THE GEOLOGY OF THE TERRESTRIAL PLANETS

Page intentionally left blank

NASA SP-469

THE GEOLOGY OF THE TERRESTRIAL PLANETS

Michael H. Carr, U.S. Geological Survey
R. Stephen Saunders, Jet Propulsion Laboratory
Robert G. Strom, University of Arizona
Don E. Wilhelms, U.S. Geological Survey

Michael H. Carr, Editor

NASA Scientific and Technical Information Branch 1984
National Aeronautics and Space Administration
Washington, DC

Library of Congress Cataloging in Publication Data
Main entry under title:

The geology of the terrestrial planets.

(NASA SP ; 469)
Includes index.
1. Planets. I. Carr, M.H. (Michael H.) II. Series.
QB601.T47 1984 559.9 83-16348

For sale by the Superintendent of Documents
U.S. Government Printing Office, Washington, D.C. 20402

FOREWORD

With the launch of Mariner 2 to Venus in August 1962, for the first time man reached beyond the confines of Earth to explore the rest of the solar system. The two decades that followed have appropriately been called the Golden Age of Planetary Exploration, for a succession of ever more sophisticated spacecraft has been sent throughout the solar system, visiting every planet as far out as Saturn. One spacecraft, Pioneer 10, has even left the solar system and is at the start of an endless journey through interstellar space.

The advance in our knowledge of the planets as a result of this activity is so enormous that it is difficult now to look back to the time of that first launch and appreciate how primitive our perception of the planets was then. Even the terrestrial planets, those closest to us, were almost unknown. Mercury was known only to have a few smudgy markings, Venus appeared as a featureless disk, and our notions about Mars were colored by a false belief in the presence of canals. Now these bodies are comfortably familiar, and we have a sound basis for hypothesizing how they might have formed and evolved to their present state. For the Moon, a planet-sized body (though actually a satellite), the advances are especially striking. In 1962, the Moon was commonly perceived as a primitive undifferentiated body, a sample of the primordial stuff of the solar system. The origin of its numerous craters—whether by impacts or volcanism—was hotly debated, and estimates of the age of the surface ranged from billions of years to relatively few. There then followed a series of spacecraft missions which culminated in the landing of men on the lunar surface during the Apollo program and the return of samples to Earth for analysis. We discovered that the Moon, like Earth, has experienced a complex geologic history which can be precisely outlined by dating returned samples. The origin of most craters was unequivocally established as impact, and the surface was found to be ancient. In several ways, the geologic history of the Moon is now more securely established than that of Earth.

Concurrent with this vigorous exploration of the solar system was a revolution in the science of geology. Indeed, the two decades following 1962 might also be called the Golden Age of Geology, for it was during this time that the theory of plate tectonics was formulated. Exploration of the sea floor, detailed monitoring of global seismicity, and discovery of reversals in Earth's magnetic field all led to the conclusion that Earth's surface is divided into large rigid plates that move with respect to each other. This perception transformed the discipline of geology by integrating a multitude of seemingly disconnected geologic observations into a single satisfying theory. Furthermore, we are beginning to realize that impacts, which have been so dominant in sculpting the surfaces of other planets, have also had a major role in the evolution of life on Earth.

Thus, the knowledge gained through space exploration is leading to the new science of comparative planetology. Although each planet is unique, all have much in common. While each can be studied independently, a greater understanding is achieved by examining the entire set. This book outlines the geologic history of the terrestrial planets in light of recent exploration and the revolution in geologic thinking. That such a volume could be written at all is a tribute to the engineering virtuosity that has made planetary exploration a reality.

Burton I. Edelson
Associate Administrator for Space
Science and Applications
National Aeronautics and
Space Administration

June 1984

Page intentionally left blank

TABLE OF CONTENTS

TABLE OF CONTENTS (continued)

TABLE OF CONTENTS (continued)

TABLE OF CONTENTS (continued)

1
INTRODUCTION

Michael H. Carr

The flight of the Mariner 2 spacecraft past Venus in December 1962 marked the start of a new era in the exploration of the solar system. At that time our knowledge of the terrestrial planets other than Earth (Mercury, Venus, and Mars) was largely astronomical in nature. Centuries of telescopic observations had established the planets' orbital motions very precisely, had determined their sizes and some of their rotational motions, but revealed almost nothing about their surfaces. Venus was completely shrouded in clouds; some vague markings had been seen on Mercury; and our perception of Mars was still colored by fanciful interpretations of its supposed canals. The Moon was the only object in the solar system, other than Earth, about whose geology we could informatively debate. By 1962 efforts were well underway to systematically decipher the geologic history of the Moon by application of stratigraphic techniques to interpretation of telescopic photographs and by comparison of lunar craters with terrestrial impact craters (Shoemaker, 1962; Shoemaker and Hackman, 1962). Even with the Moon, however, misconceptions were widespread. Lunar craters were still believed by many to be volcanic, and the Moon was commonly perceived as a primitive undifferentiated body which would yield unaltered samples of the materials from which the planets formed.

Since 1962 our perception of the solar system has been completely transformed (Beatty et al., 1981). Over 70 spacecraft have been sent to the Moon and the inner planets. They have returned an enormous amount of data, which show not only what the planets are like now, but how they might have evolved to their present state. Coincident with this period of intense exploration has been a revolution in geologic thinking about Earth. The theory of plate tectonics was formulated and new analytical techniques, particularly for measuring isotopic ratios, have led to new insights about the formation of Earth and other planetary bodies. The purpose of this volume is to summarize the geologic evolution of the terrestrial planets as we currently perceive it after these two decades of vigorous exploration.

The solar system has nine known planets (table 1.1). The four inner ones, Mercury, Venus, Earth, and Mars are relatively small; all have rocky surfaces that can be studied by geologic techniques. Beyond Mars are the four Jovian planets: Jupiter, Saturn, Uranus and Neptune—each a large gaseous ball composed mostly of hydrogen, helium, and other light elements. The outermost planet, Pluto, is a small rocky object that does not fit into the otherwise twofold planet classification. The Jovian planets comprise most of the mass of the planetary system. The mass of Jupiter alone (318 Earth masses) is greater than that of all the other planets combined. Distances in the outer solar system are also large compared with those associated with the terrestrial planets. Whereas all the terrestrial planets move on orbits within 1.52 AU[1] of the Sun, distances from the Jovian planets to the Sun range from 5.2 AU for Jupiter to 30 AU for Neptune. The terrestrial and Jovian planets differ, further, in the number of their satellites. The terrestrial planets have few, if any. Earth has one satellite, the Moon; Mars has two small ones; Venus and Mercury have none. In contrast, Jupiter has at least sixteen satellites; Saturn at least seventeen; and Uranus at least five. Moreover, the satellites of the terrestrial planets are all rocky, whereas most of the satellites of the Jovian planets contain large fractions of ice.

[1]An astronomical unit (AU) is the mean distance from Earth to the Sun (149×10^6 km).

Table 1.1. Orbital and Physical Properties of the Moon and the Planets

Object	Diameter (km)	Mass (g)	Mean density (g/cm^3)	Visual geometric albedo	Rotation period (days)	Obliquity	Revolution period	Semimajor axis (A.U. for planets; 10^3 km for Moon)	Orbit inclination (with respect to ecliptic for planets; planetary equator for Moon)	Orbit eccentricity
Sun	1 391 400	1.987 (33)	1.4	—	25.4	7°25	—	—	—	—
Mercury	4 878	3.30 (26)	5.44	0.10	58.6	~2°	0.2408 yr	0.387	7.0	0.206
Venus	12 100	4.87 (27)	5.25	0.65	243*R*	~179°	0.6152 yr	0.723	3.39	0.007
Earth	12 756	5.98 (27)	5.52	0.38	1.00	23°5	1.000 yr	1.000	0.00	0.017
Mars	6 786	6.44 (26)	3.94	0.15	1.02	25°0	1.881 yr	1.524	1.85	0.093
Jupiter	142 796	1.90 (30)	1.33	0.52	0.41	3°1	11.86 yr	5.203	1.31	0.048
Saturn	120 000	5.69 (29)	0.70	0.47	0.43	26°7	29.46 yr	9.54	2.49	0.056
Uranus	50 800	8.66 (28)	1.30	0.51	0.65*R*	97°9	84.1 yr	19.19	0.81	0.046
Neptune	46 600	1.03 (29)	1.76	0.41	0.7	28°8	164.8 yr	30.06	1.77	0.010
Pluto	3 000	1.5 (25)	1.1	0.30	6.4*R*	118°?	284.5 yr	39.53	17.15	0.248
Moon	3 476	7.35 (25)	3.34	0.115	27.3	6°7	27.3 d	384	18–29°	0.055

Data from *The Astronomical Almanac* (1984).

All solid planets retain a fragmentary record of the processes that have shaped them. The record is preserved partly in the configuration of the surface materials, partly in the chemistry and mineralogy of the planet's constituents, and partly in the planet's internal structure. The task of the geologist is to deduce the planet's history—what processes have occurred on the planet and in what sequence—from this fragmentary record. Concern is mostly with the surface since this is the only part readily accessible for study. However, conclusions must be consistent with the internal structure and chemistry as might be inferred, for example, from geophysical measurements or study of inclusions in magmas derived from great depths.

The evolution of the planet's surface can be viewed as the result of interplay of three different kinds of processes: (1) exogenic processes, which result from interaction of the surface with the external space environment, (2) endogenic processes, which result from response of the surface to changes inside the planet, and (3) interactive processes, by which the solid surface is modified by interaction with the hydrosphere and atmosphere. The relative importance of the different types of processes varies with time and from planet to planet. Around four billion years ago impact rates are believed to have been very high on all the terrestrial planets. Shortly thereafter, impact rates declined to a much lower rate, which has been roughly constant (within a factor of two) for the last three billion years. As a result the effects of impact, an exogenic process, dominate on all surfaces 3.8–4.0 billion years old. The cratered highlands of the Moon and the heavily cratered parts of Mars and Mercury are believed to date from this era. Surfaces which formed after the decline in impact rates retain a much better record of other processes. On the Moon and Mercury, the nonexogenic record is primarily the result of volcanism and deformation. However, on Earth, Mars, and presumably Venus, interaction of the surface with the atmosphere and hydrosphere has had a major effect.

The techniques used in geologic study depend on the stage of investigation of the planet. While the gains in our knowledge of the solar system in recent years are impressive, we are still in the exploration stage for most planets. The Committee on Planetary Exploration (COMPLEX) of the National Academy of Sciences has identified three stages in the investigation of a planet. The first stage, reconnaissance, reveals the major characteristics of the planet and allows us to define the goals of more detailed study. Reconnaissance is usually effected by flyby missions; this stage is now complete for all the terrestrial planets. The second stage of investigation, exploration, typi-

cally involves vehicles such as orbiters and landers, which have extended stay-times at the planet. Exploration is accomplished mainly by remote sensing data but a few in situ measurements may also be made. During this stage the geology of the planet is broadly outlined and the processes that have resulted in the present configuration of the surface are identified. We are currently in the exploration stage for Mars. It might be argued that we have reached this stage for Venus, but the remote sensing data for Venus are of such low resolution that the major geologic processes operating on that planet are still to be unequivocally identified; from a geologic viewpoint we are still in the reconnaissance stage. The final stage in the investigation of a planet is intense study, during which samples are available and the fullest range of laboratory techniques can be applied to the elucidation of the planet's geology. This stage of exploration has been reached only for the Earth and Moon.

In the reconnaissance and exploration stages, heavy reliance is placed on remote sensing data. The spectral reflectivity of the surface gives some indication of its chemical variability; some physical characteristics of the materials close to the surface can be inferred from their optical and thermal properties, and gravity variations provide clues on deeper structures. But in these early stages of exploration, the morphology of the surface provides the most definitive information on a planet's geologic history.

Geomorphology plays a relatively minor role in terrestrial geology. The Earth's surface is modified rapidly by running water so that terrestrial landforms are rarely more than a few million years old. Moreover, fluvial effects tend to dominate the landscape and destroy the geomorphic imprint of other processes. In contrast, on other planets, landforms billions of years old provide information on a variety of processes that have operated throughout the history of the planet. Each process affects the surface in a different way, and in principle, the processes can be identified from the resulting landforms. Furthermore, the sequence in which the different processes affected the surface can be determined from transection and superposition relations. The interpretation of the landforms must of course be consistent with any other data that might be available, such as gravity, reflectivity, and thermal inertia.

Generally, geomorphic reasoning is by analogy. The planet's landforms are compared with those of the Earth, whose origin is known, or with features that have been experimentally produced. The large volcanoes of Mars, for example, are clearly identifiable as volcanic by comparison with terrestrial volcanoes, and many impact features seen on other planets have natural counterparts on Earth or have been reproduced experimentally. Because of different conditions, the same processes do not necessarily have identical results on different planets. To understand other planetary bodies we must be able to extrapolate from our Earth-based experience to conditions elsewhere. Quantitative modeling of geologic processes has thus become an important element in planetary geology, helping us to predict how a particular process might be affected by variations in such factors as gravity, atmospheric pressure, or lithospheric thickness. Unfortunately, remote sensing data rarely lead to unequivocal interpretations. Several plausible explanations can commonly be devised to explain the same phenomena, so that conclusions are often frustratingly ambiguous.

Systematic stratigraphic studies are a somewhat more rigorous approach to interpreting surface morphology than simple analogy. Stratigraphy involves recognizing rock units that have a specific set of characteristics, then determining their relative ages from mutual intersection and transection relation, or from relations with impact craters and basins. The Moon lends itself well to such analysis because of its relatively simple geology and because of the presence of extensive time-marker horizons that were created during formation of the large basins; but the technique has been less successful for other bodies.

Once samples are acquired, the interpretative techniques change dramatically. Chemical and mineralogic data, which are susceptible to more rigorous analysis than geomorphologic information, become the main basis for interpreting the geology. Accurate dates are acquired, the origin of the surface rocks can be established unequivocally, and the history of the materials that make up the rocks can be traced by modeling of various geochemical anomalies. Geomorphic studies remain important, however, because the geochemical, petrologic, and impact history of the planet, as inferred from the samples, must be consistent with the present configuration of the surface.

In the chapters that follow, the geologic histories of Mercury, Venus, Earth, Mars, and the Moon are outlined. In the cases of Mercury, Venus, and Mars, the geologic history is based almost entirely on remote sensing data. The discussion therefore, is often tentative. Ages are particularly suspect. Estimates can be made from crater statistics, but without samples these

must be looked upon as no more than informed guesses. Even in the case of the Moon, from which we have samples, large uncertainties remain, partly because only six sites were sampled, partly because the record from before four billion years ago is largely destroyed, and partly because of ambiguities inherent in interpretation of the analytical data. Nevertheless, we can now reconstruct, in broad outline, the geologic history of the Moon and each of the terrestrial planets, except possibly for Venus.

2
ASTEROIDS, COMETS, AND PLANET FORMATION

Michael H. Carr

INTRODUCTION

The solar system includes numerous small objects, generally classifiable as asteroids, comets, or interplanetary dust. Asteroids and comets are of considerable importance in the study of the terrestrial planets. The impacts of these bodies with the planets have repeatedly reshaped the planets' surfaces, redistributed the surface materials and changed their chemistry and mineralogy. In addition, impacts leave scars which provide a means of assessing ages. Asteroids, and possibly old comet nuclei, continually rain on the Earth, and many thousands are preserved and are displayed in our museums as meteorites. In this chapter the nature of comets and asteroids is briefly reviewed. The formation of planets is also examined here because most of the evidence as to how the planets formed comes from meteorites. The discussion is short and general. The chapter is included mainly to provide background for the subsequent more detailed treatment of the planets.

ASTEROIDS AND COMETS

Over 2000 asteroids are known (Chapman, 1975); the largest being Ceres, about 1000 km in diameter. They appear star-like on telescopic photographs, and are recognized as a result of their motions relative to the stars. Their shapes are not known, but variations in brightness suggest that they are irregular. Most asteroids are in orbits with relatively low eccentricities (<0.3) as compared with comets, and most are in the asteroid belt between Mars and Jupiter.

Asteroids have been classified in two ways. The first is according to their orbits, which is of interest to those attempting to estimate the rate of impact on the various planets. The Amor asteroids, for example, have perihelia (the point in the orbit closest to the Sun) inside Mars' orbit but outside Earth's. Clearly, objects of this class can impact Mars but not Earth. In contrast, the Apollo asteroids have perihelia inside the Earth's orbit and so can impact both Earth and Mars. Alternatively, the asteroids are also grouped according to their albedo and spectral reflectivity. This classification is useful in that the reflectivity gives some indication of composition, and tentative correlations have been made between the asteroid groupings and various types of meteorites.

Comets have also impacted the planets throughout their history and affected their geology much in the same way as asteroids. Comets appear to be agglomerations of ice and dust that have spent most of their lifetime far beyond the orbits of the planets (Whipple, 1974). They are believed to reside in large numbers (10^{11}–10^{12}) in the most distant reaches of the solar system, in the so-called Oort cloud, which is estimated to be about 100 000 AU across. The cloud is believed to have formed early in the history of the solar system by ejection of material from the region of the planets, outward, almost to the edge of the Sun's influence. Ejection resulted from orbit perturbations induced by close passes by a planet. Distances from the Sun in the Oort cloud are so great, and motions of the comets in the cloud so slow, that perturbation of their orbits by passing stars are occasionally sufficient to cause a comet to plunge into the inner solar system on a

near-parabolic orbit around the Sun. As the ice-dust ball approaches the Sun, its surface warms and the ices start to sublime. The comet then becomes visible and develops its characteristic shape. The gases given off are ionized and swept away by the solar wind, along with any dust that is released. At this stage three parts can generally be distinguished: a bright head (coma) roughly spherical in shape, a tail of ionized gas which streams out from the head in a straight line radial to the Sun, and a tail of dust particles which extend in a slightly curved arc, also roughly radial to the Sun.

Comets are of two major kinds, periodic and nonperiodic. The nonperiodic comets constitute the vast majority. They move in parabolic orbits and make only one pass through the center of the solar system. Their inclinations are random, with prograde and retrograde orbits equal in number. From these characteristics we can conclude that the Oort cloud, their source, is spherically disposed around the solar system and not restricted to the plane of the planets. In contrast, the periodic comets are all in low-inclination, prograde orbits. They are believed to be former parabolic comets whose orbits have been perturbed by the planets, mainly Jupiter. Such perturbations are possible only for those comets which initially moved in prograde orbits with low inclinations. Periodic comets have limited lifetimes in that they lose mass each time they pass the Sun, indicating some asteroids may be burned out comet remnants.

METEORITES

Meteorites provide us with samples of asteroids and possibly burned out comets, and are of fundamental importance for understanding the formation of the planets. They provide the best evidence of the nature of the materials that accumulated to form the planets, as well as the processes of accumulation. Meteorites have a wide range of composition and mineralogy (Wood, 1979; Wasson, 1974). Some, termed differentiated meteorites, resemble terrestrial igneous rocks. They appear to have been part of a larger body that broke up at some intermediate stage in the history of the solar system, after having gone through a stage of heating and magmatic differentiation. The other main class of meteorites, the chondrites, are distinctively different from any terrestrial rock. They are mostly agglomerates of fragmental debris and typically contain chondrules—spherical mineral aggregates, 1–2 mm across, consisting mainly of olivine and orthophyroxene, but possibly with minor amounts of clinopyroxene, iron sulfide and iron-nickel. The chondritic meteorites formed very early in the history of the solar system, while the planets were forming, and so provide direct evidence of conditions at that time.

The most primitive meteorites are the carbonaceous chondrites, in which the chondrules are embedded in a fine-grained, earthy matrix. This matrix consists of hydrated, platey minerals such as serpentine and montmorillonite, together with small amounts of magnetite, iron-nickel sulfide, sulfates and carbonates. Small amounts of organic compounds are also generally present. The matrix is thus a low-temperature, volatile-rich assembly, in contrast to the high-temperature assemblage of the chondrules. The chondrules and matrix are in disequilibrium and clearly formed under very different conditions.

Some carbonaceous chondrites also have small, irregularly-shaped inclusions composed largely of Ca-Al-Ti-rich minerals. The minerals in the inclusions are those which are expected to have condensed first from the nebular gas in the early stages of cooling of the primitive solar nebula. Their formation had been predicted from thermodynamical considerations (Grossman, 1972) before they were discovered in the Allende meteorite. The Ca-Al-rich inclusions are therefore samples of the most primitive matter of the solar system. Their irregular shape indicates that they have never gone through a melting stage but formed directly from the nebular gas.

Carbonaceous chondrites resemble the Sun in composition. The only significant differences are lesser amounts of hydrogen, carbon, nitrogen, and noble gases in the carbonaceous chondrites.These elements are unlikely to have condensed in the inner solar system because of their high volatility, so their lack of incorporation into the carbonaceous chondrites is not surprising. Because of (1) the compositional correspondence between the Sun and the carbonaceous chondrites, (2) the presence of the Ca-Al-rich inclusions, and (3) the disequilibrium mixture represented by the chondrules and matrix, the carbonaceous chondrites are believed to be indicative of the primitive solar nebula composition, depleted somewhat in the more volatile elements. In models of planet formation, therefore, carbonaceous chondrites are commonly used to represent the materials from which the planets formed. All carbonaceous chondrites have ages comparable to the age of the solar system (4.6 billion years).

Carbonaceous chondrites represent only a small fraction of all chondrites; ordinary chondrites are much more common. These also contain olivine-pyroxene chondrules but their chondrules are embedded in a matrix of the same composition as the chondrules themselves. Many of the ordinary chondrites have been heated so that the boundaries between chondrules and matrix have become diffuse, and the constituent minerals have been recrystallized to form granulitic textures suggestive of high temperatures. Exposure ages for the ordinary chondrites, that is, the time the meteorite has been exposed to cosmic rays, are mostly in the 10^6–10^8 year range—far shorter than the age of the solar system.

The carbonaceous chondrites are agglomerations of chondrules, the more primitive Ca-Al-rich inclusions, and volatile-rich materials. Throughout the history of the solar system, they have never been incorporated into bodies large enough to have caused significant heating, otherwise the disequilibrium assemblage would have been destroyed. Ordinary chondrites, on the other hand, appear to have been buried within larger bodies and subjected to various degrees of heating and metamorphism. Subsequently, the larger bodies were broken up, presumably as a result of impact, and their materials dispersed. Ordinary chondrites thus have metamorphic textures and young exposure ages. Depths of burial in the parent bodies are not known but estimated to be as high as a few tens of kilometers. The major uncertainties are whether the parent body originally incorporated the volatile materials that are present in the carbonaceous chondrites, and whether the volatiles were later driven off during the heating and metamorphism.

About 15 percent of meteorites are non-chondritic. Some are breccias and appear to be lithified regolith from an asteroid surface. Other achondrites have igneous textures and appear to have formed by magmatic processes within larger bodies. They have a range of composition and texture similar to that of terrestrial igneous rocks. These igneous-textured achondrites seem, as do ordinary chondrites, to have originated within larger bodies, but at such depths that melting occurred and the normal processes of magmatic differentiation followed. There are two main types of achondrites: stones and irons. Irons generally consist of intersecting plates of two nickel-iron alloys—kamacite and taenite. From variations in the composition of the two alloys, the temperature and rate of cooling of the iron-nickel, and hence the depth of burial, can be estimated. The method is crude but suggests that the irons formed at depths of 30–50 km. These depths are probably representative of the radius of the parent body from which the meteorite formed.

In recent years the question of how bodies as small as a few tens of kilometers across could have heated up and created the metamorphic and igneous textures seen in meteorites has been resolved. It now appears that radioactive heating by the decay of short-lived radioisotopes, mainly ^{26}Al (half-life of 10^6 years), ^{244}Pu (82×10^6 years) and ^{129}I(16×10^6 years), was responsible, since the decay products of these nuclides have been found in the meteorites. Since these short-lived nuclides were incorporated into meteorites before they had decayed, the time interval between element formation and meteorite formation must have been relatively short—no more than a few million years.

FORMATION OF THE PLANETS

Our perception of how planets formed is based mainly on theoretical studies of stellar evolution and the study of meteorites. The planets are believed to have formed from a disk-like volume (nebula) of dust and gas that surrounded the protosun (see Wood, 1979; Lewis, 1974). The protosun grew by gravitational attraction of dust and gas from the surrounding interstellar medium, and during the process it inherited angular momentum from eddies in the interstellar gas. As accumulation proceeded and the protosun contracted, its angular velocity increased to preserve angular momentum, and a disk-like nebula formed around the protosun, rather than a spherically symmetrical cloud. Material outside the disc tended to move toward the protosun by gravitational attraction; material within the disc tended to assume a position where gravitational attraction was counterbalanced by centrifugal forces. A major uncertainty concerns the stability of the disc. Did local eddies within the disc cause it to fragment into numerous gaseous protoplanets, most of the solid particles being swept up to form dense solid cores, or did the disc remain continuous, allowing dust particles ultimately to accumulate into planetesimals without gaseous envelopes? The answer is not known but the latter hypothesis is the most widely held.

As the disc cooled, different materials began to condense and add to the inventory of solid particles. Grossman (1972) and Grossman and Larimer (1975) determined the sequence in which minerals would have condensed from a gas of solar composition under the expected nebular pressures (10^{-4} atm). The first

minerals to condense out are those found in the Ca-Al-rich inclusions (fig. 2.1). Last to condense are the carbonaceous compounds and ices of water, ammonia, and methane. The sequence assumes that the gases and dust are constantly in equilibrium, that is, that the higher temperature minerals react with the remaining gases as the nebula cools. If the condensed phases are removed and not able to react with the remaining gases, such as by incorporation into larger solid bodies, then the condensation sequence would be slightly different.

Recent evidence suggests some meteorites incorporate interstellar grains. Seemingly, parts of the nebula where the meteorites formed were never hot enough to vaporize all solid particles. The evidence is from the Ca-Al-rich inclusions and some chondrules which have oxygen isotope anomalies that cannot be explained by fractionation or diffusion processes within an isotopically homogeneous nebula; the oxygen in these grains is in isotopic disequilibrium with the rest of the matter in the solar system. The grains appear to have formed elsewhere, then were captured by the

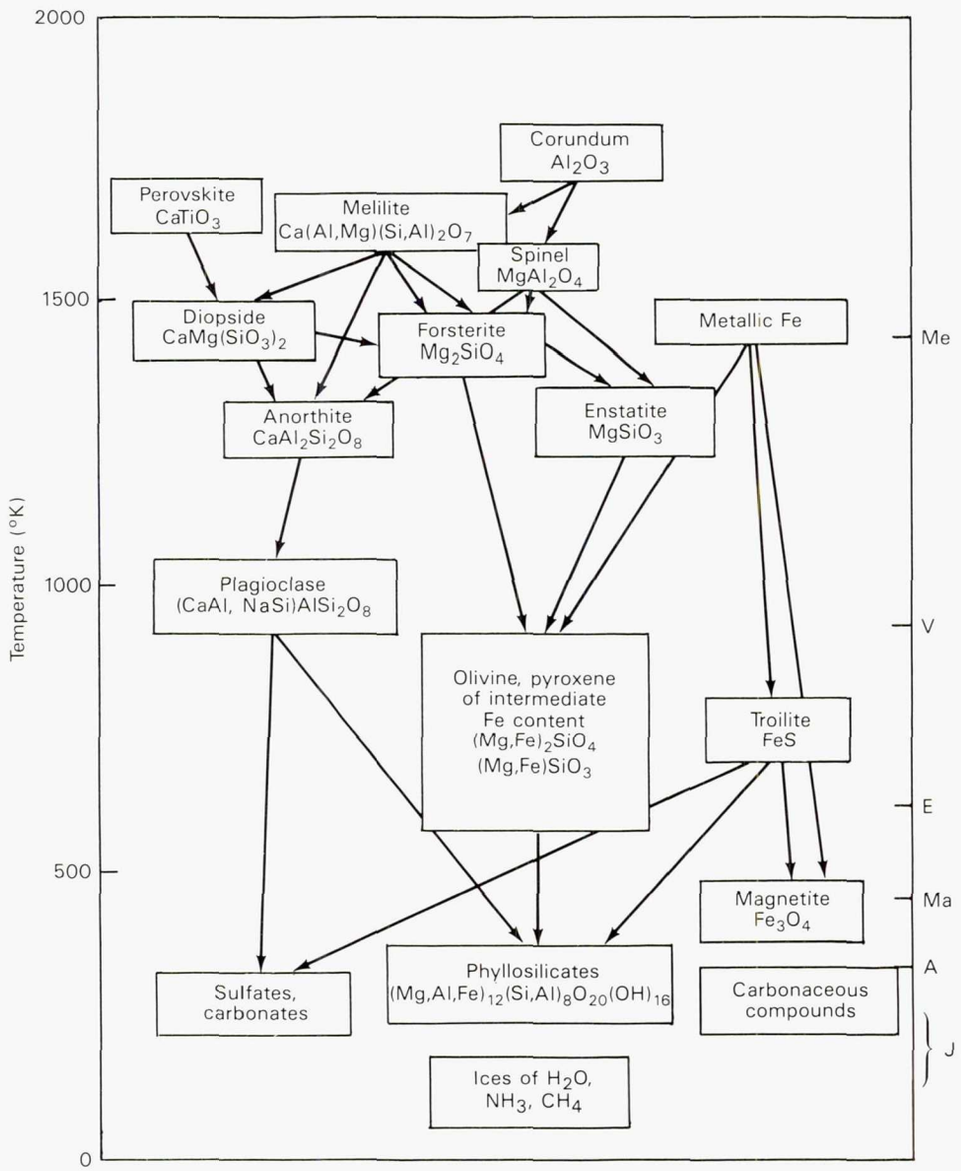

Figure 2.1. The sequence of condensation of minerals from a nebula of solar composition. As the nebula cools minerals high in the diagram react with nebular gas to form those lower in the diagram as indicated by the arrows. Many chondritic meteorites contain minerals from different levels in the diagram (different condensation temperatures), indicating their constituents were in partial disequilibrium with each other and the nebula gas. (After Wood, 1979.)

solar nebula and incorporated into meteorites without being vaporized and equilibrated with the surrounding materials.

Although chondrules, which are the dominant component of undifferentiated meteorites, are composed of minerals that are expected to condense in the 600–1500 K range, they do not appear to have been formed by simple condensation from the nebular gas. The globular shape of the chondrules suggests that they were liquid droplets, yet at the low pressures that probably prevailed in the nebula, solids rather than liquids should condense. Various suggestions have been made to explain the anomaly. First, condensation may have produced supercooled liquid droplets rather than solid crystals. Second, condensation could have occurred within gaseous protoplanets, where pressures were high enough for liquids to form. Third, the chondrules may be droplets produced during high energy impacts between small objects. Whatever the process, it had to be very efficient since a large fraction of the undifferentiated meteorites consists of chondrules, and some pre-nebular granular material had to be incorporated into the chondrules to explain their anomalous oxygen.

Thus, at some early stage in its formation, the solar system consisted of a protosun and a gaseous nebula disc, which, in the inner solar system at least, contained Ca-Al-rich aggregates and olivine-pyroxene rich chondrules. In the more distant parts of the solar system, low temperature minerals such as those found in the matrices of carbonaceous chondrites may also have been present. The next stage appears to have been the formation of asteroid-size bodies or planetesimals. Precisely how this occurred is uncertain. Gravitational instabilities may have developed and caused the particles to cluster. Growth of the clusters was aided by the presence of the nebular gas which ensured that relative velocities between particles was small. By the time asteroid size objects had accumulated, conditions in the solar system changed significantly as a result of removal of the nebular gas. After this time motions of the planetesimals were not constrained by the enclosing gas and their orbits could be perturbed by close approaches of other planetesimals. Many planetesimal orbits thus became highly eccentric and high velocity impacts became more common. Such conditions favored growth of the largest bodies. Very small bodies broke up on impact; intermediate sized bodies were eroded away because their low gravity fields allowed most of the impact-generated debris to escape. Only the largest bodies could grow by impact to ultimately form the planets.

The timing of planetary growth with respect to condensation from the nebula is unclear. Two main models have been proposed: the equilibrium condensation model in which the planets accumulated after condensation had essentially ceased, and the inhomogeneous accretion model in which accretion and condensation occurred simultaneously. According to the equilibrium condensation model, material condensed from the solar nebula following the scheme of Grossman (1972) already discussed. Condensation was arrested at different stages according to the local nebula temperature. Close in, near the orbit of Mercury, condensation ceased when temperatures were relatively high so the condensed materials consisted only of high-temperature minerals. In the more distant parts of the solar system, temperatures were low when condensation ceased so that the solid grains included low-temperature platey silicates and ices. They may also have retained high-temperature minerals that failed to react with the nebular gases as they cooled, possibly as a result of burial within the grains. The solar system was thus compositionally zoned, with predominantly high-temperature minerals in the particulates close in and with lower temperature minerals becoming more important farther out. These particulates ultimately aggregated to form the planets and resulted in the composition and density differences that are observed. In this model, accumulation is decoupled from condensation. Condensation is thought to have been accomplished in around 10^6 years; accumulation of the planets is thought to have taken around 10^8 years. The present layering of the planets is due to later heating and differentiation.

This model satisfactorily explains the density differences between the terrestrial planets (fig. 2.2). Mercury condensed largely from Ca-Al silicates and Fe-metal, materials that are expected to condense at temperatures of around 1400 K. The large proportion of metallic iron accounts for its high uncompressed density (5.4 gm/cc). Venus has accumulated largely from magnesium silicates and metallic iron, which would have condensed together at 900 K. The Earth accumulated from a 600 K assemblage of Fe-Mg silicates, troilite and metallic iron, and at the temperatures that the Mars-forming materials condensed (450 K) all the iron was oxidized to FeS, which accounts for its low uncompressed density. Two main difficulties with the equilibrium condensation model are that (1) the atmospheres of Earth and Venus require incorporation of some fraction of low temperature condensates along with the condensates which

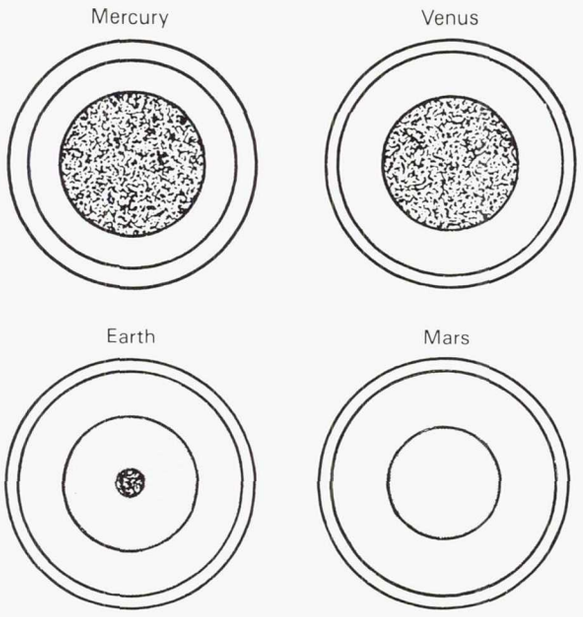

	Uncompressed density (g/cm^3)
Al-rich crust	~3.0
Mg, Fe silicates	3.2–3.8
Troilite (FeS)	~4.8
Metallic Fe,Ni	~7.8

Figure 2.2. Internal structure of the terrestrial planets as predicted by the equilibrium condensation model. Moving outward from Mercury the mantle of each planet is richer in FeO and poorer in MgO, and the core is richer in FeS and poorer in metallic Fe. (After Lewis, 1974.)

formed at the planets' characteristic temperatures, and (2) the crust and upper mantle of Earth contain a higher abundance of siderophile elements than should be present if the Earth's core formed by segregation during global melting. Other evidence of disequilibrium between the upper mantle and core also indicated that the chemical layering within the Earth cannot be due entirely to melting and fractionation (see Earth chapter).

The heterogeneous accretion model was devised to account for some of these difficulties. According to this model, accumulation of the planets kept pace with condensation. As rapidly as the material condensed from the solar nebula, the material was swept up into the planets. The planets therefore developed an onion-ring structure, with the highest temperature condensates at the center and progressively less refractory materials toward the surface. Condensation was arrested at relatively high temperatures close to the Sun. Mercury was, therefore, built mostly of refractory Ca-Al silicates and metallic iron. Further from the Sun the planets incorporated more materials from more advanced stages in the condensation sequence. Thus the density differences between the planets are explained in much the same way as the equilibrium condensation model.

The layering initially acquired by the planet was not retained. The refractory silicates were originally at the center surrounded by iron-rich material. Ultimately most of the refractory silicates reside in the crust and the iron in the core. Proponents of the model propose that the high rates of accretion caused early global heating during which the interior of the planet melted and iron fell into the center to form the core. Core formation took place before accretion was finished so that the final outer layers of the planet were never equilibrated with the core. The chemical anomalies of Earth's upper mantle are therefore resolved; while volatile-rich materials, which accumulated late, were a source of volatiles for the atmosphere.

A major problem with the heterogeneous accretion hypothesis is that no mechanism has been conceived whereby the planets could accumulate so rapidly as to keep pace with condensation. An additional problem concerns the core of Earth. The core's density implies that it is not metallic iron, as is required by the model, but instead incorporates some light element, probably sulfur, which should have been acquired late, after core formation was over.

Several attempts have been made to reconcile the two hypotheses. One such model has most of the planets accrete in around 10^8 years, roughly in accordance with the equilibrium condensation model. However, temperatures were too high in the region of the terrestrial planets for the lowest temperature condensates to form. They formed only in the asteroidal belt, or farther out, and became incorporated into planetesimals of carbonaceous chondrite composition. The last stage in accumulation of the terrestrial planets was capture of many of these planetesimals to form a volatile-rich veneer from which the atmosphere was derived. Capture of the volatile-rich material took place after core formation. The main disadvantage of the heterogeneous accretion model, the rapid accumulation, is thus avoided. At the same time the chemical disequilibrium between upper mantle and core is explained.

How the planets evolved between the time of accretion, 4.6 billion years ago, and the time when the geologic record emerged, 3.9 billion years ago, is

unclear. Meteorites tell us little about this era, and the planets themselves preserve almost no evidence of events prior to 4 billion years ago because of erasure by massive meteorite bombardment. After 4 billion years ago the bombardment rate declined thereby allowing a fragmentary record of succeeding events to be preserved. Interpretation of this record is the concern of the chapters that follow.

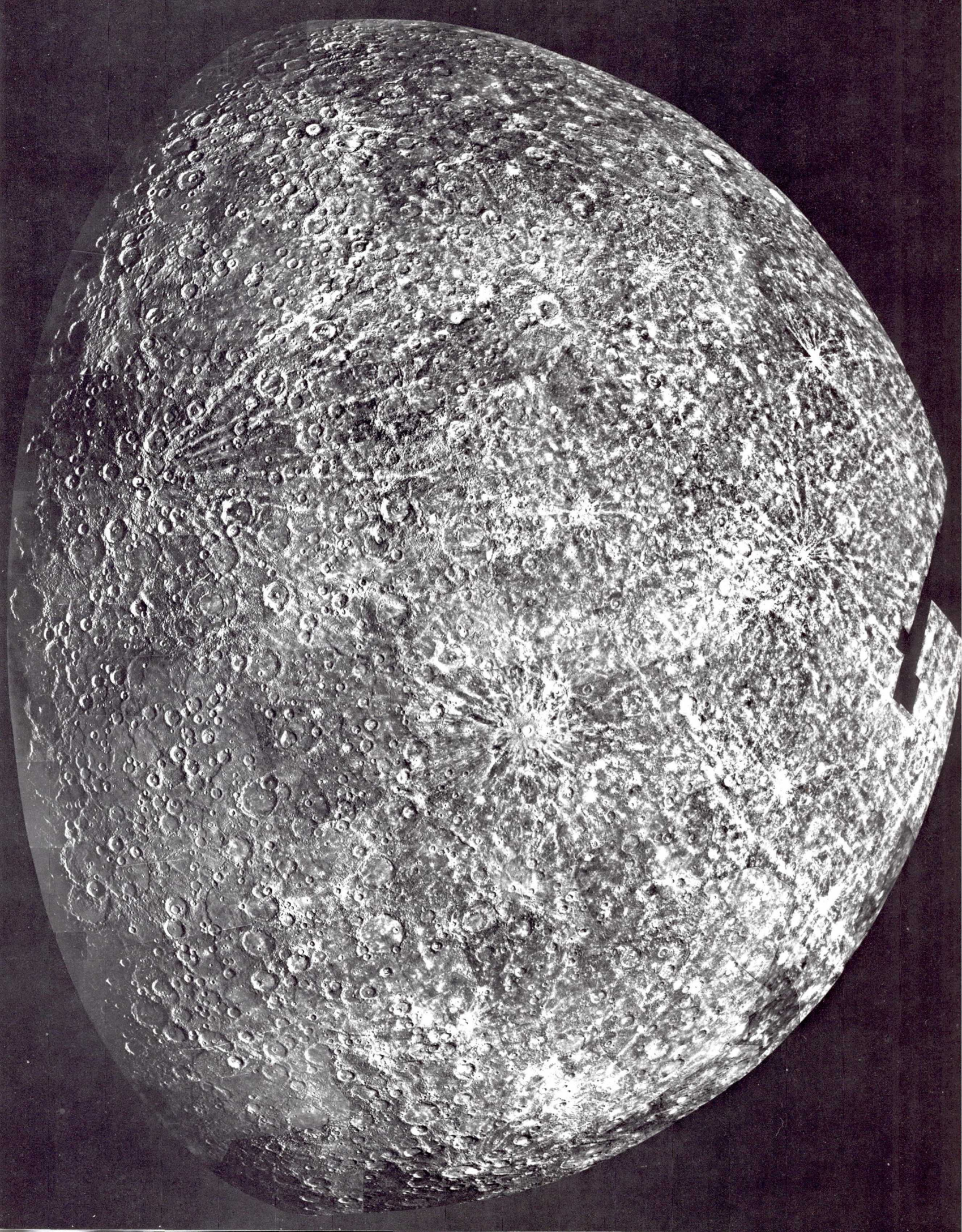

3
MERCURY

Robert G. Strom

INTRODUCTION

Prior to the flight of Mariner 10 very little was known about the smallest and innermost terrestrial planet, Mercury. At maximum elongation Mercury is no more than 28 degrees from the Sun as viewed from Earth, and therefore telescopic observations must be made during daytime or at twilight through a long path-length of the Earth's atmosphere. As a consequence of this, and because of Mercury's small size and large distance from Earth, telescopic observations provide only scanty data. However, Earth-based observations did determine three major facts about Mercury which were subsequently confirmed by Mariner 10: (1) Mercury has a very high mean density (5.44 g/cm^3) comparable to that of Venus (5.25) and Earth (5.52), and much larger than that of the Moon (3.34) and Mars (3.94); (2) Mercury's surface reflects electromagnetic radiation at all wavelengths in a similar, but not exact, manner as the Moon, when differences in their solar distances are taken into account; and (3) Mercury's rotation period is in 3:2 resonance with its orbital period. Table 3.1 lists the best current values for the more important orbital and physical properties of Mercury.

On March 29, 1974 the Mariner 10 spacecraft flew by Mercury for the first time and provided a wealth of new information about this poorly understood planet. On the first encounter, pictures were obtained of Mercury's surface at about quarter-phase illumination during its incoming and outgoing passages. Two subsequent flybys on September 21, 1974 and March 16, 1975 extended the coverage to the south polar region and provided high resolution pictures of selected areas of interest seen at lower resolutions on the first encounter. The second encounter coverage of the south polar region established a cartographic and geologic link between the incoming and outgoing sides photographed on the first encounter (Strom et al., 1975a). In addition, photographs taken during the second encounter were at significantly different viewing angles from those taken on the first encounter and so provided stereoscopic coverage of large areas of the southern hemisphere.

Over 2700 useful pictures were taken by Mariner 10 during its three encounters. The combined coverage of these pictures is about 45 percent of the surface at resolutions varying from about 4 km to 100 meters. This is approximately equivalent to Earth-based telescopic coverage and resolution of the Moon. Because of constraints imposed by Mercury's rotation period and the orbital periods of the spacecraft and Mercury, all three encounters took place when the terminator was in the same position. Consequently much of the coverage was obtained at high solar elevation angles, which made discrimination of surface morphology and topography difficult. This was somewhat offset by the stereoscopic coverage in the southern hemisphere, but in practice only about half the explored area was viewed under favorable illumination conditions. About 70 percent of Mercury is viewed under poor lighting conditions or is not visible at all, imposing difficulties in interpreting surface processes on a global scale. As a consequence, several major questions concerning the origin of certain terrains and the history of Mercury must remain open. Nevertheless, the wealth of new information from Mariner 10 has elevated Mercury from a poorly known planet to one as familiar to us as the Moon was before the era of space exploration. [An excellent

Table 3.1. Orbital and Physical Data for Mercury

Orbital data	
Semimajor axis	0.3871 AU (5.79×10^7)
Perihelion distance	0.3075 AU (4.60×10^7 km)
Aphelion distance	0.4667 AU (6.98×10^7 km)
Sidereal period	87.97 days
Synodic period	115.88 days
Orbital eccentricity	0.20563
Inclination of orbit to ecliptic	7.004 deg
Mean orbital velocity	47.87 km/s
Rotational period	58.646 days
Physical data	
Radius	2439 km
Surface area	7.475×10^7 km^2
Volume	6.077×10^{10} km^3
Mass	3.302×10^{26} g
Mean density	5.44 g/cm^3
Surface gravity	370 cm/s^2
Escape velocity	4.25 km/s
Surface temperature extremes	~90 to 740 K (− 183 to 467° C)
Normal albedo (5° phase angle)	0.125
Magnetic dipole moment	$4.9 (\pm 0.2) \times 10^{22}$ gauss cm^3

presentation of much of the imagery, cartography and nomenclature is contained in the Atlas of Mercury (Davies et al., 1978).]

In addition to the imaging experiment, Mariner 10 carried a complement of other scientific instruments that obtained information on Mercury's mass and size, atmospheric composition and density, charged-particle environment, infrared thermal radiation, and magnetic field.

Orbit

Except for Pluto, Mercury's orbit has the largest eccentricity ($e = 0.206$) and inclination to the ecliptic ($i = 7.0°$) of any planet in the solar system. These high values of e and i may be chance occurrences; or the Mercurian inclination may have a primordial link to the solar equatorial plane, which is inclined 6 degrees to the invariable plane (the plane fixed with respect to orbital precessions). Kaula (1976) has suggested that the large eccentricity is the result of very high velocity collisions between proto-Mercury and planetesimals perturbed into the inner solar system by Jupiter. An alternative explanation for Mercury's large e and i has been offered by Ward, Colombo and Franklin (1976). They suggest that Mercury's e and i have been pumped up by Venus during secular resonances between the precession rates of the lines of apsides of Mercury and Venus when, and if, the Sun had an oblateness $j_2 \sim 10^{-3}$, corresponding to a rotation rate of about five hours. This same j_2 would produce another resonance between the precession rates of the line of nodes of the two planets. For this mechanism to produce the observed e and i, the time scale for decay of the solar rotation must be about 10^6 years. By analogy with T-Tauri and other young stars, such an early rapid solar rotation and decay does not seem implausible.

Rotation

For nearly a century Mercury's rotation period was thought to be synchronous with its orbital period of 88 days. In 1965 Pettengill and Dyce (1965) measured a rotation period of 59 ± 5 days from radar observations. This period was subsequently refined by Goldstein (1971) to 58.65 ± 0.25 days from additional radar data. From shadow positions measured on consecutive Mariner 10 encounters Klaasen (1975, 1976) further refined the rotation period to 58.646 ± 0.005 days. This period corresponds to a 3:2 commensurability between the axial and orbital periods. Klaasen's (1976)

analysis of Mariner 10 pictures also determined that Mercury's rotation axis is almost perpendicular to the orbital plane (obliquity = 2° with an error ellipse of 2.6° × 6.5°).

Mercury's rotation period was probably much faster in the past (possibly as much as 8 hours), but subsequently was slowed by solar tides (Burns, 1976). For a tidal dissipation factor Q = 30, the characteristic decay time to despin Mercury to its present rate would be about 10^9 years. As a consequence of this despinning the interior temperature would have increased by 100 K, and surface stresses would have caused strains above the fracture limits (Melosh, 1977). Such stresses may have been partly responsible for some of the tectonic features seen on Mariner 10 imagery. Goldreich and Peale (1968) showed that the 3:2 resonant rotation is stable as long as the solar torque exerted on the asymmetric equatorial shape is always larger than the time-averaged tidal torque. The value of $j_2 \sim 10^{-4}$ derived from Mariner 10 data indicates that the stability criterion is satisfied. Furthermore, the capture probability of Mercury into a 3:2 resonance is much greater than into higher-order resonances for the most common tidal models. Peale (1974, 1976) also finds from obliquity histories for all realistic initial conditions that the spin axis lies near the normal to the orbit in the final state.

Internal Structure

Although Mercury superficially resembles the Moon, its internal constitution must be very different. Mercury's very high mean density of 5.44 g/cm³ is exceeded only by that of the Earth (5.52 g/cm³). However, Mercury is only about one-third the size of Earth, and its uncompressed density (5.3 g/cm³) is considerably greater than that of the Earth's (4.0 g/cm³). This indicates that Mercury's composition is 60 to 70 percent by weight of metal phases (probably iron), and only about 30 percent by weight of silicate phases. Therefore, Mercury contains proportionately twice as much iron as any other planet in the solar system. If most of this iron is concentrated in a core, then the core radius is about 75 percent (1830 km) of the planet radius and the core volume is about 42 percent of the total volume, and somewhat larger than the volume of the Moon (fig. 3.1). Virtually nothing is known about the structure of the relatively thin (610 km) outer silicate layer. If Mercury was entirely or largely molten in the past, as thermal history models suggest, then the silicate layer may be differentiated into a mantle and crust.

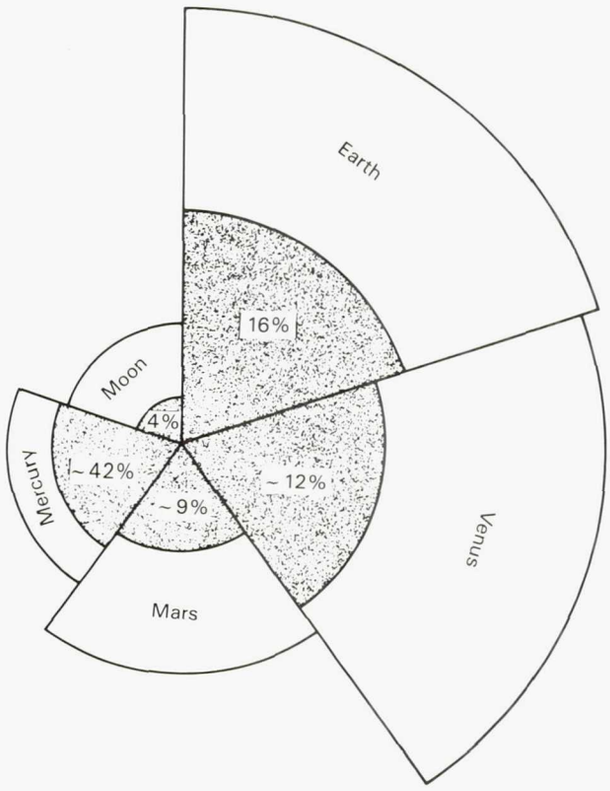

Figure 3.1. Comparison of terrestrial planet size and core radii. The percent of the total planetary volume of the core is also shown.

Magnetic Field

One of the most important discoveries made by Mariner 10 was the presence of a permanent magnetic field probably associated with Mercury's large iron core (Ness et al., 1974, 1975, 1976). Although the field is much weaker than Earth's, it is strong enough (~350 gammas) to form a magnetosheath and magnetosphere. The near-planet field is well represented by a dipole (with moment 5×10^{22}G cm³) inclined about 11° to the rotation axis, and with the same polarity as Earth's field. Although Mariner 10 did not explore this region, there are indications that the magnetosphere is elongated in the antisolar direction and may form a long magnetotail with an embedded neutral sheet. Also like Earth, there is evidence that the magnetosphere undergoes complex transient distortions (substorms) caused by interaction with the solar wind (Siscoe et al., 1975). Mercury encompasses much more of its magnetosphere than Earth. The average distance from the center of the planet to the solar wind stagnation point at the magnetopause is only 1.45 planetary radii. For Earth, the distance is about 11 Earth radii. Therefore, Mercury's magneto-

sphere is a factor of 7.5 smaller than Earth's when normalized to the planet radius. Consequently, charged particles reach Mercury much more easily than they reach Earth and no trapped radiation regions similar to the Van Allen belts occur. The solar wind may be strong enough during rare periods to actually compress the field to the surface (Siscoe and Christopher, 1975). A comparison of Earth's and Mercury's magnetic field is shown in figure 3.2.

The source of Mercury's magnetic field is not well established. By analogy with Earth and Jupiter, the favored hypothesis is an active magnetohydrodynamic dynamo within the planet (Ness, 1978). This implies a presently molten core of high electrical conductivity such as iron. Mercury is a slow rotator (58.6 days), and although rotation has been cited as a necessary condition for astrophysical dynamos, the amount necessary may be small. Gubbins (1977) has shown that for a planetary-sized dynamo of low viscosity only a slight angular velocity is required for the Coriolis force to dominate the momentum balance, a characteristic of "rapid rotation."

Another possible source of the Mercurian field is a remanent magnetization of iron-bearing rocks in the outer layers of the planet (Stevenson, 1974). Such a field can be acquired by rocks cooling through the Curie temperature in the presence of an ambient field. If Mercury once had a dipolar field caused by a dynamo which subsequently died out (possibly due to solidification of the core upon cooling) then a remanent dipolar field would be frozen in the crust. The level of magnetization necessary to support this hypothesis is comparable to that measured by Mariner 10 (Stevenson, 1976). However, this explanation requires about 5 percent free iron in the several hundred kilometer thick mantle, and whether the mantle would retain this much free iron (which is many times the typical values found in lunar basalts) is uncertain. Furthermore, estimates of the amount of contraction derived from the study of compressional surface features are not compatible with a complete or even extensive solidification of a once molten core (Solomon, 1977).

A presently active magnetohydrodynamic dynamo requires that at least the outer portion of the core is presently molten. The main problem with this explanation is the need for a concentration of heat sources in the core in order to maintain a fluid state over geologic time; a heat source density equivalent to about 2 ppb of uranium is required (Toksöz et al., 1978). Several explanations, although flawed, have been offered to account for a presently fluid core, such as the presence of K or S in the core (Toksöz and Johnston, 1977; Stevenson, 1980), a density and conductivity discontinuity at the core-mantle boundary which forms an insulating layer (Fricker et al., 1976; Gubbins, 1977), or late or extended core formation (Solomon, 1977). In any event, both explanations for Mercury's magnetic field (remanence or a magnetohydrodynamic dynamo) require that the interior is differentiated into a core and mantle, that the core was molten in the past, and very likely that it is at least partly molten at present.

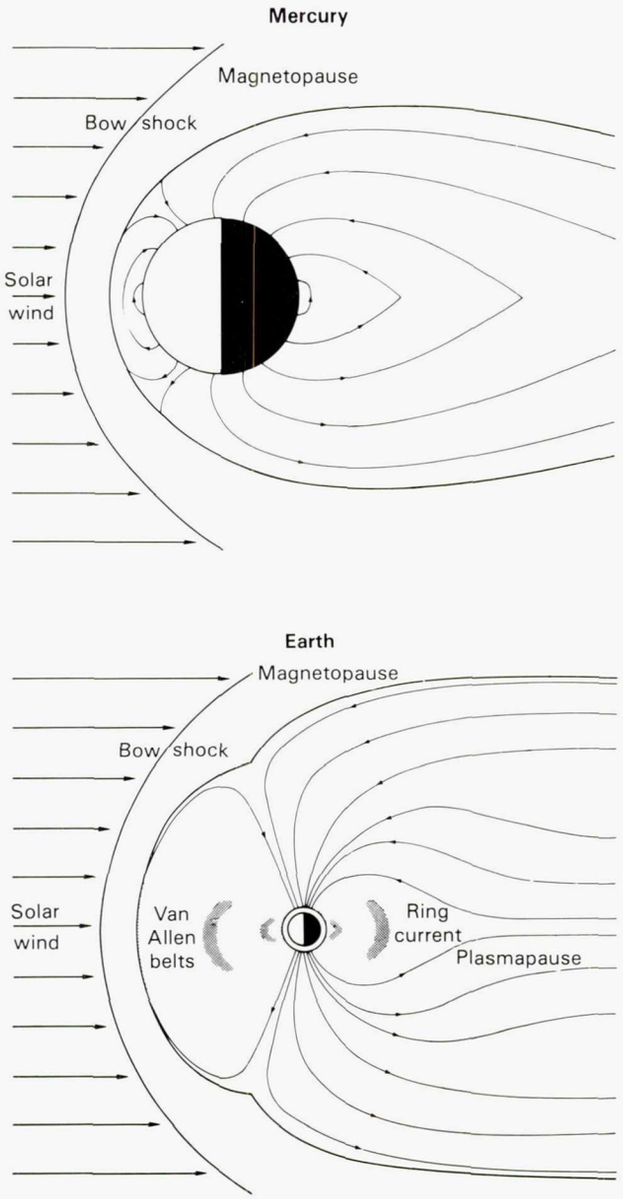

Figure 3.2. Comparison of the magnetic fields of Mercury and Earth.

Atmosphere

The ultraviolet spectrometer aboard Mariner 10 established upper limits on the atmospheric surface pressure and its composition (Broadfoot et al., 1974, 1976; Broadfoot, 1976a). The atmosphere is extremely tenuous with a surface pressure at the subsolar point less than a few times 10^{-10} mb. Consequently the gases are probably collisionless at the surface and the atmosphere essentially exospheric. Helium and atomic hydrogen have been identified in the ultraviolet spectrograms and upper limits placed on other possible constituents (H_2, O_2, Ne, Ar, O, CO_2, H_2O, and N_2). Furthermore, the Mariner 10 radio occultation experiment set an upper limit to the electron density of 10^3 cm^{-3} (Fjeldbo et al., 1976). This very tenuous atmosphere is probably derived largely from the solar wind.

Infrared Thermal Emission

The Mariner 10 infrared radiometer measured the thermal emission from Mercury at a spatial resolution as small as 40 km (Chase et al., 1974). In the equatorial regions just before dawn the minimum temperature is 90 K (at the subsolar point near perihelion the temperature is about 740 K). The temperatures thus have a range of at least 650 K (1170° F), greater than for any other planet or satellite in the solar system. The cooling curve of the surface during the night indicates the surface is composed of a homogeneous, porous material with a thermal inertia of 0.0017 cal $cm^{-2}sec^{-½}$ K^{-1}, which is similar to the value for the surface of the Moon. However, from near midnight until dawn the temperature fluctuated over a range of about 10 K, indicating regions with thermal inertias as high as 0.003 cal $cm^{-2}sec^{-½}$ K^{-1}. These observations are consistent with the presence of a layer of insulating silicate dust similar to the lunar regolith. The layer may be a few to tens of meters thick and was probably generated by impacts. The spatial variations in the thermo-physical properties of the layer indicate large-scale regions of enhanced thermal conductivity. These regions may be either areas of more compacted soil or regions where rock outcrops or boulders are not blanketed by dust.

GENERAL SURFACE CHARACTERISTICS

Although Mercury's internal constitution must be totally different from that of the Moon, its surface is remarkably similar (fig. 3.3a, b, and c). The dominant surface features are craters ranging in size from basin dimensions (1300 km) down to the smallest resolvable on Mariner 10 imagery (100 m). The craters are in various states of preservation: sharp-rimmed with extensive ray systems to highly degraded ones with very low or discontinuous rims. Antipodal to the Caloris basin is a peculiar hilly and lineated terrain that disrupts pre-existing landforms and may have been the result of focused seismic waves from the Caloris impact. Large tracts of lightly cratered smooth plains occupy low areas principally within and surrounding the Caloris basin and in the north polar regions. The larger expanses of these plains contain ridges somewhat similar to lunar wrinkle ridges. The relatively low crater densities on these plains indicate they are among the youngest surface units on the planet. Both morphologically and temporally they are very similar to the lunar maria. Unlike the Moon, Mercury has extensive intercrater areas with gently rolling planar surfaces and high densities of craters <15 km diameter. These intercrater plains appear to span a range of ages coincident with the period of heavy bombardment. They are among the oldest surface units on Mercury. Sinuous cliffs traverse the surface for hundreds of kilometers and are probably fault scarps.

Although the surface of Mercury superficially resembles the Moon, two major differences are: (1) the very great areal extent of old intercrater plains in the Mercurian highlands, and (2) the widespread distribution of lobate scarps which probably represent a period of global compression relatively late in Mercurian history. Furthermore, Mercurian crater ejecta characteristics are somewhat different from those of lunar craters, probably as a result of Mercury's greater surface gravity.

Photometry and Color

The integral optical, thermal and radar-reflecting properties of the Moon and Mercury are very similar (Hapke, 1977). These similarities indicate that Mercury is covered with a fragmental layer similar in depth and grain-size distribution to the lunar regolith. Photometric limb profiles measured from Mariner 10 data imply that small-scale slopes in the centimeter to meter size-range are about half those on the Moon, possibly caused by the influence of the stronger gravitational field of Mercury on the angle of repose of a cohesive soil (Hapke, 1977). In spite of the presence of a dipolar magnetic field, which would concentrate the solar wind

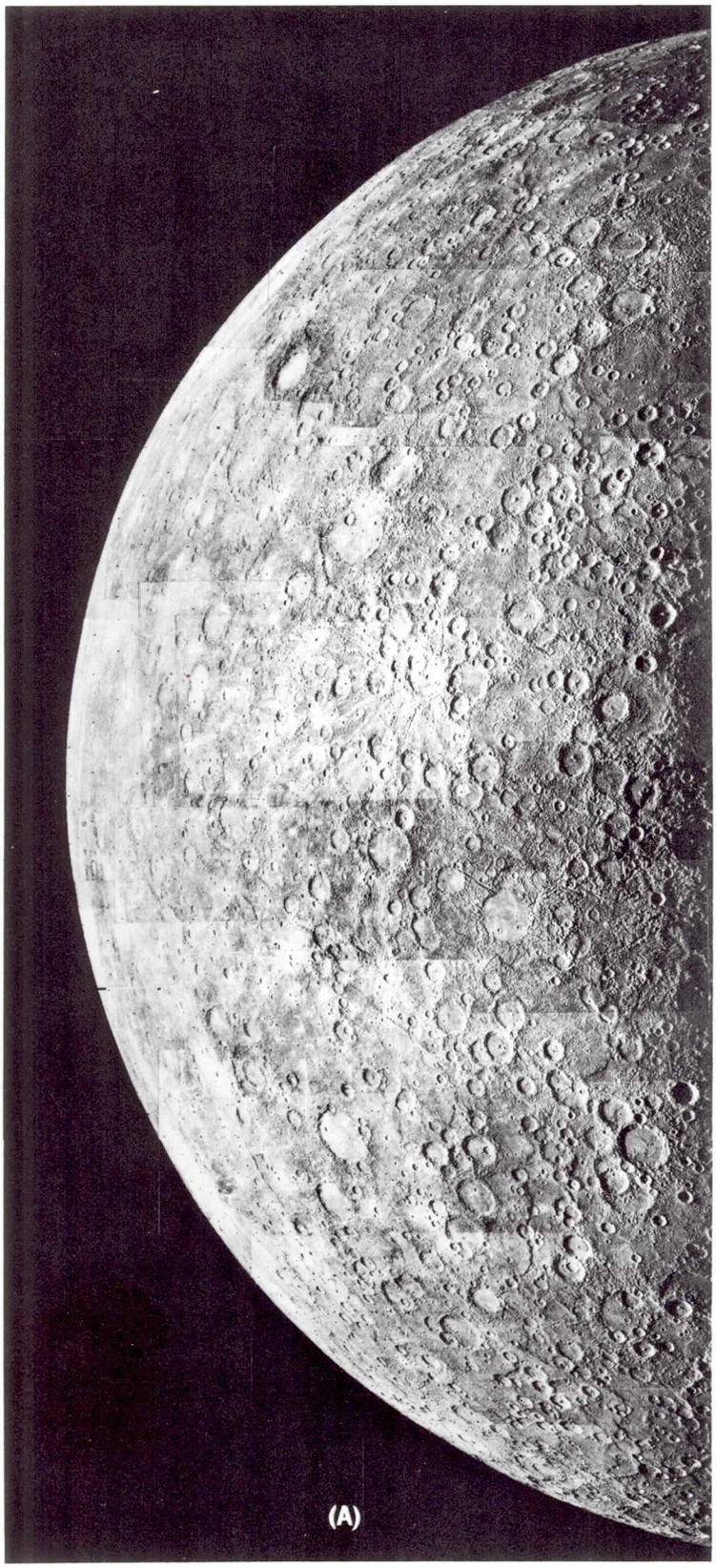

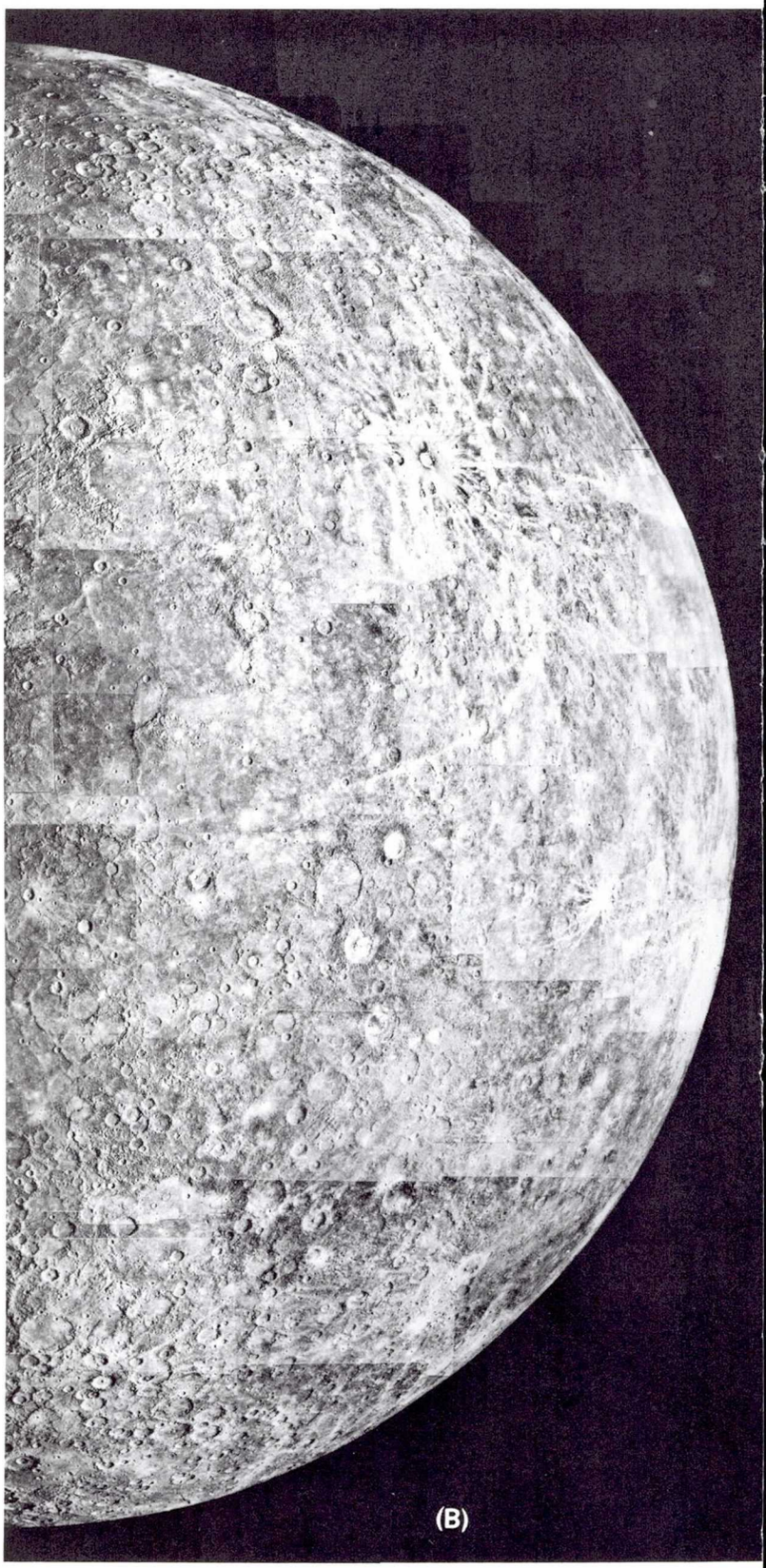

in the polar regions, Mercury displays no systematically lower albedo with increasing latitude. This implies that the dominant soil-darkening process is not dependent on the solar wind, but probably caused by processes resulting from meteoritic impact, e.g., redeposition of vaporized material.

Normal albedos were measured for various locations on Mercury using calibrated Mariner 10 images (Hapke et al., 1975). These albedos were determined for a phase angle of 5 degrees at a wavelength of 554 nm using a lunar photometric function. However, Mercury's photometric function differs enough from

Figure 3.3. Photomosaics taken by Mariner 10 of (A) the incoming side of Mercury viewed by Mariner 10, (B) the outgoing side, and (C) the southern hemisphere.

the Moon's (Danjon, 1949) so that the Mercury values should be reduced by a factor of 0.92. The normal albedos quoted here have been so corrected. Hapke (personal communication) estimates that the absolute values are accurate to within 10 percent. The Mercury values vary from about 0.08 for an area on the rim of Tolstoj basin to about 0.41 for the brightest craters. The average of 52 points is about 0.13, which is in good agreement with the integral albedo of 0.125 determined by Dollfus and Auriere (1974) from Earth-based polarimetric measurements at a similar wavelength and phase angle. Earlier Earth-based albedo measurements from photometric observations of Mercury must be systematically too low because they violate the albedo versus maximum polarization criterion (Dollfus and Auriere, 1974).

On average the Mercurian highlands, which primarily consist of intercrater plains, have albedos of about 0.16 to 0.18. There appear to be two types of smooth plains: darker smooth plains in and around the Caloris basin with albedos of about 0.12 to 0.13, and brighter smooth plains primarily on the incoming side with albedos of about 0.18. The Caloris smooth plains are therefore about 26 percent darker than the Mercurian highlands. The brighter rayed craters have albedos ranging from 0.36 to 0.41.

Normal albedos on the Moon have been determined by Pohn and Wildey (1970) and Wildey (1977) at a similar wavelength and adjusted to 0° phase angle. When these values are corrected to a 5° phase angle then the lunar maria have average albedos of about 0.06 to 0.07, but in limited areas they are as high as 0.08. The lunar highlands average about 0.10 to 0.11 while the brighter rayed craters have average values of about 0.15 to 0.16. A comparison of lunar and Mercurian albedos is listed in table 3.2.

Mercury appears to have systematically higher albedos than comparable terrains on the Moon. The Caloris smooth plains are about 90 percent brighter than the lunar maria and have an albedo about 20 percent higher than the lunar highlands. The Mercurian highlands are about 26 percent brighter than the lunar highlands, and Mercury's bright rayed craters are over 100 percent brighter than those on the Moon. At shorter wavelengths in the extreme ultraviolet from 58 to 166 nm Mercury has a significantly lower albedo (⅔) than the Moon (Wu and Broadfoot, 1977).

Color-ratio studies by Hapke et al. (1980) using Mariner 10 images taken through the orange filter (effective wavelength 578 nm) and the ultraviolet filter (355 nm) showed that color differences occur on Mercury but are smaller (25 percent) than on the Moon (40 percent). This suggests that the surface of Mercury has a more homogeneous distribution of elements

Table 3.2. Comparison of Normal Albedos on the Moon and Mercury

Terrain	Normal albedo (554 nm wavelength; 5° phase angle)
Lunar maria	0.06–0.07
Mercury Caloris smooth plains	0.12–0.13
Lunar highlands	0.10–0.11
Mercury highlands (intercrater plains)	0.16–0.18
Lunar bright rayed craters	0.15–0.16
Mercury bright rayed craters	0.36–0.41

affecting color (e.g., titanium) than does the Moon. The color difference map (fig. 3.4) compiled by Hapke et al. (1980) shows that the side of Mercury viewed by Mariner 10 on its incoming trajectory, and dominated by cratered terrain and intercrater plains, is more homogeneous than the outgoing side which has large areas of smooth plains. Except in a few instances there is little correspondence between color boundaries and geologic boundaries.

Surface Composition

Data on the composition of the Mercurian surface are extremely limited. Spectra of Mercury show a continuous increase in reflectance with increasing wavelength from the visible to the infrared (McCord and Adams, 1972; Vilas and McCord, 1976; McCord and Clark, 1979). Spectra of lunar highlands regolith also display a similar rise in the continuum with wave-

Figure 3.4. Color difference maps of Mercury. The side of Mercury viewed by the approaching Mariner 10 is shown in (A) and should be compared with fig. 3.3a. The side viewed by the departing spacecraft is shown in (B) and should be compared with fig. 3.3b. The maps were compiled from the ratio of brightness at 578 nm (orange) to the brightness at 355 nm (UV). Areas with the highest spectral ratio are light orange, while those with the lowest ratio are black. Areas with the average ratio are medium brown. (From Hapke et al., 1980; with modifications.)

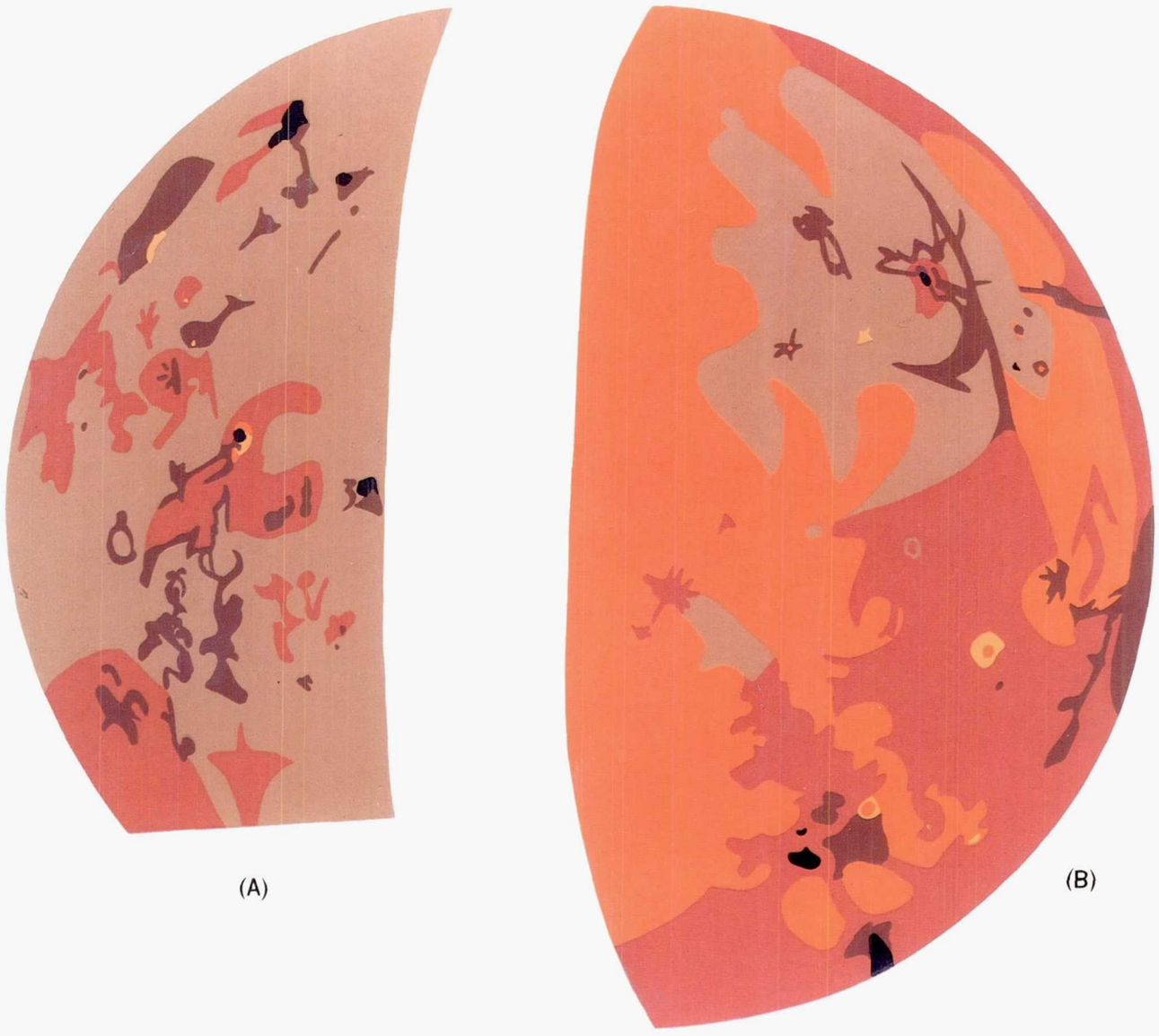

length. No other solar system objects yet observed have similar spectra. McCord and Clark (1979) reported a weak absorption feature between 0.75 and 0.95 μm, centered at 0.89 μm, which they attribute to Fe^{2+} ions in a pyroxene. A close comparison of this feature with an absorption band in lunar highlands regolith (Apollo 16 site) implies that both soils have the same amount of Fe^{2+}, suggesting an upper limit of about 5.5 percent FeO in average Mercurian regolith. Currently there is no evidence on Mercury for a 1.05 μm absorption band where Fe^{2+} absorbs in olivine.

The color ratio of Mariner 10 images discussed above show that, unlike the Moon, all Mercurian ray systems are blue relative to average (Hapke et al., 1975). Hapke et al. (1975) found that as the FeO abundance and Ti^{4+} abundance in Fe^{2+}-bearing materials increases, the spectrum reddens and the albedo decreases. Also, a relatively small amount of ilmenite ($FeTiO_3$) powder will cause the spectrum to become bluer and the albedo to drop significantly. Because all Mercurian ray systems possess the unique combination of bluish color and high albedo while those on the Moon are mostly red, Hapke et al. (1975) concluded that Mercury's surface is low in Ti, Fe^{3+}, and metallic Fe relative to the Moon's. This is also consistent with Mercury's lower ultraviolet reflectivity mentioned earlier. More recent studies by Hapke (1977) indicated that vapor-phase deposition accompanying micrometeorite impacts is an important darkening process on both Mercury and the Moon, and requires at least 3 percent FeO in the target material. Because comparisons of lunar and Mercurian reflection spectra indicate an average FeO content in the Mercurian soil of less than 6 percent, Hapke (1977) concluded that the average FeO content on the surface of Mercury is between 3 and 6 percent. These data suggest that on average at least the outer layers of Mercury are depleted in iron and titanium relative to the Moon. This also appears to be consistent with the albedo, color variations, and thermal history models.

CRATERS AND BASINS

The general morphology of Mercurian craters and basins is similar to that of their lunar counterparts (fig. 3.5). The craters range in size from as small as 100 m (highest resolution obtained by Mariner 10) up to basins over 1000 km in diameter. Small craters are bowl-shaped, but with increasing size they develop central peaks, terraces on their inner walls, and ejecta deposits with hummocky radial facies and swarms of secondary impact craters. Many fresh craters larger than about 100 km in diameter display interior concentric rings. As on the Moon, the craters and basins unquestionably represent the products of impacts by the complete size-range of meteoritic material. Similarly, crater morphologies become less sharp with increasing age until most of the crater elements are barely discernible. The dominant degradational process is apparently erosion and ballistic sedimentation by meteoritic bombardment, although in at least some cases the emplacement of plains units, viscous relaxation and possibly isostatic adjustments have contributed. Craters can be classified according to the degree of degradation of morphological components such as rays, secondary craters, various ejecta facies,

Figure 3.5. Comparison of a lunar (A), Mercurian (B), and Martian (C) crater. The width of the Mercurian continuous ejecta blanket (B) is less than that of the Moon (A) due to the reduced ballistic range. The Martian ejecta blanket (C) has a lobate form indicating flowage across the surface possibly due to impact in a subsurface permafrost layer. (Lunar crater is Copernicus, 93 km; Mercurian crater is Brahms, 75 km; Martian crater is Cerulli, 115 km.)

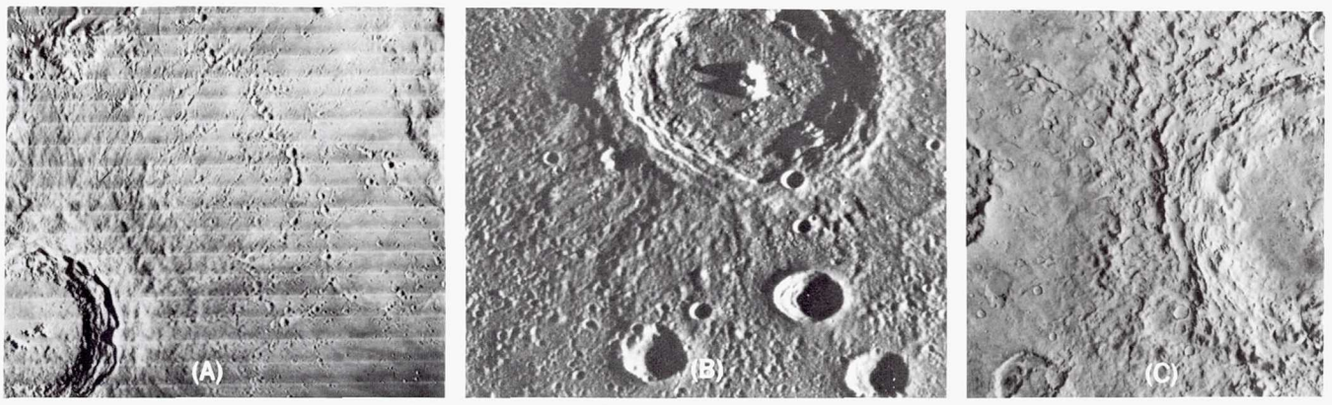

rim sharpness, and the state of interior terraces. Craters of similar size and state of preservation are considered to be about the same relative age.

In the 1960s, the Lunar and Planetary Laboratory (University of Arizona) developed a five-fold classification scheme for lunar craters (Arthur et al., 1963). The LPL classification designates Class 1 craters as the freshest and Class 5 craters as the most degraded. The U.S. Geological Survey has developed a somewhat similar five-fold classification designating the degradational state of craters as C_5 through C_1; C_5 being the freshest crater and C_1 being the most degraded (the reverse of the LPL scheme). Fortunately, the classification used by both organizations is based on somewhat similar criteria and therefore the crater classes are fairly interchangeable. However, investigators have used one or the other classification in various papers leading to extreme confusion for those unfamiliar with the two schemes. Because the LPL classification is found more frequently in the literature, it will be used here.

The freshest craters have well-developed and extensive ray systems; many extend hundreds of kilometers and some over 1000 km (fig. 3.3). Surrounding some craters are dark halos resembling those associated with such lunar craters as Tycho and Aristarchus. Other fresh-appearing craters have lost their ray systems and dark halos. Several relatively fresh craters have very bright patches on their floors. Unlike the Moon, color ratios from Mariner 10 images (Hapke et al., 1975) show that Mercurian ray systems and bright halos are bluer than their surroundings, and that the bright patches on the crater floors are redder than their surroundings.

Ejecta Deposits

One of the main differences between lunar and Mercurian craters is the character of their ejecta deposits (Gault et al., 1975). Lunar craters have outer rims of hummocky terrain grading outward into a radially ridged facies. These two facies comprise the continuous ejecta blanket. The continuous ejecta blanket, in turn, grades outward into discontinuous ejecta deposits where secondary impact craters form crater clusters and chains. For a given rim diameter the radial extent of Mercurian continuous ejecta blankets is uniformly smaller than that for the Moon (fig. 3.5) by a factor of about 0.65 (Gault et al., 1975). This reduced width is the result of the greater gravitational field on Mercury (370 cm/sec^2) which reduces the ballistic range of ejecta.

The distribution and characteristics of secondary impact craters of the discontinuous ejecta deposits also differ from their lunar counterparts (fig. 3.6). On Mercury the maximum areal density of secondary craters occurs closer to the primary crater's rim than for similar-sized lunar craters. The maximum density occurs at about 1.5 crater radii from the rim of Mercurian primaries, while on the Moon the maximum density occurs at about 2–2.5 crater radii. Furthermore, the maximum density of secondaries is over twice that of lunar craters of comparable size, but beyond two crater diameters the areal densities are about the same. The restricted distribution and enhanced areal density of Mercurian secondaries relative to those on the Moon can also be explained by the smaller ballistic range. This tends to reduce the dispersion between individual ejected fragments and concentrate them in a smaller area surrounding the crater (Gault et al., 1975). Long linear crateriform grooves near the rims of many Mercurian craters are probably the result of this reduced dispersion for larger ejected fragments. In a lower gravity field the secondaries would not overlap as much and would tend to form chains of more discrete craters as observed on the Moon.

Scott (1977) has noted that Mercurian secondaries are larger, deeper, and better preserved than those for primary craters on the Moon of similar size and degradation. He suggests that the difference is caused by greater secondary impact velocities on Mercury. For equivalent ranges, ejection velocities and therefore impact velocities are about 1.5 times greater on Mercury. These higher velocities may produce larger secondary craters which degrade more slowly than on the Moon.

Figure 3.7 illustrates the different ballistic ranges (R) for fragments launched at various ejection angles and velocities on the Moon and Mercury. The curves were derived from the ballistic equation for airless bodies and take into account the change in gravity with height and the radius of curvature of the surface. Because only gravitational forces modify the trajectories, an ejected fragment returns to the surface along a segment of an elliptical orbit. The apoapse of this orbit corresponds to the maximum height of the fragment while, in general, the periapse is within the body of the planet (Wright et al., 1963). Consequently,

$$R = 2r \tan^{-1}\left(\frac{V \sin\theta \cos\theta}{1 - V \cos^2\theta}\right)$$

where $0 \leq \theta \leq \pi/2$

and $V = V_e^2/rg$

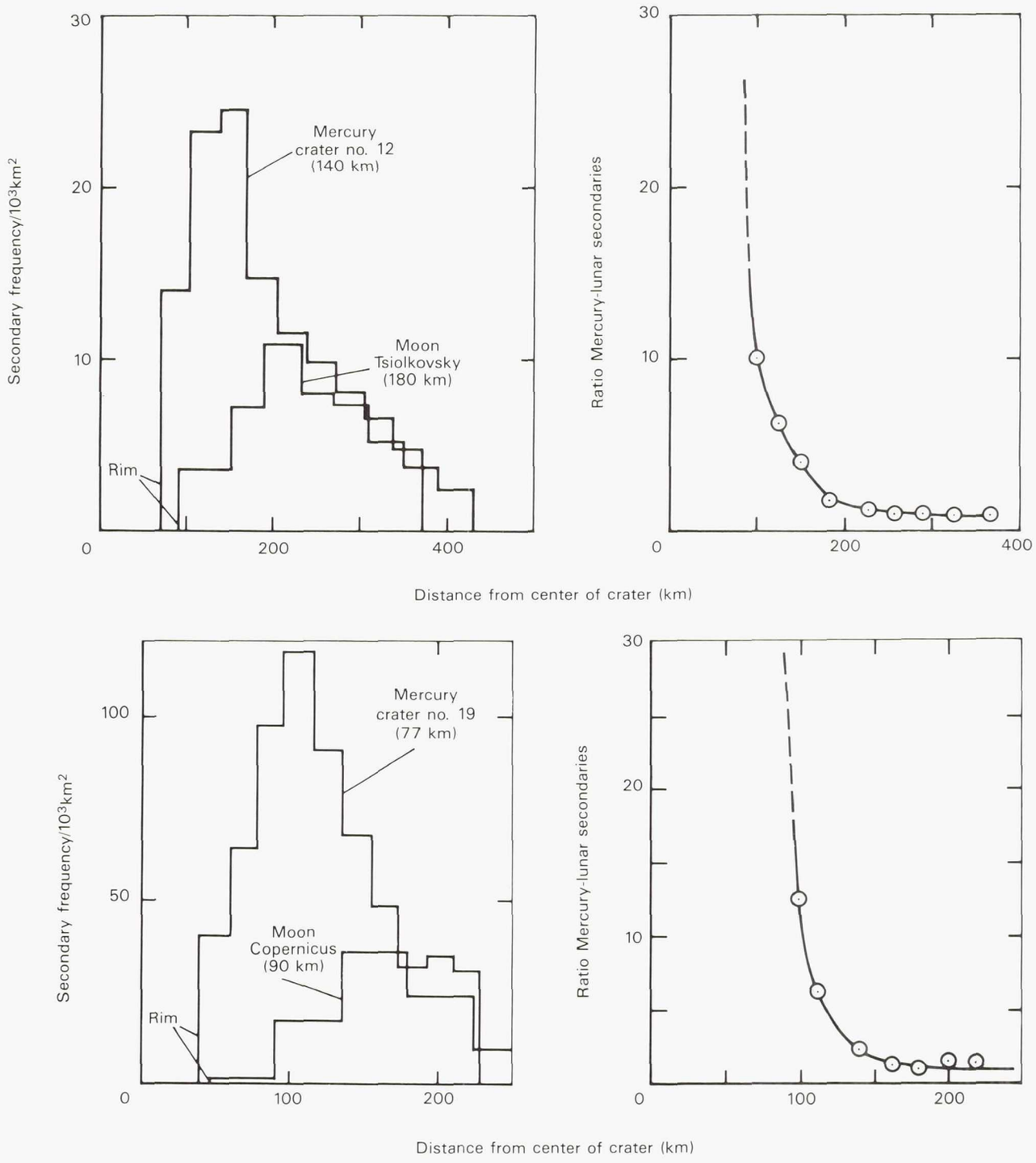

Figure 3.6. Radial variations in the areal density of secondary craters and the ratios of Mercurian to lunar secondary craters for Mercurian craters 12 (Verdi) and 19 (March) and for lunar craters Copernicus and Tsiolkovsky. (From Gault et al., 1975.)

V_e is the ejection velocity, g is gravitational acceleration (Moon = 162 cm/sec²; Mercury = 370 cm/sec²), r is the planet radius (Moon = 1738 km; Mercury = 2439 km), and θ is the ejection angle from the horizontal.

Experimental hypervelocity impacts (Gault et al., 1968) indicate that most material is ejected at angles between 30° and 45° from the horizontal. The curves in figure 3.7 show that for a given range at these ejection angles the ejection velocity is constrained within

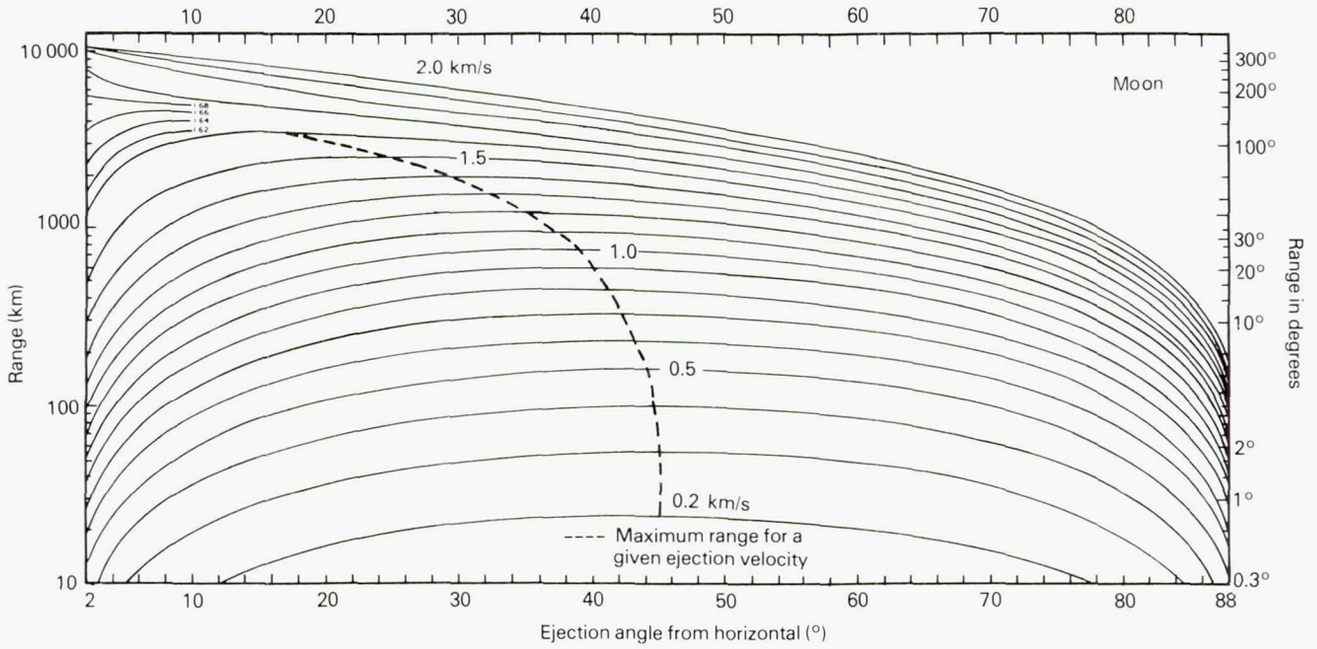

Figure 3.7. Plot of the range versus ejection angles from the horizontal for various ejection velocities for the Moon and Mercury.

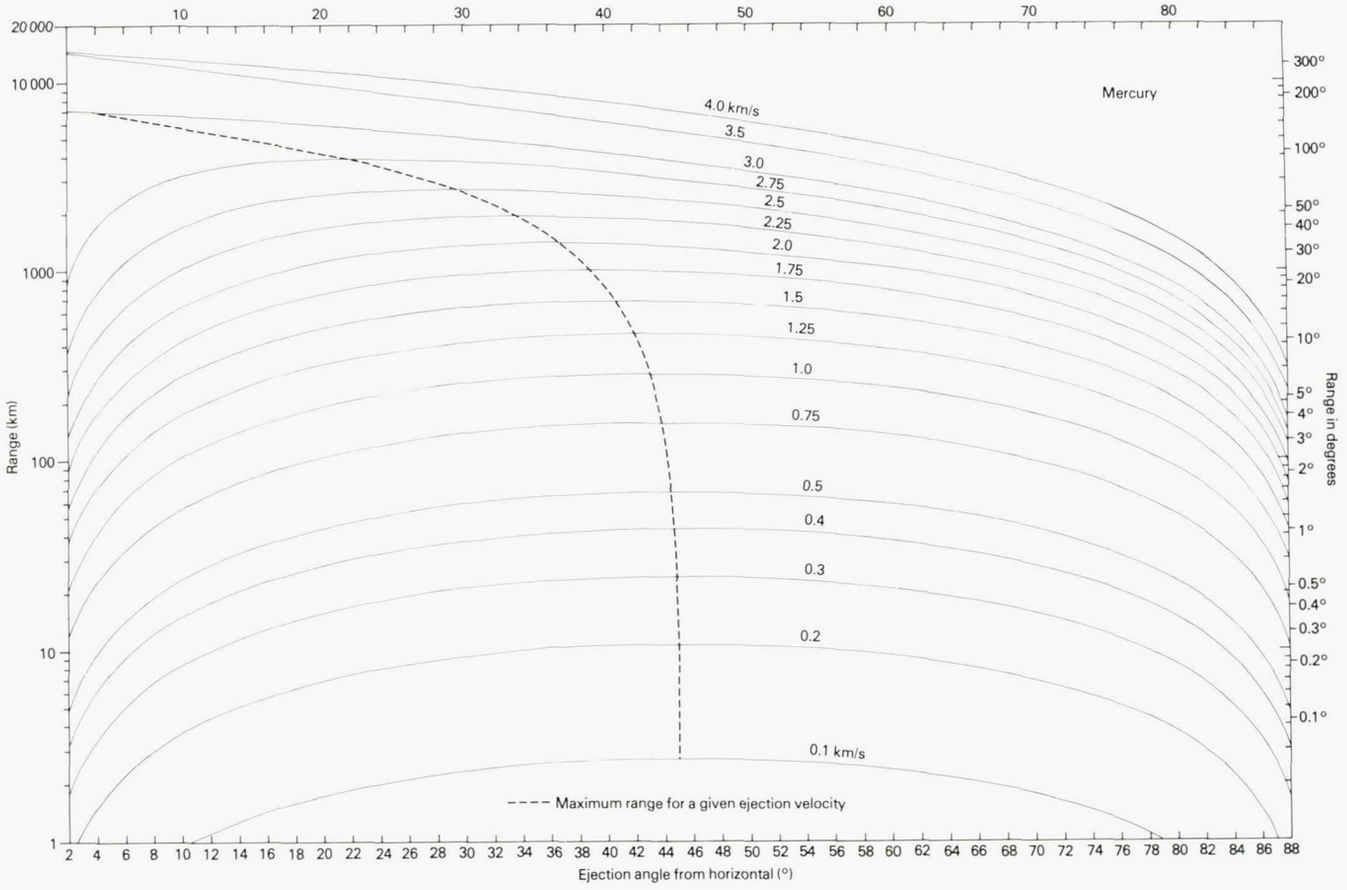

narrow limits. Even between ejection angles of 20–70° the ejection velocities are rather tightly constrained. Furthermore, with increasing ejection velocities above about 0.4 km/sec the maximum range occurs for progressively smaller ejection angles (less than 45°). Gault's studies indicate that the maximum secondary crater density occurs at about 1.5 crater radii on Mercury and about 2.0–2.5 crater radii on the Moon. Therefore, for both lunar and Mercurian craters in the diameter range 20–200 km, most of the larger fragments appear to have been ejected at velocities between 0.2–0.6 km/sec. For a given range, however, the ejection velocities are about 1.5 times greater on Mercury.

Interior Structure

The interior structure of Mercurian craters (terraces, central peaks, and rings) is similar to that of lunar craters (fig. 3.5) but the frequency of occurrence of some morphological features appears to be different. Fresh simple bowl-shaped craters have a depth/diameter ratio (1:5) similar to that for both lunar and Martian craters (Pike, 1980). The transition from simple bowl-shaped craters to complex craters (terraces and central peaks) occurs at about the same diameter on the Moon and Mercury (16–19 km), but at a much smaller diameter on Mars (6 km). Many other morphological and statistical differences occur between Martian craters and lunar and Mercurian craters. The most notable difference is the peculiar lobate ejecta blankets associated with Martian craters over a wide range of diameters and terrain types (fig. 3.5). These ejecta blankets have been attributed to impacts penetrating a subsurface ice layer and ejecting material with a high volatile content which flowed across the surface (Carr et al., 1977). Other differences include a much smaller diameter at which double ring basins occur on Mars compared to the Moon and Mercury (Wood, 1980), and a greater abundance of central peaks on Mars (Wood et al., 1978). These contrasts are probably due to differences in the physical properties of the target material including volatile content and stratification, although gravity and impact velocity may also have an effect.

Although the depth/diameter relationships and onset diameters of central peaks and terraces appear similar for both lunar and Mercurian craters, the diameter/frequency distribution of central peaks, terraces, and scalloped crater rims (slump features) is different. Smith and Hartnell (1979) found Mercury has a significantly higher percentage of fresh craters with central peaks than the Moon in the 5–75 km

Figure 3.8. Histogram of the central peak (A) and terrace (B) frequency versus crater diameter for the Moon and Mercury. (From Smith and Hartnell, 1979.)

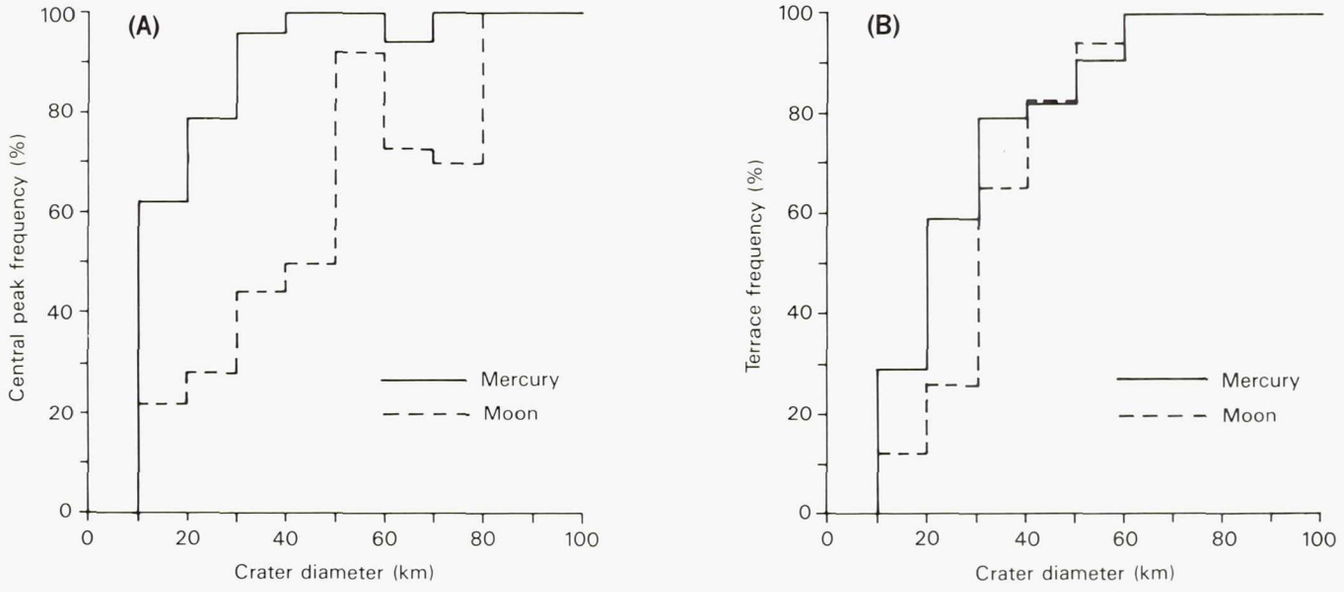

diameter range. Above a diameter of 75 km, all fresh craters on the Moon and Mercury have central peaks. Terraces are more abundant in Mercurian than lunar craters up to a diameter of 45 km (fig. 3.8). They concluded that gravity, terrain type, and impact velocity are important in influencing crater shape. Moreover, that gravity may be a critical factor because of similarities in the terrace and central peak plots that suggest wall failure and hence gravitational potential energy is important. Hale and Head (1980) found that the ratio of central peak diameter to crater diameter is the same for Mercury and the Moon. This, together with a similar peak height to rim height relation (Malin and Dzurisin, 1976, 1978), suggests to them that gravity is not the controlling factor in central peak formation, but rather dynamic rebound plays the major role.

Smith and Hartnell (1979) and Cintala et al. (1977) have found significant differences in the abundances of central peaks, terraces, and scalloped crater rims between fresh craters in the lunar maria and highlands (figs. 3.9 and 3.10). Both studies attribute these contrasts to differences in physical properties of the target materials; the lunar highlands consisting of a thick regolith and breccia (the megaregolith) and the maria consisting of only a thin regolith underlain by unbrecciated volcanic flows.

In a similar comparison of analogous terrain types on the Moon and Mercury, Cintala et al. (1977) found that the morphologies of craters formed in the lunar maria, the Mercurian smooth plains, and the Mercurian cratered terrain are similar. They also found, however, that large differences exist between craters formed in the lunar highlands and the analogous Mercurian cratered terrain (fig. 3.10). This suggests that a difference in the physical properties of the target material, rather than gravity, is a major factor affecting the formation of crater interior morphologic features. Accordingly, they suggested that the similar morphologies of craters formed in Mercurian smooth plains, lunar maria, and Mercurian cratered terrain indicate similar physical properties for all three terrains, but that large differences in Mercurian cratered terrain and the lunar highlands imply dissimilar physical properties. The main difference between the lunar highlands and the Mercurian cratered terrain is the great abundance of intercrater plains on Mercury. Because the lunar maria are volcanic lava flows, they reason that both the young Mercurian smooth plains and the older intercrater plains may also be volcanic deposits.

In summary, the formation of interior and exterior crater morphology is probably a complex interaction of two or more factors such as surface gravity, impact velocity, physical properties of the substrate, and subsurface crustal structure or discontinuities. The differences in the ejecta deposits of Mercurian and lunar craters are almost certainly due to the differences in

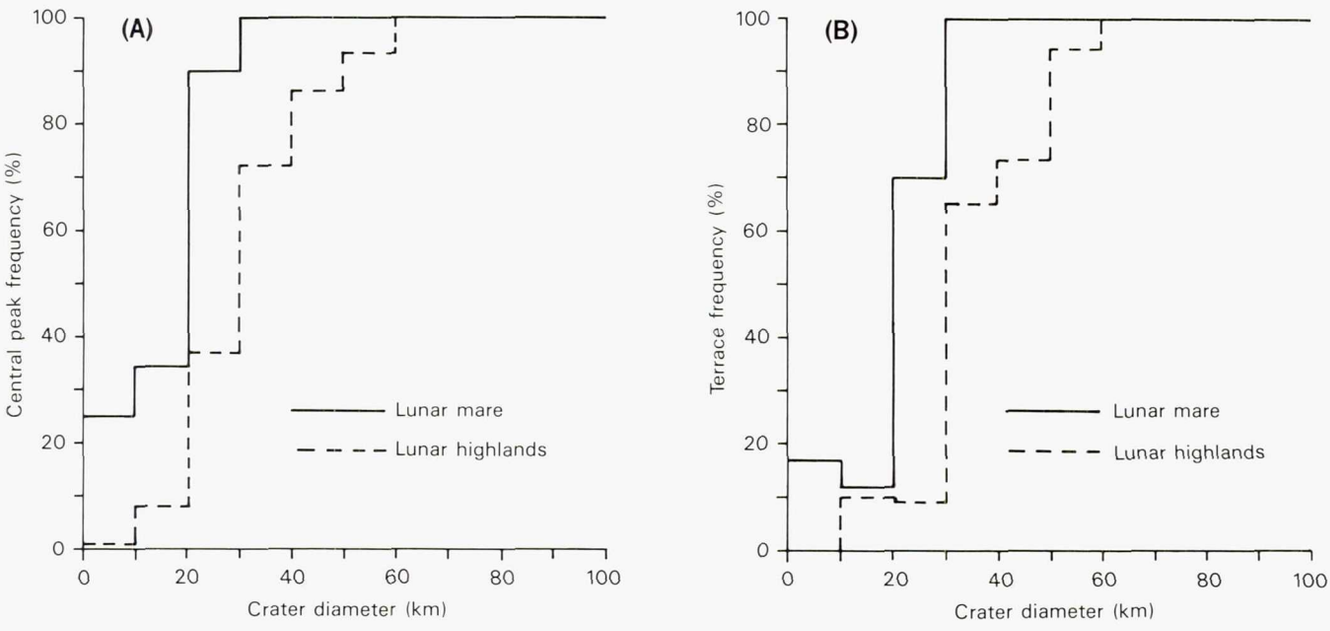

Figure 3.9. Histogram of the central peak (A) and terrace (B) frequency versus crater diameter for the lunar highlands and mare. (From Smith and Hartnell, 1979.)

gravitational acceleration, which reduces the ballistic range and increases the secondary impact velocity for a given range on Mercury compared to the Moon. The frequency of occurrence of interior structures such as slump structures and central peaks in craters appears to be related primarily to differences in the physical properties of the substrate, although gravity and impact velocity may play a role. Similar onset diameters of these features and similar depth/diameter relationships on the Moon and Mercury, together with other observations, suggest that gravitational potential energy and impact velocity are not significant factors affecting these attributes. Comparisons of interior morphologic features between lunar and Mercurian craters suggests that Mercurian smooth and intercrater plains and the lunar maria have similar physical properties that are different from those of the lunar highlands.

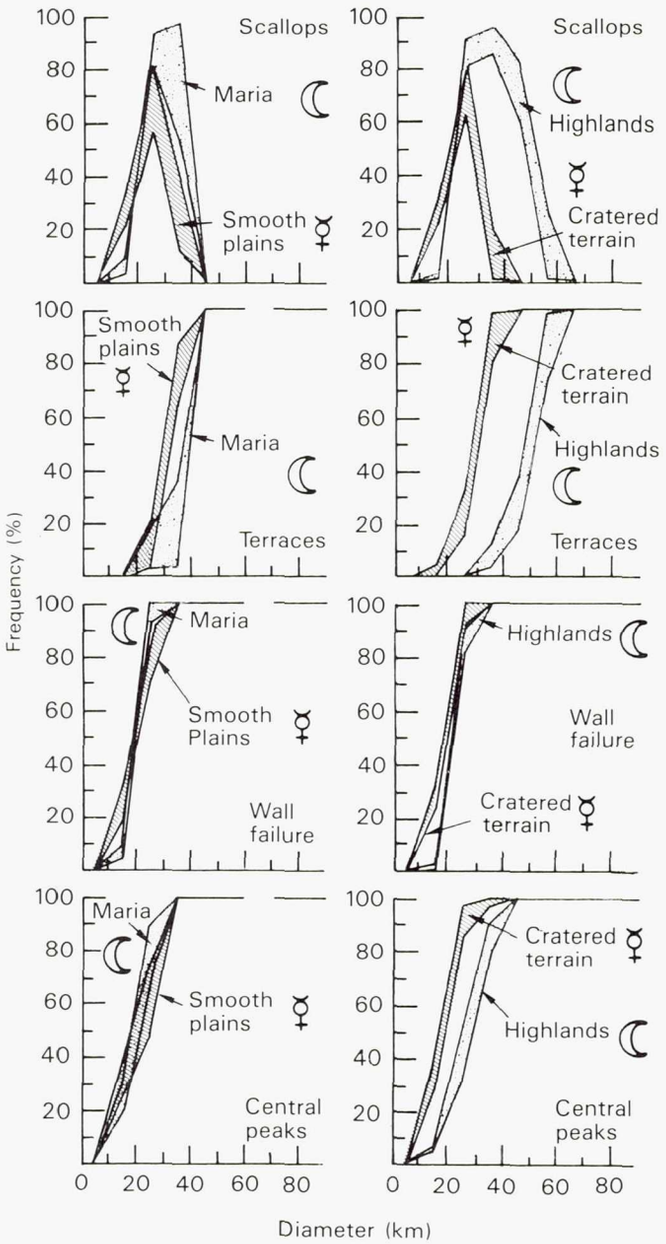

Figure 3.10a. Morphology/frequency distribution comparing craters on the lunar maria to those in the Mercurian smooth plains (left), and craters in the lunar highlands to those in the Mercurian cratered terrain (right). (From Cintala et al., 1977.)

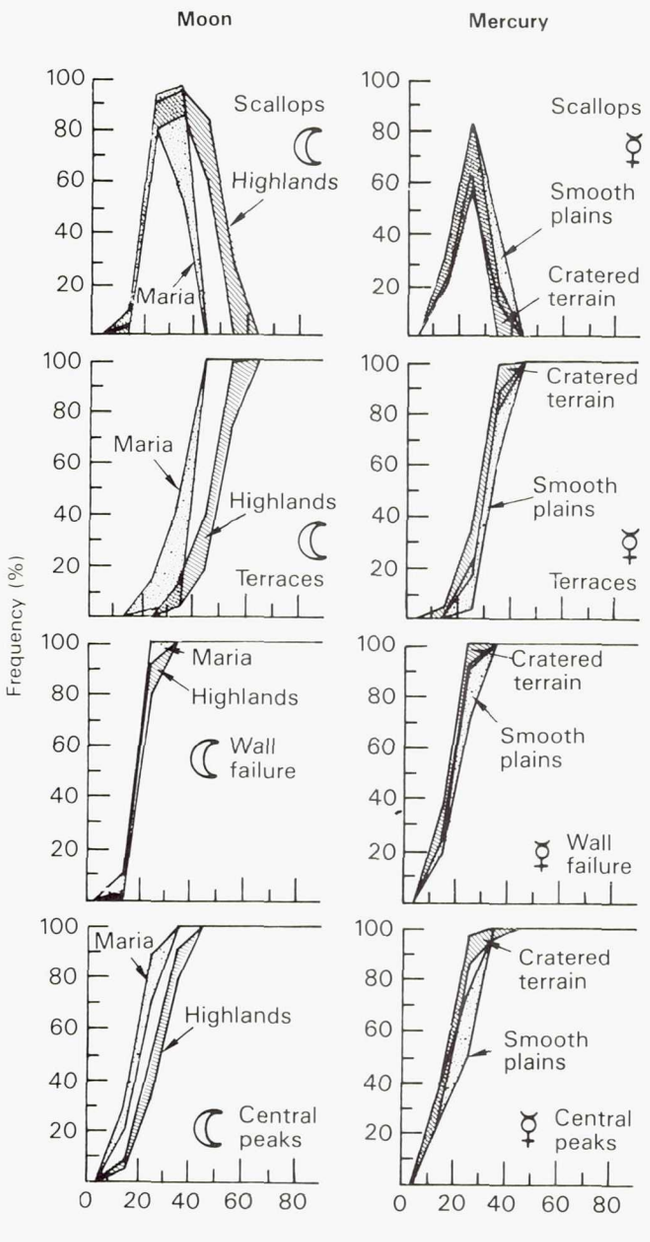

Figure 3.10b. Morphology/frequency distribution, illustrated as $\pm 1\sigma$ envelopes around the mean values, for craters on the Moon (left) and Mercury (right). (From Cintala et al., 1977.)

The Caloris and Other Large Basins

Basins are nothing more than very large craters, making the definition of a basin somewhat arbitrary. Hartmann and Kuiper (1962) defined the term as a large circular depression with distinctive concentric rings and radial lineaments. Wood and Head (1976) followed this definition but place special significance on the development of concentric rings. Other investigators (e.g., Murray et al., 1974) considered any crater larger than an arbitrary diameter (in their case 200 km) as a basin.

With increasing size, craters with diameters larger than about 100 km show a gradual transition from a central peak surrounded by an irregular ring of peaks, to single concentric rings of peaks to multiple concentric rings at the largest diameters (fig. 3.11). Wood and Head (1976) termed craters with a central peak surrounded by an irregular ring of peaks as *central peak basins,* and craters with a single concentric ring of peaks as *peak ring basins.* On Mercury, central peak basins first occur at about 90 km diameter, whereas on the Moon they first appear at about 140 km diameter (Wood and Head, 1976; Gault et al., 1975). Multi-ring basins have two or more rings with at least the outer rings being asymmetric in profile (more scarp-like). Only two structures on Mercury have been identified as multi-ring basins: Caloris

Figure 3.11. Comparison of lunar central peak basin Compton (A) and Mercurian central peak basin Hitomaro (B) with lunar peak ring basin Schrödinger (C) and Mercurian peak ring basins Strindberg and Ahmad Baba (D). Compton is 175 km in diameter; Hitomaro is 58 km in diameter; Schrödinger is 320 km in diameter; Strindberg is 165 km in diameter; and Ahmad Baba is 115 km in diameter.

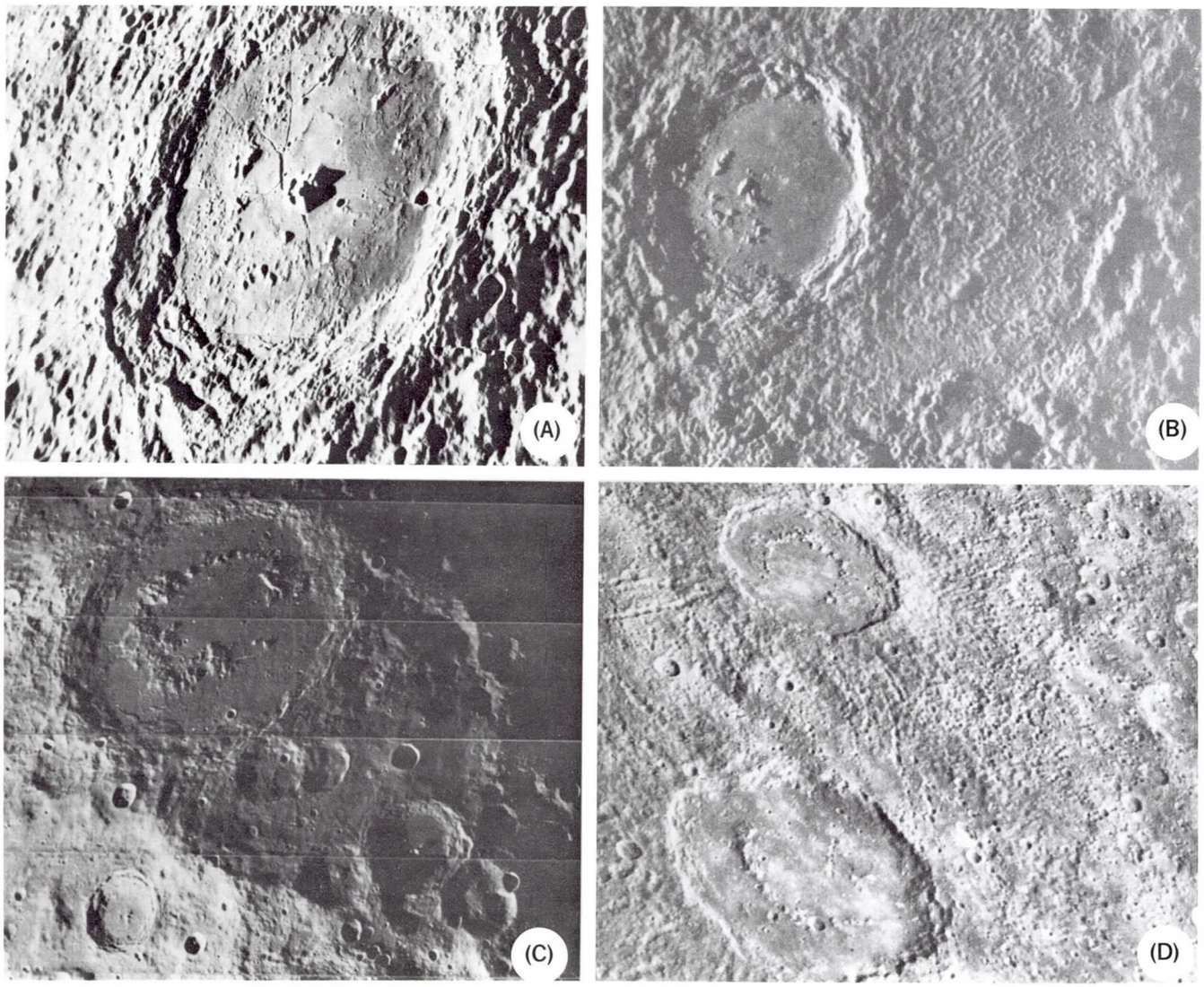

(1300 km diameter) and Tolstoj (400 km diameter). The apparent lack of such structures may be due in part to the poor photographic coverage, adverse lighting conditions, or burial of ring structures by subsequent basin infill. The ring spacing of these basins is significantly less than those on the Moon and Mars. Based on ring tectonic theory, McKinnon (1981) considered this smaller spacing to indicate a relatively thin (< 50–125 km) lithosphere at the time of formation.

The largest structure viewed by Mariner 10 is the Caloris basin (1300 km diameter) (fig. 3.12). This basin has many characteristics in common with the

Figure 3.12. Photomosaic of the Caloris basin. Unlike other planetary basins, the floor is highly ridged and fractured. Both ridges and fractures display a concentric and radial pattern.

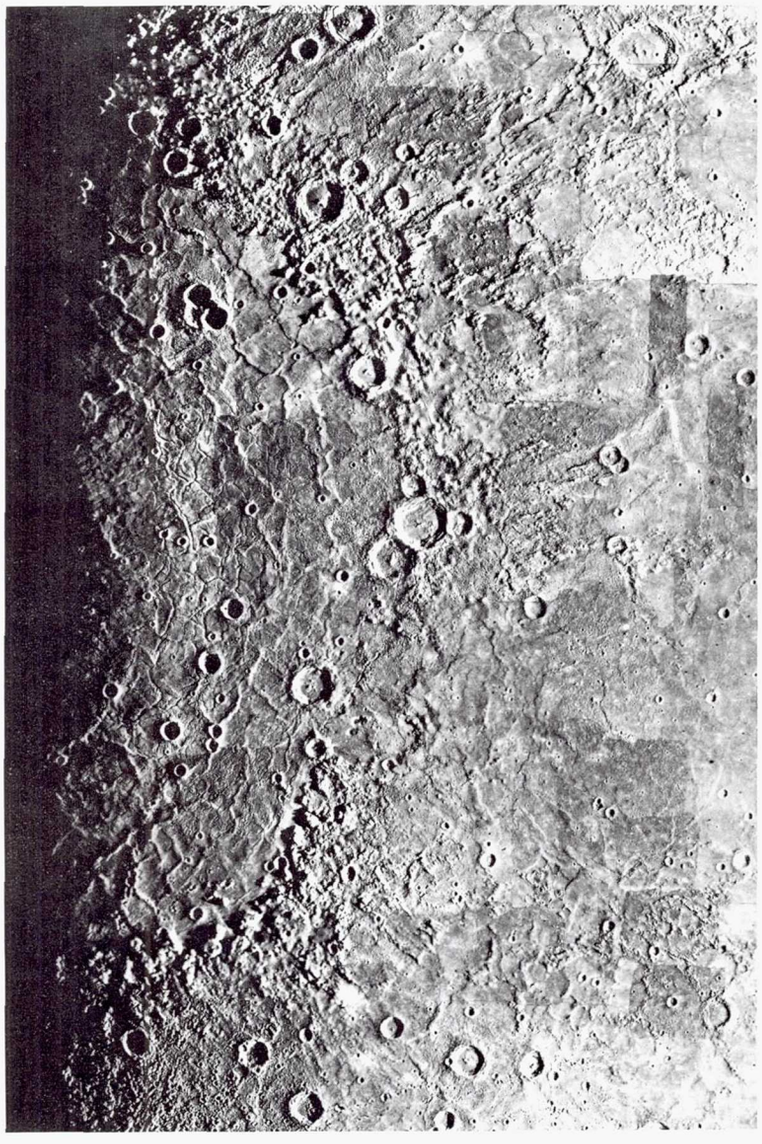

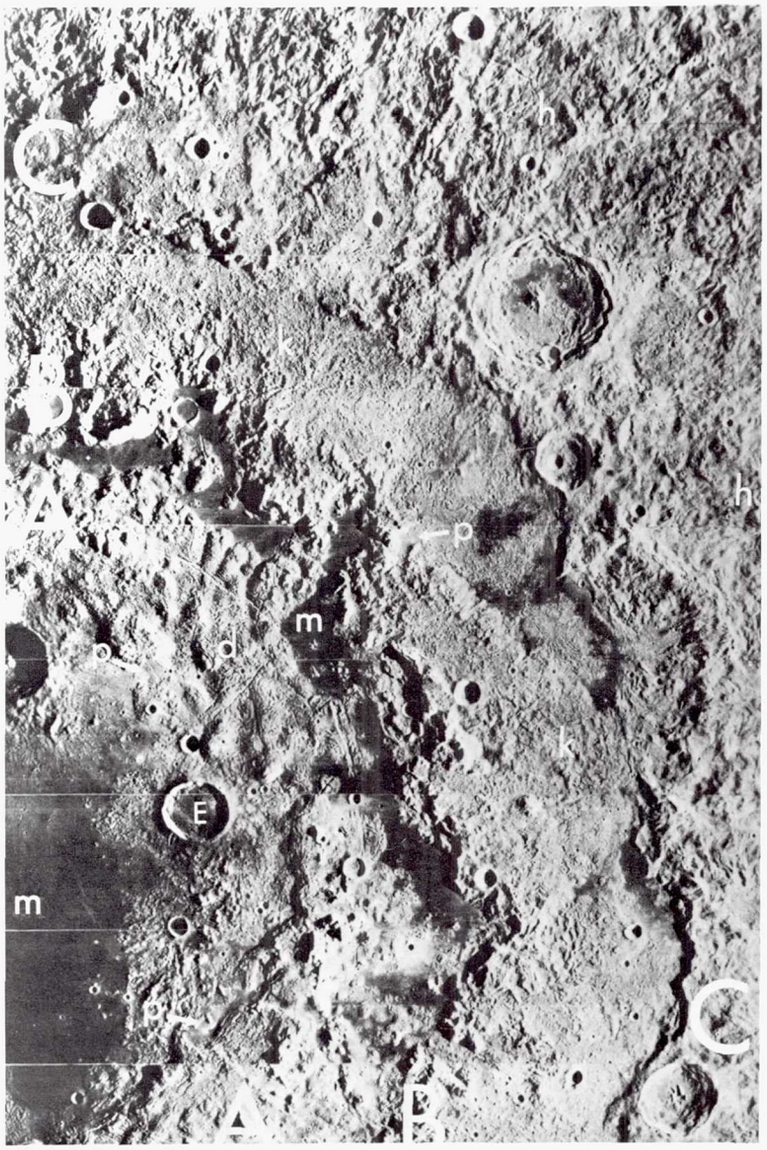

Figure 3.13. Lunar Orbiter 4 photograph (M 181) of a portion of the lunar Orientale basin showing the multi-ring structure and various geologic units associated with the basin. The diameter of the Cordillera ring (C) is about 920 km. The crater Kopff (E) is 40 km in diameter. Geologic units are A, Inner Rook Mountains; B, Outer Rook Mountains; C, Cordillera Mountains; m, mare basalts; d, domical and fractured terrain; k, knobby and hummocky terrain; h, radially lineated and braided continuous ejecta deposits (Hevelius Formation); p, small patches of light smooth plains.

lunar Orientale (fig. 3.13) and Imbrium basins (Strom et al., 1975b; McCauley, 1977). The main ring consists of segmented massifs with rectilinear outlines about 30 × 50 km in size and average about 1–2 km in height above the basin floor. The basin interior is filled with smooth plains that are extensively ridged and fractured. This type of floor structure appears to

be unique to Caloris; it is not present in any other basin on Mercury, Mars or the Moon. A weakly developed outer scarp occurs at about 100–160 km from the main scarp, and is best seen in the northeastern part of the basin (fig. 3.14). The area between the two scarps consists of a blocky to knobby terrain grading outward beyond the outer scarp into a radially lineated terrain (fig. 3.14). This lineated terrain extends to about one basin diameter from the main Caloris scarp and is embayed by both smooth and hummocky plains (Trask and Guest, 1975). Hummocky plains appear as large lobes around the basin and consist of numerous smooth equidimensional knobs set in a matrix of rolling plains (fig. 3.15). Smooth plains form a broad belt that is circumferential to the basin and extend outward for over one basin diameter (fig. 3.16). Numerous poorly-preserved crater clusters, chains, and irregular troughs lie within the cratered terrain beyond one basin diameter and are probably secondary impact craters from Caloris (McCauley, 1977). With the possible exception of the smooth plains, all these terrains probably represent materials or structures produced by the impact that formed the Caloris basin. The units have been assigned a formal rock-stratigraphic nomenclature (McCauley et al., 1981) patterned after that used in geologic mapping of the Imbrium basin (Wilhelms and McCauley, 1971) and the Orientale basin (Scott et al., 1977).

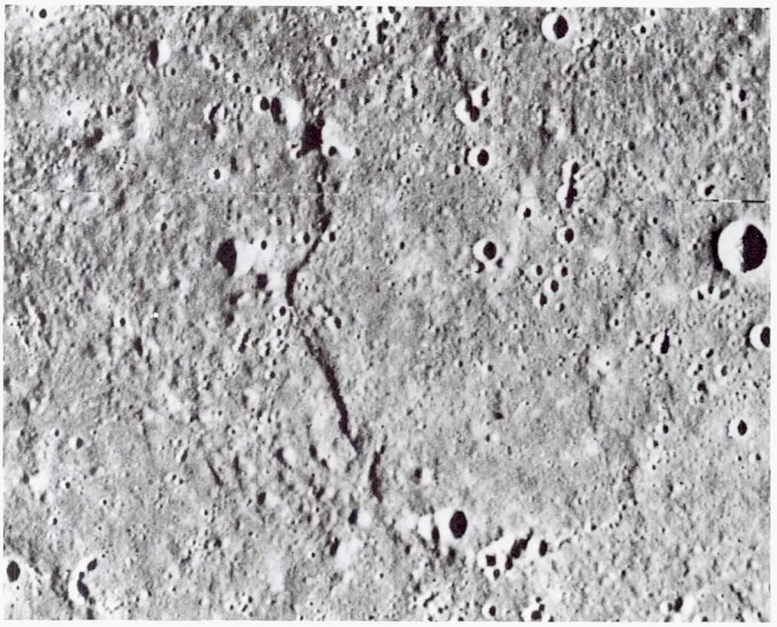

Figure 3.15. The Caloris hummocky plains; a basin ejecta facies. The large hill left of the scarp is about 1.4 km high. The area is located about 200 km east of the rim of the Caloris basin. The area covered by this picture is 153 × 115 km. (FDS 72)

Based on morphologic similarities, McCauley (1977) considered the main Caloris scarp and the weaker outer scarp to be the structural equivalents of the lunar Orientale Montes Rook and Montes Cordillera scarp, respectively (figs. 3.12 and 3.13). The radially lineated terrain extending outward from the outer scarp is thought to be the eroded equivalent of the Orientale radially-braided continuous ejecta deposit termed the Hevelius Formation (fig. 3.13).

Figure 3.14. The Caloris basin Knobby (K) and Lineated (L) terrain. The inner Caloris ring is denoted by A-A' and the outer ring by B-B'. (FDS 193)

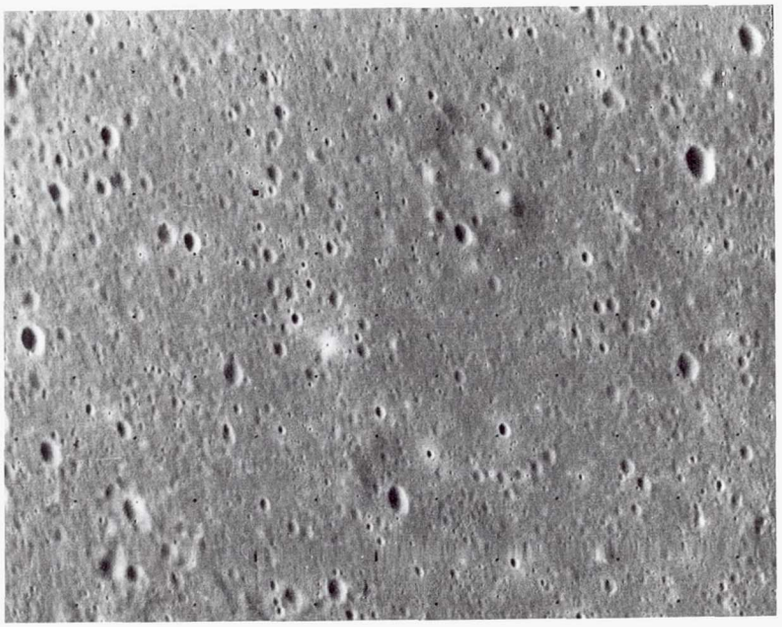

Figure 3.16. Smooth plains located about 700 km east of the Caloris basin. The vertical and horizontal dimensions of this picture are about 50 and 85 km, respectively. (FDS 45)

Its position and extent relative to the outer scarp is essentially the same as that of the Hevelius Formation relative to the Montes Cordillera scarp. The large lobes of hummocky plains have a distribution outside the basin rim similar to that of the Alpes Formation around the lunar Imbrium basin. The Alpes Formation is the textural counterpart of the knobby terrain primarily found between the Outer Rook Mountains and the Cordillera scarp in the Orientale basin (fig. 3.13). However, unlike the Orientale knobby terrain, the Caloris hummocky plains embay and are interspersed with the lineated terrain out to at least one basin radius. McCauley (1977) and McCauley et al. (1981) considered the main Caloris scarp to be the rim of the excavation crater while the hummocky plains and radially lineated terrain are ejecta deposits laid down contemporaneously with the formation of the outer scarp by slumping. McKinnon (1981) pointed out, however, that the basin floor subtends 0.53 radius and the geometry of the shock that would create such a crater is inconsistent with a transient depth less than 90 km (the line of sight depth from the Caloris Montes rim). The volumetric adjustment required to compensate for this transient depth is inconsistent with the weak deformation observed beyond the main scarp. Therefore, the limit of excavation was probably within the main scarp and buried by the smooth plains that fill the basin.

Although it is not possible to date unambiguously the Caloris impact on an absolute time scale, its age relative to the general crater population can be estimated by superposition relationships of ejecta deposits on pre-existing terrain and the degradational state of craters superposed on the ejecta deposits. McCauley et al. (1981) found that numerous craters in the 30 to 100 km size-range are superposed on the Caloris ejecta assemblage and that most of these are Class 1 (USGS C_5 type) and Class 2 (USGS C_4 type). A few smaller craters primarily 30 to 50 km in size are designated upper Class 3 (USGS upper C_3 type) and also are superposed on Caloris ejecta. Therefore, the Caloris impact seems to have occurred near the end of formation of Class 3 craters. Wood et al. (1977), in a study of degradational crater types, found that on both the Moon and Mercury extensive crater degradation occurred during the formation of Class 5 to Class 3 craters, and a lower level of modification has occurred since then. They concluded that the period of intense bombardment ended on both the Moon and Mercury during the transition from Class 3 to Class 2 craters. However, the absolute time represented by this transition is not necessarily the same on both bodies. In any event, the Caloris impact seems to have occurred near the end of intense bombardment on Mercury.

The origin of the smooth plains which fill and surround Caloris is not clear. Both impact (Wilhelms, 1976; Oberbeck et al., 1977) and volcanic (Strom et al., 1975b; Trask and Strom, 1976; Cintala et al., 1977; Hawke and Cintala, 1977) origins have been suggested. However, as mentioned earlier, the structure of the smooth plains that fill Caloris appears to be unique. Although the plains superficially resemble the Orientale Maunder Formation interior to the Outer Rook Mountains and interpreted as impact melt, their overall appearance is dissimilar (Strom et al., 1975b; McCauley, 1977). They have a much more extensive and coarser concentric and radial fracture pattern which transects numerous mare-like ridges not present in the Maunder Formation (fig. 3.17). The fractures become progressively more pronounced (wider and deeper) toward the basin center (Strom et al., 1975b). Mare-like ridges also form concentric and radial patterns. Transection relationships indicate that most of the ridges predate the formation of the fractures. Strom et al. (1975b) suggested that the ridges are compressional features formed by subsidence of the basin floor, and that the fractures represent tensional features produced by subsequent uplift of the central basin. Dzurisin (1976) hypothesized that the subsidence was caused by withdrawal of magma beneath Caloris and subsequently extruded to form

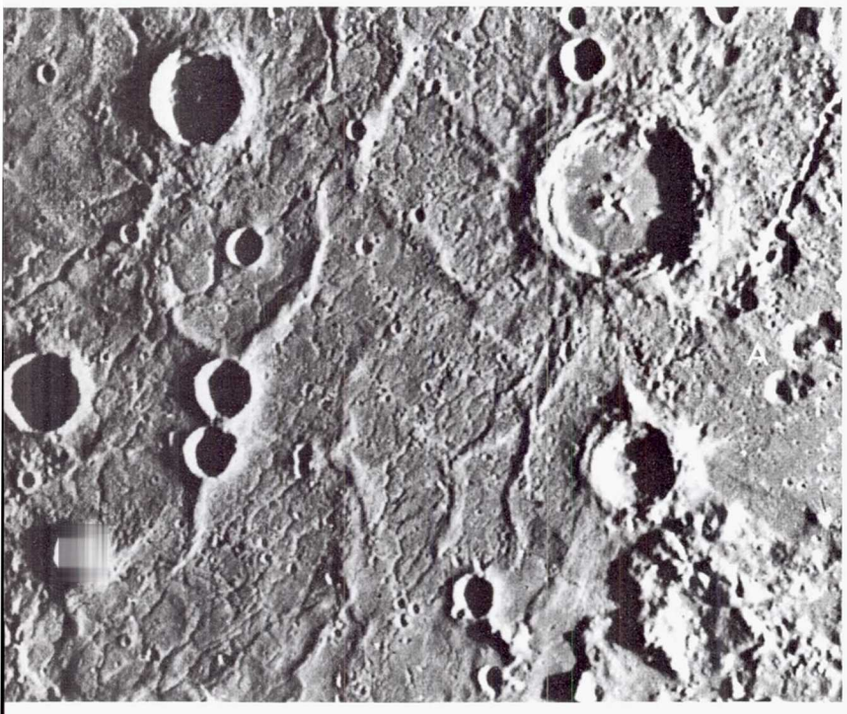

Figure 3.17. Part of the Caloris basin floor showing the ridges and fractures. The length and width of the fractures increase toward the center of the basin (lower right to upper left) and the fractures transect the ridges indicating they are younger. The irregular depressions at A are rimless and probably originated by collapse rather than impact. The largest crater is about 60 km in diameter. (FDS 126)

the smooth plains outside the basin. The central basin uplift is presumed to be caused by relaxation toward isostatic equilibrium following this event. Based on this hypothesis and the fact that Caloris is located near Mercury's axis of minimum moment of inertia, Melosh and Dzurisin (1978a) suggested there may be an annular positive gravity anomaly associated with isostatically uncompensated material constituting the smooth plains surrounding the basin. They hypothesize that it is this positive gravity anomaly, rather than a mascon associated with the basin interior as postulated by Murray et al. (1974), which may account for the coincidence of the Caloris basin with the long axis of the planet's dynamical figure. They assume that the uplift responsible for the fracture pattern is due to isostatic adjustments, but it also may be driven by the annular load itself (McKinnon, 1979). It is also possible that the uplift resulted from an intrusion of basic or ultrabasic magma following the initial subsidence of the floor.

Other large basins on Mercury are more degraded than Caloris, contain a higher density of superposed craters, and so appear to be older. Furthermore, most are filled with unfractured smooth plains that often embay post-basin craters. This, together with the fact that the smooth interior plains often have a much lower crater density than the exterior terrain, indicates the plains are often younger than the basins they occupy (Strom et al., 1975b; Trask and Strom, 1976).

Two very degraded basins about 800 km in diameter have been recognized primarily by circular patches of smooth plains (Schaber et al., 1977; DeHon, 1978). Trask and Strom (1976) suggested that the large area of smooth plains in the north polar region (Borealis Planitia) may occupy an ancient basin about 1000 km in diameter, but identification is uncertain because of incomplete photographic coverage in this region. Figure 3.18 shows another large basin (Beethoven, 630 km diameter) about half the size of Caloris which has been described by Strom et al.

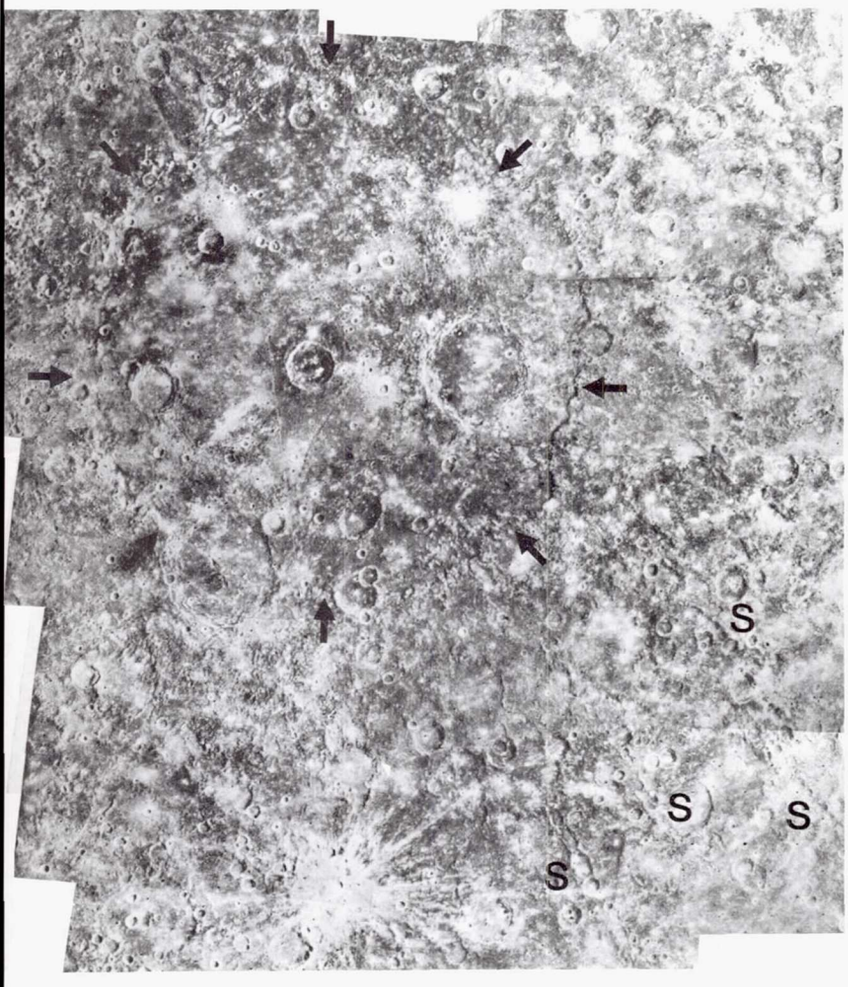

Figure 3.18. Photomosaic of the 625-km-diameter Beethoven basin. The basin is indicated by arrows. Remnants of radial sculpturing (s) occur southeast of the basin and consist primarily of crater chains.

(1975a). Although Mariner 10 photographed this basin under a high illumination (70°), the rim and other basin structure are discernible. The basin is filled with plains that have been moderately cratered by large impacts. No large expanses of exterior plains comparable to those surrounding Caloris are recognized. However, a radial sculpture in the form of crater chains 150–180 km long and about 12 km wide are visible to the southeast of the basin. The chains extend at least one basin diameter from the rim, and are probably secondary impact craters.

Crater Statistics

The crater diameter/frequency distribution of the Mercurian highlands is similar to that of the lunar highlands and the heavily cratered provinces of Mars (fig. 3.19). All show a highly structured curve that cannot be represented by a single distribution function. Recent computer modeling, together with statistical and observational crater investigations, strongly suggest that the lunar highlands are not at saturation density, but instead basically represent a production

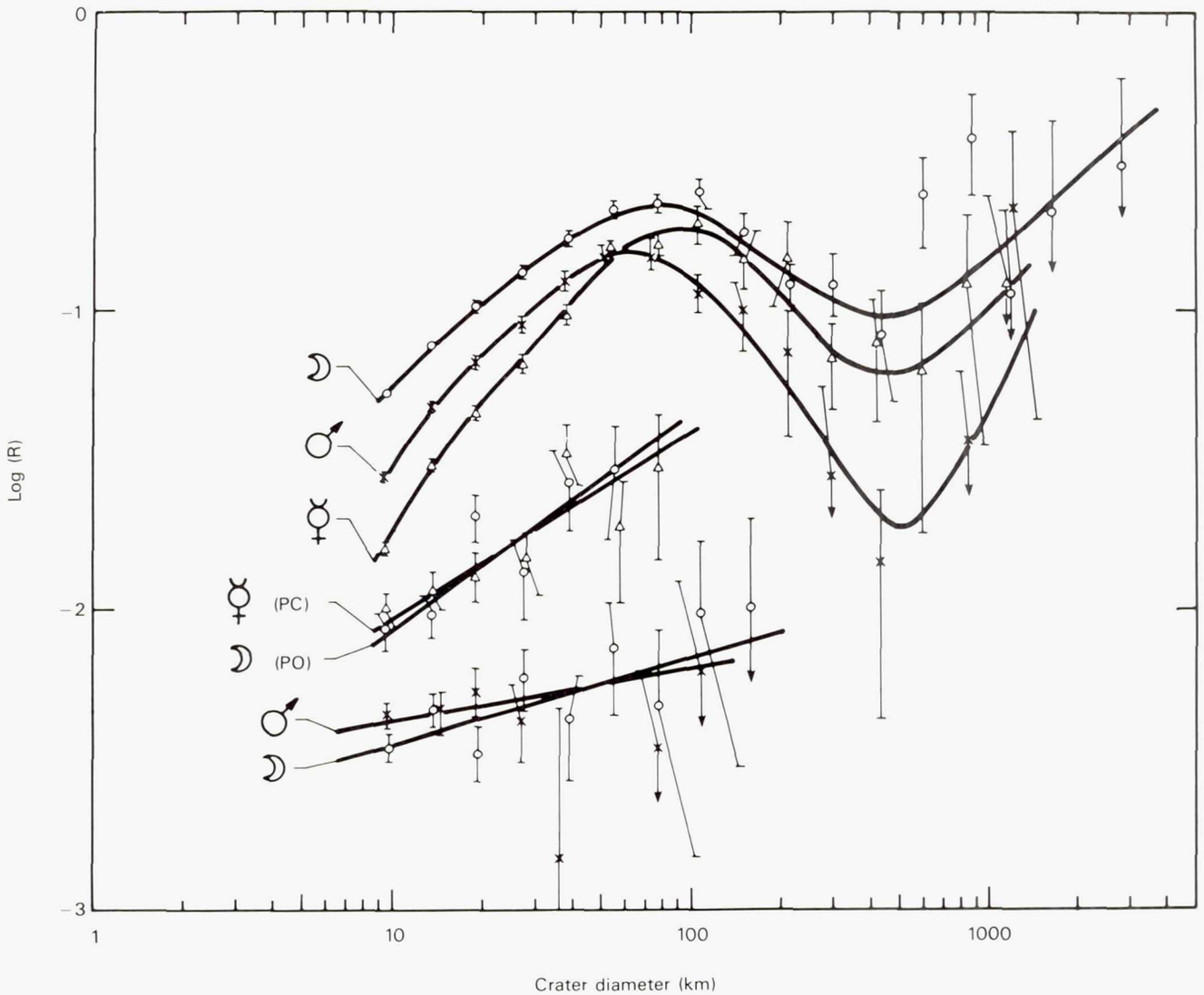

Figure 3.19. Comparison of the crater diameter/density distribution of the lunar, Mercurian, and Martian highlands; the post-Caloris (PC) and post-Orientale (PO) crater populations; and the post-mare and sparsely cratered areas of Mars. The R value is the ratio of the observed distribution function to the function $N = D^{-3}$, where N is the number of craters per unit area and D is the crater diameter.

population (Woronow, 1978; Oberbeck et al., 1977; Strom, 1977; Strom et al., 1981; Woronow et al., 1982). The same conclusion also applies to Mercury and Mars. The similarity in the overall structure of the crater diameter/frequency distribution between the Moon, Mars, and Mercury therefore suggests all three bodies were impacted by the same family of objects. One anomalous feature of the Mercurian highland curve is that at diameters less than about 80 km there is a paucity of craters compared to the Moon and Mars (fig. 3.19). Trask (1975) and Oberbeck et al. (1977) believed that the Mercurian curve more closely represents the true crater production population analogous to a lunar highland curve from which widely distributed basin secondaries have been subtracted.

Alternatively, Strom (1977) considered that the paucity of Mercurian craters relative to the Moon resulted from the obliteration of a fraction of Mercurian craters by emplacement of the intercrater plains. Locally on Mercury a crater excess occurs below a diameter of about 15 km and probably reflects the high density of craters below this diameter, which are superposed on intercrater plains. This excess has been interpreted as predominantly secondaries from craters and basins of the heavily cratered terrain (Trask, 1975; Strom, 1977). Although the overall shape of the Martian curve for the heavily cratered provinces is similar to those of the Mercurian and lunar highlands, the crater density is significantly less at both small and large diameters. It is unlikely that eolian or fluvial erosion and deposition are primarily responsible for this lower density because these processes would not obliterate all crater sizes equally. Three possible explanations are: (1) the total cumulative impact flux was less on Mars than on the Moon and Mercury, (2) an almost complete resurfacing occurred sometime after the onset of the period of heavy bombardment, or (3) surface solidification after accretionary melting occurred later on Mars than on the Moon and Mercury. The latter possibility assumes the period of heavy bombardment was contemporaneous on all three bodies. Both the post-Caloris and the lunar post-Orientale crater populations have a diameter/frequency distribution that is virtually identical in both shape and density (PC and PO in fig. 3.19). Their shapes are very similar (at the 90 percent confidence level) to those of the lunar and Martian highlands over the same diameter range and must represent production populations because of their low crater densities. This lends support to the contention that (1) the lunar and Martian highlands crater population basically represents a production population, and (2) in the case of Mercury, the paucity of craters less than about 80 km diameter resulted from obliteration of a fraction of craters by intercrater plains formation.

For the younger, more sparsely cratered surfaces of the Moon and Mars, the crater populations are quite different from those of the highlands. Both the lunar maria and Martian sparsely-cratered plains display essentially identical diameter/frequency distributions which differ significantly from those of the highlands (fig. 3.19). A Chi-squared test indicates they are different at the 99 percent confidence level. This suggests that at least the Moon and Mars were impacted by two families of objects—one primarily responsible for the period of late heavy bombardment, and the other primarily impacting after mare formation on the Moon and young plains formation on Mars. The flux history of these families on Mercury and Mars is uncertain, because it depends on the origin and source regions of the impacting objects.

In one scenario, the possibility is raised that the period of late heavy bombardment on Mercury may have been longer than that on the Moon and Mars due to an extended period of sweep-up of a family of accretional remnants (Vulcanoids) in the dynamically stable region between Mercury and the Sun (Leake et al., 1981). In spite of attempts to detect objects remaining in the region, none have yet been observed. If the impact flux history of early and late populations on the Moon was broadly similar on the other inner planets, then the earlier population consisted of short-lived objects, which were swept up in about the first billion years of solar system history, while the later population consists of long-lived objects, which have been impacting over about the past four billion years. On Mercury, the signature of this latter population has not yet been identified (Strom, 1979). Perhaps it never reached Mercury in numbers large enough to leave a recognizable signature; or the youngest surfaces on Mercury formed earlier than the lunar maria when the objects responsible for heavy bombardment still dominated. Judging by the cumulative crater density on the lunar maria, the number of objects for post-mare craters was very small compared to the earlier population, and therefore it may be mixed in with the post-Caloris craters.

However, Allen (1977) found that the diameter/frequency distributions of the rayed craters (the freshest craters) on the Moon and Mercury are different. On the Moon the rayed craters have the same distribution function as the post-mare craters; on Mercury

they appear to have a distribution function similar to the post-Caloris craters. Although this tends to support the possibility that the post-mare population never reached Mercury, the statistics these conclusions were based on are poor, and therefore the question should remain open. In any event, the two populations may represent two separate and distinct families of impacting objects or they may represent one family that evolved with time through mutual collision. If the late arriving population is missing from Mercury, it is more likely that they represent two separate and distinct families of objects.

Data on the populations of large craters and basins (>200 km in diameter) suggests that Mercury has a lower basin density than the Moon. Assuming that the unobserved part of Mercury is cratered to the same extent as the observed side, Schaber et al. (1977) found that there are 1.2 times more craters >200 km diameter on Mercury than on the Moon. However, when the difference in surface area between the Moon and Mercury is taken into account, Mercury's crater density is only 0.7 times that of the Moon. Furthermore, the areal density of basins larger than 400 km in diameter on Mercury is only 0.3 times that of the Moon, and for basins between 400 and 700 km the areal density is only 0.2 times that of the Moon. These values are in fair agreement with those of Malin (1976) and Wood and Head (1976) although there are differences among the three data sets. However, the number of basins is small, and the statistical significance questionable.

Malin (1976) observed that the areal densities of the large craters and basins on Mars, Mercury, and the Moon appear to be inversely proportional to the surface areas of the planets. Possible explanations are: (1) each planet swept separate regions of space containing a similar number of objects, (2) there was a resurfacing of the planets which varied proportionally with the area of the planet, or (3) the crusts of each planet solidified at different times during the period of heavy bombardment. Schaber et al. (1977) favored the latter explanation based on large degraded craters and basins which display well-defined secondary crater fields (fig. 3.20). They interpret the

Figure 3.20. The double-ringed basin Ma Chih-Yuan (170 km diameter) has a degraded rim but relatively well-preserved secondary impact craters. This may be the result of isostatic adjustments which have affected the large structure but not the smaller secondaries. (FDS 166665)

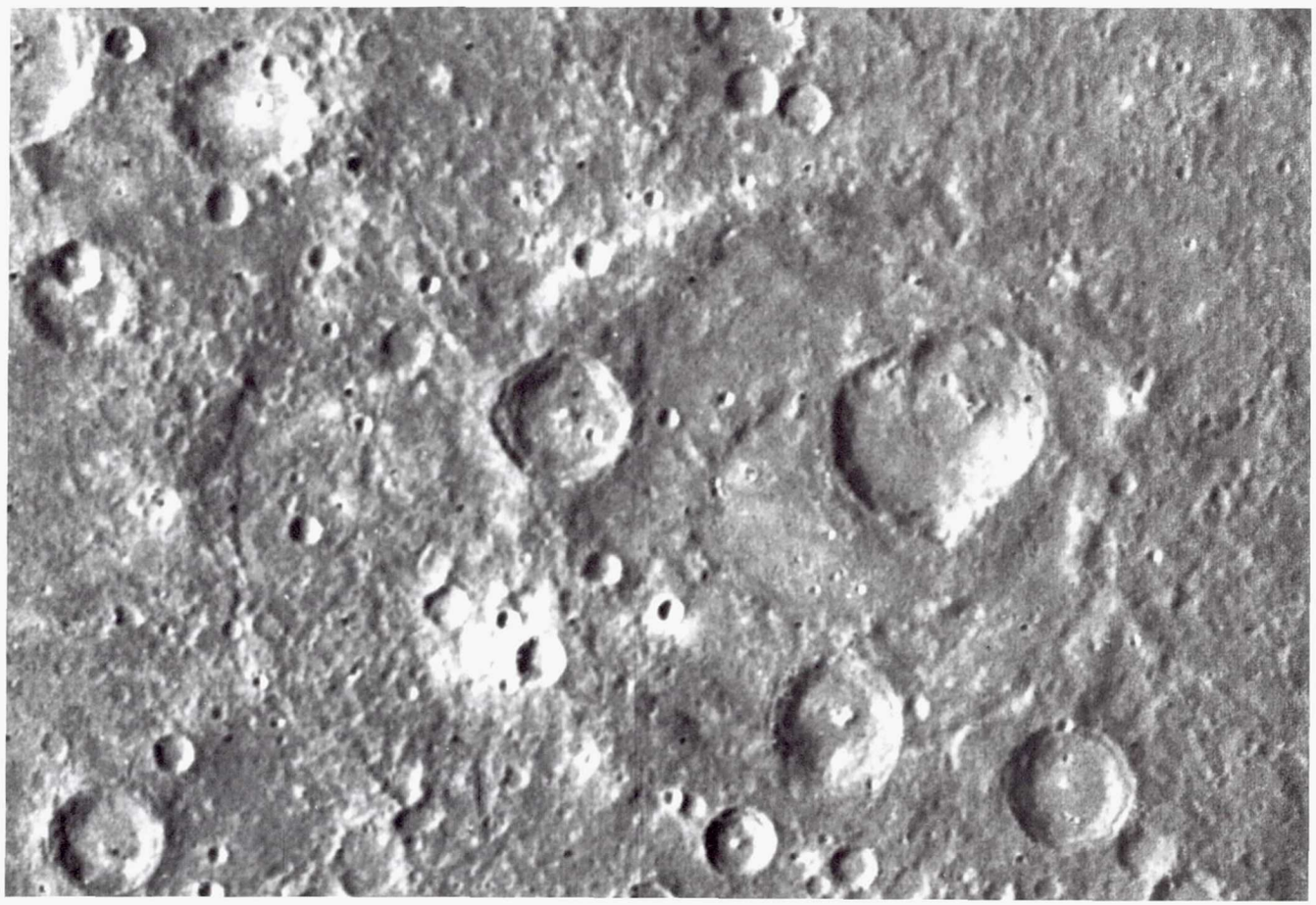

degradation of these craters as resulting from isostatic adjustments in a thermally active crust, which degraded the primary craters but preserved the secondaries. According to this explanation, the paucity of large basins and craters relative to the Moon may have been caused by a very early efficient isostatic adjustment. However, the observation that intercrater plains were, at least in part, emplaced during the period of heavy bombardment and probably obliterated at least a fraction of pre-existing craters suggests that resurfacing played a role in shaping the crater diameter/frequency distribution (Malin, 1976; Strom, 1977). In fact, Schaber et al. (1977) suggested that the viscosities of the lunar and Mercurian crusts were the same over the past 4.4×10^9 years, i.e., during the period of intense bombardment and when at least some of the intercrater plains were deposited.

MAJOR SURFACE UNITS

Four major and several local terrain types have been recognized on Mercury. Local units associated with the Caloris basin were discussed earlier. Although detailed geologic mapping may reveal sub-units of the main terrain types, the major surface units first described by Trask and Guest (1975) adequately represent the general characteristics of Mercury's surface and will be used here.

In general, Mercury's surface can be divided into two plains units, heavily cratered regions, and a peculiar hilly and lineated terrain (fig. 3.21). The plains were divided into two units, termed smooth plains and intercrater plains by Trask and Guest (1975). The smooth plains are sparsely cratered, occur primarily on the side of Mercury viewed by the outgo-

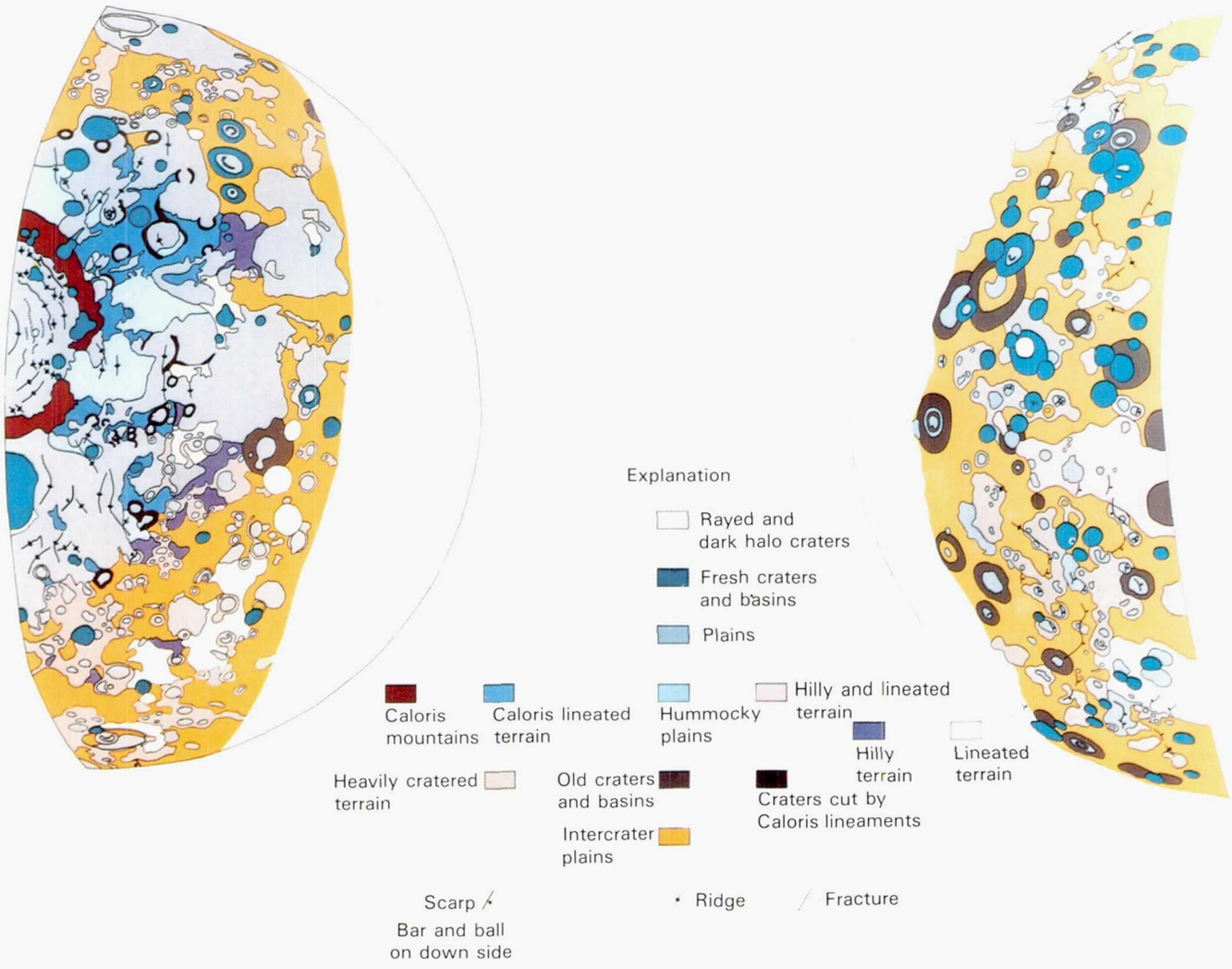

Figure 3.21. Generalized terrain map of outgoing (left) and incoming (right) sides of Mercury. The units shown on these maps are discussed in the text. The intercrater plains are contemporaneous with much of the heavily cratered terrain, not the oldest unit as indicated on the map. (From Trask and Guest, 1975.)

ing Mariner 10 spacecraft, and clearly constitute one of the youngest surface units on the planet. The intercrater plains mingle with heavily cratered regions, have a high density of superposed craters less than about 15 km diameter, and are among the oldest surface units on the planet. Because the heavily cratered terrain and intercrater plains are closely associated, they will be discussed together. The hilly and lineated terrain consists of angular to irregular hills, which disrupt many crater rims. It is locally distributed antipodal to the Caloris basin and is probably related to the impact that formed the basin.

Smooth Plains

In several respects Mercury's smooth plains resemble the lunar maria. They form relatively sparsely cratered, essentially level surfaces, overlapping more densely cratered areas (fig. 3.22). Therefore, they are one of the youngest surface units on the planet. All the larger areas of smooth plains have about the same overall density of superposed craters. They may, however, have been deposited over an extended period of time; the lunar maria, which also have similar crater densities, were deposited over a period of 1 billion years. The smooth plains display numerous ridges that grossly resemble lunar wrinkle ridges (fig. 3.22), except for the general absence of crenulated crests (Strom et al., 1975b). No regions of anomalous polarization or color occur within the smooth plains, such as those occurring in the lunar maria; suggesting a fairly uniform composition probably low in titanium. However, the smooth plains within and surrounding the Caloris basin and in the north polar region are redder than average. However, the color boundary does not always coincide with the boundary between smooth plains and other geologic units (Hapke et al., 1980).

Figure 3.22. Smooth plains southeast of the Caloris basin showing a mare-like wrinkle ridge. The dimensions of the picture are 111 × 148 km. (FDS 70)

The most extensive tracts of smooth plains occur in and around the Caloris basin and in the north polar region (fig. 3.21). Earth-based radar profiles located about 5° south of the Caloris basin and extending about 60° into the unilluminated region show a relatively smooth surface with height differences less than 1 km (Zohar and Goldstein, 1974). This suggests that plains materials extend over 2000 km beyond the terminator and possibly surround the entire basin. On the portion of Mercury viewed by Mariner 10, the smooth plains are concentrated in the northern hemisphere between 120° and 190°W (Strom et al., 1975a). Mercury, like the Moon and Mars, may therefore have an asymmetric distribution of smooth plains. However, numerous relatively small patches occur over the rest of Mercury viewed by Mariner 10. These occur especially within the heavily cratered terrain and intercrater plains; while many, if not all the interiors of large basins and old circular depressions contain smooth plains.

The origin of Mercurian smooth plains is controversial; both impact and volcanic origins have been suggested. Preliminary analyses of Mariner 10 photography prompted Murray et al. (1974) and Strom et al. (1975b) to propose a volcanic origin based primarily on their widespread distribution, morphological similarities to the lunar maria, and the observation that relatively large areas of smooth plains are younger than the basins they occupy. Wilhelms (1976) and Oberbeck et al. (1977), on the other hand, proposed that the majority of smooth plains are basin ejecta deposits similar to the lunar Cayley Formation and smooth ejecta facies associated with the Orientale basin (fig. 3.23).

The controversy over the origin of the smooth plains centers primarily on the plains within and surrounding the Caloris basin. Wilhelms (1976) correctly pointed out that the morphology of the smooth plains is similar to that of the lunar light plains, which are probably mostly basin ejecta deposits. However, a detailed investigation of thorium abundances from the gamma ray spectrometer experiment indicates that thorium concentrations in lunar light plains in the vicinity of Mare Smythii to be more consistent with volcanic deposits (Haimes et al., 1978). Furthermore,

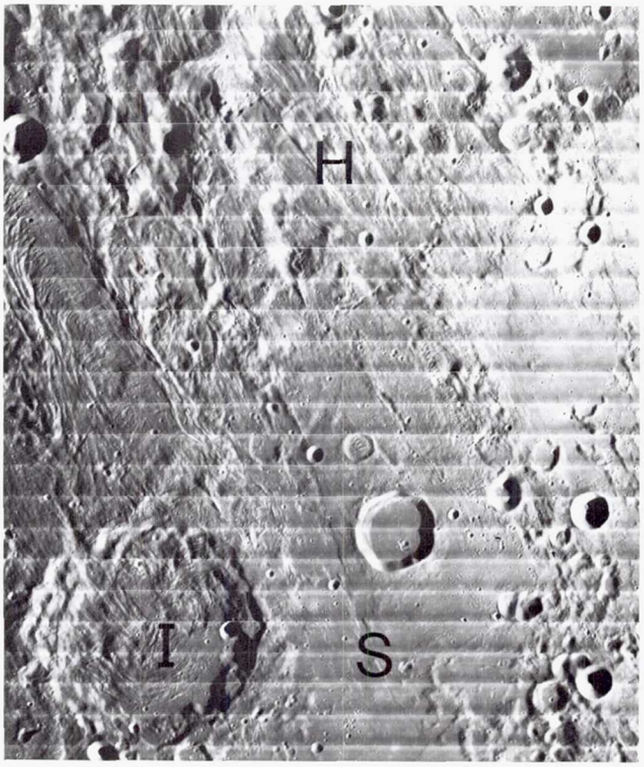

Figure 3.23. The radially braided continuous ejecta blanket (H) grades into a smooth ejecta facies (S) southeast of the lunar Orientale basin. The light smooth ejecta has the same morphology and albedo as the Cayley light plains surrounding the Imbrium basin. The crater Inghirami (I) is 91 km diameter. (LO IV, H 172)

Hawke and Head (1978) and Spudis (1978) presented evidence that the light plains comprising the Apennine Bench Formation are the result of KREEP (K = potassium, REE = rare earth elements, P = phosphorus) volcanism. Wilhelms attributes the Mercurian wrinkle-like ridges to compressive stresses and notes that they are somewhat similar to ridges in some lunar light plains. Furthermore, some Mercurian smooth plains and highlands terrain have similar albedos as have lunar light plains and highlands.

A major difference between the two deposits is that the Mercurian smooth plains cover a proportionately larger area (~15 percent of the surface viewed by Mariner 10) than do the lunar light plains (~4 percent). (See figs. 3.21 and 3.24.) Wilhelms (1976) speculated that this results because Mercurian basin ejecta was more fluid than lunar ejecta, perhaps consisting of mobilized clastic material or partly melted material. According to Wilhelms, this may be the result of large, slow impacts which could produce more partly melted material than on the Moon. However, the similar crater populations on the terrestrial planets indicate the impacting objects had a common origin (see section on crater statistics). If these objects were in heliocentric orbits of large eccentricity (e.g., asteroids or comets), then their impact velocities would have been considerably *greater* on Mercury than the Moon (Wetherill, 1975). If they were in heliocentric orbits of small eccentricity (e.g., accretional remnants), then the impact velocities would have been similar at both the Moon and Mercury. It is therefore unlikely that impact velocity can account for differences between the areal distribution of smooth plains on the Moon and Mercury.

Furthermore, Hawke and Cintala (1977) tentatively identified ponded material exterior to Mercurian craters ranging from 17 to 250 km in diameter. This material is similar to impact melt found in and around lunar craters and appears to be of comparable volume. They concluded that unless the Caloris basin formed under circumstances that did not occur on the Moon, the smooth plains cannot be completely explained by impact melt. Oberbeck et al. (1977) considered the smooth plains surrounding Caloris to have been the result of ballistic erosion and sedimentation by basin ejecta rather than emplacement of impact melt. Under this hypothesis the smooth plains formed by saturated secondary cratering, which eroded the surface and

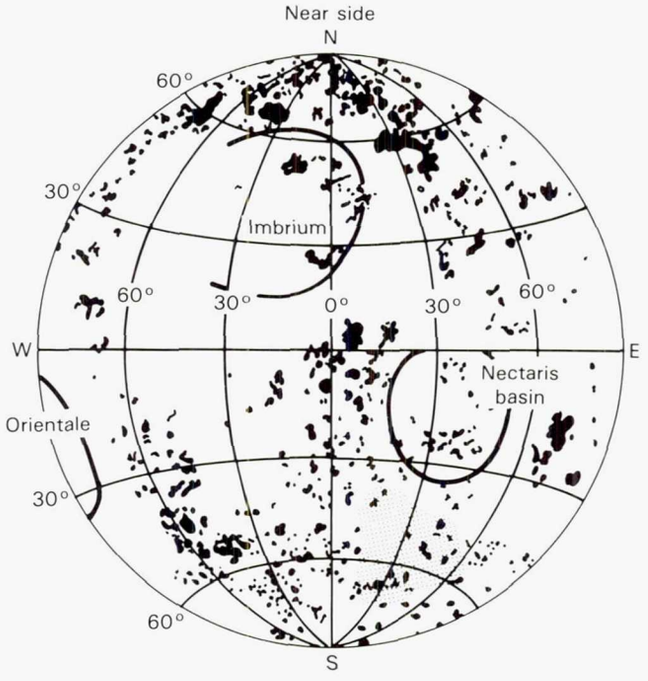

Figure 3.24. Distribution of light plains (black areas) and a region of intercrater plains (stippled area) on the near side of the Moon. (After Howard et al. (1974) with modifications.)

deposited the erosion products in low-lying areas such as craters. The greater surface gravity of Mercury concentrates the ejecta closer to the basin and thus accounts for the greater volume of smooth plains compared to similar deposits on the Moon. However, other large basins do not show a proportionately large volume of smooth plains exterior to their rims (Trask and Strom, 1976; Hawke and Cintala, 1977). One would expect comparable deposits if smooth plains are related to basin ejecta.

The volcanic hypothesis is based primarily on similarities in morphology, distribution, and age relationships between Mercurian smooth plains and the lunar maria. No unambiguous volcanic landforms such as flow fronts or domes have yet been identified in association with smooth plains. However, the apparent lack of these features may be due to the restricted coverage, constant solar elevation angle, and relatively low resolution of the available photography which is similar to Earth-based telescopic observations of the Moon. Under such observing conditions there is little evidence for a volcanic origin of the lunar maria. Several irregular rimless depressions in smooth plains within the Caloris and Tolstoj basins (see figs. 3.12 and 3.25) are probably of internal origin. Similar features on the lunar maria are thought to be caused by volcanic processes. It is possible that internally modified craters, similar to floor-fractured and mare-filled lunar craters, may be present near several plains-filled basins (Schultz, 1977). They often contain bright patches on their floors (normal albedo = 0.36–0.41) which Schultz (1977) and Dzurisin (1977) believed may result from some type of post-impact volcanic activity.

The age relationship of smooth plains relative to basins with which they are associated bears strongly on the origin of the plains. If the plains are of impact origin, then they must be the same age as their associated basin. If they are volcanic, then they must be younger than the associated basin, although the age difference need not be great. The plains interior to the Caloris basin show no flooded craters (Archimedean type craters); all craters display ejecta blankets superposed on the plains and therefore clearly postdate the emplacement of the smooth plains (Strom et al., 1975b). However, only half the basin was photographed by Mariner 10; Archimedean craters may be present on the unphotographed half. Crater statistical studies seem to indicate that the smooth plains in and around Caloris are of different relative ages and younger than the Caloris impact. Wood et al. (1977) found that, like the Moon, the number or density of Class 1 craters (the freshest) on smooth plains around Caloris is about half that in the Mercurian highlands. They concluded that the smooth plains were emplaced after the epoch of Class 1 crater formation had already begun. As previously discussed, McCauley et al. (1978) placed the Caloris impact in late Class 3 time. If these relative age assignments are correct, then the majority of smooth plains were emplaced after the Caloris impact and therefore are probably volcanic. In a recent statistical study of post-Caloris crater densities on the smooth plains and Caloris ejecta facies, Watkins and Strom (1984) found significant age differences. The two Caloris ejecta units (hummocky plains and lineated terrain) apparently have the same crater densities and are therefore the same relative age. However, the smooth plains within and immediately surrounding the Caloris basin have a variety of crater densities, which are less than those on the ejecta units. This suggests not only that the smooth plains were emplaced after the Caloris impact in agreement with the study by Wood et al. (1977), but that they were deposited over a relatively extended period.

Figure 3.25. Photomosaic of the Mercurian Tolstoj basin (400 km diameter) showing post-basin craters flooded by smooth plains (arrows) and a large elliptical and rimless depression (A) probably caused by collapse.

The normal albedo of the smooth plains within and around the Caloris basin is systematically lower than the Mercurian highlands. Most of the values of the Caloris smooth plains are about 0.12 to 0.13, whereas the Mercurian highlands (intercrater plains) are about 0.16–0.18 (see table 3.2). Also two of the three albedos listed by Hapke et al. (1975) under hummocky plains (a Caloris ejecta facies) are higher (0.14–0.15) than the plains. The anomalously low value (0.10) is found to lie not within the hummocky plains, but in the adjacent smooth plains. Although the number of measured areas is small, the current evidence indicates that the Caloris smooth plains have a different albedo and therefore possibly a somewhat different composition than the highlands and Caloris ejecta, which is consistent with, but does not necessarily prove, a volcanic origin.

Hapke's (1980) color-ratio studies showed that although the area dominated by smooth plains surrounding the Caloris basin and in the north polar region is more reddish than average, the color boundary does not generally correspond to the boundary between smooth plains and other geologic units (fig. 3.4). However, the color boundaries on the Moon derived from photographs taken at similar wavelengths also vary in correspondence to geologic boundaries where known differences in composition occur (fig. 3.26). The abundance of titanium is primarily responsible for the color differences observed on the Moon. High titanium abundances give rise to bluish mare while low titanium abundances produce reddish mare, which is indistinguishable from the color of the highlands. For instance, Sinus Iridum and contiguous portions of Mare Imbrium have the same color as the surrounding highlands as shown in figure 3.26. If the surface of Mercury is depleted in titanium relative to the Moon as Hapke's (1977) study indicated, then one would not expect good correspondence between color and geologic boundaries.

Stratigraphic studies clearly indicate that some large tracts of smooth plains in other basins post-date the basins with which they are associated. Strom et al. (1975b) and Trask and Strom (1976) noted several regions where smooth plains embay craters that post-date the basins in which they occur. Figure 3.27 is a rectified photomosaic of the Borealis Planitia region near the north pole. The smooth plains occupy a circular depression about 1000 km in diameter which contains the 300 km diameter crater Goethe, near the terminator. The plains have flooded craters within the circular depression and the Goethe crater. Furthermore, the crater density is much less on the plains than on the adjacent cratered terrain. Therefore, these smooth plains clearly post-date the formation of the 1000 km circular depression and Goethe. Wilhelms (1976) speculated that these plains were ballistically emplaced by a basin in the terminator. This basin would have to be about the same age and size as Caloris in order to produce these extensive lightly cratered plains. Because the hilly and lineated terrain antipodal to Caloris was probably produced by focused seismic waves from the Caloris impact, one would expect a similar terrain antipodal to this hypothetical basin. This terrain would occur in the sunlit portion of the south polar area, but no such terrain is found there.

The smooth plains within the 350 km Tolstoj basin show relationships similar to those at the Borealis Planitia region; i.e., embayed craters on the floor and a much lower crater density than the adjacent terrain (fig. 3.25). Furthermore, there is a good correspondence between the color boundaries and the interior fill on the north, south, and eastern edges of the basin. Also, the lowest measured albedo (0.08) occurs on the

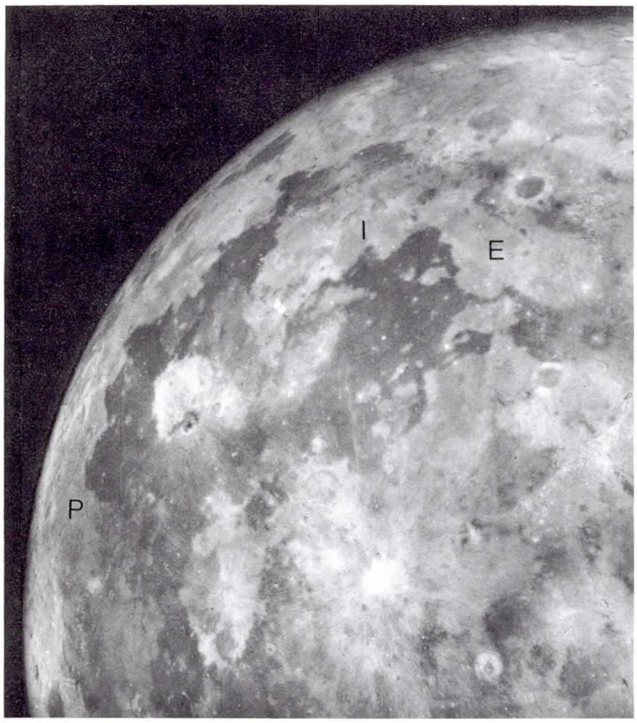

Figure 3.26. Color difference picture of the Moon centered on Mare Imbrium. This photograph is a color ratio image constructed from UV (370 nm) and red (610 nm) negatives. The light regions are reddish and the dark regions are bluish relative to the average of the whole Moon. As on Mercury (fig. 3.4) the color boundaries do not always coincide with geologic boundaries. For example, the color of Sinus Iridum (I), the eastern part of Mare Imbrium (E) and the western portion of Oceanus Procellarum (P) is indistinguishable from that of the adjacent highlands. (From Whitaker, 1972.)

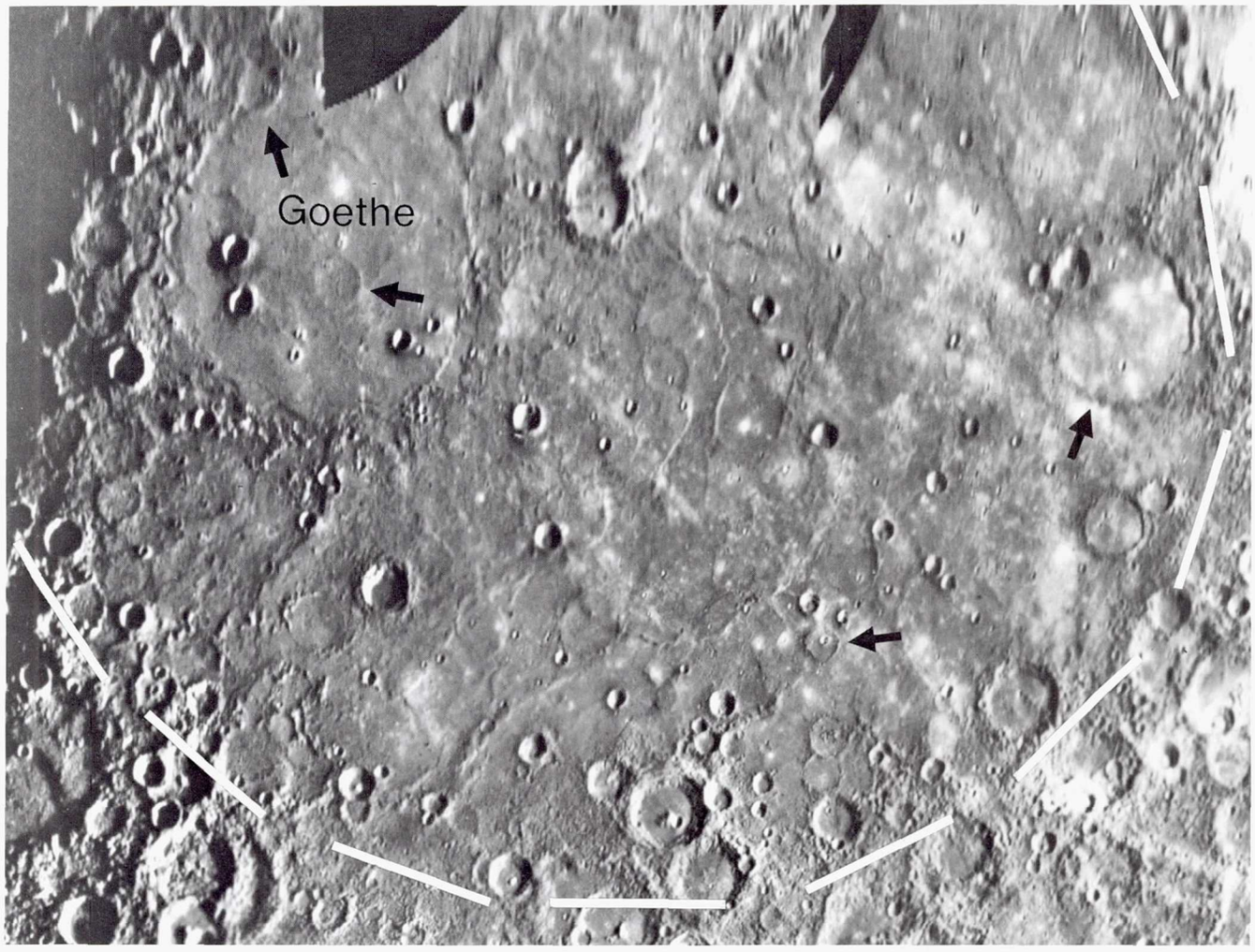

Figure 3.27. Photomosaic of the north polar region of Mercury showing numerous craters flooded by smooth plains. Craters (arrows) on the floor of the Goethe basin (340 km diameter) as well as the basin itself have been flooded by smooth plains. These plains may occupy a large circular depression about 1000 km in diameter (dashed white lines) and obviously post-date this structure and the Goethe basin.

eastern rim of Tolstoj (fig. 3.25) where the topography is very subdued and closely resembles the dark mantling material at similar locations on the Moon (such as Sulpicius Gallus and Taurus Littrow on the rim of the Serenitatis basin and in the vicinity of Rima Bode on the edge of Sinus Aestuum). These lunar materials are probably volcanic pyroclastic deposits (Head, 1976) and it is possible that the Mercurian deposits have a similar origin.

Other areas of smooth plains (i.e., Petrarch crater within the hilly and lineated terrain) show similar stratigraphic relationships and indicate in many instances that smooth plains are younger than their associated basins. Although it has been suggested that in these cases the plains were deposited ballistically from some exterior source, no evident source basins exist nearby. This suggested to Strom et al. (1975b) and Trask and Strom (1976) that at least large areas of smooth plains are volcanic deposits emplaced in a manner similar to the lunar maria.

The current evidence favors a volcanic origin for most smooth plains; a smaller proportion of smooth plains being basin ejecta or impact melt as suggested by Wilhelms (1976) and Oberbeck et al. (1977). The evidence favoring a volcanic origin is summarized as follows: (1) widespread distribution; (2) age differences between smooth plains and the basins they occupy or are adjacent to; (3) age differences between Caloris smooth plains and Caloris ejecta facies; (4) morphological similarity between smooth plains and lunar maria; (5) similarity in the physical properties of mare basalts and smooth plains suggested by comparative crater morphology; (6) apparently similar volumes of impact related deposits around lunar and Mercurian craters of equal size; (7) possible internal modifications of craters near areas of smooth plains; and (8) albedo differences between smooth plains in and around Caloris and other geologic units.

Although no single line of evidence by itself proves a volcanic origin, the combined observations tend to

support this hypothesis. Until more definitive evidence is presented to the contrary, the volcanic origin of much of the smooth plains appears to be a good working hypothesis.

Intercrater Plains and Cratered Terrain

The most widespread terrain type on Mercury is the intercrater plains first described by Trask and Guest (1975). It consists of level to gently rolling plains with a high density of superposed craters less than about 15 km diameter (figs. 3.28 and 3.29). These plains occupy about 45 percent of the highland surface viewed by Mariner 10 and occur between and around clusters of large craters in the more heavily cratered terrain. Many of the superposed small craters form chains or clusters suggestive of secondary impact craters. The high density of superposed craters and stratigraphic relationships clearly indicates that the intercrater plains are older than the smooth plains and that they form some of the oldest terrains on Mercury. Both the Moon and Mars also have intercrater plains. On the Moon, the intercrater plains, termed Pre-Imbrium Pitted Plains, have an extremely limited distribution (see figs. 3.24 and 3.30). Both a volcanic (Scott, 1972; and Strom, 1977) and impact (Howard et al., 1974) process have been suggested for their origin. The intercrater plains on Mars have a somewhat different morphology. They lack the high density of superposed small craters and often contain lunar-like wrinkle ridges (fig. 3.31). Martian inter-

Figure 3.28. Large areas of Mercurian intercrater plains (IP). (FDS 27328)

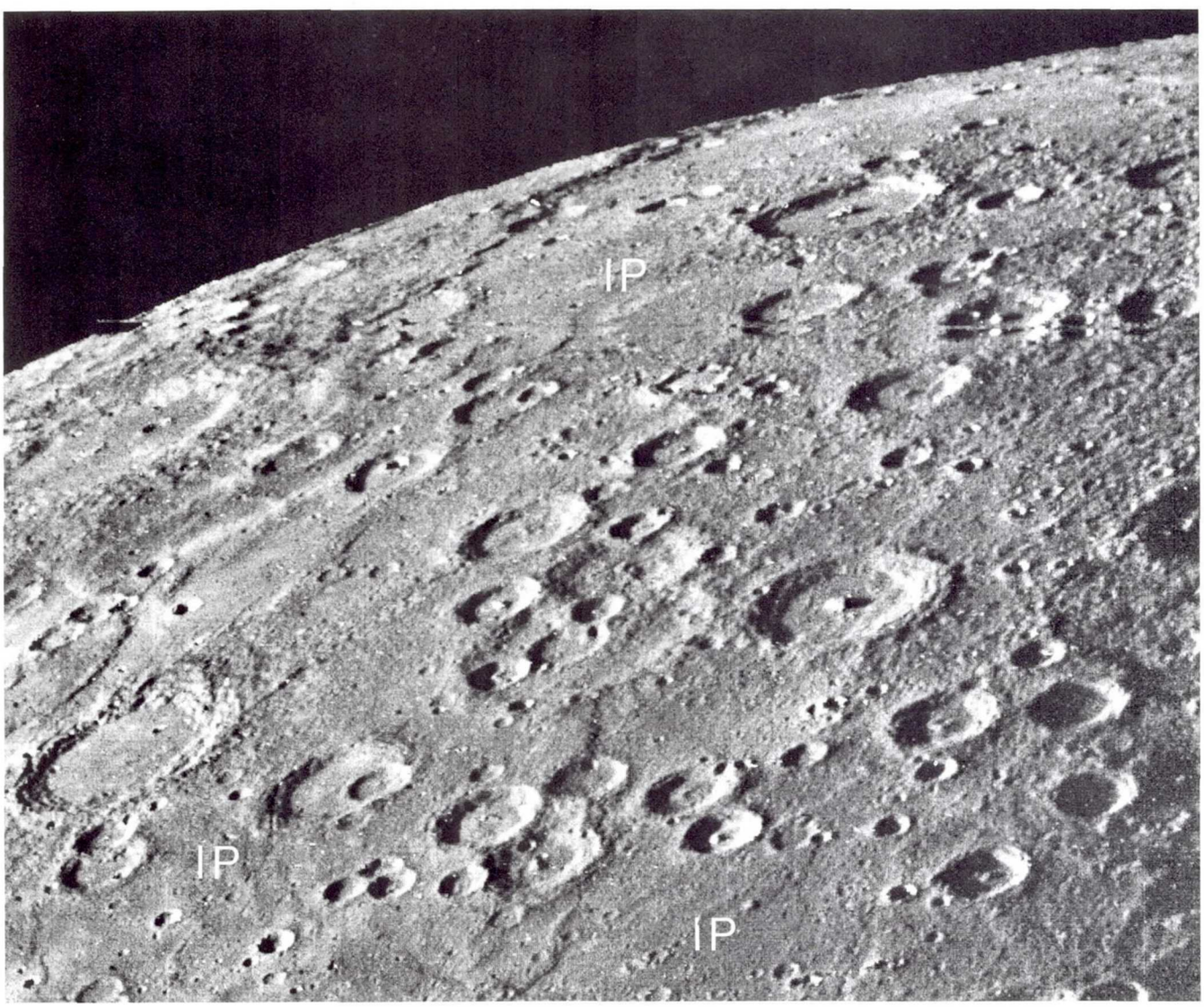

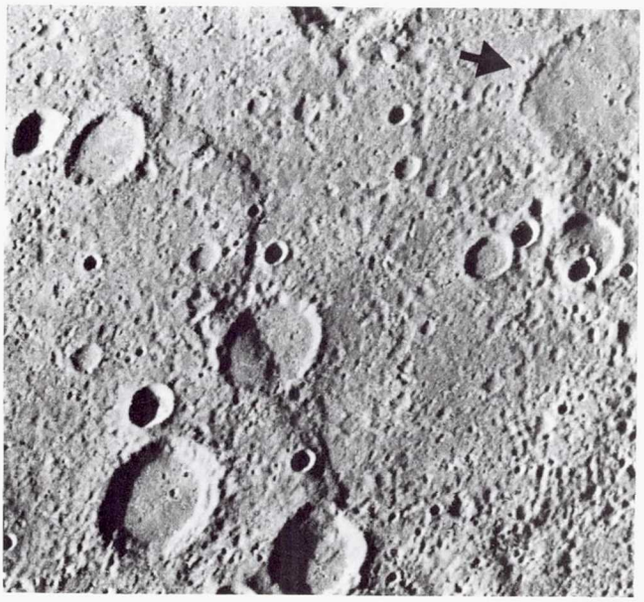

Figure 3.29. High resolution picture of typical intercrater plains. Abundant shallow elongate craters and crater chains are present on the intercrater plains and are probably mostly secondary impact craters from fresher craters and basins of the more heavily cratered terrain. The arrow indicates a 90 km diameter crater which has been embayed by intercrater plains, and therefore, pre-dates the intercrater plains. (The photo is 400 km across.) (FDS 27448)

crater plains have been attributed to early volcanic activity (Wilhelms, 1974).

The age of Mercurian intercrater plains relative to the heavily cratered terrain has important implications for the early history of Mercury. Trask and Guest (1975) and Trask (1976) considered most of the intercrater plains to be older than the craters comprising the heavily cratered terrain because of the abundance of superposed secondaries which they believed were derived from these craters. However, Malin (1976a), Strom (1977), and Leake (1981) noted many old craters which have been embayed by intercrater plains (fig. 3.29). Therefore, some highland craters must predate at least a portion of intercrater plains. In the diameter range of about 20–50 km, the lunar highlands are more heavily cratered than the highlands of Mercury (Murray et al., 1974; Trask, 1976; Oberbeck et al., 1977; and Strom, 1977). Trask (1976) and Oberbeck et al. (1977) considered the Mercurian crater population to more closely represent the original production population in this size range and that the greater crater density in the lunar highlands is due to basin secondaries. However, Strom (1977) showed that the distribution function of the lunar post-Orientale production population is about the same as that of the lunar highlands, suggesting that the crater

Figure 3.30. Region of lunar intercrater plains (IP) southwest of the Nectaris basin in the lunar highlands. (Compare with figs. 3.29 and 3.31.) The crater Nicolai (N) is 42 km diameter. (LO IV, H-88)

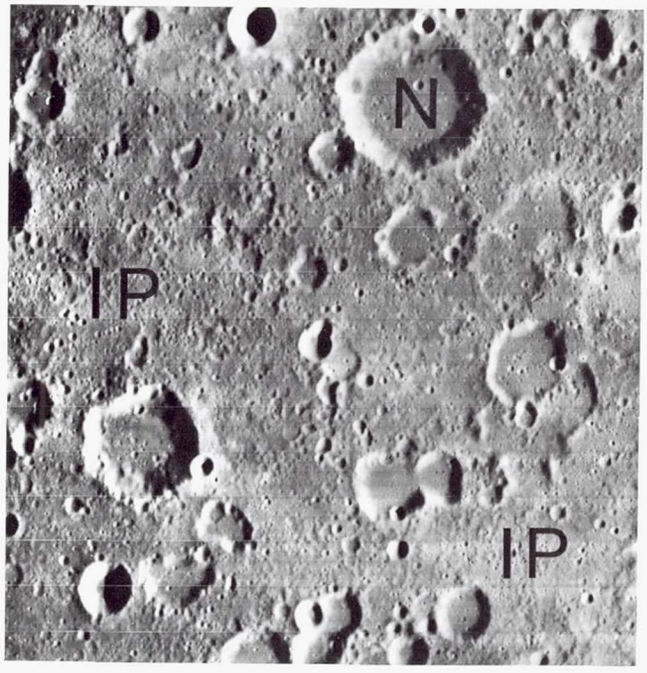

Figure 3.31. Region of Martian intercrater plains in the heavily cratered southern highlands of Mars. (Photo is 260 km across.) (VO97A05).

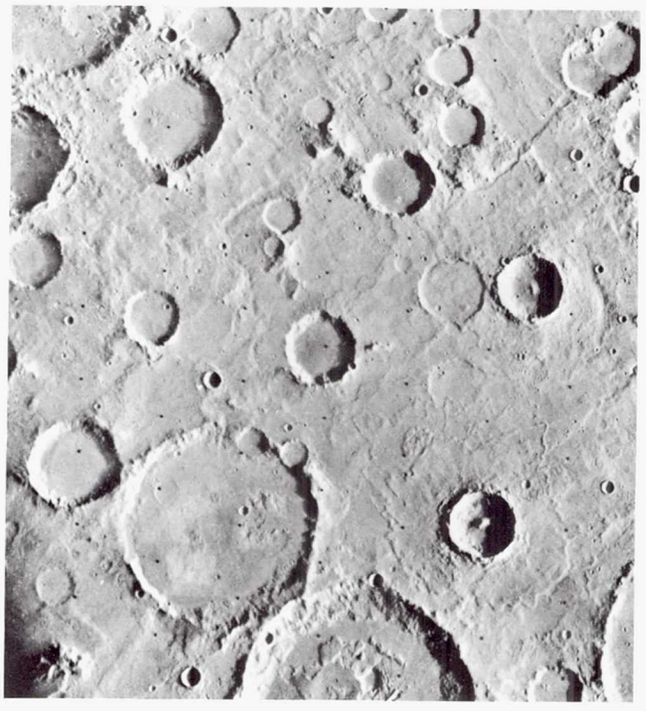

population in the lunar highlands is also basically a production population. Strom suggested that because the Mercurian intercrater plains have embayed some craters, a certain fraction of pre-existing craters must have been obliterated and therefore the paucity of craters relative to the lunar highlands is the result of obliteration by intercrater plains formation. Furthermore, Leake (1981) attempted to date the intercrater plains relative to the various crater degradational classes by superposition of ejecta blankets and embayment relationships. Leake found that intercrater plains were emplaced *during* the formation of Class 5 through Class 3 craters and that the volume of plains generally decreases as age decreases (fig. 3.32). The secondary craters superposed on the intercrater plains appear to be derived mainly from the Class 1-3 craters and Class 4 basins of the heavily cratered terrain. Patches of plains emplaced during the formation of Class 1 and 2 craters are equivalent to the smooth plains discussed earlier. The embayment of certain craters and basins by intercrater plains, their age relative to crater degradational classes, and the paucity of 20–50 km craters relative to the lunar highland crater population strongly suggest that the intercrater plains span a range of ages. They appear to have been emplaced *during* the period of heavy bombardment but the volume apparently decreased with time. The formation of intercrater plains and smooth plains may *not* represent two distinct plains-forming episodes. Instead they may represent a more or less continuous period of plains formation lasting from sometime during the period of heavy bombardment through the emplacement of the youngest smooth plains.

The origin of intercrater plains is less certain than that of the smooth plains. As in the case of smooth plains, both an impact and volcanic origin have been suggested. Wilhelms (1976) and Oberbeck et al. (1977) considered them to be an older basin ejecta facies

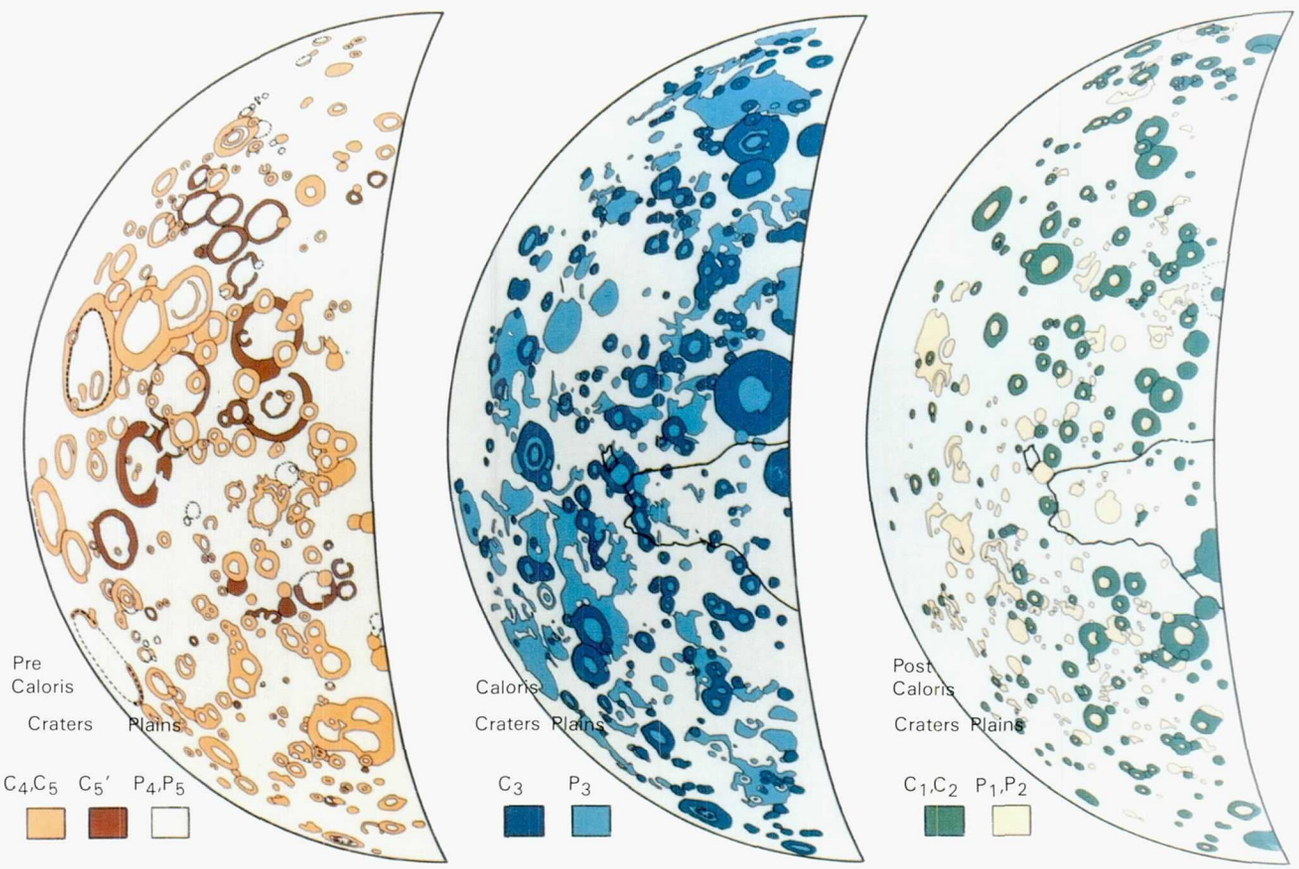

Figure 3.32. Paleogeologic maps of Mercury's incoming side showing the distribution of craters and plains of various relative ages. The oldest craters (C_4–C_5) and plains (P_4–P_5) predate the hilly and lineated terrain outlined by the solid line and are probably pre-Caloris age. C_5 craters predate P_4–P_5 plains. The youngest craters (C_1–C_2) and plains (P_1–P_2) post-date the hilly and lineated terrain and are probably post-Caloris age. The P_5–P_3 plains are equivalent to intercrater plains and P_2–P_1 plains are smooth plains. (From Leake, 1981.)

formed during the period of heavy bombardment. However, a major drawback to this hypothesis is the apparent lack of source basins to account for such a widespread distribution of these plains. Schaber et al. (1977) found that the density of basins <400 km diameter on Mercury is only 30 percent of that on the Moon, and for basins between 400 and 700 km in diameter the density on Mercury is only 21 percent of the lunar basin density. Although the lunar highlands contain small areas of intercrater plains (particularly southwest of the Nectaris basin), their distribution is extremely limited compared to that on Mercury (compare figs. 3.21 and 3.24); yet the density of basins is considerably greater on the Moon. Wilhelms (1976) accounted for this difference by speculating that the crust of Mercury was more plastic than that of the Moon, and that impacts in this "softer" and "hotter" material would produce more impact melt than on the Moon. However, based on apparent total isostatic compensation of ancient basins 800 km in diameter, Schaber et al. (1977) calculated that the average viscosity of the Mercurian crust was about the same as that for the Moon. This suggests that during the period of intense bombardment (during intercrater plains formation) the lunar and Mercurian crusts had similar viscosities.

Evidence for a volcanic origin of intercrater plains is based upon the tentative identification of volcanic landforms, the areal coverage of intercrater plains relative to coverage by craters of the same age, and the overall widespread distribution of these deposits. Malin (1978) and Leake (1981) identified several features in the Mercurian highlands which may be volcanic. These are primarily domical structures, one of which is 30 km in diameter, 2 km high, and has concave lower slopes and convex upper slopes. Malin and Leake considered these features to be volcanic constructs. Dzurisin (1976) also identified linear ridges associated with intercrater plains which he considered to be the sites of extrusive activity. However, the evidence for volcanism associated with these features is not as compelling as that for Martian constructs and the question of their origin should remain open. The main argument for a volcanic origin of intercrater plains is their very widespread distribution compared to lunar deposits considered to be basin ejecta. Leake's (1981) paleogeologic maps of intercrater plains and craters on Mercury show their distribution at various times (fig. 3.32). The areal extent of intercrater plains appears to decrease as age decreases, but there is little relationship between their distributions and craters of similar age. The proportion of intercrater plains to craters of the same age varies greatly from region to region and does not correlate with crater size. This suggests the emplacement of intercrater plains was unrelated to the formation of craters, which implies an internal origin for intercrater plains. Similar relations (fig. 3.32) suggest at least some of the smooth plains may be volcanic. Furthermore, from crater morphological studies (Cintala et al., 1977), the physical properties of intercrater plains appears to be more similar to those of the lunar maria and Mercurian smooth plains than the megaregolith of the lunar highlands. However, impact melt may have properties similar to volcanic flows. In short, the geological evidence is not sufficient to decide between the basin ejecta or volcanic origin of intercrater plains, although a volcanic origin is favored based on the evidence presented above. Thermal history models suggest a magma source and tectonic setting which could produce volcanic activity on a global scale early in Mercurian history.

Hilly and Lineated Terrain

The most peculiar terrain viewed by Mariner 10 consists of hills and depressions which disrupt preexisting landforms, particularly crater rims (Trask and Guest, 1975). This terrain forms a slightly elongated area which is directly antipodal to the Caloris basin (figs. 3.21 and 3.33). The hills are 5–10 km wide and 0.1–1.8 km high (fig. 3.34). Linear depressions with scalloped rims display a rough orthogonal pattern trending northeast and northwest. Several large craters, whose rims have been severely broken up into hills and depressions, contain smooth plains which have not been disrupted (fig. 3.33). Clearly these smooth plains post-date the formation of hilly and lineated terrain.

Schultz and Gault (1975) identified similar terrain antipodal to the lunar Imbrium and Orientale basins. However, the Mercurian hilly and lineated terrain covers a larger area and is more pronounced than its lunar counterpart. They suggest that the terrain is the result of focused seismic waves caused by large basin-forming impacts. Lagrangian computer simulations of shock wave propagation indicate that antipodal seismic effects are significantly enhanced by focusing and are of a magnitude sufficient to cause vertical ground motion of about a kilometer or more and accelerations approaching lunar gravity (Hughes et al., 1977). Furthermore, the seismic effects are significantly more pronounced for a molten planet than a

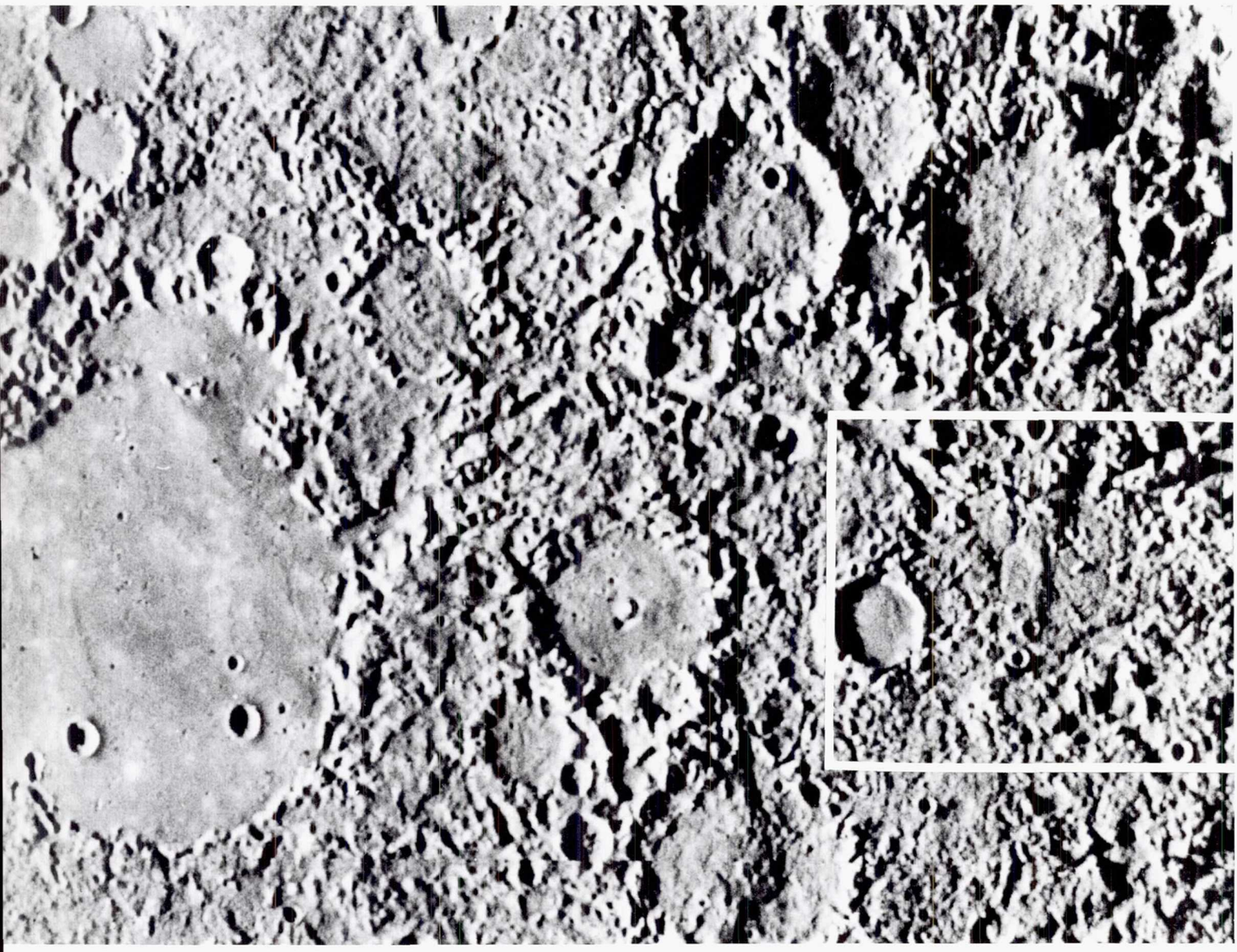

Figure 3.33. Hilly and lineated terrain antipodal to the Caloris basin. Crater rims have been broken up into hills and valleys but in certain cases the smooth plains filling the craters have not been. Therefore these smooth plains post-date the craters in which they lie. (The picture is 543 km across.) (FDS 27370)

solid one, and tensile failure may occur at depths of tens of kilometers below the antipode. Leake (1981) found that Class 1 and 2 craters are superposed on the hilly and lineated terrain, whereas craters of Class 3 and 4 straddling the boundary have had part of their rims disrupted. This places the formation of the hilly and lineated terrain approximately between the production of Class 2 and 3 craters, which is in agreement with the age of the Caloris impact derived by McCauley (1978). Although Wilhelms (1975) suggested that the hilly and lineated terrain is the result of the dissection of the surface by ejecta from basins hidden in the terminator, its Caloris antipodal location, lunar analogs, similar age relative to the Caloris impact, and computer modeling strongly suggest that it was caused by the disruption of the surface induced by focused seismic waves from the Caloris impact. If the smooth plains within several large craters disrupted by this terrain are volcanic deposits, as suggested by Trask and Strom (1976), then it is possible that the tensile fracturing caused by the seismic waves tapped a magma source and provided egress for the eruption of these deposits.

TECTONICS

Of the terrestrial planets explored to date, Mercury displays a unique tectonic framework. This tectonic framework is characterized by the widespread (probably global) distribution of large lobate scarps. These scarps are found on virtually all types of terrain viewed by Mariner 10 and often reach lengths of several hun-

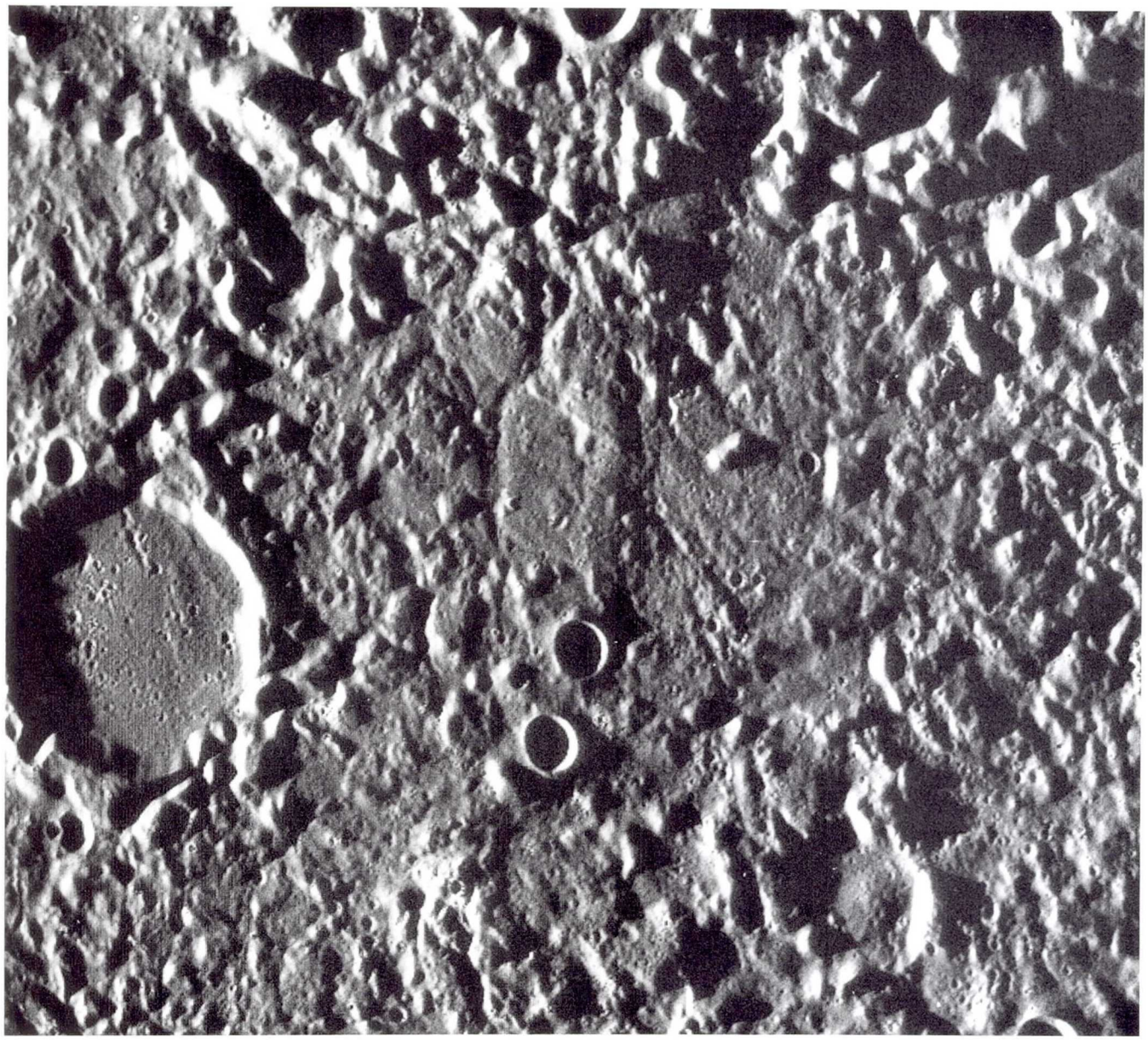

Figure 3.34. High resolution picture of the hilly and lineated terrain. The region has been broken up into hills from about 0.1 to 1.8 km high which are interspersed with smooth material. The largest crater is 31 km in diameter. (FDS 27463)

dred kilometers and heights of about 1 km or more. A system of probably older structural lineaments also has been recognized. These lineaments are primarily represented by linear ridges, valleys, and segments of crater rims showing preferred orientations. To a large extent this tectonic framework is either the direct or indirect result of the formation of Mercury's large iron-rich core and consequent thermal history. However, crustal stresses produced by planetary despinning from an earlier, more rapid rotation rate also may have contributed to Mercury's surface structure.

Lobate Scarps and Lineaments

Lobate scarps are relatively steep escarpments, which generally have a lobate outline on a scale of a few tens of kilometers (Strom et al., 1975b). They vary in length from about 20 km to over 500 km and have heights of a few hundred meters to about 1 or 2 km (figs. 3.29 and 3.35). The crests of the scarps are rounded and the slope of the terrain behind the scarps varies from flat to gently dipping away from the scarp. Often individual scarps transect several terrain types including craters, intercrater plains, and smooth plains. Dzurisin (1976) classified lobate scarps into three types based on large-scale planimetric geometry. However, in detailed morphology they all display the characteristics described above and probably have a common origin. Some scarps are confined to the smooth plains comprising the floors of craters. Although some of these scarps may be flow fronts, a

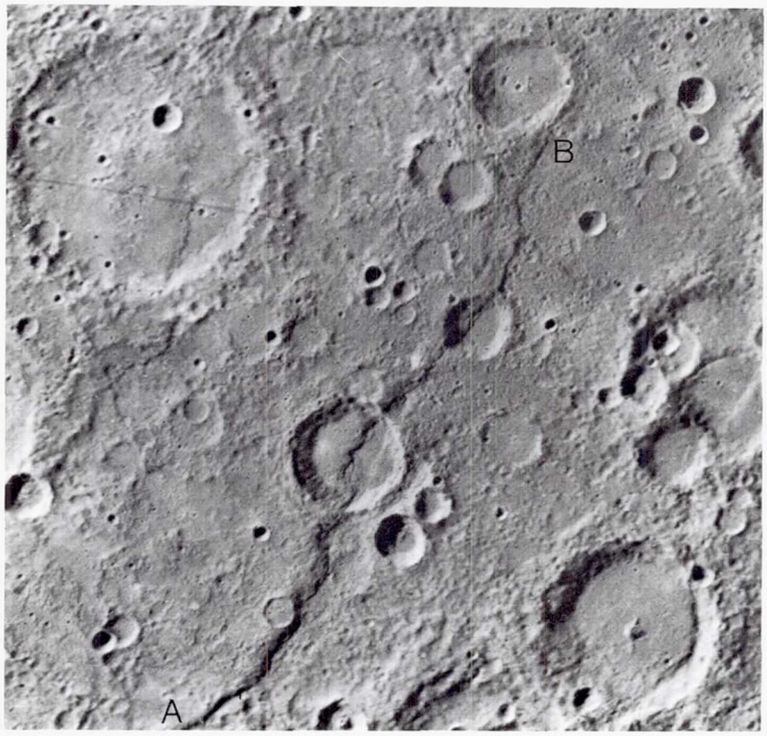

Figure 3.35. Photomosaic of Discovery scarp (A-B). This lobate scarp is one of the largest scarps on Mercury and is probably a thrust fault. It is about 2 km high and over 500 km long, and transects two craters 55 and 35 km in diameter.

tectonic origin is likely for most. The majority of lobate scarps show transection relationships, a general linear trend, large dimensions, and in one case a horizontal offset of a large crater's rim, which indicates a tectonic origin. Strom et al. (1975b) noted that the morphology and overall geometry of these scarps are unlike normal faults seen on the Moon and Mars, and propose that they are thrust or reverse faults caused by compressive stresses. In fact, the southwestern part of the crater wall of Guido d'Arezzo has been horizontally displaced 10 km by Vostok scarp (fig. 3.36). This is consistent with thrusting of the northeastern part of the crater over the southwestern part, causing a shortening of the radius of the crater and the apparent horizontal offset of the wall. By analogy, the vast majority of lobate scarps are probably thrust or reverse faults caused by compressive stresses. Furthermore,

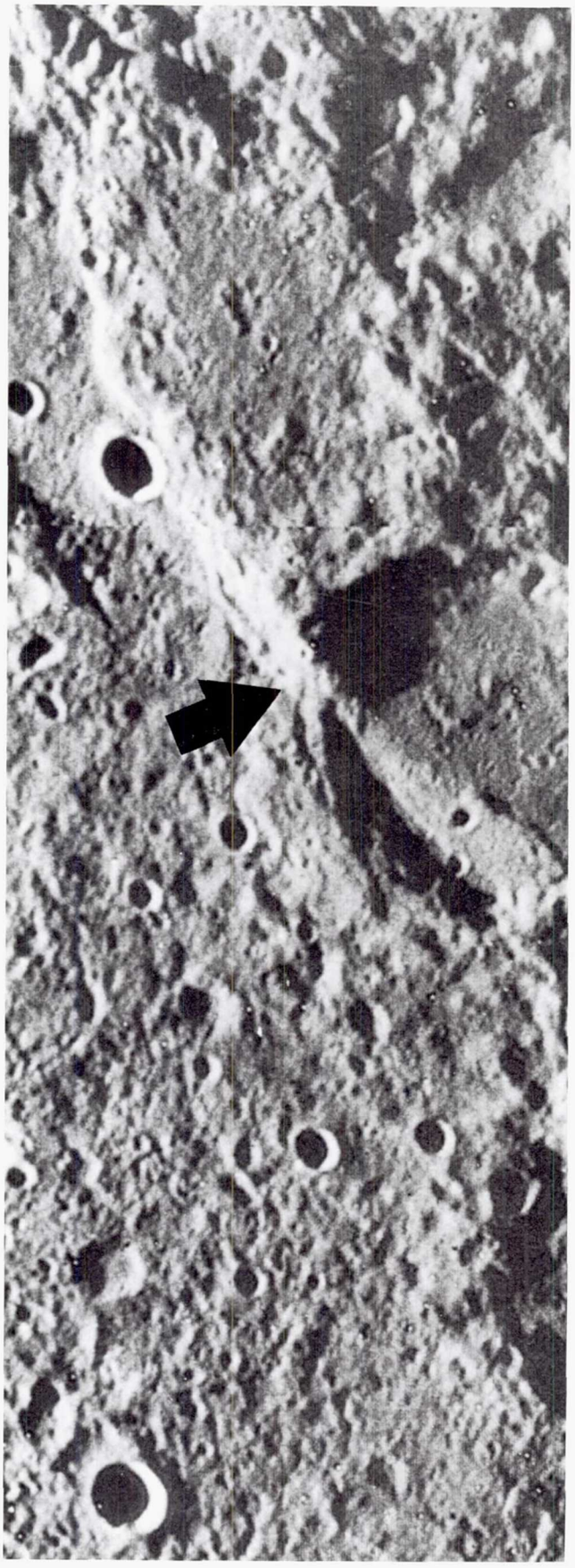

Figure 3.36. The 130 km long Vostok scarp transects two craters (lower crater is Guido d'Arezzo) 80 and 65 km in diameter. The northwestern rim of Guido d'Arezzo has been offset about 10 km by the scarp (arrow). This offset was probably caused by shortening of the crater due to thrusting of the eastern part of the crater over the western part. (FDS 528858)

the lobate scarps are more or less evenly distributed over the surface viewed by Mariner 10 (fig. 3.37), and therefore the entire planet appears to have been subjected to compressive forces which caused a general crustal shortening. From estimates of the fault plane inclination, average height, and measured lengths of lobate scarps, and assuming that the area measured is representative of the planet as a whole, Strom et al. (1975b) estimated that there has been a total decrease in surface area of about 6.3×10^4 to $1.3 \times 10^5 km^2$ (equivalent to a 1–2 km decrease in the radius of Mercury). This value is remarkably close to that calculated for a radius decrease based on thermal history models (Solomon, 1976). In addition to lobate scarps, Dzurisin (1976), and Masson and Thomas (1977) recognized a system of structural lineaments having preferred orientations and closely resembling the lunar lineament system (Strom, 1964). The lineaments consist of ridges, troughs, and linear segments of crater rims. They have at least three, possibly five, preferred orientations trending northeast, northwest, and north-south. The lunar lineament system also shows the same three orientations (Strom, 1964). Dzurisin (1976) considered the Mercurian lineaments to represent modifications of linear crustal joints formed in response to stresses induced by tidal spindown.

The lobate scarps transect intercrater plains, craters, and smooth plains, but in several instances they also have been disrupted by moderate-sized impact craters. However, the craters which disrupt scarps are primarily of Class 1 and 2 degradational types. No intercrater plains have been observed to embay the scarps. This suggests that scarp formation began after inter-

Figure 3.37. Map of the lobate scarps, ridges, plains, and the hilly and lineated terrain on the outgoing (A) and incoming (B) sides of Mercury. (After Strom et al., 1975.)

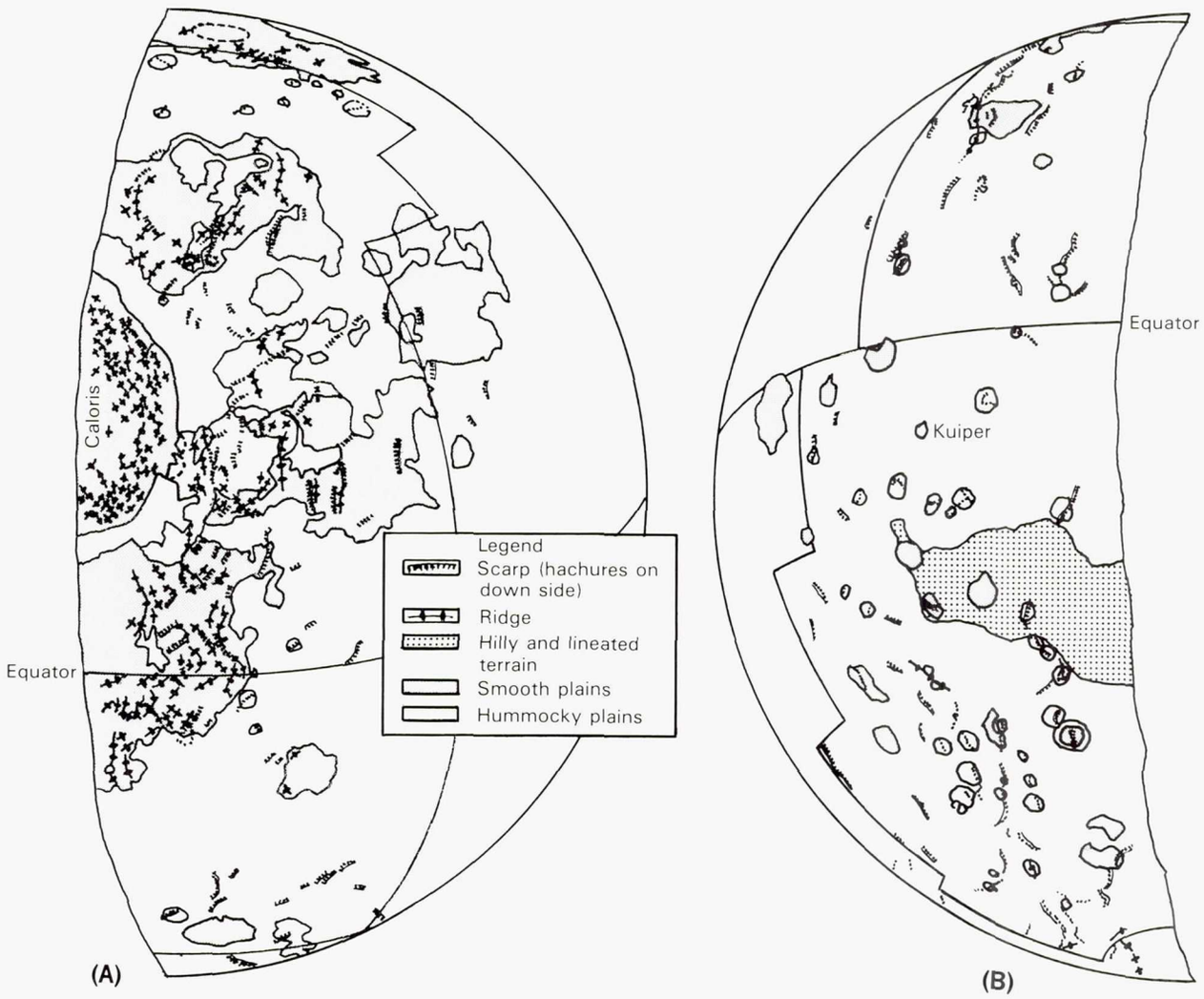

crater plains emplacement, sometime near the end of heavy bombardment, and extended some undetermined time beyond smooth plains emplacement. Lobate scarps transect the smooth plains around the Caloris basin but they are apparently smaller and fewer than those found in the Mercurian highlands. In general, the lineament system is probably older and pre-dates most of the lobate scarps. Dzurisin (1976) pointed out that many large degraded craters and basins show polygonal outlines, suggesting that the joint pattern was established well before the end of heavy bombardment. Furthermore, several lobate scarps have linear segments with trends similar to nearby lineaments, suggesting that some scarps formed along pre-existing joints. Also linear troughs in the hilly and lineated terrain are aligned along trends defined by lineaments elsewhere, and may have formed along pre-existing joints during seismic jostling from the Caloris impact.

The surface of Mercury viewed by Mariner 10 is remarkably free of structures resulting from tensile stresses. Only two areas contain structures which were probably produced by tension and both are associated with Caloris (figs. 3.17 and 3.33). The fractures on the floor of the Caloris basin are probably graben, resulting from an uplift of the floor; troughs in the hilly and lineated terrain antipodal to Caloris may be graben which formed along pre-existing joints during vertical ground motions induced by focused seismic waves from the Caloris impact. No circumferential graben or normal faults are found exterior to basins, as often occurs on the Moon, nor are there systems of radial graben, as occur on Mars. The present surface of Mercury appears to have been dominated by compressive stresses.

Causes of Crustal Deformation

Two main hypotheses have been proposed to account for the tectonic framework of Mercury: (1) a change in the shape of the planet due to despinning from an initially higher rate, and (2) global contraction due to cooling from an initially higher temperature. According to the first hypothesis, tidal slowing of the rotation from an initially higher rate (20 hrs) results in a decrease in polar flattening, producing crustal stresses well above the fracture limit (Burns, 1976; Melosh, 1977; Melosh and Dzurisin, 1978b). Depending on the value of the planetary dissipation constant (Q) the time required to despin Mercury from a rotation period of 20 hours to the present period of 58.6 days is 0.2 to 2.0 billion years (Goldreich and Soter, 1966). The stress regime resulting from despinning produces three zones of faulting: (1) an equatorial zone of compression containing north-south trending thrust faults, (2) a mid-latitude zone of shearing stress containing an orthogonal set of NW and NE trending wrench faults, and (3) polar zones of tensile stress containing east-west trending normal faults (Melosh, 1977; Melosh and Dzurisin, 1978b). However, the south polar region of Mercury displays numerous lobate scarps (thrust faults) but no evidence of normal faulting, although structural lineaments are present here as well as in other areas of the planet. As a result it has been necessary to invoke a combination of despinning and global contraction to account for compressive stresses in the polar regions (Pechmann and Melosh, 1979). The relative importance of despinning and contraction to the development of Mercury's tectonic framework depends on various parameters such as the ratio of the time constant for despinning to that for contraction.

The hypothesis of global contraction to explain the tectonic framework initially invoked a partial solidification of the large iron core (Murray et al., 1979; Strom et al., 1975b). However, Solomon (1976) found that cooling of the lithosphere following core formation alone can account for the radius decrease estimated by Strom et al. (1975b). A solidification of an inner core up to 60 percent of the radius of the outer core, or more likely a combination of lithospheric and inner core cooling (1050 km radius) would satisfy the estimated limits on global contraction (Solomon, 1977). Complete or even extensive solidification of a once molten core is excluded by the limitation on total radius change. This is consistent with a convective dynamo mechanism for the generation of Mercury's magnetic field (Ness, 1978). Global contraction should lead to a more or less random distribution of compressive stresses to produce an azimuthally random distribution of thrust faults on a global scale. Contrary to measurements of Melosh and Dzurisin (1978b), Cordell and Strom (1977) found that the azimuthal distribution of lobate scarps is more or less random (fig. 3.38). Furthermore, the lineament system is an apparently ancient fracture system and predates the formation of lobate scarps (Dzurisin, 1976), whereas they should be more or less contemporaneous under the spindown hypothesis. Although despinning may have influenced the tectonics of Mercury, the azimuthal and areal distribution of lobate scarps, together with their age relationships, suggests that contraction

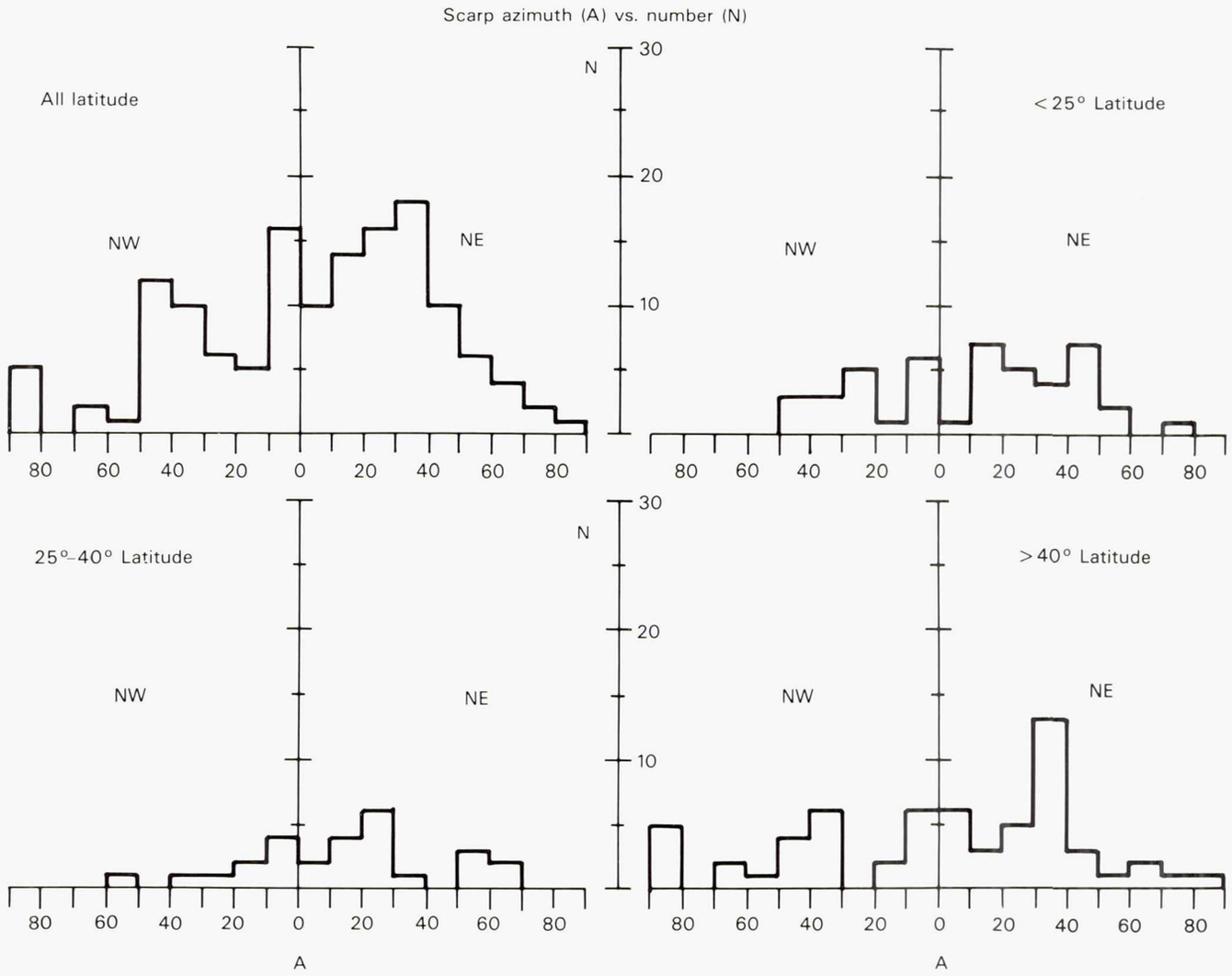

Figure 3.38. Azimuth-frequency histograms of lobate scarps for all latitudes (− 90° to ± 60°), latitudes between ± 25° (< 25° plot), latitudes between + 25 to + 48° and − 25 to − 40° (the 25–40° plot), and latitudes between − 40 to − 90° and + 40 to + 60° (> 40° plot) on the incoming side of Mercury. (After Cordell and Strom, 1977.)

due to cooling of the lithosphere and/or core following core formation was the dominant mechanism responsible for the presently observed tectonic framework.

SURFACE HISTORY AND THERMAL EVOLUTION

The surface history of Mercury is a reflection of its thermal history. If both the smooth and intercrater plains originated by impact basin ejecta processes, then it is likely that little or no volcanic activity occurred on Mercury, at least during the history recorded on its surface. This would imply that either the thermal regime throughout most of its history has led to little melting or there were no means by which magmas could reach the surface in any large quantity. Mercury would then be unique among the terrestrial planets because all others have experienced thermal histories which resulted in extensive volcanic activity over large areas of their surfaces. Indirect evidence suggests, however, that Mercury has experienced considerable melting comparable to, if not more than, the other terrestrial planets. Melting models for the terrestrial planets based on a comparison of various heating mechanisms relative to the Moon indicate that Mercury would be more likely to have experienced global melting than the Moon or other terrestrial planets (Hostetler and Drake, 1980). Compositional information, although meager, indicates that Mercury's surface is composed of silicates low in FeO and titanium, compared to the Moon, suggesting that Mercury is a differentiated planet with a silicate crust

and iron-rich core. The widespread distribution of lobate scarps indicates Mercury was subjected to a period of global contraction. The contraction was probably due, at least in part, to cooling of the interior. These two pieces of evidence together suggest Mercury experienced widespread melting and differentiation followed by cooling.

The discovery of Mercury's dipolar magnetic field also provides strong evidence that Mercury is differentiated into an iron-rich core and a silicate mantle. As discussed earlier, the two most reasonable explanations for its origin are: (1) the field is the result of remanent magnetization due to an ancient dynamo, or (2) it is a presently active magnetohydrodynamic dynamo. Both explanations for Mercury's magnetic field require that the interior is differentiated into a core and mantle and that the core was at least molten in the past and quite probably the outer portion is still molten.

The thermal history of Mercury is highly dependent on the abundance of radioactive isotopes. Thermal models suggest that a core will not form with a uranium abundance of only 30.4 ppb, whereas a core always forms with an abundance of 44 ppb, regardless of values of thermal conductivity and initial temperature (Siegfried and Solomon, 1974). If Mercury retained the uranium and thorium (Th/U$\sim$4) predicted by current cosmochemical models of solar nebula condensation and planetary accretion (Lewis, 1972, 1973; Grossman, 1972; Grossman and Larimer, 1974), then differentiation and core formation are probable for all likely initial temperature distributions and thermal conductivity values (Siegfried and Solomon, 1974). The consequences of core formation on the thermal history of Mercury are dramatic. In a model where the parameters were chosen to favor early differentiation Solomon (1976) found that core formation begins 1.2 billion years after planetary origin and is complete by 1.8 billion years. Most of the differentiation occurs within 200 million years and a temperature rise of about 700° C results from the release of gravitational potential energy. Most of the mantle is melted which should lead to substantial surface modification. However, if the surface of Mercury is as old as the period of heavy bombardment on the Moon (4.0 billion years ago), then core formation would have to have been complete at least 1 billion years earlier than indicated by this model. As a result, extensive early heating is required, which must have involved a much larger fraction of the planetary volume than for the Moon. Core infall would be accompanied by substantial melting of the mantle, and an increase in the planet radius by as much as 17 km (Solomon, 1976). Subsequent to core formation, cooling of the lithosphere or a combination of lithospheric and core cooling leads to a decrease in radius of perhaps 2 km or more (Solomon, 1976, 1977). A somewhat similar thermal model by Toksöz et al. (1978) reached similar conclusions. In any event, thermal history models involving differentiation into a core and mantle predict large scale melting of the mantle, leading to an increase in volume and widespread extensional fracturing of the crust. This provides ideal conditions for extensive volcanic activity; a ready source of lavas and tensional fracturing to provide egress to the surface. Under these conditions it is difficult to understand how Mercury could not have sustained widespread volcanism when the Moon experienced extensive volcanism under a much less severe tectonic and thermal regime.

Figure 3.39 is a schematic representation of the relative age of various events discussed elsewhere in the text. As Chapman (1976) correctly pointed out, absolute chronologies of planets cannot be determined from photogeologic studies alone. Because they depend on a rather accurate knowledge of the impact flux history, which is uncertain, no attempt was made to relate these events to an absolute time scale. However, it is highly likely that the age of Mercury's surface is comparable to that of the Moon's and formed sometime during the first 2–2.5 billion years after planetary formation (Murray et al., 1975). If large tracts of intercrater plains are volcanic then it is possible that this period of volcanism coincided, at least in part, with the period of heavy bombardment. Much of the intercrater plains pre-date or are contemporary with the oldest craters (Classes 4–5) of the heavily cratered terrain, while other large tracts appear to post-date these craters. Perhaps the plains material was extruded along fractures caused by expansion of Mercury during or shortly after core formation. Crustal fracturing during spindown also may have aided the process. The absence of extensional fracturing in the Mercurian highlands may be due to several factors. Crustal expansion and therefore tensional fracturing may have been nearly complete by the time of emplacement of the oldest intercrater plains units. Furthermore, the emplacement of volcanic plains may have covered their source fractures, as have the mare lavas on the Moon. Subsequent cratering (both primary and secondary) also could obliterate fractures.

The Caloris basin and the hilly and lineated terrain appear to have formed near the end of heavy bombardment—when the crust was being subjected

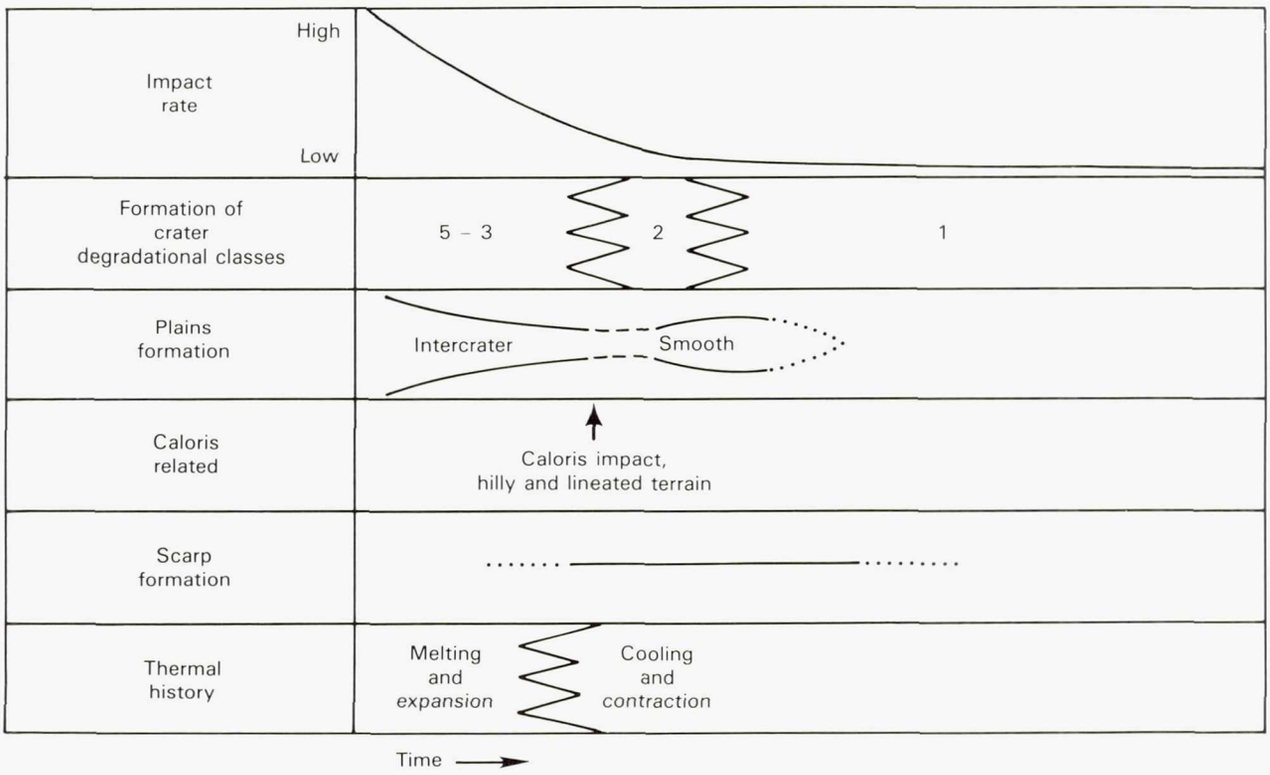

Figure 3.39. Diagram of the relative age of various events in Mercury's history. No attempt has been made to relate these events to an absolute time scale, but they all probably occurred early in the planet's history. The relative ages are interpretations based on investigations by various authors and are independent of the origin of plains units.

to global compression due to cooling of the core and/or lithosphere. Cooling and global compression probably began toward the end of heavy bombardment but before the formation of Caloris and continued past the formation of smooth plains. In general, global compression would tend to close off magma conduits and inhibit surface volcanism except for local areas of tension, e.g. seismic wave focusing at the Caloris antipode (Solomon, 1978). The majority of smooth plains appear to have been emplaced during the period of global compression. However, as Solomon (1977) pointed out, thermal stress will readily allow upward migration of magma to shallow levels where it can move to the surface if the fluid pressure exceeds the lithostatic pressure, or if the crust is weakened by impacts. Since the majority of smooth plains are concentrated in and around large impact basins, they may have been emplaced along fractures produced by the large impacts. Subsequent to smooth plains emplacement, crustal compression waned and died out at some indeterminate time. Since then only occasional impacts have modified Mercury's surface. A diagrammatic representation of this history is shown in figure 3.40.

Although thermal history models predict extensive mantle melting and crustal extensional fracturing, an alternative history can be developed in which little or no volcanism has occurred since the onset of heavy bombardment. In this scenario, the period of planet expansion, mantle melting, and crustal extensional fracturing would have ceased prior to the oldest craters preserved on the surface. This early period of melting may have completely resurfaced the planet. Subsequent cratering would be retained only after the surface was sufficiently solidified. The early, large craters would be more isostatically compensated, which would account for their degraded appearance but well-preserved secondaries. Under this view, the oldest intercrater plains would be the main remnants of the resurfacing, while the later intercrater plains would be ejecta deposits from as yet unidentified basins. Global compression due to cooling would be occurring during this period, and subsequent formation of basins (most of which have not been identified) would produce the smooth plains by impact melt and/or ballistic emplacement. Although this scenario is conceivable, the relatively late onset of compression suggested by crater-lobate scarp transection relationships, the evidence for a volcanic origin of at least large tracts of plains, and the difficulty of accounting for plains formation by impact processes, suggests that the first alternative is a more likely hypothesis.

DISCUSSION

The surface of Mercury closely resembles the Moon in two important respects: (1) the presence of ancient, heavily cratered regions with a lunar-like crater den-

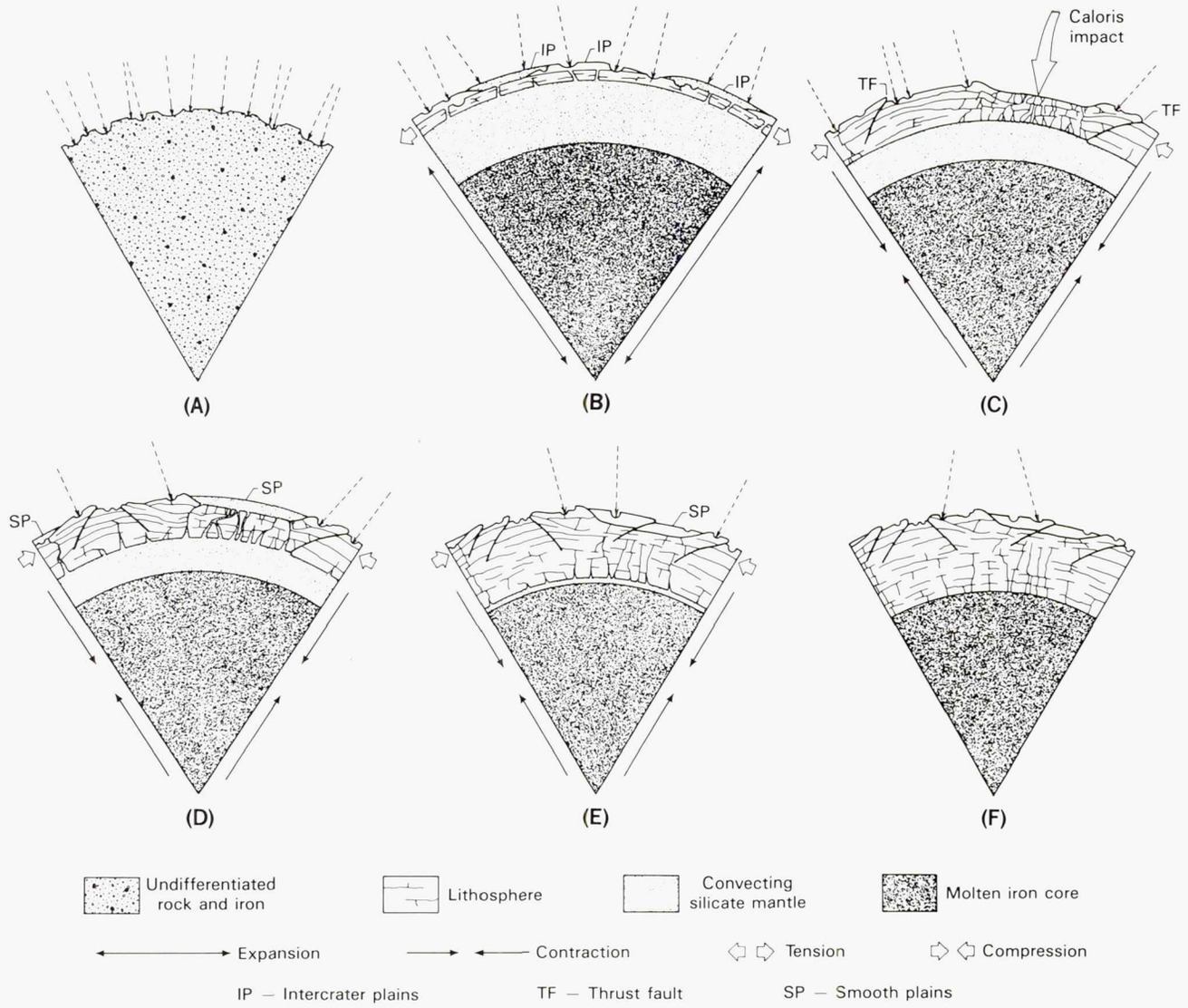

Figure 3.40. Diagram of the possible history of Mercury described in the text. In (A) Mercury has just formed with a large percentage of iron uniformly distributed throughout the planet. In (B) the large iron core has formed and largely melted the silicate mantle causing global expansion and tensional fracturing in a thin solid lithosphere. Volcanic eruptions along these fractures produce the intercrater plains (IP) during the period of heavy bombardment. In (C) the convecting mantle cools sufficiently to cause global contraction which results in compressive stresses and thrust faulting (TF). About this same time the Caloris impact occurs. Soon afterward new eruptions fill the Caloris basin and other areas with smooth plains (SP) near the end of heavy bombardment as shown in diagram D. In (E) further cooling and contraction produce compressive stresses strong enough to close off the volcanic conduits. Finally, cooling and contraction are complete and the planet becomes inactive except for occasional impacts which scar the surface (F).

sity and size distribution, and (2) large areas of younger, smooth plains resembling the lunar maria in both morphology and mode of occurrence. This superficial resemblance can lead to an overemphasis, and possibly an overinterpretation, of the similarities at the expense of the great differences which make Mercury unique in the solar system. Among these differences is Mercury's high mean density, which implies an iron content per unit volume greater than any other planet or satellite in the solar system. This large concentration of iron is probably a consequence of equilibrium condensation processes in the early solar nebula at Mercury's distance from the Sun. Furthermore, the presence of a relatively strong dipole magnetic field implies that the iron is concentrated into an enormous core some 75 percent of the total radius. The early formation of such a large core leads to thermal histories which predict large-scale melting consuming a much larger fraction of Mercury's lithosphere than that of the Moon. As a consequence, Mercury's tectonic regime and internal dynamics must have been very different from the Moon's. This might be expected to produce surface characteristics which differ in important respects from those on the Moon.

The two main differences between the surfaces of Mercury and the Moon are the tectonic framework and the widespread distribution of ancient intercrater plains on Mercury. Both of these characteristics may

be either the direct or indirect result of core formation on Mercury, which leads to extensive lithospheric melting, global expansion, and crustal extension. These conditions might be expected to yield extensive volcanism on a global scale, perhaps producing much of the intercrater plains. The origin of the tectonic structures is more firmly based, and is almost surely the result of compressive stresses due to crustal shortening. Although planetary despinning may have played a role in developing the tectonic framework, global contraction due to cooling of the lithosphere and/or core must have played an important part in order to explain the areal and azimuthal distribution of compressional features. Global contraction is also an indirect consequence of core formation because a significant decrease in radius results from cooling following the extensive melting induced by core formation. Furthermore, the relative age of intercrater plains emplacement and the onset of compression deduced from stratigraphic and transectional relationships is consistent with the stress history predicted by core formation in Mercury.

As Solomon (1978) pointed out, global compression would act to shut off volcanism associated with local stress systems faster than for a planet under global extension; therefore, the time duration of smooth plains emplacement (if volcanic) should be relatively short for Mercury compared to that for volcanic plains on the Moon and Mars. Both the post-Orientale and the post-Caloris surfaces record the same crater population with the same crater density and were imprinted near the end of late heavy bombardment on both bodies (see fig. 3.19). If the flux and decay rate of late, heavy bombardment were the same at Mercury and the Moon (a circumstance which is still uncertain), then both surfaces are about the same age (3.8 billion years). Crater densities on these surfaces are about a factor of three greater than that of the lunar maria (fig. 3.19), and the post-Caloris population is primarily superposed on the smooth plains. Therefore, the Caloris smooth plains may have been emplaced earlier than most of the lunar maria.

The paucity of iron and titanium on Mercury's surface relative to the Moon (Hapke, 1977) is consistent with the higher albedo of Mercury's surface units. Minerals containing these elements contribute to darkening the surface, and the titanium abundance is primarily responsible for the color differences observed on the Moon (see fig. 3.26). A low titanium abundance on Mercury could well account for the much smaller color differences and the poor correspondence between color and geologic boundaries. The depletion of these elements in crustal rocks relative to the Moon may have been the result of greater lithospheric melting leading to more efficient differentiation, particularly by gravity settling under Mercury's greater gravitational acceleration. This process could result in a stratified mantle with the heavier elements concentrated at greater depths (Herbert, 1980). Intercrater and smooth plains emplacement may represent one continuous epoch of volcanism, which tapped source regions depleted in iron and titanium relative to the Moon, and terminated when compressive stresses became strong enough to close off the conduits. In this case, Mercury, unlike the Moon, did not experience a period of late stage iron- and titanium-rich mare-like volcanism. Instead the source region for the older intercrater plains volcanism may have been at a shallower more differentiated level; while at least the younger Caloris smooth plains may have originated from a deeper level where slightly more iron and titanium were concentrated. Although the major differences between the surfaces of Mercury and the Moon can be readily explained in terms of the formation of a large Mercurian core, our current state of knowledge does not preclude other interpretations discussed earlier.

The flight of Mariner 10 has advanced our knowledge of Mercury a thousand fold and provides new insight into terrestrial planet evolution. However, the answers to major questions regarding the origin and composition of some of its surface features must await further investigation. Only an orbital mission with a diverse complement of scientific instruments is capable of providing the information to help answer these questions. Until then we must rely on existing data to sharpen our interpretations and improve theoretical models.

ACKNOWLEDGMENTS

The author thanks Charles Wood, Donald Gault, Mark Cintala, Bruce Hapke, Eugene Smith, Ewen Whitaker, Martha Leake and Newell Trask for providing several illustrations used in the text. Discussions with Ewen Whitaker, Bruce Hapke and Faith Villas on the photometry and spectroscopy of Mercury were very useful. Reviews of the text by Sean Solomon, Charles Wood, William McKinnon, Michael Carr, Donald Wilhelms and Ewen Whitaker are greatly appreciated. Portions of the research were conducted under NASA Grant NSG-7146.

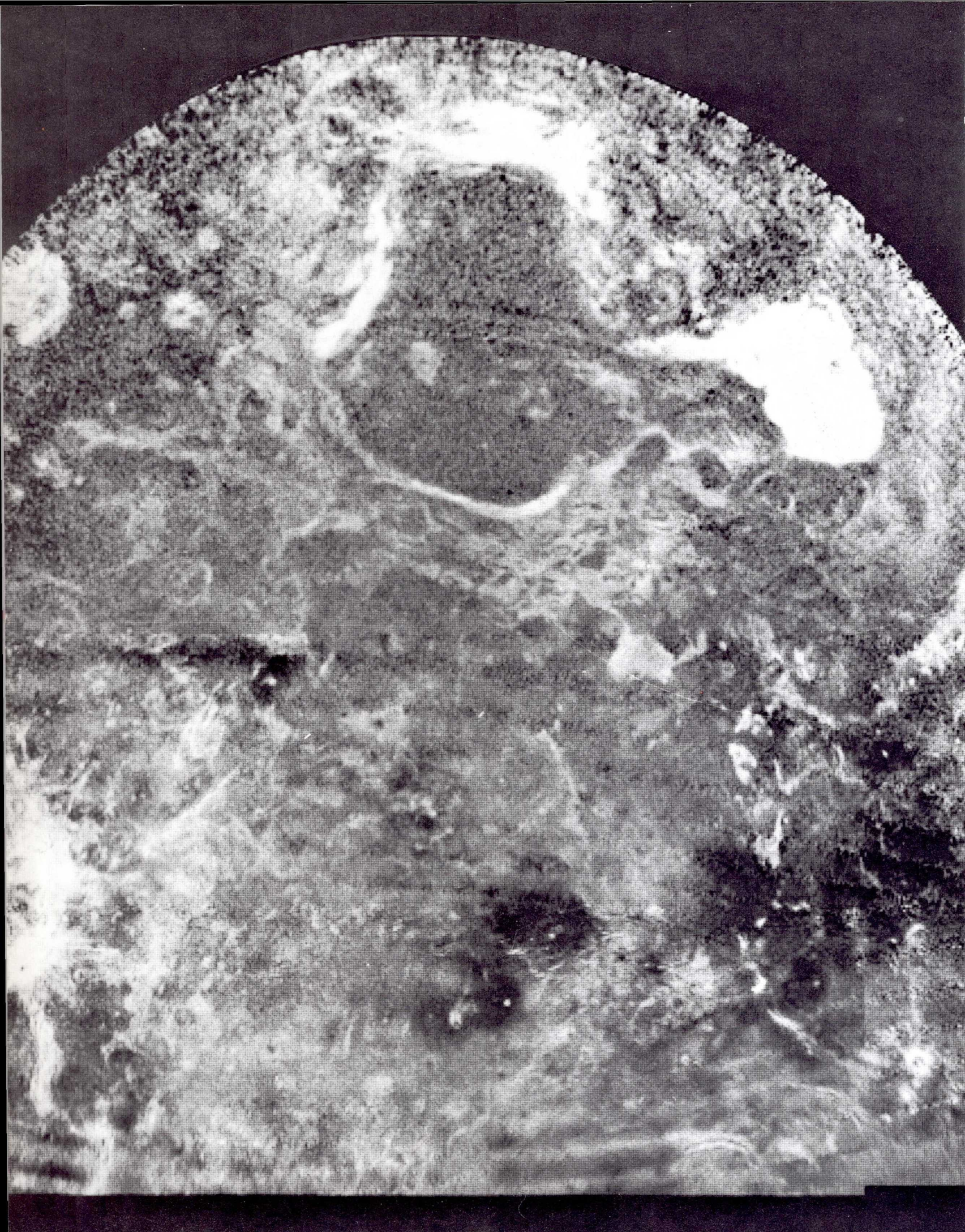

4
VENUS

R. Stephen Saunders and Michael H. Carr

INTRODUCTION

Venus is of special interest to the geologist for the contrast it presents with Earth and for the clues it provides concerning Earth's origin and evolution. Both bodies are of similar size, composition, and distance from the Sun yet they have evolved to remarkably different states; one developed into a prolific haven for life, the other into a sterile inferno. Unfortunately, we are far from understanding why this happened. Geologic study of Venus is particularly difficult. The main obstacle is its thick atmosphere which prevents us from seeing the surface with either optical telescopes or conventional spacecraft imaging systems. Only in recent years, with the development of radar imaging techniques and deployment of landers on the surface, have we been able to get a glimmer of Venus' surface, and to begin its geologic study.

Venus is the brightest object in the heavens, after the Sun and the Moon. Because it lies inside Earth's orbit, its angular distance from the Sun is always small ($<47°$), so it is visible only at dawn and dusk. In ancient Egypt, Venus was seen as two objects—the evening star and the morning star. To the Phoenicians, Venus was Astarte; to the Chaldeans (Babylonians) it was Ishtar. The Chinese called it Tai-pe, which means Beautiful White One. The most ancient observations known were recorded by the Babylonians on the Venus Tablets around 1900 B.C. The correct reference to Venus is a matter of some debate. Moore (1961) used *Cytherean* as the adjectival form, a word derived from the old Sicilian name for Venus. As that term is probably unfamiliar to most, the more straightforward *Venusian* is used here.

Observations of Venus played a key role in testing the Copernican theory of the solar system against the hypothesis that Earth lies at the center. The test proposed by Copernicus was to observe the phases on Venus and thus demonstrate that it revolves around the Sun. Galileo observed the phases and revealed his discovery in a message to Kepler, which Galileo coded to allow more time to confirm the discovery and to establish his priority. The message to Kepler was "Haec immatura, a me, iam frustra, leguntur—o. y.," which translates to "These things not ripe are read by me.", ignoring the two letters "o. y." that do not fit into the anagram. The message can be rearranged to read "Cynthia figuras aemulatur Mater Amorum," the real message, or "The Mother of Love emulates the phases of Cynthia."

EARLY TELESCOPIC OBSERVATIONS

Astronomers have been observing Venus through the telescope since the instrument was invented in the early part of the seventeenth century. Among the best known of the early observers is Christiaan Huygens, who reported that Venus is featureless. However, many subsequent observers noted markings of various kinds, including bright patches and polar caps, although the best observers reported none that were reliably repeated. The watchers of the bright spots attempted to determine the length of the Venusian day, and a surprising number deduced rotation periods nearly the same as those of Earth and Mars. These included Giovanni Cassini (23 hr 21 min), J. J. Cassini (23 hr 28 min), Schroter (23 hr 21 min), and Trouvelot (24 hr).

The most extreme estimate of the Venusian day was by Schiaparelli, the discoverer of the Martian canals, who suggested in 1891 that Venus has a rotational period equal to its orbital period of 224 days 16 hr

48 min. A short time later Lowell built his observatory in Flagstaff, Arizona, primarily to study Schiaparelli's Martian canals. Lowell also saw canals on Venus and in 1897 published a map of them. Although Lowell's Venusian canals were never confirmed by others using large telescopes, Lowell appears to have been convinced that the markings were real and further, that the 225 day period was correct. Moore (1961) argued, in discussing Lowell's beliefs, that Schiaparelli's estimate of close to 225 days could not be correct since thermal observations of the dark side of Venus gave no indication that the dark side is colder than the sunlit side. In the early 1960s several astronomers documented retrograde atmospheric motions of 100 m/s at the equator, which gives a four day cloud circulation period (Young and Young, 1975), but still gave no indication as to the rotation rate.

The first published speculation that Venus has an atmosphere appears to have been by Schroter in 1796. The first conclusive indication of its thickness was through spectroscopic work in the 1930s, which revealed at least 300 times as much CO_2 as in Earth's atmosphere. In the early literature, the high albedo of the planet was variously attributed to a variety of causes including dust clouds, formaldehyde, or salts such as NaCl or MgCl from dried oceans.

Another frequently cited phenomenon was the Ashen Light. Apparently first described by Father Johannes Riccoli in 1643 (Moore, 1961), the Ashen Light is a faint phosphorescence of the night hemisphere, normally seen when Venus is a thin crescent. The light appears to vary in intensity and has been ascribed to extensive twilight or to electrical phenomena such as aurora or lightning activity.

Many of the early observers were concerned with predicting and accurately measuring the timing of transits—the passages of Venus across the Sun's disc. Transits of Venus are infrequent because of the relatively large inclination of its orbit (3.4°). Currently, they occur in pairs separated by eight years (1631, 1639; 1761, 1769; 1874, 1882; 2004, 2012). Kepler was the first to predict a transit, the one on December 7, 1631, which Gassendi unsuccessfully attempted to observe. Horrocks was successful, however, in predicting and observing the next transit in 1639.

By the mid-eighteenth century there was great interest in careful observation of the transits of Venus for the purpose of determining the astronomical unit, and the transits of 1761 and 1769 were widely observed for this purpose. The 1768 expedition of Captain James Cook, for example, was charged by the Royal Society with the responsibility of observing the transit of Venus from Tahiti. The observations were made on June 3, 1769.

The most poignant story among those of the early transit watchers is related by Moore (1961). The French astronomer Guillaume Legentil set out for Pondicherry, India, in 1760. Delayed by the Seven Years' War, he arrived too late for the 1761 transit and decided to wait eight years in India for the next one. Unfortunately, on the day of the transit, June 3, 1769, it was cloudy, and a presumably despondent Legentil departed India for home, but was shipwrecked twice en route. Eleven years after setting out for India, he reached Paris only to discover that he had been presumed dead and his property distributed to his heirs.

ORBITAL AND ROTATIONAL MOTIONS

Venus moves around the Sun in an orbital period of 224 days 16 hr 48 min, an eccentricity of 0.0068, and an inclination of 3° 24′. The eccentricity is less than any other planet, and the inclination is greater than that of any other planet's but Mercury and Pluto. There are about 584 days between inferior conjunctions, the times of closest approach of Venus and Earth. The exact time varies by about four days because of orbit eccentricities. At the time of closest approach, the Earth–Venus distance is 44 million km, and the Venus disc, although not visible, is 64″ across. At superior conjunction, when Venus and Earth are on opposite sides of the solar system, Venus has an angular diameter of 9.5″. As seen from Earth, the greatest angular distance of Venus from the Sun is at dichotomy when the angular separation is 47°. When seen in the evening, Venus is waning; in the morning it is waxing as it approaches superior conjunction. It is most brilliant at an angular distance of 40° from the Sun.

The semi-major axis of the orbit is 0.723 AU, so the planet receives about twice as much solar radiation as Earth. However, Venus has a high albedo (0.71), compared with Earth (0.39) and the Moon (0.07), because of its continuous cloud cover. As a consequence, despite its closer proximity to the Sun, Venus absorbs less radiation than Earth, giving it an effective radiation temperature of only 224 K as compared with Earth's 253 K.

The Venusian day has been only recently determined from radar observation. As noted above, early telescopic estimates ranged from 23 hours to 225 days,

and this situation prevailed until the late 1950s. In the early 1960s, radar started to be used to observe Venus. W. B. Smith of the Massachusetts Institute of Technology looked for a Doppler shift in the radar echo as evidence of rotation. Although the period was not determined, there was an indication that the motion was retrograde. During the conjunction of 1962, several workers (Carpenter, 1964; Goldstein, 1964; Muhleman, 1964; Drake, 1964) confirmed that Venus' rotation was retrograde and estimated the period as close to 250 days. The estimate was later refined to 242.6 ± 0.9 days (Goldstein, 1965). The best current estimate is very close to 243 days, with the rotation axis inclined at 177°. Because of the similarity in the orbital and rotational periods, the sidereal day differs significantly from the solar day, which lasts 116.8 Earth-days. To an observer on the surface of Venus, the Sun would rise in the west, and daylight would persist for 58.4 Earth-days with a sky resembling that of a dark overcast day on Earth.

EARTH-BASED RADAR OBSERVATIONS OF THE SURFACE

Radar observations from Earth, besides providing us with a measure of the Venusian day, gave us our first information about the planet's surface. Radar studies of Venus have since been carried out in the U.S. mainly at three observatories: Arecibo in Puerto Rico, which has a 300 m diameter antenna using mostly 70 cm wavelength; Goldstone in the Mohave Desert of California, which has a 64 m antenna and operates primarily at 12.5 cm wavelength; and Haystack in Massachusetts, which has a 43 m antenna that is used at 3.8 cm wavelength. High resolution radar data can only be obtained around inferior conjunction, or about every 19 months. At inferior conjunction, the same hemisphere of Venus always faces the Earth.

The first Venus observations were ranging for ephemeris development. These range determinations had about one kilometer accuracy by the late 1960s. By 1970, images had been obtained by each of the three major observatories. These images had a resolution of about 50 km and showed only that Venus has fixed features and that the radar reflectivity varies from place to place. The technique used is to separate the echo into range bins representing circular regions on the planet equidistant from Earth. The range bins are subdivided by Doppler provided by the slow rotation of Venus. This still leaves a north-south ambiguity, in that each resolution element in the northern radar hemisphere has a counterpart with the same range and Doppler in the southern hemisphere. This ambiguity is now removed by an interferometry technique first developed by Rogers and Ingalls (1969, 1970) using the MIT Haystack telescope. The technique was subsequently used by Campbell et al. (1970) at Arecibo and by Goldstein and Rumsey (1970, 1972) at Goldstone. The theory behind the technique was described by Shapiro et al. (1972) and had been previously applied to the Moon (Zisk, 1972). The first images of Venus showed several circular features that resemble impact craters. Reflectivity and altimetry maps have since been made of small regions, showing numerous other surface features (Rumsey et al., 1974; Goldstein et al., 1976, 1978).

The highest resolution mode of the Goldstone images is about 10 km linear radar resolution and the images typically cover about 8° radius or regions of the planet about 1600 km in diameter (fig. 4.1). The theory and data processing operations of three station interferometry for obtaining the topography is described in Jurgens et al. (1980). The standard error of their altimetry is about 35 m near the sub-radar point increasing to about one kilometer at 6°. Recent Goldstone radar images (Jurgens et al., 1980) reveal small mountains 30–60 km in diameter, 1–2 km high, with mean slopes of 2.5° to 3.5°. A strong dependence of reflectivity on incidence angle is observed, suggesting that the surfaces are relatively smooth at the 12 cm-wavelength used.

The highest resolution images are those from Arecibo, which range in radar resolution down to 3 km (Campbell and Burns, 1980; Head and Campbell, 1982). These have substantially better resolution than the Pioneer Venus radar images, although obviously restricted to the hemisphere that faces Earth during opposition. Campbell and Burns used Arecibo images to construct a mosaic that covers about 25 percent of the planet's surface at a resolution of 10–20 km (fig. 4.2). The area covered stretches from 260° to 30°E between latitudes 70°N and 50°S.

The radar images show considerable surface detail reflecting mostly roughness variations. Freyja and Akna Montes, north of Lakshmi Planum, Maxwell Montes, and Theia and Rhea Montes are particularly prominent, implying rough surfaces at radar wavelengths. Two types of circular features are present: large, smooth, quasi-circular regions with diameters between 200 and 1300 km, and bright regions generally less than 300 km. Especially intriguing in the

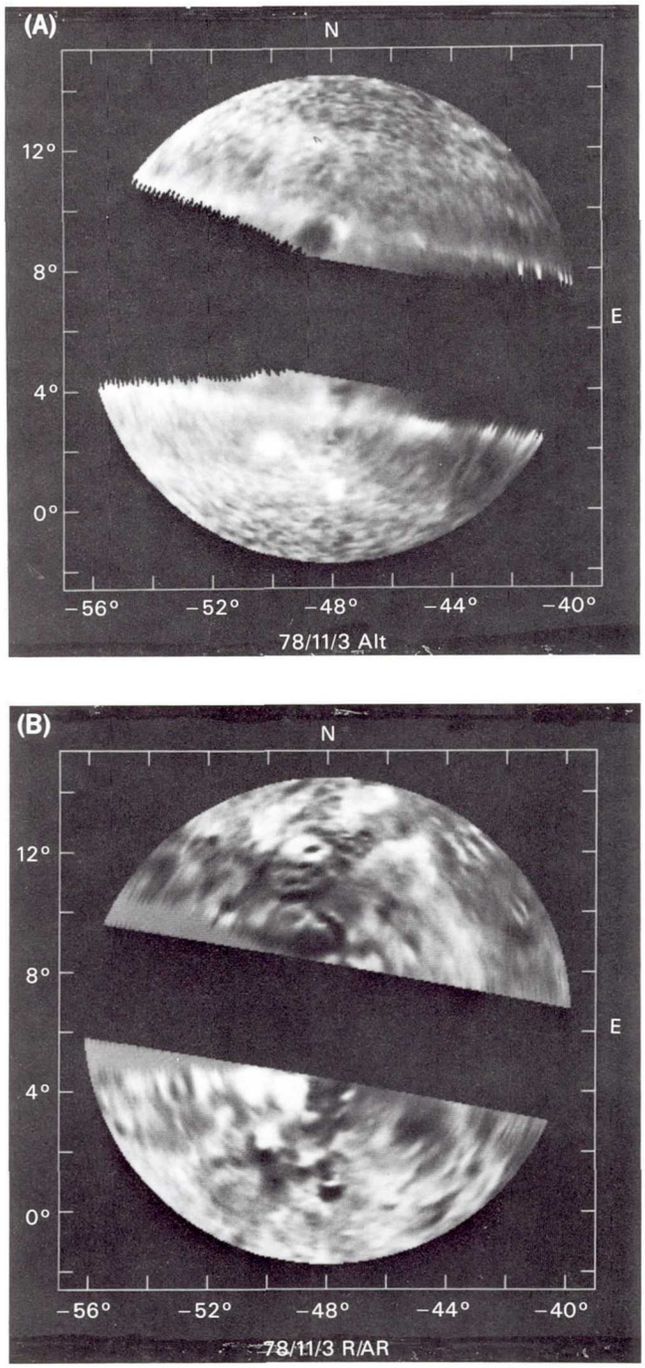

Figure 4.1. Goldstone radar images of a segment of the Venusian lowlands centered at 6°N, 312°E. (A) shows altimetry, the dark areas being low and the bright areas high. In the upper half is a crater 150 km in diameter and 750 m deep. Two bright spots in the lower half are isolated mountains, probably volcanoes. (B) shows variations in radar reflectivity for the same area. The variations are probably caused mainly by surface roughness, with bright areas rougher than dark areas.

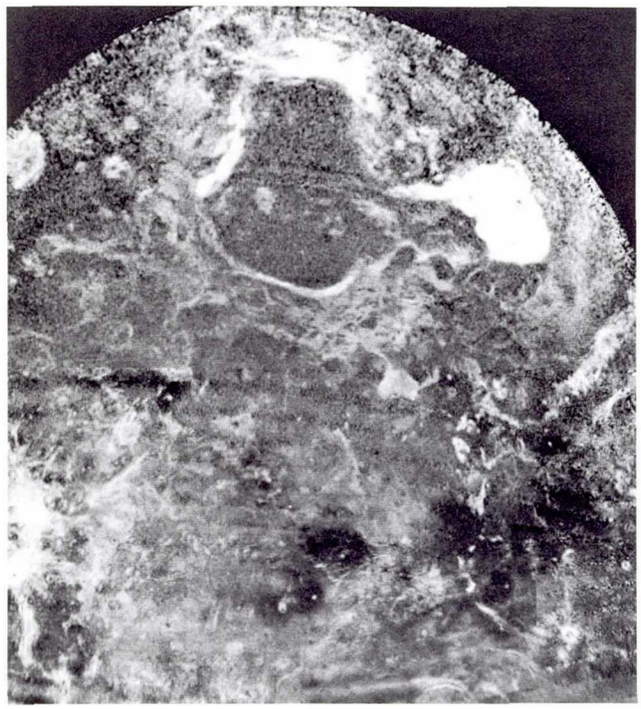

Figure 4.2. Mosaic of Arecibo radar images which covers about 40 percent of the northern hemisphere about the 330° longitude. The image shows variations in reflectivity of the surface at radar wavelengths. The prominent dark feature at the top center is Lakshmi Planitia with the very bright Maxwell Montes to the east. The bright marking at the lower left edge is Beta Regio. (Refer to fig. 4.6 to correlate with relief.)

highest resolution pictures are some banded terrain, suggestive of folded or faulted rock sequences (Head and Campbell, 1982).

SPACECRAFT OBSERVATIONS

The first U.S. spacecraft to observe Venus was Mariner-Venus 2, which flew by the planet on December 14, 1962 (table 4.1). It carried two primary experiments: a microwave radiometer to measure the surface temperature and the atmospheric structure and an infrared radiometer to determine the cloud structure and temperatures. The principal scientific results were the determination of a surface temperature of around 400 K and an indication that the magnetic field, or at least the dipole moment, must be less than 10 percent that of Earth. Mariner 2 also provided an order of magnitude improvement in the mass estimate for Venus (e.g., Anderson et al., 1964).

Table 4.1. Missions to Venus (from Colin, 1980)

Spacecraft	Launch	Encounter	Type	Encounter characteristics
Mariner 2	August 27, 1962	December 14, 1962	flyby	closest approach: 34 833 km
Venera 4	June 12, 1967	October 18, 1967	bus	burn-up
		entry probe	hard lander, nightside	
Mariner 5	June 14, 1967	October 19, 1967	flyby	closest approach: 4100 km
Venera 5	January 5, 1969	May 16, 1969	bus	burn-up
		entry probe	hard lander, nightside	
Venera 6	January 10, 1969	May 17, 1969	bus	burn-up
		entry probe	hard lander, nightside	
Venera 7	August 17, 1970	December 15, 1970	bus	burn-up
		entry probe	soft lander, nightside	
Venera 8	March 27, 1972	July 22, 1972	bus	burn-up
		entry probe	soft lander, dayside	
Mariner 10	November 3, 1973	February 5, 1974	flyby	closest approach: 5700 km
Venera 9	June 8, 1975	October 22, 1975	orbiter	periapsis: 1560 km; apoapsis:
		entry probe	soft lander, dayside	112 200 km; period: 48 hr, 18 m; inclination 34°10′
Venera 10	June 14, 1975	October 25, 1975	orbiter	periapsis: 1620 km; apoapsis:
		entry probe	soft lander, dayside	113 900 km; period: 49 hr, 23 m; inclination 29°30′
Pioneer Venus 1	May 20, 1978	December 4, 1978	orbiter	periapsis: <200 km; apoapsis: 66 000 km; period: 24 hr; inclination: 105°
Pioneer Venus 2	August 8, 1978	December 9, 1978	bus	burn-up, dayside
			entry probes	4 hard landers, dayside and nightside
Venera 11	September 9, 1978	December 25, 1978	flyby	closest approach: 25 000 km
		entry probe	soft lander, dayside	
Venera 12	September 14, 1978	December 21, 1978	flyby	closest approach: 25 000 km
		entry probe	soft lander, dayside	
Venera 13	October 30, 1981	March 1, 1982	entry probe	soft lander
Venera 14	November 4, 1981	March 5, 1982	entry probe	soft lander
Venera 15	June 2, 1983	October 10, 1983	orbiter	24 hr orbit, 1000 km periapsis
Venera 16	June 7, 1983	October 4, 1983	orbiter	24 hr orbit, 1000 km periapsis

Mariner 5, a spare Mariner-Mars 1964 spacecraft, was launched on June 14, 1967, and arrived at Venus on October 19, 1967. The main objective was to investigate the atmosphere, ionosphere, and magnetosphere of Venus; for the geosciences, an important result was an improved radius. Previous telescopic measurements had yielded a radius of 6120 ± 7 km (DeVaucouleurs, 1964). The radar determined radius was 6056 km (Ash et al., 1968). By combining the radio tracking of Mariner 5 with Earth-based radar reflections, a radius of 6054 ± 2 km was determined (Anderson et al., 1968). A high priority was to determine the atmospheric density and pressure at the surface. During an exciting five day period in October 1967, Mariner 5 arrived at Venus and the Soviet Venera 4 made a hard landing on the Venus surface. The Soviets put down a pressure sensor for a direct measurement of surface pressure, while the U.S. used radio occultations of the Mariner spacecraft. The surface temperature was about 700 K and the pressure about 100 bars. The cloud top was at 67 ± 10 km, and CO_2 was confirmed as the predominant atmospheric

constituent. Measurements made by Venera 4 indicated that the magnetic field of Venus is <0.00001 that of Earth.

Over the next few years the Soviets sent several additional spacecraft to Venus and achieved the first soft landing on another planet when Venera 8 soft landed on the Venus surface on July 22, 1972. In addition to measuring various properties of the atmosphere during entry, the lander was able to measure the radioactivity of the surface materials with a gamma ray spectrometer (Vinogradov et al., 1973), and to obtain a measure of their density (1.5 g/cm^3).

The first spacecraft to orbit Venus were Veneras 9 and 10, placed in orbit in October 1975. They were in elliptical orbits with periapses of about 1500 km. The orbiters were not tracked continuously and were operated in a 3-axis stabilized mode only near periapsis. Elsewhere in the orbit they rotated slowly about the Venus–Earth direction. Veneras 9 and 10 also released landers to the surface and both successfully soft-landed. These landers carried an imaging system in addition to the gamma ray spectrometer/densitometer carried on Venera 8, and both spacecraft returned excellent pictures from the surface. In 1978 the Soviets sent two additional spacecraft, Veneras 11 and 12, to Venus, but neither returned useful data.

The U.S. also sent two spacecraft, Pioneer-Venus' 1 and 2, to Venus in 1978 (Colin, 1980). Pioneer 1 was an orbiter carrying a wide array of scientific instruments to examine the atmosphere, the surface, and the interaction of the planet with the solar wind. Of main geologic interest was a radar mapper designed to systematically map the elevation of the surface and its roughness. Pioneer 2 consisted of five separate spacecraft—a bus, a large atmospheric probe, and three small probes. The probes entered the atmosphere of Venus at different locations, two on the night side and two on the day side. Each carried several instruments designed primarily to determine the composition and structure of the atmosphere.

In 1981 the Soviets launched two more spacecraft to Venus, Veneras 13 and 14. In March 1982, both successfully soft-landed on the surface and photographed their surroundings. Both spacecraft carried an X-ray fluorescence instrument, which provided the first chemical analyses of the Venusian surface.

The most recent Soviet Venus missions are Venera 15 and 16. Identical spacecraft were placed in polar orbits to image the northern hemisphere using a radar system. Other experiments included a radiometer to measure surface brightness temperature, and altimeter to map surface topography, and an infrared spectrometer to obtain data on atmospheric composition.

The image resolution of Venera 15/16 radar is about 1.5 km. This is about the same as the best currently available Earth-based resolution from Arecibo (Campbell et al., in press). In comparable terms, the NASA Venus Radar Mapper will have a resolution of 180 to 460 m depending on position in orbit from periapsis.

Preliminary releases of the Soviet images show craters and linear tectonic features.

CONSTRAINTS ON THE COMPOSITION OF VENUS

The terrestrial planets are characterized as much by their differences as by their similarities and each must have started out on its unique evolutionary path as a result of conditions that prevailed very early in their history. Before examining the Venusian surface in detail, and trying to reconstruct the geologic history from the surface record, we will briefly examine what might be deduced about the planet's early history from models of formation of the planets. General models for compositional and density trends in the solar system have been developed by Lewis (1972, 1974) and Cameron (1963, 1973). In these models solid dust condensed in equilibrium with gas of the solar nebula at temperatures and pressures that varied with heliocentric distance (see Introduction). The dust grains accreted to form larger objects and ultimately planets. The more volatile the elements, or compounds, the farther out they condensed.

Condensation within a solar nebula that is cooling outward and with time, satisfactorily explains the gross compositional trends in the solar system, but the rare gases appear to follow an inverse trend. Pioneer-Venus discovered a large excess of nonradiogenic rare gases in the Venusian atmosphere. Neon and the nonradiogenic argon isotopes ^{36}Ar and ^{38}Ar are one hundred times more abundant on Venus than on Earth. In contrast, the mixing ratios for nitrogen and carbon dioxide are remarkably similar for the two planets. The volatile rare gases decrease in abundance outward rather than increase as the simple model predicts. The cause must be connected with the origin of planetary atmospheres. Pollack and Black (1979) outlined the basic theories of origin.

(1) Condensation/capture. Planets acquired their atmospheres from the primordial nebula or solar wind. Either source must have had a composition different from today's Sun.

(2) Cometary impact. Volatile-rich objects entered the inner solar system from the more distant parts where they had condensed. The objects accreted onto the inner planets, providing them with atmospheres. This model does not, however, explain the observed rare gas gradients.
(3) Grain-accretion. Pollack and Black (1979) proposed a grain-accretion hypothesis in which the rare gases became adsorbed on grains which were later accreted by the planets. The solar nebula, they postulated, had a relatively uniform temperature gradient but a steep pressure gradient, decreasing outward. Adsorption of volatiles is pressure dependent so that the grains that accreted nearest the center where the pressures were highest would have more adsorbed volatiles. Most of the non-rare gas volatiles such as nitrogen and water were chemically bound within the grains, and so their abundances were not as sensitive to the pressure gradient as the rare gases. The rare gases were thus fractionated with respect to the other volatiles.

Wetherill (1981) alternatively proposed that the solar wind accretion model best accounts for the observed trends. During the early stages of development of the solar system, material condensed from the nebula gas to form particles which accumulated into larger bodies (planetesimals), which in turn accumulated to form the planets. Wetherill suggested that the excess inert gases were implanted by an enhanced solar wind bombardment during planetesimal growth, and that the decreasing outward rare gas trends were produced by a geometric shading effect, causing implantation to be less efficient with increasing distance from the Sun because of shielding by particles closer in. Each planet preferentially incorporated material that had condensed in its part of the solar system, so that the planets nearer the Sun incorporated relatively more rare gases.

The origin of a planet's atmosphere is strongly coupled to its outgassing history. In general, the atmosphere does not represent the composition of the total inventory of degassed volatiles because most gases react with the surface materials or are lost by exospheric processes. Only the rare gases, except for He, are conserved. The isotopic abundance of rare gases, therefore, provides the best clues concerning atmospheric history but even these do not provide a unique solution. The outgassing history of Venus remains obscure, and will remain so until we obtain much more compositional information about the surface and the interior.

Presently, the composition of the interior of Venus is constrained only by the bulk density and inferences drawn from compositional determination made by the Soviet landers. After making corrections for the effects of compression, the density of Venus appears to be about 2 percent less than if it were compositionally identical to Earth (Ringwood and Anderson, 1977). Ringwood and Anderson argued that even if the high surface temperatures had persisted since the formation of the planet, the thermal wave could have penetrated only about 500 km. Temperature deeper than 500 km would be about the same as on Earth so that the density differences cannot be explained simply on the basis of the high surface temperatures. This argument assumes that heat is lost mainly by conduction, but the conclusion would be the same if heat transport was mainly by convection since the temperature at which mantle materials flow should be similar on both planets. Removing the effect of thermal expansion due to the higher near-surface temperatures on Venus lowers the bulk density somewhat, but still leaves an uncompressed density 1.7 percent smaller than Earth's.

The Lewis (1972, 1974) equilibrium condensation model qualitatively explains why Venus has a lower uncompressed density than Earth. Earth incorporated more sulfur than Venus, so has a higher sulfur to silicate ratio. Since sulfur has a greater atomic weight than the mean atomic weight of the silicates, Venus is less dense. However, Ringwood and Anderson suggested that there are problems with the equilibrium condensation model because they calculated the decrease in density resulting from removing all the sulfur from Earth's core and still concluded that Venus remains less dense. On the other hand, support for equilibrium condensation is provided by a model of sulfur chemistry in the atmosphere-lithosphere system based on Pioneer-Venus (Lewis and Kriemendahl, 1980) which suggested that the Venus lithosphere must have a far lower FeO content than Earth's. This is expected from the equilibrium condensation model, which predicts that FeO would not condense at the Venus distance.

Goettel et al. (1981) showed that the density differences between Earth and Venus can be eliminated by assuming a different temperature structure and a deeper basalt to eclogite transition. In addition, the low FeO content expected for Venus would tend to result in a lower observed (uncorrected) density for

Venus, since the depth to phase transitions involving olivine to spinel and perovskite structures is increased with decreasing FeO/(FeO + MgO) (Phillips and Malin, 1982). A low FeO content could also result in higher interior temperatures because iron-poor olivines have higher melting temperatures, and probably a higher viscosity at a given temperature, than iron-rich olivines. Temperature profiles may therefore stabilize at higher values in the iron-poor Venus mantle as compared with the iron-rich Earth mantle.

VENERA LANDER RESULTS

The Venera spacecraft have provided close-up views at four locations. Venera 9 landed on a rocky, sloping surface at 32°N, 291°E, on the eastern flanks of Beta Regio. The rocks are mostly flat and slab-like, ranging in size up to 70 cm in diameter and 20 cm high (Florensky et al., 1977). Many have fractures and grooves suggestive of layering. Between the rocks is a seemingly fine-grained, low-albedo material. Florensky et al. suggested that the slabs were in the process of slowly moving downslope by mass wasting. Three days later, on October 25, 1975, a second spacecraft was set down at 16°N, 291°E on a flat plain to the south of Beta Regio. The plain appears to be composed of scattered flat outcrops with darker, fine-grained material between. The outcrops are typically 1 to 3 m across and constitute about half the surface. The fine-grained material at this site also had a very low albedo (< 3 percent); that of the rocks was close to 5 percent. After both landings, gamma-ray detectors were deployed to determine the radioactivity and density of the surface materials. At the Venera 10 site the material on which the detector rested has an estimated density of 2.8 ± 1 g/cm^3, which is typical of coherent silicate rocks (Surkov et al., 1977). Light levels decreased shortly after landing, probably as a result of the spacecraft engines raising dust. Some of the local materials are thus fine-grained and loosely consolidated. Both sites are at an elevation close to 6053 km. Surface temperatures ranged from 730 to 740 K and the pressure ranged from 88 to 94 atm.

Venera 13 landed at 7°S, 303°E on a flat plain at a similar elevation to the Veneras 9 and 10 sites; the Venera 14 site at 13°S, 311°E is at a somewhat lower elevation (fig. 4.3). Both sites resemble the Venera 10 site except that at the Venera 13 site there was a large area of dark regolith close to the spacecraft. Regolith is almost absent at the Venera 14 site and layering in the outcrops is more obvious (fig. 4.4).

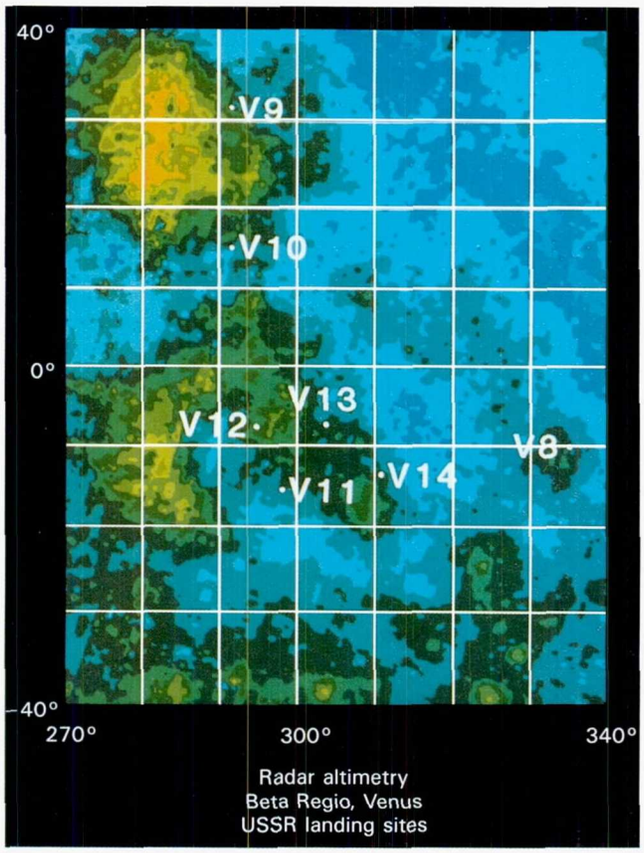

Figure 4.3. Location of the different Venera landing sites. (For key to the color coding of relief, see fig. 4.6.)

The abundances of U, Th, and K suggested by the gamma-ray results of Veneras 8, 9, and 10 (table 4.2) are more similar to those of terrestrial rocks than to those of lunar rocks and meteorites. The Venera 8 abundances are typical of terrestrial continental rocks, whereas the Veneras 9 and 10 abundances more closely approach the values for the terrestrial oceanic crust (see Earth chapter). However, these comparisons should be viewed with caution, for the precisions indicated in table 4.2 may not be a true reflection of the accuracies of the analyses.

More complete chemical analyses were obtained from the X-ray fluorescence instruments on Veneras 13 and 14 (table 4.3). The analyses from both sites are similar except for the K values. They resemble those of terrestrial ocean floor basalts, although the Venera 13 rocks have significantly more K and less Si.

EOLIAN EROSION AND TRANSPORT

At the Veneras 9 and 10 sites surface winds were measured directly by anemometers. They ranged from

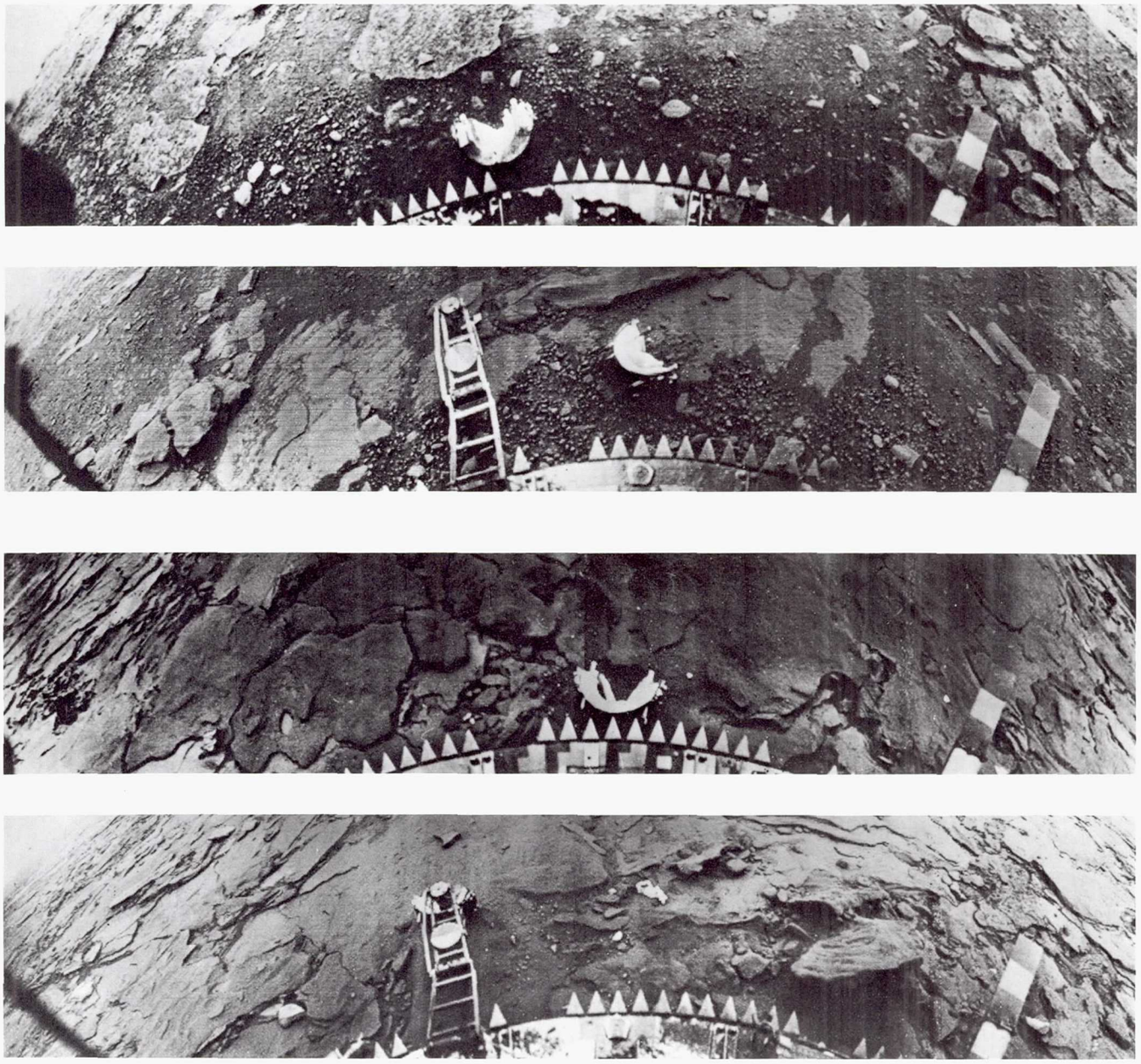

Figure 4.4. Views from the Venera 13 (top) and Venera 14 (bottom) spacecraft. Both spacecraft landed on a level plain with mostly flat, slabby rocks at the surface. The Venera 13 site is also partly covered with a fine-grained regolith.

0.4 to 0.7 m/sec^{-1} at the Venera 9 site and from 0.8 to 1.3 m/sec^{-1} at the Venera 10 site (Keldysh, 1977). In addition, surface winds could be estimated from the tracking of the Venera and Pioneer spacecraft as they descended through the atmosphere. Counselman et al. (1980) showed that the wind profile was similar at all four locations sampled by the Pioneer probes. They ranged from about 100 m/sec at an altitude of 65 km, down to 5 m/sec at an altitude of 10 km, and 1 m/sec at the surface. The dominant motion in the lower atmosphere is retrograde zonal (E–W) rotation. Meridional (N–S) velocities are small throughout the profile and appear to be due mostly to eddies.

These surface winds, though small, are sufficient to raise dust from the surface and to dislodge and move debris. Wind tunnel experiments that simulate Venusian conditions (Williams and Greeley, 1982; Greeley et al., 1982) show that the optimum particle size for wind transport on Venus is 70 μm. The minimum friction wind speed capable of moving particles is about 2 cm/sec (fig. 4.5), close to an order of magnitude less than on the Earth and two orders of magnitude less

Table 4.2. Venera Measurements of Uranium, Thorium, and Potassium Abundances (from Surkov, 1977)

Venera	U($x10^{-4}$ wt.%)	Th($x10^{-4}$ wt.%)	K(wt.%)	K/U($x10^4$)
8	2.2 ± 0.7	6.5 ± 0.2	4.0 ± 1.2	+1.65 1.82 −0.85
9	0.60 ± 0.16	3.65 ± 0.42	0.47 ± 0.08	+0.47 0.78 −0.27
10	0.46 ± 0.26	0.70 ± 0.34	0.30 ± 0.16	+1.65 0.65 −0.46

Table 4.3. Composition of Surface Materials at the Venera 13 and 14 Sites on Venus Compared With Terrestrial Oceanic and Continental Crust (from Barsukov, 1982)

Constituent	Venera 13	Venera 14	Terrestrial oceanic basalt	Average continental crust
MgO	10 ± 6	8 ± 4	7.56	2.2
Al_2O_3	16 ± 4	18 ± 4	16.5	16.0
SiO_2	45 ± 3	49 ± 4	51.4	63.3
K_2O	4 ± 0.8	0.2 ± 0.1	1.0	2.9
CaO	7 ± 1.5	10 ± 1.5	9.4	4.1
TiO_2	1.5 ± 0.6	1.2 ± 0.4	1.5	0.6
MnO	0.2 ± 0.1	0.16 ± 0.08	0.26	0.08
FeO	9 ± 3	9 ± 2	12.24	3.5
Total (%)	92.7	95.56	99.86	92.68

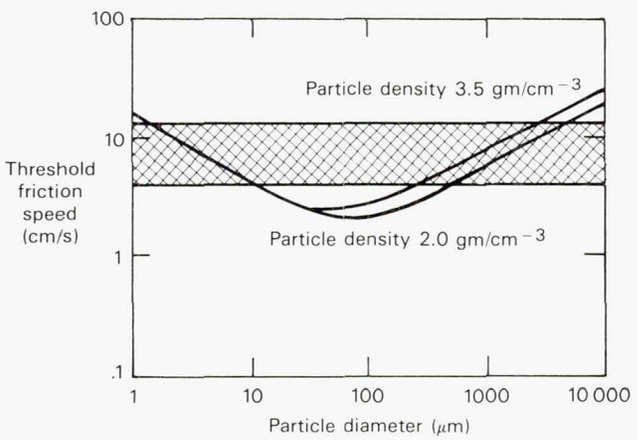

Figure 4.5. The threshold frictional wind speeds required to move particles of different diameters on the Venusian surface. Curves are given for particle densities of 3.5 and 2.0 gm/cm^{-3}, which spans the expected range. The shaded area shows the range of frictional wind velocities expected from the Venera wind data.

than on Mars, a reflection of the high atmospheric density at the Venusian surface. The Venera velocity measurements were made at a height of 1 m above the surface; the frictional wind velocity right at the surface should be about an order of magnitude lower. Thus the Venera measurements imply wind speeds in the 4 to 13 cm/sec range, well above the experimentally derived threshold speed of 2 cm/sec. Theoretical extrapolation of threshold friction speeds as a function of particle diameter to Venusian conditions, based on the work of White et al. (1976) and White (1979), give similar results.

One way in which eolian transport under Venusian conditions appears to differ from Earth and Mars is in the action of the particles after the threshold speeds for saltation are achieved. Particles tend to roll across the surface rather than saltate (Greeley et al., 1982). In other words, their saltation path lengths are

very short. This effect which had been predicted on theoretical grounds (White, 1979) must affect the geometry of eolian features such as dunes and ripples. Ripples should, for example, have higher amplitudes and shorter wavelengths than on Earth.

While winds can readily move particulate debris across the Venusian surface, unconsolidated wind-blown debris appears to constitute only a small part of the surface. The dielectric constant of the Venusian surface has been estimated as 4.7 ± 0.8 (Kuzmin and Marov, 1974) which is more consistent with dry rock than poorly consolidated regolith. The dielectric constant of the Moon, for example, ranges from 2.6 to 2.8, a reflection of the presence of a fine-grained regolith. Dielectric constants of rock materials roughly correlate with density, and the range of dielectric constant for the Venusian surface implies densities that range from 1.3 to 3 g/cm^3 with a mean value of 2.2 g/cm^3, which is more consistent with porous rocks than unconsolidated sediments. Although unconsolidated eolian sediments appear to cover only a small fraction of the surface, many of the exposed rocks may be of eolian origin. The densities and dielectric constants are consistent with cemented fragmental debris. The layering observed in the rocks of the Venera sites could be sedimentary. Warner (1980, 1983) suggested that the low-lying dark plains of Venus are eolian sinks, with mostly cemented eolian deposits at the surface.

CHEMICAL WEATHERING

Several attempts have been made to deduce weathering processes at the Venusian surface by searching for plausible reactions that might occur between gases in the atmosphere and normal rock-forming minerals under Venusian conditions. Urey (1952) suggested that the Venus atmosphere might be buffered by the following reaction

$$\underset{\text{wollastonite}}{CaSiO_3} + CO_2 = CaCO_3 + SiO_2$$

The equilibrium pressure for this reaction at 740 K is 90 bars, which is remarkably close to the conditions on the surface. However, as pointed out by Nozette and Lewis (1982), wollastonite is not a common rock-forming mineral and the efficacy of the reaction in buffering the atmosphere is questionable.

The question of how (or if) the Venus atmosphere is buffered is a complex one and intimately coupled with weathering reactions. Rates of reaction between the atmosphere and the surface under the high temperature conditions at the Venusian surface are likely to be high, despite the generally dry conditions. As pointed out by Warner (1983), although the mixing ratio of water vapor in the lower atmosphere, 10^{-3} to 10^{-4}, is up to a factor of 100 lower than in the Earth's atmosphere, the pressure is a factor of 90 higher, so that the partial pressure of water at the surface is about the same on the two planets. Since the temperature is about 450° C higher on Venus, the activity of water is considerably greater. If reaction rates are high, then the rate of fixation of carbon dioxide by reaction with silicates will depend on the rate at which new silicate materials are exposed at the surface by processes such as volcanism, mechanical weathering, and eolian transport. Venus maintains a thick carbon dioxide atmosphere (table 4.4). This could simply be a reflection of extremely low reaction rates of carbon dioxide with silicates at the surface. However, if reaction rates are fast, as has been proposed, then the carbon dioxide must be efficiently recycled back into the atmosphere either by deep-seated processes such as burial followed by volcanism, or by processes at the surface which result in carbon-dioxide-fixing reactions under some conditions, and carbon-dioxide-yielding reactions under other conditions. Several authors have suggested that the lower atmosphere of Venus is complexly buffered and that several gases (H_2O, CO, HF, HCl, SO_2, COS), in addition to CO_2 are buffered by reactions with each other and with the surface. The specific reactions involved are uncertain partly because of the lack of knowledge of the chemistry of the lower atmosphere and the surface rocks. Any equilibrium achieved is likely to be dynamic, depending to some

Table 4.4. Composition of the Atmosphere of Venus (from Nozette and Lewis, 1982)

Species	Mole fraction	Source (6, 7)
CO_2	0.97	Pioneer and Venera
CO	2×10^{-4}	Earth-based
H_2O	2×10^{-5} to 5×10^{-4}	Pioneer and Venera
HCl	$>10^{-6}$	Earth-based
HF	$>10^{-8}$	Earth-based
N_2	0.03	Pioneer and Venera
$SO_2 + S_2$	$<3 \times 10^{-4}$	Pioneer and Venera
H_2S	10^{-6}	Pioneer
COS	$>3 \times 10^{-6}$	Pioneer

extent on the rate of turnover of the surface rocks, and to some extent on reaction rates.

Nozette and Lewis (1982) identified several reactions, involving common rock forming minerals and constituents identified in the lower atmosphere, that could take place at the surface (table 4.5). Some of the reaction could go in opposite directions at different elevations. At high elevations, for example, forsterite reacts with CO_2 to produce magnesite and enstatite but at elevations below 6052 km, where temperatures are higher, magnesite and enstatite recombine, giving off CO_2. Nozette and Lewis suggested that such reversible reactions could contribute to buffering of CO_2 in the atmosphere. In high areas, the surface reacts with the atmosphere to produce weathered products which are removed by creep or by the wind and deposited in the lowlands where the reactions are reversed.

Despite considerable attention given to weathering processes on the Venusian surface, large uncertainties remain, and have little chance of being resolved until better analyses are obtained of the lower atmosphere, and until we have good mineralogical analyses of the surface at various elevations.

GLOBAL TOPOGRAPHY AND SURFACE ROUGHNESS

Because of the near resonance between the rotation period of Venus and Earth's orbital period, the same side of Venus always faces Earth at closest approach. As a result, Earth-based elevation measurements and radar backscatter images are restricted to a limited region—between latitudes 50°S and 75°N, and 130° of longitude between 260° and 30°. Such restrictions do not, of course, apply to spacecraft data, and much of our recent increase in knowledge of planetwide variations in Venus surface properties results from the Pioneer mission. The Pioneer-Venus radar mapper operated at a wavelength of 17 cm and in two modes, altimetry and imaging (Pettengill et al., 1979a). In the altimetry mode, radar reflections from near the subspacecraft point were observed. Signal delay gives a

Table 4.5. Possible weathering reactions on Venus. Reactions marked with an asterisk proceed to the right at high altitudes and to the left in the hotter lowlands. Tremolite may, for example, form at high altitude but break down at low altitude (from Nozette and Lewis, 1982)

$Mg_2SiO_3 + 2CO_2 \quad 2MgCO_3 + SiO_2$ (forsterite; magnesite; quartz)	(1)
$Mg_2SiO_4 + CO_2 \quad MgCO_3 + MgSiO_3$ (enstatite)	(2)*
$Fe_2SiO_4 + 4\ COS \quad 2FeS_2 + SiO_2 + 2CO + 2CO_2$ (fayalite; pyrite)	(3)*
$MgSiO_3 + 2HF \quad H_2O + MgF_2 + SiO_2$ (sellaite)	(4)
$CaCO_3 + MgSiO_3 + CO_2 \quad CaMg(CO_3)_2 + SiO_2$ (dolomite)	(5)
$2CaAl_2Si_2O_8 + 5MgSiO_3 + SiO_2 + H_2O \quad Ca_2Mg_5Si_8O_{22}(OH)_2 + 2Al_2SiO_5$ (tremolite)	(6)*
$2CaMgSi_2O_6 + 3MgSiO_3 + SiO_2 + H_2O \quad Ca_2Mg_5Si_8O_{22}(OH)_2$ (diopside)	(7)*
$KAlSi_3O_8 + 3MgSiO_3 + 2HF \quad KMg_3AlSi_3O_{10}F_2 + 3SiO_2 + H_2O$ (orthoclase; fluorophlogopite)	(8)*
$Mg_2SiO_4 + 2CO_2 + SO_2 \quad 2MgSO_4 + SiO_2 + 2CO$	(9)
$CaAl_2Si_2O_8 + SO_2 + CO_2 \quad CaSO_4 + Al_2SiO_5 + SiO_2 + CO$ (anhydrite)	(10)*
$CaMgSi_2Si_2O_6 + SO_2 + CO_2 \quad CaSO_4 + MgSiO_3 + SiO_2 + CO$	(11)*
$Mg_2SiO_4 + 1/2CaMgSi_2O_6 + CO_2 \quad 1/2CaMg(CO_3)_2 + 2MgSiO_3$	(12)*

measure of surface elevation; backscatter efficiency gives an indication of slopes in the meter- to decameter-scale. Elevations were measured to an accuracy of about 200 m. The areal resolution cell ranged from 23×7 km to 101×101 km, depending on the altitude of the spacecraft during the observations (Pettengill et al., 1979b, 1980). In the imaging mode, the antenna was rotated to observe the surface on either side of the ground track, thereby enabling scattering efficiencies at relatively high angles (30°–58°) to be measured. At these angles scattering by small-scale (cm) roughness elements dominates.

The orbiter started mapping in December 1978 and continued, with some interruptions, until July 1980 (Colin, 1980). For most of the mission, the spacecraft was in a 24 hr orbit with an inclination of 140°; periapsis was maintained at altitudes between 140 and 190 km. As the planet rotated and moved in its orbit, the ground track of the orbiter was offset in longitude by 150 km at the equator. The orbit periapsis, about which most of the measurements were made, completed two and one-half passes around the planet during the course of the mission. On the second or third periapsis passes over the same area, gaps in the previous coverage were filled or new observations interleafed between the previous tracks. The mission data have now been integrated into relief maps (figs. 4.6 and 4.7) and meter-decameter-scale roughness maps, which cover over 90 percent of the planet's surface at a spatial resolution of 100–200 km. Maps have also been compiled of the cm-scale roughness of the area between 10°S and 50°N, at resolutions as low as 30 km (Pettengill et al., 1980, 1982; Masursky et al., 1980).

Much of the Venusian surface is a rolling plain of relatively uniform elevation. As a result, 60 percent of the planet's surface is within 500 m of the modal radius of 6051.1 km; 20 percent is within 125 m (fig. 4.8). Deviations from the modal value are biased heavily toward high elevation; about 20 percent of the surface has an elevation more than 1 km above the modal value, whereas less than 1 percent has elevation more than 1 km below it. The higher areas form a few continental size masses and smaller islands that stand above the global plain. The highest point so far measured (radius of 6062.1 km) is in the Maxwell Montes at 64°N, 2°E. The lowest point measured is in Diana Chasma at 14°S, 156°E, where the planet's radius is 6049.0 km.

The single mode of the elevation histogram for Venus is in sharp contrast to the strongly bimodal distribution of Earth's topography (fig. 4.8, table 4.6). The distributions for all the terrestrial planets have a high elevation tail, a phenomenon that appears to occur at all scales on natural topographic surfaces. On Mars, Earth, and the Moon, the elevation distributions are largely controlled by the various crustal provinces—continents and ocean basins on Earth; uplands and maria on the Moon; lowland plains, cratered uplands, and Tharsis plateau on Mars. The simple elevation distribution for Venus, and the similarity in its skewness to terrestrial continents, suggest a single global crustal province that is topographically similar to Earth's continents. Venus appears to have the same proportion of rugged, youthful mountains as Earth, although the mechanisms that created and modified them may be very different.

Masursky et al. (1980) divided the Venus surface into three major components on the basis of elevation. Their lowland province includes all areas below the reference radius of 6051.0 km and constitutes 27 percent of the surface. The most extensive lowland basin, Atalanta Planitia, centered at 65°N, 165°E is about the size of the Gulf of Mexico. Its surface averages 1.4 km below the datum, and like the surface of most other low areas of the planet, it is sparsely cratered and radar dark. Masursky et al. suggested that these low areas are volcanic plains analagous to the lunar maria, although as already noted, eolian deposits may preferentially accumulate in these low areas and be widely exposed at the surface. Their presence could in part account for scarcity of crater-like dark rings on this unit as compared with the rolling plains.

The second major component of the surface is the rolling plains, which include all those areas with radii between 6051.0 and 6053.0 km, about 65 percent of the planet. The unit is characterized by Root Mean Square slopes of 1°–3° in the meter- to decameter-scale, and probably gently rolling topography at the kilometer scale. Circular features 20–300 km in diameter, with shallow flat floors and radar-bright rims, are more common on this unit than on any other part of the surface. In addition to these crater-like features are several circular radar bright areas, 200–300 km across and up to 1.5 km high. Some have a central dark region of lower elevation and are tentatively interpreted as volcanoes.

The third major component of the surface is the highlands. These occur in three continent-size areas. The first is Ishtar Terra, centered at 70°, 340°E. Its highest part consists of the Maxwell Montes, which

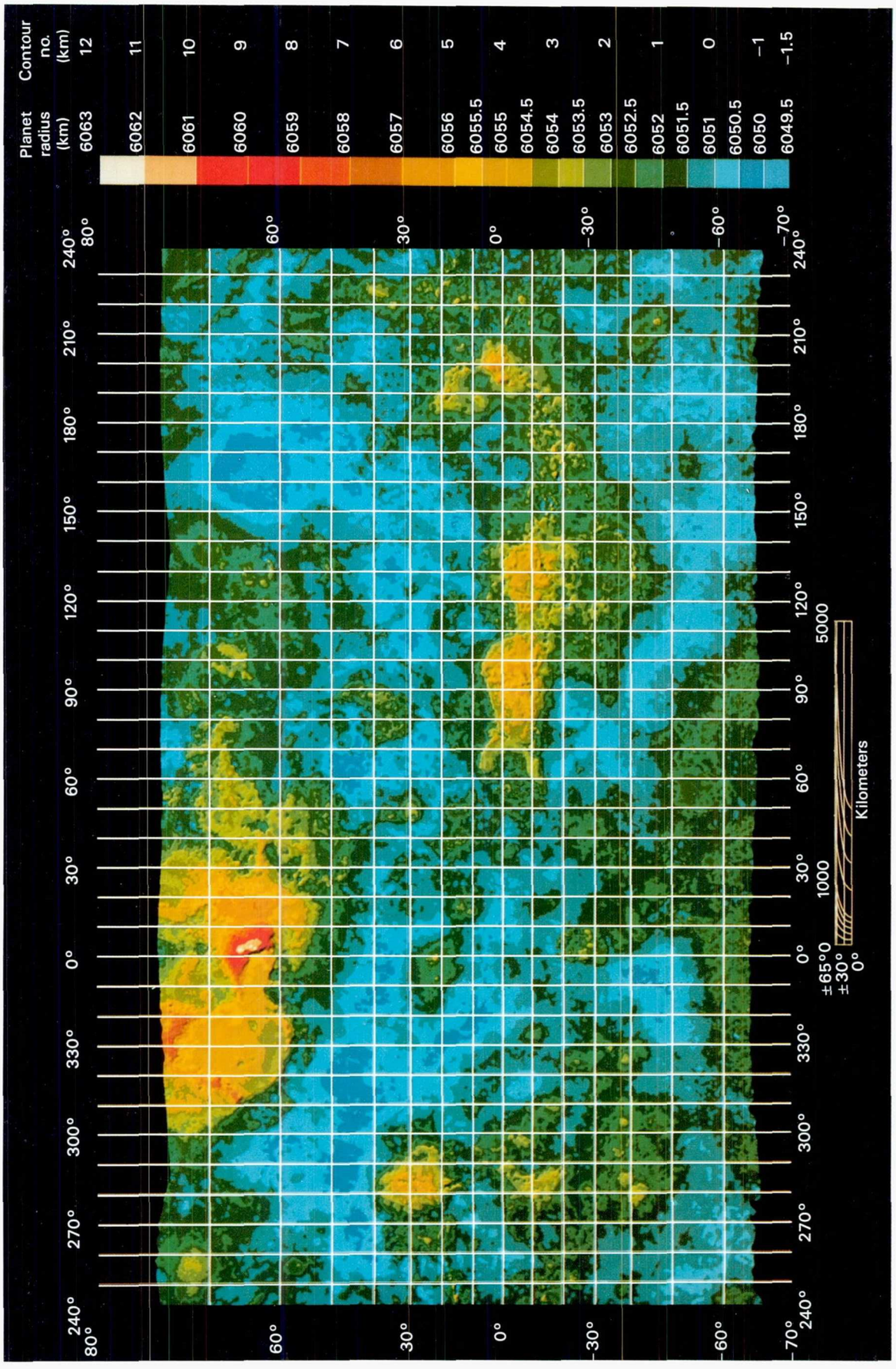

Figure 4.6. A color-coded contour map of elevations of the Venusian surface. High areas are shown in reds and yellows, low areas in blues.

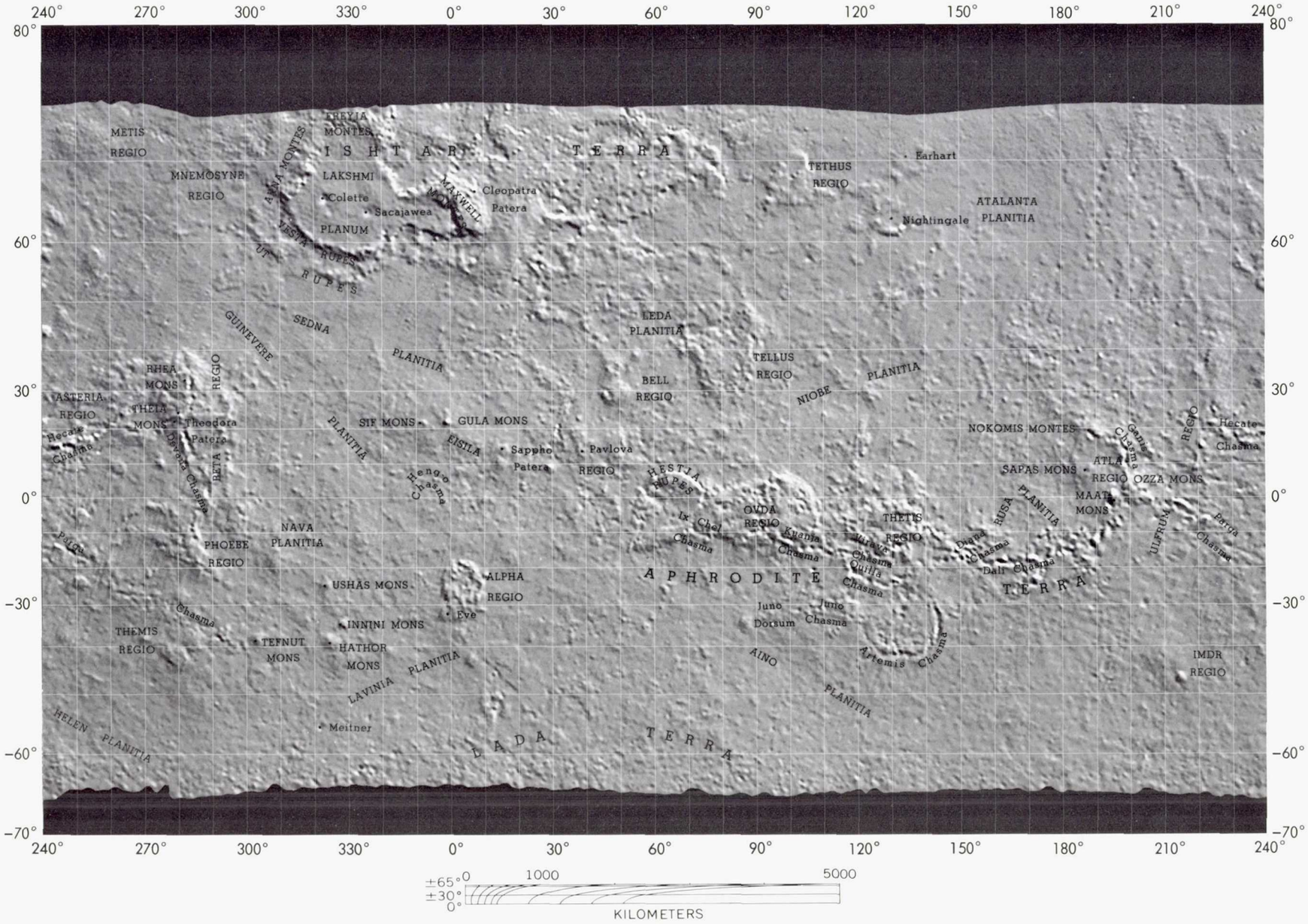

Figure 4.7. The same data as in figure 4.6 but depicted as shaded relief with illumination from the northeast.

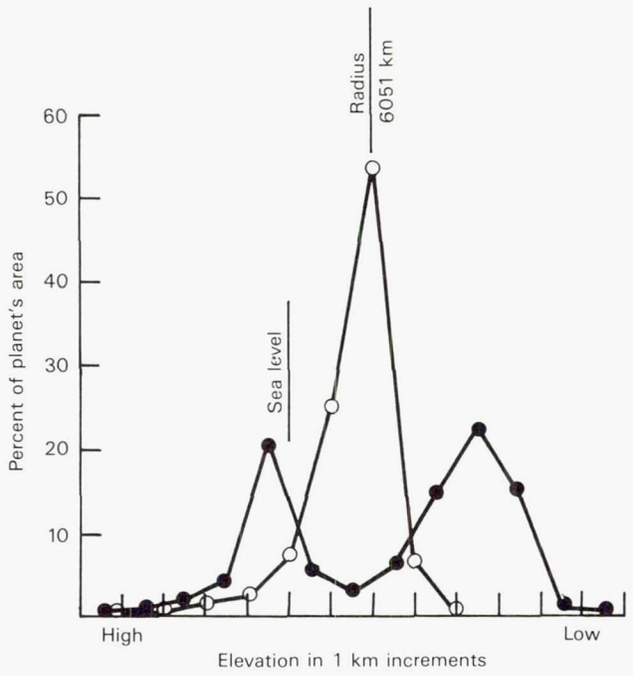

Figure 4.8. Hypsometric curves for Earth and Venus. The curve for the Earth is bimodal with peaks near sea level and at the depths of mature ocean floors. The Venus data are unimodal as skewed toward higher elevations.

extend to heights of 11 km above the datum. The mountains are radar bright and have meter-decameter slopes in the range of 4°–10°; a dark circular feature, possibly a caldera, is situated 2–4 km below the summit. To the west of Maxwell Montes is a dark, roughly circular plain, Lakshmi Planum, standing 4–5 km above the datum. The plain appears to be cratered and is bounded on the south and west by an abrupt, arcuate scarp. Masursky et al. (1980) interpret Lakshmi Planum as an ancient uplifted surface covered with a thin veneer of younger flows. To the east of the Maxwell Montes is some topographically complex terrain, 2–3 km above the datum and consisting of numerous closed depressions with no consistent regional trends.

The second and largest major upland area is Aphrodite Terra, which is about the size of Africa and elongates in a roughly E-W direction between 70° and 210°E just south of the equator. Western and central mountainous regions named Ovda Regio and Thetis Regio, respectively, are separated by a low saddle. South and east of the central mountains are a complex of linear troughs and ridges, the most prominent being the semi-circular Artemis Chasma. The ridges and troughs merge eastward with the mountains of Atla Regio, which mark the eastern end of Aphrodite

Table 4.6. Percentage of Mapped Area of Venus Within Topographic Intervals (from Masursky et al., 1980)

Planetary radii class interval (km)	Percent area in interval	Cumulative percent area in and above interval
6061.9–6061.5	00.004	00.004
6061.5–6061.0	00.005	00.009
6061.0–6060.5	00.007	00.016
6060.5–6060.0	00.006	00.022
6060.0–6059.5	00.010	00.032
6059.5–6059.0	00.008	00.040
6059.0–6058.5	00.010	00.050
6058.5–6058.0	00.007	00.057
6058.0–6057.5	00.013	00.070
6057.5–6057.0	00.016	00.086
6057.0–6056.5	00.047	00.133
6056.5–6056.0	00.106	00.239
6056.0–6055.5	00.327	00.566
6055.5–6055.0	00.594	01.160
6055.0–6054.5	01.106	02.266
6054.5–6054.0	00.965	03.231
6054.0–6053.5	01.692	04.923
6053.5–6053.0	02.440	07.363
6053.0–6052.5	05.376	12.739
6052.5–6052.0	08.982	21.721
6052.0–6051.5	17.376	39.097
6051.5–6051.0	33.664	72.761
6051.0–6050.5	20.533	93.294
6050.5–6050.0	06.091	99.385
6050.0–6049.5	00.607	99.992
6049.5–6049.0	00.008	100.000

Terra. Here the terrain has a dominantly N–S trend, in contrast to the mainly E–W lineaments in the rest of Aphrodite. The eastern mountains are slightly higher (5.7 km above datum) than the western and central mountains (5.5 km above datum). All of Aphrodite exhibits complex patterns of topography, RMS slopes, and backscatter efficiency—patterns that suggest an abundance of steep blocky slopes.

The third major upland region is Beta Regio, centered at 30°N, 285°E. It is composed of two shield-shaped mountains, Theia Mons and Rhea Mons, which reach elevations of 4–5 km above the datum. Both have been interpreted as possible volcanoes (Malin and Saunders, 1977). Smaller elevated areas, Phoebe Regio and Themis Regio, occur to the south of Beta and appear connected to it by a N–S linear disruption zone upon which the two supposed volcanoes lie (McGill et al., 1981).

A vast series of canyons and linear disruption zones connect most of the high ground at low latitudes (fig.

4.9). The largest troughs, the Diana and Dali Chasmata, are 3000–3500 km long and 75–100 km wide (Schaber, 1982). They are part of a broad (1000–1500 km) linear zone of disruption that extends from the west end of Aphrodite through Atla Regio to Beta Regio over 20 000 km to the east. The fracture system thus extends almost three-quarters of the way around the planet in a roughly E–W direction. A second disruption zone, with a prominent rift, Devana Chasma, extends south from Beta Regio at the west end of Aphrodite. The most prominent of all the rifts, the semi-circular Artemis Chasma, does not lie on any of the disruption zones just outlined, but rather lies just to the south of the main E–W system.

SURFACE ROUGHNESS

To first order, roughness correlates strikingly with elevation; elevated regions are much rougher than low regions. This is true, both of the Pioneer-Venus data measured at a wavelength of 17 cm and Earth-based data. Venus is smoother at the centimeter- to meter-scale than the Moon or the rough regions of Mars. Most of the planet has meter-scale RMS slopes between 1° and 3° (Masursky et al., 1980). According to the Apollo bistatic radar experiment, the Moon has slopes of 3° to 4° (Moore et al., 1980; Tyler, 1979). Meter-scale roughness on the Moon is dominated by impact debris. The youngest craters, mostly of Copernican and Eratosthenian age, appear as bright rings in the radar images, but older craters do not, probably because continual break-up of blocks in the floor and rim ejecta reduces the surface roughness. Mars has regions that are much rougher than is typical for Venus, and regions that are perhaps smoother. The volcanic plains in the Tharsis region of Mars, for example, have 10° to 15° slopes, whereas the plains of Elysium and Syrtis Major have slopes of 1° to 2° at 12 cm wavelength (Downs et al., 1973, 1975; Simpson et al., 1978). An aging process that reduces roughness appears to occur both on Mars and the Moon. Older volcanic plains may be smoothed by sand blasting, the removal of weathered products by the wind, and

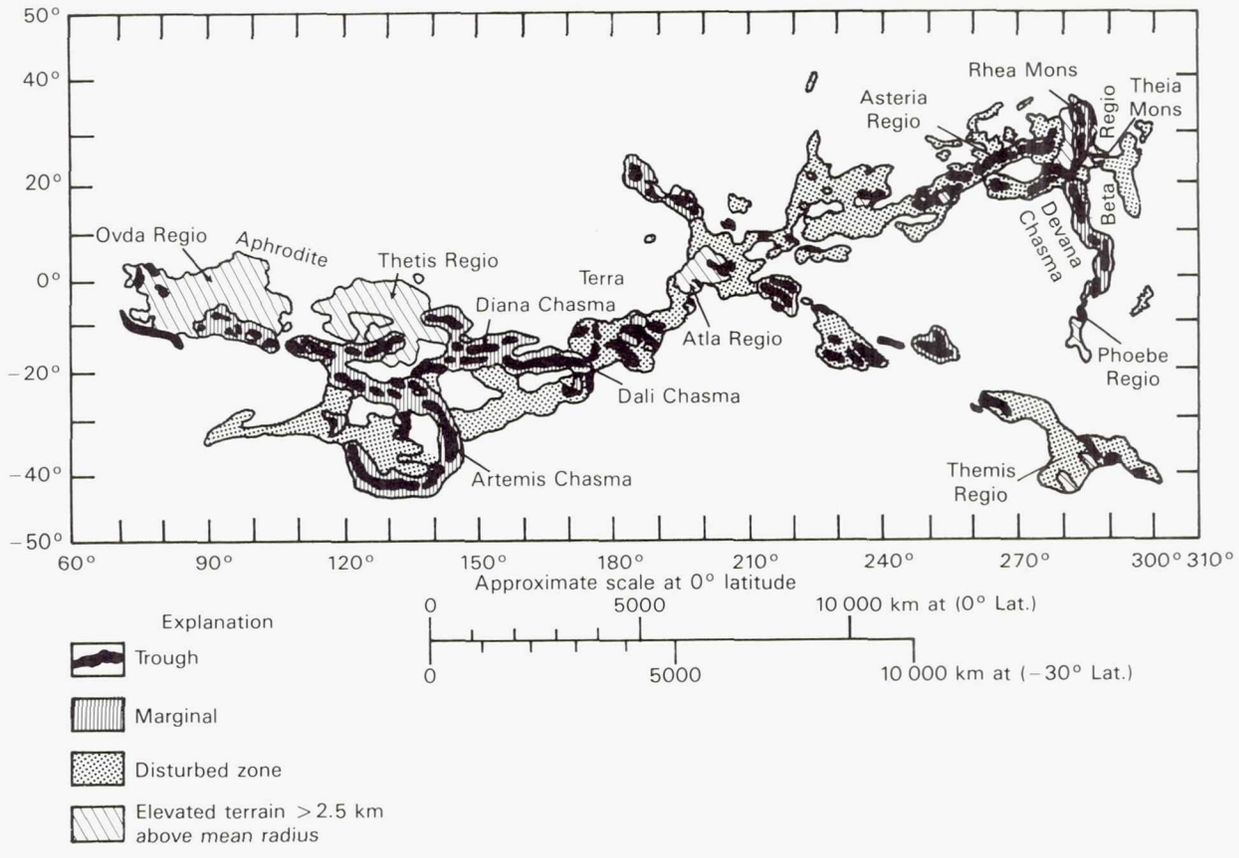

Figure 4.9. Structural sketch map showing interconnected troughs, marginal ridges, disturbed zones, and elevated terrain between Beta Regio and Themis Regio to the east and Aphrodite Terra to the west. The interconnected system stretches in a roughly E–W direction around roughly two-thirds of the planet near the equator (from Schaber, 1982).

through mantling by the products of eolian and chemical processes.

Venus has a wide range of roughness. The highest regions are probably rough, primary volcanic surfaces, but most of the surface has probably been smoothed by weathering and sedimentary mantling as on Mars. Numerous bright circular features have been interpreted as impact craters. If their present size frequency distribution (Campbell and Burns, 1980) represents an equilibrium between crater production and destruction by erosion and sedimentation, then crater obliteration rates of 10^{-5} to 10^{-7} cm/yr are implied, which are more comparable to Mars rates than terrestrial rates.

BRIGHT RADAR RINGS

Bright rings are prominent on many radar images of Venus (Rumsey et al., 1974; Campbell et al., 1979; Goldstein et al., 1976, 1978). They are common on the rolling plains unit but generally absent in the elevated regions. If they are impact craters, then they provide a means of assessing the age of the surface, and the rates of erosion and viscous relaxation of the lithosphere, so that their origin is of crucial importance for understanding the evolution of the surface.

A number of roughly circular bright rings can be seen in Goldstone images of the equatorial region (Rumsey et al., 1974; Goldstein et al., 1976, 1978). The incidence angles are generally less than 6°, and at these angles the backscatter is strongly slope dependent. The ratio of rim width to crater diameter is typical of that for impact craters on other planets, and generally different from that for volcanic features. The bright rings thus appear to be impact craters with raised rims (Saunders and Malin, 1977), but an impact origin is far from proven (McGill et al., 1982). Campbell and Burns (1980) identified 33 bright rings on Arecibo images which generally have higher incidence angles than the Goldstone images, and tend to emphasize variations in backscatter rather than slopes. Several large (>300 km) radar-dark circular features have also been interpreted as impact basins (Masursky et al., 1980).

Thompson et al. (1980, 1981) and Cutts et al. (1981) investigated radar images of lunar craters, and these may provide a basis for interpreting the Venus images. The radar signature of lunar craters is initially a continuous radar-bright region up to 20 times the diameter of the associated crater. Cutts et al. reported that most lunar crater signatures shrink with age rather rapidly until only the crater rim is bright and then this gradually fades. The floor signature has a much greater lifetime than that of the ejecta zone. Radar bright rings are rare on the Moon, and Cutts et al. suggested that they occur only where a crater has been embayed by mare material. This observation might lead to the conclusion that bright-ring features on Venus are volcanically filled craters. However, Cutts et al. suggested a similar result would follow from mantling of rough, radar-bright areas with fine impact debris produced during basin formation.

Saunders et al. (1982) examined the bright ring radar features in 3.8 cm lunar images (Zisk et al., 1974; Thompson, 1974). About 30 radar-bright rings were identified that met the selection criteria that they be complete rings encompassing darker floors and not be at extreme ranges of radar incidence angles. The features found in this study do not occur preferentially on maria, plains, or terra. Somewhat surprisingly, only three of the features have mare-flooded floors. With one exception, an Imbrian crater, all the rings are associated with Copernican and Eratosthenian craters. The diameter distribution of these craters falls along a production curve. Comparison with topography suggests that the inner diameter corresponds to the crater floor diameter, as suggested by Cutts et al. (1981). The outer diameter corresponds to the diameter of the raised crater lip. The implication is that, on the Moon, relatively level areas such as crater floors and the surrounding ejecta deposits quickly become dark to the 3.8 cm radar as a result of impact comminution. Slope appears to be the major contributor to radar brightness.

Saunders et al. (1982) proposed that the evolution of the radar signature of lunar craters is largely slope controlled. Impact craters are initially an extensive radar-bright region. The ejecta and floor become relatively smooth in a short time, but the rim lip and crater walls remain rough until their slopes have been so reduced by erosion that downslope movement of erosion products no longer continuously exposes blocky material.

The processes of crater erosion on Venus are not known. However, it might be expected that, as on the Moon, only a fraction of the total number of circular features is detected, and that their radar signature changes with time as the craters are eroded. The strong correlation between elevation and reflectivity apparent in the Pioneer-Venus data (Pettengill et al.,

1980) suggests that slope is a major factor in controlling backscatter. The radar-bright rings are therefore likely to be caused by steep slopes surrounding a relatively flat circular feature, and impact craters are the most plausible candidates.

If the radar-bright rings are impact craters, then estimates can be made of resurfacing rates on Venus and the ages of different Venusian surfaces. The flux of objects in the size range that would have produced the observed craters has been essentially identical for Earth and Venus, and affected little by the atmosphere (Tauber and Kirk, 1976). Assuming lunar fluxes, Campbell and Burns (1980) estimated from the density of radar-bright rings that the rolling plains have an impact age of 600–800 million years. However, Saunders and Malin (1976) found that the densities varied greatly, and while the plains overall have a crater density that is less by a factor of ten than that of the lunar highlands, densities in small areas may approach those of the lunar highlands. If the rings are of impact origin, the Campbell and Burns "age" is probably a minimum age, being more indicative of the lifetime of the radar-bright signatures than of the surface itself. Presumably older craters that have lost their radar signature could still be present, but remain undetected.

The impact crater hypothesis therefore leads to the supposition that the rolling plains are older than the highland regions and that some of the plains may date back to the decline in impact rates 3.8 billion years ago. Clearly, if a significant fraction of the rings are volcanic, then none of these conclusions are valid. The relative ages of highlands and lowlands remain unknown as well as the absolute ages.

The case for an impact origin for the large (>200 km) dark, quasi-circular features is far less convincing than that for the bright rings. Solomon et al. (1982) recognized two types: (1) circular areas of low radar backscatter and little topographic relief, and (2) large, roughly circular depressions, such as Atalanta Planitia, which is 4000 km across and over 2 km deep. Masursky et al. (1980) likened these dark features to lunar impact basins, and from their size frequently concluded that they were at least 3.8 billion years old. However, Solomon et al., demonstrated that if surface temperatures throughout much of Venus' history were comparable to those that presently prevail, then viscous relaxation would eliminate almost all topographic relief in basins larger than a few hundred kilometers across within 3 billion years. They conclude, therefore, that the large topographic basins, such as Atalanta Planitia, are geologically young and have formed by some process other than impact. One possibility is that they are analagous to terrestrial platform basins, produced by lithospheric extension and thermal subsidence.

GRAVITY

The gravity field of Venus shows strong correlation with topography, large gravity highs coinciding with large topographic highs (Ananda et al., 1980; Sjogren et al., 1980; Phillips et al., 1981; Reasenberg et al., 1981; Esposito et al., 1982). The situation thus differs from that on Earth where gravity is only poorly correlated with the regional-scale topography. The Venusian anomalies are generally smaller than those on the Moon and Mars where 100 mgal anomalies are common. The largest, that associated with Beta Regio, is 135 mgal at a reference altitude of 200 km (Esposito et al., 1982). For comparison, a 500–600 mgal anomaly, referenced to the global mean, occurs over Olympus Mons on Mars.

Simulation of the anomalies that would be produced by the observed topography implies that significant compensation of the topography has taken place. Phillips et al. (1981) attempted to place limits on lithosphere thickness and rigidity by comparing topography and gravity at different wavelengths. They showed that depths of compensation of 100 km or more are required if the topography is supported by density variations alone. If compensation is at shallower depths, then a combination of density differences and flexural rigidity of the lithosphere is required to support the topography. They concluded that, because of creep within the lithosphere, the topography can be supported passively only if it is very young, on the order of 10^7 years, or if the heat flow is considerably less than that on Earth, which they consider unlikely. Another possibility is that the lithosphere is supported dynamically from below, such as by convection beneath the lithosphere (McGill et al., 1981). These conclusions are reinforced by the more recent work of Esposito et al. (1982) who demonstrated that compensation depths of 300–400 km are required to explain the large anomaly over Beta Regio. Weertman (1979), however, questioned the use of terrestrial creep rates in estimating the strength of the Venusian crust. He suggested that, despite the higher temperatures, creep rates in the Venusian lithosphere may be sub-

stantially less than in Earth's because of the lower water content.

PLATE TECTONICS ON VENUS

Much of the speculation about the evolution of the Venusian surface has focused on whether plate tectonics have ever occurred on the surface (McGill, 1979; McGill et al., 1982; Phillips et al., 1981; Solomon and Head, 1982). The speculation is triggered by several considerations. First, the similarity in size of Venus and Earth should lead to similar surface heat flows if compositions are comparable. Second, the vast rift systems on Venus could be analogous to the divergent rift zones of Earth. Third, strong correlation of gravity and topography, coupled with some estimates of young crater ages, suggests the topography might be young. Fourth, early chemical analysis of the surface materials, from Venera 8, pointed to the possibility of granitic materials.

Head et al. (1981) and Arvidson and Davies (1981) assessed the likelihood of detecting present-day plate tectonics on Venus solely from the topography. They reconstructed images of Earth using digital terrain data with elements 100 km on a side in order to simulate the Pioneer-Venus resolution. In their simulations many of the diagnostic features of plate tectonics, such as mountain chains and island arcs, disappear. The continents look level and featureless but ocean floor ridges and some trenches are resolved. Arvidson and Davies asserted that a ridge system comparable to the ocean ridges of Earth should be discernible in the existing data even after correcting for the temperature of the Venusian surface and the lack of loading by ocean water. On the other hand, Head et al. (1981) and Solomon and Head (1982) believed several factors in addition to surface temperature and water loading could affect the configuration of the ridges; maintaining that a ridge system could be easily masked on the rolling plains.

Some care must be taken in the application of these analog studies. It is important to understand that the altimeter used by Pioneer-Venus has a horizontal resolution that is determined by the effective length of the pulse. In general, the range that is detected will be that of the nearest surface in the beam. Elevated features tend to be smeared out and depressions such as trenches appear narrower because of the geometric effects of the altimeter system. Experience with radar suggest that the smallest features that can be resolved have dimensions of many radar resolution elements, although linear features may require only three or four depending on how irregular they are.

Other reasons for exercising care in the application of Earth analogs to the interpretation of Venus data is that we do not fully understand the effects of the hydrosphere, atmosphere, and biosphere on Earth's topography. The major fold mountain systems would not appear as they do without the influence of any one of these factors. Of the highest peaks on Earth, the top one hundred or more consist primarily of marine sedimentary rocks.

Phillips et al. (1981) cited differences in profile between the oceanic ridges of Earth and possible counterparts in the Venusian highlands as evidence of their being of different origins. The flanks of the oceanic ridges are concave upward, reflecting contraction by cooling, whereas the elevated areas of Venus, such as Aphrodite and Beta Regio, are convex upward. The ridges of Venus are also convex upward. Kaula (1981) added that the ridges on Venus do not have a narrow distribution about a mode in crest height as do terrestrial oceanic ridges. But both these arguments are relevant only if the Venusian highlands are believed to be the analogs of the terrestrial oceanic ridges, which is doubtful (Solomon and Head, 1982). Furthermore, Brass and Harrison (1982) asserted that the general form and detectability of tectonically created features depend on the balance between erosion rates and rates of plate motion. If erosion rates on Venus are relatively high, linear trenches and rift valleys will fill and not be recognizable.

Theoretical arguments have also been raised against plate tectonics. Anderson (1981) argued that the high surface temperatures will prevent plate tectonics, because the lithosphere can never cool to a low enough temperature to become negatively buoyant. Thus, the currently favored mechanism for driving plate tectonics, drag of negatively buoyant lithosphere into subduction zones, cannot work. Weertman (1979) showed that plate tectonics could occur on Venus only if the rocks were extremely dry, for only then would the lithosphere have the required rigidity at the relatively high Venusian lithosphere temperatures. Finally, Kaula (1981) showed, from the number of possible spreading centers and the dimensions of the observed ridges, that if the ridges formed by spreading, which he doubts, the amounts of internal heat lost through plate tectonics can be no more than 15 percent of the total lost by the planet. On Earth, 70 percent of the internal heat is lost through plate motion.

While acknowledging that plate tectonics are unlikely at present, Phillips et al. (1981) speculated that plate tectonics may have occurred in the past. As we saw above, counts of large craters suggest the rolling plains are ancient, whereas the highlands are relatively young. Phillips et al. suggested that equatorial highlands may have been former zones of divergence, and that at some relatively ancient time in Venus' history, plate tectonics ceased and basalt crusts tended to accumulate over the former divergent zones to form the relatively young equatorial highlands. Possible causes for cessation of plate motion are crustal thickening, loss of water from the interior, destabilization of water at the surface, and rise in surface temperatures as the extreme greenhouse developed.

Kaula (1981) compared the evolution of Venus with that of other terrestrial planets. He noted that on the basis of size and composition Venus might be expected to have evolved along a path similar to Earth. Yet, Venus is more Mars-like than Earth-like. He suggested that the contrast between Earth and Venus is largely due to the thicker atmosphere and consequent higher surface temperatures. These result in a greater depth to the basalt-eclogite transition, which in turn inhibits recycling of the crust. Venus has therefore a thicker crust than Earth, which coupled with the higher surface temperatures, increases the buoyancy of the lithosphere and prevents subduction.

ACKNOWLEDGMENTS

G. McGill of the University of Massachusetts and S. Solomon of the Massachusetts Institute of Technology made several suggestions for improving the chapter. Part of the work was performed by the Jet Propulsion Laboratory, California Institute of Technology and sponsored by NASA.

5
EARTH

Michael H. Carr

INTRODUCTION

The geologic evolution of Earth is vastly different from that of other planets. The surface of Earth is undergoing constant change; new crust is continually formed at mid-oceanic ridges and old crust is resorbed into the mantle at subduction zones; high ground is eroded by running water and the erosion products transported across the surface to be deposited in low areas; the surface rocks are chemically altered by interaction with the atmosphere and hydrosphere, and the weathered products become buried and reconstituted to form new high-temperature assemblages. On other terrestrial planets, with the only possible exception of Venus, because we know so little about it, the pace of geologic activity is orders of magnitude slower.

Earth's distinctive geologic features and processes are the result primarily of plate tectonics—the lateral movement of large, rigid lithospheric plates with respect to one another—and the presence of a relatively thick atmosphere and hydrosphere. Life may have also had a secondary effect, by changing the chemistry of the atmosphere and near-surface waters. The results of plate tectonics are deformation, magmatic activity, and slow mixing of materials within the outer few hundred kilometers of the planet. The action of water tends to reduce surface relief and to redistribute and fractionate surface materials. Neither of the two processes appears to have operated on other planets for any significant length of time. There may have been incipient plate tectonics on Venus (Phillips et al., 1981), and water may occasionally have flowed across the surface of Mars, but in neither case were these processes sufficiently sustained to produce global modifications of the surface.

The intent of this chapter is to provide some basic information about Earth and the nature of the geologic processes that have resulted in its present configuration so that its style of geologic activity can be contrasted with the other planets. The perspective is global. Specific processes such as sediment transport, generation of magma, and weathering are discussed only insofar as is necessary for depiction of the general geologic framework. The emphasis is on the forces that control the evolution of the entire planet and give Earth its distinctive geology. Plate tectonics is discussed in some detail because of its importance in understanding Earth's present tectonic framework, although to what extent plate tectonics has operated throughout the planet's history is still very uncertain. The early history of Earth also receives special emphasis because of its importance in understanding how Earth set off on an evolutionary path so different from that of the other planets. The chapter is somewhat shorter than the others because the subject has been treated so extensively elsewhere, and many of the sources quoted are secondary because of the vast literature on Earth.

This section starts with a few general comments about the topography and physiography of the surface and then goes on to an account of plate tectonics. This mostly concerns the planet's recent history, although the discussion concludes with some extrapolations back 600 million years. Next follows an examination of Earth's interior, followed by a review of various theories for the origin of Earth. Earth's early history is then discussed and this leads us through the Archean and Proterozoic Eons up to the start of the Paleozoic Era where the plate tectonics section left off. The chapter concludes with a brief examination of the evolution of the atmosphere and hydrosphere.

GENERAL PROPERTIES

Earth is slightly pear-shaped with an average equatorial radius of 6378 km and an average polar radius of 6275 km. The most distinctive feature of the surface is the division into land and sea. Only 29 percent of the solid surface is exposed; the rest is under water. The land is also unevenly distributed, with over 65 percent in the northern hemisphere. To emphasize the asymmetry, dividing Earth into two hemispheres, one with a pole near Spain at 0° longitude, 38°N, and the other with a pole near New Zealand, puts 81 percent of the land on the Spain-centered hemisphere. The distribution of land and sea roughly corresponds to the distribution of continental and oceanic crust. However, because the sea extends onto the continental margins, the fraction of Earth's surface that is continent (41 percent) significantly exceeds that which is land.

The continents can be divided into three main components: (1) shield areas which consist mostly of exposed, highly deformed and metamorphosed Precambrian (>570 million years old) rocks, (2) platform areas, where the shieldlike basement is covered with a relatively thin (generally <2 km) veneer of mostly unmetamorphosed deposits of late Precambrian or younger age, and (3) linear ranges of highly folded and metamorphosed Phanerozoic rocks. These are in two main belts, one around the Pacific (Andes, Rockies, Alaska, Japan, and Philippines) and the other extending roughly east-west, south of Eurasia (Alps, Turkey, Iran, Himalayas, and Indonesia).

The oceans can similarly be divided into three main components. The deep ocean basins constitute around 40 percent of the sea floor. They range in depth from 4 to 6 km and have low gradients broken only by an occasional volcanic mountain. The second major component consists of broad ridges that form an interconnected global network. The axes of the ridges are sites of plate divergence, where new lithosphere is currently being formed. Most ridges are 1000 to 4000 km across with elevations 1–2 km above the floors of the ocean basins. Along their axes is commonly a rift valley. The third and deepest parts of the oceans are within ocean trenches. These form where plates converge, and one plate dips under the other, dragging down the ocean floor. Examples are the Kermadec-Tonga trench north of New Zealand, and the Java trench south of Java and Sumatra.

The relief forms of Earth are thus mainly linear—mountain chains of folded and metamorphosed rocks, ocean ridges, and ocean trenches, separated by areas of low relief. This topographic style contrasts markedly with the other terrestrial planets on which circular impact structures dominate the landscape. Earth's topography is also mostly young, which is the reason why impact craters are rare. The ocean trenches are forming today, the ocean floors are mostly less than 200 million years old, and most of the extreme relief on the land results from volcanic and tectonic activity that occurred during the last 100 million years. The high rates of volcanism and deformation are complemented by high rates of erosion and deposition. Average erosion rates for North America are estimated at 3×10^{-3} cm/yr (Menard, 1961). For comparison, erosion rates for the Chryse basin on Mars are estimated at no more than 10^{-7} cm/yr (Arvidson et al., 1979). Rates for Mercury and the Moon are even lower.

The hypsometric curve for Earth is markedly bimodal with one peak at sea level and a second at 4 km below sea level (fig. 5.1). The first peak results because 71 percent of the land is at an elevation within 1 km of sea level, a reflection of the efficacy of water in reducing relief on the land. The second peak at about 4 km below sea level is much broader than the first and is an indication of the average depth of the ocean basins. Extremes of elevations occur along plate boundaries; the highest mountains occur where surface materials are folded and squeezed between convergent plates, and the deepest ocean trenches are at subduction zones where one plate dips under another. The total relief is about 20 km, measured from the 8.85-km summit of Mount Everest to a depth of 11 km in the Marianas trench. The relief is in large part isostatically compensated. Topographic highs are at least partly compensated by low density rocks at depths. Similarly, topographic lows are partly compensated for by dense materials. Free-air gravity anomalies are thus mostly small and the free-air gravity is only poorly correlated with topography, in contrast to the close correlation on the other terrestrial planets. Most of the compensation appears to take place within 35 km of the surface, the mean thickness of the continental crust.

Most of the tectonic activity of Earth, as indicated by both relief and earthquakes, is concentrated along plate margins (fig. 5.2). A narrow zone of relatively shallow earthquakes occurs along the axis of the oceanic ridges. Subduction zones, where old oceanic crust is being ingested into the mantle, are marked by intense seismic activity, much of it in relatively deep

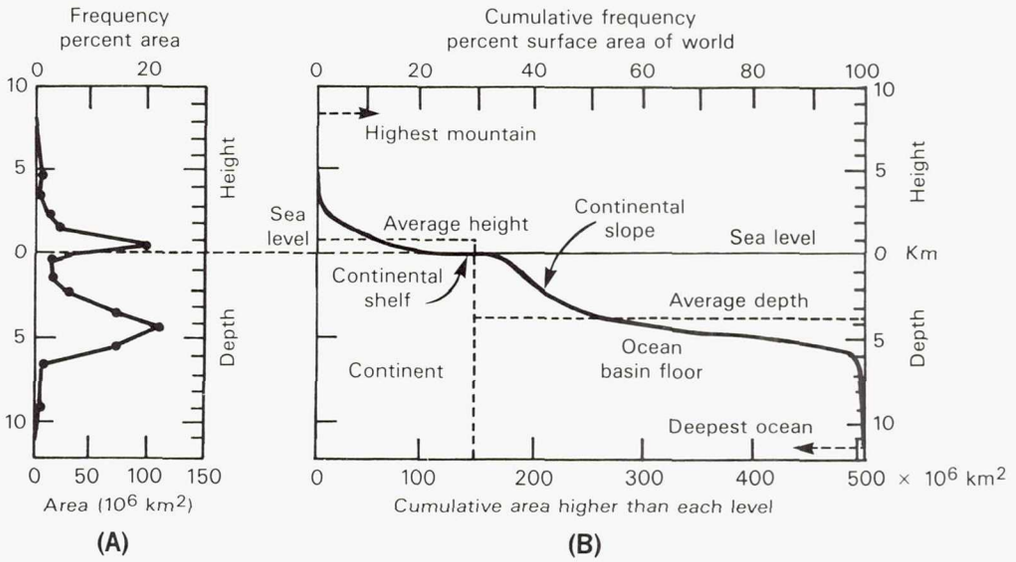

Figure 5.1. Distribution of areas of solid Earth according to surface elevation. (A) Frequency distribution. (B) Cumulative hypsographic curve (Wyllie, 1971).

Figure 5.2. Plot of earthquake epicenters from 1961 to 1967 (Baranzangi and Dorman, 1969). Most occur at plate junctions so their locations outline plate boundaries.

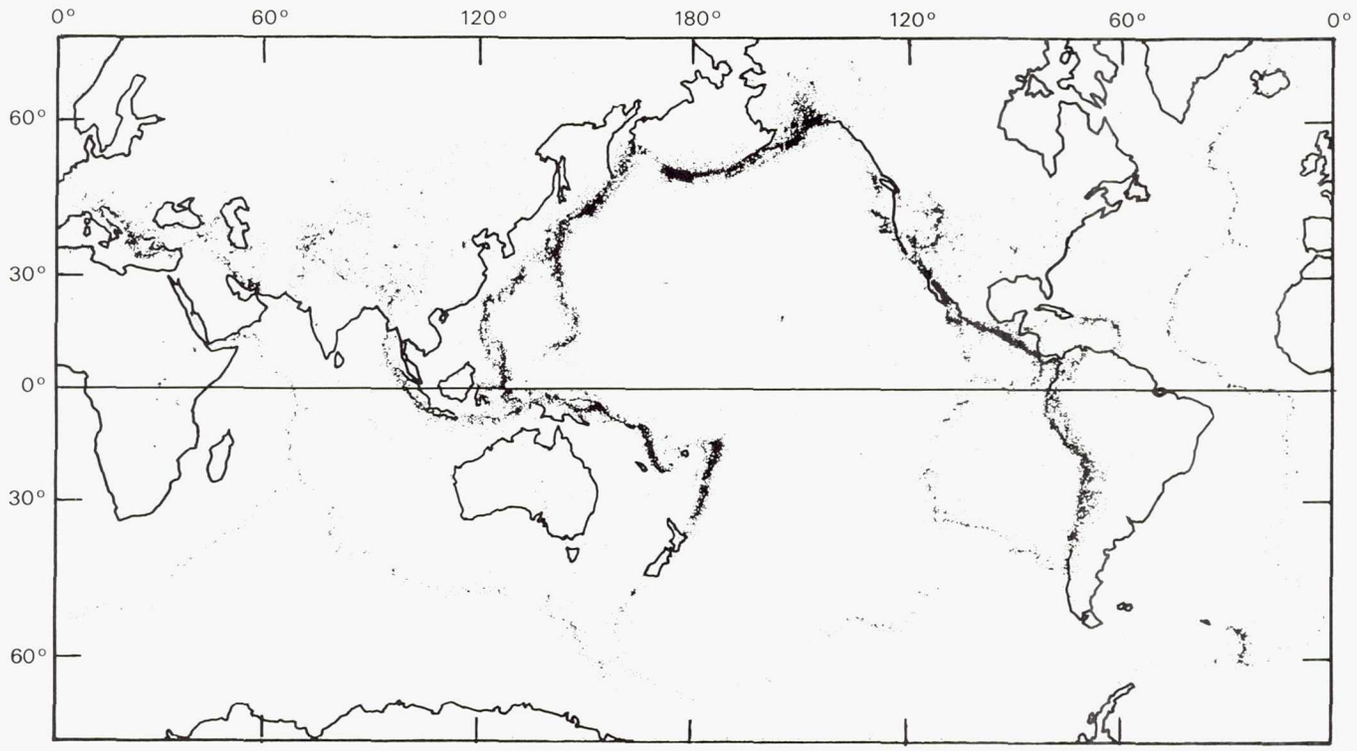

(>100 km) earthquakes. Transform faults, which form where plates slide by one another, are characterized by relatively shallow earthquakes. From maps of the incidence of earthquakes, therefore, the outline of the lithospheric plates can readily be discerned (fig. 5.2). The northern and western boundaries of the Pacific plate, for example, are delineated by seismic activity along subduction zones; the eastern margin is indicated by seismic activity along the western margin of North America and along the East Pacific Rise. Where two continents converge, as in the cases of Africa–Arabia and India approaching the southern edge of Eurasia, seismic activity is spread over a broad belt and plate boundaries are not clearly marked.

Volcanic activity is also concentrated along plate boundaries. Of the more than 800 volcanoes active

today, over 75 percent are along subduction zones that form the "ring of fire" around the Pacific. Volcanoes are also common along other convergent margins as in Indonesia, the Caribbean, and the Mediterranean. The distribution of active volcanoes may, however, be misleading as far as indicating where most volcanic activity occurs. Almost certainly most volcanism is along the mid-oceanic ridges, where high rates of volcanic activity have resulted in formation of the entire ocean floor within the last 200 million years. However, activity on the ridges is generally not localized at a point. Volcanoes on the ridges rarely rise above sea level, as in Iceland, so that named volcanoes astride oceanic ridges constitute only a small fraction of all the volcanoes known. Intra-plate volcanoes, such as those in Hawaii, are even less common.

The relatively high rates of geologic activity coupled with interaction of the surface materials with the atmosphere and hydrosphere result in recycling of materials at rates that are comparable with, or shorter than, the age of Earth. Materials at or near the surface are reworked by the processes of weathering erosion, transport, deposition, metamorphism and so forth, but there is also a much longer term, deeper seated recycling caused by subduction of the lithosphere into the mantle and regeneration of lithosphere at spreading centers.

As a result of the recycling, the crust can be envisaged as an array of different sized reservoirs (carbonates, shales, granites, oceans, etc.) with different elements moving from reservoir to reservoir on different time scales. Each element has a characteristic residence time in a given reservoir that depends on the amount of the element in the reservoir and the rate at which it is added and removed. Sodium, for example, has a residence time of 10^8 years in the oceans, whereas iron may have a residence time of only a few hundred years (Siever, 1974). Quartz is recycled relatively rapidly, with the average quartz grain retracing its path through the geologic cycle every 10^8 years (Pettijohn et al., 1972). Clearly the average residence time of quartz in the various crustal reservoirs (mainly sandstone) is comparable to or less than this. On most other planetary bodies, Io being the only exception, recycling rates are far slower, and average residence times probably far exceed the life of the planet.

Accompanying the relatively near surface cycling of materials within the lithosphere is a much larger scale recycling of parts of the lithosphere through the upper mantle. Seismic tracing of subducted plates suggests that the outer 300–350 km of the mantle, or 150×10^9 km^3, absorbs most of the ingested lithosphere. Assuming an average subduction rate of 2 cm/yr, a 100-km-thick lithosphere, and 29 000 km as the length of the subduction zones, Siever (1974) estimated that 58 km^3 of lithosphere is ingested each year. At this rate, complete turnover of material down to a depth of 350 km would take around 3 billion years, or almost the age of the planet. If the turnover depth is greater, the turnover rate is even slower. Earthquakes are detected to 700 km depth in some subducted zones, and mixing with the deeper mantle may occur.

Subduction involves mostly oceanic crust (and upper mantle) but Armstrong (1968), Armstrong and Hein (1973), and O'Nions et al. (1979) argued that continental crust is also recycled. Their arguments are based on the strontium, lead, and neodymium isotope record, which indicates some degree of equilibration of isotopes between continental crust and mantle. Acknowledging that continental crust is not normally subducted because of its buoyancy, they suggested that recycling is effected by subduction of sediments derived from the continents and deposited on the ocean floor. They further argued that the rate of recycling of the continental crust has slowed with time and that most of the continental crust formed early in the history of the planet (>3 billion years ago).

PLATE TECTONICS

Our present perception of the geology of the Earth is dominated by the theory of plate tectonics. It provides a unifying framework within which all the numerous aspects of geology, from the chemistry of lavas to sedimentation rates, from styles of deformation to faunal migrations, assume a comprehensible whole. In essence, the outer rind of Earth is perceived as being divided into rigid plates that move laterally with respect to one another. Where plates diverge, at the mid-oceanic ridges, new materials form; where plates converge, at ocean trenches, near-surface materials may be ingested into the hotter mantle below; where plates slide by one another, large transform faults occur. There are at present six plates of continental dimensions or larger, and many smaller plates.

Formulation of the Theory

The theory of plate tectonics has had a revolutionary impact on geology. The story of how the theory evolved has been recounted in detail elsewhere

(Hallam, 1973; Condie, 1976; Wilson, 1968; Dewey, 1972; Wyllie, 1971) and is summarized only briefly here. Although the theory was formulated mainly in the 1960s, elements had been perceived much earlier. It was not until abundant paleomagnetic and seismic data became available and a vigorous exploration of the sea floor undertaken that the entire system could be visualized. As early as the mid-nineteenth century Snider (1858) published maps showing Africa and South America joined and attached to the other continents to form a single land mass which he suggested had broken apart in the great biblical flood. Taylor (1910) proposed that creep of Earth's crust was the cause of most of the mountain chains of Earth, and his maps of creep directions are remarkably similar to the present-day maps of plate motions. Wegener was, however, the most influential of the early "mobilists," publishing his ideas in several papers including the widely read book *The Origin of the Continents and Oceans*. In this book he postulated that before the Mesozoic era, all the continents formed one large supercontinent Pangaea. During the Mesozoic, the mass started to break up and the pieces slowly drifted apart to their present positions. Wegener's ideas met considerable resistance, particularly in North America, and although they were subsequently elaborated on and refined by various geologists (Du Toit, 1937; Holmes, 1944) before the second world war, they were never widely accepted. It was not until acquisition of paleomagnetic data in the 1950s that continental drift started to gain some respectability in the geologic community.

Many rocks become permanently magnetized as they form and so record the relative position of the magnetic pole at the time of their formation. By the mid-1950s techniques had been developed whereby these fossil directions of magnetization could be measured on a range of rock types. Pioneering work by groups at Cambridge and the University of London showed a systematic shift of magnetic pole position with time (Blackett et al., 1960). Moreover, the pattern of the shift was different on the different continents, suggesting that the relative positions of the continents had changed. The most plausible explanation of the observations was continental drift (Runcorn, 1962). A puzzling aspect of these early paleomagnetic results was the mixed polarity of the directions of magnetization but this was shortly resolved as Cox et al. (1963) showed that Earth's magnetic field reverses polarity on a relatively short time scale, an observation that was to play a crucial role in achieving an understanding of the growth of the oceans.

Meanwhile a vigorous exploration of the sea floor had begun. The vast system of interconnected mid-oceanic ridges had been discovered, and the ridges were found to be sites of high heat flow, active seismicity, local volcanism, and rifting. Mapping of the ridge system and its unique properties stimulated Hess (1962) to propose sea-floor spreading. He suggested that the ridges mark the positions of upwelling in the mantle, and that new crust forms at the ridges and is carried away on either side. Old oceanic crust, he proposed, is destroyed in the deep oceanic trenches. Most of the ocean floors are thus relatively young, having formed as a result of relatively recent volcanic activity along the ridges.

Hess' ideas received strong support from paleomagnetic data. As noted above, periodic reversals of Earth's magnetic field had been conclusively demonstrated. Extensive surveying of the ocean floor revealed magnetic anomalies with a characteristic striped pattern adjacent to all the ridges examined. Vine and Matthews (1963) suggested that the magnetic anomalies were a record of the magnetic reversals that had occurred while the ocean floor was being formed. The floor in effect acted as a slowly moving tape recorder, maintaining a record of fluctuations in Earth's magnetic field from the present backwards in time, and could be used to calculate the spreading rates. Thus the stage was set for formulation of the theory of plate tectonics.

Wilson (1965) proposed that the mobile belts of Earth, where much of the deformation, seismic, and volcanic activity occur, are interconnected and divide Earth's surface into several large rigid plates. He identified three types of mobile belts: mountain ranges, including island arcs; mid-oceanic ridges; and faults with large horizontal displacements. The faults he called transform faults since they transform the horizontal motions accompanying sea-floor spreading at the ridges and compressions at the island arcs into horizontal shear. Morgan (1968) and McKenzie and Parker (1967) took these ideas and analyzed the plate motions in quantitative terms by means of a theorem of Euler. The theorem states that motion of a rigid block on a sphere can be described by rotation about a single axis through the center of the sphere and that the amount of displacement of any part of the block varies according to its angular distance from the rotation pole. They asserted that spreading rates along the mid-oceanic ridges should vary in a systematic way with

respect to the rotation poles of the rigid blocks. There followed a rapid testing of this theory against observed spreading rates, seismic activity, and location of plate boundaries. Variations in spreading rates predicted for the mid-Atlantic and the Indian ocean ridges were confirmed by direct observation (Heirtzler et al., 1968). Le Pichon (1968) used the spreading rates and the directions of shear on transform faults to identify six major plates and their rotations with respect to one another. He was also able to trace the motions on a global scale back 70 million years. Meanwhile Isacks et al. (1968) had reinterpreted global seismic data in light of the new theory. They distinguished the rigid lithosphere from the more mobile underlying asthenosphere and showed that the seismic data were consistent with tension along the mid-ocean ridges, shear along the transform faults, and downbuckling of the lithosphere under island arcs. They identified the major zones of underthrusting and the directions of motions of the lithosphere into the regions now known as subduction zones. With these papers most of the major elements of plate tectonic theory were perceived, and the path of geology since that time has been largely a reinterpretation of all aspects of the field in light of the new theory.

Present View

Earth's surface appears to consist of several rigid plates of lithosphere delineated by the major earthquake belts (fig. 5.2). The lithosphere consists of both upper mantle and crust, and any one plate may contain both continental and oceanic crust. Plate boundaries do not necessarily coincide with continental boundaries, although some do; the continents are simply rafted along with the rest of the crust. The lithospheric plates slide over the more mobile asthenosphere, mostly at rates between 1 and 10 cm/year, although the rates may be as high as 20 cm/yr. The plates range in thickness from a few kilometers under the mid-oceanic ridges to more than one hundred kilometers under the continents. The lower boundary of the plates is not a compositional boundary but a mechanical one. The thin lithosphere close to the ridges yields by ductile flow at a relatively shallow depth because of the high heat flows; as the lithosphere is carried away from the ridges it cools and thickens, as ductile flow occurs at greater depths. In the Pacific basin, for example, 50-million-year-old lithosphere is 60 km thick, and 100-million-year-old lithosphere is 85 km thick (Leeds et al., 1974).

At the mid-oceanic ridges, where the plates diverge, new oceanic crust and upper mantle is formed at the plate's trailing edges. Heat flow at the ridge crest is mostly in excess of 6 μcal/cm^2/sec as compared with around 1 μcal/cm^2/sec for oceanic crust 150 million years old (Sclater et al., 1980). Sclater and Francheteau (1970) suggested that the relief on the ridges is caused largely by thermal expansion of mantle materials as a result of the anomalously high heat flows and consequent high subsurface temperatures. The ridges are commonly offset by transform faults that are also the sites of shallow (< 50 km) earthquakes.

The most voluminous volcanic rocks erupted along the mid-oceanic ridges are low-K tholeiitic basalts. As the rocks cool through the Curie point for most magnetic minerals (500–600° C), they become magnetized along the ambient field direction and are carried away from the ridge preserving a record of the eruption history. The ridge tholeiites generally have relatively high Al_2O_3 and Cr compared with island and continental tholeiites and relatively low K, Rb, Cs, Sr, Ba, Zr, U, Th, and REE, and low Sr^{87}/Sr^{86} ratios, mostly in the range of 0.702 to 0.704 (Kay et al., 1970; Peterman and Hedge, 1971). While drill cores have not been obtained to any great depths on the ridges, sections of oceanic crust probably are preserved in the so-called ophiolite sequences found in many mountain belts (table 5.1). The sequences start with ultramafic igneous rocks at the base. These pass upward into gabbro, then into the sheeted complexes of

Table 5.1. Typical Ophiolite Sequence

Rock type	Interpretation
Cherts and reconstructed clays	Sea-floor sediments
Basaltic lavas and pillow lavas	Lavas mostly erupted at mid-oceanic ridges
Diabase dikes and sills	Feeders for the mid-oceanic ridge eruptions
Gabbros	Rocks formed within magma chambers below the mid-oceanic ridges
Cumulus peridotite	Rocks formed by crystal fractionation in the magma chamber
Sheared peridotite	Mantle rocks from the magma chamber walls

closely spaced diabase dikes, and ultimately into tholeiitic pillow lava. The latter may be overlain by sedimentary rocks that are presumably deposited on the ocean floor. The ophiolite sequences are believed to be pieces of ocean floor that originally formed along the mid-oceanic ridges, but later were thrust onto the continent at a zone of convergence.

New plates form as old ones start to break up and drift apart. The rift valleys of Africa are, for example, believed to form along a zone of incipient divergence and are characterized by updoming, rifting, and volcanism. The continental-rift volcanic rocks are generally enriched in alkalis and rare earths in contrast to the alkali poor oceanic tholeiites. Silica-rich members such as trachyte and rhyolite are also much more common than along the mid-oceanic rises. The distinctive chemistry of the continental-rift volcanics probably results largely from their depth of origin (Green, 1972b); the continental magmas form at relatively great depths (>70 km) below a relatively cool and thick continental lithosphere, whereas the rise tholeiites have a relatively shallow depth of origin. The various alkali-rich magmas may form by removal of varying amounts of olivine, pyroxene, and garnet from the deep-seated melts (Green and Ringwood, 1968). Contamination of the magmas with the continental rocks may also add to the magmatic variety of the rift volcanics. The rift valleys are also sites of clastic sedimentation, with possible formation of red beds, and sites of temporary lakes or arms of the sea, with accompanying formation of evaporites.

If separation continues, then oceanic crust forms between the diverging continental masses and a series of distinct geologic environments are ultimately formed, as typified by the margins of the Atlantic Ocean. The former edge of the continent survives as the continental slope. Along the slope, the rifts and coarse clastic debris that formed during the early stages of separation are buried by younger, fine-grained sediments and turbidites. On the ocean side of the continental slope, mud, clay, and organic ooze bury the newly formed oceanic crust. Toward the continent, sedimentary sequences consisting of shallow-water sandstone, shale, and limestone, which are typical of quiet sedimentary environments, are deposited on the shelf. Being within a moving plate, the shelf experiences little tectonic or volcanic activity as it is passively rafted away from the divergent zone at the mid-oceanic ridge.

At convergent plate junctions, geologic activity is far more complicated and varied. It is the processes at these junctions that ultimately result in the linear mountain chains and metamorphic belts of the world. The simplest form of convergent junction is one where a plate with oceanic crust rides under another plate (fig. 5.3). Complications arise when continents or island arcs are carried into the subduction zone to encounter the opposing plate. The continent or arc materials are relatively buoyant and so resist subduction. The horizontal motion of the plates is therefore translated into intense compression near the surface, overthrusting, and possibly a reversal in the direction of subduction. Deformation becomes extreme when two continental blocks collide, as in the case of India and Asia. Because the continental crust resists subduction, a substantial fraction of the continents survive from early in the planet's history and the continents may have grown periodically as new material was welded to the old in the convergence zones.

Consuming plate margins may be either along the edge of a continent, as along the west coast of South America, or along island arcs separated from the con-

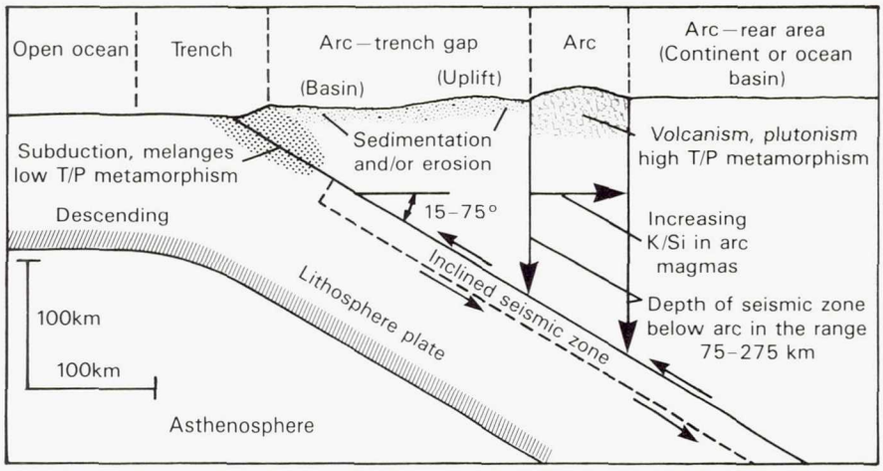

Figure 5.3. Generalized section across an arc-trench system showing the relation of magmatism and metamorphism to the subduction zone (Hallam, 1973; after Dickinson, 1971a).

tinents by marginal seas, as in the western Pacific. A trench, usually 5–8 km deep, normally forms where the plate being consumed dips under the opposing plate, and movement of the subducted slab can be traced to considerable depths by means of earthquakes. The earthquake hypocenters generally are located in a tabular volume, the Benioff zone, that dips under the arc or continental margin at a wide range of angles, but averaging around 45°. In some cases, as in the Mariana and Tonga arcs, and along the west coast of South America, earthquakes are detected in the Benioff zone to depths of 700 km; along other subduction zones such as the Aleutians, the earthquakes are mostly at depths less than 300 km. First motions of the earthquakes indicate tension within the slab near the axis of the trench and compression at greater depths (Oliver et al., 1973). In some arcs, as under the North Island of New Zealand, a gap in the Benioff zone suggests that a piece of lithosphere has detached from the main slab (Isacks et al., 1968; Oliver et al., 1973).

As the downgoing slab moves into the subduction zone, pelagic sediments and slivers of oceanic crust are scraped off the downgoing plate and stacked in a sheared, telescoped sequence or melange on the opposing side of the trench. As the sequence is compressed and buried, it is metamorphosed under conditions of relatively low temperature, but high pressure, to form rocks typically of the blueschist or low greenschist facies. Such sequences can be recognized in the fossil record as a heterogeneous, sheared rock mass in which blocks of diverse types including greywacke, chert, greenstone, and serpentine are juxtaposed in an almost random fashion (Dickinson, 1971a,b). Also incorporated almost intact may be ophiolite slices, representing the former ocean crust. Typical of such melanges is the Franciscan Formation of California, most of which is believed to have been plastered against the continental margin in a subduction zone parallel to the California coast in the Mesozoic (Hamilton, 1969). The thick stack of low-density rocks of the trench causes a negative gravity anomaly along its length, and if subduction slows or ceases, the sequence will rise isostatically. The trench area is also characterized by low heat flows because of the presence of the cold downgoing lithospheric slab.

Beyond the trenches is a magmatic arc, which may form a string of islands or, where located on continental crust, a thick stack of subaerial volcanic rocks. Between the arc and the trench is the so-called, arc-trench gap, 75 to 275 km wide. This is a region of relatively quiet sedimentation between the zone of deformation just inside the trench and the active volcanic region that constitutes the arc. Fossil arc-trench gap sequences are thus relatively unmetamorphosed sequences of sedimentary rocks, sandwiched between the melanges of the subduction zone and the volcanics of the arc. Toward the arc they grade laterally into volcanic or volcaniclastic strata; the contact with the melange rocks is generally tectonic.

The volcanic arcs themselves are generally about 75 km wide and the sites of both volcanism and intrusion of magma at depth. It is these arcs that make up the "ring of fire" around the Pacific. The extrusives are typically andesitic, and the intrusives are granite and granodiorite, but variations occur. Where the arc is built on oceanic crust, the volcanics may contain significant amounts of tholeiitic basalt in addition to andesite; where the arc is on a continental margin, significant amounts of dacitic and rhyolitic products may be erupted. In general the K and Si content of the lavas of the arc increase with distance from the trench (Dickinson, 1971a). Much of the volcanism of the arcs is pyroclastic. Some of the volcanic products accumulate on the arcs in volcanic cones, but much is also dispersed over wide areas as ash. Where the arcs are deeply eroded, granite batholiths may be exposed together with metamorphic rocks of the upper greenschist and amphibolite facies, which formed at relatively high temperatures.

Myashiro (1972, 1973) noted that metamorphic belts around the Pacific are commonly paired. One belt contains minerals typical of low temperatures and high pressures (glaucophane, lawsonite, aragonite, and jadeite) and the other parallel belt contains metamorphosed sediments and volcanics with minerals such as sillimanite, indicative of high temperatures. These two belts, he suggested, form respectively at the trenches and the arcs, indicating which side of a previous convergent junction was subducted.

The region behind the arc (away from the trench) may evolve in two basically different ways. Behind some arcs, such as Japan (the Marianas and the Tonga-Kermadec chain) there is extension, and new oceanic crust and ocean basins are formed there (fig. 5.4). Where such an arc was originally along a continental margin, the result of the extension can be migration of the arc away from the continent to form a marginal ocean basin (Karig, 1971). In contrast, compression occurs behind other arcs, such as the Andes, and rocks in a broad belt behind the arc are folded and thrust onto the continental foreland (fig.

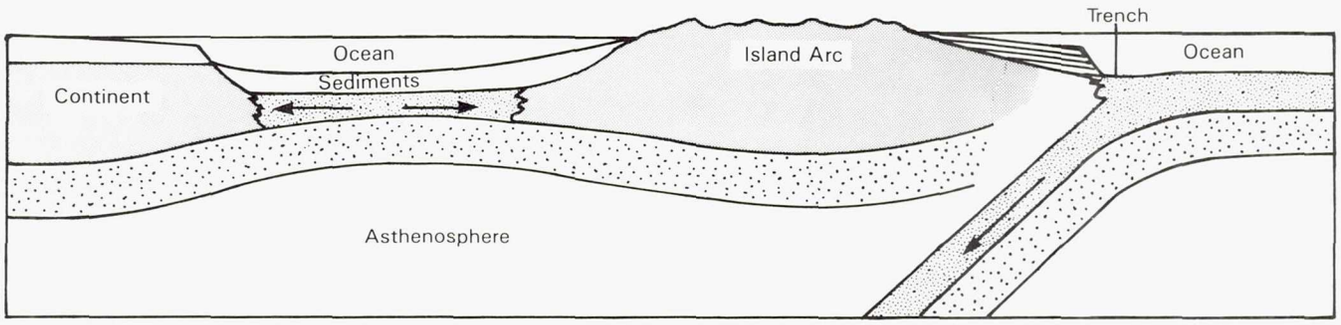

Figure 5.4. Generalized cross section across the edge of a continent bordered by an island arc. New oceanic crust is created between the arc and the continent by back-arc spreading (adapted from Dewey, 1979).

Figure 5.5. Generalized cross section of an active continental margin where subduction results in cordilleran style tectonics inland (adapted from Dewey, 1979).

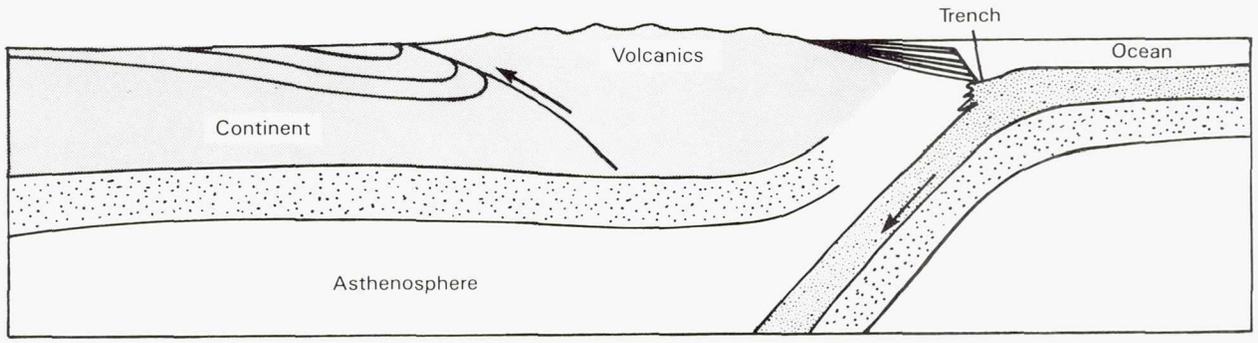

5.5). The reason for the different back-arc tectonic environments is not clear. Coney (1971) proposed that the broad belt of cordilleran folding and overthrusting of Mesozoic age that extends down the western part of North America was caused by active driving of the continental North American plate over the underlying asthenosphere. He suggested that had the plate been stable with respect to the asthenosphere, island arcs would have migrated off the continental margin, and the cordilleran style of deformation would not have occurred. Molnar and Atwater (1978), on the other hand, demonstrated that back-arc spreading occurs where relatively old (>100 million years) lithosphere is being subducted, whereas cordilleran style tectonics develop where young lithosphere is being subducted. They attribute the different styles to differences in buoyancy of old and young lithosphere.

The processes occurring at island arcs and active continental margins can, of themselves, lead to formation of mountain chains. However, many orogenic belts are the result of additional complications, particularly where island arcs or continents that are rafted along on moving plates encounter a subduction zone. In these cases, passive continental margins of the Atlantic-type are involved in the collisions. If the approaching continent meets oceanic crust of the opposing plate at the subduction zone, then oceanic crust may be thrust up onto the continent (fig. 5.6) to form a wedge of ophiolites as in Papua and New Caledonia. Continued convergence of the two plates must then result in reversal of the polarity of subduction, since the continental crust cannot be subducted. The continental margin thus changes from a passive margin to an active one with the oceanic crust thrust under it. Alternatively, the approaching continental margin may collide with an island arc at the subduction zone so that island-arc volcanics and sediments are thrust over the continental margin, which itself undergoes compressional deformation. Again, if the convergent motion is sustained, the polarity of the subduction must change. Dewey and Bird (1970) suggested that this occurred in north New Guinea in Miocene time. In both cases new material may be welded onto the continental margin.

The final major way in which mountains are built is by collision of two continents; that is, where an inactive Atlantic-type of continental margin is driven toward a subduction zone on an active continental

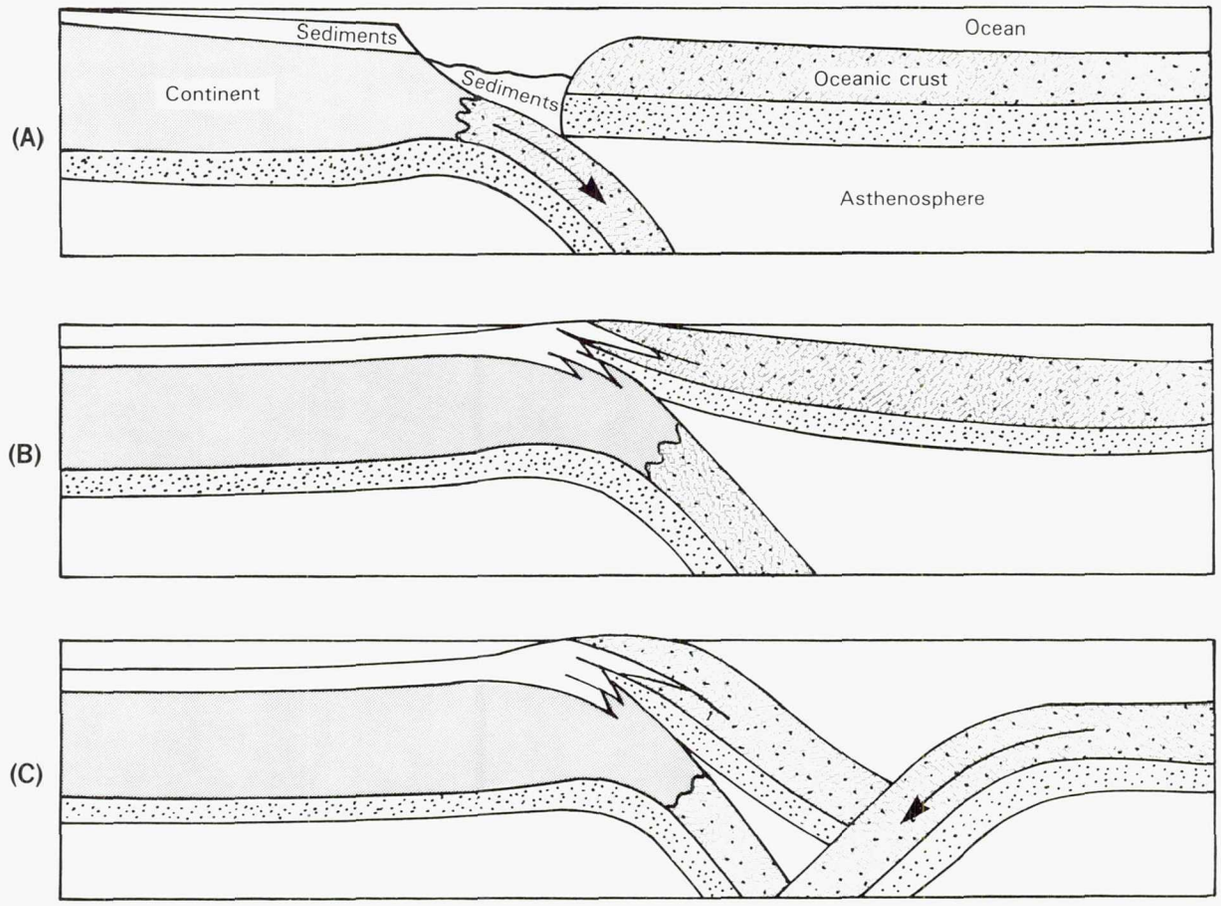

Figure 5.6. Possible sequence of events when a continent rafted along on a plate being subducted encounters the subduction zone. Oceanic crust is thrust onto the continental foreland as ophiolites (B) and ultimately the polarity of the subduction is reversed (C) (Dewey, 1979).

margin (fig. 5.7). Collision causes the continental basement to be sheared and thrust in both directions away from the join. Slivers of oceanic crust may also be involved in the thrusting. The sediments on the former continental shelf become compressed and folded, then thrust to form gigantic nappes (detached and recumbent folds). Rapid erosion of the trapped, deformed, and uplifted rocks may result in deposition of a thick, sedimentary sequence composed of mixed rock-types termed molasse, adjacent to the growing pile of deformed rocks. Plutonic activity may occur at depths below the massive pile to form granitic batholiths. Eventually, the buoyancy of the continental masses prevents further underthrusting and what is left of the subducted plate may break off and sink into the asthenosphere (Isacks et al., 1968). Relative motion between the two continents ceases and the global motions of the plates must then become reorganized. The present Himalayan mountain chain is the result of such a continent–continent collision. India collided with Asia along a former subduction zone, south of Tibet, during the Cenozoic. A similar collision may now be occurring in the Mediterranean, although here the situation may be more complicated. Ophiolite-blueschist zones are complexly interleaved with slivers of continental crystalline rocks and folded sediments, suggesting that several island arcs of microcontinents may have been trapped between the converging African and Eurasian masses (Dewey and Bird, 1970).

Mountain belts can thus form in a variety of ways. New continental crust can be welded to old at active margins and old continents can become welded together along so-called suture belts during continent–continent collisions. These collisional events, which result in reversal of the polarity of subduction or cessation of the relative motions of the two continental masses, must cause episodic large-scale reorganization of plate shapes and motions. Furthermore, the sizes and shapes of the plates are constantly changing as a general result of divergence and convergence. The African plate, for example, is presently growing larger as a result of spreading at the surrounding

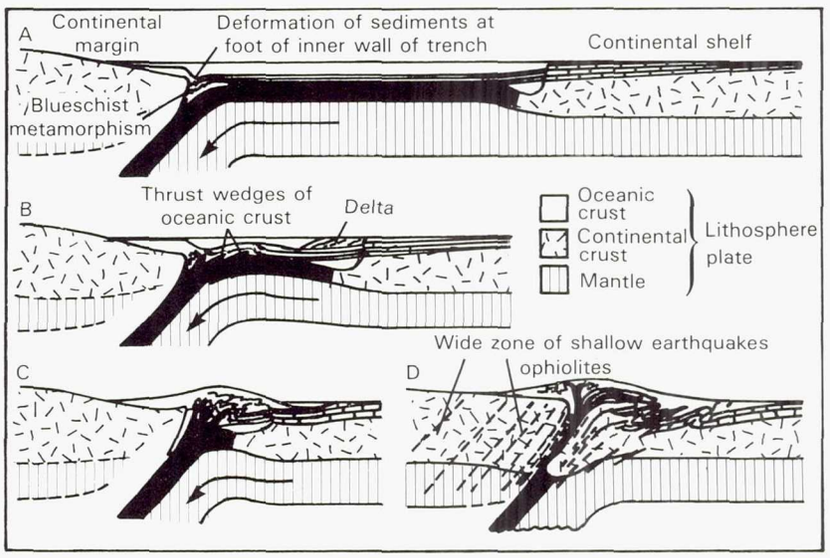

Figure 5.7. Possible sequence of events in a continent-continent collision. The sedimentary sequence on the underriding plate becomes juxtaposed with the sequence on the overriding plate, and slivers of oceanic lithosphere are caught between. The combined section is intensely folded and overthrust onto the continents. Ultimately deep burial, metamorphism and plutonic activity lead to suturing of the two plates and the global plate motions become reorganized.

divergent boundaries. Moreover, motion into a subduction zone is rarely at right angles; the resulting shear must be accommodated by transform motion along the plate boundaries. The plate geometry is thus constantly changing, and one of the tasks of geology is to reconstruct former configurations and trace how the surface evolved to its present state.

Past Motions

Smith et al. (1973) attempted to reconstruct world geography back to the beginning of the Phanerozoic on the basis of present-day plate geometries and motions, paleomagnetic data, location of orogenic belts, and indices of past climates. Some of the reconstructions are given in figures 5.8 and 5.9. Reconstructions for the last 250 million years—back to the Permian—can be made with some confidence because they are constrained by magnetic anomaly patterns on the ocean floors and by the present plate positions and spreading rates. During the Permian and Triassic all the continents formed essentially one supercontinent, termed Pangaea by Wegener (1966). The continental mass was crudely crescent-shaped with Eurasia forming the northern horn and the southern continents, which constituted a long-lived land mass termed Gondwanaland, forming the southern horn. Between the two horns was the ancient ocean of Tethys. The subsequent history of the continents can be described in terms of three main events: the opening of the Atlantic, the closing of Tethys, and the break-up and dispersal of Gondwanaland. The exact timing of the events is uncertain but the broad outlines are as follows. In the Jurassic (140–200 million years ago), the north Atlantic started to open and Eurasia rotated clockwise toward Tethys, hinged on the western Mediterranean. By mid-Cretaceous time (90 million years ago) the North Atlantic had grown to be 1000–2000 km across, whereas Tethys had narrowed to less than 1000 km across in the Mediterranean and the Middle East. Also during the Cretaceous, Gondwanaland broke up and underwent rapid dispersal over the southern hemisphere. India started its northward drive toward Asia, South America split from Africa to form the South Atlantic, and Antarctica and Australia drifted away from Africa to the south and west. By the Eocene (50 million years ago), India was about to collide with Asia, only narrow disconnected remains of Tethys were trapped between the converging plates of Eurasia and Africa-Arabia, and the South Atlantic was over 1000 km wide. Since that time, further convergence of Africa-Arabia and India with Eurasia has resulted in formation of the almost continuous belt of mountains across southern Europe, Anatolia, Iran, and the Himalayas.

Reconstructions for the pre-Permian are far less certain because of the absence of surviving ocean floor of that age and our inability to extrapolate subsequent motions backwards as a result of all the continents being together in one land mass in the Permian. The reconstructions of Smith et al. (1973) for this period are based on the position of orogenic belts and on paleomagnetic data from the continents. The paleomagnetic data, however, give only paleolatitudes. The continents are positioned at the latitude necessary to place the magnetic pole at the geographic pole; longitudes are assigned somewhat arbitrarily. It appears

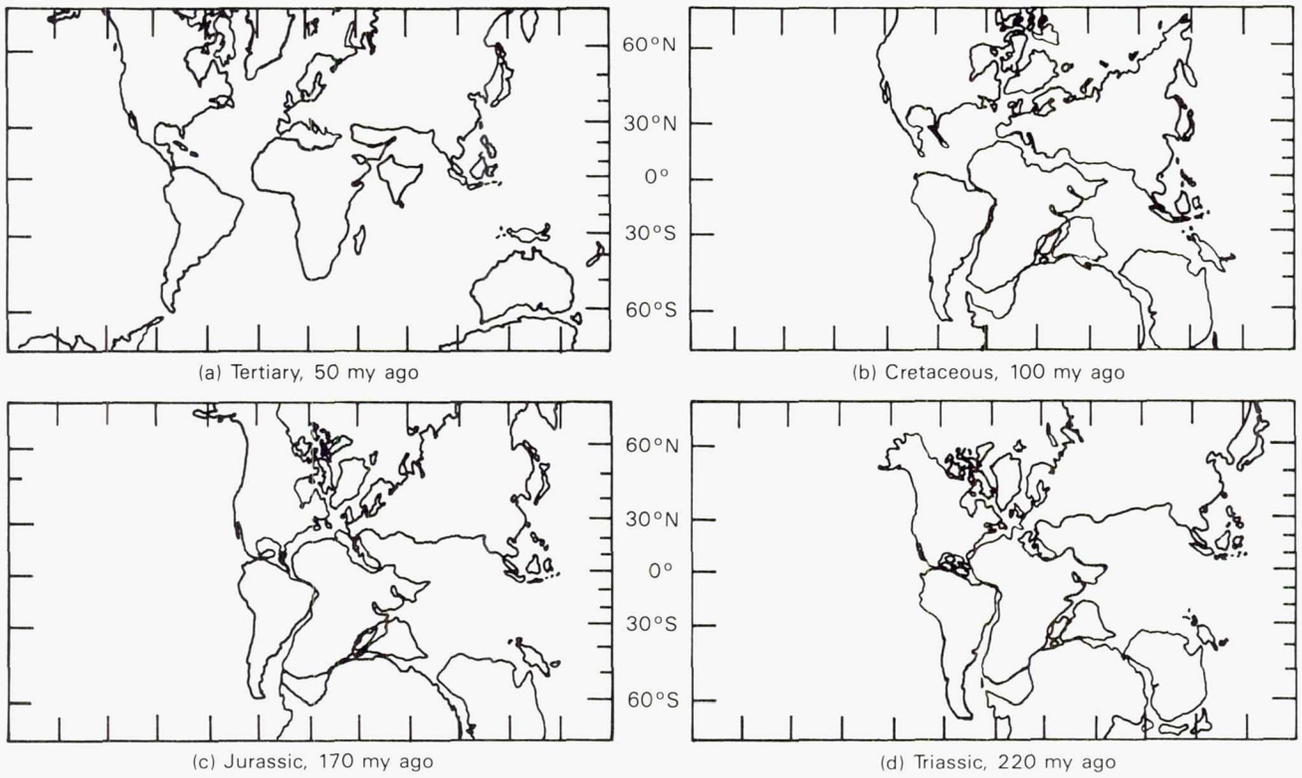

Figure 5.8. Configuration of the continents back to Triassic time. The configuration is tightly constrained by data from the ocean floors (Smith et al., 1973).

Figure 5.9. Possible configuration of the continents between the Permian and the Cambrian. The configuration is poorly constrained because of the lack of data from the ocean floors (Smith et al., 1973).

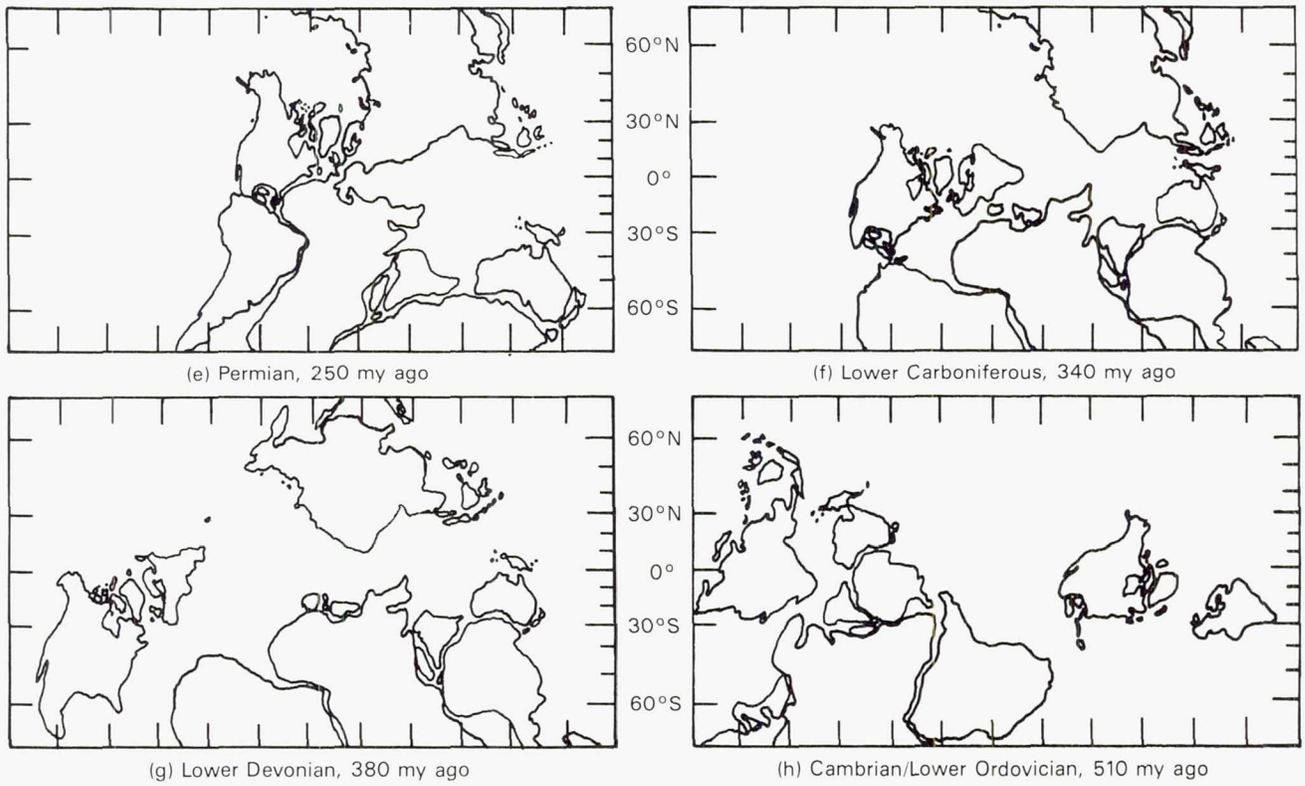

from the magnetic poles that the southern continental mass remained essentially intact throughout the Paleozoic. However, the northern continents successively broke up and reassembled. During most of the Paleozoic (230–570 million years ago) Europe was separated from Asia by an ocean, which closed in the Permian to produce the Urals. During the Mississipian, northern Europe and North America were joined but separated from southern Europe by an ocean which finally closed during the Hercynian orogeny (230–300 million years ago). Somewhat earlier, in the Ordovician, northern Europe had been separated from North America but fused with it during the Caledonian orogeny (350–400 million years ago). Extrapolation back into the Precambrian is extremely speculative, but continuity of ancient (1.8 to 3.0 billion years) orogenic belts across Gondwanaland suggested that much of that land mass, at least, remained intact for most of the Proterozoic.

Plate tectonics have clearly played a major role in the evolution of Earth during the last 500 million years. Much less clear is the role of plate tectonics before 500 million years ago, an era that constitutes almost 90 percent of the planet's history. The rest of this chapter discusses formation of Earth, then traces its history from the time of formation through the Archean and Proterozoic Eons to the start of the Phanerozoic. A continuing concern is the extent to which plate tectonics affected geologic evolution during the early periods.

THE INTERIOR OF EARTH

Although the results of geologic processes operating at Earth's surface can be observed directly, our knowledge of the interior is obtained by indirect means—from seismic data, Earth's moment of inertia, comparisons with meteorites, and study of inclusions in volcanic rocks. Division of Earth into crust, mantle, and core has been known for over 70 years from seismic data. The Mohorovicic discontinuity, or Moho, defines the base of the crust, which is generally at a depth of 5–7 km under the oceans and 35–40 km under the continents. At the Moho both shear (S) and pressure (P) waves undergo an abrupt change in velocity, as a result of the compositional boundary between the ultramafic mantle and the more Si- and Al-rich rocks of the crust. The mantle extends from the Moho down to the Gutenberg discontinuity at a depth of around 2900 km. Below this depth, S-waves are not transmitted and P-waves undergo a sharp drop in velocity. The discontinuity separates a liquid, dominantly metal, outer core from the lower mantle. Other seismic discontinuities have been detected and will be discussed below. The variation of seismic velocities with depth is given in figure 5.10.

The distribution of density within Earth is constrained by the mass of Earth, its moment of inertia, the travel time of seismic waves (although the relation between elastic constants and density is not precisely known), and the free oscillations of Earth. The densities at the top of the mantle range from 3.2–3.6 gm/cm^3 and they increase slowly to a depth of 400 km, then more rapidly to a depth of 700 km below which they increase slowly to a value of 5–6 gm/cm^3 at the base of the mantle. At the core boundary density jumps to 9–10.5 gm/cm^3 and then increases steadily to a central density of 12–14 gm/cm^3 (Wyllie, 1971). In most models of the internal distribution of density the mantle constitutes around 67 percent of the mass of the planet, the core 32 percent, and the crust only about 0.5 percent.

Internal temperatures are less well constrained. Deep temperatures (>300 km) have little influence on surface heat flow, which is quite well known. Most estimates of internal temperatures are based on theoretical models for the thermal evolution of Earth; methods that relate geophysical properties such as seismic wave velocities and electrical conductivity to temperature, or on petrologic arguments that relate the composition and depths of origin of magmas to phase relations in ultramafic magmas at different temperatures.

Figure 5.10. Variations of S- and P-wave velocities with depth within Earth (Wyllie, 1971).

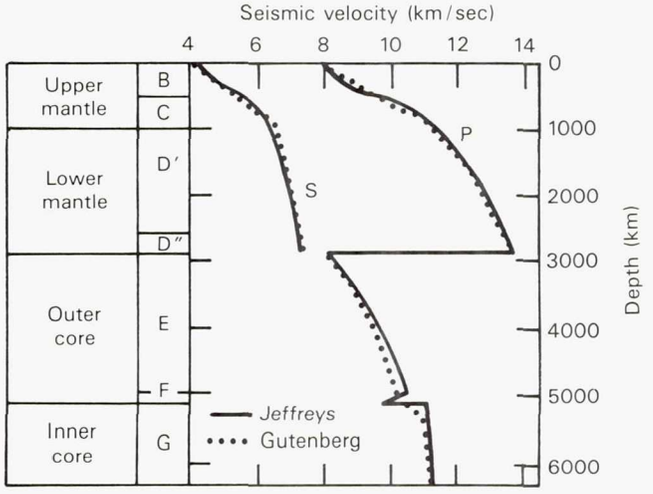

The total heat loss from Earth is around 10^{13} cal/sec, of which 70 percent is through the deep oceans and marginal basins and 30 percent is through the continents and continental shelves. Creation of new lithosphere accounts for 90 percent of the heat lost through the oceans and therefore, about 60 percent of the total heat lost. Only 20 percent of the heat loss is by conduction through the lithosphere (Sclater et al., 1980).

The Crust

Two major kinds of crust are distinguished, a thin oceanic crust and a thicker continental crust. The oceanic crust is relatively uniform in its properties. It consists of a basal layer, averaging 4.7 km thick, of gabbro and basalt with P-wave velocities of 6.7–6.9 km/sec. Above this is a layer of consolidated sediments and volcanics, averaging 1.7 km thick, with P-wave velocities in the 4–6 km/sec range (Turekian, 1976). This may be covered by a thin layer of unconsolidated sediments which becomes thinner toward the ridges. The total mass of the oceanic crust is estimated as 7×10^{24} g (Turekian, 1976). Its composition (table 5.2) is reasonably well known, the crust having formed largely by eruptions of low-K tholeiitic basalt along the mid-oceanic ridges.

Continental crust is more varied. A large fraction consists of stable, ancient, crystalline basement that may be partly overlain by relatively undeformed Phanerozoic sediments. Much of the basement appears to have formed by successive Precambrian orogenies that created linear belts of deformed and metamorphosed rocks of relatively uniform age. It is mostly 35–40 km thick and has P-wave velocities of 6.0–6.9 km/sec. Overlying sediments, if present, have P-wave velocities mostly in the 2–4 km/sec range.

Welded to the central shields of the continents may be Phanerozoic orogenic belts and mountain chains. Paleozoic orogenic belts are generally underlain by crust that is similar in properties to that of the shields. Under the younger orogenic belts however, the crust is thicker, up to 100 km under the Himalayas. The greater thickness in these areas reflects isostatic compensation of the mountain chains by low-density roots. Areas of crustal extension, such as the Basin and Range Province of the United States and the African rift valleys, have unusually thin (<30 km) crusts. Because the continental crust is thicker than the oceanic crust it constitutes 70–80 percent of the crustal mass, estimated at 2.5×10^{25} g.

Heat flow in the continental crust averages 1.4 μcal/cm^2/sec, but varies according to age (Sclater et al.,

Table 5.2. Estimates of the Chemical Composition of the Crust (from Condie, 1976). Major Elements Are Given in Weight Percent; Minor Elements in ppm.

	1	2	3	4	5
SiO_2	60.2	63.3	48.8	61.3	57.9
TiO_2	0.7	0.6	1.4	0.8	0.9
Al_2O_3	15.2	16.0	16.3	16.3	15.4
Fe_2O_3	2.5	1.5	2.0	1.5	2.4
FeO	3.8	3.5	6.6	4.2	4.4
MgO	3.1	2.2	7.0	3.2	4.0
CaO	5.5	4.1	11.9	5.3	6.8
Na_2O	3.0	3.7	2.7	3.7	3.0
K_2O	2.9	2.9	0.2	2.3	2.3
H_2O	1.4	0.9	1.0	0.8	1.3
Rb	95	85	4	70	75
Sr	340	350	170	310	300
Ba	670	1150	65	920	540
U	3	1.8	0.2	1.4	2.5
Th	100	6	0.5	4.8	8.0
Ni	50	20	100	35	60

1. Average continental crust. 1:1 basalt-granite mixture assumed for lower crust.
2. Average continental crust assuming lower crust is granulitic.
3. Average oceanic crust.
4. Total Earth's crust assuming granulitic lower continental crust.
5. Total Earth's crust assuming granite-basalt mixture for lower continental crust.

1980). In young orogenic belts the heat flow is mostly in the range of 1.6–2.4 μcal/cm^2/sec but it decreases to around 1.1 μcal/cm^2/sec after a billion years. The areas of crustal extension have relatively high heat flows (1.5–2.5 μcal/cm^2/sec).

The composition of the continental crust has been estimated in various ways. Estimates of the sedimentary layer (table 5.2) are based on the relative proportions of different sedimentary rocks observed at the surface and in drill holes. Sampling of the Canadian shield (Eade and Fahrig, 1971) and modeling the distribution of different rock types (Ronov and Yaroshevsky, 1969) show that the upper continental crust is close to granodiorite or quartz diorite in composition. The composition of the lower continental crust is more difficult to assess (two models are given in table 5.2). One assumes that the lower crust consists of a mixture of granitic and basaltic rocks. The other assumes that metamorphic rocks of the granulite facies in the Canadian shield, which appear to have formed at depths of 20–35 km, can be taken as indicators of the composition of the lower crust (Eade and Fahrig, 1971). The granulite model is more Al-Si-rich and Fe-Mg-poor than the granite-basalt model. Both are consistent with the seismic velocities of the lower crust. Estimates of the relative abundances of different rock types and normative minerals for the crust as a whole (ocean and continent) are given in table 5.3. The normative mineralogy, with quartz and feldspar constituting 63 percent of the total, reflects the dominance of continental crust.

The Mantle

The composition and structure of the mantle are inferred from several kinds of data. First, its vertical density profile is constrained by the moment of inertia. Second, the variations in seismic properties give indications of the physical state and phase changes at different depths. Third, studies of phase equilibria suggest possible mineral assemblages at different depths and parent materials for magmas derived by partial melting and brought to the surface. Finally, certain ultramafic inclusions in some igneous rocks and kimberlites are demonstrably samples of the upper mantle as shown by the presence of high-pressure minerals such as diamonds, and of coexisting mineral pairs that provide a measure of the depth at which they crystallized.

Table 5.3. Abundances of Main Rock Types and Minerals in the Crust (Data from Ronov and Yaroshevsky, 1969)

Rocks	% Volume of crust
Sedimentary	
Sands	1.7
Clays and shales	4.2
Carbonates (including salt-bearing deposits)	2.0
Igneous	
Granites	10.4
Granodiorites, diorites	11.2
Syenites	0.4
Basalts, gabbros, amphibolites, eclogites	42.5
Dunites, peridotites	0.2
Metamorphic	
Gneisses	21.4
Schists	5.1
Marbles	0.9
Totals	
Sedimentary	7.9
Igneous	64.7
Metamorphic	27.4

Minerals	% Volume of crust
Quartz	12
Alkali feldspar	12
Plagioclase	39
Micas	5
Amphiboles	5
Pyroxenes	11
Olivines	3
Clay minerals (+ chlorites)	4.6
Calcite (+ aragonite)	1.5
Dolomite	0.5
Magnetite (+ titanomagnetite)	1.5
Others (garnets, kyanite, andalusite, sillimanite, apatite, etc.)	4.9
Totals	
Quartz + feldspar	63
Pyroxene + olivine	14
Hydrated silicates	14.6
Carbonates	2.0
Others	6.4

Most parts of Earth have a relatively high seismic velocity zone that extends from the Moho down to depths of 50–70 km. Pressure-wave velocities in this zone are mostly in the 7.9–8.1 km/sec range and shear-wave velocities are around 4.6 km/sec. This uppermost mantle together with the crust makes up the lithosphere. Beneath the rigid lithosphere, in most places, is a low-velocity layer that extends down to 200–300 km (fig. 5.11). At the top of the layer, P-wave velocities are around 7.6 km/sec and S-wave velocities are around 4.2 km/sec. The seismic waves also have relatively high rates of attenuation. These properties suggest that the low-velocity layer is partly molten (1–10 percent liquid). It corresponds, in part, to the asthenosphere—the mobile layer over which glide the rigid plates of the lithosphere. The asthenosphere may, however, extend to greater depths in some places because earthquakes caused by subducted slabs of lithosphere moving down into the asthenosphere can be detected in some areas to depths of 600–700 km.

From the base of the low-velocity layer down to 400 km the S- and P-wave velocities increase slightly owing to the increasing pressure, but at 400 km there is a sharp discontinuity. Pressure-waves increase from 8.5 to 9.6 km/sec and S-waves increase from 4.5 to 5.5 km/sec. The velocity jump is probably caused by the transition from olivine, as the dominant mineral of the upper mantle, to spinel (Ringwood and Major, 1970). Aluminum-rich pyroxene in the upper mantle may also be replaced by garnet below this discontinuity (Smith and Mason, 1970). Other discontinuities at 650 km and 1050 km are probably the result of phase changes also. The precise nature of the latter changes is not known, but it likely involves transformation of Fe-Mg silicates, in which Si is in 4-fold coordination, into denser phases with Si in 6-fold coordination.

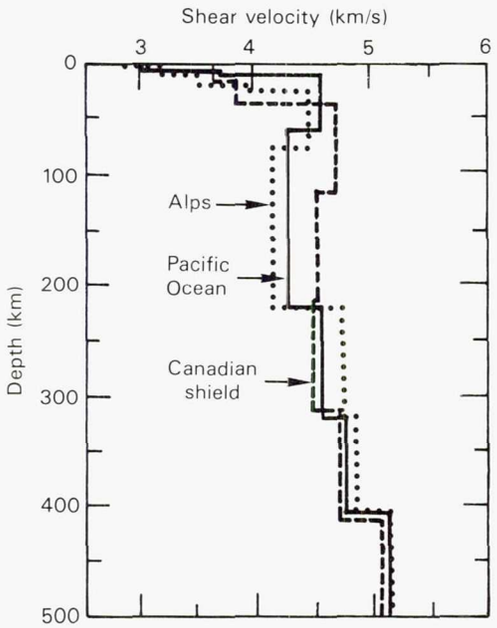

Figure 5.11. Variations in shear wave velocities in the outer 500 km of Earth (Wyllie, 1971).

Theoretical studies of phase equilibria and the generation of basaltic magma, together with ultramafic inclusions carried up by deep-seated magmas and kimberlites give a good indication of upper mantle mineralogy (Smith, 1979). The mantle probably is complex, with a mineralogy that changes according to depth and location as might be expected from repeated episodes of partial melting and ingestion of the lithosphere. The dominant rock types are relative Ca-Al-rich peridotite (rock composed chiefly of olivine), relative Ca-Al-poor harzburgite (peridotite consisting of olivine and orthopyroxene), and very small amounts of eclogite (clinopyroxene and garnet), dunite (nearly all olivine), and other ultramafic rocks. The peridotite has Mg/Fe ratios around 10 and generally contains spinel or garnet depending on their depth of formation.

Ultramafic inclusions provide a basis for estimating the bulk composition of the upper mantle at depths less than 200 km (Boyd, 1973). Comparing table 5.2 with table 5.4 shows the extreme enrichment of the upper mantle in Mg with respect to the crust. Of special interest, because of their importance in understanding core formation and different models for accretion of Earth, are the chalcophile and siderophile elements. The Fe/Ni ratios in mantle-derived olivine are close to the cosmic ratios, which suggests that Ni has not been selectively removed from upper mantle silicates by partitioning between silicates and metal or sulfides. Any such partitioning would result in selective depletion of Ni in the silicates, which is not observed. Similarly, the noble metal contents of mantle derived inclusions are higher than would be expected for equilibration of the silicates of the mantle with sulfides or metal. These relations suggest first, that there is little sulfide or metal within the upper mantle, and second, that upper-mantle materials were never equilibrated with significant amounts of metal or sulfide at any time in the past. The upper-mantle materials are in disequilibrium with the core. Thus, either the Ni and noble metals now in the upper mantle were added after the core formed, or the core

Table 5.4. Some Estimates of the Bulk Composition of the Upper Mantle (Smith, 1977)

	1	2	3	4	5	6
P_2O_5	—	—	—	0.04	0.06	—
SiO_2	45.1	42.86	44.66	45.19	43.97	44.2
TiO_2	0.2	0.33	0.19	0.054	0.07	0.1
Al_2O_3	4.6	6.99	2.80	1.52	1.64	2.7
Cr_2O_3	0.3	0.18	0.45	0.39	0.49	0.30
Fe_2O_3	0.3	0.36	—	0.92	0.89	1.1
FeO	7.6	8.97	7.92	4.74	6.03	7.3
MnO	0.1	0.14	0.12	0.10	0.13	0.15
NiO	0.2	0.20	0.31	0.26	0.36	0.20
MgO	38.1	35.07	40.97	41.8	44.73	41.3
CaO	3.1	4.37	2.59	1.04	1.10	2.4
Na_2O	0.4	0.45	0.30	0.18	0.12	0.25
K_2O	0.02	0.003	0.12	0.16	0.06	0.015

Note: Estimates are all from inclusions, except that given in column 1, which is a hypothetical rock, pyrolite, obtained by mixing one part basalt with three parts peridotite (Ringwood, 1975).

1. Average mantle pyrolite, Ringwood (1975).
2. Volatile-free, undepleted upper mantle from partial fusion—partial crystallization model for xenoliths at Kilbourne Hole, New Mexico.
3. Mean of 20 garnet peridotites from various countries.
4. Average garnet lherzolite in kimberlite.
5. Average of eight garnet lherzolite nodules at Lashaine, Tanzania.
6. Estimated undepleted upper mantle (Harris et al., 1967).

formed after accretion was over and a barrier was present between the upper mantle and the core-forming materials at greater depths (Smith, 1977).

Deeper in the mantle, P-wave velocities increase progressively as the density increases until they reach a value of around 13.7 km/sec at the Gutenberg discontinuity, which marks the base of the mantle at a depth of 2920 km. The mineralogy of the lower mantle is very uncertain. All the silicates normally present in peridotites must transform to denser phases at depth, but precisely which phases cannot be specified, partly because of a lack of knowledge of phase equilibria at the prevailing high pressures. Uncertainties also arise because the temperature profile is poorly constrained, and because of the possibility that the Mg/Si and Fe/Mg ratios may vary considerably with depth (Smith, 1977).

The Core

The core constitutes around 32 percent of the mass of the planet and can be divided into inner and outer regions. The outer liquid core has P-wave velocities mostly in the 8–10 km/sec range and does not transmit S-waves. The inner core, defined by the Lehmann discontinuity at 5200 km, does transmit S-waves, although at low velocities, suggesting that it is near the melting point or partly molten. While the core is almost certainly rich in Fe and other siderophile elements, it is less dense than a pure Fe-Ni liquid. The most likely explanation is that the core incorporates significant amounts of sulfur (Murthy and Hall, 1972). Fe and Ni sulfides occur in most meteorites and their incorporation into an accumulating Earth would have resulted in formation of liquids which could have sunk to form the core. A sulfur content of 9–12 percent is sufficient to explain the low density. Ringwood (1977) alternatively suggested that oxygen may be the cause of the low density.

FORMATION OF EARTH

Earth is estimated to be 4.6 billion years old on the basis of the following evidence. (1) Most meteorites have solidification ages close to 4.6 billion years and are thought to have accreted around the same time as Earth, and from the same primitive condensation products of the solar nebula. (2) The evolution of terrestrial lead isotopes follows a curve which, when

extrapolated back 4.6 billion years, matches the composition of primordial lead, as determined from U-deficient meteorites (Patterson, 1956). (3) Globally averaged U and Pb isotopic abundances in the crust give an age of 4.6 billion years. (4) The oldest rocks found on the lunar surface are 4.6 billion years old (Taylor, 1975).

The oldest rocks found on Earth are close to 3.8 billion years old (Moorbath, 1976), and so postdate the formation of Earth by about 800 million years. Despite the lack of direct evidence from between 4.6 and 3.8 billion years ago, we can infer what might have happened during this early era from geochemical evidence, from modeling of Earth's accretion and its subsequent thermal history, and from conditions at the start of the geologic record 3.8 billion years ago.

In recent years the sequence of condensation of materials from the solar nebula and their accretion to form meteorites and planets have received considerable attention. Lewis (1972), Grossman (1972), and Grossman and Larimer (1974) examined the condensation sequence in the primitive solar nebula. They assumed that the nebula was uniform in composition and that the temperature and pressure fell off with increasing distance from the proto-sun. According to their models, as the nebula cooled, different materials condensed: the refractory metals and Ca, Al, and Ti oxides first, then Mg silicates at intermediate temperatures, then Fe, and lastly the more volatile material such as Na, K, S, and Se. The condensed materials remained in contact with the nebula gas and were able to react with it in the later stages of condensation. Thus, some of the Fe metal that condensed was later oxidized or sulphurized to produce FeO and FeS. Condensation was arrested when the remaining nebula gas was removed by the solar wind. The solar system was thus left compositionally zoned, with dust in the inner solar system preferentially enriched with early, high-temperature condensates and the outer solar system enriched with low-temperature condensates. Accretion of the planets from these materials resulted in the planets closer to the Sun being formed from a larger proportion of the high-temperature fraction.

How the planets accreted from the condensed dust is controversial. According to the inhomogeneous accretion model (Turekian and Clark, 1969), the planets accreted rapidly while condensation was occurring so that each developed an ''onion ring'' structure as successive condensation products accumulated. Accretion times required for Earth in their model are on the order of 10^3 to 10^4 years. This model has been criticized on several grounds, mainly because of the abundant evidence from meteorites of formation of planetesimals, up to hundreds of kilometers in diameter, as an intermediate stage in the formation of the planets, as originally suggested by Urey (1952), and because of dynamical problems inherent in such rapid accretion.

According to the homogeneous accretion model, the planets accumulated slower than the material condensed. They formed from planetesimals—aggregates of the various materials that formed at different stages of the condensation sequence. The condensed particles are believed to have accumulated into clods as a result of gravitational instabilities in the nebular disc. As the clods grew in size, gravitational attraction and energy dissipation in a developing regolith probably allowed larger bodies to grow faster than the smaller (Hartmann, 1978). Ultimately, an array of planetesimals, tens to hundreds of kilometers in diameter formed, as is evident from the mineralogy of some meteorites, which clearly demonstrates that they formed within much larger bodies. Carbonaceous chondrites may be representative of the most primitive planetesimals; meteorites such as the basaltic and iron meteorites are the products of melting and fractionation within planetesimals.

According to one model by Safronov (1977), a small number of planetesimals gained advantage over others, largely because of their size. They initially grew by low-velocity capture of other planetesimals in orbits similar to their own, but as their size grew, so did their zone of influence; capturing objects in orbits more and more dissimilar to their own. In the final growth stages of these protoplanets, their zones of influence greatly overlapped. Earth, for example, was able to capture objects in orbits that overlapped that of Mars, and vice versa. Safronov (1977) estimated that by these means 98 percent of Earth accumulated in 10^8 years. Accretion times of that order must have caused substantial internal heating during the final stages of accretion, because re-radiation of collisional energy back to space is inefficient.

Bulk Composition of Earth

The bulk composition of Earth provides clues concerning formation of Earth and events that immediately followed.

Smith (1977) critically examined different ways of estimating the bulk composition of Earth and provided estimates based on several different assumptions. Es-

timates of Earth's composition have been approached in two basic ways. The first, exemplified by Ganapathy and Anders (1974), is to assume that Earth formed in the same way as chondritic meteorites, by accretion of debris condensed from the primitive solar nebula, then to calculate the proportion of the different components from the estimated abundance of certain key elements in Earth. The second technique, exemplified by Smith (1977), is to estimate the bulk composition from estimates of the composition of the crust, mantle, and core, as described above, although here also meteoritic data must be used, particularly to estimate the composition of the core.

Ganapathy and Anders (1974) assumed that Earth formed from different materials that condensed out of the solar nebula as it cooled, according to the scheme of Grossman and Larimer (1974). Then they used terrestrial evidence to estimate the relative proportions of the different components that accumulated to form Earth. The abundance of U in Earth (18 ppb (Larimer, 1971)) is, for example, taken as an index of the overall abundance of the refractory elements. The fraction of volatile elements incorporated is estimated from the Tl/U ratio in surface rocks, since Tl tends to follow U in the geochemical cycle. The proportion of metal is based on modeling of Earth's core. The resulting bulk composition is given in table 5.5.

The estimates of bulk composition by Smith (1979) are based more directly on terrestrial evidence. Estimates are made of the crust and mantle composition from sampling of different rock types and geophysical evidence as outlined in the previous section. Because of the lack of geochemical data on the core, however, Smith was forced to draw on analogies with meteorites to estimate its composition. He examined three models, each based on analogy of the inner core with a different type of meteorite. The results of his modeling are also shown in table 5.5. Differences between the Ganapathy and Anders model and the Smith model are elaborated on in Smith (1979) and will not be explored here. The models agree within a factor of two for most elements.

Some general conclusions drawn by Smith (1979) from the bulk chemistry are as follows. (1) There was only slight fractionation in the nebula of the early condensate, silicate, and metal components although Earth is substantially depleted with respect to Cl chondrites in elements that condensed below 1000° C. (2) Major crustal-liquid differentiation of Earth resulted

Table 5.5. Estimates of the Composition of Earth's Hydrosphere, Crust and Mantle, and Two Different Estimates of the Bulk Composition. Columns 1–4 are from Smith (1977), column 5 is from Ganapathy and Anders (1974). Abundances are given in weight fractions.

	1 Hydrosphere	2 Crust	3 Mantle	4 Bulk	5 Bulk
H	0.1082	0.0015	0.0005	6.6(− 5)	7.7(− 5)
C	2.8(− 5)	0.0052	1.0(− 4)	1.1(− 3)	0.0344
N	1.6(− 5)	2.0(− 5)	1.0(− 5)	2.2(− 5)	8.99(− 6)
O	0.859	0.4688	0.4387	0.296	0.282
Na	0.011	0.0213	0.0022	2.5(− 4)	0.00158
Mg	1.3(− 12)	0.0233	0.2458	0.165	0.129
Al	1.0(− 9)	0.0808	0.0147	0.102	0.0177
Si	3.0(− 6)	0.2686	0.2076	0.140	0.143
P	9.0(− 8)	0.0010	0.0003	6.1(− 4)	0.00213
S	9.0(− 4)	0.0004	0.0012	0.0435	0.0183
Cl	0.019	1.8(− 4)	2.3(− 4)	1.6(− 5)	2.49(− 5)
K	4.0(− 4)	0.0130	0.0010	1.3(− 4)	1.69(− 4)
Ca	4.0(− 4)	0.0499	0.0184	0.0125	0.0191
Ti	1.0(− 9)	0.005	0.0011	7.9(− 4)	0.00101
Cr	2.0(− 10)	1.0(− 4)	0.0031	0.0033	0.00471
Mn	4.0(− 10)	0.0012	0.0009	6.5(− 4)	5.84(− 4)
Fe	3.0(− 9)	0.0509	0.0612	0.3043	0.358
Ni	7.0(− 9)	7.5(− 5)	0.0024	0.0164	0.0202
Zn	5.0(− 9)	7.0(− 5)	4.2(− 5)	4.0(− 5)	9.16(− 5)
U	3.0(− 9)	1.3(− 6)	2.8(− 7)	2.6(− 8)	1.8(− 8)

in preferential separation of elements that enter basaltic liquids, and these formed much of the crust and upper mantle. (3) Volatilization of a major fraction of Earth is ruled out except in the early stages of growth (i.e., the depletion of volatiles is the result of the process of accretion rather than of a subsequent event). (4) Substantial amounts of siderophile and chalcophile elements were retained in the upper mantle and crust at a late stage of accretion (did not all enter the core). (5) Major amounts of Ca, Al, Na, and Ti were retained in the lower mantle. To what extent the radial zoning is the result of heterogeneous accretion and how much is due to crystal-liquid segregation is not clear.

Formation of the Core

Formation of the core probably took place very early in Earth's history as a natural consequence of the thermal state of Earth during the late stages of accretion (Murthy, 1976), although other models such as early accretion of core-forming materials (Clark et al., 1972) and slow growth throughout geologic time (Runcorn, 1962a) have been proposed. Early core formation is indicated by the following lines of evidence. (1) Significant segregation of core material could not have taken place late in the planet's history for it would have greatly perturbed the evolution of Pb isotopes in the mantle since Pb preferentially enters metallic phases whereas U enters silicate phases (Oversby and Ringwood, 1971). (2) Because of the great release of energy during core formation, it almost certainly was over before formation of the oldest rocks presently preserved on the surface (3.8 billion years). (3) The older rocks have remanent magnetism. (4) Rb would have preferentially entered the core, but Rb-Sr systematics of mantle rocks give a mantle age of 4.45 billion years (Hurst, 1978). These lines of evidence suggest that mantle temperatures were high enough to cause extensive melting of silicates and complete melting of Fe and FeS within 100–200 million years of planet formation. This timing is also consistent with evidence of accretion of some materials after core formation, as is implied by the abundances of siderophile and chalcophile elements in the upper mantle.

Core formation was probably close to catastrophic. When temperatures reached the Fe-FeS eutectic, an iron-rich melt would have separated and descended toward the center of the planet as a result of its high density, thereby releasing gravitational energy. The energy released would have caused further melting, segregation, and energy release, resulting in a runaway effect. According to Murthy (1976) the total energy released is sufficient to raise the temperature of the entire planet by 1200° C.

The extent to which the planet melted would have depended on the rate at which the core formed. The U-Pb systematics indicate that there was extensive melting, but evidence from the volatile elements is more equivocal. The upper mantle and crust are strongly depleted in alkalis and sulfur, carbon and nitrogen with respect to chondrites (Gast, 1960; Murthy and Hall, 1972) while other volatiles such as the halogens and water are in chondritic proportions. Such selective depletion, which appears unrelated to thermal volatility (Smith, 1979), is unlikely to have resulted from complete global melting. One possibility is that core formation took place after accretion and during the process only the interior was pervasively melted. Volatile elements from the interior were driven off, but a significant fraction was trapped in the cooler outer parts of the planet.

A second possibility is that accretion continued after core formation was largely over. An excess of siderophile elements in lunar highland breccias has been attributed to large accretion of metal-rich planetesimals (Morgan et al., 1972; Ganapathy et al., 1973). The outer regions of Earth also appear to have excess siderophiles. Ringwood (1966) estimated that the Ni content of the upper mantle is one to two orders of magnitude larger than if it were a silicate residue left behind after removal of siderophiles to form the core. Other siderophiles (Co, Cu, Au, Re, etc.) are similarly enriched. Murthy (1976) ascribed the enrichment to late accretion of metallic planetesimals and suggested a similar cause, late accretion, for enrichment of the outer parts of Earth in refractories (Gast, 1960). All these late additions to the planet would have been mixed into the outer few hundred kilometers as a result of the high impact rate.

Events subsequent to core formation are very hazy until a concrete record emerges from around 3.8 billion years ago. Murthy (1976) suggested that during the era of core formation a protocrust may have formed that was largely basic and ultrabasic in composition as a result of the pervasive mantle melting. Later, the high water content and high temperatures in the mantle may have been conducive to production of anorthositic melts, but Murthy (1976) doubted that Earth ever had an anorthositic outer layer like the Moon, because of Earth's steep pressure gradient. At depths greater than 35 km, sub-solidus reactions would tend to destroy the plagioclase-rich assemblages.

He suggested, alternatively, that any early crust would have formed from Ca- and Fe-rich melts and been basic to ultrabasic in composition. However, any such crust would be unstable because of the high impact rates prior to 3.9 billion years ago and because the crust would have been thin as a result of high thermal gradients caused by residual heat from the early thermal events and higher U and K contents than at present.

THE ARCHEAN

The geologic record starts with the Archean, which extends from the time of formation of the oldest rocks, 3.8 billion years ago, until 2.5 billion years ago. Archean rocks are exposed within all the shield areas, but the largest exposures are in central and south Africa, western Australia, and around Hudson Bay in Canada (fig. 5.12). The oldest rock known is a 3.824-billion-year-old metavolcanic boulder from a conglomerate in the Isua Series of West Greenland (Moorbath et al., 1977). Rocks in excess of 3 billion years have also been found in South Africa (Sinha, 1972), Zimbabwe (Hawkesworth et al., 1975), and Minnesota (Goldich and Hedge, 1974). The origin of Archean rocks is controversial. Ideas range from a view, on one extreme, that the Archean crust was stable, that all the continental material was in one supercontinent, and that this distribution reflects a global asymmetry imposed by early impacts (Goodwin, 1976). On the other extreme is a plate tectonic view, in which the Archean Eon is perceived as one in which numerous microcontinents repeatedly collided and broke apart at rates that far exceeded those in the Phanerozoic. All agree that heat flows during the Archean were substantially greater than at present, with estimates ranging from 2.5 to 5 times the present rate (Gast, 1960; Wasserburg et al., 1964). In this section the nature of the Archean rocks is reviewed, as well as some of the possible implications for both the tectonic environment and conditions at the surface. Most of the material is abstracted from reviews by Tarling (1978) and Windley (1976, 1977).

Two kinds of Archean rock associations are generally distinguished, high-grade metamorphics and low-grade greenstone belts. In many areas both types occur, but the temporal and spatial relations between the two are not always clear. The most common type of rock in the high grade terranes are quartzofeldspathic gneisses of calc-alkaline affinity. The gneisses are typically foliated and banded at a scale of 1 cm

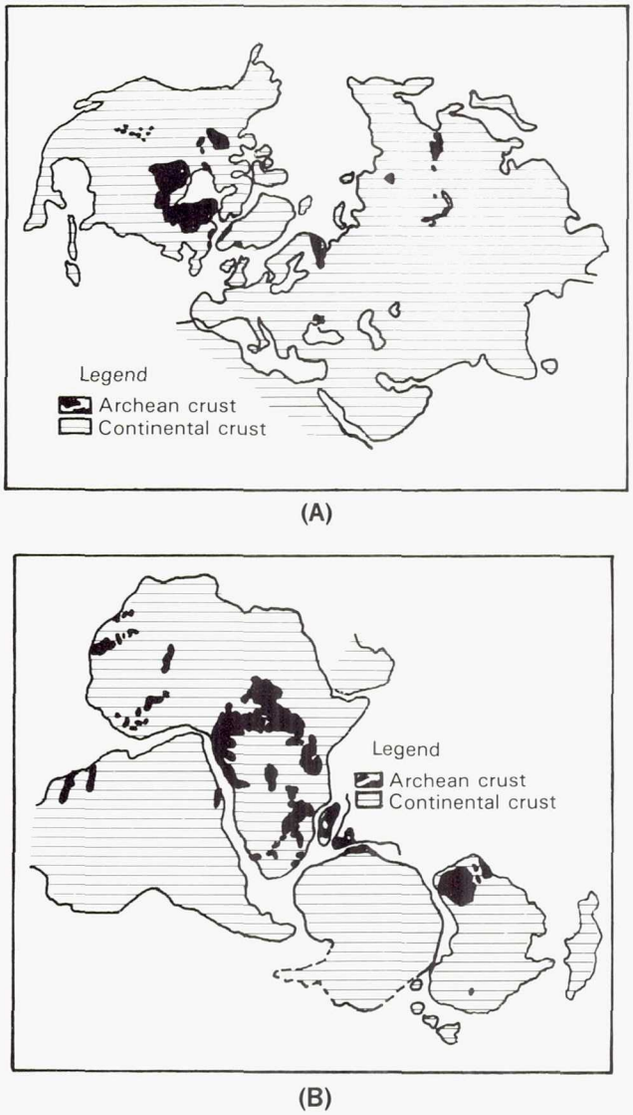

Figure 5.12. Distribution of exposed Archean crust in (A) Laurasia and (B) Gondwanaland (Goodwin, 1976).

and commonly have undergone various degrees of partial melting so are penetrated by granite veins. Intercalated with the gneisses are a wide variety of metamorphosed volcanics and sediments. Included are amphibolite, which has a chemistry similar to modern tholeiites, marble, quartzite, and mica schist. Many of the schists are graphitic, although whether the graphite is biogenic or not is not known.

Included also among the sediments are banded iron formations, which consist of alternating quartz-rich and iron-rich layers. These have no modern equivalent, but are almost ubiquitous in the Archean. They have been found in India, Zimbabwe, Norway, Sierra Leone, Guyana and elsewhere, many as economic deposits. Cloud (1968) suggested that the banded iron

formations formed by precipitation of iron as a result of reaction with oxygen produced by photosynthesizing organisms. The oldest known banded iron formation, one from the Isua area of West Greenland, is 3.76 billion years old (Moorbath et al., 1973). If Cloud is correct, therefore, life had started by the time the geologic record emerged from the era of high impact rates, around 3.8 billion years ago. Biogenic or not, the banded iron formations, like the other associated sediments, appear to have been deposited in stable, near-shore environments.

Cutting many of the high-grade sequences are layered intrusions. Most are composed primarily of plagioclase and hornblende, with minor chromite. The plagioclase is very calcic, ranging from An_{80} to An_{100}. Eclogite and komatiites (ultramafic and mafic rocks with quenched textures, high MgO and high CaO/Al_2O_3) have also been reported at some locations. Komatiite is of interest in that its formation requires a high degree of mantle melting, estimated by Green (1972b) at 60–80 percent for ultramafic and 40–60 percent for mafic komatiite. Their abundance in the Archean may result from the high heat flows and steep geothermal gradients expected for this time.

Moorbath (1976) argued on the basis of Rb/Sr data that the younger (3.1 billion years) gneisses of west Greenland are not remobilized older (3.8 billion years) gneisses but formed from juvenile mantle derivatives. Because the early gneisses have a higher Rb/Sr ratio than the mantle, the Sr isotopes in the gneisses and mantle must have evolved along different paths. The initial Sr isotopes of the younger gneisses fall on the evolutionary track of the mantle rather than that of the older gneisses. The implication is that during this period (3.8 to 3.1 billion years ago), crustal material was accumulating at the expense of the mantle and not being merely recycled.

The second type of major rock association of the Archean, the greenstone belts, occur in most shield areas and range in age from 2.3 to 3.4 billion years. The belts occur as irregularly shaped, elongate slivers, embedded in a matrix of gneissic or granitic rocks. They range in size from up to 1000 km across and up to 250 km wide, although the best studied, the Barberton belt of South Africa, is only 120 km by 40 km. Structural relations with the surrounding rocks are commonly unclear. Most of the belts are synform in shape, but they may be complexly interfolded with the surrounding rocks and not true synclines (Stowe, 1974).

While stratigraphic sequences are different in different belts, most sequences can be divided into a lower, predominantly volcanic group and an upper, mainly sedimentary group (Anhaeusser, 1971; Glickson, 1976). At the base are mainly peridotite and basaltic komatiites, some with pillow structures. These are usually followed by low-K rocks of the basalt-andesite-dacite-rhyolite sequence, which may be interbedded with chert and banded iron formations. The upper, predominantly sedimentary sequence consists mainly of deep-water sediments such as shale and graywacke, at the base, followed by shallower water sediments including conglomerate, quartzite, and limestone. Thus the sediments in the high-grade areas resemble the stable continental shelf deposits of the Phanerozoic, whereas those in the low grade greenstone belts resemble deposits found on active plate margins.

Models of the evolution of the Archean crust and formation of the sequences just described are of two basic types: fixist models, which assume a fixed crust and formation of the greenstone belts primarily by vertical tectonics, and mobilist models, which draw close analogies with plate tectonics and assume large lateral motions. The various fixist theories (Anhaeusser et al., 1969; Viljoen and Viljoen, 1969; Glickson and Lambert, 1973; Green, 1972a) differ in detail but most portray the greenstone belts as developing in linear downwarps in an unstable, thin, primitive, sialic crust. Accumulation of sediments and volcanics in the basins caused downsagging, burial and possibly partial melting of the deeper materials. The basal komatiites in some models are viewed as relics of a primordial oceanic crust. At a late stage the greenstone belts are thought to have been intruded by granite diapirs, which caused compression and local folding. One variant of the fixist models is that the greenstone belts are terrestrial equivalents of lunar maria. Green (1972a) suggested that impact-triggered melting beneath large impact craters caused mafic and ultramafic eruptions within the craters. After further magmatism, sedimentation, and metamorphism, these evolved into the observed greenstone belts.

Several authors have attempted to explain Archean tectonics in terms of plate tectonics, notably Anhaeusser (1973), Talbot (1973), Rutland (1973), Burke et al. (1976), and Windley (1977). At the start of the Archean, two to five times as much heat was produced by radioactive decay as is produced today. At present twice as much heat is dissipated through

ocean ridges as through the rest of the crust. Burke et al. (1976) suggested that a similar situation should have prevailed in the Archean, for there is no evidence of any heat dissipative processes peculiar to those times. One of the principal differences between present-day and Archean tectonics concerns rates. To allow faster heat dissipation, spreading rates would have had to be greater or the length of the oceanic ridges longer, or both. Because of the higher thermal gradients, the lithosphere—both continent and ocean—was probably slightly thinner than at present. It should be noted in passing, however, that other authors (Molnar and Atwater, 1978; Hargraves, 1981) used the high heat flows postulated for the Archean to argue against Archean plate tectonics. They claim that the main driving force behind modern-day plate tectonics is the negative buoyancy of old oceanic lithosphere, which in effect drags a moving plate into a subduction zone. The higher heat flows in the past would result in a thin, relatively warm lithosphere which would not have sufficient negative buoyancy to be passively subducted.

Burke et al. (1976), Tarney et al. (1976), and Windley (1977) all suggested that greenstone belts formed in back-arc spreading centers analogous to those in the western Pacific (Karig, 1971, 1974). They argued that the belts would not have survived if they formed either within the main ocean basins, or along arcs, because they would be subducted or destroyed by uplift and erosion. Moreover, the sequences within the greenstone belts are very similar to those that form in back arc areas (fig. 5.13). Tarney et al. (1976) demonstrated close similarities between the Rocas Verdes marginal basins of South America and various greenstone belts, and Burke et al. (1976) drew similar comparisons with the Paleozoic Round Pond area of Newfoundland and with the Mesozoic rocks of the northwestern Sierra Nevada of California. According to Windley (1977), the high-grade sequences are the equivalents of rocks formed at modern arcs, the Archean sequences having undergone deep burial and extensive plutonic activity. The greenstone belts are thus caught between different arcs or between arcs and the continental foreland, and ultimately become embedded in the high grade sequences.

According to the plate tectonic model, the Archean Eon is one of formation and consolidation of continental material, and of declining magmatic and tectonic activity. The era started with numerous microcontinents formed largely by arc volcanism and tectonism. With rates of plate motion two to three times the present, frequent collisions between the arcs resulted in progressive consolidation of the continental materials into larger masses. With the decline in heat production was a corresponding decline in tectonic and magmatic activity, and a decline in the rate of continental growth. By the end of the era, Burke et al. (1976) estimated one-third of Earth's surface was covered by continental crust, as compared to the present 41 percent, and most of it was in large continental masses. According to the "fixist" models, the Archean was an era of intense volcanic activity, during which thick piles of lava erupted through fissures onto a thin, globe-encircling crust. As a result of outpouring of basalt above, and remelting below, crustal materials were recycled relatively rapidly, resulting first in tonalities and trondjhemites, and ultimately granites, from which protocontinental crust could form (Hargraves, 1981).

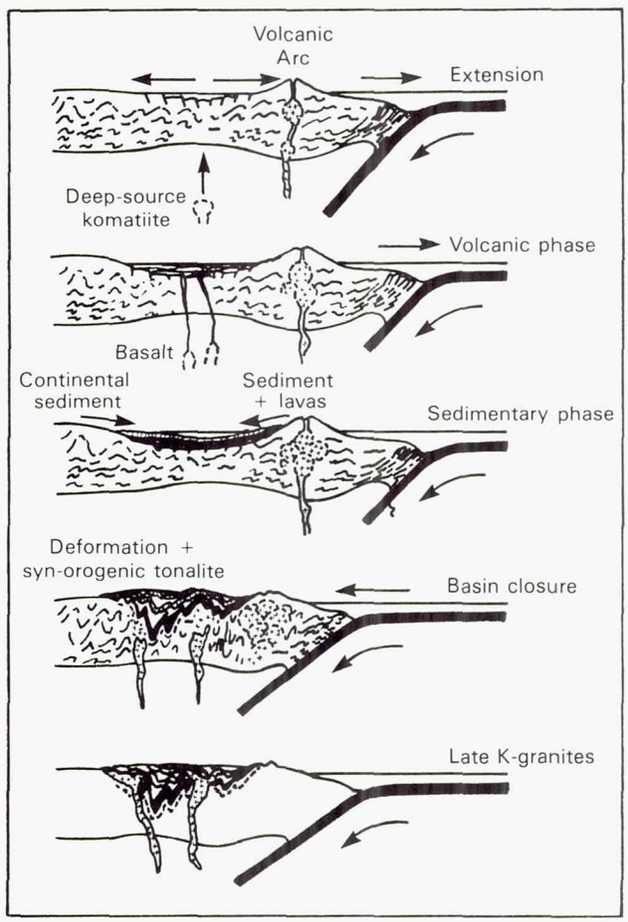

Figure 5.13. Possible development of greenstone belts by back-arc volcanism, sedimentation and compression (Tarney et al., 1976).

THE PROTEROZOIC

The Proterozoic Eon extends from 2.5 billion years ago to the start of the Cambrian 570 million years ago, constituting almost half of the planet's history. Generalizations about the Proterozoic are more difficult to make than about the Archean, possibly because much more is known. Anhaeusser (1973) emphasized that the synclinal greenstone belts and high-grade gneisses that characterize the Archean do not continue into the Proterozoic. Instead the early Proterozoic was characterized by thick sequences of gently dipping sediments and volcanics that appear to have been deposited in broad downwarps of the old sialic crust. The sediments are mainly stable platform types with large fractions of conglomerate, orthoquartzite, and sandstone. Associated with them are commonly flood basalt of tholeiitic type, and potash-rich andesite and rhyolite. Hunter (1974) estimated that such sedimentary sequences in South Africa (Swaziland, Pangola, and Witwatersrand Groups) are 10–20 km thick and accumulated for periods of 70–300 million years. Similar stable platform sediments also characterize the Huronian and Animikie systems of southeastern Canada, which are around 2.3 billion years old (Card et al., 1972). Absent from all these deposits are ophiolites and any flysch or molasse types of deposits that are indicative of contemporaneous tectonic activity. These South African and Canadian early Proterozoic sequences are thus difficult to reconcile with conventional plate tectonics.

More typical of Phanerozoic sequences are the circum-Ungava and Coronation geosynclines of Canada (Davidson, 1972; Hoffman et al., 1974). The circum-Ungava structure is asymmetric, having quartzite, dolomite, and iron formations adjacent to the Ungava craton in the west, and mafic volcanics, shale, and graywacke farther to the east. During the Huronian orogeny, 1.6 to 1.75 billion years ago, the geosynclinal sequence was thrust onto the Ungava foreland and became highly deformed and metamorphosed. Accordingly, Hoffman et al. (1974) suggested that horizontal movements, such as those associated with plate tectonics, were involved. Similarly, they used the depositional and deformational history of the Coronation syncline of northwestern Canada to demonstrate the existence of plate motion 2 billion years ago. They showed that its depositional and structural history was similar to that of the Phanerozoic Cordilleran geosyncline of North America, which is characterized by early platform-derived sediments, followed by platform-directed sedimentation derived from offshore magmatic arcs, followed by platform-directed overthrusting. Thus the early Proterozoic preserves evidence both of large-scale intracratonic sedimentation involving vertical movements, and of horizontal movements such as result from plate motion.

Several distinctive characteristics of early Proterozoic sediments are worth noting. Banded iron formations continued to form until around 1.8 billion years ago, and Goldich (1973) estimated that they make up 15 percent of all the early Proterozoic sediments. They are found throughout the world, wherever Archean and early Proterozoic sequences occurred. Around 1.7 to 2.0 billion years ago, red beds appeared for the first time in the geologic record on several continents. These are sandstones with a hematite pigment, which generally forms a coating around individual grains. Their appearance is generally taken as indicative of oxygen-rich conditions at the surface. Thus two oxygen-sensitive events occurred at about the same time (1.7–2.0 billion years ago): the last banded iron formations formed and the first red beds formed.

Cloud (1968) suggested that the early atmosphere was oxygen-deficient and that iron weathered to Fe^{+2}, which was relatively mobile because of its greater solubility compared with Fe^{+3}. The ferrous iron, he suggested, reacted with photosynthetically produced oxygen in the primitive ocean, thereby producing the banded iron formations and preventing toxic buildup of oxygen. Migration of oxygen from the hydrosphere to the atmosphere, however, ultimately led to free oxygen being available for weathering. As a result, Fe^{+3} was produced directly by weathering and red beds formed. The cessation of banded iron formations and the start of red bed deposition may therefore be connected.

During the middle to late part of the Proterozoic (1.8 to 0.57 billion years ago) a series of medium- to high-grade mobile belts formed across Laurasia and Gondwanaland. Included are the Churchill and Grenville belts of Canada, the Laxfordian of Scotland, and the Svecofennides and Karelides of Sweden and Finland (Windley, 1977). Many of the belts appear to consist of reactivated basement, but igneous rock suites are also present, including characteristically anorthosite, rapakivi granite (alkali-rich granite with megacrysts of K-feldspar), and alkali complexes, some with carbonatite. Accumulation of thick sequences of coarse, red, continental sandstone also took place within the intra-cratonic troughs. Examples are the

Belt-Purcell Groups (1.0–1.45 billion years) of western Canada and the United States and the Keweenawan sediments of the middle United States. Layered igneous complexes such as the Muskox Intrusion of northwestern Canada and the Duluth complex of Minnesota are also relatively common. Both the late and the early Proterozoic are also characterized by extensive glaciations. The later ones appear to be concentrated in the periods 900–1000 million years ago, 730–820 million years ago, and 580–650 million years ago (Steiner and Grillmair, 1973). The glacial deposits occurred widely, having been found in Siberia-China, Scandinavia, Brazil, western North America, South Africa, and Australia.

To what extent the Phanerozoic style of plate tectonics is applicable to the Proterozoic is unclear, although much of the evidence suggests that the continents moved as very large units, possibly as one unit, a Proterozoic Pangaea, and that some of the mobile belts formed interior to the continent, with little or no horizontal movement. Evidence of horizontal movement, or the lack of it, is from paleomagnetic data and from matching of structural trends across the belts. Paleomagnetic poles from widely spaced locations within the Laurentian shield, with dates ranging from 2.2 to 1.0 billion years ago, all lie on the same track, thereby suggesting that the Laurentian shield remained intact during this period (Irving and Lapointe, 1975). The track is irregular with numerous hairpins, indicating that the shield was in motion and that it changed direction periodically. Dewey and Burke (1973) have, nevertheless, argued that the Grenville belt can be compared with the Hercynian and Himalayan fold belts, which formed by intercontinent collisions. Their model does not appear, however, to apply to the rest of the Canadian shield, nor to some of the folded belts of the southern continents.

Clifford (1970) and Shackleton (1973) showed, by several examples from Africa, that older belts can be traced through younger ones, or that older belts can be matched on either side of younger belts. Both relations preclude extensive horizontal movement during formation of the younger mobile belt. Clifford and Shackleton therefore suggested that most of the Proterozoic mobile belts formed by remobilization of the pre-existing crystalline basement with little or no horizontal movement. The absence of ophiolites, melanges, and blueschist is also cited as supporting evidence for this model. Engle and Kelm (1972), Goodwin (1973), and others have further asserted that the coherent grouping of Archean provinces of different ages, the continuity of tectonic patterns within the shields, and the linear array of banded iron formations stretching from continent to continent, indicate that the continents could not have continually drifted apart and reassembled during the Proterozoic. They propose that from around 2.2 billion years ago to around 1.0 billion years ago there existed one Proterozoic supercontinent. Sea floor spreading and subduction may have occurred during the period, as suggested by Dewey and Burke (1973), but only the periphery of the continental mass was affected by plate motion, as possibly exemplified by the Grenville Province.

Windley (1977) suggested that around 1.0 billion years ago the postulated Proterozoic supercontinent(s) started to break up. The evidence is the widespread occurrence of basalt, diabase dikes, alkalic igneous complexes, and red beds; the latter being a rock association that commonly formed during the break-up of Pangaea during the Mesozoic. (For possible positions of the pieces of continent at the end of the Proterozoic (570 million years ago) see section on plate tectonics.) At the close of the Proterozoic, animals with hard shells had developed so that fossils are common in the subsequent record. The geology from then to the present is dominated by plate tectonics, at least for the last 250 million years, and the main characteristics of the prevailing tectonic regime were described above. It should be emphasized that this most familiar era of Earth's history represents only the last 13 percent of the planet's lifetime.

EVOLUTION OF THE ATMOSPHERE AND HYDROSPHERE

Before 1970 it was widely believed, largely through the pioneering work of Rubey (1951), that Earth's atmosphere and ocean accumulated slowly over geologic time, and that accretionary processes played a negligible role in planetary outgassing. This belief arose from the following observations. (1) Earth is greatly depleted in nonradiogenic rare gases with respect to the Sun so that the atmosphere is not simply a remnant of primordial nebular gas. (2) The atmosphere is greatly enriched in ^{40}Ar with respect to the nonradiogenic rare gases, which indicates that gas is released from the interior. (3) Volcanic activity is known to release volatiles. (4) The then accepted thermal models of Earth required cold accretion of Earth. (5) The volume of gas in the atmosphere is far greater than could

be released by weathering during the lifetime of the planet. During the 1970s however, considerable evidence accumulated for catastrophic outgassing of Earth within a few hundred million years of its formation, followed by relatively trivial juvenile outgassing for the rest of its history. Fanale (1971) showed that the nonradiogenic rare gas content of Earth is similar to chondritic meteorites if one assumes that the nonradiogenic rare gases currently in the atmosphere represent the total inventory for Earth. In this respect Earth is typical of the meteoritic array. If Earth and the meteorites formed of similar parent materials then it follows that Earth is thoroughly outgassed with respect to Ne, Ar, and Kr, and the nonradiogenic rare gas inventory has been conserved and not blown off to space as suggested by Ringwood (1966). Nor has the inventory been significantly added to by the solar wind as suggested by Cameron (1964), otherwise the atmosphere would be preferentially enriched in ^{20}Ne with respect to meteorites, which is not observed. Ne and Xe are somewhat anomalous, which Ozima and Nakazawa (1980) attributed to incorporation into Earth of a small amount of nebular gas that was trapped within planetesimals during later stages of accretion.

Given that Earth is completely outgassed with respect to the nonradiogenic rare gases, the question arises as to when this occurred. Fanale (1971) used several lines of evidence to demonstrate that outgassing took place early. Geochemical arguments for early pervasive melting and outgassing have already been reviewed in the section on core formation. Fanale showed in addition that early outgassing is indicated by the isotopic composition of rare gases trapped in modern and ancient beryls. Damon and Kulp (1958) showed that Precambrian beryls have significantly greater radiogenic ^{4}He and ^{40}Ar contents than recent beryls, but negligible amounts of the nonradiogenic rare gases. They suggested that the high radiogenic gas content in the old beryls is due to the greater release rates of the accumulated radiogenic gases, which in turn resulted from higher radioactive heat production in the Precambrian. The nonradiogenic gases are missing because they had all been outgassed in an earlier catastrophic episode.

While the evidence of early catastrophic outgassing is convincing, there remains the problem of the fate of volatiles other than the rare gases such as C, N, O, and H. Their near-surface abundances fall far short of those that would result from complete outgassing of the interior. Fanale (1971) suggested that significant quantities of these gases remained dissolved in silicate melts during the early melting event. In effect, an equilibrium developed between the melted interior and the developing atmosphere. Smith (1979) alternatively argued that, as the outer parts of the planet cooled, volatiles from the still-outgassing interior would be captured near the surface and form minerals such as micas and amphiboles. In addition, he suggested, large amounts of volatiles outgassed to the surface could be resorbed into the crust and upper mantle by subduction, during an early era of rapid recycling of the lithosphere.

The compositions of the early atmosphere and hydrosphere are not known, although what little evidence exists suggests that the oceans had approximately the same composition as now, whereas the atmosphere differed from the present mainly by being oxygen-free. A roughly constant composition for sea water is suggested by casts of gypsum and halite in sedimentary rocks 2 billion years old, the presence of limestone in ancient Precambrian sediments, and the sequence of minerals in the oldest evaporite deposits (Holland, 1976). A significant difference between present marine deposits and those of the Precambrian is that the Precambrian carbonates have consistently higher dolomite/calcite ratios. Holland (1976), after examining several possibilities, suggested that the most likely explanation of the difference is that the CO_2 available for carbonation did not keep pace with the supply of Mg^{+2} and Ca^{+2} and from weathering. This he attributed to a progressively slower recycling of CO_2 with time and distribution of carbonates to progressively deeper levels in the lithosphere, both as a consequence of a decreasing thermal gradient with time.

Evidence for an early oxygen-deficient atmosphere is mainly from two sources: (1) banded iron formations, which as we have already seen, may require weathering and transport of Fe^{+2} and, occurring only under anoxic conditions, and (2) the presence of detrital uraninite in early Proterozoic sediments such as the Witwatersrand and Transvaal Systems of South Africa, which may require oxygen partial pressures of less than 10^{-3} atmospheres for its survival in the weathering cycle (Holland, 1976).

The buildup of oxygen in the atmosphere probably resulted largely from photosynthesis (Cloud, 1968; Schidlowski, 1971). If banded iron formations were acceptors of photosynthetically produced oxygen, as suggested by Cloud (1968), then photosynthesis

started at least as far back as the oldest known banded iron formations, the 3.76-billion-year-old Isua Formation of west Greenland (Moorbath et al., 1973). The organisms responsible were probably limited to primitive, stromatolite-building procaryotes. Procaryotes have their genetic materials dispersed throughout their cells in contrast to the eucaryotes whose genetic material is concentrated in a nucleus. The period from 3.7 billion years ago to the end of the Archean, 2.5 billion years ago, may have been one where a rough balance was maintained between production of oxygen by photosynthesis and its fixation by reaction with Fe^{+2}. However, as we have seen, red beds started to appear in the Proterozoic, suggesting oxidizing conditions. The amount of oxygen in the atmosphere may still have been extremely small, most of the oxidation being by ultraviolet-generated ozone, which has reaction rates in weathering far greater than O_2 (Windley, 1977).

During the early to mid-Proterozoic there appears to have been a steady buildup of oxygen in the atmosphere, probably as a result of proliferation of procaryotic blue-green algae. By 1.5 billion years ago, the oxygen content of the atmosphere was sufficient to support life forms with primitive oxidative metabolisms, and the first oxygen-employing organisms with organized nuclei (eucaryotes) appear at this time (Schopf, 1974). The appearance of the eucaryotes was a major step in the evolution of life, for these organisms can reproduce sexually so have a greater potential for diversification than procaryotes. Schidlowski (1976) suggested that in order to support the oxygen-metabolizing organisms the oxygen content of the atmosphere must have reached 1 percent of the present level.

Accumulation of oxygen in the atmosphere would have resulted in development of a protective ozone layer by late Precambrian times, thereby opening up shallow waters and ultimately the land to colonization. During the period from 1.5 billion years ago to the end of the Precambrian there was considerable diversification of plant life (Schopf, 1974), probably largely among the eucaryotes. Toward the end of this period the first animals appeared (jellyfish, worms, sponges), and Cloud (1968) estimated that oxygen levels in the atmosphere must have been around 3 percent of the present. According to Berkner and Marshall (1967), oxygen contents reached 10 percent of the present levels by the Silurian (450 million years ago), and around this time there are the first indications of land plants. Oxygen appears to have reached its present level in the atmosphere around 350 million years ago.

SUMMARY

Earth is an active and evolving planet. During the final stages of accretion, around 4.6 billion years ago, the planet was heated enough to trigger core formation. This was probably catastrophic, resulting in pervasive melting and outgassing of the interior. No record remains of the first 700 million years of Earth's history, but it must have been an era of intense bombardment that resulted in efficient mixing of the outer 200 km. The era from 3.8 billion years ago, when the oldest known rocks formed, to around 2.5 billion years ago was probably one of relatively rapid continent growth. The atmosphere probably lacked oxygen and life forms were restricted to the primitive procaryotes. Much of the ocean formed before this time as a side effect of core formation, and was similar in composition to present seas. From 2.5 to 1 billion years ago, continental material appears to have been consolidated into a few (possibly one) large mass(es). Parts of the continental basement were episodically mobilized along linear belts, mainly by vertical movements, not the large horizontal motions associated with plate tectonics. Paleomagnetic evidence indicates, however, that the continents were in motion, and subduction and Phanerozoic-style mountain building may have occurred around the periphery of the continents. During the Proterozoic Eon the atmosphere became oxidizing and the first eucaryotes appeared. After 1 billion years ago there was partial breakup of the large continental masses into pieces that continued to disperse and reassemble throughout the Phanerozoic. The oxygen content of the atmosphere continued to increase until it reached the present level around 350 million years ago. Around this time (400–350 million years ago) the land was first colonized by plants and shortly thereafter by animals, and Earth's surface began to assume its present appearance.

ACKNOWLEDGMENTS

This chapter was substantially improved by suggestions from R. Hargraves of Princeton University and K. Howard, H. Wilshire and E. Shoemaker of the U.S. Geological Survey.

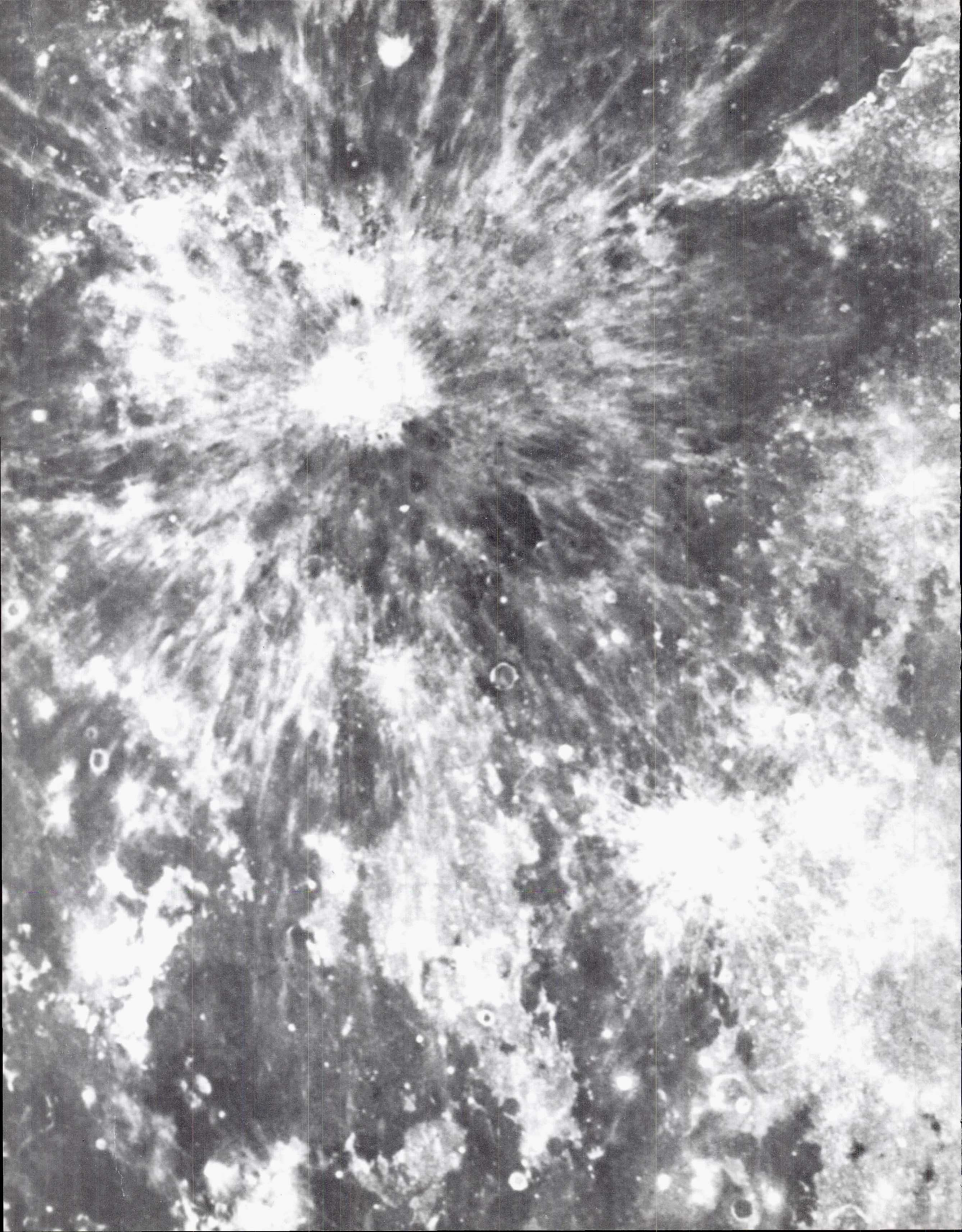

6
MOON

Don E. Wilhelms

INTRODUCTION

Scope and Organization

This chapter emphasizes the present state and evolution of the physical features which are visible on the Moon's surface, that is, the geology and geologic history. It is directed at a geologically educated audience, but most of it should also be comprehensible to the general scientific reader. All terms specific to the Moon and space exploration are defined as are all but the most basic terms common to both terrestrial and lunar geology. References cited include books, review papers, some important first presentations of ideas, and the most recent paper in a series on a given subject.

The chapter is organized in recognition that deposits of craters, basins, and maria dominate the stratigraphy of the Moon's crust just as the corresponding landforms dominate its appearance. Each section includes information intended to answer the basic questions (1) what do the units or their constituent rocks look like, (2) where are they located on the Moon, (3) how, in general, were they emplaced, and (4) when were they emplaced? The more fundamental question why—that is, the basic causes originating in the Moon's interior and in interplanetary space which combined to shape the surface—are addressed only where relatively well understood. The poorly understood origin of the Moon is not discussed.

Some recent book-length works explore the Moon from other viewpoints. It is viewed in its solar system context by Hartmann (1972, 1983), Wood (1979), Murray, Malin, and Greeley (1981), Beatty, O'Leary, and Chaikin (1981), and Glass (1982). The Basaltic Volcanism Study Project (BVSP, 1981) and Taylor (1975, 1982) have presented comprehensive, scholarly treatises emphasizing lunar petrology and geochemistry. Unreferenced books by French (1977) and Cadogan (1981) summarize these and other topics for the general scientifically inclined reader. The geologic topic of the present chapter is explored in greater detail by Mutch (1970), Guest and Greeley (1977), Wilhelms (in press b), and in the superbly illustrated and comprehensively captioned volume edited by Masursky, Colton, and El-Baz (1978). Schultz (1976a) presented an elaborate earlier compilation of Lunar Orbiter photographs and accompanying interpretations. Finally, the contemporary reader will find that the classic works of Baldwin (1949, 1963) contain amazingly current and useful data and interpretations of the Moon's near side.

Two Decades of Lunar Investigations

Answers to longstanding questions about the Moon's surface have been learned during the last two decades of intensive study. Processes originating above and under the surface have combined to shape it. *Primary impacts* of projectiles from space have formed circular depressions, termed craters if one rim dominates their form, and ringed basins or simply basins if other rings lie inside the main topographic rim. *Secondary impacts* of ejecta thrown from the primary crater or basin have excavated swarms of smaller, circular and noncircular craters. Basins are the principal component of the *terrae*—the light-colored, rugged uplands or highlands of the Moon. Craters scar the terrae and, in lesser numbers, the other major type of terrane, the dark, generally level and smooth *maria*. The mare plains were formed by eruptions of basaltic magma from the interior, the second major lunar process. The

surface, jointly created by impacts and volcanism, is topographically complex (figs. 6.1–6.3) but geologically simpler than the surfaces of Earth or Mars.

The dual origin of lunar surface features has not always seemed obvious. Before the advent of intensive lunar exploration, most observers sought a common origin, either impact or volcanic, for all features. The sometimes immoderate arguments for one or the other side were reminiscent of the earlier neptunist-plutonist contention in terrestrial geology (Mutch,

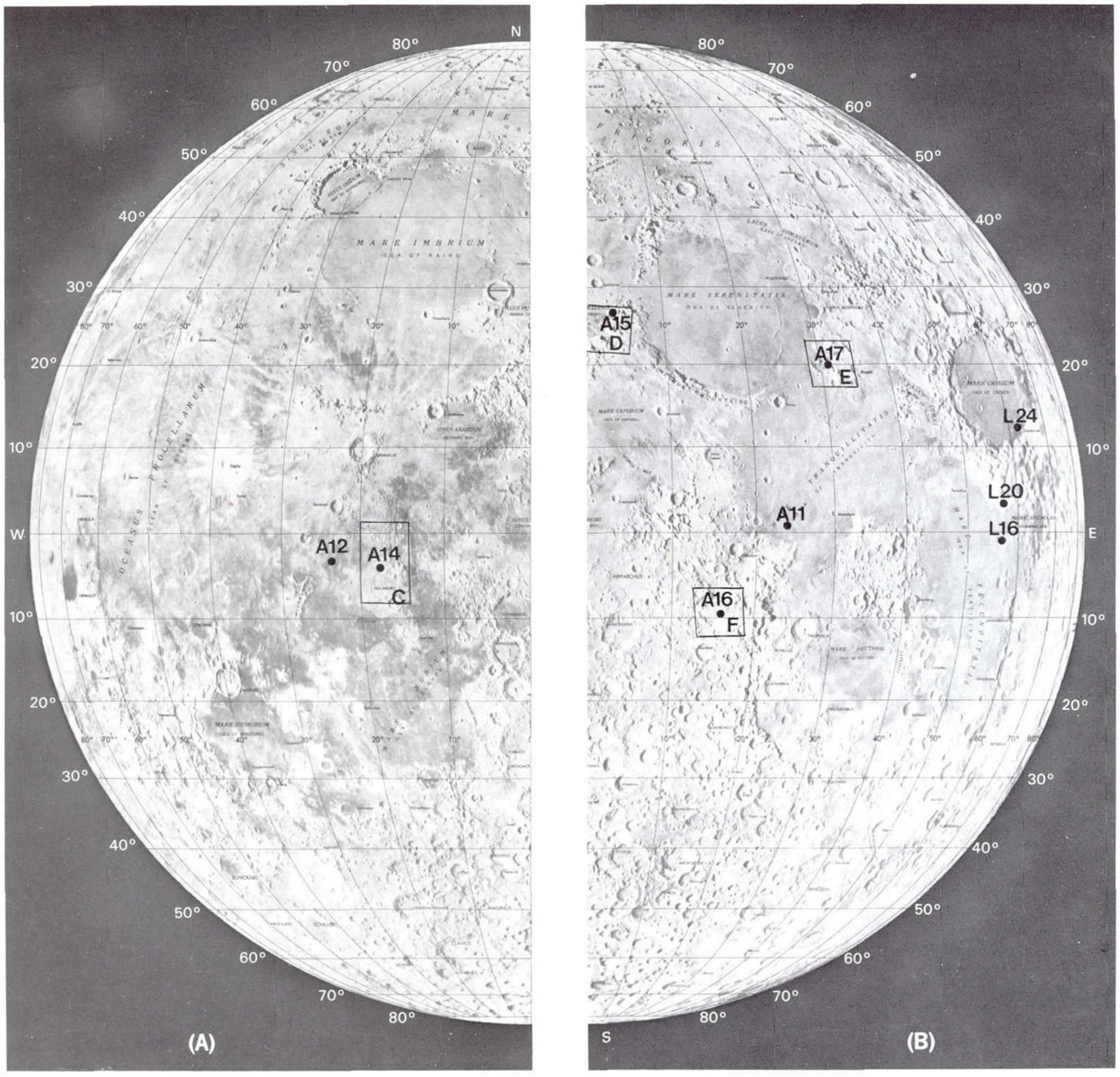

Figure 6.1. Landing sites of spacecraft that returned samples of the Moon. A = Apollo; L = Luna. (A). Western hemisphere, longitudes 90°W (left edge) to 0° (right edge). Note: *Before 1961, this hemisphere was considered the eastern. North is at the top in this and all other illustrations in this chapter except as noted; before 1961 north was usually placed at the bottom as it is seen in astronomical telescopes. Some maps and catalogs use a 360° convention, whereby longitudes increase eastward from 0° longitude; the convention used here is more common and corresponds to the terrestrial convention. (B). Eastern hemisphere, longitudes 0° (left edge) to 90°E (right edge). A and B are parts of LEM-1, prepared by U.S. Air Force Aeronautical Chart and Information Center in 1962.*

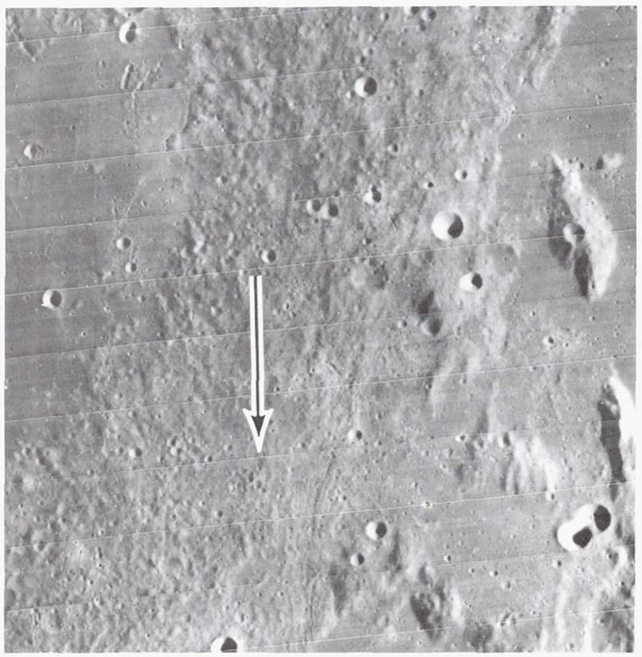

C. Fra Mauro peninsula, site of Apollo 14 landing (arrow). Largest crater is Fra Mauro, 95 km. Orbiter 4 H-120.

Note: *Unmanned Lunar Orbiter (Orbiter) frames are identified in this chapter by the mission number (1, 2, 3, 4, 5), a letter H for high resolution or M for medium (moderate) resolution, and the frame number. Each Orbiter H-frame is centered in an M-frame having the same number (Mutch, 1970).*

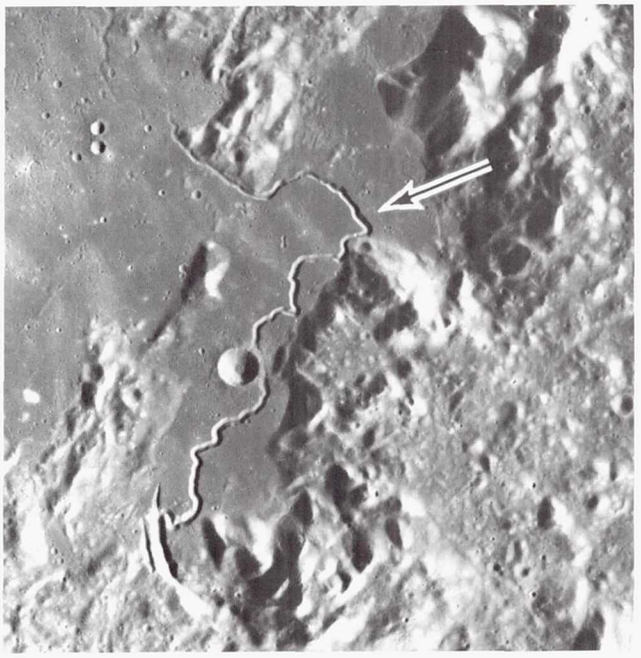

D. Montes Apenninus (rugged terrain) and Rima Hadley (sinuous rille), site of Apollo 15 landing (arrow). Scene 160 × 160 km. Apollo 15 M-1135.

Note: *The orbiting spacecraft of Apollo missions 15, 16, and 17 carried mapping or metric (M) cameras, which provided photogrammetric-quality stereoscopic photographs in a square format, and panoramic (P) cameras, which provided very high-resolution photographs in a strip format (Masursky et al., 1978). All missions carried hand-held or bracket-mounted Hasselblad (H) cameras.*

E. Montes Taurus (rugged terrain) and Taurus-Littrow valley, site of Apollo 17 landing (arrow). Scene 170 × 170 km. Apollo 17 M-446.

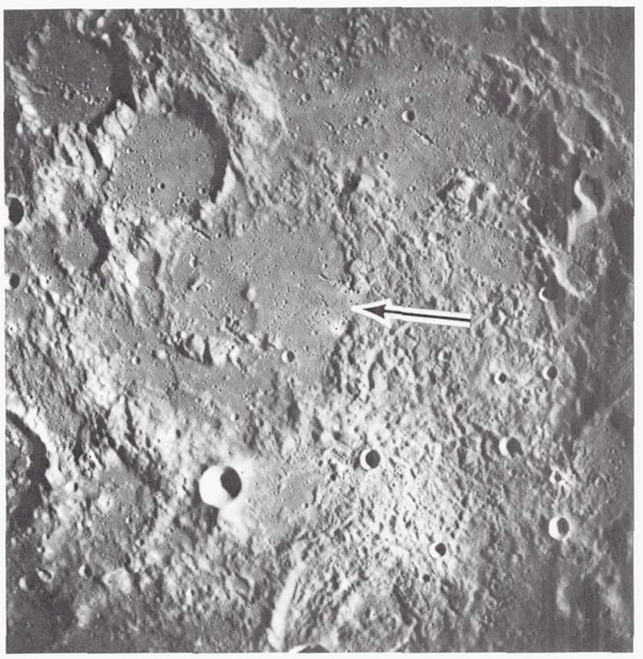

F. Descartes highlands, site of Apollo 16 landing (arrow). Landing point is on Cayley plains; rugged terrain north, east, and south of point is Descartes Mountains. Scene 160 × 160 km. Apollo 16 M-440.

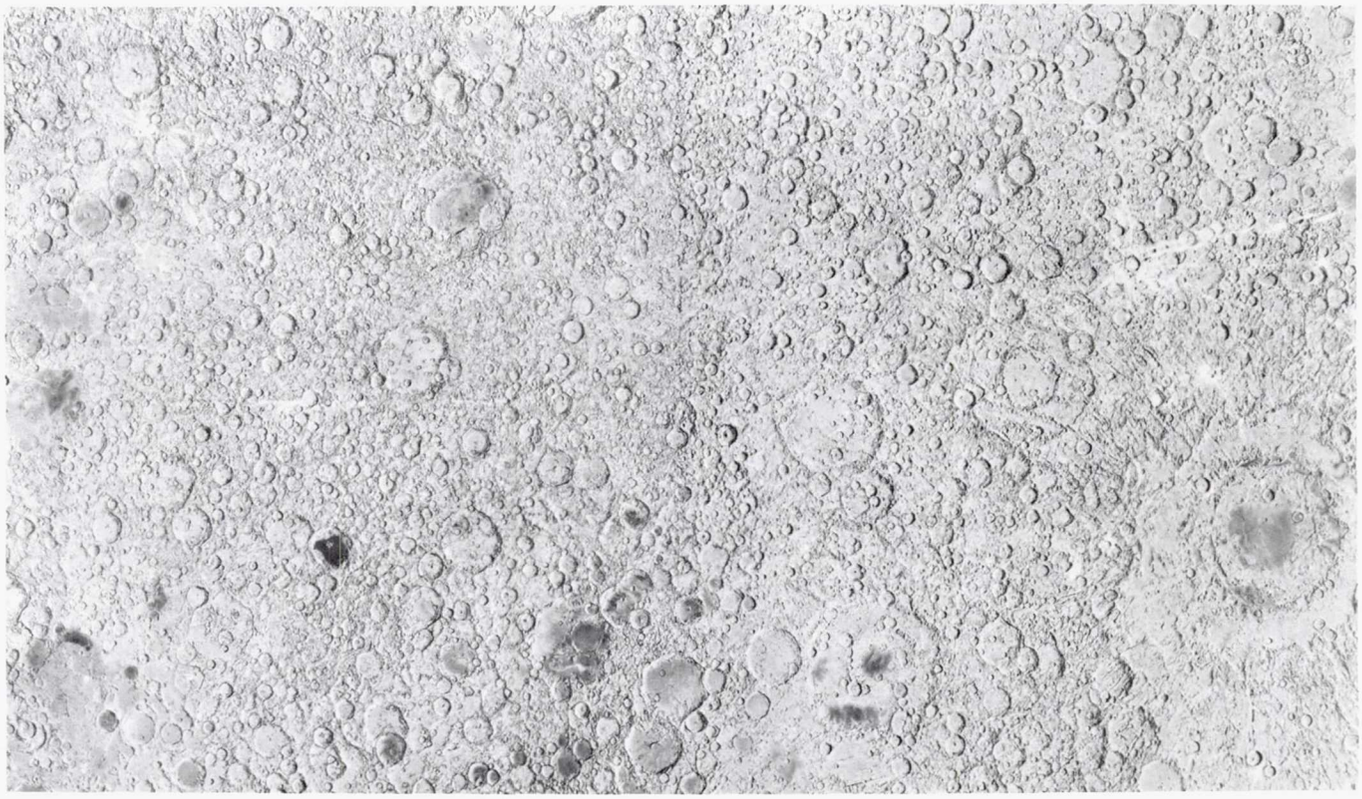

Figure 6.2. Shaded-relief map of far side of Moon. Latitude coverage 50°N–50°S. Prepared 1980 by U.S. Geological Survey, Map I-1218A. Longitude 80°E (left) to 80°W (right), increasing to 180° in center.

1970). For both planets, the extreme views yielded to compromises embracing both types of processes when more facts became available. Synoptic and objective studies by Baldwin (1949, 1963), Kuiper (1959), Hartmann and Kuiper (1962), and Shoemaker (1962a,b; Shoemaker and Hackman, 1962; Shoemaker et al., 1963) laid the foundation for much of our current picture of the Moon.

The work of Shoemaker and Hackman (1962), foreshadowed by a brief but brilliant study by Gilbert (1893), established the present perception of the Moon as a geologic body. That is, its visible crust consists of rock units which formed in sequence according to the same natural laws as do rocks on Earth, although often by different processes. Impacts did not merely excavate depressions and raise circular ridges, but also ejected materials which were deposited around the crater or basin as discrete, three-dimensional beds of fragmental and melted rock. The beds overlap one another in the order in which they were deposited (fig. 6.4). Mare volcanism formed beds of lava and pyroclastic material that are even more like rocks on Earth. This stratified character of the Moon's crust now seems obvious but became widely accepted only gradually as telescopic and spaceflight studies advanced during the 1960s. It was the basis for targeting many American spaceflights (Wilhelms, in press a) and led to the results presented here. A globally valid lunar stratigraphic column based on the original scheme (Shoemaker and Hackman, 1962) and subsequent amendments is given in table 6.1.

Each successive spaceflight added new data for the present synthesis (table 6.2). The space age opened with the Earth-orbit flight of the Soviet Sputnik 1 in October 1957. Mostly in response to this success, the United States established the National Aeronautics and Space Administration (NASA) a year later. Direct lunar exploration can be thought of as starting in 1959, when the Soviet spacecraft Luna (Lunik) 2 struck the surface, Luna 3 photographed the far side for the first time, and Project Ranger was established as the first major American lunar exploration program (Kopal and Mikhailov, 1962; Lipsky, *in* Middlehurst and Kuiper, 1963; Hall, 1977).

Telescopic studies accelerated about the same time (Kuiper et al., 1960; Kuiper and Middlehurst, 1961; Fielder, 1961; Markov, 1962; Kopal, 1962; Kopal and Mikhailov, 1962; Shoemaker, 1962a,b, 1964; Shoe-

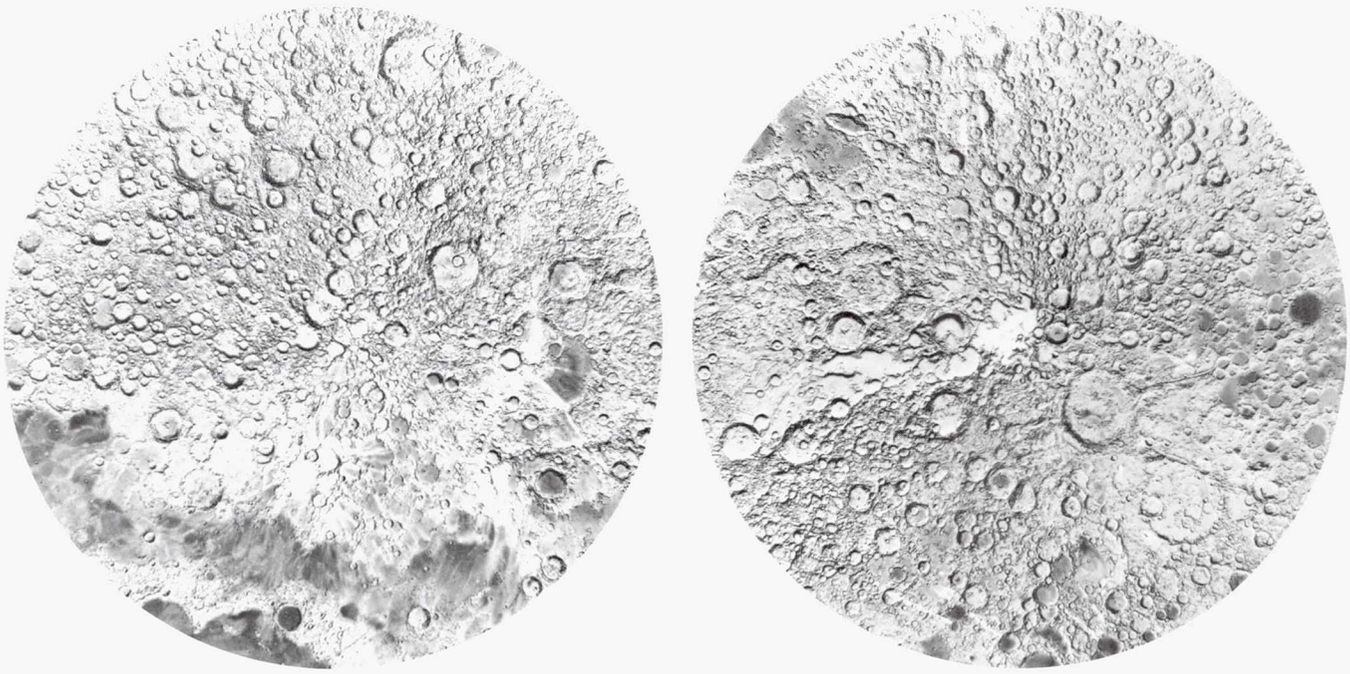

A. Latitudes 45°N–90°N. *B. Latitudes 45°S–90°S.*

Figure 6.3. Shaded relief maps of polar regions of Moon. Prepared 1981 by U.S. Geological Survey, Map I-1326B.

maker and Hackman, 1962; Baldwin, 1963; Middlehurst and Kuiper, 1963). After failures or partial failures of Rangers in 1961 and 1962, Rangers 7, 8, and 9 successfully returned the first detailed pictures of the Moon's surface before impacting the surface in 1964 and 1965 (table 6.2; Heacock et al., 1965, 1966; Hall 1977). The Soviet Luna 9 and the U.S. Surveyor 1 achieved nondestructive soft landings in 1966. Soviet flyby and orbital missions had taken place in 1965 and 1966, and then the highly successful American Lunar Orbiter program returned some 1500 high- to medium-resolution photographs during an intensive program between August 1966 and August 1967 (Mutch, 1970). Orbiter photographs cover about 99 percent of the lunar surface at varying resolutions. They provide the only available views of much of the far side and the only better-than-telescopic views of much of the near side. U.S. and Soviet soft landers continued to examine the surficial materials in the same time period. The high-resolution Surveyor photographs contain still-valuable information about processes of generation and reworking, thickness, blockiness, albedo, and other properties of the regolith, the ubiquitous fragmental overburden (Shoemaker et al., 1969; March 1970 issue of *Icarus*). Surveyors 5, 6, and 7 also provided the first—and quite accurate—direct analyses of lunar materials (Gault et al., 1968a; Turkevich, 1971).

Although not designed primarily as a scientific program, Project Apollo marked, of course, the culmination of lunar exploration. Apollo 11 landed in Mare Tranquillitatis on July 20, 1969, and obtained several important keys to lunar history (30 January 1970 issue of *Science*). Most Tranquillitatis rocks are basaltic lavas between 3.55 and 3.85 aeons old (1 aeon = 10^9 years), yet are younger than geologic units on three-fourths of the Moon's surface (see "Mare Basalts").[1] Prior lunar history therefore was far more eventful than subsequent history. Primeval materials differentiated in the first 0.35 aeons after lunar accretion (see "Terra

[1]Absolute ages are given in this report as if they had been calculated by the radioactive decay constants for the Rb-Sr and K-Ar systems adopted by the International Union of Geological Sciences in 1977 (Steiger and Jaeger, 1977). The ages may, therefore, differ numerically from values given in earlier literature. For example, a "new" age of 3.85 aeons corresponds to "old" ages of 3.91 aeons as determined by the ^{40}Ar-^{39}Ar method (Turner, 1977) or 3.93 aeons as determined by the Rb-Sr method (Papanastassiou and Wasserburg, 1971a,b; Nyquist, 1977). Ages determined by the Sm-Nd method (Lugmair, 1974; DePaolo, 1981) remain unchanged.

Breccias'') into a feldspathic terra crust and an ultramafic mantle that later became the source of the mare basalts. The intense cratering visible on the terrae must have taken place in a much shorter time than the enormously long time which has elapsed since the lavas appeared on the surface. The only events in those last 3½ aeons have been relatively minor cratering and development of a few meters of regolith, in contrast to the enormously active and intricate evolution of Earth in the same period. Thus the antiquity and the recent inactivity of the lunar surface were demonstrated on this first mission.

The second manned mission, Apollo 12 in November 1969, returned pieces of compositionally different lavas (e.g., lower in titanium) that are younger by half an aeon than those from Tranquillitatis. The great age gap—almost as long as the Phanerozoic on Earth—proved once and for all that the maria are not the product of a single event such as a basin impact, as had been thought by many previous observers who equated ringed basins with the maria.

Apollo 13 suffered a mishap on the way to the Moon in April 1970 and did not land. After a delay caused by the accident, Apollo 14 landed in February 1971 at Apollo 13's intended target, a geologic unit that had long been scrutinized by lunar geologists—the Fra Mauro Formation (fig. 6.1C). This was Apollo's first excursion from the relatively simple lunar maria onto the generally older, intensely impacted terrae. The returned material was probably ejected 3.85 aeons ago from the largest ringed basin on the near side of the Moon, Imbrium.

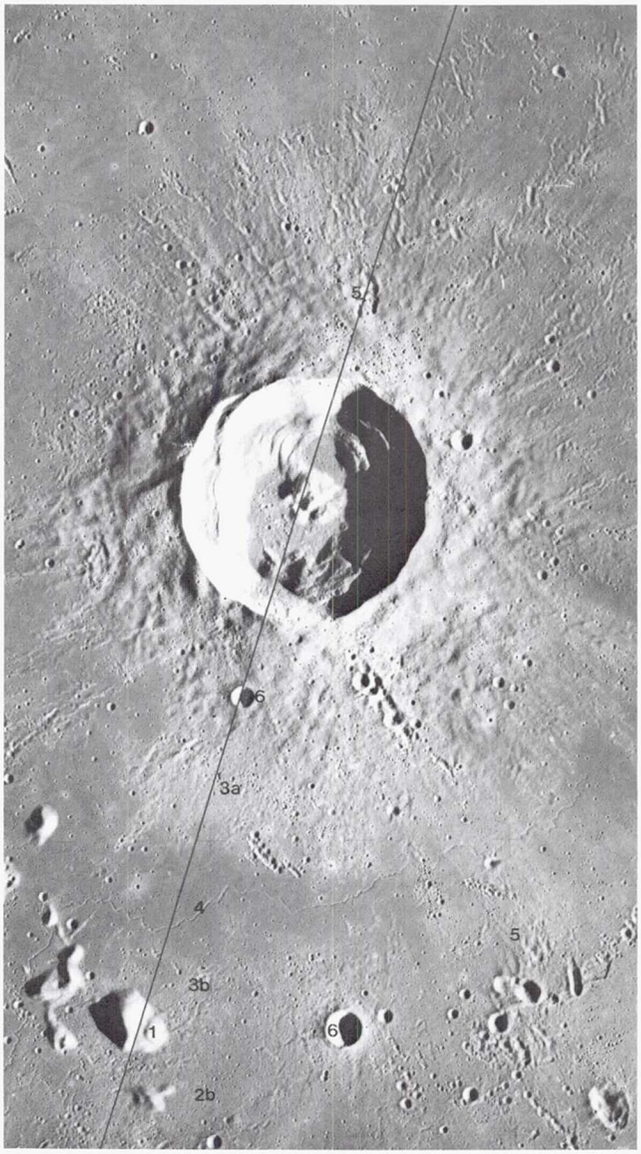

Figure 6.4. Stratigraphic relations at crater Euler (28 km, 23°N, 29°N).

Units numbered in order of decreasing age:

(1) Terra massifs of an Imbrium-basin ring.

(2) Old mare material exposed as fractured ''kipuka'' (2a) and overlain by Euler ejecta (2b).

(3) Materials of crater Euler, composed of rock derived from units 1 and 2.

(4) Younger mare unit encroaching on units 1–3; truncates Euler ejecta and forms avenue, containing sinuous rille, between Euler flank (3a) and distal ejecta (3b).

(5) Secondary craters of Copernicus (centered 500 km to southeast) superposed on units 3 and 4.

(6) Small, simple crater superposed on all other units.

A. Apollo 17 M-2922.

B. Geologic cross section.

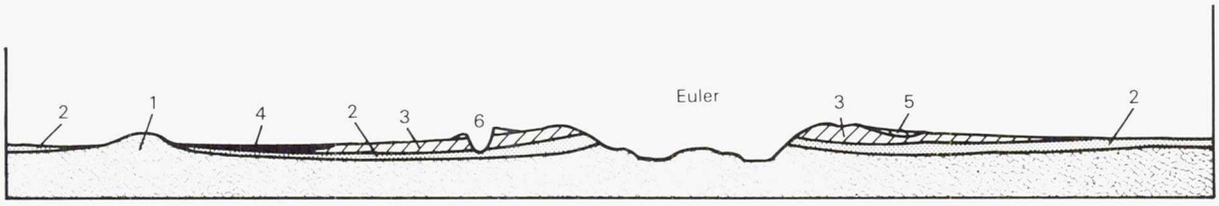

Apollo 15 in July 1971 was a much more complex mission that afforded geologically trained astronauts an opportunity to explore systematically. With the help of a roving vehicle and a long stay time of almost three days, they visited both the rim of the Imbrium basin (Montes Apenninus) and a small mare (Palus Putredinis) cut by a large lunar rille (Rima Hadley; fig. 6.1D).

Table 6.1. Lunar Stratigraphic Column. Time-stratigraphic units contain all the rock-stratigraphic units formed on a planet within a given time interval (American Commission on Stratigraphic Nomenclature, 1970; Mutch, 1970; Wilhelms, 1970, in press b)

Time-stratigraphic unit	Defining reference	Representative rock-stratigraphic units	Estimated duration (aeons)
Copernican System	Shoemaker and Hackman (1962); Wilhelms (in press b)	Crater materials (figs. 6.7, 6.9, 6.15, 6.16, 6.44, 6.57, 6.60) Minor mare materials	1.0
Eratosthenian System	Shoemaker and Hackman (1962); Wilhelms (1980a)	Mare materials (table 6.7; figs. 6.4, 6.52, 6.69) Crater materials (figs. 6.4, 6.15, 6.52, 6.57)	2.2
Upper Imbrian Series	Wilhelms (in press b)	Mare materials (table 6.7; figs. 6.53–6.55, 6.60, 6.62, 6.64, 6.66) Crater materials (figs. 6.15, 6.16, 6.64)	0.6
Lower Imbrian Series	Wilhelms (1970, in press b)	Orientale basin materials (fig. 6.20) Schrodinger basin materials (fig. 6.21) Imbrium basin materials (figs. 6.1C, D; 6.18, 6.38)	0.05
Nectarian System	Stuart-Alexander and Wilhelms (1975)	Crater materials (figs. 6.16B, 6.27) Basin materials (table 6.4; figs. 6.1E, 6.22–6.26) Nectaris basin materials (figs. 6.27, 6.32)	0.07
Pre-Nectarian system	Informal	Basin materials (table 6.4; figs. 6.22, 6.31, 6.32) Crater materials (figs. 6.16B, 6.27, 6.30)	0.63

Table 6.2. Spaceflights That Provided Lunar Data. Dates are beginning of mission activities at the Moon (Ranger 7 impacted on 1 August, Universal Mean Time)

		Principal mission	Landing location or orbital parameters
Luna 2	September 1959	First impact	Flank of Autolycus, lat 30°N, long 0°
Luna 3	October 1959	First unmanned flyby photography	Far side and eastern limb, altitude 65 000 km
Ranger 7	July 1964	First pre-impact photography	Mare Nubium (Cognitum), lat 10.6°S, long 20.7°W
Ranger 8	February 1965	Pre-impact photography	Mare Tranquillitatis, lat 2.6°N, long 24.7°N
Ranger 9	March 1965	Pre-impact photography	Interior of Alphonsus, lat 12.9°S, long 2.4°W
Zond 3	July 1965	Unmanned flyby photography	Far side and western limb, altitude 9960 km to 11 570 km
Luna 9	February 1966	First unmanned landing	Oceanus Procellarum (Planitia Descensus), lat 7.1°N, long 65.4°W
Luna 10	April 1966	First unmanned orbital flight; gamma-ray	Perilune 350 km, apolune 1015 km

Table 6.2 (continued). Spaceflights That Provided Lunar Data. Dates are beginning of mission activities at the Moon

		Principal mission	Landing location or orbital parameters
Surveyor 1	June 1966	Unmanned landing	Flamsteed P, lat 2.5°S, long 43.2°W
Lunar Orbiter 1	August 1966	First unmanned orbital photography	Inclination 12°, perilune 190–40 km, apolune 1865–1815 km
Luna 11	August 1966	Unmanned orbital photography	Perilune 165 km, apolune 1195 km
Luna 12	October 1966	Unmanned orbital photography	Perilune 100 km, apolune 1740 km
Lunar Orbiter 2	November 1966	Unmanned orbital photography	Inclination 12°, perilune 50 km, apolune 1855 km
Luna 13	December 1966	Unmanned landing	Oceanus Procellarum, lat 18.9°N, long 62.1°W
Lunar Orbiter 3	February 1967	Unmanned orbital photography	Inclination 21°, perilune 55 km, apolune 1845 km
Surveyor 3	April 1967	Unmanned landing	Oceanus Procellarum, lat 3.2°S, long 23.4°W
Lunar Orbiter 4	May 1967	Unmanned orbital photography (synoptic)	Inclination 85°, perilune 2705 km, apolune 6115 km
Explorer 35	July 1967	Unmanned orbital magnetics	Perilune 830 km, apolune 7650 km (returned data until February 1972)
Lunar Orbiter 5	August 1967	Unmanned orbital photography	Inclination 85°, perilune 195–100 km, apolune 6065–1500 km
Surveyor 5	September 1967	Unmanned landing	Mare Tranquillitatis, lat 1.4°N, long 23.1°E
Surveyor 6	November 1967	Unmanned landing	Sinus Medii, lat 0.5°N, long 1.5°W
Surveyor 7	January 1968	Unmanned landing	Flank of Tycho, lat 40.9°S, long 11.5°W
Zond 6	November 1968	Unmanned flyby, first returned film	Altitude $\geq$3300 km
Apollo 8	December 1968	First manned orbital flight	Inclination $\sim$13°, perilune 110 km
Apollo 10	March 1969	Manned orbital flight	Inclination $\sim$1°, perilune 110–15 km
Apollo 11	July 1969	First manned landing	Mare Tranquillitatis (Statio Tranquillitatis), lat 0.7°N, 23.4°E
Zond 7	August 1969	Unmanned flyby, returned film	Western limb and southern far side, altitudes 2200 and 10 000 km
Apollo 12	November 1969	Manned landing	Oceanus Procellarum, lat 3.2°S, long 23.4°W
Apollo 13	April 1970	Manned flyby (aborted landing)	
Luna 16	September 1970	First unmanned sample return	Mare Fecunditatis, lat 0.7°S, long 56.3°E
Zond 8	October 1970	Unmanned flyby, returned film	Altitude $\geq$1120 km
Luna 17	November 1970	Lunokhod 1, unmanned rover	Sinus Iridum, lat 38.3°N, long 35.0°W
Apollo 14	February 1971	Manned landing	Fra Mauro highlands, lat 3.7°S, long 17.5°W
Apollo 15	July 1971	Manned landing	Palus Putredinis (Apenninus-Hadley region), lat 26.1°N, long 3.7°E
Luna 19	October 1971	Unmanned orbital flight	Perilune 140–77 km, apolune 140–385 km
Luna 20	February 1972	Unmanned sample return	Crisium basin rim, lat 3.5°N, long 56.5°E
Apollo 16	April 1972	Manned landing	Descartes highlands, lat 9.0°S, long 15.5°E
Apollo 17	December 1972	Manned landing	Taurus-Littrow valley, lat 20.2°N, long 30.8°E
Luna 21	January 1973	Lunokhod 2, unmanned rover	Mare fill of Le Monnier, lat 25.8°N, long 30.5°E
Luna 24	August 1976	Unmanned sample return	Mare Crisium, lat 12.7°N, long 62.2°E

Of all the missions, Apollo 16 (April 1972) landed farthest from a mare, though not far from a basin (Nectaris; fig. 6.1F). It was expected to return volcanic materials of the terra from a planar deposit and some distinctive hilly and furrowed terrain (Cayley and Descartes Formations, respectively). However, the mission encountered severely brecciated material like that of previously sampled terra. This discovery went far toward clarifying the relative roles of impact and volcanism on the Moon. Coupled with continued photogeologic and theoretical studies, it led to the current model that only the maria are volcanic; whereas the terrae, after an igneous beginning, have been shaped almost entirely by impacts. Photogeologic observations discussed here show that the Apollo 16 rocks were emplaced by basins like other terra rocks.

Apollo 17 then closed off the manned landing program in December 1972 by studying terra massifs of the Serenitatis basin and mare lavas and pyroclastic deposits in an embayment from Mare Serenitatis (fig. 6.1E). Serenitatis is the only pre-Imbrium basin from which abundant material was returned.

Lunar exploration did not end with Apollo 17. The Soviet unmanned lunar program has included the return of regolith samples to Earth. Successful sample returns began with a probe of Mare Fecunditatis in September 1970 (Luna 16) and of the Crisium basin rim in February 1972 (Luna 20). Surface exploration ended with the return of bits of Mare Crisium by Luna 24 in August 1976. The small Soviet samples add significantly to knowledge of lunar materials beyond that acquired from the Apollo samples by indicating areal variations and adding absolute ages to the lunar stratigraphic column (French, 1977). One hopes that some nation or group of nations will continue to explore the Moon. Although most of the major questions asked two decades ago about its general history, composition, and internal state have been answered, the Moon is not yet understood in detail.

CRATERS

General Features and Origin

Most lunar craters are characterized by radial symmetry. Small craters consist of smoothly contoured, bowl- or cone-shaped interiors, and commonly a small flat floor (fig. 6.4, locality 6; fig. 6.5). They are considerably deeper than the surrounding terrain unless subsequently filled. Related to the crater proper are exterior deposits which slope away from the rim crest (fig. 6.5). The outer parts of the deposit contain grooves, pits, and subcircular secondary craters which become increasingly numerous about one radius from the rim crest and dominate the circumcrater terrain for greater distances.

Morphologies of larger craters are basically similar but more complex (figs. 6.6 and 6.7). The classic example of a large, fresh lunar crater is the 95-km-wide Copernicus (fig. 6.7; Shoemaker, 1962a). Copernicus-type craters are characterized by a roughly circular rim crest surrounded by coarsely hummocky debris and by radially lineated outer flanks, beyond which are numerous loops and strings of secondary craters (figs. 6.4 and 6.7). The main crater has a central peak surrounded by a roughly flat floor, and the walls are terraced. The depth/diameter ratios decrease in larger craters along with the increasing morphologic complexity (Pike, 1980a,b; fig. 6.8). Most simple lunar craters are smaller than 16 km and most complex craters are larger than 21 km; the transitional size range contains transitional types (figs. 6.6, 6.8; Pike, 1980a,b). Complex craters appear at smaller diameters on the maria than on the terrae and at different diameters on different planets (Pike, 1980b).

The origin of craters occupied more attention before Apollo exploration than any other lunar topic. This major debate has been settled decisively in favor of impact origin for most craters by the following evidence.

(1) Meteorites and astronomically observed objects are still so numerous that impacts on all planets are inevitable, and must have been much more abundant in the early solar system.

(2) The circularity, radial symmetry, and radial ejecta textures indicate origin of all crater features from a relatively small central source. Impact energy is released from a zone much smaller than the final crater, whereas volcanic eruptions or magma withdrawals create depressions which more closely assume the sizes and shapes of the controlling structures.

(3) The coarse concentric and radial structures of ejecta blankets of large craters and basins indicate displacement of large amounts of material from the crater. Furthermore, many secondary craters occur thousands of kilometers from their point of origin, their relation to a fresh primary crater being shown by their position along bright subradial rays (figs 6.4 and 6.9). These

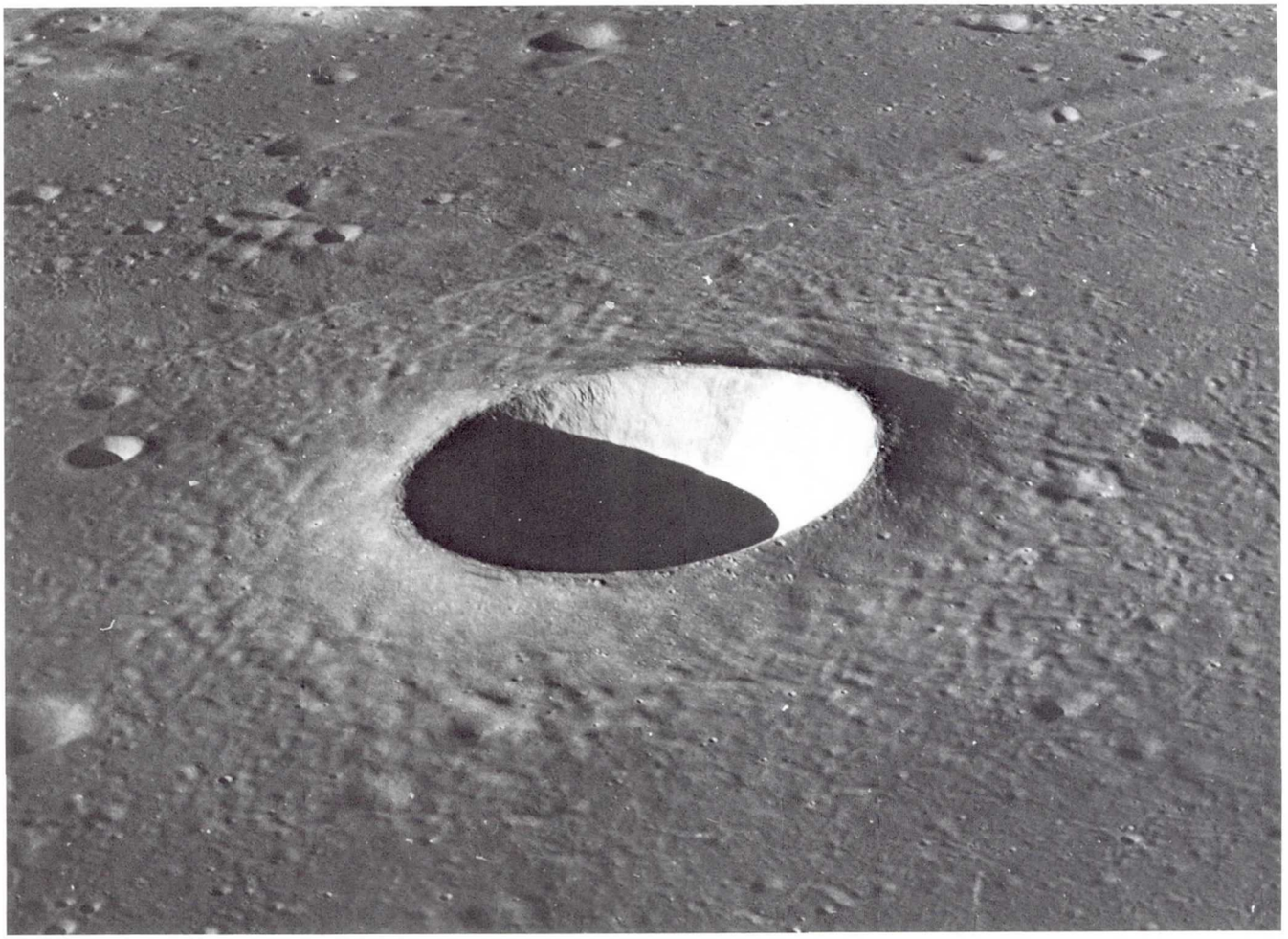

Figure 6.5. Simple crater Moltke (7 km), near southern border of Mare Tranquillitatis (0.5°S, 24°E). Inner, dunelike texture grades outward into subconcentric secondary craters. Rille is one of Rimae Hypatia, part of border rille system of Mare Tranquillitatis. South-looking oblique, Apollo 10 H-4324.

relations show that the generating process was enormously energetic. High ejection velocities approaching the lunar escape velocity (2.4 km/s) are required to produce the most distant secondary craters. Only hypervelocity impacts from space are capable of releasing such energies from a small central zone; the Copernicus impact is estimated by Shoemaker (1962a) to have released 7.6×10^{28} ergs (7.6×10^{21} J). Sufficient internal energy could not accumulate in the low confining pressures of a planetary crust without being released in amounts too small to create the observed features. Collapse could create large circular depressions but not the external features.

(4) Origin of the secondary craters and their attendant rays from structural cracks is excluded by the birdsfoot or herringbone pattern of the secondary craters' ejecta, which is directed away from the primary crater (fig. 6.7B) and which has been reproduced by simultaneous impacts in the laboratory (Oberbeck and Morrison, 1973). The pattern of nonradial groups of secondary craters such as loops (fig. 6.7A) is consistent with ballistic theory (Shoemaker, 1962a).

(5) Morphologic features more closely resemble those of terrestrial impact craters and large explosion craters than volcanic morphologies. Some particularly significant examples are the central peaks, which superficially resemble subsidiary volcanoes in craters but are much more like the energetically uplifted centers of impact and explosion craters.

(6) Crater dimensions are also more nearly matched by impact and explosion craters than by volcanic craters (Pike, 1980a). In particular,

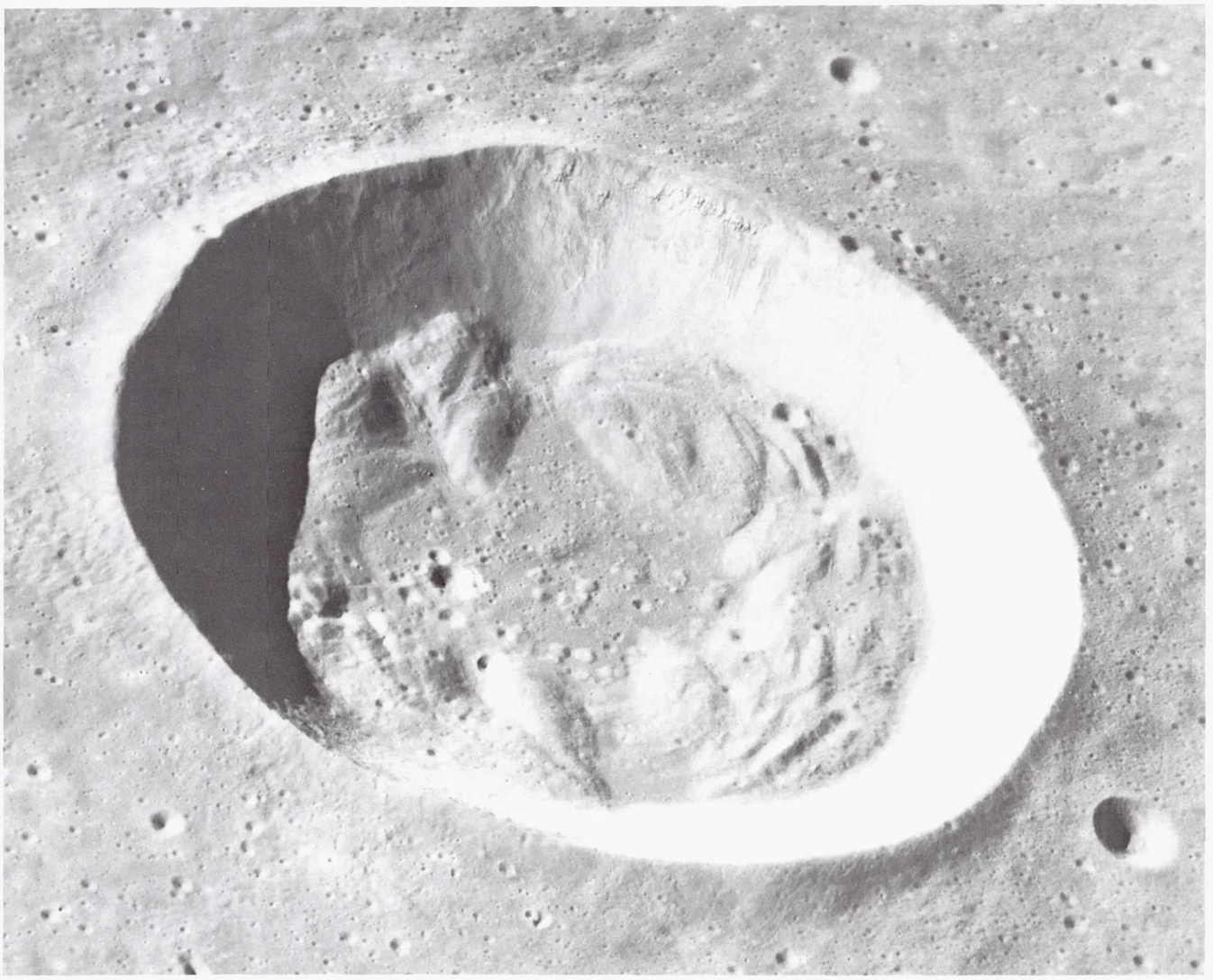

Figure 6.6. Crater Bessel in Mare Serenitatis (16 km, 22°N, 18°E), containing flat floor and debris accumulated from walls. Represents transition between simple and complex craters. Apollo 15 P-9328.

floors lie below the level of the surrounding terrain in fresh impact craters, but in few, if any, known volcanic craters.

(7) Repetition of the same pattern around almost all craters is consistent with impact; whereas volcanism produces more diverse landforms.

(8) Most primary craters are randomly distributed, on a surface of a given age, in numbers which increase exponentially with decreasing size. The characteristic inverse size-frequency distribution matches the mass distribution of cosmic projectiles (Öpik, 1960; Baldwin, 1963; Shoemaker et al., 1963; BVSP, 1981, ch. 8). Structurally controlled internal forces would create nonrandom groupings.

(9) Shock-metamorphosed materials found ubiquitously on the terrae and commonly on the maria were formed at pressures exceeding any possible volcanic pressures (French and Short, 1968; King, 1976; Taylor, 1982) and in amounts that require major impacts at every terra site visited.

Some exceptions prove the rule. Some distinctive small craters alined along fractures or located amidst or near volcanic deposits (dark mantling materials) are probably of internal origin (see "Mare Basalts"). Most of these small craters differ morphologically from primary and secondary impact craters, being less regular and having lower rims. They lack thick, roughly textured ejecta and rays. A minority of small, simple craters lacking distinctive morphologies and

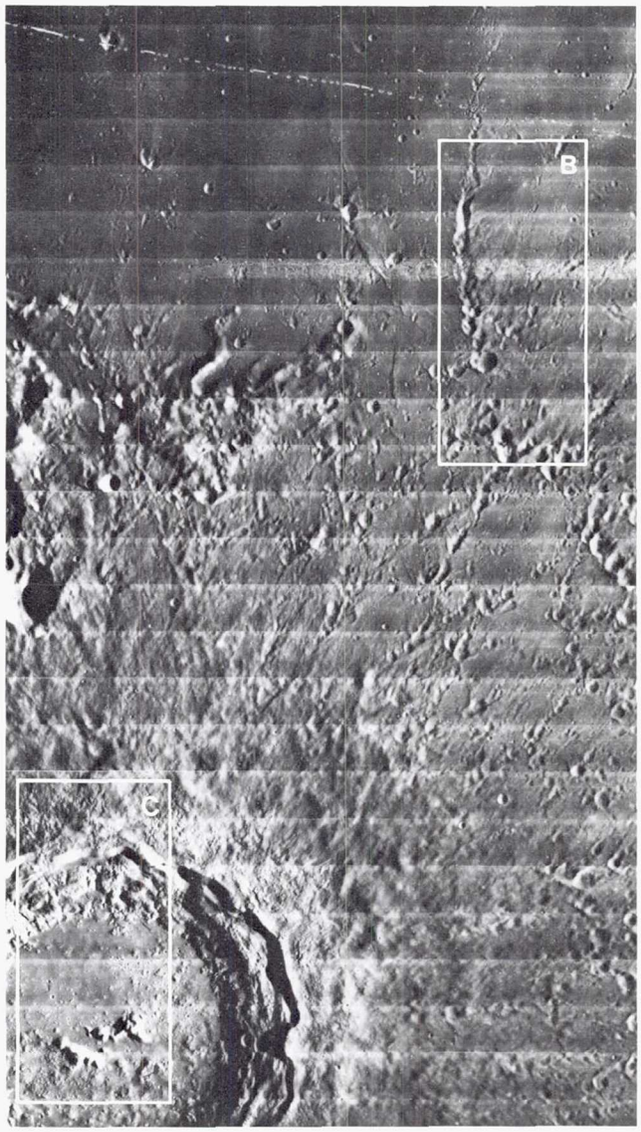

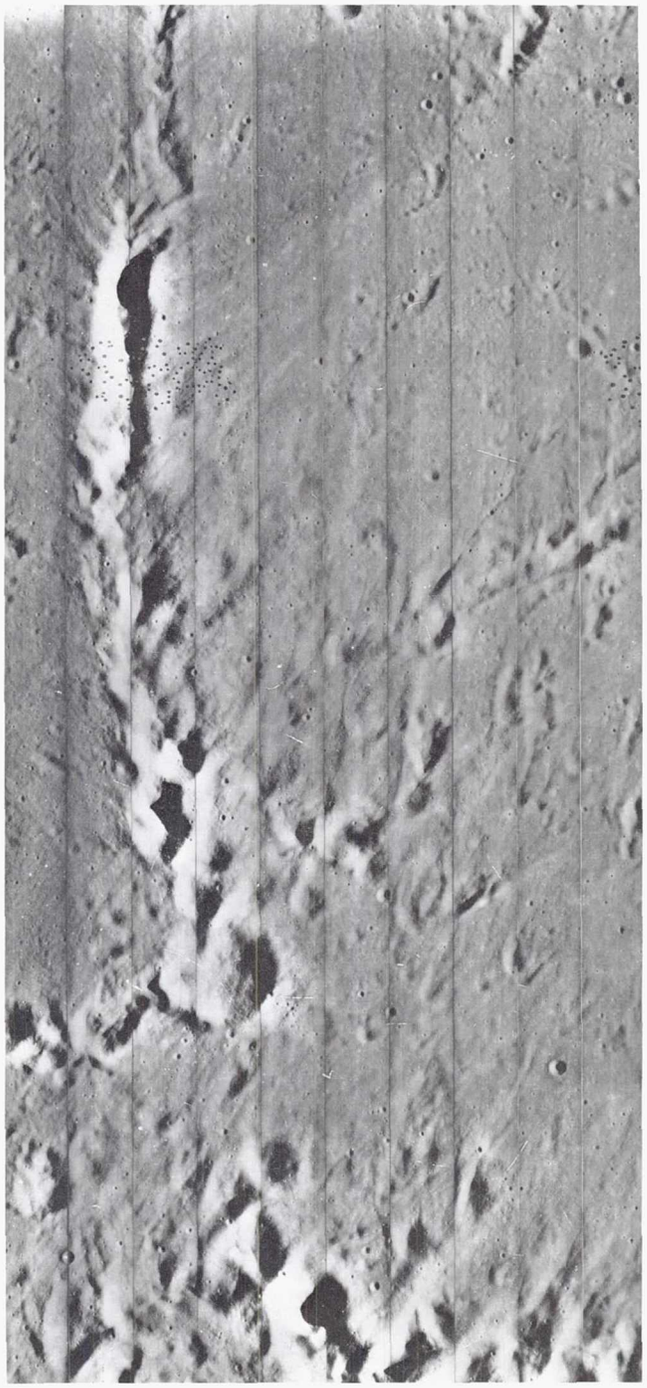

Figure 6.7. Crater Copernicus (95 km, 10°N, 20°W) and its secondary craters.

A. Regional view. Conspicuous secondary chains are not radial to primary crater but are sources of radial ray elements. Areas of B and C outlined. Long, thin line above box B is artifact of photo processing in spacecraft. Orbiter 4 H-121.

B. Detail of secondary craters outlined in A showing "herringbone" pattern of ejecta produced by interference of secondary ejecta during nearly simultaneous impacts. Orbiter 5 M-144.

unassociated with secondary craters may also be endogenic. Endogenic floor uplift may create a variety of landforms which have been considered volcanic, but which are actually impact features altered by the uplift (see "Tectonism"; Brennan, 1975; Schultz, 1976b).

Cratering Processes

Simple craters

The appearance of craters and the lithologies of lunar terra samples are best understood in light of impact cratering mechanics. Following is an idealized description based on extensive studies of natural and experimental craters (Baldwin, 1949, 1963; Shoemaker, 1962a; Gault et al., 1968b; Gault, 1974; Oberbeck, 1975; Roddy et al., 1977; Grieve, 1980; Melosh, 1980).

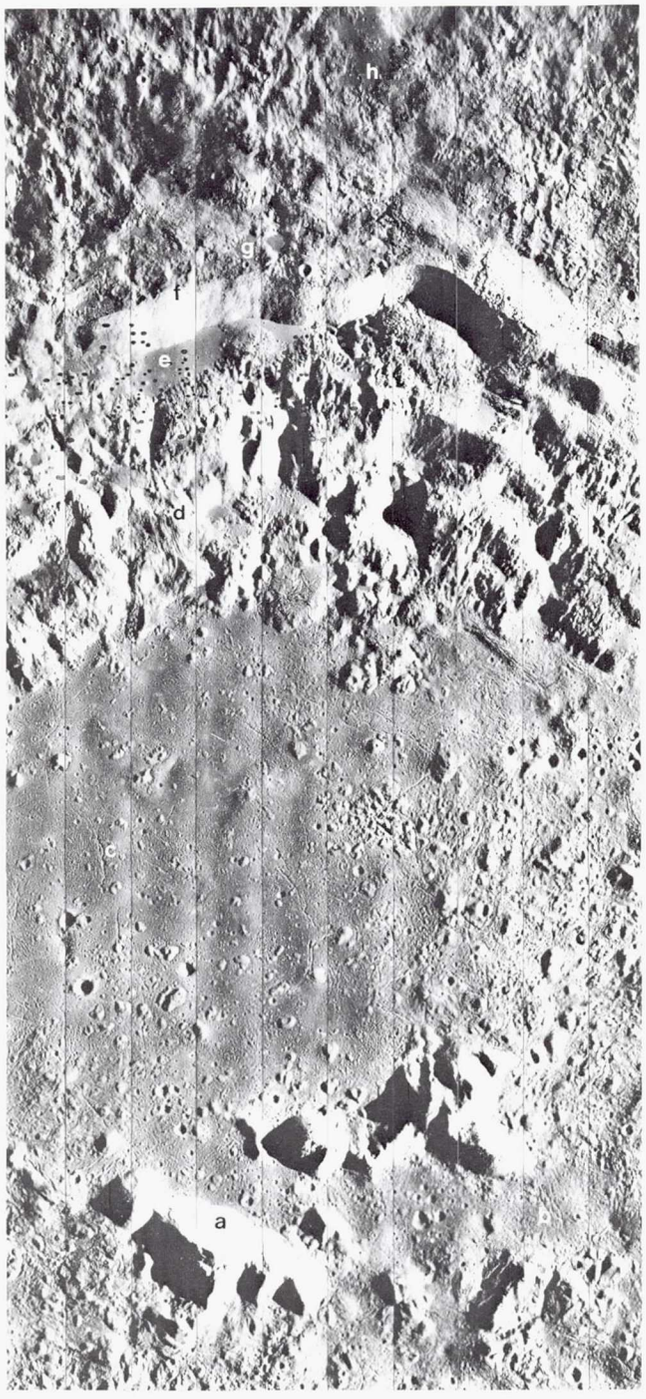

C. Detail of central peak (a), fissured floor material (b, c), cascades (d) and pools (e) of melt on walls, rim crest (f), and melt pools on rim flank (g, h). Orbiter 5 M-154.

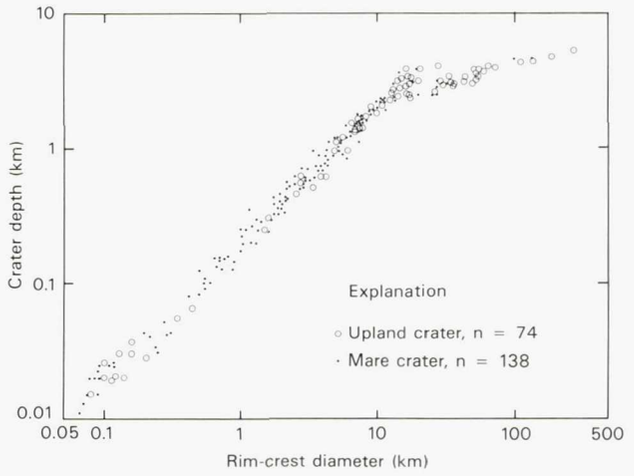

Figure 6.8. Depth/diameter ratios of lunar craters. Distinct inflection at 15–20 km marks transition between simple and complex craters (from Pike, 1980a).

An impact of a hypervelocity projectile generates shock waves with pressures of several megabars that propagate rapidly into both the projectile and the target and intensely compress them. Melted material of both projectile and target may be immediately jetted from the contact zone (fig. 6.10A). Then much larger amounts of target and projectile material are ejected along the cavity walls as it expands (fig. 6.10B–F). Ejection is the result of decompression along free surfaces, in contrast to explosion craters where ejection is the direct result of expansion around the explosive source (Shoemaker, 1962a). Zones of target material progressively farther from the impact point are ejected as the cavity expands. The shallow material around the impact encounter zone is ejected first, deeper material later. After maximum depth has been reached, the cavity continues to grow laterally. Material from the upper wall may be the last to be ejected (fig. 6.10F; Orphal, Piekutowski, Swift, *in* Roddy et al., 1977).

The outward decay of the shock wave means that the target material is shocked progressively less-intensely outward. Material near the encounter zone is melted, whereas sizable blocks are only weakly fractured at the radial distance of the final wall (fig. 6.11). However, shock grades are generally mixed. For example, during cavity growth, partly melted, intensely shocked, compressed, and sheared materials may be injected into zones farther from the cavity surface, and unmelted crushed debris may be injected into fractures (fig. 6.11; Wilshire and Moore, 1974; James, 1977; Stöffler, 1981). The mixed zones may then be ejected in a later stage of cavity expansion.

At least for a simple crater, ejecta is deposited in reverse order from ejection. Late-derived material from near the wall is lobbed or pushed out at low velocities and lands near the rim. The first materials ejected attained the highest velocities, and are the last to impact the surface, farther from the crater. The ejecta forms an expanding curtain that maintains

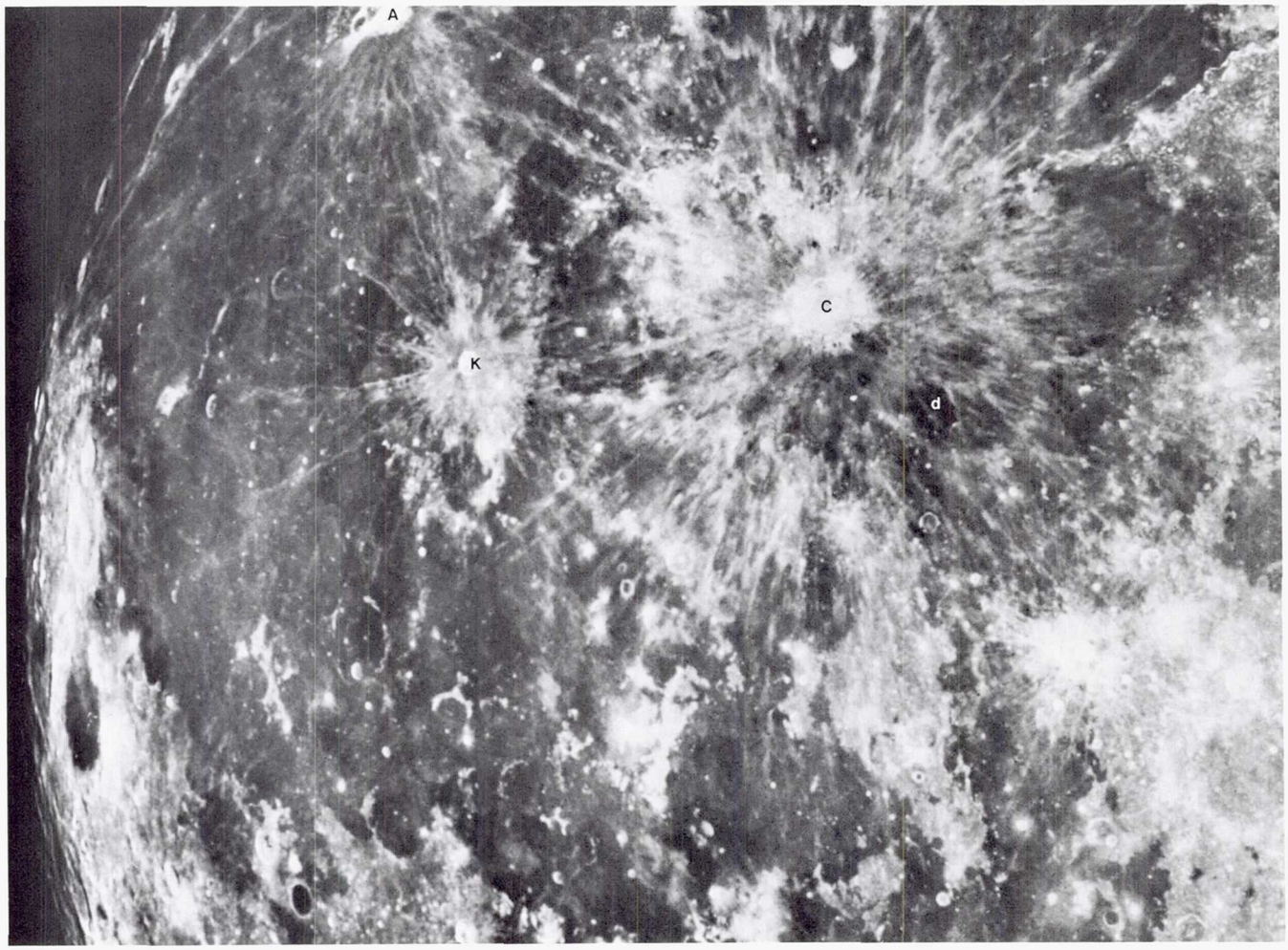

Figure 6.9. Full-Moon photograph showing extent of bright rays. Source craters include Aristarchus (A), Copernicus (C; compare fig. 6.7), and Kepler (K; compare fig. 6.16). Rays fainter on dark-mantle units (d) southeast (lower right) of Copernicus and mare south of Kepler than on other maria and terrae (see "Maria").

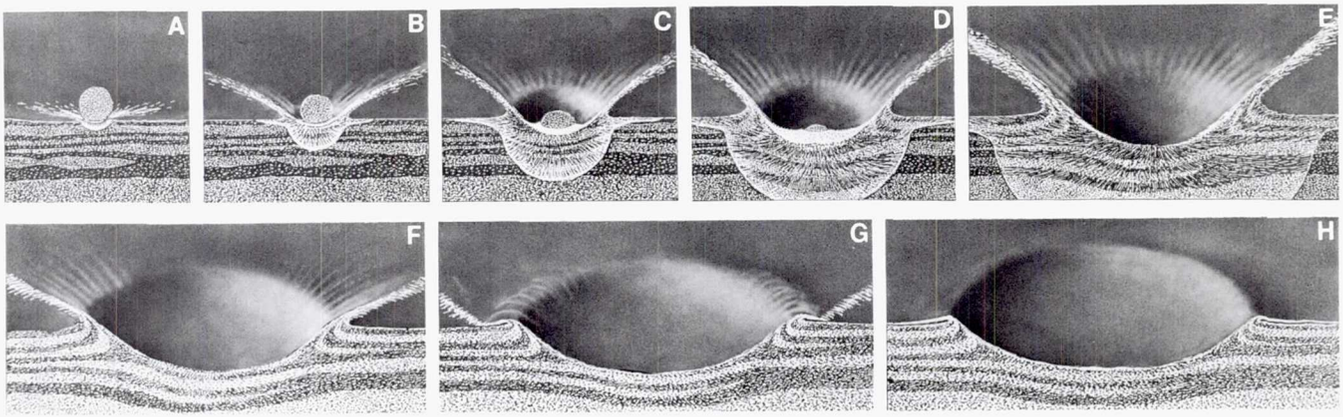

Figure 6.10. Stages in formation of an ideal simple impact crater. (Drawn by Donald E. Davis.)

A. Initial contact; highly shocked material jetted.

B., C., D. Compressional shock wave propagates outward and cavity grows by rarefaction behind shock wave while projectile is consumed.

E. Cavity continues growth after projectile consumed.

F. Maximum crater size.

G. Curtain of debris shaped like inverted lampshade continues outward expansion after cavity growth ceases and overturned flap of ejecta comes to rest.

H. Final configuration.

roughly the angle with the surface that it acquired when ejected along the cavity walls (Oberbeck, 1975). Material in the curtain is deposited from the crater rim outward, and the deposit thins outward from the rim. The result is a continuous rimflank deposit containing mixed shock grades, including impact melt.

Furthermore, molten materials may be ejected from the crater late in the cavity growth because they remained pressed against the expanding cavity wall (fig. 6.11; Grieve et al., *in* Roddy et al., 1977). They pond in depressions in the rim deposit (fig. 6.7C; Howard, 1975; Howard and Wilshire, 1975; Hawke and Head, *in* Roddy et al., 1977).

Cavity growth ceases when the attraction of gravity overcomes the force of ejection. The shock wave decays outward into an elastic wave and fractures the rock around the cavity (fig. 6.11). The deformation ceases when the stresses induced by decompression fall below the tensile strength of the surrounding rock. Then the crater walls may slump and the remaining melts may flow down the walls and collect in depressions.

After cavity growth has ceased, the curtain of ejecta may continue to move outward (fig. 6.10G). With increasing distance from the rim, ejecta strikes the surface with increasing velocity so that ejecta and surface materials are mixed. During outward movement, the debris curtain becomes progressively separated into filaments, which produce chains and loops of secondary craters upon impact farther than one or two radii from the crater. These projectiles probably consist of highly shocked material from near the impact encounter zone.

Complex craters

Complex craters like Copernicus possess features not accounted for in the foregoing idealized description. Interpretations of central-peak origin (volcanic hypotheses aside) generally fall into two categories, "push" or "pull" (Pike, 1980b). Push mechanisms envision collapse of the crater walls to form terraces or subcrater fault blocks that converge on the center and push up the peak. Pull mechanisms entail peak uplift by some type of rebound of the subcrater material which pulls the walls inward, causing their collapse. The geometries of the motions and the final configuration might be similar in the two cases.

Pull mechanisms are supported by several lines of evidence. Both in terrestrial craters (Roddy, *in* Roddy et al., 1977) and lunar craters (Pike, 1980a), peaks probably came first; craters with peaks but no terraces are relatively common whereas few craters with large terraces but no peaks are observed. Also, large craters were probably never deep enough to initiate wholesale collapse. Field studies of terrestrial craters formed in sedimentary targets suggest that the relatively shallow floors of complex craters are in about their original stratigraphic position and are not severely deformed (Milton et al., 1972; Wilshire et al., 1972; Offield and Pohn, 1979). In contrast, materials in the peaks are extremely deformed and were derived from substantial depths (fig. 6.12; Engelhardt et al., 1967; Wilshire et al., 1972; Roddy, 1976). Several terrestrial craters

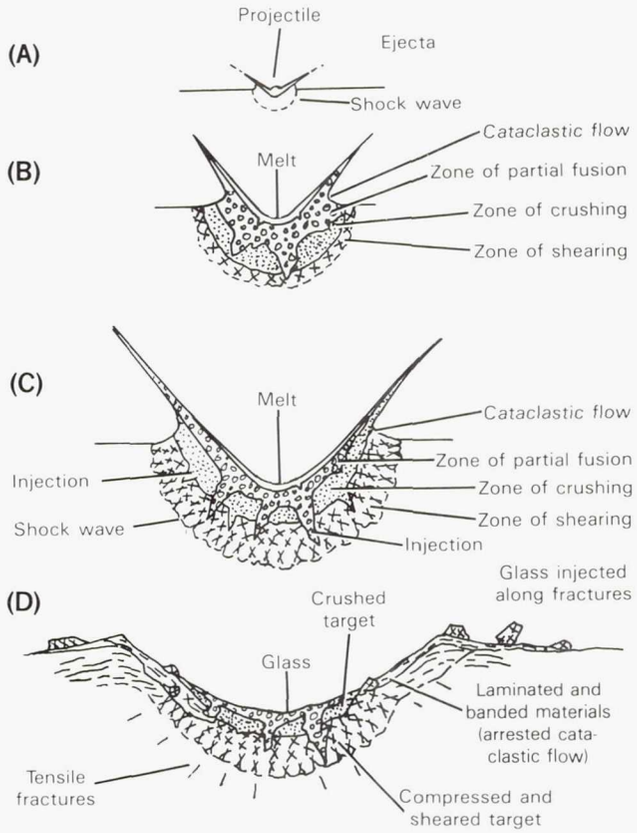

Figure 6.11. Relation of breccia lithologies to sources in simple crater (Wilshire and Moore, 1974). Shock grades decrease outward from impact encounter zone. Successively lower shock grades ejected at each stage (A–C), the highest grades being ejected first and traveling farthest. Final crater (D) contains rough outward gradation from impact melt through melt-rich breccias, melt-poor breccias, monomict breccia, and finally to fractured rock little altered from the pre-impact state. Pattern complicated by injection of higher shock grades into less highly shocked zones. Interior and "megablocks" ejected in late stages may contain dikes of glass injected along fractures, forming dimict breccias. Figure shows floor covered by impact-melted glass and wall and rim covered by breccia laminated and banded during ejection; in addition, crystalline rock solidified from impact melt coats many crater walls and rims.

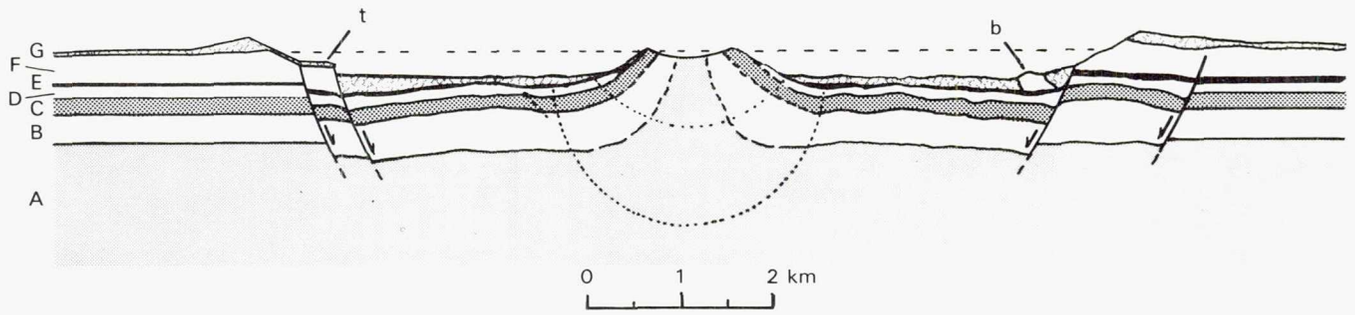

Figure 6.12. Geologic section of complex crater as interpreted by Pike (1980b), based on four terrestrial craters. Strata above E excavated in broad, shallow part of crater. Stratum G is the ejecta and intracrater breccia. Intense, deep deformation occurs only within semicircular dotted lines; sharply uplifted strata A, B, and C constitute most of central uplift. Inward movement of crater floor results in terracing (t) and faulting. Stratum F forms slump block (b).

also show evidence of centripetal, subhorizontal movement of the floor materials (Roddy, 1976; Offield and Pohn, 1979).

In summary, much evidence points to a sharp uplift of only a small central region, accompanied by inward movement of the rest of the floor. The major terraces presumably result from withdrawal of support from the walls by the inward movement (fig. 6.12).

The ejecta and melt of complex craters may also behave differently from those of simple craters, but terrestrial evidence is sparse because of erosion. The complex crater Rieskessel or Ries, in southern Germany, has the best preserved ejecta (Engelhardt, 1967; Dennis, 1971; Chao, 1974, 1977; Roddy et al., 1977; Hörz and Banholzer, 1980). A fragmental, almost unshocked deposit called the Bunte Breccia surrounds the 25-km crater and also occurs locally inside. The breccia is derived from strata (mainly Mesozoic and Tertiary sediments) that lay at shallow depths. The breccias also contain material derived from the surface outside the crater and incorporated during ground flow (Chao, 1977) or secondary impact (Oberbeck, 1975). The Bunte Breccia is not markedly zoned like the overturned flaps of some simple craters but is chaotically structured. Overlying the Bunte Breccia inside and outside the crater is more highly shocked rock called Suevit (suevite), which was derived from the crystalline materials underlying the Mesozoic sediments and which fell back after having been lofted in high trajectories. Large "megablocks" containing injected shocked material lie inside and outside the crater rim.

Other carefully studied terrestrial complex or ringed craters are in the Canadian Shield. They are distinguished by large, thick sheets of melted rock consisting of homogenized target materials (Dence, 1971; Simonds et al., 1976; *Journal of Geophysical Research,* 1978, v. 83, n. B6). Melt was deposited on and injected into the brecciated floors (fig. 6.11; Grieve, 1980; Stöffler, 1981).

Distribution and Stratigraphy

Superposition relations

Relative dating of craters is, of course, a key to establishing lunar stratigraphic sequences. One set of dating methods depends on superposition relations among individual craters and secondary-crater clusters. The relations are obvious where the rimcrest of one crater is truncated by that of another. Where the rims of both craters are complete, relative ages can commonly be determined by partial filling of one crater by the ejecta of another. At greater separations, secondary craters extend the stratigraphic reach of their parent primary craters by pitting underlying craters or other surfaces and by being themselves overlain by younger units (fig. 6.4).

Crater frequency

Most units, however, are not in contact. Isolated lunar units must be dated by methods based on craters that are akin to terrestrial stratigraphic correlations based on fossils (McGill, 1977; BVSP, 1981, ch. 8). The most common approach is to count the craters of a given size superposed on a given area. Dating by means of "crater counts" and related methods is based on the relation, which follows from the random production of primaries, that the older the surface the more craters are superposed. In this respect primary craters contrast with secondary craters, which are nonrandomly distributed near their parent primary and form nonrandomly in "bursts" when each pri-

mary forms. Only "background" secondaries having numerous unknown parents and which are theoretically scattered in great numbers over the Moon also accumulate as a function of time (Shoemaker, 1965). Crater counts are depicted by graphs of several types of which cumulative plots are the most commonly used. In these plots, the logarithm of the number of craters per unit area having a given diameter or larger is plotted against the logarithm of that diameter (fig. 6.13). The negative slopes reflect the proportionally smaller number of large craters in any given population.

The ideal of reading relative ages from the counts is seldom achieved without considerable interpretation either of the craters before counting or of the plotted results. First, there is no point in counting craters which are older than the surface being dated. Therefore, partly buried craters should be identified and eliminated from the counts (Neukum et al., 1975a; Wilhelms et al., 1978). An alternative approach is to include the buried craters in the counts and detect them by a flattening of the size-frequency curve (fig. 6.13D). Second, as soon as there are enough craters of the size being counted to approach

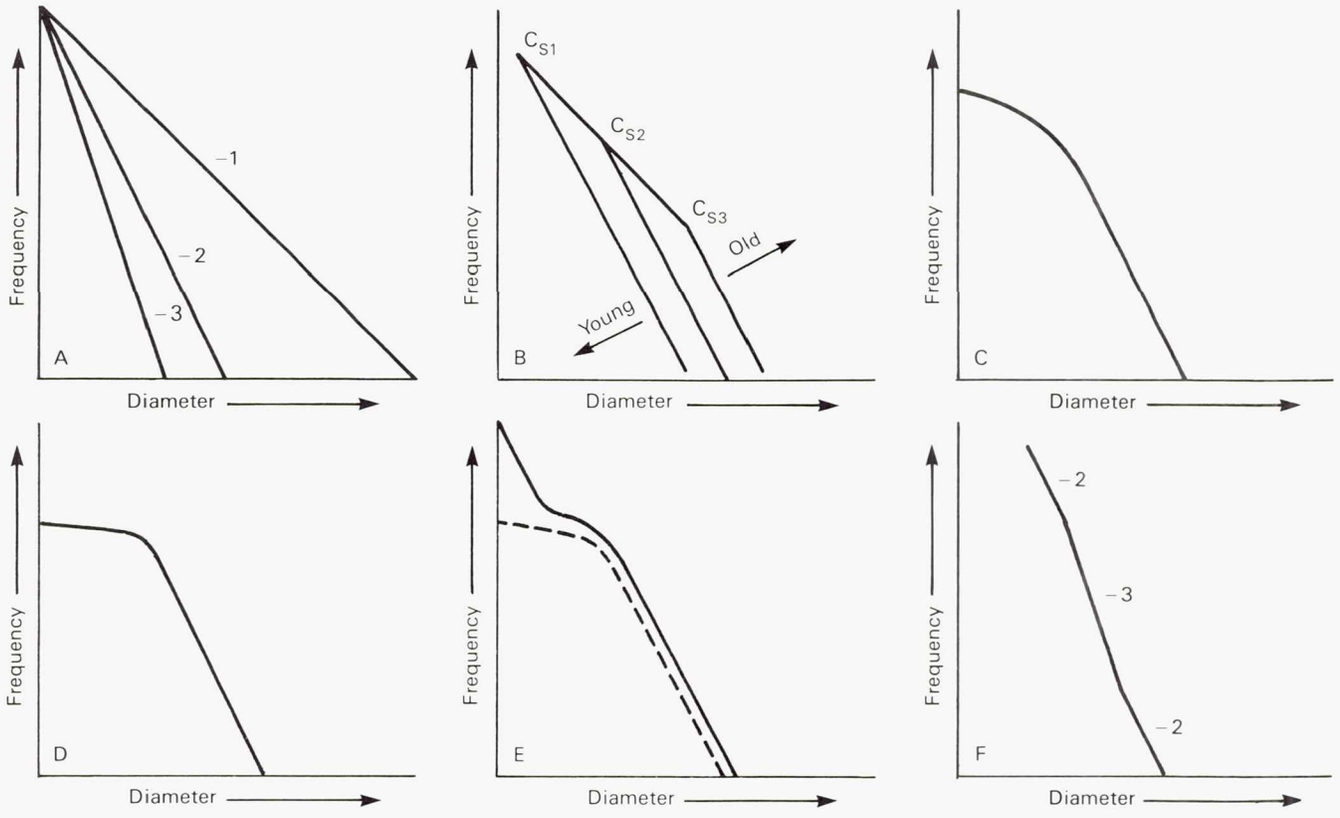

Figure 6.13. Diagrammatic size-frequency distributions of craters; cumulative form.

A. Three different production functions having slopes indicated.

B. Production curves of three ages are truncated by shallower curve which is the same for all ages; it portrays an idealized steady-state or equilibrium distribution. Craters of all sizes form in each time interval, but many craters smaller than the limiting diameter for the steady-state (C_s) are destroyed. The small craters' size-frequency distribution therefore slopes more gently than the production distribution.

C. A turndown at the small-diameter end of the production curve may arise from equilibrium effects as in B or from inability to observe the small craters.

D. Burial by a younger unit obliterates the smaller craters of a population.

E. Cratering resumes with same production size-distribution as before the burial, so craters are added to the curve of D (dotted) at each diameter interval. An offset of the curve remains.

F. Different production functions in three diameter intervals. For 0.1–2.0-km craters on the Moon, the steep slope of the middle field (−3 slope here) results from a mixture of secondary craters having steep production distributions and primary craters having shallower production functions. Different slopes may also be caused by different production distributions of primaries as in A.

overlap, some craters which have formed will be obscured. Ultimately, a surface becomes saturated with craters and a *steady state* is achieved in which craters below a certain size are destroyed as rapidly as they form (Shoemaker, 1965; Trask, 1966, 1971). This condition is detected on plots by a turndown to flatter slopes at the end of the size-frequency curve which represents small diameters (fig. 6.13B, C). However such flattening is usually indistinguishable from flattening caused by a real diminishment of small crater-forming projectiles relative to larger objects. Because of the saturation of old surfaces, it is not clear whether the objects that created craters and basins on the early lunar terrae had the same production distribution as those of the more recent flux. Third (but not last in a list of possible hazards to crater counting), only randomly distributed craters are direct recorders of surface age; counts of secondary craters concentrated along stringers or loops, for example, would give false ages. Primaries and secondaries must therefore be distinguished either before the craters are counted or in the completed plots. Criteria for recognition of secondaries (table 6.3) have been applied by some workers to eliminate them from the counts (e.g., Neukum et al., 1975a,b; Wilhelms et al., 1978). Other practitioners have noted that the production populations of primaries and secondaries differ in such a way that curves reflecting inclusion of many secondaries are steeper than those for the production population of primaries (-3.6 to -4.0 for the secondaries ver-

Table 6.3. Crater Identification Criteria

Property	Primary impact	Secondary impact	Internal
Spatial distribution	Random on a geologic unit	Concentrated about primary in clusters, chains, loops; basin secondaries commonly grouped radially to basin	Amidst dark material and/or alined along rilles
Slope of size-frequency distribution (cumulative)	-1.8 for post-mare craters $\gtrsim 2$ km	-3.6 to -4.0	Insufficient data
Circularity	Circular <10 km; crenate >10 km	Variable	Variable
Depth	Much deeper than surrounding terrain when fresh	Shallow except far from source	Variable
Interior profile	Smooth, conical $\lesssim 16$ km; terraced, peaked, flat-floored $\gtrsim 21$ km (fresh craters)	Smooth except where filled by deposits of primary or other secondary craters	Variable; mostly smooth
Rimflank profile	Rugged near crest, then concave out to ~ 2 radii	Inconspicuous	Variable; mostly gentle
Rimflank texture	Concentric, hummocky near crest, radial to ~ 1 radius	Linear or V-shaped intercrater ridges	Inconspicuous
Ejecta distribution	Predominately symmetrical	V-shaped or linear away from source	Widespread
Mutual relations	Clear overlap or "push-through"; interference features rare	Interference features common; downrange overlap common	Variable
Size	Any	Mostly <30 km; proportional to source crater or basin	Mostly <20 km

sus −1.8 to −2.0 for the primaries; Shoemaker, 1965; Oberbeck et al., 1977; Wilhelms et al., 1978).

Crater morphology

Related dating methods depend on the assumption that impacts which formed primary and secondary craters too small to be seen have eroded surfaces in proportion to duration of the surface's exposure. A technique widely used by the U.S. Geological Survey to date mare and other plains units accepts the inevitability that small craters are saturated and that primaries and secondaries are mixed. Areally small geologic units often cannot be dated accurately by counts of craters because too few have formed after the units were deposited. The technique is based on a model for crater erosion developed by Soderblom and Lebofsky (1972) and refined and applied by Boyce (1976; Soderblom and Boyce, 1972; Boyce et al., 1974; Moore et al., 1980). The method is a quantitative descendant of a system for dating small craters devised by Trask (1969, 1971) which was successfully applied to mare surfaces being considered for Apollo landings (fig. 6.14). The model predicts the net effects of the repeated bombardment by fine particles of all origins upon the slopes of craters in the hundreds-of-meters diameter range, taking solar lighting into account. The age of a crater can be determined by measuring shadows on its walls and floor. Small craters are flattened and obliterated more quickly than large ones. Thus, the size of the largest crater of a given state of degradation on a surface is a measure of the relative age of the surface. Most commonly, the diameter of the largest crater on a surface that hypothetically would be eroded to a slope of 1° is computed from measured slopes. The diameter is referred to in the literature and here as D_L. The larger the D_L the older the surface. The method has proved useful in dating mare units too small to date by size-frequency counts, and in extrapolating absolute ages of mare units that were sampled to those that were not (fig. 6.15).

Large craters are also commonly dated by morphology. One qualitative morphology-age scheme assumed

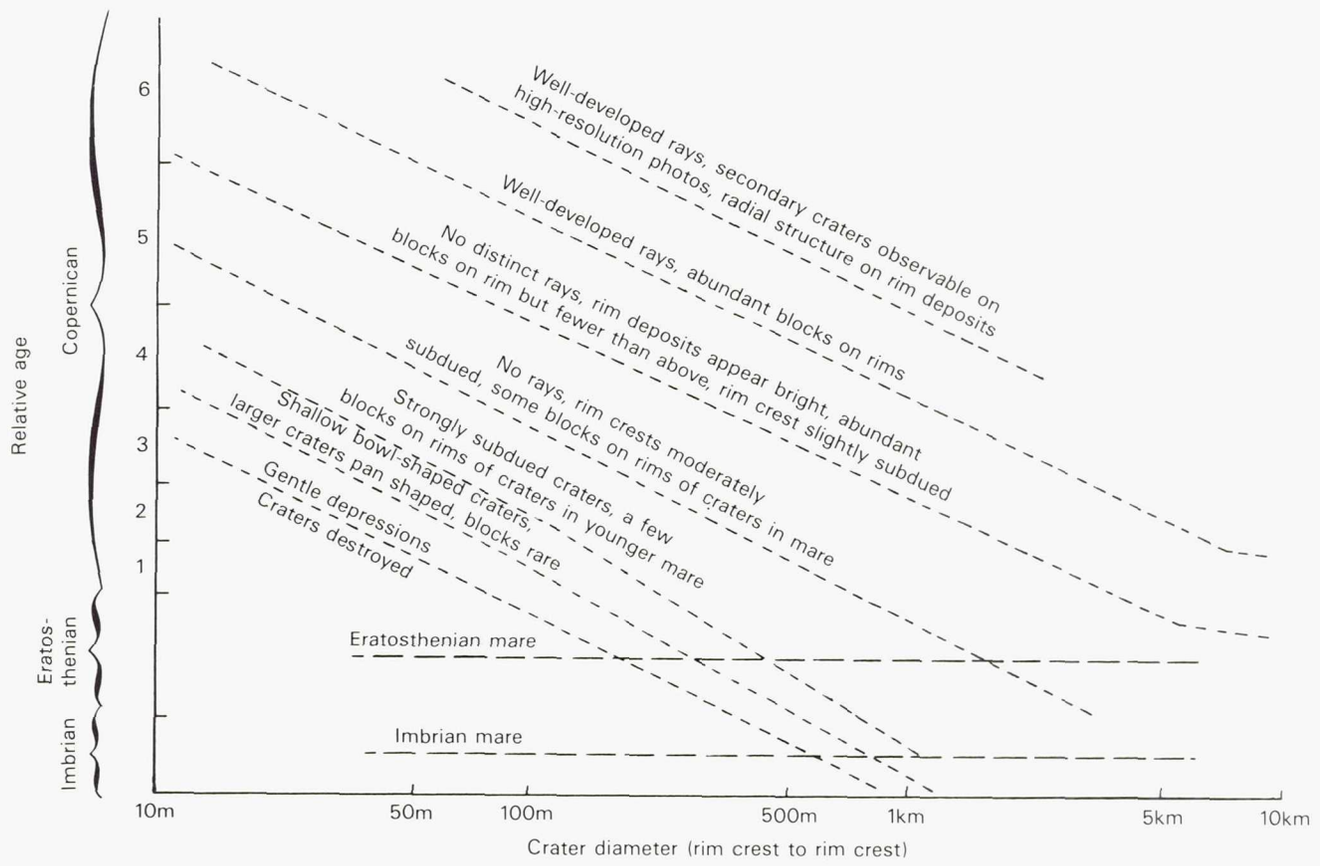

Figure 6.14. Relations among age, size, and morphology of small craters (Trask, 1971). Horizontal lines are examples of isochrons; their intersections with diagonal lines bounding morphology classes indicate what crater morphologies are superposed on average Imbrian mare and Eratosthenian mare. Morphology categories are gradational and may vary according to substrate properties.

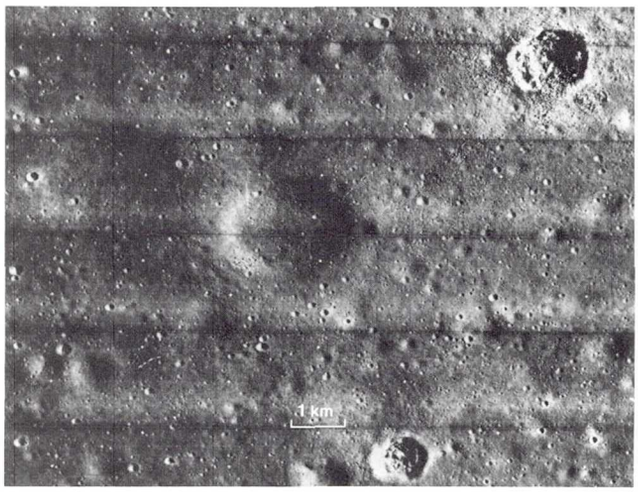

Figure 6.15. Examples of fresh and degraded craters on a mare surface. Reference to figure 6.14 shows that 1-km crater below scale bar, which is strongly subdued or bowl-shaped, is probably Eratosthenian; 1-km crater to its right is moderately subdued and blocky so belongs to Copernican class 1 or 2; larger, very blocky crater in upper right corner is probably Copernican class 4; and the 3-km, pan-shaped crater with a few blocks near center of picture must be Imbrian. This last crater and the almost invisible crater of the same size to its left limit the age of the underlying mare to Imbrian; such craters could not have reached their advanced state of degradation on an Eratosthenian mare surface. East of Apollo 12 site; Orbiter 3 H-143.

a gradual subduing of originally similar crater features with increasing age (Pohn and Offield, 1970; Offield and Pohn, 1970). Some examples of the progressive degradation are given in figure 6.16. Estimating age from morphology can be successful only if the regional setting of a crater is considered, particularly its relation to basin deposits (Wilhelms, in press b).

Summary

If the morphologic and size-frequency criteria for age are correctly interpreted, each geologic unit should, of course, be overlain only by craters having properties typical of stratigraphic intervals younger than the unit. This consistency has been approached in a series of iterations (summary by Wilhelms, in press b). Topographically sharp craters are superposed on all units; large subdued craters are superposed only on old units (unless they are anomalously buried by still-younger deposits). Units of successively older ages support successively more craters above the steady-state size for that age.

Below or near the steady-state size, successively larger craters disappear on successively older units (figs. 6.14 and 6.17). For example, an Eratosthenian unit is unlikely to display Eratosthenian craters smaller than 100 m, and the basal Imbrian unit (the Fra Mauro Formation) is unlikely to display <1 km Imbrian craters (fig. 6.14; Trask, 1971). Nectarian craters smaller than 20 km or 30 km are obviously deficient relative to Imbrian craters of the same size (fig. 6.17), and no Nectarian craters <5 km were identified with certainty during systematic examination of the Moon. The pre-Nectarian curve shows a deficiency in sizes as large as 50 km (fig. 6.17; Wilhelms et al., 1978). Nectarian and pre-Nectarian units can therefore be dated only by frequencies of craters larger than about 20 km. Consequently, only areally extensive (basin-scale) units of these ages can be dated by size-frequency counts. Morphologies of individual large superposed craters help date some of the old units, and craters in the hundreds-of-meters to 2-km range help date young planar units.

Some buried units, small units, rugged units (on which craters are not preserved), and poorly photographed units cannot be dated at all by crater-based methods. Stratigraphic relations determined by geologic mapping may help bracket their ages.

BASINS

Introduction

Understanding most aspects of lunar geology depends on understanding ringed impact basins. This results simply from the fact that basins are the largest features of the Moon. All well-exposed lunar impact excavations 300 km and larger possess at least one ring inside the rim and by definition are basins. Their deposits constitute most of the upper terra crust. Basins are also the sites of most mare volcanism and tectonism.

Most investigators were aware of the importance of crater and mare deposits by the early 1960s, but appreciation of the dominant role of basin deposits on the terrae has come more slowly. Gilbert (1893) traced an extensive near-side system of grooves and ridges (fig. 6.18B) to the Imbrium basin and correctly hypothesized that this "Imbrium sculpture" was created by Imbrium ejecta. Baldwin (1949, 1963) repeated Gilbert's observations and showed that ringed basins with concentric and radial structure characterize other regions as well. Another landmark study showed the basic similarity of the ring pattern of basins and raised the number of identified basins

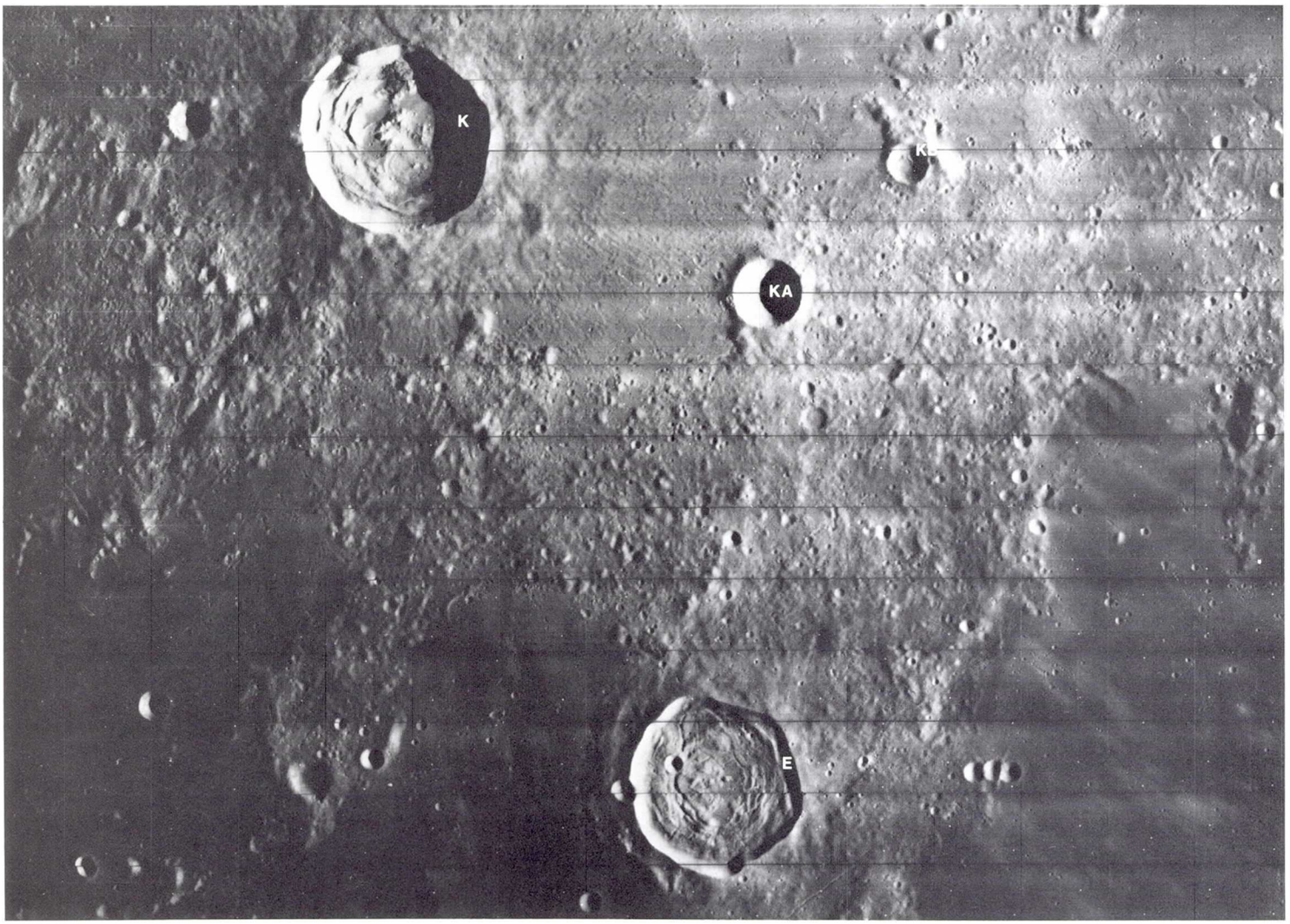

Figure 6.16. Examples of large craters of different ages.

A. Kepler (K, 32 km, 8°N, 38°W), shown to be Copernican by radial bright-ray pattern (fig. 6.9) and conspicuous, sharply-textured ejecta and secondary craters, which extend more than one crater diameter from rim crest. In contrast, Imbrian crater Encke (E, 28 km) has smooth ejecta truncated by mare flooding; floor also uplifted and fractured. Simple crater Kepler A (KA, 11 km) appears fresh but is overlain by Kepler secondary craters and lacks conspicuous ejecta; therefore Eratosthenian or Upper Imbrian. Kepler B (KB, 7 km) much more degraded, undoubtedly Imbrian. All four craters superposed on Imbrium-basin ejecta. Orbiter 4 H-138.

B. Schorr (S, 53 km, 20°S, 90°E); Upper Imbrian age indicated by moderately sharp interior detail coupled with lack of well defined ejecta or secondary craters. Overlies Nectarian crater Schorr A (SA, 64 km), whose rim crest is well defined but which lacks textural detail. Large crater partly in view at right is Curie (C, 139 km, 23°N, 92°E); considering size, Curie is much more degraded than Schorr A, therefore undoubtedly pre-Nectarian. Almost entire scene except Schorr overlain by large secondary-crater chains of early Late Imbrian crater Humboldt, centered outside of lower left corner. Apollo 15 M-2369.

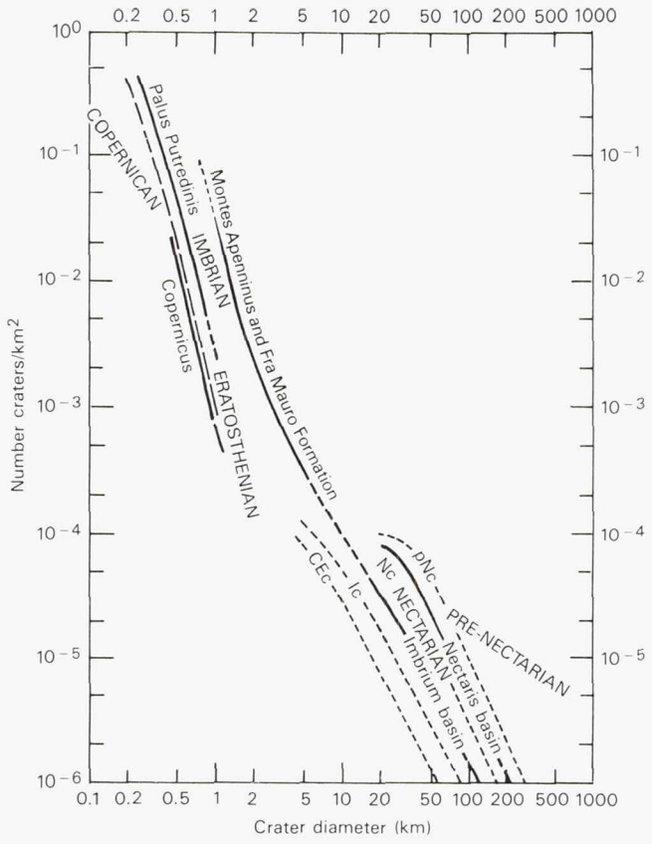

Figure 6.17. Size-frequency distributions of craters in each lunar time-stratigraphic system. Deposits of Nectaris and Imbrium basins define pre-Nectarian–Nectarian and Nectarian–Imbrian boundaries, respectively (table 1); frequencies of ≥ 20 km craters determined by Wilhelms (1979, in press b); frequencies of small craters determined on two Imbrium-basin units (Montes Apenninus and Fra Mauro Formation) by Neukum et al. (1975a, b); dashed where extrapolated from observations. Mare material of Palus Putredinis (Neukum et al., 1975a) lies very near Imbrian-Eratosthenian boundary (Wilhelms, in press b). Frequencies of units at Eratosthenian-Copernican boundary (long-dashed line; Wilhelms, in press b) poorly defined but somewhat greater than those on crater Copernicus determined by Neukum and König (1976).

Short-dashed curves show average frequencies of four groups of ≥ 4.5 km primary-impact craters (Wilhelms et al., 1978); pNc = pre-Nectarian, Nc = Nectarian, Ic = Imbrian, CEc = Copernican and Eratosthenian combined. Smaller craters included for CEc and Ic than for Nc and pNc because small craters of old populations are destroyed; diminishment of small sizes also shown by turndowns of left-hand parts of curves for Nc, Nectaris basin, and pNc (compare fig. 6.13C); CEc and Ic < 4.5 are visible but have not been systematically counted. In general, graph reflects fact that smaller craters can be counted on young units than on old. Therefore valid counts require larger areas for old units than for young units. Dating based on overall crater morphology and D_L method is required where exposed areas are too small for valid counts.

to 12 (Hartmann and Kuiper, 1962). Shoemaker and Hackman (1962) explicitly stated the similarity of deposits surrounding the Imbrium basin to those of craters and added the concept of rock units. However, they and most other workers of the 1960s considered the radial grooves to be fractures induced by the impact (Shoemaker and Hackman, 1962; Hartmann and Kuiper, 1962; Hartmann, 1964; Strom, 1964; Wilhelms, 1970). McCauley (1967a,b) identified another ejecta deposit around the Orientale basin, which is almost out of telescopic view on the Moon's west limb. Lunar Orbiter photography raised the number of basins recognized on the whole Moon to 27 or 29 (Stuart-Alexander and Howard, 1970; Hartmann and Wood, 1971). Nevertheless, as late as 1969, the only basin deposits identified with certainty were those of Imbrium, Orientale, and Humorum (Mutch, 1970; Wilhelms, 1970). Most of the terrae were considered assemblages of crater deposits, whose monotony was relieved only by the conspicuous material which forms light-colored plains, then thought to be volcanic. Later, basin deposits were traced over greater areas. Apollo orbital photographs showed that the seemingly straight Imbrian sculpture consists of elliptical secondary-impact craters. The sculpture and the inner deposits of all basins grade outward into fields of subcircular secondary craters, which are like those around craters except that they are larger and more nearly radial (Wilhelms, 1976; Wilhelms et al., 1978). Indistinct deposits and secondary craters of old basins have been recognized as the analogs of the young; overlapping deposits of basins have been mapped over the whole terrae (fig. 6.19; Wilhelms and McCauley, 1971; Wilhelms and El-Baz, 1977; Scott et al., 1977; Lucchitta, 1978; Stuart-Alexander, 1978; Wilhelms et al., 1979; Wilhelms in press b).

Orientale

Introduction

Just as Copernicus is often used as the standard of comparison for complex lunar craters, the ten-times-larger Orientale is the model for basins (fig. 6.20). Imbrium was studied first because of its favorable position for telescopic viewing, but Orientale displays basin features much better because of its lesser degradation and flooding. Although detected by telescopic studies and Soviet Zond-3 images (Hartmann and Kuiper, 1962; Hartmann, 1964; McCauley, 1967a), Orientale was not well observed until Lunar

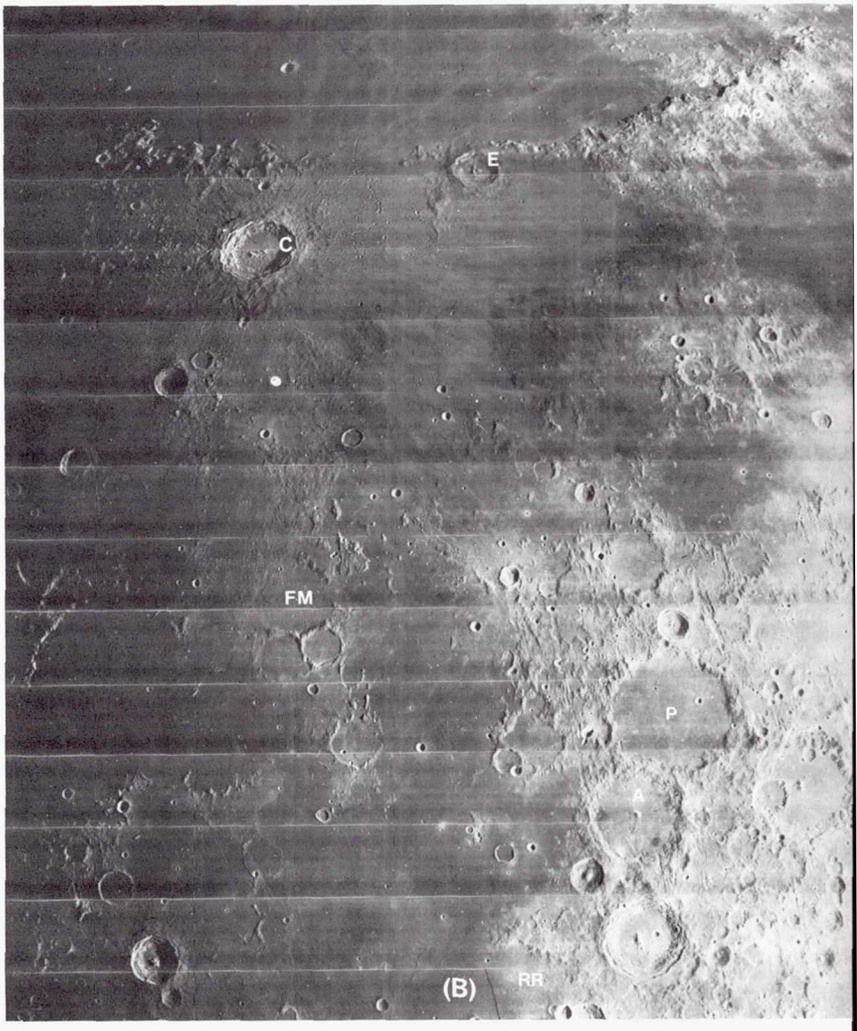

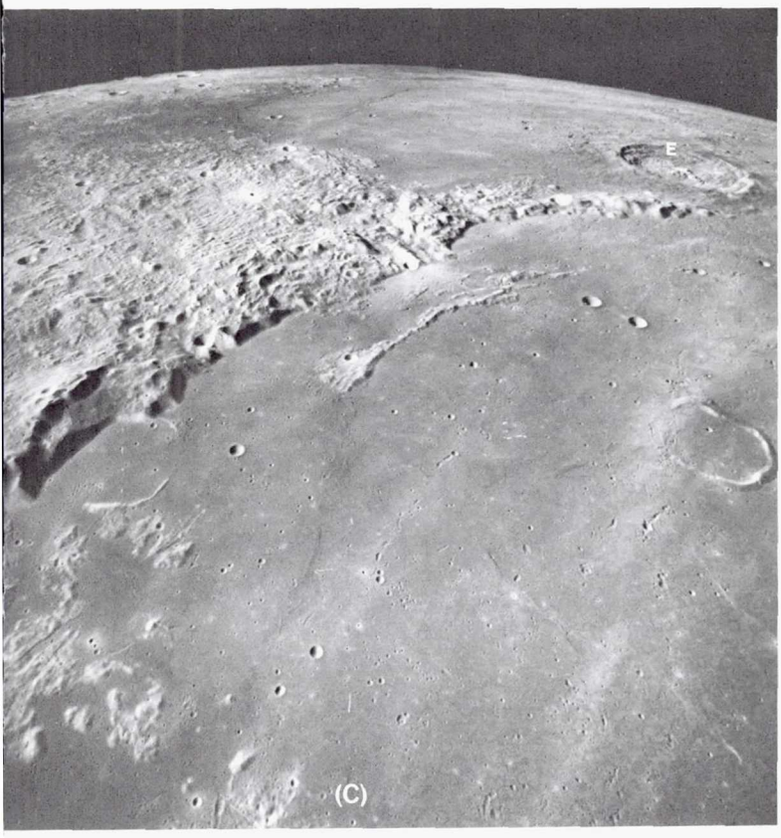

Figure 6.18. Imbrium basin and periphery on lunar near side.

A. View centered on Mare Imbrium (MI). Southern basin rim consists of Montes Apenninus (MAp) and Montes Carpatus, the range north of (above) Copernicus (C, 93 km). Alternatively, north rim may be (1) north shore of Mare Frigoris (MF) or (2) Montes Alpes (MAl) plus the terra overlain by Plato (P) and the crater containing Sinus Iridum (SI). Rim may split in Montes Caucasus (MC) and continue as both of the above. Center as given here (38°N, 19°W, under letters MI) is center of circle best fit to Carpatus and Frigoris north shore. Inner ring(s) marked by mare ridges and unburied summits of rings such as Montes Recti (MR) and the rugged elevation on the Apennine Bench (AB) south of Archimedes (A). VA = Vallis Alpes (Alpine Valley). Rectified telescopic photograph courtesy Lunar and Planetary Laboratory, University of Arizona (Hartmann and Kuiper, 1962).

B. Overall view of southern periphery including Montes Apenninus (MAp, compare fig. 6.1D), Fra Mauro peninsula (FM; compare fig. 6.1C), and Imbrium sculpture cutting rims of Ptolemaeus (P, 153 km) and Alphonsus (A; compare fig. 6.56). C = Copernicus; E = Eratosthenes (58 km); RR = Rupes Recta (Straight Wall). Orbiter 4 M-113.

C. Montes Apenninus viewed from north-northwest; E = Eratosthenes. Apollo 17 M-2433.

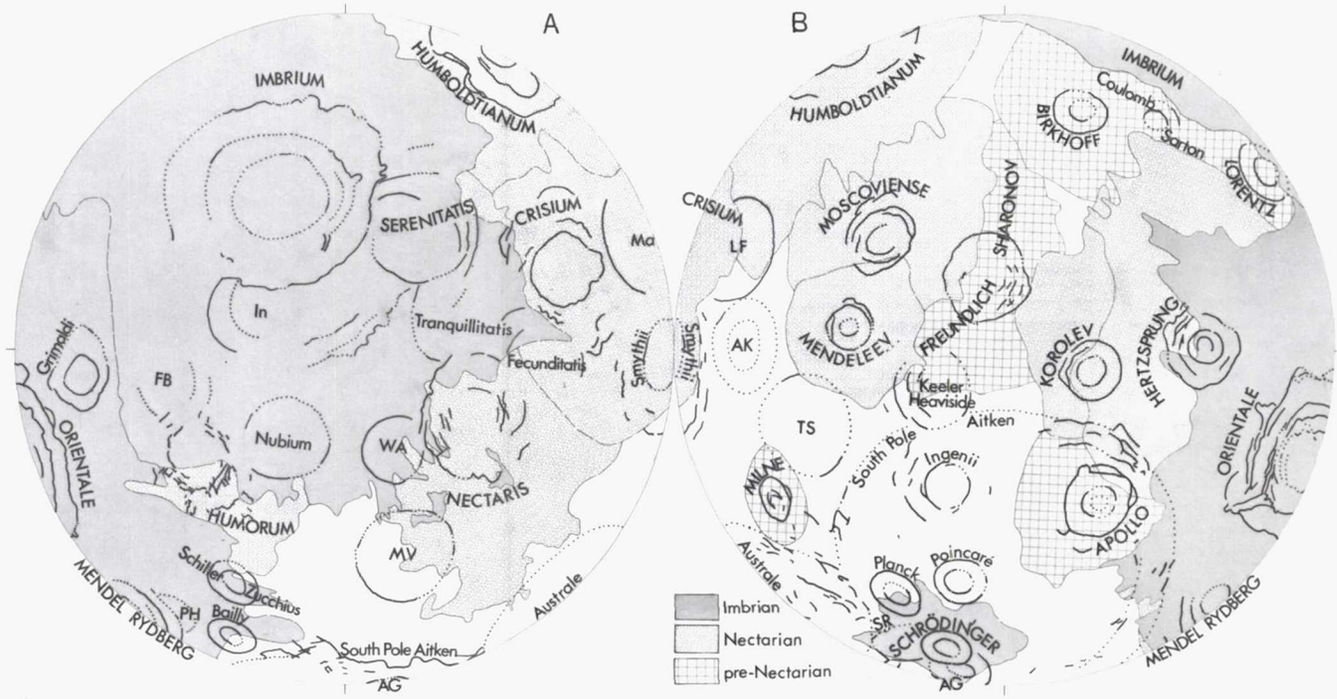

A. Near side *B. Far side*

Figure 6.19. Map of lunar basins (Wilhelms, 1980b). Rings and ring arcs solid where exposed, dotted where buried or inferred. Mapped deposits include continuous, primary ejecta and densest concentrations of secondary craters; dashed where uncertain. Names of basins having mapped deposits are in capitals. Names of other definite basins are written out in lower case. Initials refer to indefinite basins: AG = Amundsen-Ganswindt; AK = Al-Khwarizmi–King; FB = Flamsteed-Billy; In = Insularum; LF = Lomonosov-Fleming; Ma = Marginis; MV = Mutus-Vlacq; PH = Pingré-Hausen; SR = Sikorsky-Rittenhouse; TS = Tsiolkovskiy-Stark; WA = Werner-Airy. Procellarum basin not shown (see fig. 6.63).

Orbiter 4 exposed the full beauty of this almost unmodified impact basin (fig. 6.20). About the eastern two-thirds of the ring system and its encompassing deposits and secondary craters were well photographed (fig. 6.20A). The impact origin of Orientale and other basins was demonstrated by energy considerations like those applied to Copernicus, multiplied many times over. The thousand-kilometer extent of radially disposed ridges, grooves, craters, and plains should have ended all doubts about the origin of basins by enormous impacts.

Rings

Although the rings of Orientale are commonly cited as type examples of lunar multiple basin rings, they are more regular than is usual. Four well-defined rings characterize the sector photographed by Orbiter 4 (fig. 6.20A). The outermost is Montes Cordillera, a nearly complete ring 930-km across that is the topographic ring of the basin; that is, most of the depressed terrain generally thought of as the basin interior lies inside this ring. Whether the Cordillera is also the basin rim in the sense of the boundary of the excavation is another matter. The Cordillera ring is scarplike in places, and in other places rises in arcuate massifs. It marks the inner limit of the coarsely textured exterior basin ejecta.

Next inside the Cordillera is the outer of the two rings called Montes Rook. The peaks of this 620-km ring are rugged, jagged, and stand higher above their bases than those of the Cordillera. The inner Rook ring (480-km diameter) is similar but considerably less massive in most sectors. An innermost ring 320 km in diameter is delineated partly by scarps and partly by massifs. The ring spacing of Orientale supports the "rule" (Hartmann and Wood, 1971) that lunar basin rings are regularly spaced by factors of 2 or its square root.

The poorly photographed western sector is less regular (fig. 6.20B). The four rings are vaguely identifiable, but the general appearance is chaotic and a basin depression is not obvious. If this sector had been well photographed instead of the eastern, interpreta-

tions of basin rings might have followed a different path.

Interior deposits

Two kinds of materials in addition to massif materials (and the later mare materials) characterize the Orientale interior. One is the Montes Rook Formation, a hummocky- or knobby-textured unit concentrated between the outer Rook and Cordillera rings but extending locally beyond both (Scott et al., 1977). Its interpretation has been difficult. It must have been partly ejected, for it locally lies upon the Cordillera scarp (McCauley, 1977). It also shows concentric features where banked against the scarp, and some radial texture. The knobs resemble similar ones on the floors of fresh craters such as Copernicus and Tycho (fig. 6.7C; Murray, 1980). Those crater-floor materials are commonly interpreted as impact melt because the knobs appear draped by fissured material, which probably shrank during cooling (Howard and Wilshire, 1975). Thus the Montes Rook Formation probably includes impact melt and was thrown over the rim in some sectors.

Another basin floor material, the Maunder Formation, forms smoother, light-colored plains and fissured, hilly materials (fig. 6.20C). The Maunder probably consists of pooled impact melt like that in the large lunar and Canadian Shield craters (fig. 6.7C; Scott et al., 1977).

Exterior deposits

Textures of the external deposits and their relations to older and younger terranes are especially clear around Orientale. A thick blanket, the Hevelius Formation (McCauley, 1967a,b; Scott et al., 1977), completely obscures underlying features on Montes Cordillera, but the formation thins farther out and becomes indistinct 300 to 600 km from the Cordillera. The Hevelius abundantly displays evidence of flow along the surface (fig. 6.20D). Pre-Orientale craters deflect radial flow ridges and grooves into concentric patterns which may resume a radial orientation after bypassing the obstacle. Textures are coarse near the basin and progressively finer outward. Ultimately the Hevelius Formation grades into smooth planar deposits, strong evidence for the basin-ejecta origin of light plains deposits in general, including those at the Apollo 16 site, once thought volcanic.

Secondary chains locally extend to the Cordillera rim (Vallis Bouvard; fig. 6.20A), where, like the pre-basin craters, they are blanketed by the continuous ejecta. Most secondaries, however, appear from beneath the continuous deposits at about the same radial distance where fine textures give way to plains (fig. 6.20E). Some secondary crater groups have interfered with each other as have crater secondaries, but more Orientale secondaries form radial than herringbone patterns (compare figs. 6.7B and 6.20E). Other Orientale secondaries, recognized by similar sizes, clustering, and rim shapes, are considerably subdued through partial burial by the continuous Hevelius Formation or deposits of other secondaries. The secondary-impact field eventually degenerates outward into discontinuous patches, and finally into thin mantles barely distinguishable from the older, subjacent terrain. A few strings of fresh craters many hundreds of kilometers from Orientale are probably also Orientale secondaries.

Basin-Forming Processes

Ring origin

Rings of other basins show both similarities to and differences from those of Orientale. The discussions here concentrate on cavities $\geq$300-km wide, but some smaller cavities with small rings or partial rings have also been called basins. Examples are Antoniadi (135 km) and Compton (162 km), each having a peak centered inside the inner ring; Schwarzschild (235 km), with an arcuate partial ring; and Milne (262 km), characterized by several subconcentric partial rings.

These features have commonly been cited as evidence for a transition between the central peaks of craters and the rings of basins (e.g., Hartmann and Wood, 1971; Hodges and Wilhelms, 1978). The jagged peaklike morphology of inner rings like those of the 320-km fresh basin Schrödinger (fig. 6.21) also suggests an origin as expanded central peaks. However, most craters in the 200- to 300-km diameter range have a poorly developed, inconspicuous inner structure (Murray, 1980). Basin rings and crater peaks may form by different, though related, processes.

Understanding the origin of basin rings is important for estimating the extent to which the lunar crust and mantle were excavated and deformed during very large impacts. The identity of the boundary of excavation is particularly significant. Theories of ring origin fall roughly into the following categories: (1) an inner ring, or the former position of an inner ring, marks the excavation limit (Hartmann and Wood, 1971; Howard et al., 1974; Moore et al., 1974; Head,

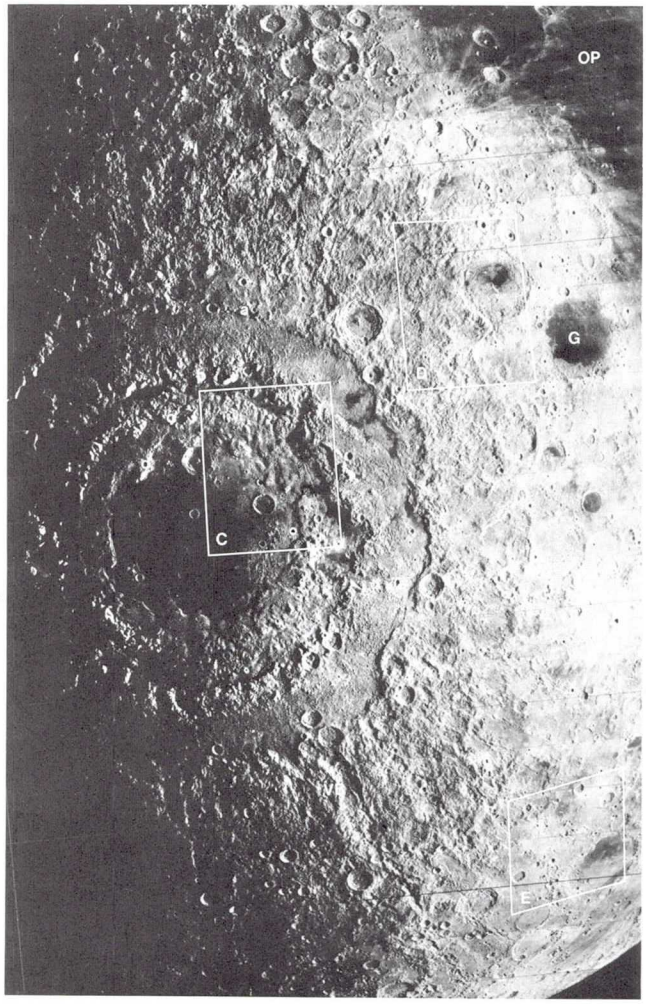

Figure 6.20. Orientale basin, centered 20°S, 95°W.

A. Regional view centered on eastern part of basin. Rings are Montes Cordillera, 930 km diameter (a); outer Montes Rook (620 km, b); inner Montes Rook (480 km, c); and innermost ring (320 km, d). VB = Vallis Bouvard, a chain of Orientale secondary craters. Areas of C-E outlined. Part of southwestern Oceanus Procellarum in upper right (OP); mare fill of Grimaldi at G. Orbiter 4 M-187.

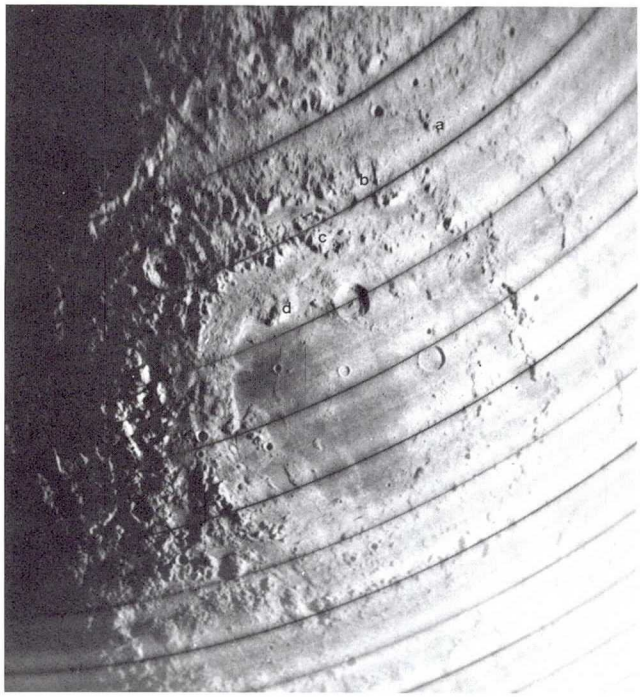

B. Regional view centered on western part of basin. Eastern rings labeled as in A; ring structure less distinct in west. Orbiter 4 M-194, rectified by Lunar and Planetary Laboratory, University of Arizona; courtesy E. A. Whitaker.

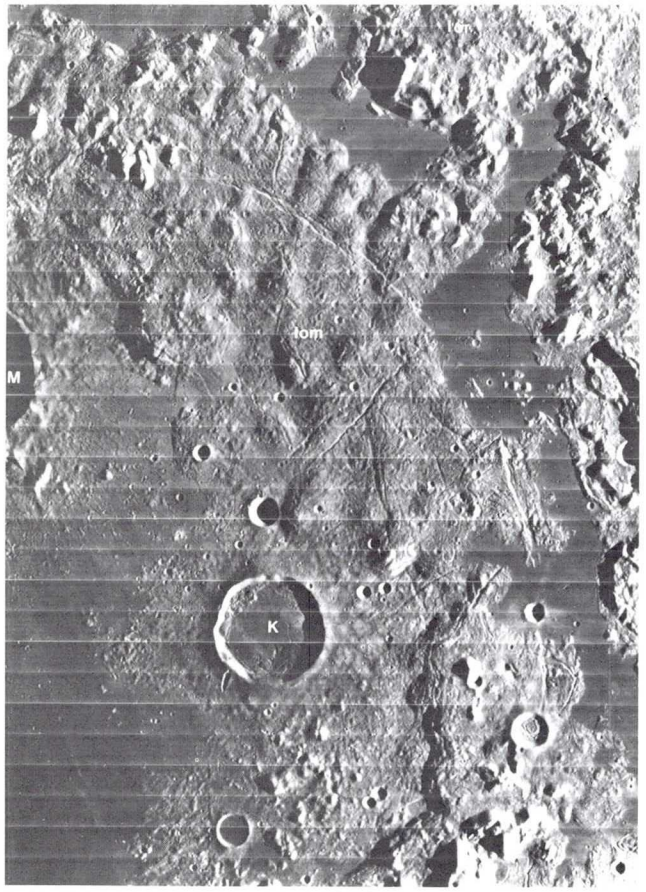

C. Part of northeastern interior, showing fissured swells of impact melt (Maunder Formation, Iom), knobby Montes Rook Formation (Ior), and rugged, irregular massifs where both Rook rings are amalgamated (upper right; compare fig. 6.20A). Craters are Kopff (K, 42 km, 17°N, 90°W) and Maunder (partly in view at M). Crescentic mare is Lacus Veris. Orbiter 4 H-187.

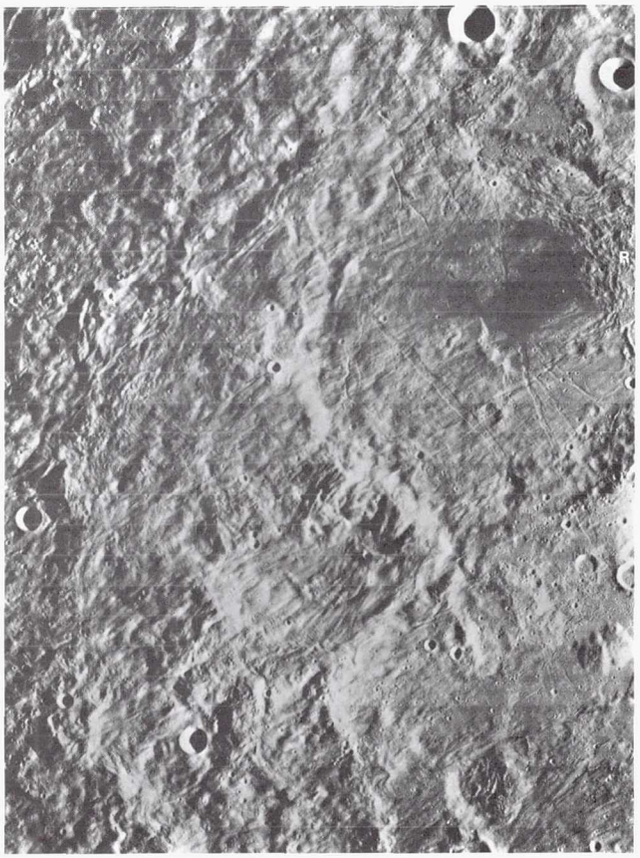

D. Hevelius Formation, lineated ejecta of Orientale basin. Surface flow evinced where obstacles have deflected otherwise radial ridges and grooves. Radial Hevelius grades into dunelike forms accumulated against distal wall of crater Riccioli (R, 146 km, 3°S, 74°W).

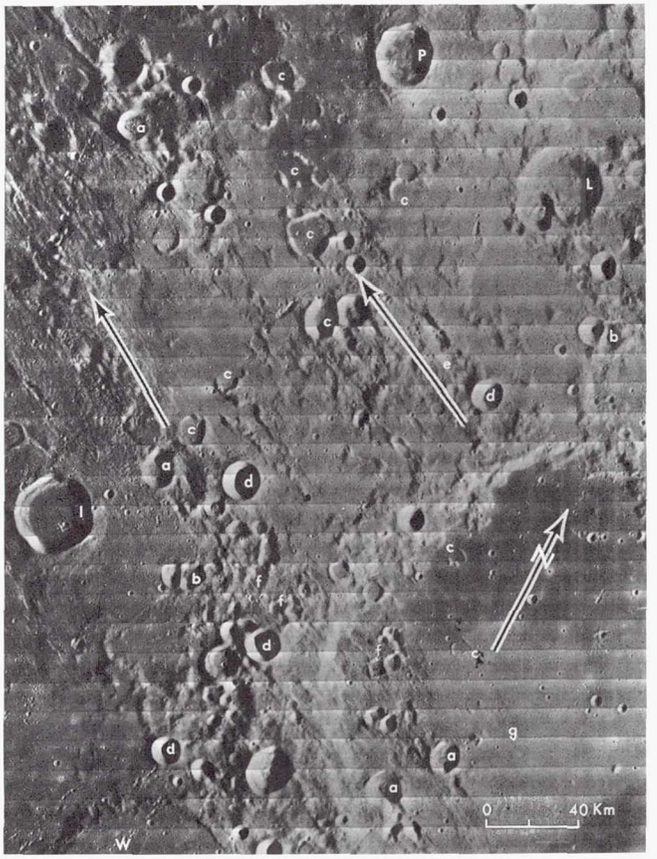

E. Secondary craters of Orientale southeast of basin near crater Schickard (lower right, 227 km, 44°S, 55°W). Two left-hand arrows lie along linear, radial secondary-crater ejecta and point to Orientale center, 1200 km away. Secondary craters include typical well formed individuals partly filled by ejecta (a); pairs forming linear intercrater septa (b); similar but partly buried groups and individuals (c); very sharp craters which may be secondaries or postbasin primary craters (d); buried, linear chains (e); and diverse clusters of small secondaries (f). Plains (g) also probably secondary ejecta. Prebasin primary craters are Schickard, Inghirami A (I), Lacroix (L), and Wargentin (W). Only large postbasin primary crater is Piazzi C (P). Orbiter 4 H-167; after Wilhelms (1980a).

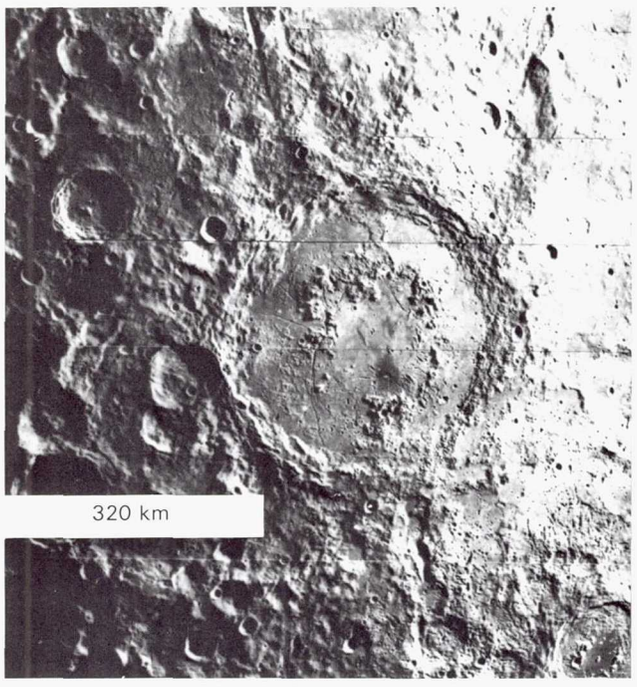

Figure 6.21. Schrödinger basin (320 km, 76°S, 134°E), showing double-ring structure. Outer rim resembles crater rims; inner ring consists of rugged peaks. Radial valleys formed by secondary impact. Orbiter 4 M-8.

1974a; McCauley, 1977; Scott et al., 1977); the outer rings formed like terraces of craters by collapse into the cavity, either (a) during (McCauley, 1977) or (b) after (Head, 1974a) excavation; (2) the main, topographic basin rim is the boundary of excavation, and interior rings are (a) nested subcavities (Hodges and Wilhelms, 1978) or (b) floor uplifts (Baldwin, 1974; Murray, 1980).

The resemblance of the main, 320-km rim of Schrödinger to the rims of craters is obvious, and they must be equivalent in origin. That is, the Schrödinger rim is the boundary of excavation as modified (widened by terracing). The morphology of the inner ring indicates floor uplift. It is very unlikely that excavation was contained within the inner, 160-km ring, because the cavity would be smaller than many craters which lack a second ring. Schrödinger-type double-ring structure persists until about 450 km, the diameter of the Korolev and Moscoviense basins (table 6.4; figs. 6.22, 6.23). The inner ring is generally half as wide as the topographic rim (Wood and Head, 1976).

Hertzsprung (570 km) represents the next step in the complexity series. This relatively young but pre-Orientale basin has an intermediate ring, or a zone of irregular hills between the rim (570 km), and a distinct inner ring (265 km; fig. 6.24). The great extent of ejecta and secondary craters beyond the 570-km rim shows that this rim is equivalent to crater- and Schrödinger-type rims—the boundary of excavation. Uplift is the mechanism most consistent with the interior structure, especially the irregular zones.

Interior irregularities of this sort also appear in all larger basins. Perhaps the clear division of basin structure into rings has been overemphasized considering the poorly defined patterns of hills, peaks, and ridges that characterize large tracts of western Orientale (fig.

Table 6.4. Known and Possible (parentheses) Lunar Ringed Impact Basins. Listed in order of age (youngest at top); basins with mappable deposits in capitals

Basin[1]	Center Lat.	Center Long.	Diameters (km)[2] Main rim	Diameters (km)[2] Other ring(s)	Age[3]	Remarks
ORIENTALE	20 S	95 W	930	620–480–320	1-I	Fig. 6.20
SCHRÖDINGER	75 S	134 E	320	150	2-I	Fig. 6.21
IMBRIUM	33 N	18 W	1200–(1500)	670	3-I	North rim dual? Fig. 6.18
(Sikorsky-Rittenhouse)	69 S	111 E	310	—		Fig. 6.21
Bailly	67 S	68 W	300	150		—
HERTZSPRUNG	2 N	129 W	570	(410)–265		Fig. 6.24
SERENITATIS	27 N	19 E	740	420	4-N	Rings, age doubtful; double?
CRISIUM	18 N	59 E	1060?	635–500–380		Figs. 6.25, 6.61
HUMORUM	24 S	40 W	820?	440–325		Complex rings; fig. 6.26
HUMBOLDTIANUM	61 N	84 E	600	275		Complex rings; double basin; fig. 6.25
MENDELEEV	6 N	141 E	330	140	5-N	—
MENDEL-RYDBERG	50 S	94 W	630?	460–200		—
KOROLEV	5 S	157 W	440	220	6-N	Fig. 6.22
MOSCOVIENSE	26 N	147 E	445	210		Fig. 6.23
NECTARIS	16 S	34 E	860	600–450–350		Fig. 6.27
APOLLO	36 S	151 W	505	250	7-pN	Fig. 6.22
Grimaldi	5 S	68 W	430	230		—
FREUNDLICH-SHARONOV	19 N	175 E	600	?	8-pN	Fig. 6.31
BIRKHOFF	59 N	147 W	330	150		—
Planck	58 S	136 E	325	175	9-pN	Fig. 6.31
Schiller-Zucchius	56 S	45 W	325	165		—
(Amundsen-Ganswindt)	81 S	120 E	355			Fig. 6.21
LORENTZ	34 N	97 W	360	185	10-pN	—
Smythii	2 S	87 E	840	(660)–360	11-pN	Fig. 6.32
Coulomb-Sarton	52 N	123 W	530?	400–180		—

6.20B), Hertzsprung (fig. 6.24), Crisium (fig. 6.25), Humboldtianum (fig. 6.25), Humorum (fig. 6.26), Nectaris (fig. 6.27), and Serenitatis (fig. 6.18B,E). Partly regular and partly random processes of floor uplift seem required to explain their combinations of ringlike and chaotic patterns.

Recently, a wavelike process of basin ring formation first proposed by Van Dorn (1968) and Baldwin (1972, 1974) has been revived (Grieve, 1980; Murray, 1980). Highly shocked, fluidized or nearly fluidized material of most of the cavity rebounds, then a smaller central zone partly collapses. The collapsed part rises again in its center, and so on for as many cycles as are consistent with basin size, strength, layering, and other properties of the target. The uplift freezes from the outside in because the inner part is the most highly fluidized. This explanation nicely accounts for both the regular structure, where controlled by layering or some other anisotropic factor, and the irregular structure, where the target is more homogeneous and the oscillations are imperfect.

In the version of the model favored here, the topographic rim is also the boundary of excavation and not an exterior scarp. The rim of Orientale, Montes Cordillera, cannot have formed after cessation of ejecta deposition as claimed by many workers (e.g., Head, 1974a), because it is mantled with ejecta (McCauley, 1977). It is a major structure and not an external byproduct of the basin formation. It is a nearly complete ring that demarcates the inner boundary of the thick, coarsely textured Hevelius Formation, the most conspicuous stratigraphic unit on the Moon. Pre-basin craters are numerous outside and absent inside (Baldwin, 1974). If we consider the extent of the Orientale deposits and secondary craters (fig. 6.20) and accept appearances at face value, the

Table 6.4 (continued). Known and Possible (parentheses) Lunar Ringed Impact Basins. Listed in order of age (youngest at top); basins with mappable deposits in capitals

Basin[1]	Center Lat.	Center Long.	Diameters (km)[2] Main rim	Other ring(s)	Age[3]	Remarks
Keeler-Heaviside	10 S	162 E	780?	540		Fig. 6.31
Poincaré	58 S	162 E	340	175	12-pN	Fig. 6.31
Ingenii	34 S	163 E	560?	325		Fig. 6.31
Lomonosov-Fleming	19 N	105 E	620			—
Nubium	21 S	15 W	690			—
Fecunditatis	4 S	52 E	690		13-pN	—
Mutus-Vlacq	52 S	21 E	700			—
Tranquillitatis	7 N	40 E	775?			—
Australe	52 S	95 E	880	(550)		Fig. 6.32
(Al Khwarizmi-King)	1 N	112 E	590			—
(Pingré-Hausen)	56 S	82 W	300?			—
(Werner-Airy)	24 S	12 E	500?			—
(Balmer-Kapteyn)	16 S	69 E	550?			—
(Flamsteed-Billy)	8 S	45 W	570?		14-pN	—
(Marginis)	20 N	84 E	580			Fig. 6.25
(Insularum)	9 N	18 W	600?			—
(Grissom-White)	40 S	155 W	600?			—
(Tsiolkovskiy-Stark)	15 S	128 E	700?			—
South Pole-Aitken	56 S	180	2500		15-pN	Fig. 6.22
(Procellarum)	26 N	15 W	3200	2400–1700		Fig. 6.63

NOTES

1. Basins named from two superposed, unrelated craters (Wilhelms and El-Baz, 1977) or from contained mare. Older names and references to first mention given by Wilhelms (in press b).
2. Main rim refers to topographic basin rim, which is the boundary of excavation in the author's opinion. Other major rings given; in parentheses if partial.
3. I = Imbrian; N = Nectarian; pN = pre-Nectarian. Fifteen age groups also given; basins cannot be accurately ranked within a group (Wilhelms, 1981, in press b). Each group is headed by a basin which can be dated by crater frequencies (Wilhelms, 1979, in press b); other basins in group are ranked in order of increasing size.

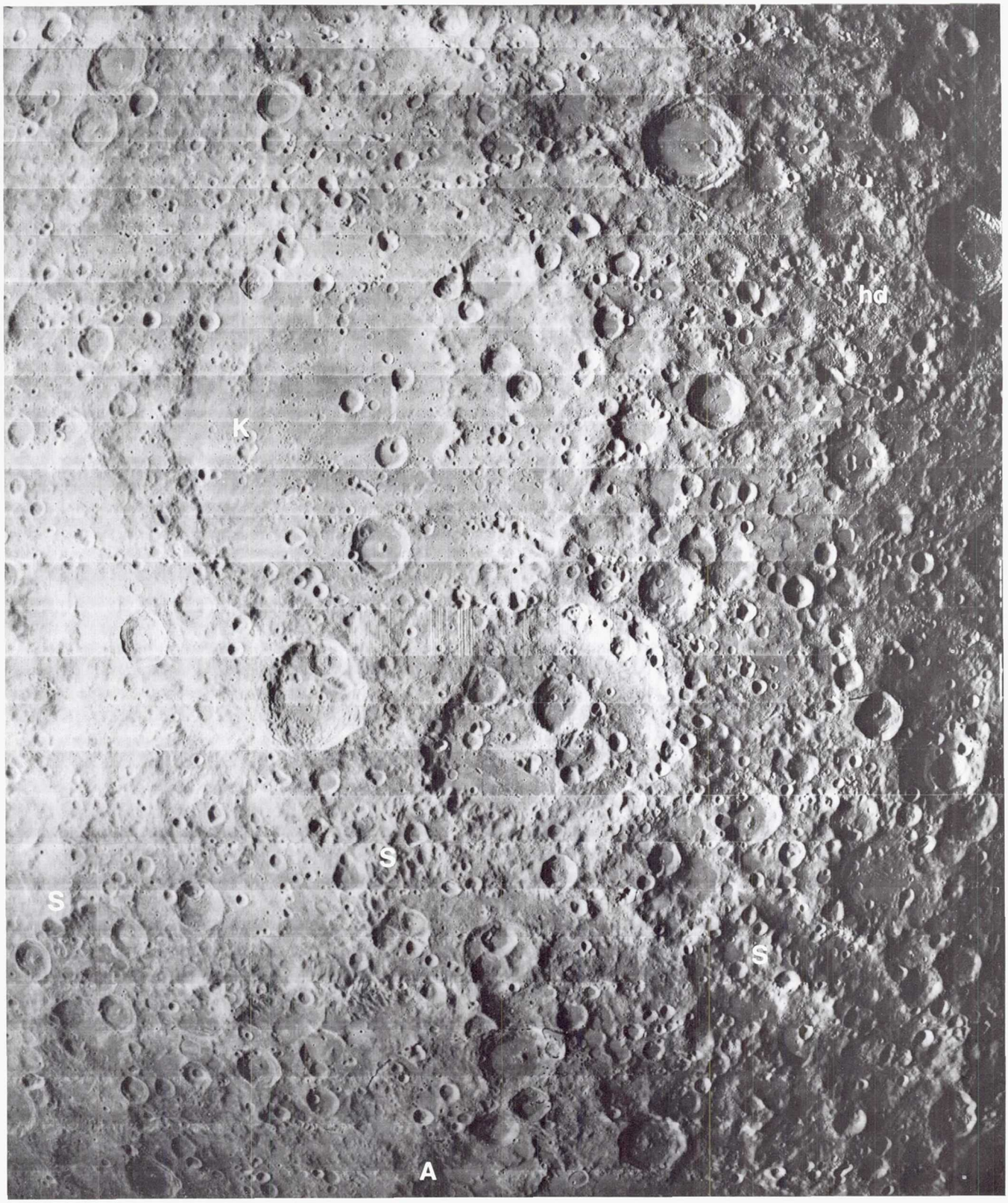

Figure 6.22. Korolev basin (K; 440 km; 5°S, 157°W), showing double-ring structure. Outer ring is subdued, contains downdropped "terrace" in west (left of K). Inner ring is ridgelike and incomplete, some sectors being buried by plains (under K). Basin filled by light-colored plains deposits. Northern rim of Apollo basin (A), massifs of South Pole-Aitken basin (S), and deposits of Hertzsprung basin (hd; compare fig. 6.24) also in view. Orbiter 1 M-28.

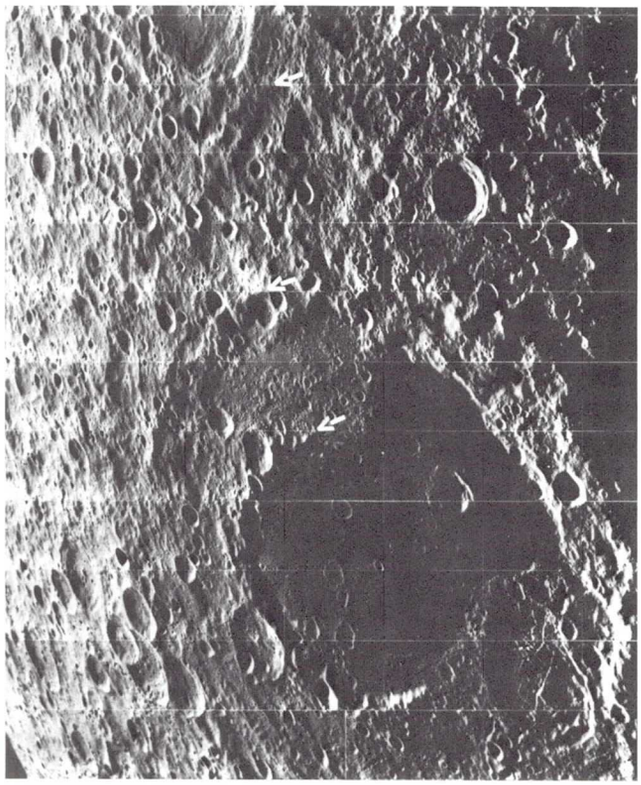

Figure 6.23. Moscoviense basin (445 km; 26°N, 147°E). Arrows mark three rings; terrain between outer two rings variable in width, and contains arcuate partial rings. Inner basin and probably the outer structure indicate figure-8 structure, probably resulting from twin impact. Orbiter 5 M-124.

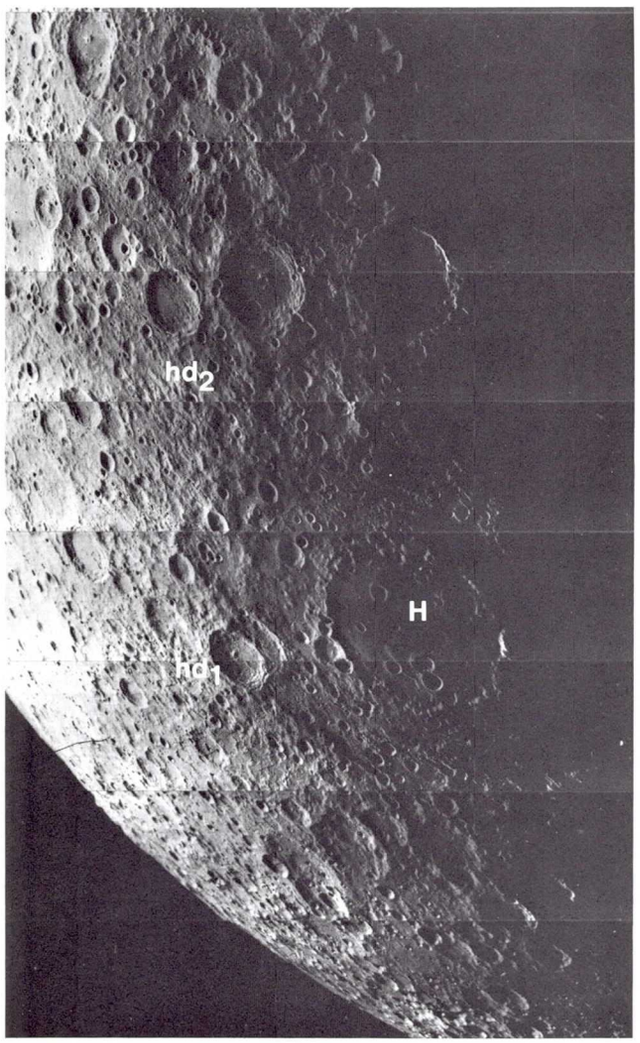

Figure 6.24. Hertzsprung basin (H, 570 km, 2°N, 129°W). Inner ring and outer ring in southwest conspicuous (below and left of H); other ring structure less well defined. Basin deposits shown in figure 6.22 at hd_1; more conspicuous, typical deposits at hd_2. Interior filled by marelike plains material (light-colored when seen under higher sun illumination). Orbiter 5 M-28.

Cordillera is the boundary of excavation of the Orientale basin. The same is true of Montes Apenninus, the Moon's most prominent range, which is the inner boundary of the Imbrium basin ejecta and must form the boundary of excavation in its sector. Around all relatively fresh basins (see table 6.4), distinct ejecta begins at the topographic rim, extends an average of one basin radius farther, and is succeeded outward by densely concentrated secondary craters which extend an additional one or two basin radii.

Problems remain in identification of many large basin rims. Crisium and Humorum, for example, have multiple rings and irregular zones that extend out to 530 and 410 km, respectively, from the basin centers (figs. 6.25 and 6.26). Rimlike structure is well defined at this distance in some sectors and not in others. Apparently, the behavior of large impacts is affected by properties of target and projectile in complex and largely unpredictable ways.

Sequence of events

Following is the inferred sequence of events in the development of a large ringed basin, exemplified by Orientale (fig. 6.28).

(1) Impact and development of a craterlike cavity, whose depth/diameter ratio may initially resemble those of simple craters.

(2) Lesser deepening but vigorous lateral cavity expansion, with ejection of massive ejecta at low angles. Forms chainlike secondary craters (Vallis Bouvard) overlain by lineated ejecta (Hevelius Formation).

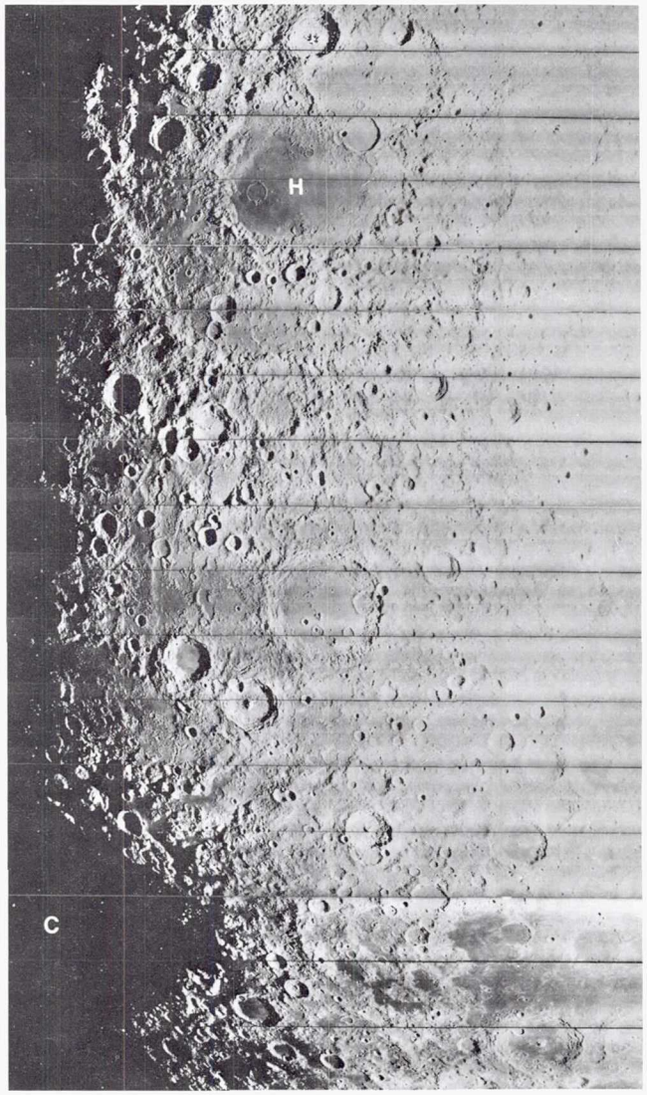

Figure 6.25. Humboldtianum (H) and Crisium (C) basins on Moon's east limb. Terminator (irregular line between dark and illuminated regions) about at longitude 61°E. Concentric and radial structure of both basins evident. Orbiter 4 M-23.

(3) Rebound of interior and ejection of knobby ejecta (Montes Rook Formation) at higher angles and lower velocities.
(4) Several oscillations of interior, each having successively lower amplitude and extending to smaller radius. Hinge line of each oscillation recorded by an interior ring (outer Rook, inner Rook, 320-km ring).

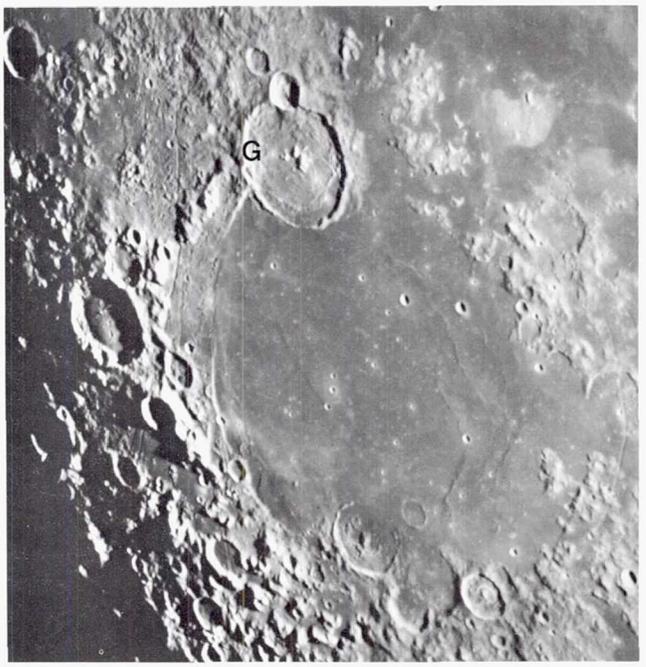

Figure 6.26. Humorum basin. Concentric structure includes parts of mountainous terra rings (below and left of Gassendi, G, 110 km), mare ridges, and arcuate rilles (see "Tectonics"). Catalina Observatory photograph 1607.

(5) Last oscillation leaves a central uplift in basins of certain size (fig. 6.20A).
(6) Impact melt (Maunder Formation) settles into place.
(7) Early-launched ejecta impacts distant terrain, forming secondary craters. May overlap with stages 4–6.

Distribution and Stratigraphy

Most of the near side and part of the far side are dominated by the relatively well-preserved deposits of the Imbrium, Orientale, and Nectaris basins (figs. 6.18, 6.20, 6.27). They divide the lunar stratigraphic column into four time-stratigraphic blocks, the three oldest of which (pre-Nectarian, Nectarian, and Lower Imbrian) contain other basin materials as well (table 6.1). The 28 definite and 16 probable or possible basins have been ranked into a minimum of 15 unnamed, informal subdivisions of these systems (table 6.4). Basins of a group appear distinct in age from

Figure 6.27 (next page). Nectaris basin (centered 16°S, 34°E), bounded on southwest by conspicuous scarp, Rupes Altai (RA). Dotted lines indicate additional rings. Limit of most conspicuous ejecta and secondary craters south of basin outlined. A 16 = Apollo 16 landing site. Nectarian crater Rheita (R, 70 km, 37°S, 47°E) superposed on Vallis Rheita (VR), a secondary-impact chain of Nectaris basin. Pre-Nectarian crater Janssen (J) buried by Nectaris basin deposits (the Janssen Formation). After Stuart-Alexander and Wilhelms (1975). Orbiter 4 M-83.


A16
Mare Nectaris
R
VR
J

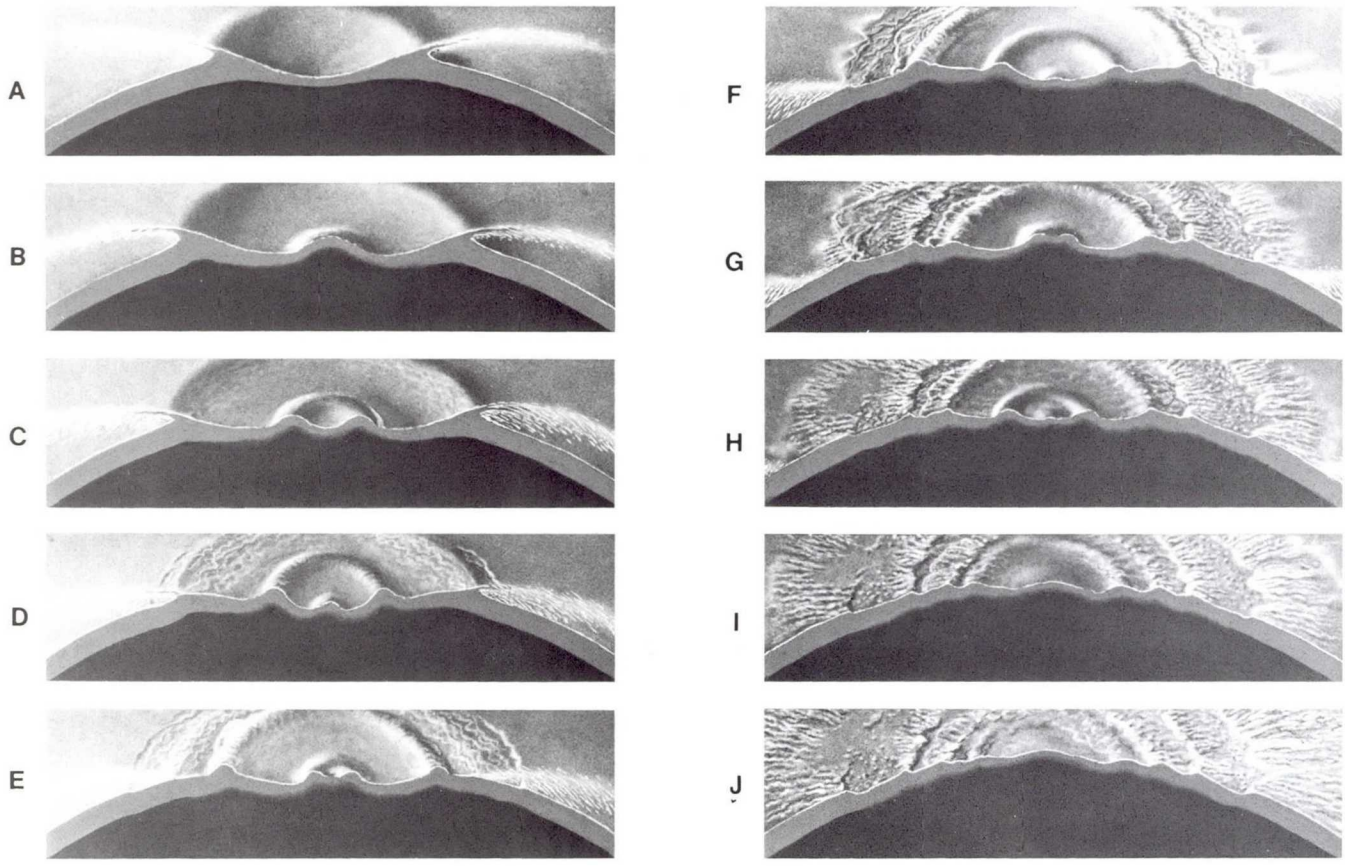

Figure 6.28. Stages in formation of typical ringed impact basin (modeled on Orientale) according to oscillatory uplift model. (Drawn by Donald E. Davis.)

A. Early stages of growth, resembling simple crater. Target rock greatly weakened by shock wave.
B. Cavity grows and becomes shallower relative to depth, ejection angle decreases, and central uplift begins as in complex crater.
C. Central uplift collapses, forming temporary double-ring basin like Schrödinger.
D. Center rebounds as in water-drop crater.
E. Wavelike motion enlarges inner ring of C and D, new innermost ring forms from central peak of D, bounding ring of excavation becomes lower, and ejecta blankets basin walls and exterior. Temporary three-ring basin is formed.
F. Excavation boundary reaches final size, and two inner rings and a central uplift have formed.
G. Ejecta continues to move beyond excavation and interior continues to oscillate, enlarging innermost ring and causing surge of ejecta from intermediate ring (Montes Rook Formation at Orientale).
H. Exterior deposits (Hevelius Formation at Orientale) mostly in place and two rings inside excavation boundary have frozen, but innermost ring continues to grow and center rises once again.
I. Innermost ring has grown to final size and central uplift relaxes into low, broad mound.
J. Final configuration.

those of the other groups; basins are not ranked within a group.

Counts of superposed craters, as described in the "Craters" section, are necessary for establishing relative age of many basins (fig. 6.29; Wilhelms, in press b). Statistics of craters ≥ 20 km are used in the counts because some smaller superposed craters of the original population have been obliterated on the older basins (fig. 6.17), and because many photographs are inadequate for distinguishing craters which record the time since the basin formed (primary craters superposed on the basin) from craters which do not (secondaries and buried primaries).

As many basins as possible are ranked by superposition relations. Basin ejecta can be recognized both from its distinctive texture and from subdual of the

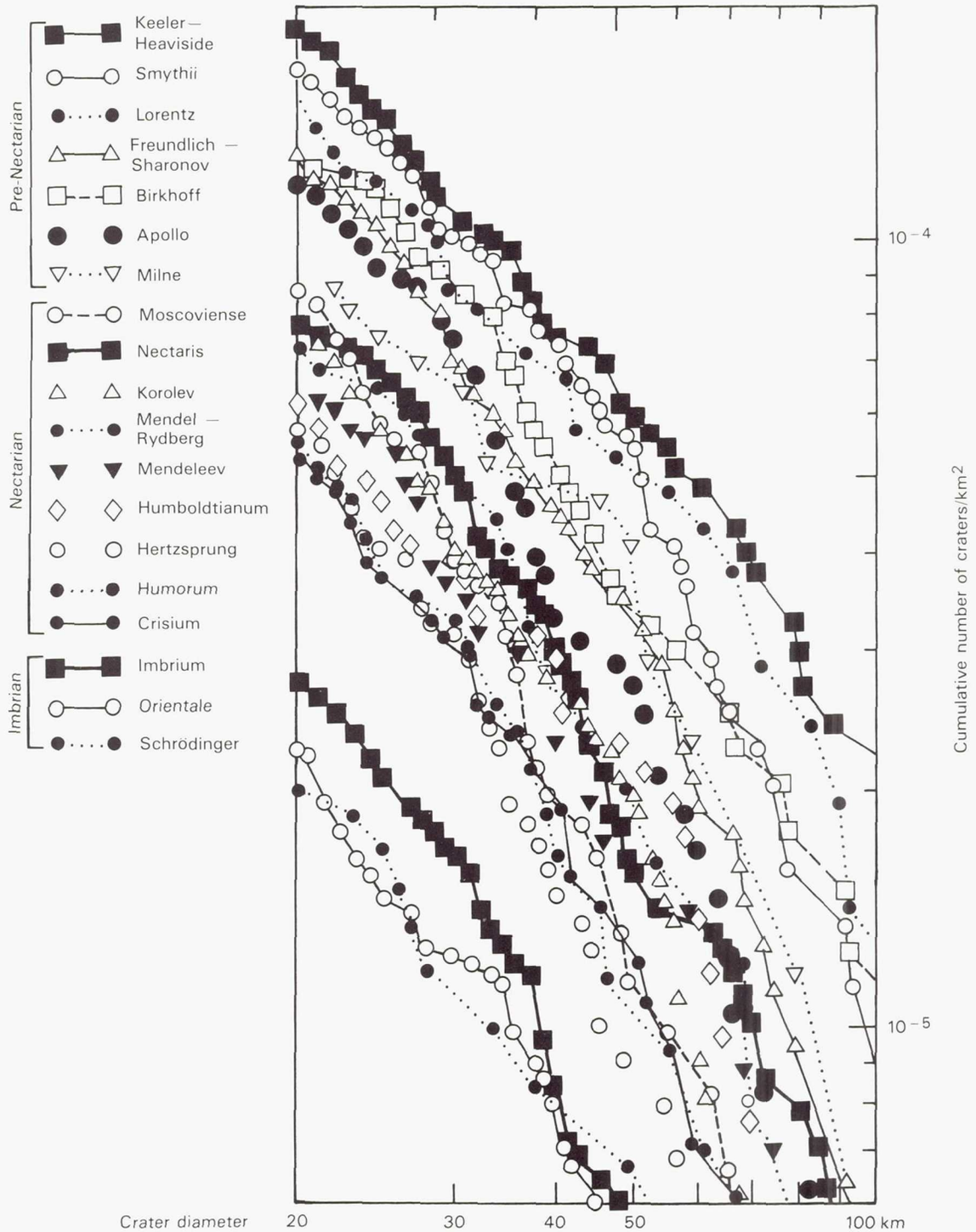

Figure 6.29. Size-frequency distributions of primary impact craters 20–100 km superposed on lunar basins (Wilhelms, 1979).

underlying topography. Although textures in the older and smaller ejecta blankets are indistinct, they are commonly detectable. The degree of obscuration of older craters provides clues to the presence of ejecta even where the textures are absent. Ejecta thins outward, so craters and other landforms close to the rim are buried more deeply than those farther away. The degree of obscuration varies at a given radial distance around a given basin, as it does around Copernicus-type craters, because of the lobate depositional pattern of ejecta (figs. 6.7A, 6.20). Heavy obscuration extends an average of one basin radius from a basin

rim. Geologic mapping is commonly required to find this obscuration pattern and rank the ejecta blankets stratigraphically. Craters are dated by morphology, and those too fresh to be modified by basin materials are distinguished from those which have lost some of their original, fine-scale features (fig. 6.16). In some cases, systematic obscuration was noted before the presence of a basin was detected from its rings.

Secondary craters extend the range to which superposition relations can be determined (fig. 6.30). Secondary craters surround all fresh, well-photographed craters and basins. Approximately similar but more degraded craters or subdued depressions around older basins, such as Freundlich-Sharonov (fig. 6.31), are assumed to have similar origins. Age sequences are clear when grooves radial to one basin transect part of another basin (fig. 6.31). The interpretation of the grooves does not matter for relative dating, provided they do not postdate the basin from which they radiate. The fact that they are synchronous with the basin is now believed to be well established by the morphologies of Imbrium sculpture and the Orientale secondary field.

Basins are increasingly numerous in successively older time-stratigraphic units. None are of Copernican, Eratosthenian, or Late Imbrian age. The three model basins—Orientale, Schrödinger, and Imbrium—are Early Imbrian. Nectarian basins and their deposits are much more widespread. They dominate the Moon's east limb region (Nectaris, Humboldtianum, Crisium; figs. 6.25, 6.27) and a broad belt of the far side (Moscoviense, Mendeleev, Korolev, Hertzsprung; figs. 6.22—6.24). On the near side, they are mostly obscured by Imbrium and Orientale deposits except in the southeast (Nectaris) and parts of the Humorum basin (figs. 6.19, 6.26, 6.27). Nectaris-basin deposits are exposed in an extensive area, so that crater densities and superposition relations can be determined relatively accurately. Frequencies and morphologies of superposed craters are important standards for discriminating other Nectarian units from pre-Nectarian units (figs. 6.17, 6.29).

Pre-Nectarian deposits are common in a broad strip between Nectarian deposits on the far side (fig. 6.31) and on the southern near side and east limb beyond the reach of the Imbrian and Nectarian deposits (figs. 6.19, 6.32). Pre-Nectarian and Nectarian craters are scattered randomly wherever not obscured by younger basin deposits. Most of the premare Moon is probably covered by basin ejecta (fig. 6.19).

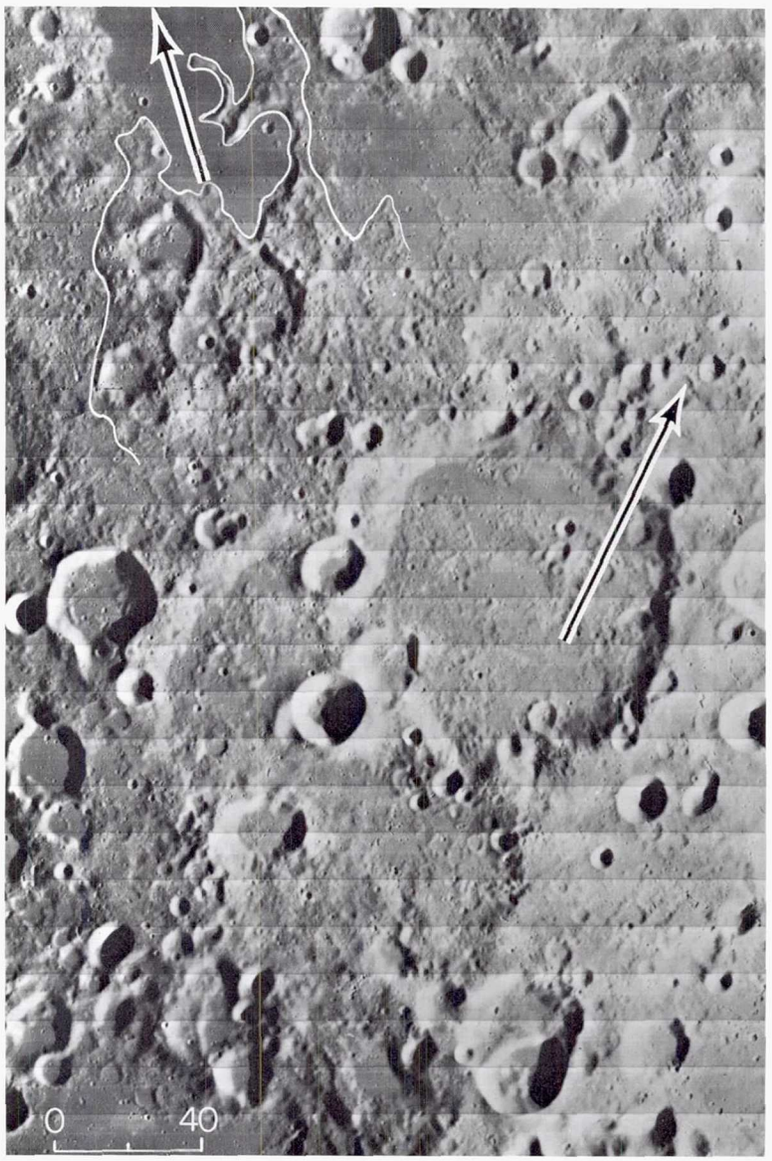

Figure 6.30. Secondary craters of Humorum basin (outline, basin centered 600 km in direction of left arrow) and Imbrium basin (left of right-hand arrowhead; basin centered 2500 km due north, direction of arrow). Right-hand arrow crosses rim of pre-Nectarian crater Wilhelm (107 km, 43°S, 21°W). After Wilhelms (1976). Orbiter 4 H-131.

The two largest pre-Nectarian basins are also the two largest geologic features of the Moon. The 2500-km South Pole-Aitken basin (Big Backside Basin) encloses a depression of the far side terra up to 5–7 km below the average lunar radius of 1738 km and is rimmed by some of the Moon's largest mountains (Howard et al., 1974; Stuart-Alexander, 1978; Wilhelms et al., 1979). It is also the site of about half of the far side's maria, which are contained in super-

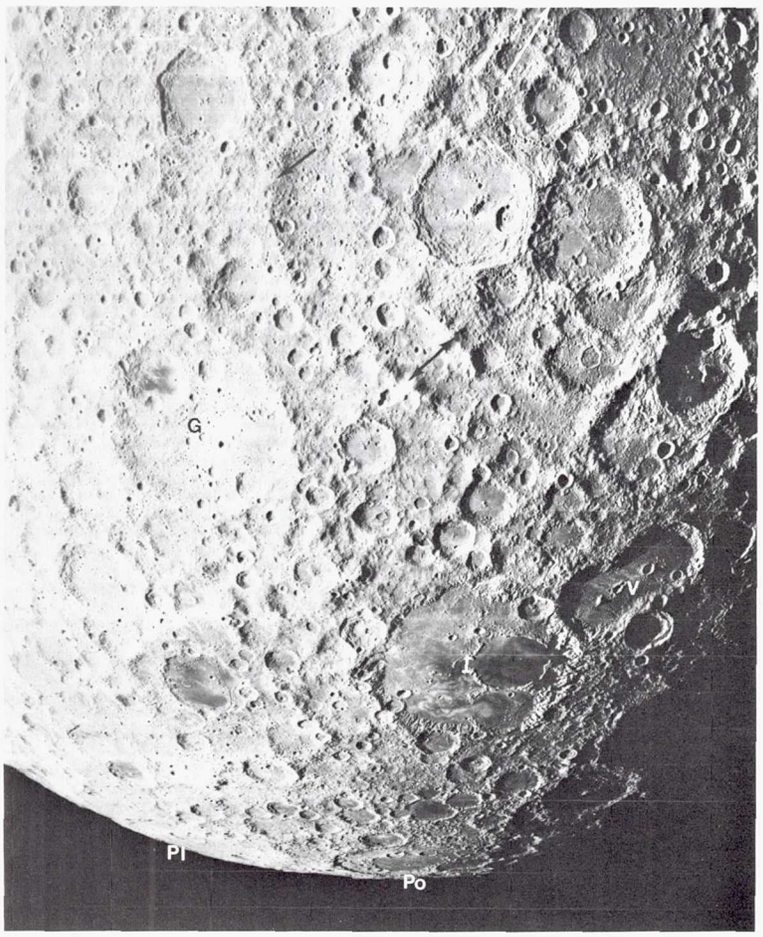

Figure 6.31. Pre-Nectarian basins and densely packed craters on lunar far side. Radial grooves of Freundlich-Sharonov basin (white arrow points to basin center), massifs of Keeler-Heaviside basin (black arrows), Ingenii basin surrounding Mare Ingenii (I), and smaller Planck (Pl) and Poincaré (Po) basins. Craters include Gagarin (G, 272 km, 20°S, 149°E) and Van de Graaff (V). Orbiter 2 M-75.

posed craters and small basins such as Apollo, Planck, and Poincaré. As drawn by Whitaker (1981), the near-side Procellarum basin is still larger, enclosing a geologically complex area 3200 km in diameter and centered at 23°N, 15°W. This basin, which Cadogan (1974) called Gargantuan and drew somewhat differently, accounts for many arcuate mountains of the near side and encloses about 80 percent of the Moon's maria. Ejecta of these two giant basins may cover most of the terrae, though the ejecta textures are not observed. Subsequent sections describe further major phenomena ascribable to the South Pole-Aitken and Procellarum basins.

TERRA BRECCIAS

Crustal Structure

A terra rock is both a sample of the lunar crust, which had an igneous beginning, and a sample of a stratigraphic deposit, which originated by impact. This dual origin may confuse the petrologist attempting to distinguish effects of the two processes and has led to an ambiguous nomenclature for lunar terra materials. Both phases in terra history are discussed here, with emphasis on the impact processes and lithologies.

The terra crust is crudely stratified. Uppermost is a regolith more than 5 m thick having seismic velocities of about 100 m/s (Cooper et al., 1974). Regoliths on both terrae and maria consist of loose fragments, breccias, glass droplets, and glass-welded aggregates, which are generated by innumerable small impacts from the underlying bedrock and from earlier regolith fragments (Shoemaker et al., 1969; Shoemaker and Morris, 1970; Heiken, 1975; Taylor, 1975, 1982; French, 1977; Cadogan, 1981). Regoliths contain meteoritic trace chemistry, solar-wind particles, cosmic-ray tracks, and other evidence of exposure to the space environment (Burnett and Woolum, 1977; Crozaz, 1977). Some are randomly structured but most consist of thin layers, each of which is part of the ejecta blanket of a small crater (Duke and Nagle, 1975).

The part of the subregolith bedrock accessible to study consists of much larger ejecta blankets generated by fewer and larger impacts. Each forms a laterally continuous bed of relatively coherent, lithologically related, brecciated material. The brecciated nature of the upper 2 or 3 km of the crust has led to the term "megaregolith" (Short and Foreman, 1972; Hartmann, 1973). This term is partly appropriate because regoliths and bedrock breccias both consist of fragmental materials generated by impact, but is not used here in order to stress the extent and continuity of the photogeologically detectable beds. The coarse-scale beds are probably interbedded with true regoliths that were formed by small impacts in the intervals between the major impacts.

Spacecraft exploration has provided some data on the layering, composition, and density of the deeper lunar interior, though all conclusions are tentative (fig. 6.33; summaries by Goins et al., 1979; BVSP, 1981, pp. 666–678; Taylor, 1982). The density of the terra crust is estimated at between 2.90 g/cm^3 and 3.05 g/cm^3, as compared with 3.34 g/cm^3 for the bulk

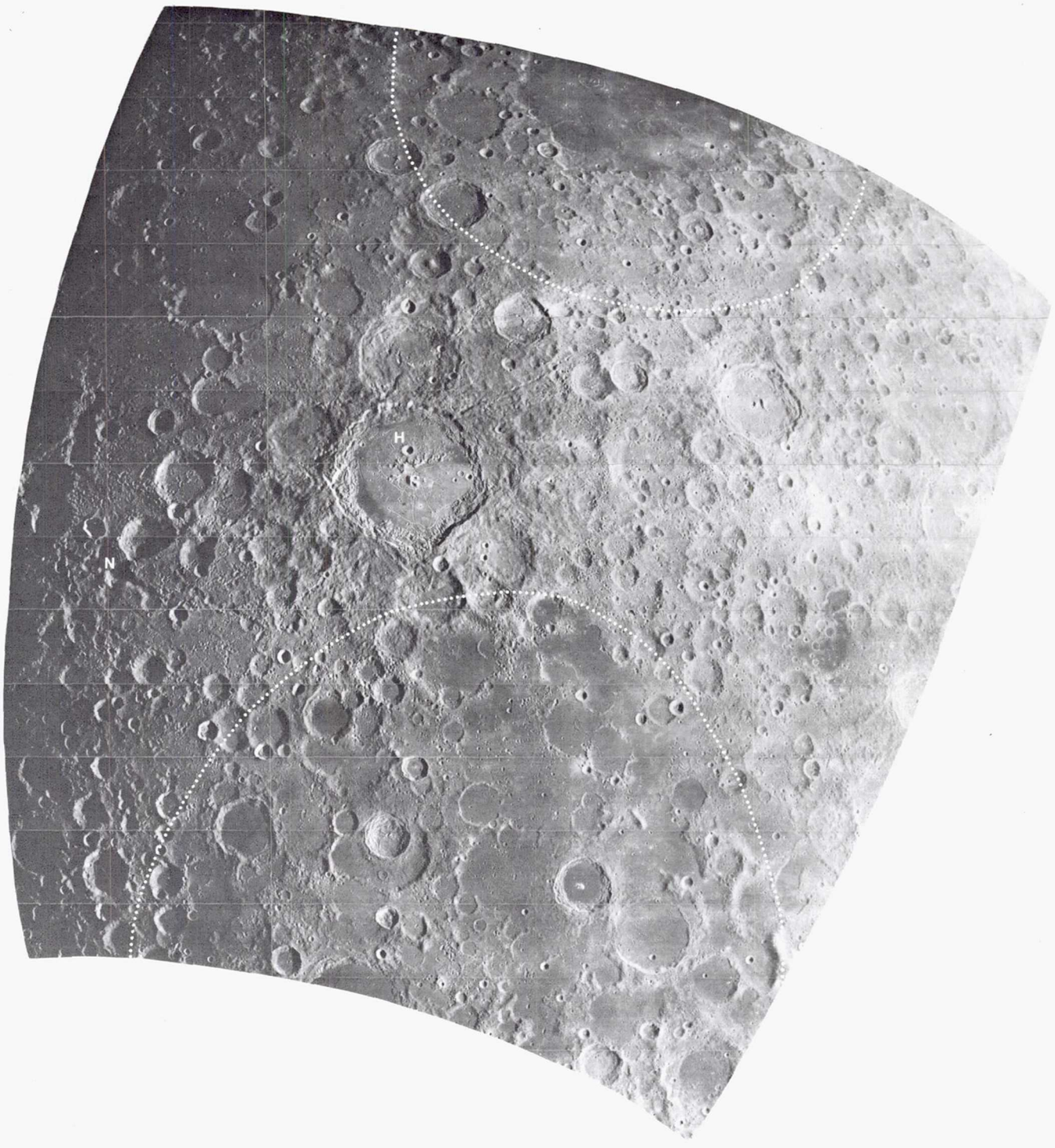

Figure 6.32. Dots indicate main rims of southern Smythii and northern Australe basins. Mare Smythii defines its basin and small mare patches help outline Australe. Crater Humboldt (H, 207 km, 27°S, 81°E) and radial grooves of Nectaris basin (N) are superposed on Australe basin. Orbiter 4 M-9.

Moon. Its average thickness is estimated as 74 ± 12 km (BVSP, 1981, p. 671), corresponding to 10 to 14 percent of the Moon's volume. The crust in the southwestern near-side (where most seismic data were collected) is estimated as between 45- and 60-km thick (Toksöz et al., 1974; BVSP, 1981, p. 669). Beneath the Apollo 16 site, it appears to be about 75 km, close to the lunar average (Goins et al., 1979). The far-side crust is thought to be thicker than the near-side crust, and a hemispherical dichotomy is generally assumed

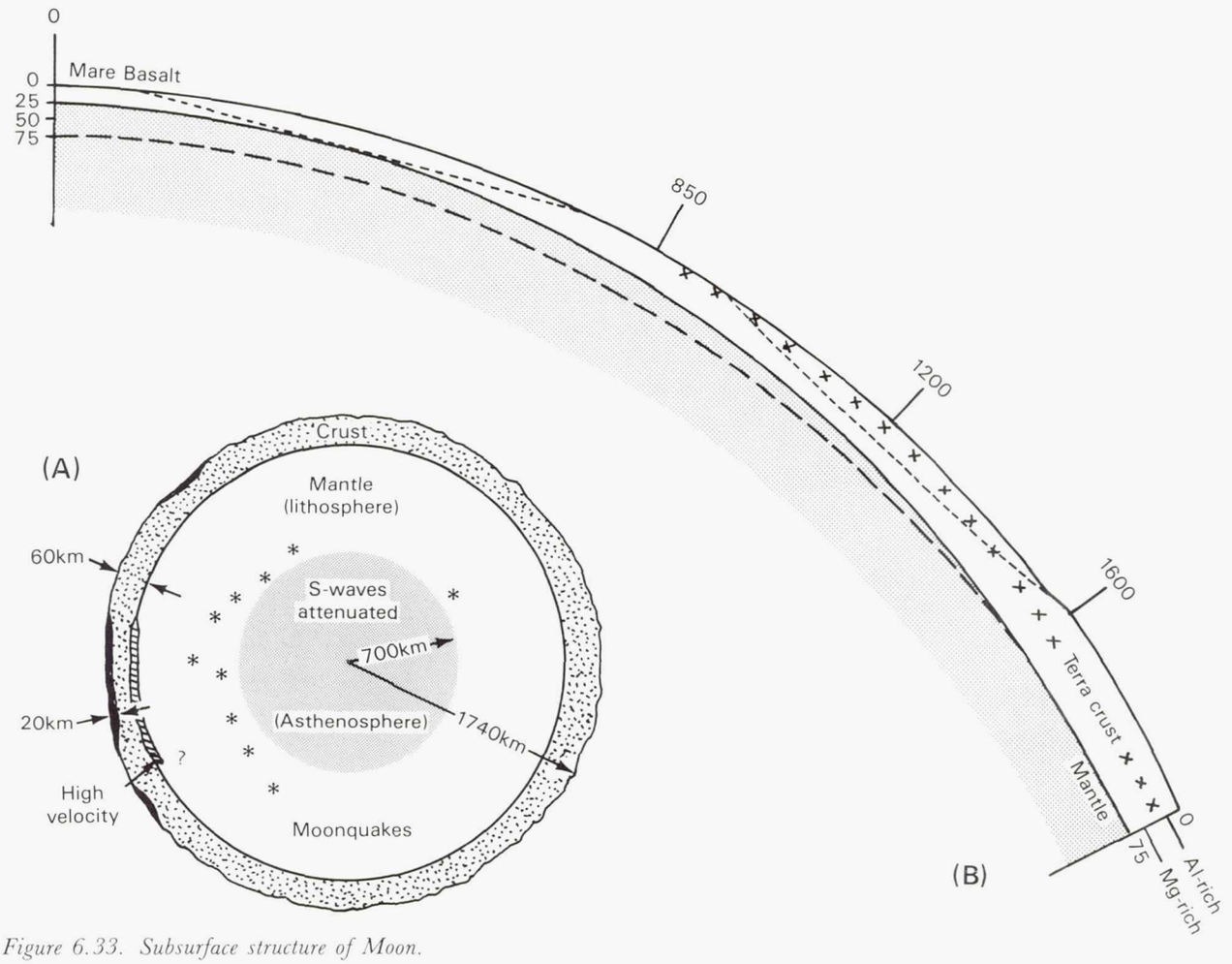

Figure 6.33. Subsurface structure of Moon.

A. Diagrammatic section of globe (Toksöz et al., 1974). Crustal thickness exaggerated. Since publication of this interpretation, mare basalts (black) have been shown to be much thinner than 20 km (see "Maria").

B. Detail of crust and upper mantle showing variable crustal thickness beneath and near Procellarum basin (center at 0). True scale and curvature. Vertical scale refers to depth beneath average lunar terra surface, radius 1738 km. Dashed line at 75 km depth indicates estimated position of mantle-crust boundary before Procellarum basin formed. Present crustal thickness of about 75 km near rim of Procellarum basin (1600-km radius) based on estimates for Apollo 16 region (Nakamura, 1981). Thickness averaging 50 km between rings of 850- and 1200-km radius based on seismic data from southern Oceanus Procellarum (Koyama and Nakamura, 1979). Thickness of 25 km beneath central basin is an upper limit derived by assuming another 25-km decrease between troughs. Dotted lines diagrammatically represent excavations by two later basins; basins of same size may reach mantle in central Procellarum but excavate only crustal material in outer troughs.

Hypothetical transition zone between concentrations of Mg-rich rock (lower crust) and Al-rich rock (upper crust) marked by x's. KREEP possibly also concentrated in lower or lowermost crust. Procellarum basin has stripped off highly aluminous material and exposed Mg-suite and KREEP. Composition of later basin ejecta depends on which remaining levels are intersected by the basins.

(Kaula et al., 1974; Bills and Ferrari, 1977; Haines and Metzger, 1980). Where measured, the far-side surface generally lies higher above the Moon's center of mass than the near-side surface. However, it can be suggested that the Procellarum and South Pole-Aitken basins may exert greater control over crustal thickness and surface elevation than does a hemispherical factor (fig. 6.33B).

Seismic velocities increase from about 300 ± 50 m/s to about 6 km/s at 20 or 25 km depth, then rise further to about 7 km/s and remain relatively constant to the base of the crust. The 20–25 km discontinuity may mark either a physical difference (cracks and pores open above, closed below) or a chemical difference (less dense above, more dense below) (Todd et al., 1973; Herzberg and Baker, 1980; Taylor, 1982).

Composition and Mineralogy

Lunar compositions are usually compared with chondritic meteorites, assumed to represent the primordial composition of the solar system (table 6.5). Sampling results starting with the Apollo 11 mare-basalt analyses showed strong depletion of volatile elements (Na, K, Pb, Rb, many trace elements, and H_2O) relative to chondrites (Wetherill, 1971). Refractory elements (Al, Ba, Ca, Hf, Sr, U, Th, Zr, rare earths, and others) seemed correspondingly enriched. Depletion of volatiles still seems likely to most investigators (Warren and Wasson, 1979a; Wood, 1979; Taylor, 1982). Data from Surveyor (Turkevich, 1971), returned-sample analyses, and orbital geochemical sensing (see "Maria") combine to indicate a terra composition high in Al, accounting for the relatively low terra density. Taylor (1982) estimates the Al_2O_3 content of the terra crust to be about 25 percent, as opposed to ≤ 11 percent for the most common types of mare basalt (see "Mare Basalts"). The orbital geochemical instruments suggest that the terra is richer in Al on the far side and on other terrain outside the Procellarum basin, than over that basin (Adler et al., 1973; Hubbard et al., 1978). The impact mixing characteristic of the Moon assures that the few samples (12 including three analyzed remotely by Surveyors 5–7) are more nearly representative than would be the same number of samples from Earth.

Starting with the mare landing by Apollo 11, all the sample-return spaceflights contributed to the present picture of terra chemistry and petrology. The otherwise basaltic Apollo 11 regolith included small fragments of plagioclase or plagioclase-rich rock. An impact into the terra ≥ 45 km away presumably had ejected the fragments, which were called anorthosite and anorthositic gabbro (Wood et al., 1970). Similar fragments were found in the Apollo 12 regolith. The much larger Apollo 15 collection from the Apennine front provided abundant samples of these and related rocks. The regolith sample returned by Luna 20 from the Crisium basin rim also added to understanding of the feldspathic terra materials (Prinz et al., 1973; Taylor et al., 1973). The words anorthosite, norite, and troctolite are used in various combinations, as adjectives or nouns, to describe rocks with different proportions of the three major minerals (fig. 6.34, Prinz and Keil, 1977; Stöffler et al., 1980). Accordingly, the rock suite has been given the acronym ANT. ANT is the predominant material of the lunar terra crust.

The three major lunar terra minerals (plagioclase, low-Ca pyroxene, olivine; Frondel, 1975; Smith, 1974; Smith and Steele, 1975; Cadogan, 1981; Taylor, 1975, 1982) commonly appear as petrographically identifiable minerals (modes). However, a source of constant confusion for the nonspecialist reading the lunar petrologic literature is that the ANT rock names are commonly used as normative names signifying only the bulk chemical composition of rocks, including glasses and complex breccias. In other words, nonigneous rocks are given igneous rock names. In ANT

Table 6.5. Estimated Compositions of Moon Compared With Cl Meteorites and the Parent Body of Eucrite Meteorites

Oxide[1]	Bulk Moon[2]	Terra crust[3]	Mare basalts[4]	Cl[5]	EPB[6]
SiO_2	43.3–48.7	45.0	37.8–48.8	33.3	39.0–46.0
TiO_2	0.2–0.4	0.6	0.4–13.0	0.1	0.1–0.2
Al_2O_3	3.7–7.6	24.6	5.3–14.4	2.4	2.4–3.1
FeO	11.3–13.9	6.6	10.7–22.3	34.0	14.4–28.3
MgO	25.3–33.4	6.8	5.7–20.0	23.4	28.5–32.5
CaO	3.4–6.1	15.8	6.3–12.5	1.9	1.2–2.5
Na_2O	0.05–0.15	0.5	tr–1.0	1.1	0.04–0.07
K_2O	$\sim$0.01	0.1	tr–0.3	0.1	$\lesssim$0.01
Cr_2O_3	0.3–0.4	0.1	0.2–0.9	0.5	0.5–0.8

NOTES:

1. Weight percent. Other elements given by BVSP (1981) and Taylor (1982).
2. Range of estimates from Taylor (1982, table 8.2) and three models given by BVSP (1981, tables 4.3.2e and 4.5.8).
3. Taylor (1982, tables 5.5 and 8.2).
4. Reference suite of mare basalt samples (BVSP, 1981, table 1.2.9.1).
5. Type Cl carbonaceous chondrite, excepting volatiles (Taylor, 1982, table 8.2).
6. Eucrite Parent Body, a presumed asteroid believed to be source of eucrite meteorites and which may be the closest compositional relative of Earth and Moon. Range for four model estimates (BVSP, 1981, table 4.3.2e).

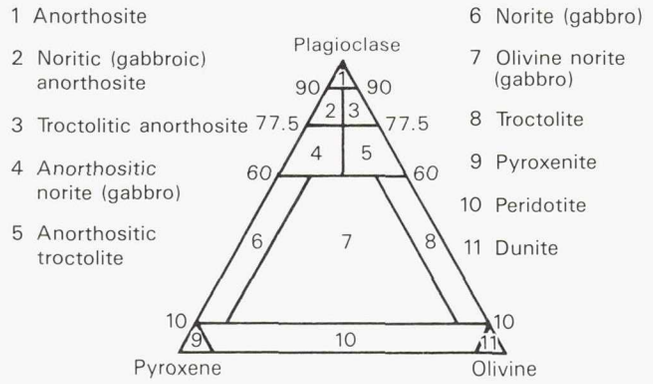

Figure 6.34. Terminology of ANT suite (Stöffler et al., 1980). Each rock term is based on contents of the three minerals shown at the corners of the diagram. Compositions are normative, referring to chemistry and not necesssarily to actual crystals of the minerals. Norites and gabbros distinguished according to whether pyroxene is low in Ca (orthopyroxene; norites) or high in Ca (clinopyroxene; gabbros).

terms, the average normative composition of the lunar terra is an anorthositic norite dominated by plagioclase and low-Ca pyroxene. The terms anorthosite and highland basalt are commonly but incorrectly used as synonyms for the average terra composition.

A few small samples of pristine igneous rocks have been found in impact breccias (Norman and Ryder, 1979; Warren and Wasson, 1979b). They suggest that two major magma systems, an anorthositic and an Mg-rich suite, formed the early crust. These materials have been intensively reworked and mixed by impacts.

Some important deductions were made even before these pristine components were identified. A major key is the rare earth element europium, which is underabundant in mare basalts and overabundant in terra plagioclase, relative to chondritic abundances. Even before the terrae were visited, the complementary Eu anomalies were observed in the Apollo 11 regolith and ascribed to extensive, early differentiation of primitive lunar material into the plagioclase-rich terra crustal material and the more mafic source of the mare basalts (Smith et al., 1970; Wood et al., 1970; Taylor, 1975). This early differentiation is commonly ascribed to a "magma ocean" (Wood, 1975a,b; Walker et al., 1975) that did not solidify until about 4.4 to 4.2 aeons ago, or 0.15 to 0.35 aeons after the Moon's origin (Nunes et al., 1975; Herbert et al., 1977; Carlson and Lugmair, 1979, 1981). This simple picture has been modified (Warren and Wasson, 1980; James, 1980), but remains a leading working hypothesis for the differentiation of the crust and mare-basalt source rocks (Taylor, 1982).

Another compositional class of terra material also appeared first as a fragment at the Apollo 11 site, then more abundantly in the Apollo 12 regolith, and very abundantly in the nearby Apollo 14 regolith and bedrock breccias; that is, KREEP (K = potassium, REE = rare earth elements, P = phosphorus; Hubbard et al., 1971). These and other trace elements characteristic of KREEP (for example, U, Th, Zr, Ba, Rb) do not easily enter the most common lunar minerals and so are concentrated either in the first partial melts or in the last residual liquids of fractionating magma systems (the magma ocean or other, smaller, later systems; Taylor, 1975, 1982; Irving, 1975, 1977; Meyer, 1977; Warren and Wasson, 1979c). The trace elements U, Th, and ^{40}K make KREEP much more radioactive than ANT, and KREEP was detected from orbit by gamma-ray spectrometers carried on Apollos 15 and 16 (Metzger et al., 1973, 1977). In keeping with its surface abundances, the orbital data reveal most KREEP in the vicinity of Mare Imbrium and Oceanus Procellarum, both in the Imbrium basin materials and in units derived therefrom. KREEP is generally intermediate in alumina content between the terra and mare materials. It has been plagued with synonyms (Taylor, 1975). From the Apollo 14 site it got the name Fra Mauro basalt, but it is neither always from the Fra Mauro Formation or always basalt in the sense of an igneous rock emplaced by volcanism.

Low-K, medium-K, and high-K varieties are recognized (Taylor, 1975). Low-K KREEP was found at most sampling sites, and has been considered the second most abundant crustal material after the ANT suite (Taylor, 1975). It may have been concentrated near the base of the crust or elsewhere, or may have been assembled by impacts from higher-grade KREEP and ANT (Reid et al., 1977). Medium-K KREEP appeared at the Apollo 14 site and in the Apollo 15 regolith (Irving, 1977). High-K KREEP was collected in small quantities by Apollo 12 and in large quantities by Apollo 14. Model ages suggest origin of most or all sampled KREEP at about 4.36 aeons (Carlson and Lugmair, 1979). Only minor terra compositions other than ANT and KREEP have been identified.

A crude chemical stratification of the crust (Ryder and Wood, 1977; Warren and Wasson, 1980) may be supported by the surface distribution of chemical types. The Procellarum (fig. 6.33B) and South Pole-Aitken impacts may have stripped off shallow, Al-rich material (Apollo 16 anorthositic samples) and exposed

a deeper KREEP-rich zone (Apollos 14, 15 and 17). Few or no mantle materials have been found in the sample collections except in recycled, remelted form as mare basalts. Some ultramafic materials have been considered mantle rocks, but most evidence indicates that they formed in the crust (e.g., Warren and Wasson, 1979a; Herzberg and Baker, 1980). Thus not even the giant basins seem to have had deep excavated cavities.

Texture and Structure

General features and nomenclature

Most terra samples are complex breccias (James, 1977; Stöffler et al., 1979, 1980). The majority are polymict (contain several components with different compositions), but some are monomict (one component) or dimict (two components). Terra breccias are bedded, banded, and lensed at all scales from outcropping ledges to small clasts. They display a wide variety of textures, grain and clast sizes, and a range of matrices from coherent, glassy, and dark to friable, fragmental, and light (figs. 6.35—6.37). The literature commonly distinguishes between "breccia" and "melt rock" in reference to individual samples, but clast-free melts and melt-free breccias were probably mechanically separated from polymict breccias by impacts in the regolith. An example is a white boulder of impact melt with an igneous-appearing texture and a uniform composition (samples 68415 and 68416).[2] Examples of dimict rocks are "black and white rocks" at the Apollo 16 site, whose dark melt rock and friable, feldspathic clastic material display mutual intrusion and inclusion relations (James, 1977, 1981; Stöffler et al., 1979, 1981). One expects such intermingling from the cratering process (fig. 6.4). Polymict breccias (fig. 6.36) defy ready categorizing, but Stöffler et al. (1980) have provided a useful classification and a much needed (and long) list of synonyms from earlier literature.

Some order relative to the varying shock intensities during cratering appears among the complexities. In some breccias, both clasts and matrices consist of friable, fragmental, usually feldspathic materials, and impact melt appears only as clasts (e.g., North Ray

Figure 6.35. A KREEP-rich impact-melt rock (sample 14310) collected from Fra Mauro Formation near Apollo 14 landing site.

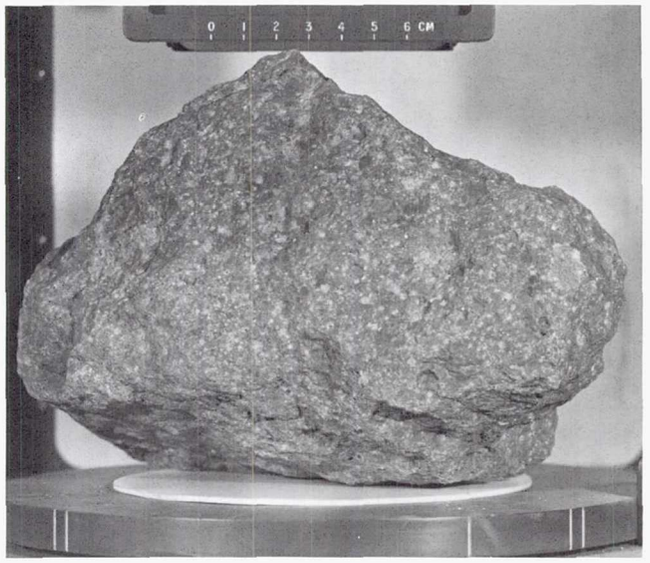

A. "Mug shot" of entire sample after arrival from Moon. Small white spots are "zap pits" made by micrometeoroid impacts. Surface otherwise nearly featureless. (Courtesy Lunar and Planetary Institute, Houston.)

B. Thin section of sample 14310,34 showing textures typically associated with igneous rocks, including subophitic texture (s; compare fig. 6.65B). Field of view 1.5 mm; transmitted light; crossed polarizers. (Courtesy P. D. Spudis.)

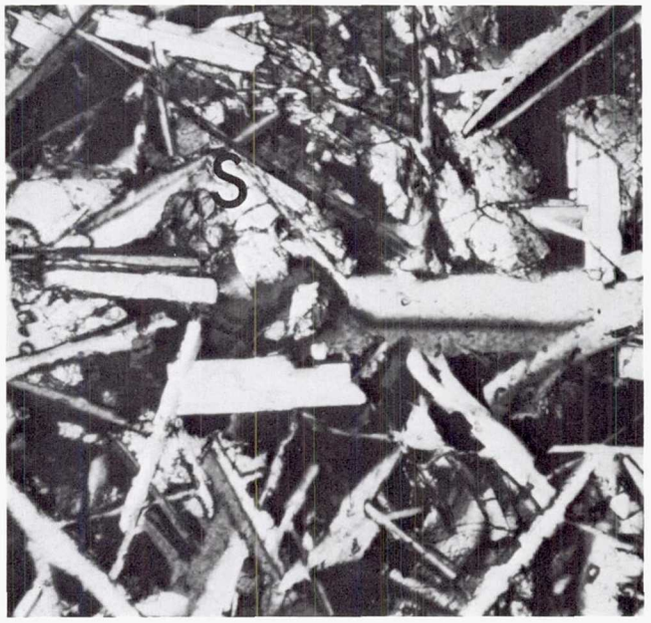

[2]Apollo samples are given five-digit numbers beginning with a code for the mission number: 10 = Apollo 11; 12 = Apollo 12; 14 = Apollo 14; 15 = Apollo 15; 6 = Apollo 16; 7 = Apollo 17. Some Apollo 15 and almost all Apollo 16 and 17 numbers have the collection station as the second digit, except that Apollo 16 station 11 is designated by 7 and station 13 by 3. For example, sample 68415-68416 was collected by the Apollo 16 astronauts at station 8 (South Ray crater ejecta) and sample 67015 at station 11 (on the rim of North Ray crater). Commas and additional digits following the five-digit number denote splits of the sample. Cadogan (1981, pp. 123–134) summarizes sample-handling procedures.

Figure 6.36. A feldspathic fragmental breccia (sample 67015) collected from rim of North Ray Crater, superposed on Descartes Formation, north of Apollo 16 landing site.

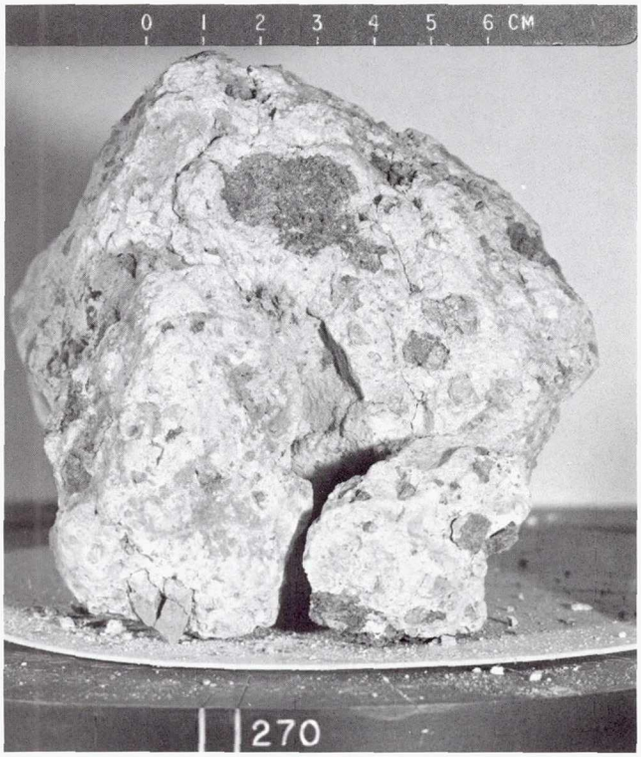

A. "Mug shot" of entire sample. Melt-rich clasts are dark. Light material includes feldspathic matrix and clasts. (Courtesy Lunar and Planetary Institute, Houston.)

B. Thin section of sample 67015,88. Matrix is seriate-textured, cataclastic plagioclase with minor pyroxene. Clasts include glassy-matrix breccia (g), clast-laden, crystalline, impact-melt breccia (m), and numerous monomineralic plagioclase clasts (p). Field of view 1.5 mm; transmitted plane-polarized light. (Courtesy P. D. Spudis.)

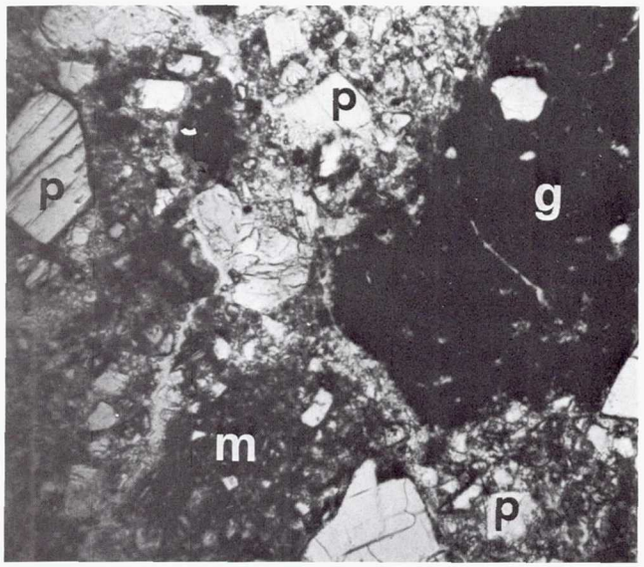

crater samples, Apollo 16, fig. 6.36; Stöffler et al., 1981). Presumably these breccias were formed near the walls or floor of a crater or basin and were ejected in the later stages of cratering. The melt clasts may have formed during the event that ejected and assembled the breccias, as in the suevite at the Ries; or may have been acquired from an earlier deposit, as were materials in the unshocked Bunte Breccia of the Ries (Stöffler et al., 1979).

Evidence of high shock grades abounds in lunar terra breccias. Many samples contain matrix material that crystallized in the fashion of an igneous rock but from an impact melt (figs. 6.35, 6.37). Some, like samples 68415-68416 or the Apollo 14 sample 14310 (fig. 6.35), are clast-free and closely resemble endogenic igneous rocks. Much more common are *fragment-laden* or *clast-rich* impact melts containing rock and mineral debris in chaotic mixtures evocative of their origin. Textures of impact melts appear to have been influenced by clast content (Nabelek et al., 1978). Those with few clasts commonly have *ophitic* or *subophitic* textures indicative of relatively few nucleation sites (fig. 6.35). *Poikilitic* textures are considered a sign that many minute clasts were incorporated in impact melts (fig. 6.37). Melts with few clasts may

Figure 6.37. Thin section of sample 65015,77, a poikilitic impact-melt rock from Apollo 16 landing site. Pyroxene "oikocrysts" (o) poikilitically enclose plagioclase "chadocrysts" (c) and plagioclase clasts (p). Compare fig. 6.1E. Field of view 1.5 mm; transmitted light; crossed polarizers. (Courtesy P. D. Spudis.)

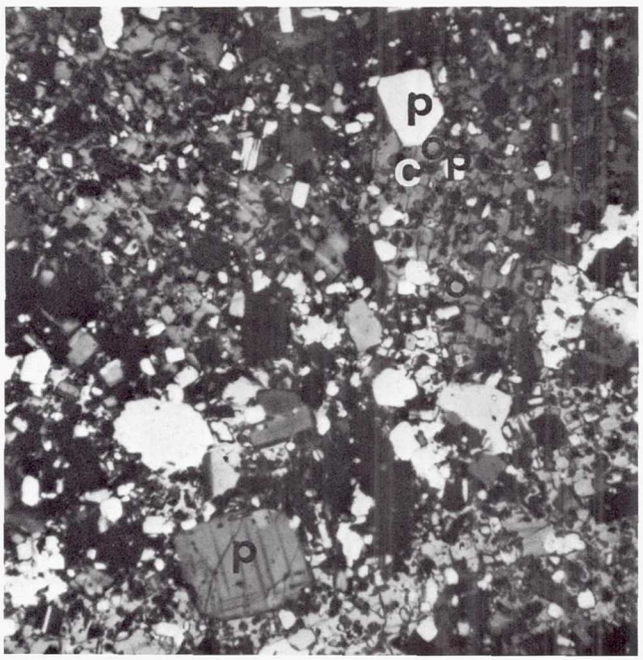

have formed closer to the impact point than melts with many clasts (Stöffler, 1981). Finally, there are *granoblastic* or granulitic textures indicating metamorphism after emplacement (Taylor 1982).

Assembly and emplacement

The question of how many events are required to make the observed breccias is of general interest to lunar geology. The first studies of terra breccia samples showed that they have a complex texture wherein clasts in breccias themselves consist of breccias. This relation was interpreted as the result of multiple brecciation events (Wilshire and Jackson, 1972). A basin-scale impact on any part of the present and past Moon, except perhaps on a thick mare deposit, would redistribute overlapping ejecta blankets consisting of already complex breccias (fig. 6.19; Eggleton and Offield, 1970). Almost any impact would redistribute already complex interiors and deposits of craters. Such recycling could be repeated many times. Regoliths would be melted and recycled. Some impact targets would contain beds and dikes of mare or nonmare basalts. Any new deposit would be a complex mixture of all these components.

Another complicating factor is that secondary impacts can form a combined deposit of primary and secondary ejecta (Oberbeck, 1975). Such deposits would be identical in general character to a primary-ejecta deposit composed of pre-existing complex materials.

During study of the later collections of terra breccias, the likelihood emerged that great complexities can also arise in a single large impact (Simonds, 1975). Materials from all parts of the excavation, from the totally melted and homogenized to the unshocked, are thoroughly mixed during cavity growth, shearing from the walls, ballistic flight, and flow along the surface (fig. 6.11; Wood, 1975c). Matrices may be broken after quenching and incorporated as clasts in other matrices of the same deposit. Heterogeneities in thermal metamorphism and annealing also arise even after deposition because of sharp thermal gradients in the cooling melt (Simonds, 1975; Simonds et al., 1976).

Hopes for distinguishing the number of impacts in a breccia deposit's history rest mostly on analysis of the impact melts. Similarity of melt compositions throughout a deposit suggests origin in a single melt, because impact melting may homogenize target chemistry near the impact zone (Grieve and Floran, 1978). Melt sheets can theoretically be distinguished by their contents of *siderophile elements,* which accompany metallic Fe in the geochemical cycle. Highly siderophile elements (for example, Au, Ge, Ir, Ni, Os, Re) are thought to come from iron and chondritic meteorites, because silicate planetary crusts should be depleted in elements which migrated to the core along with the Fe.[3] Each meteorite and therefore each melt sheet would presumably have a unique composition (Morgan et al., 1977). The converse, however, is not necessarily true; diverse compositions of major or siderophile elements do not necessarily indicate multiple melt sheets. Only the totally melted parts of the internal melt sheets of craters are sufficiently homogenized to retain the distinctive geochemical signature for that event (Grieve and Floran, 1978). Ejected melts may be incompletely melted and therefore diverse in composition.

The melts are crucial to the dating of deposits. The effects of impact on isotopically determined ages are uneven. The impact melts found in any deposit are likely to have inherited isotopic and chemical compositions from earlier events (impact brecciations, impact melting, endogenic melting). Impacts heat only part of the target materials sufficiently to completely reequilibrate the Ar, K, Rb, and Sr isotopes used in dating lunar stratigraphic deposits (Shoemaker et al., 1963; Kirsten and Horn, 1974; Turner, 1977). Ages spreading over 300 million years were found in one rock (Jessberger et al., 1977). The best hope of identifying times of impact is to perform many analyses on melts (not combined with clasts as has often been done) and seek the youngest cluster of ages (Jessberger et al., 1977). This age will approximate the age of the deposit, provided the melts are actually part of it and were not introduced by a later impact.

In my opinion, all samples of terra breccias were emplaced in deposits of basins. The following four sections explore how the lithologies and absolute ages of the samples may be related to the morphologies and relative ages of the photogeologic units from which they were obtained.

Fra Mauro Formation (Apollo 14)

The first basin ejecta blanket discovered by mapping was the Fra Mauro Formation. First called the

[3]The relation to meteorites of the highly siderophile element, iridium, has recently been the center of much interest in terrestrial geology and biology. Strong Ir anomalies have been discovered in several places in the transition strata between the Cretaceous and Tertiary Systems, suggesting that a large impact struck Earth at that time and somehow caused the extinction of large-bodied Mesozoic species such as most dinosaurs (Alvarez et al., 1980).

Imbrian system, or the Apenninian series, it was recognized as similar to crater blankets by Shoemaker and Hackman (1962), and is taken as the dividing horizon between pre-Imbrian and post-Imbrian materials—a role predicted for Imbrium basin ejecta by Gilbert (1893). Appreciation of the distinctiveness of the Fra Mauro Formation persisted during the planning stages for Lunar Orbiter and Apollo exploration, and a landing site for Apollo was chosen near its type area (figs. 6.1C, 6.38, 6.39). First Apollo 13 and then Apollo 14 were scheduled to collect samples of this important rock unit. The returned materials were expected to yield the age of the Imbrium basin, to provide samples of the deep lunar crust or mantle, and to reveal something about the mechanism of emplacement of lunar basin deposits (Eggleton and Offield, 1970).

The samples were returned to Earth in February 1971, but controversy about their significance persists. They are richer in KREEP than any other lunar sample collection. Alternative views are that a KREEP-rich layer deep in the crust was tapped by this largest sampled basin (Ryder and Wood, 1977); that volcanic KREEP was reejected by Imbrium (Wood, 1972; Cadogan, 1981); and that KREEP's distribution in the Moon is local and laterally variable (Wetherill, 1981). The Imbrium basin formed inside the huge pre-Nectarian Procellarum, or "Gargantuan" basin (Cadogan, 1974; Whitaker, 1981). Therefore, the Procellarum basin seems a likely cause of KREEP localization, either because it served as a receptacle for volcanic KREEP (Cadogan, 1974) or because it removed much of the crust that overlay deep, KREEP-rich zones (fig. 6.33).

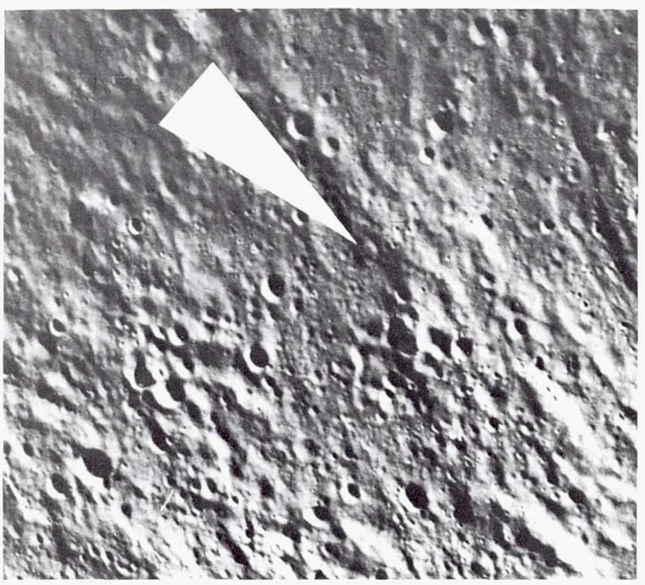

Figure 6.38. Apollo 14 landing site. Arrow (12 km long) indicates Cone Crater (370 m; barely visible); right edge of arrow oriented same as arrow in figure 6.1C and points away from center of Imbrium basin; Imbrium rim (Montes Carpatus) 550 km north of Cone Crater. Hummocky ridges radial to Imbrium; they are intrinsic depositional topography of Fra Mauro Formation. Apollo 12 H-7597.

The processes that emplaced the samples remain controversial despite the clear photogeologic stratigraphy and setting of the Fra Mauro Formation. The largest rocks were collected from ejecta of the 25-million-year old (Arvidson et al., 1975), 370-m wide crater known as Cone Crater (figs. 6.39, 6.40). They grade from clast-free impact melts to melt-rich breccias heavily laden with clasts (Chao, 1973). Some of the breccias are friable, but coherent matrices, either crystalline or aphanitic, are more common. As mentioned, their complexity has been ascribed to reworking of similar, previously brecciated blankets that lay in the Imbrium target area before being ejected by the Imbrium impact (Wilshire and Jackson, 1972). Some of the clast-free melt rocks have been thought volcanic, but are now generally considered to be impact-melt rocks (fig. 6.35; James, 1973). Many of the textures were initially ascribed to metamorphism and annealing by heat generated in the Imbrium impact and retained in the ejecta blanket (Wilshire and Jackson, 1972; Warner, 1972). Crystallization in igneous fashion from impact melts is now thought more important in producing the textural, compositional, and mineralogical relations (Ryder and Bower, 1976).

The impact melts are the focus of a debate about whether the Fra Mauro samples consist of (1) primary ejecta of Imbrium (Eggleton and Offield, 1970; Wilshire and Jackson, 1972; Wilhelms, in press b), or (2) a mixed deposit consisting partly of material at or near the Apollo 14 site and reworked by Imbrium secondary impacts (Morrison and Oberbeck, 1975; Stöffler et al., 1976; Head and Hawke, 1975; Simonds et al., 1977). The proponents of this "local" origin, cite rarity of impact melting in the Ries Crater ejecta and the inferred confinement of melt-sheets to the interiors of Canadian Shield craters (the rims have been obliterated by erosion) as evidence that abundant impact melt of Imbrium origin should not be present at the Apollo 14 site. They also believe that the Fra Mauro melt rocks are too diverse in composition to have originated in a single impact, because individual Canadian Shield melts show little variability.

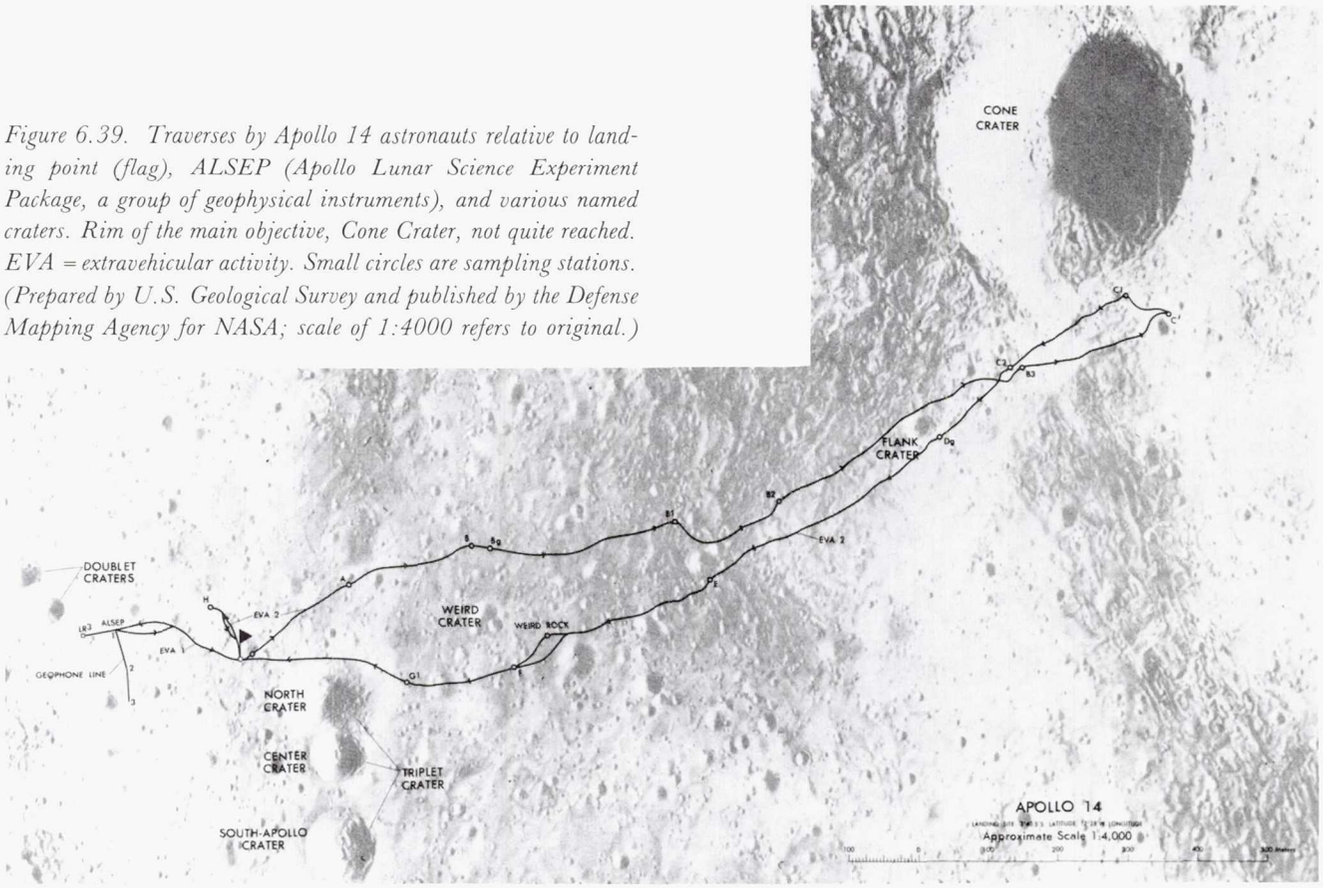

Figure 6.39. Traverses by Apollo 14 astronauts relative to landing point (flag), ALSEP (Apollo Lunar Science Experiment Package, a group of geophysical instruments), and various named craters. Rim of the main objective, Cone Crater, not quite reached. EVA = extravehicular activity. Small circles are sampling stations. (Prepared by U.S. Geological Survey and published by the Defense Mapping Agency for NASA; scale of 1:4000 refers to original.)

I believe that the original primary impact interpretation is more probable because the Fra Mauro is more like the thick ground-flow deposits of the Orientale basin (fig. 6.20D) than like the Orientale secondary deposits, which are discontinuous and traceable to visible secondaries (fig. 6.20E). Secondary craters are deeply buried both by the Fra Mauro Formation at the Apollo 14 site (fig. 6.38) and by the inner deposits of Orientale. Some local material originating outside the basin may have been incorporated either by ballistic re-excavation (Oberbeck, 1975) or during ground flow (Chao, 1977), but primary ejecta must dominate such coarsely textured, thick deposits.

Furthermore, each of the theoretical arguments against abundant Imbrium melt at the Apollo 14 site is debatable (Wilhelms, in press b): (1) The Canadian Shield impacts homogenized the target materials by total melting near the impact zone, but incompletely digested materials partly preserve diverse original target compositions. Preimpact materials could hardly have been totally mixed over the entire target area of a large lunar basin. From this viewpoint, the Imbrium melt compositions (Simonds et al., 1977) seem, in fact, to be surprisingly uniform. (2) The Ries Crater did not form coherent melt sheets because its target material contained volatile materials, whose expansion disperses silicate melts (Kieffer and Simonds, 1980); and volatiles are absent on the Moon. Moreover, the Ries at 25 km is at least 50 times smaller than Imbrium. (3) Abundant ejected melt is observed on the Moon (a) as fissured pools on the Orientale flank (Moore et al., 1974); (b) on rims of all fresh craters larger than a few kilometers wide (fig. 6.7C; Howard and Wilshire, 1975; Hawke and Head, *in* Roddy et al., 1977); (c) probably as lobes of fluid, admittedly not necessarily molten, material segregated from the Hevelius Formation at distances from Orientale equal to distances of the Apollo 14 site from Imbrium (Eggleton and Schaber, 1972; Hodges et al., 1973; Moore et al., 1974; Wilhelms et al., 1979); and (d) probably on the floors of some secondary craters distant from their Orientale sources (Moore et al., 1974). (4) Large impacts may generate proportionally more incomplete melt (Baldwin, 1963) than small impacts, which result in only small amounts of total melt (O'Keefe and Ahrens, 1975). (5) Deep materials on the Moon at the time of the basin impacts may have been close to melting temperatures as a result of postulated high heat flows at that time (Wood, 1975c). It seems evident that much impact melt could indeed have been created by and ejected from Imbrium and deposited at the Apollo 14 site.

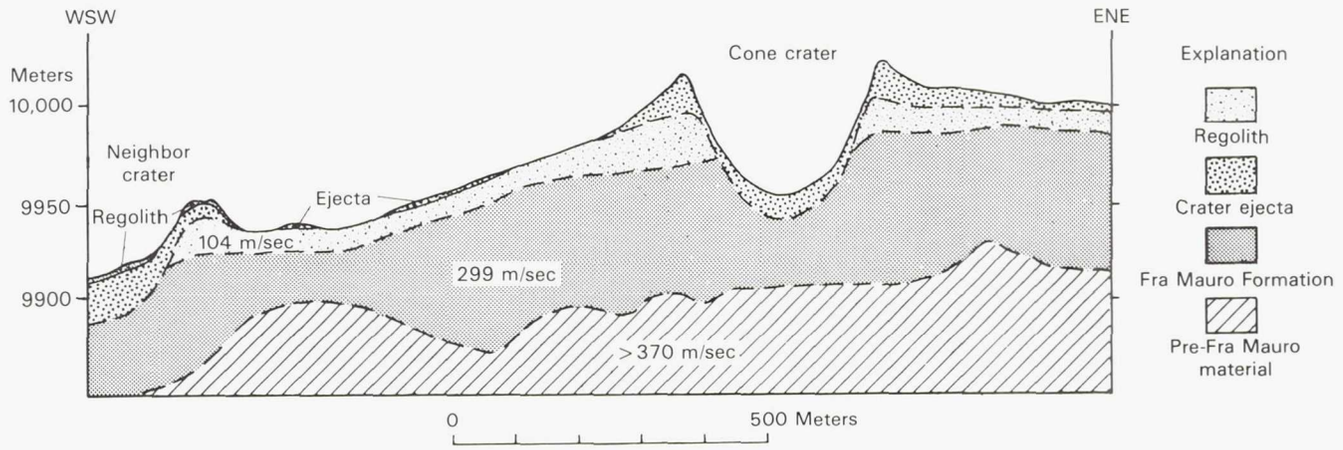

Figure 6.40. Interpretation by Chao (1973) of seismically detected layers at Apollo 14 site. Vertical scale relative to lunar radius of 1738 km.

The amount of Imbrium melt likely at the Apollo site bears on the interpretation of the isotopic ages of the samples. Two age clusters have been identified in the Apollo 14 rocks by both ^{40}Ar–^{39}Ar (Turner, 1977) and Rb-Sr (Papanastassiou and Wasserburg, 1971b) methods (table 6.6). The younger cluster was found mainly in clast-poor KREEP-rich impact-melt rocks (14073, 14276, and 14310; fig. 6.35). The measured ages group closely between 3.79 and 3.85 aeons. If the melts did not form in the Imbrium impact, they must have been formed by a single pre-Imbrium impact around 3.82 ± 0.03 aeons ago, then were transported together to the site, without dispersal, in either the primary or the secondary Imbrium ejecta. This coincidence seems unlikely. The samples were probably melted in the Imbrium target zone and transported to the site in the Imbrium primary ejecta 3.82 ± 0.03 aeons ago.

The best dated older group of samples are several clasts of mare basalt (Ridley, 1975; Ryder and Taylor, 1976; Taylor, 1975, 1982; Ryder and Spudis, 1980). All have Ar-Ar and Rb-Sr ages of 3.85–3.98 aeons. Thus they differ in age from the younger cluster and have a wider spread of ages. They are also compositionally different, having less alumina than the younger melts (though more than most mare basalts) and lower initial Sr ratios (Papanastassiou and Wasserberg, 1971b; Simonds et al., 1977). The old clasts are presumably fragments of pre-Imbrian mare basalt incorporated in the bedrock breccias before deposition of the breccias at the site of the future Cone Crater (Wetherill, 1977). The basalt-in-breccia relation is consistent with either the primary-ejecta or secondary-ejecta models; beds of basalt could have existed before the Imbrium impact either in the Imbrium target area (Wilshire and Jackson, 1972) or the vicinity of the Apollo 14 site (Head and Hawke, 1975). In either model, the age of Imbrium is constrained as ≤ 3.85 aeons.

The following working hypotheses seem to be consistent with available data and Moon-wide geologic relations: (1) The ridge deposit at the Apollo 14 site, the Fra Mauro Formation, contains abundant primary ejecta from the Imbrium basin including rock melted by that impact; (2) the Fra Mauro Formation was sampled both in Cone Crater ejecta and the regolith elsewhere near the landing site; (3) the cluster of old isotopic ages records a pre-Imbrian volcanic eruption or eruptions in the Imbrium target between 3.85 and 3.98 aeons ago; and (4) the cluster of young ages records the Imbrium impact 3.82 ± 0.03 aeons ago.

Imbrium Massifs and Apennine Bench (Apollo 15)

Montes Apenninus

Samples were collected from massifs of two basins, Imbrium and Serenitatis, to help determine their emplacement process, composition, content of primitive rock, and emplacement ages. Massifs are thought to consist partly of uplifted prebasin rock and partly of new basin ejecta (Carr et al., 1971). Although Apollo 15 landed near the base of the Moon's most spectacular mountain range, Montes Apenninus, very little definite Apennine material was collected (figs. 6.1D, 6.41, 6.42). The collections came from the regolith or colluvial aprons of slope debris, with the result that most collected rocks were small and the positions of their source beds on the slope are unknown. The largest samples of massif material are

Table 6.6. Adopted Absolute Ages of Major Sampled Lunar Geologic Units

System or series	Rock unit	Site	Age (aeons)[1]	Basis	Reference[3]
Copernican	Small craters[2]	Apollos 14, 16	≤0.05	Exposure ages	Ar 75
	Tycho	Apollo 17	0.11	Exposure ages	Ar 76
	Copernicus	Apollo 12	0.81	Ar-Ar ages	Eb 73 Al 77
Eratosthenian	Pigeonite, olivine, and ilmenite basalt	Apollo 12	3.17	Average of best Rb-Sr and Ar-Ar ages	BVSP 81
Upper Imbrian	Olivine basalt	Apollo 15	3.26	do	BVSP 81
	Pigeonite basalt	Apollo 15	3.30	do	BVSP 81
	Green glass	Apollo 15	3.30	Ar-Ar ages	Hn 74
	VLT basalt	Luna 24	3.30	Ar-Ar age	BVSP 81
	Feldspathic basalt	Luna 16	3.41	Ar-Ar age	BVSP 81
	Orange-black glass	Apollo 17	3.64	Ar-Ar ages	Hn 78 Al 80
	High-K high-Ti basalt	Apollo 11	3.57	Rb-Sr and Sm-Nd ages	BVSP 81
	High-Ti basalts	Apollo 17	3.72	Average of best Rb-Sr and Ar-Ar ages	BVSP 81
	Low-K high-Ti basalts	Apollo 11	3.67 3.70 3.79	Averages of best Ar-Ar ages for 3 units	BVSP 81
Lower Imbrian	Low-K high-Ti basalt	Apollo 11	3.84	Average of best Ar-Ar ages	BVSP 81
	Apennine Bench Fm. (KREEP basalt)	Apollo 15	3.85	Average of best Rb-Sr, Sm-Nd, and U-Pb-Th ages	C/L 79
	Imbrium basin ejecta	Apollos 14, 15	3.85	Best ages from young cluster, Apollo 14, and black-white breccia, Apollo 15	P/W 71b Al/K 74
Nectarian	Crisium basin	Luna 20	3.84 ± 0.04	Ar-Ar age	Po 73
	Serenitatis basin	Apollo 17	3.87	Youngest Ar-Ar ages	Hn 78 Ei 79 St 79
	Volcanic clasts	Apollos 14, 17	3.85–3.98	Individual ages	R/S 80
	Nectaris basin	Apollo 16	3.92 ± 0.03	Interpretation of 2–4 mm fragments; Ar-Ar ages	J 81
Pre-Nectarian	Plutonic clasts	Apollos 15, 16, 17	4.17–4.54	Individual ages	C/L 81

NOTES:

1. Ages computed with "new" decay constants recommended by International Union of Geological Sciences (Steiger and Jäger, 1977; BVSP, 1981, p. 902):
   ^{40}Ar-^{39}Ar method: $\lambda = 0.5543$/aeon
   Rb-Sr method: $\lambda = 0.0142$/aeon
   Sm-Nd method: $\lambda = 0.00654$/aeon
2. Best determinations (Arvidson et al., 1975) are for:
   South Ray Crater (Apollo 16): 2 million years
   Cone Crater (Apollo 14): 25 million years
   North Ray Crater (Apollo 16): 50 million years
3. *Reference abbreviations:*
   Al 77, 80 = Alexander et al. (1977, 1980)
   Al/K 74 = Alexander and Kahl (1974)
   Ar 75, 76 = Arvidson et al. (1975, 1976)
   BVSP 81 = Basaltic Volcanism Study Project (1981, table 7.3.1)
   C/L 79, 81 = Carlson and Lugmair (1979, 1981)
   Eb 73 = Eberhardt et al. (1973)
   Ei 79 = Eichhorn et al. (1979)
   Hn 74 = Huneke et al. (1974)
   Hn 78 = Huneke (1978)
   J 81 = James (1981)
   Po 73 = Podosek et al. (1973)
   P/W 71b = Papanastassiou and Wasserburg (1971b)
   R/S 80 = Ryder and Spudis (1980)
   St 79 = Staudacher et al. (1979)

probably the black and white breccias (Ryder and Bower, 1977). Whether the black and white rocks are really Imbrium basin ejecta or parts of a pre-Imbrian bed uplifted in the massifs is not certain. An Ar-Ar date of 3.86 ± 0.04 aeons may date their assembly as breccias (Alexander and Kahl, 1974), a reasonable date for the Imbrium impact according to the Apollo 14 results.

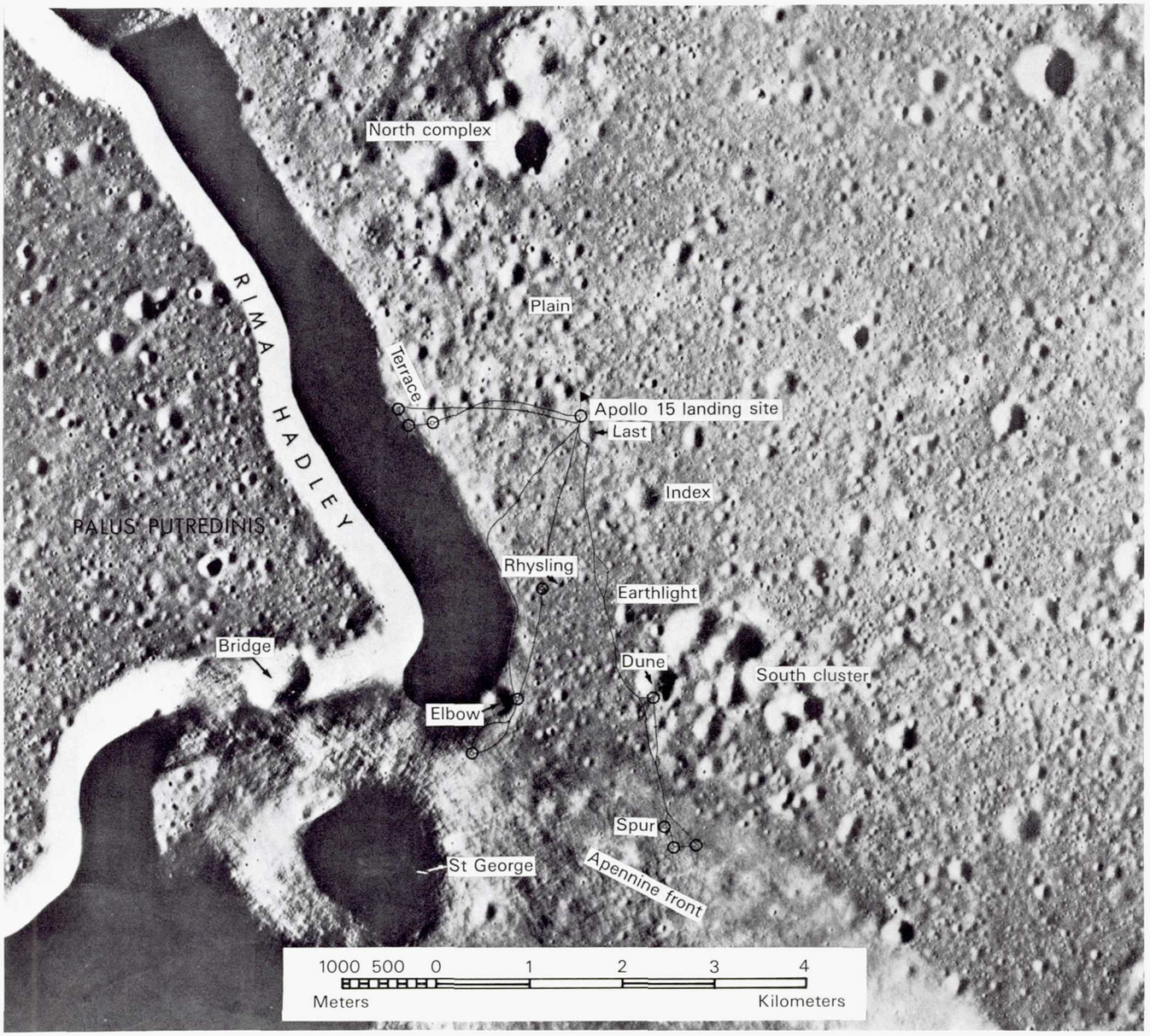

Figure 6.41. Detail of Apollo 15 site showing routes traversed by astronauts. Small circles are sampling stations. (Base is lunar photomap 41B4S4(25) prepared by Defense Mapping Agency (2nd edition, April 1975).)

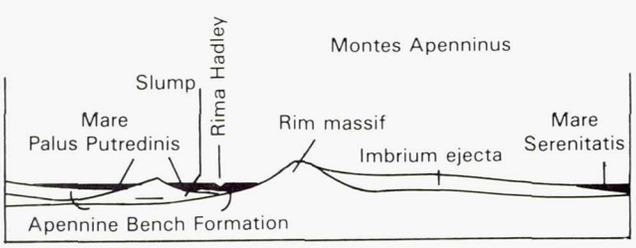

Figure 6.42. Diagrammatic geologic section drawn across figure 6.1D in direction of arrow. Sequence of events, from earliest to latest, was (1) uplift of massif, immediately followed by (2) deposition of ejecta on basin flanks and (3) slumping of major blocks from the Apennine front; (4) emplacement of Apennine Bench Formation, which followed immediately after event 3 if formation consists of impact melt or within a few million or tens of millions of years if consists of volcanic basalt; (5) mare volcanism, hundreds of millions of years later.

Apennine Bench Formation

An interior plains deposit may also have been sampled. Some medium-K KREEP fragments in the regolith at the Apollo 15 site may have come from a light-colored planar deposit known as the Apennine Bench Formation (Spudis, 1978; Hawke and Head, 1978). This unit is exposed west of the site where it is clearly seen to be older than mare materials and Archimedes ejecta but younger than parts of the Apennine front (fig. 6.42; Hackman, 1966). Wilhelms (1980) suggested, on the basis of morphology and position, that it is the equivalent of the Maunder Formation of Orientale, which probably consists of impact melt. The Apennine Bench Formation has also been interpreted as volcanic (Hackman, 1966; Wilhelms and McCauley, 1971). Most KREEP returned from the Moon was emplaced at the collection sites as fragment-laden impact-melt rock, but the Apollo 15 fragments may be bits of true endogenic volcanic basalt since they have clast-free igneous textures and lack meteoritic siderophiles (Dowty et al., 1976; Irving, 1977; Meyer, 1977). If the KREEP is volcanic and if the fragments were derived from the Apennine Bench Formation, the formation is volcanic as originally proposed. It would then be post-basin, pre-mare deposit of KREEP basalt (Spudis, 1978; Hawke and Head, 1978). The fragments have been dated at about 3.85 aeons (Dowty et al., 1976; Carlson and Lugmair, 1979), close to the ages of the black and white rocks and just within the younger Apollo 14 cluster of ages. Imbrium cannot be younger than the KREEP regardless of whether that well-dated material is impact or endogenic melt, and cannot be older than the Apollo 14 rocks. The range from 3.82 to 3.86 aeons is within the interlaboratory analytical uncertainty of the ^{40}Ar-^{39}Ar method (G. W. Lugmair, personal communication, 1982) and within the stated intralaboratory errors. An age of 3.85 aeons is adopted here for the Imbrium basin.

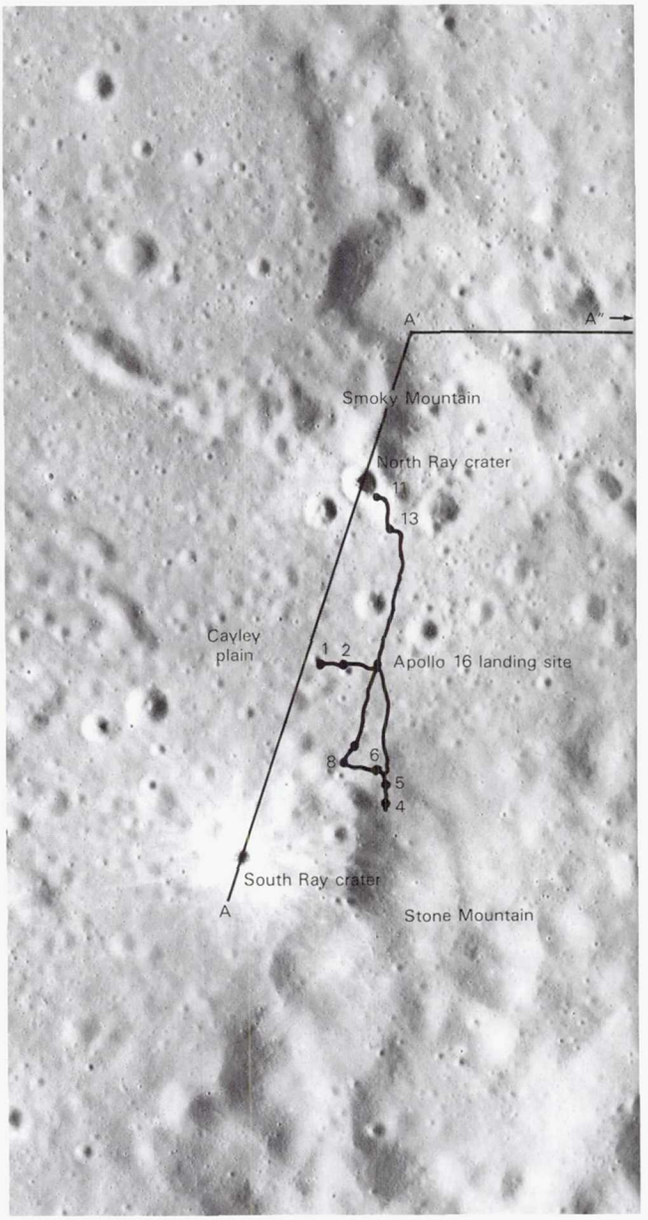

Figure 6.43. Apollo 16 landing region, showing principal sampled features and paths traversed by astronauts. Numbers refer to sampling stations. North Ray and South Ray craters 10 km apart. A-A'-A" is line of section in figure 6.45; point A" lies off photograph. Apollo 16 P-4623.

Cayley and Descartes Formations (Apollo 16)

The stratigraphic context and the emplacement processes and ages of the planar Cayley and hilly-and-furrowed Descartes Formations sampled by Apollo 16 remain poorly known (figs. 6.1F, 6.43–6.45). Imbrium-basin origin was suggested early in lunar stratigraphic studies (Eggleton and Marshall, 1962) and after the mission (Eggleton and Schaber, 1972; Hodges et al., 1973), but was less popular than volcanic interpretations in the mid-1960s when the mission was being planned (summaries by Wilhelms and McCauley, 1971; Hinners, *in* NASA, 1972c, sec. 1; Hodges et al., 1973; Muehlberger et al., 1980; Ulrich et al., 1981; Wilhelms, 1980a, in press a, b). However, no igneous rocks were found, except as highly reworked relics of the early crustal plutonism (James, 1980). The returned rocks are dimict and polymict breccias with widely varying amounts of impact melts in clasts and matrices (fig. 6.36).

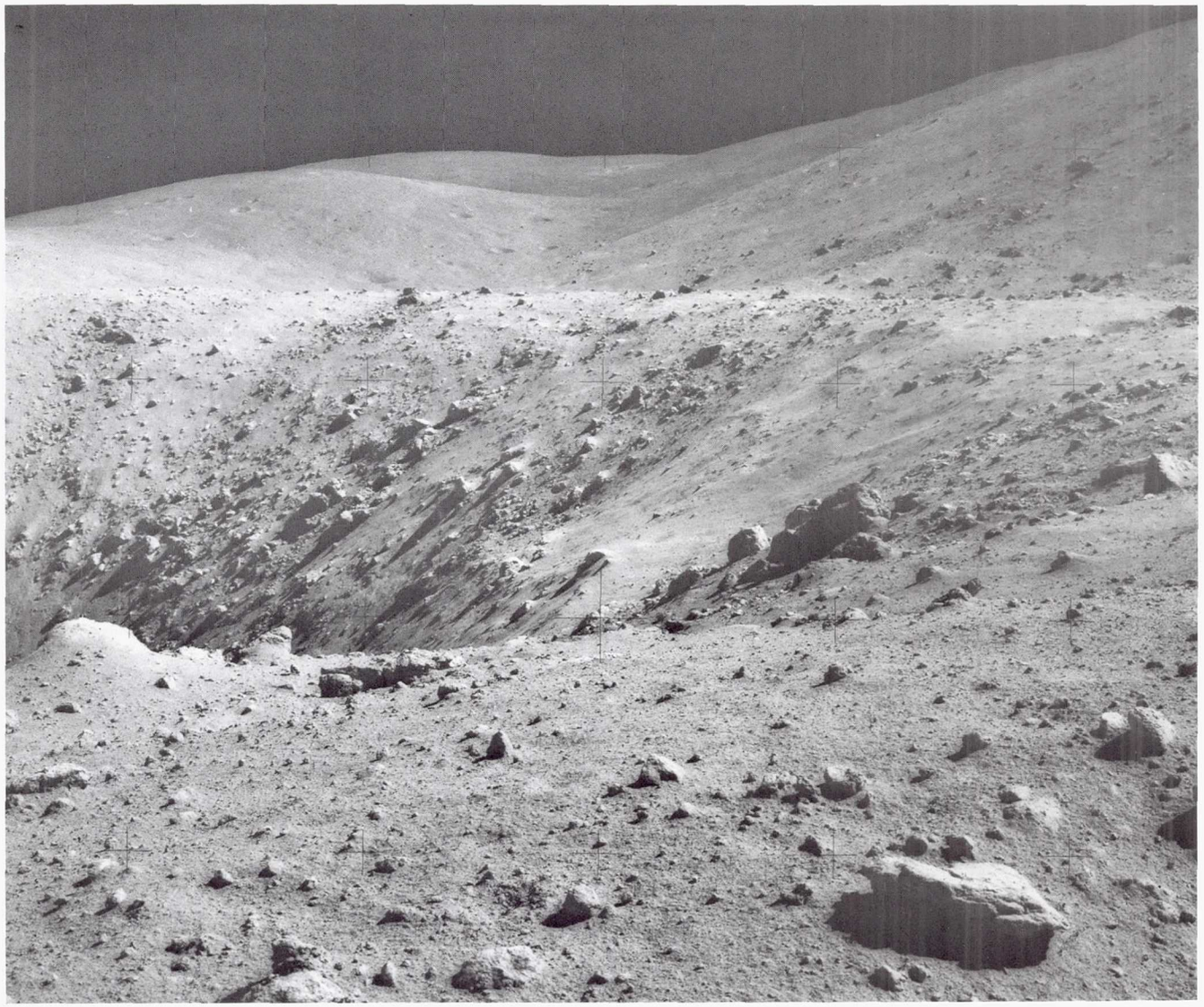

Figure 6.44. View of North Ray Crater and Smoky Mountain (background), Apollo 16 landing region. Rock inside and on rim of North Ray Crater probably consists of material of Descartes Formation excavated by the crater, and may contain Nectaris-basin material. Apollo 16 H-17264.

Of the sample suites believed collected from the two units, those from the Cayley Formation seem more melt-rich and those from the Descartes Formation (fig. 6.36) more fragmental (James, 1981; Stöffler et al., 1981; Ulrich et al., 1981). The melt-rich lithology of the Cayley is consistent with origin as partly fluidized primary ejecta which segregated from the Fra Mauro Formation and flowed into depressions (Eggleton and Schaber, 1972). Gradation of circum-Orientale plains with the Hevelius Formation provides a convincing analog. A good Orientale analog is also available for surface-flow emplacement of the Descartes, which resembles Orientale basin deposits that crumpled into transverse dunelike landforms upon meeting crater walls and other obstacles (fig. 6.20D; Hodges et al., 1973; Moore et al., 1974). The distance from the Imbrium basin, although great (1050 km), is no greater proportionately than the distance of some of the Orientale analogs from the Cordillera ring, about two-thirds of the basin diameter in both cases. A relation to Imbrium is indicated by the ages, textural gradations, and regional setting of the Cayley and Descartes amidst a concentration of other Imbrium-related landforms (figs. 6.1F, 6.43).

A different source of the material and a different, though related, emplacement process are also possible: primary ejecta of the Nectaris basin may have been incorporated in the Cayley and Descartes For-

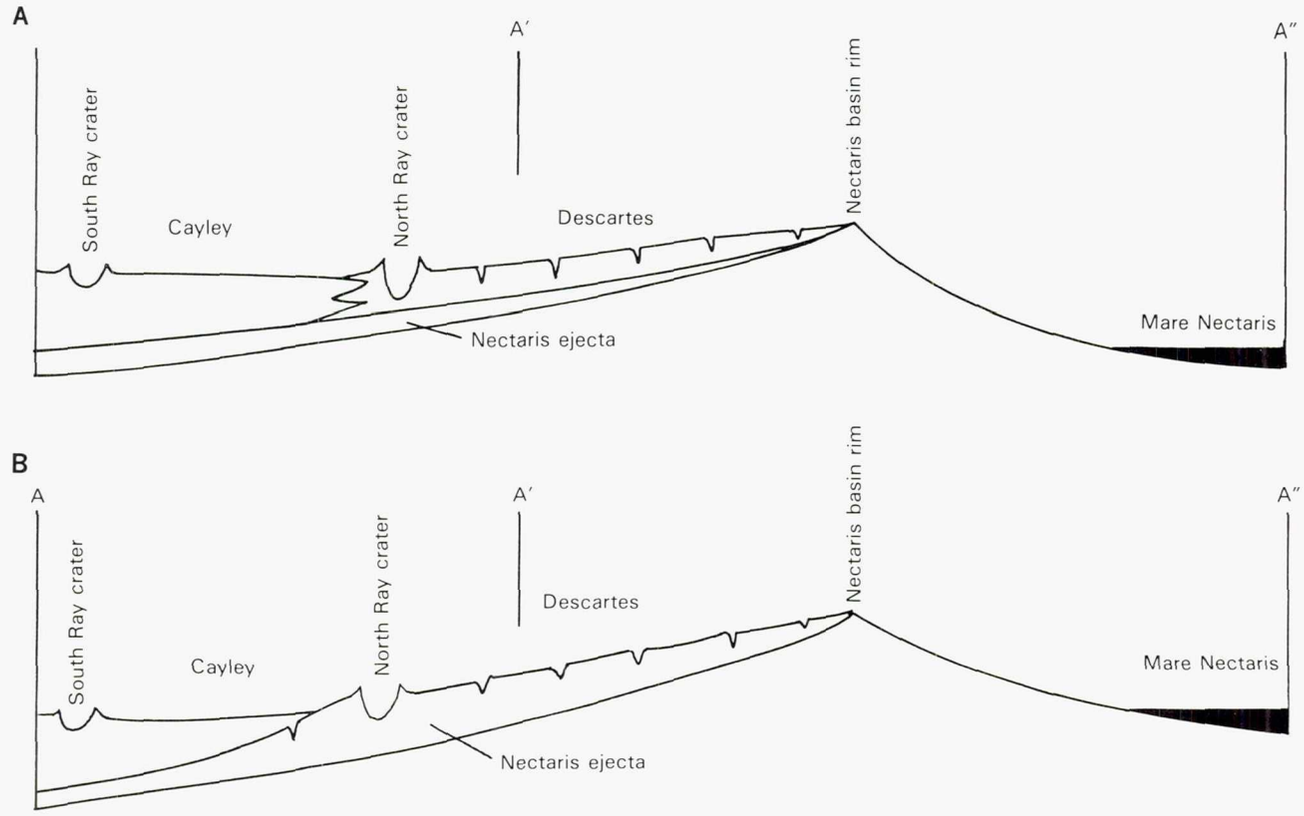

Figure 6.45. Diagrammatic geologic sections giving alternative interpretations for emplacement of Cayley and Descartes Formations. Notches indicate secondary craters of Imbrium basin. Line of section drawn on figure 6.43.

A. Both formations are intergradational facies of same deposit, originating as primary or secondary ejecta of Imbrium basin. North Ray Crater excavates this deposit and does not reach Nectaris ejecta.

B. Descartes Formation originates as Nectaris ejecta and is modified by Imbrium-ejecta impacts; Cayley Formation originates as later deposit of Imbrium origin as in A. North Ray Crater excavates Nectaris ejecta.

mations. Nectaris ejecta is conspicuous considerably south of the Apollo 16 site (fig. 6.27). Like the Orientale and Imbrium ejecta, the Nectaris deposits subdue older craters, are radially textured, and grade outward into secondary craters. The landing site is only about 60 km west of the western rim of the Nectaris basin, which is a continuation of parts of the rim that bound the conspicuous ejecta. The Apollo 16 region must therefore be swamped with Nectaris ejecta, unless the ejecta was distributed asymmetrically. The question is, how deeply is it buried at the Apollo 16 site?

If deeply buried by Imbrium material, Nectaris ejecta may not have entered the sample collection. If unburied or thinly buried, Nectaris ejecta may compose much of the material of the photogeologic units. Although the spatial relation to Imbrium and crater densities show that the Cayley Formation was emplaced in the Imbrian Period long after Nectaris, it may nevertheless *consist* largely of reworked Nectaris ejecta. A debris surge initiated by secondary impacts of Imbrium would mix small amounts of Imbrium ejecta (Oberbeck et al., 1974; Morrison and Oberbeck, 1975) with the Nectaris material. The resulting deposits' geometry would be similar whether they were emplaced as primary or secondary ejecta of Imbrium and whether they incorporated large or small amounts of Nectaris material (fig. 6.45).

The possible nature of the local material incorporated by the debris surge has been widely misunderstood. A popular model for the origin of the Apollo 16 materials is that they are parts of an "unnamed crater B," said to dominate the site, and of other obscure craters (Head, 1974b). Head states that "B" cuts the southern, Stone Mountain facies of the Descartes material, which he believes to be of Nectaris origin, and is cut by grooves of the northern Smoky Mountain facies, which he believes to be of Imbrium origin, as do other observers. However, even if "B" exists, it does not cut the Stone Mountain

Descartes; the furrows of the Smoky Mountain and Stone Mountain facies are gradational and were formed in the same event (fig. 6.1F). Furthermore, "B" cannot have furnished much material to deposits which bury it deeply. If secondary impacts churned up local material that was redeposited as the Cayley and Descartes, the local material must be predominantly Nectaris ejecta.

The Apollo 16 samples that have been the most thoroughly dated by the ^{40}Ar-^{39}Ar method are "coarse fines" (2–4 mm) from the rim of North Ray crater (fig. 6.44; Maurer et al., 1978; James, 1981). The ages of these and other samples at the site range widely from 3.89 to 4.14 aeons plus a scattering of younger ages. Feldspathic fragment-laden melts cluster around 4.1 aeons. A number of other types cluster around 3.9 aeons. Although some of the materials may be from the Imbrium basin, most of these ages are too old to have been set by the Imbrium impact. If the radiometric dating is accurate and the material was emplaced originally as Nectaris basin ejecta, the Nectaris impact occurred 3.9–4.1 aeons ago. Melt and clast were inevitably analyzed together in these small samples so that the significance of the dates is uncertain. Considering the many compositional, radiometric, and geologic factors, James (1981) favors an age of 3.92 aeons. Wetherill (1981) believes that 4.1 aeons is more consistent with likely early impact rates.

Unfortunately, the final conclusion about these complex deposits must be that neither their absolute ages nor chemical and petrologic relations are well understood and that none of the above possibilities may be the correct one. The units from which the samples came, especially in the case of the Descartes, are uncertain. The emplacement was initiated by the Imbrium impact and both Imbrium and Nectaris materials are present at the site. Crater materials are subordinate in the bedrock though occur in the regolith (and prebasin crater materials were undoubtedly entrained in the primary ejecta, as in all lunar ejecta). The primary–secondary and the Imbrium–Nectaris proportions are not known, and the age of Nectaris is very uncertain. I believe that the result of James' (1981) work is the best available working hypothesis, with appropriate margin for error, and in this paper estimate 3.92 ± 0.03 aeons as the age of the Nectaris basin.

Serenitatis Massifs (Apollo 17)

Abundant materials were obtained from North and South Massifs on the Serenitatis rim at the Apollo 17 site (figs. 6.46—6.48). Many of the samples came from boulders which were traced by color or tracks to ledges visible on the massif flanks (Wolfe et al., 1981). Thus the geologic context of the rocks is known much better than at the Apennines, and much more material in larger pieces was gathered. Compositionally, the Apollo 15 and 17 terra suites are more alike than those of any other pair of Apollo sites, but whether this suggests common origin of the two sample suites is unclear (Ryder and Wood, 1977). Derivation from the ledges on the massif flanks suggests that the samples came either from the Serenitatis cavity or from an older basin or crater whose materials were uplifted to form the present Serenitatis rim. A single event is indicated by the compositional (not textural) kinship of all large samples, and most authors believe that the event was the Serenitatis impact (Wood, 1975c; James et al., 1978). A few odd rocks (73255) are not traced to specific ledges and may be from Imbrium (Spudis and Ryder, 1981) or from Serenitatis (James et al., 1978).

Absolute ages of the samples also reflect dominance of a single event. The ^{40}Ar-^{39}Ar and Rb-Sr ages are

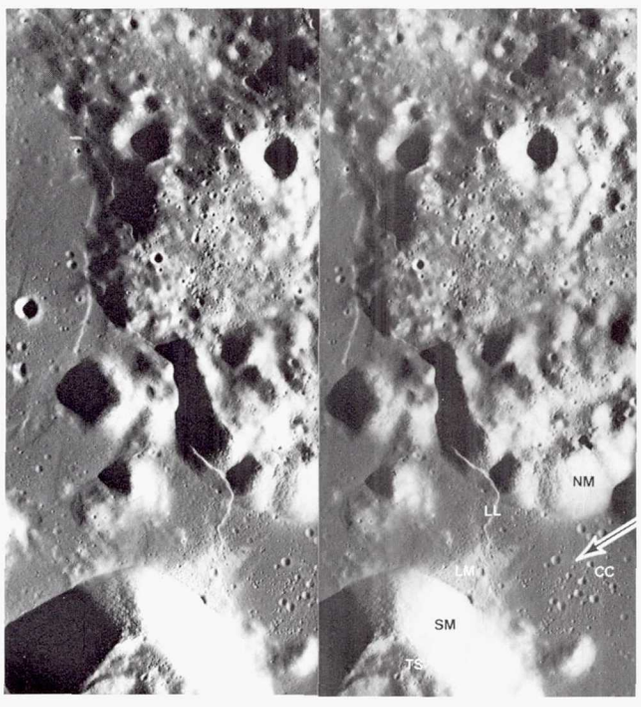

Figure 6.46. Stereoscopic photographs of Apollo 17 landing region, including landing point (arrow), Central Cluster of craters (CC, secondary to Tycho 2250 km to southwest), Lee-Lincoln scarp (LL), light mantle (landslide) (LM), North Massif (NM), South Massif (SM), and Tycho secondaries atop South Massif (TS). Interpretations from Wolfe et al. (1981). Apollo 17 P-2309 (right) and P-2314 (left).

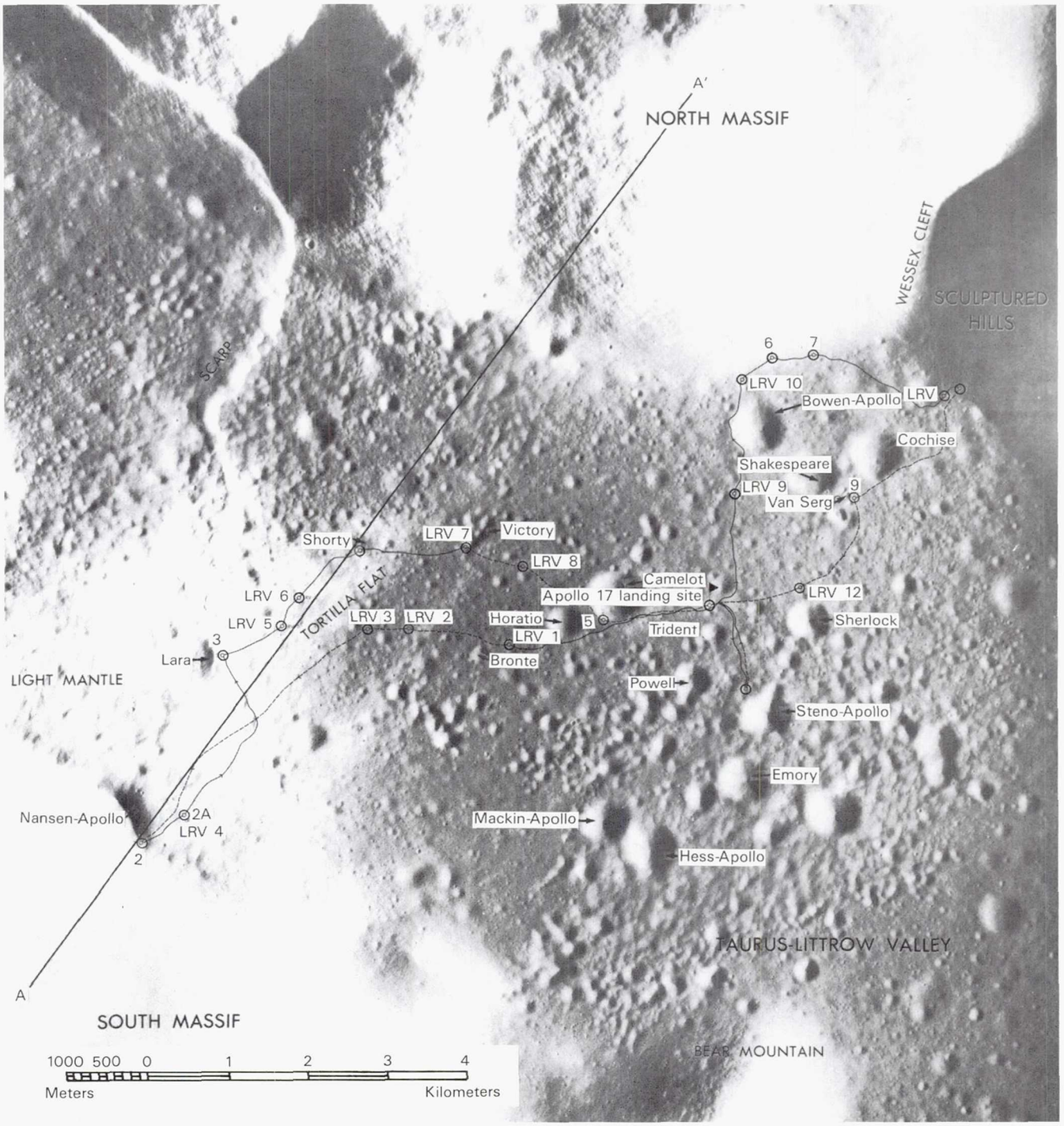

Figure 6.47. Traverses by astronauts at Apollo 17 landing site. LRV = Lunar Roving Vehicle stations; other numbers refer to major sampling stations. Line A-A' is the line of section of figure 6.48. Lunar Photomap 43D1S2(25) prepared and published by Defense Mapping Agency (March 1975).

spread quite widely between about 3.85 and 3.95 aeons. The spread arises from unequal degrees of isotopic equilibration between various clasts and matrices, and may be displayed by a single rock (Jessberger et al., 1977). There is no distinct field relation or texture-lithology relation pointing to separate impacts. If the variation is due to incomplete equilibration then the youngest ages are from the most nearly equilibrated samples, and should date the impact. The youngest reliable ages, 3.86–3.87 $\pm$ 0.03 aeons, come

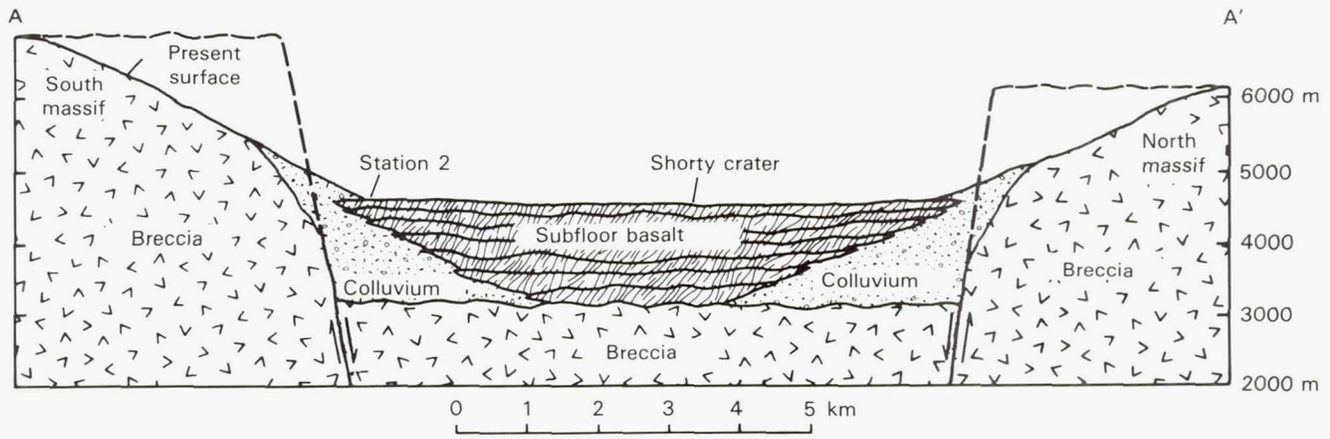

Figure 6.48. Geologic section along line A-A' in figure 6.47 according to Wolfe et al. (1975; also Wolfe et al., 1981, fig. 242). "Breccia" is Serenitatis-basin material. "Subfloor basalt" is the mare-basalt fill of the Taurus-Littrow Valley; it is overlain by the light-colored landslide, dark-mantling material, and regolith. Steep faults bounding massifs are highly inferential, and massifs were probably never as square-cornered as shown.

from two clasts not traceable to a ledge (73215 and 73255; Jessberger et al., 1977; Eichhorn et al., 1979; Staudacher et al., 1979). In addition, a date of 3.86 ± 0.04 aeons has been obtained from the matrix of a boulder definitely from the massifs (72435; Huneke, 1978). The Serenitatis impact probably occurred 3.86 or 3.87 aeons ago.

Summary of Emplacement Times

Nectarian and Imbrian basins supplied all the samples by which the older part of the stratigraphic column is calibrated in years. No pre-Nectarian basins were sampled because they were inaccessible to Apollo and Luna landings. The oldest basin which may have been sampled is Nectaris. Two interpretations given above and in figure 6.49 set its age at between 3.9 and 4.1 aeons, the younger end of the range being favored here.

The three younger basins that were probably dated radiometrically have similar absolute ages, and so their sequence is best determined stratigraphically. The oldest of the three may be Crisium, from whose rim Luna 20 returned small fragments of regolith dated at 3.84 ± 0.04 aeons (Podosek et al., 1973). While the precise origin of these fragments is uncertain, a post-Nectaris age is consistent with the crater densities (fig. 6.29) and the superposition of probable Crisium secondaries on Nectaris (Wilhelms, 1976).

The next youngest basin in the sequence is probably Serenitatis. Serenitatis is probably a double basin (Scott, 1972b, 1974; Wolfe et al., 1981) whose parts may have formed simultaneously as did, more clearly, the two or three parts of the Humboldtianum basin (fig. 6.25). Sparse crater-density data from the limited area of exposed Serenitatis materials east of the basin support its relative youth; only three craters believed younger than Serenitatis and older than Imbrium are known in the area of figure 6.50. The rest of the many craters in the area are either Imbrium secondaries or pre-Serenitatis in age (Wilhelms, 1976, 1980a). Additional evidence comes from superposition relations of craters identified by their radiality to Serenitatis as Serenitatis secondaries (fig. 6.50; Wilhelms, 1976). Moreover, if Crisium were younger than Serenitatis, then Crisium ejecta would be expected at the Apollo 17 site, but none has been recognized there.

The age of 3.86–3.87 aeons is very close to that of the Imbrium basin. Numerous investigators have taken this similarity and the discovery of a great many other similar radiometric dates on terra samples to indicate that most or even all ringed basins formed in an impact "cataclysm" (Tera et al., 1974). This conclusion was based in part on the assumption that Serenitatis is an old basin, or, naively, the oldest ringed basin. The estimate of the old age of Serenitatis is based largely on the fact that it is severely modified (Stuart-Alexander and Howard, 1970). However, most of the modification is due to burial by deposits of the neighboring Imbrium basin (fig. 6.1B). Serenitatis may be one of the youngest pre-Imbrian basins, and therefore, not surprisingly, separated in age from Imbrium by only 10–20 million years.

The only basin that is well dated both relatively and absolutely is Imbrium. Its age of 3.85 is the best calibration point in the pre-mare stratigraphy. It is used

Figure 6.49. Estimates of early cratering rate. Each box represents possible ranges in size-frequency distribution of superposed craters (box height) and absolute age (box width). Included absolute ages are those having reported error ranges < 0.1 aeon (BVSP, 1981, table 7.3.1). Frequencies for Imbrium basin, Nectaris basin, and Al-Khwarizmi—King (basin?) surface (AK-K; highest known crater frequencies) are based on ≥ 20 km craters (Wilhelms, 1979; in press b); lower edge of box is actual count; upper edge is extrapolation from larger craters assuming many 20–40-km craters have been destroyed and production distribution was same as for young craters (-1.8 cumulative; fig. 6.17). Frequencies for basalts sampled by Apollo (Ap) based on ≥ 1-km craters (Neukum et al., 1975a, b). Frequencies in the two size ranges calibrated by means of Imbrium-basin counts in both ranges (bar). Crosses represent author's estimates for most likely values (table 6.1).

Heavy line drawn through crosses. Dashed lines touch corners of boxes and enclose envelope of likely values. Interpolations between data and extrapolation of AK-K assume constant decline in cratering rate (straight lines). Constant rate assumed after 3.2 aeons. Radical decrease in rate between Imbrium impact and 3.2 aeons poorly constrained by Apollo 11 and 17 measurements. Age of AK-K probably between 4.0 and 4.1 aeons. Time elapsed between formation of oldest basins and AK-K surface unknown.

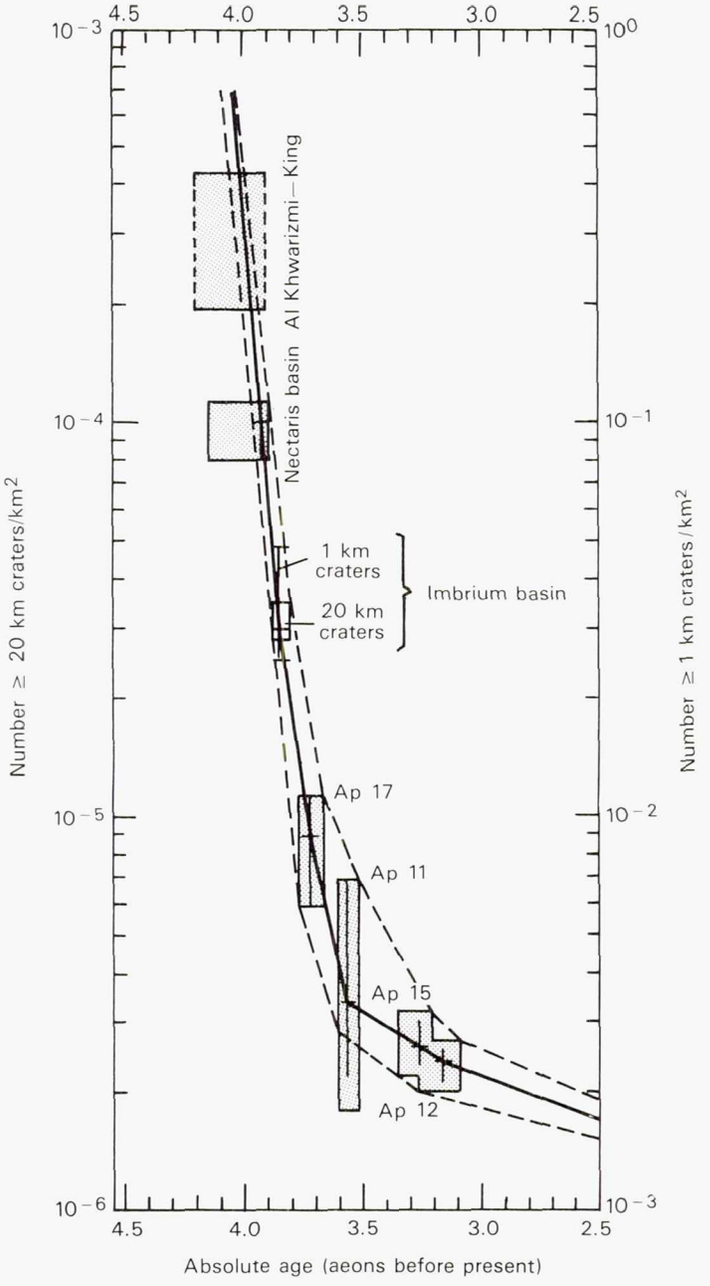

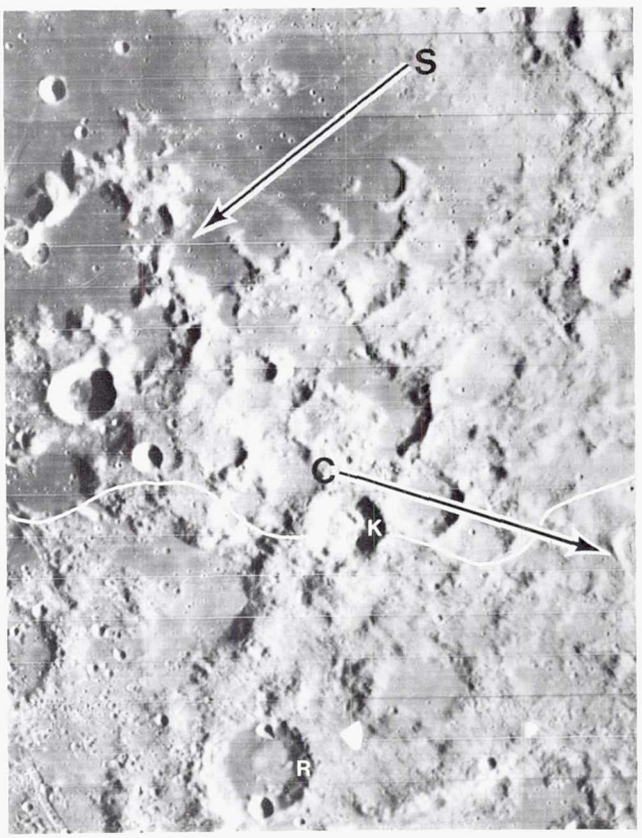

Figure 6.50. Secondary craters of Serenitatis basin northeast of Mare Serenitatis. Relatively unmodified secondaries displaying Serenitatis-radial texture (direction of arrow, S, below arrow). Lineations at bottom of picture not closely radial to Crisium basin (arrow, C) but are more closely radial to Imbrium. Only conspicuous post-Serenitatis, pre-Imbrium craters are Kirchhoff (K, 25 km, 30°N, 40°E) and Romer A (R, 35 km, 27°N, 28°E). Orbiter 4 H-74.

to calibrate the cratering rate in pre-mare times (fig. 6.49).

MARIA

Introduction

The dark, smooth maria are topographically and geologically simpler than the terrae. The visible maria cover 16 percent of the lunar surface (fig. 6.51) and are younger than the terrae. They cover 30 percent of the near side but only 2 percent of the far side. Most mare materials flood centers and peripheral shelves of large basins. The lavas flood along contours, forming complex embayments with the complex terra topography.

The obvious spatial relation between mare and basin led to a genetic confusion which has persisted as a semantic confusion between the terms mare and basin in some literature. Many early observers who knew that impacts formed the basins (see "Craters" and "Basins") furthermore assumed that the impacts also formed the maria (e.g., Urey, 1952). Others who correctly perceived from landforms that the maria are volcanic assumed that the basins were also formed gradually by volcanism (e.g., Fielder, 1965). Dual origin was proved by some simple stratigraphic observations which showed that the maria substantially postdate the containing basins (Baldwin, 1949, 1963; Hackman and Mason, 1961; Mason and Hackman, *in* Kopal and Mikhailov, 1962; Shoemaker and Hackman, 1962). The maria are less densely cratered, and fill craters which in turn are superposed on the basins (fig. 6.32).

Surveyor, Apollo, and Luna exploration has proved that the mare materials are basalts (Gault et al., 1968a; 30 January 1970 issue of *Science*). This section describes the mare properties observable from a distance; the returned samples are described in the following section.

General Features

Morphology

The generally smooth and level mare surfaces are interrupted by certain areally minor but genetically significant landforms. The most significant are lobate lava flows, which are similar to terrestrial flows. The largest known lunar flows, demarcated by scarplike fronts, are in Mare Imbrium (fig. 6.52; Kuiper and Strom, *in* Heacock et al., 1965, pp. 29-32; Whitaker, *in* Hess et al., 1966, pp. 79-83; Schaber, 1969, 1973). The scarps are from 10 to >35 m high, and individual flows are up to 1200 km long. Each may have been formed by rapid eruption of fluid lava from a single, large vent (Schaber, 1973). Shorter and thinner flows are observed in other maria, but most lunar maria lack topographically expressed flow units (Schaber et al., 1976). Floodlike eruptions may have formed massive lava lakes (Greeley, 1976).

Several types of elevated landforms, mostly formed by extrusion of basalt, are scattered in several maria and are concentrated in a few. Many domes are circular, subtle features with low profiles commonly topped by small, smooth-rimmed craters (fig. 6.53). These low mare domes are concentrated in Mare Tranquillitatis and western Mare Insularum, but occur in other maria as well. Steeper, rough-surfaced features usually called cones are concentrated in the Marius Hills (fig. 6.54; McCauley, 1967a,b; McCauley, 1968) and are scattered in several maria and also in the terrae. The difference between the domes and cones presumably results from variants in composition or eruptive process. The Marius Hills were a favored site for Apollo missions in hopes that they would yield differentiated volcanic petrologies. The morphologies of domes or cones are mimicked by *kipukas* or *steptoes,* synonyms for islands of older terra or mare surrounded by younger mare materials (fig. 6.4). The positive landforms occur mostly in shallow maria (Arthur, *in* Kopal and Mikhailov, 1962, p. 322; Head, 1976; Head and Gifford, 1980). The Moon has no large shield volcanoes like those of Earth and Mars.

Although most lunar craters are of impact origin, endogenic craters do exist. Most endogenic craters lie amidst or near maria or small patches of dark material in the terrae (figs. 6.55, 6.56). This association with volcanic materials or alinement along faults demonstrates their internal origin. For example, random impact is unlikely to be responsible for the many craters exactly centered on what are obviously volcanic domes (fig. 6.53). Too many craters or rimless pits are alined exactly along some fissures to be coincidental impacts (figs. 6.55, 6.56). They may have formed entirely by collapse without extruding any volcanic material. Single craters situated along rilles, located amidst dark materials, and having elongate or irregular shapes are also surely endogenic (fig. 6.56). On the other hand, many clustered or alined craters are of secondary impact origin (figs. 6.53, 6.56). Geologic setting is therefore the clue to origin

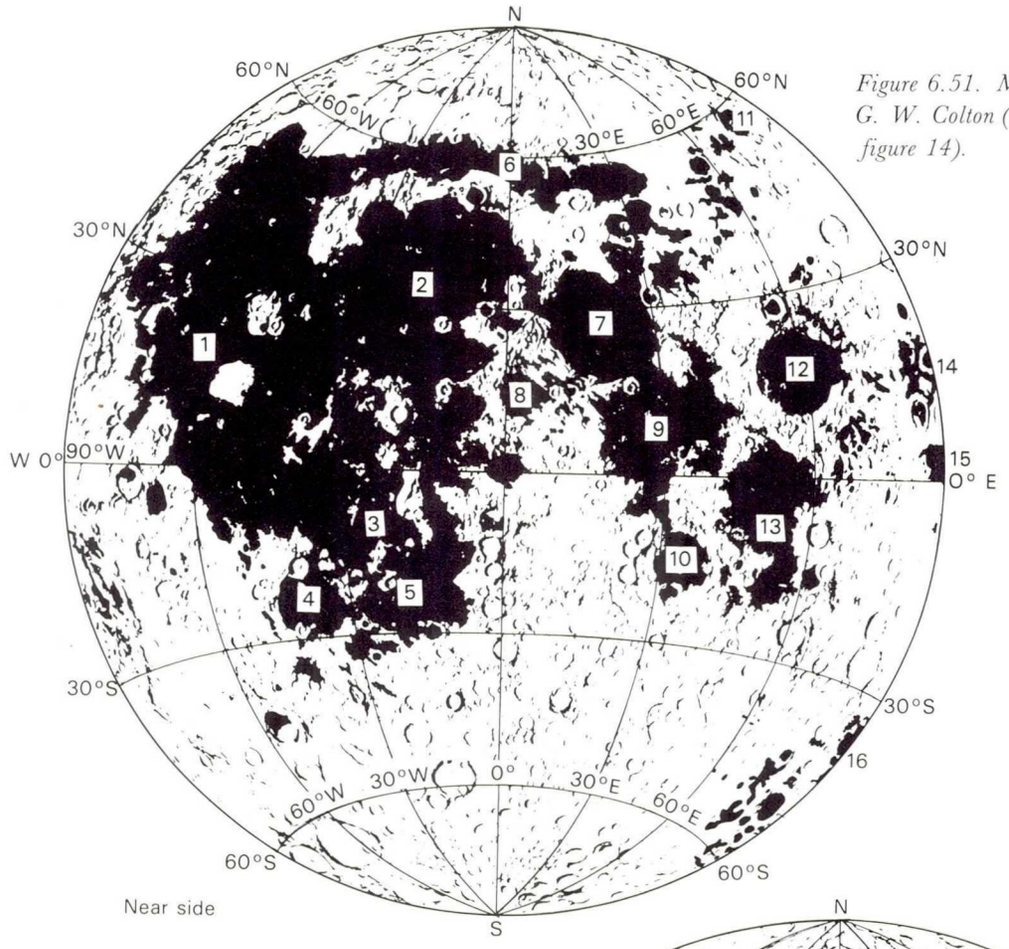

Near side

Figure 6.51. Map of lunar maria. Prepared by G. W. Colton (in Masursky et al., 1978, figure 14).

Legend:

1 Oceanus Procellarum
2 Mare Imbrium
3 Mare Cognitum
4 Mare Humorum
5 Mare Nubium
6 Mare Frigoris
7 Mare Serenitatis
8 Mare Vaporum
9 Mare Tranquillitatis
10 Mare Nectaris
11 Mare Humboldtianum
12 Mare Crisium
13 Mare Fecunditatis
14 Mare Marginis
15 Mare Smythii
16 Mare Australe
17 Mare Moscoviense
18 Mare Ingenii
19 Mare Orientale

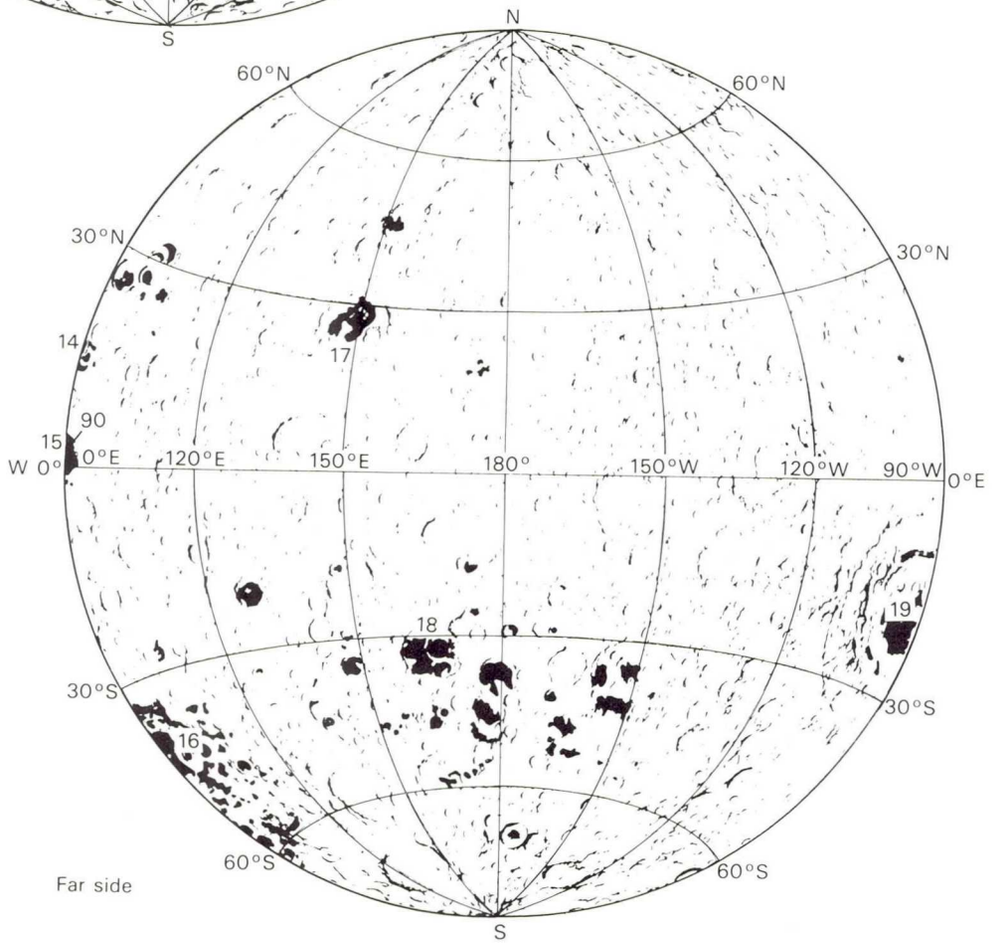

Far side

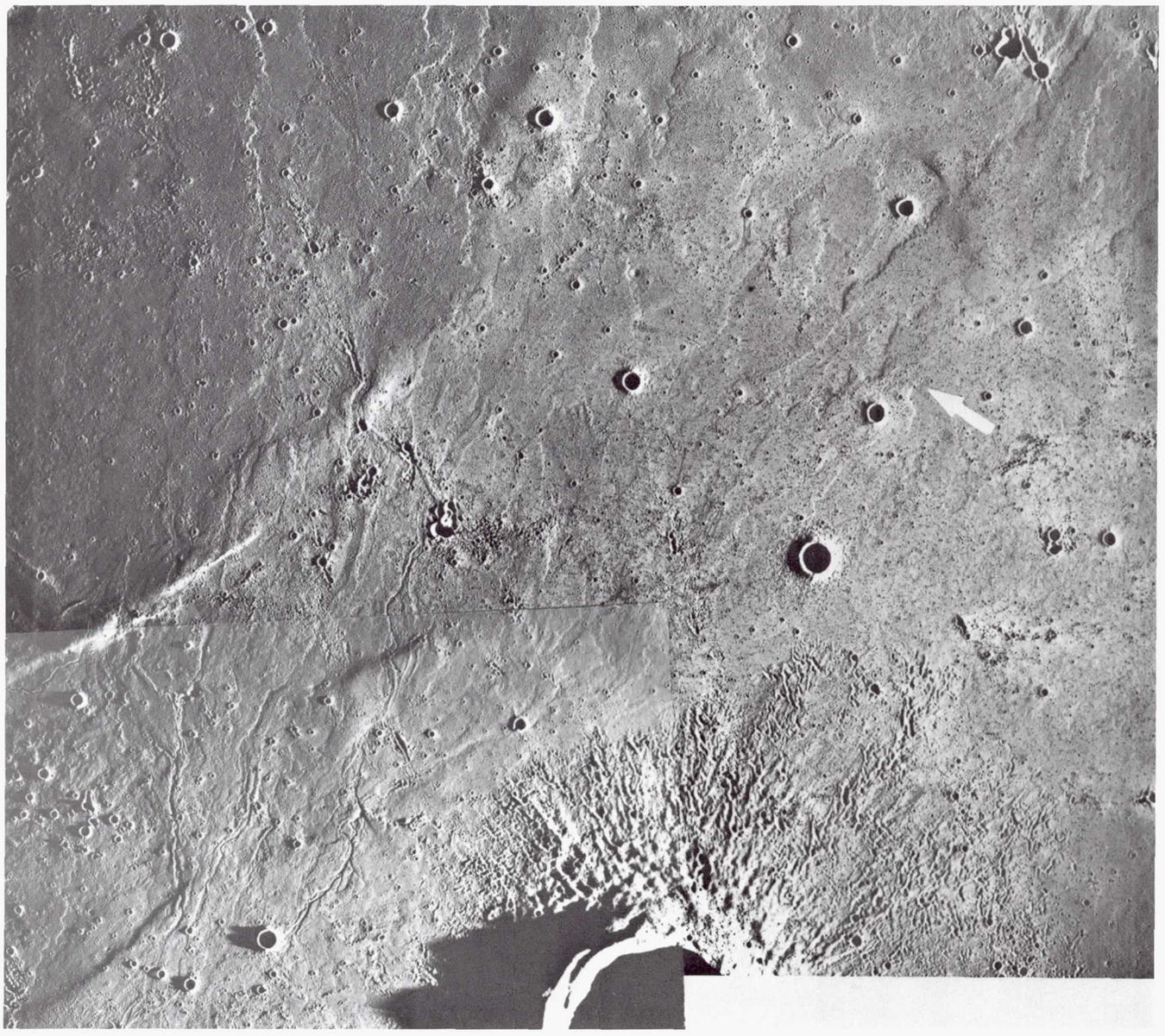

Figure 6.52. Lobate flows in Mare Imbrium. Arrow marks southeast boundary of intricate, overlapping Eratosthenian flows, the Moon's most conspicuous (Schaber et al., 1976). Fine detail enhanced by low sun elevation (about 4° in center of picture). Northwest ejecta of crater Euler (28 km, 23°N, 19°E; compare figure 6.4) sharply truncated by the young flows. Mosaic of Apollo 17 M-2295 (lower left) and Apollo 15 M-1701 (remainder); courtesy Gerald G. Schaber.

of many craters. Almost all recognized endogenic craters are smaller than 10 km.

Many larger craters having features atypical of impact craters, such as elevated floors and smooth rims, have been thought to be calderas (fig. 6.56). Instead, they are impact craters whose floors have been tectonically elevated in or near basins or which have been modified by mare volcanism (see "Tectonism"). Large calderas are not expected on the Moon. Calderas form by collapse or magma withdrawal into shallow magma chambers, but lunar basalts probably do not accumulate in such chambers (Head, 1976).

Sinuous rilles are another areally minor but conspicuous type of mare feature which has attracted much attention (figs. 6.4, 6.54). The Apollo 15 landing was targeted next to a large sinuous rille, Rima Hadley (fig. 6.41). Sinuous rilles are probably lava tubes or channels (Kuiper et al., *in* Heacock et al., 1966, p. 199; Murray, 1971; Howard et al., 1972; Guest and Greeley, 1977, pp. 62–68). Some lunar rilles including Hadley display alternately roofed and unroofed segments. The sources of Hadley and numerous other sinuous rilles border the terrae, and other sources lie amidst the terrae (Aristarchus-Harbinger

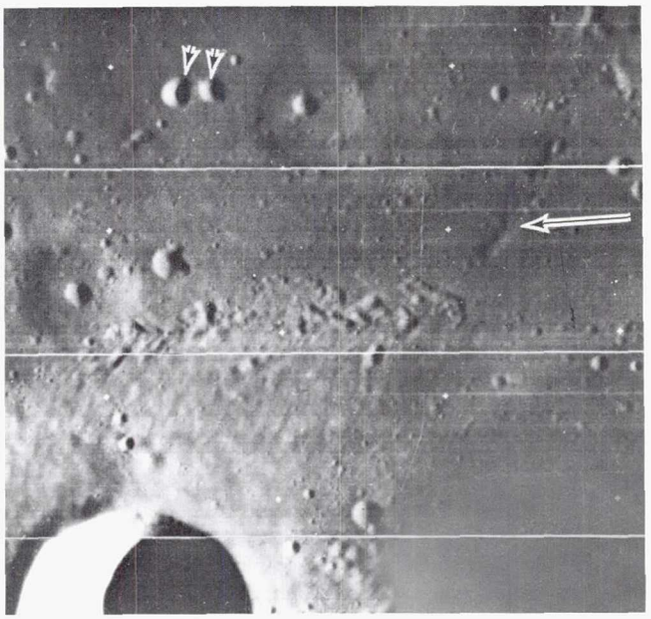

Figure 6.53. Low mare domes and line of cones north of crater Hortensius (lower left). A smooth-sloped crater is centered in each dome, and similar craters (two arrowheads) may also be volcanic. Long arrow marks chain of cones. East-west crater group with herringbone structure in center of frame is secondary to a large primary impact crater outside right edge of frame. Orbiter 4 H-126.

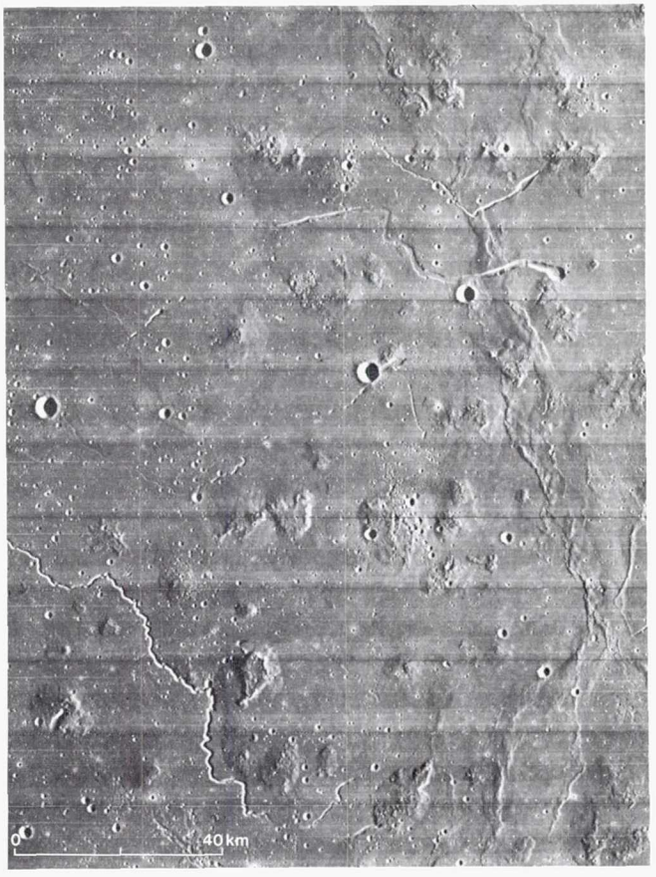

Figure 6.54. Part of Marius Hills centered at 13°N, 56.5°W. Domes and cones having rough topography are concentrated more densely here than in any other area. Sinuous rilles also characterize the volcanic complex. Orbiter 4 H-157.

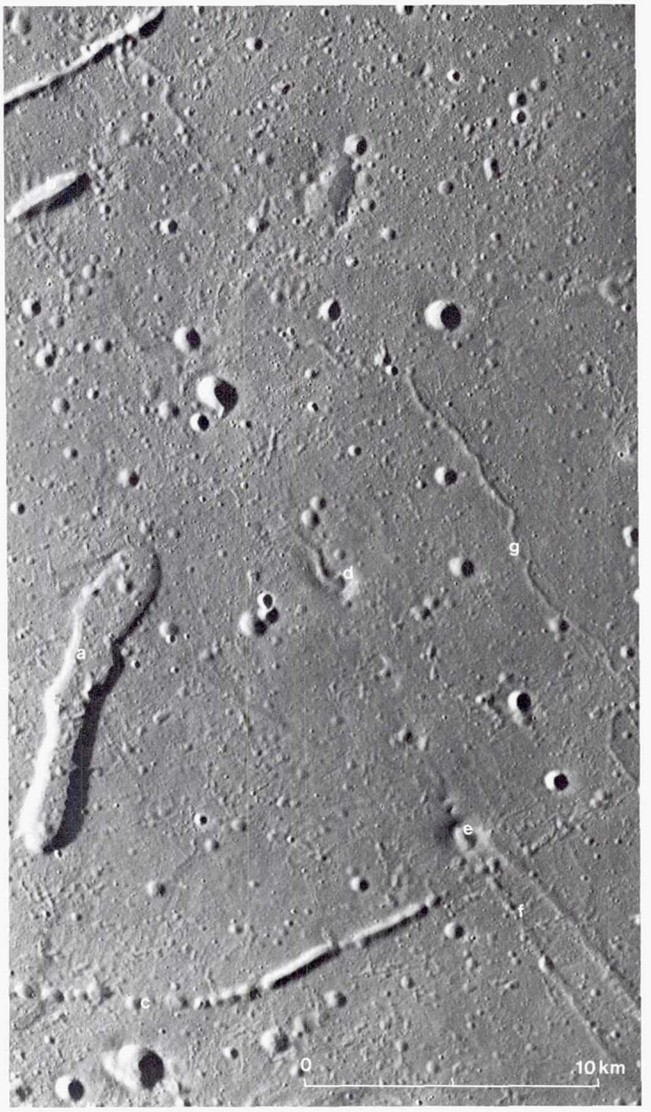

Figure 6.55. Variety of endogenic landforms at margin of Mare Serenitatis, including broad subsidence feature shaped like a tongue depressor (a), probable subsidence or drainage rilles and craters (b, c), small cinder cones (d, e), two grabens (f), radial to the mare center, which may have localized one of the cones, and a sinuous rille (g) (see NASA, 1973, sec. 30, parts B, C; sec. 31, part A). Located on figure 6.60. Apollo 17 P-2317.

Figure 6.56. Endogenic dark-halo craters (arrows) in crater Alphonsus (119 km, a floor-fractured, pre-Imbrian crater scored by Imbrium sculpture). L = crater Lalande, once thought a caldera but probably an impact crater whose floor has been uplifted and covered by thin mare material. Foreground feature at lower right (D) is Rima Davy and Davy A, possibly of secondary-impact origin. Boom of gamma-ray spectrometer protrudes from left edge of photograph. Apollo 16 M-2478.

region; east of crater Plato). Sinuous rilles and other small volcanic landforms of the maria are thoroughly described and illustrated by Lowman (1969), Fielder (1971), Strom (1971), Head (1976), Schultz (1976a), Masursky, Colton, and El-Baz (1978), and the Basaltic Volcanism Study Project (BVSP, 1981).

Other landforms characteristic of the maria are not depositional but tectonic in origin. These faults and folds are discussed under "Tectonism."

Remote sensing

The term remote sensing is usually construed as instrumental observation of various parts of the electromagnetic spectrum with a telescope or from a spacecraft (or airplane in the case of Earth). Recognition of mare units depends more on remotely sensed optical, spectral, and geochemical properties than on intrinsic morphology (Head et al., 1978b). They differ

in this respect from impact units, because mare units are igneous rock bodies whose compositional unity arises from their mode of origin and is altered little during emplacement.

The most obvious optical property of the maria is their low albedo—the brightness or reflectance under high-angle illumination. By strict definition, albedo is the reflectance at nearly vertical illumination, but can be estimated sufficiently for most purposes when the Sun is higher than about 45°. Because of the contrast between exposures of feldspathic terra breccias and mafic mare basalts, the maria can be delineated even by unsophisticated observations of surface brightness (figs. 6.9, 6.57).

Before Apollo exploration, the causes of the albedo differences between terra and mare and among mare units were not fully known. Examination of the regolith shows that albedo is controlled both by composition and by duration of exposure to the unique lunar surface environment. Albedo depends on the amount and composition of agglutinates developed in regoliths from crystalline bedrock (Adams and McCord, 1973). Agglutinates are complex glass-bonded aggregates of regolith particles formed when small impacts melt and weld rock and mineral fragments. Up to a point, agglutinates accumulate in proportion to the time the regolith is exposed to impact peppering. Eventually, the amount accumulated

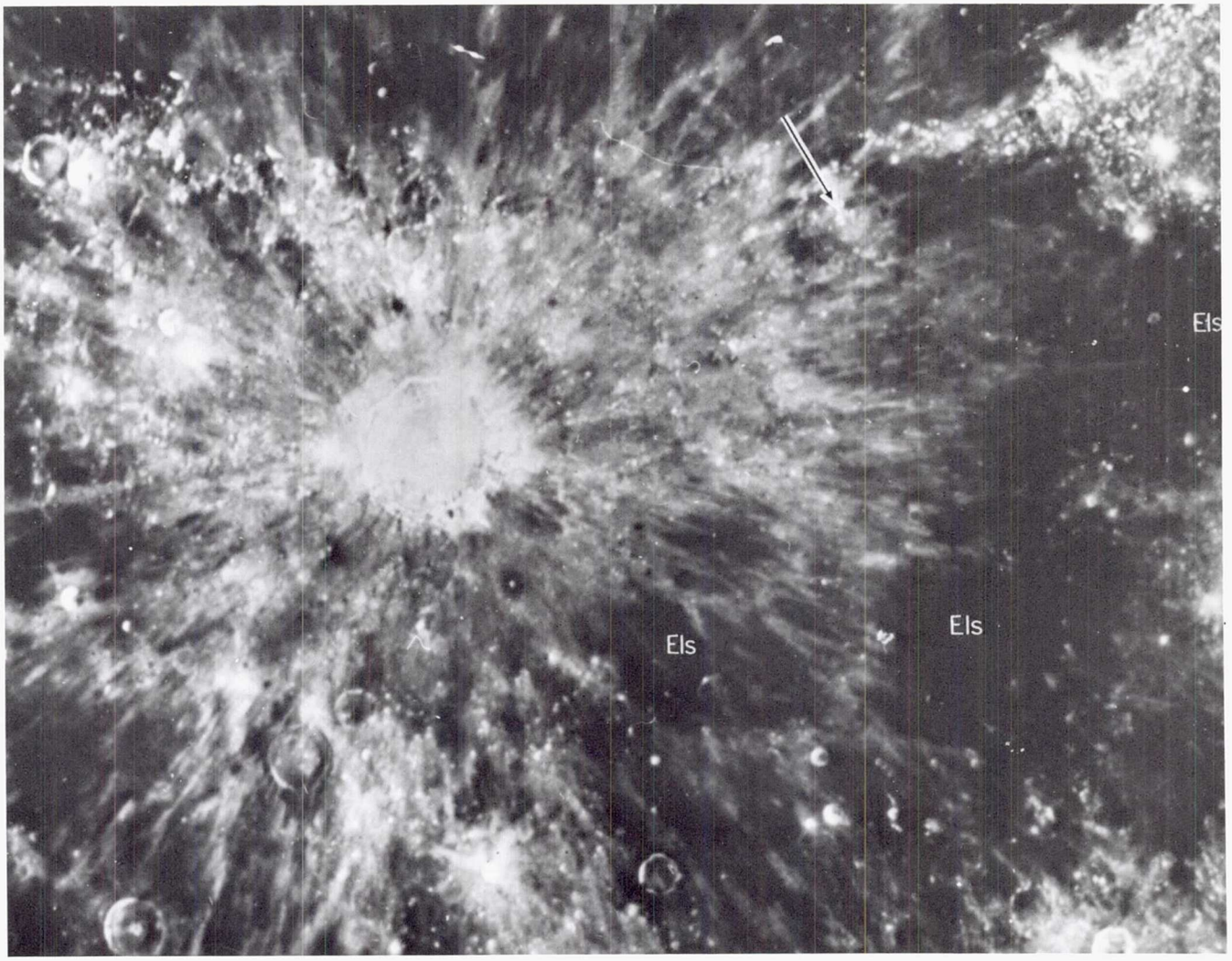

Figure 6.57. Full-Moon photograph of Copernicus region showing albedo differences. All terra and crater walls are bright because they are steep. Copernicus and most of its rays are bright because they are young. In both cases, fresh crystalline material is exposed. Maria and dark-mantling units are dark because mature, Fe-Ti rich regolith is developed on their surfaces. Eratosthenes (arrow) darkened almost to disappearance because it is much older than Copernicus. The dark-mantling materials (shown here by a superseded symbol EIs) are not brightened where crossed by Copernicus rays because the darkening process has operated more effectively on those Fe-Ti-rich units than on other units.

reaches a steady state in which new micrometeoroid impacts destroy as much agglutinitic material as they produce. Regoliths in this steady state are termed mature. In mature regoliths, composition of the agglutinates strongly affects the albedo; regoliths highest in iron and titanium are the darkest (Adams and McCord, 1973; Pieters, 1978). As all undisturbed mare regoliths are believed mature, the darkest regoliths form from the lavas that are highest in Fe and Ti. Higher content of these elements also explains why the maria are darker than the terrae. Although Fe may be the greater contributor to total darkening, the differences in albedo among mare units may be due more to differences in Ti content, because Ti varies more among mare-basalt units than does Fe (Pieters, 1978).

This correlation between darkness and Fe-Ti content applies only to mature regoliths developed on mare basalts. Fresh exposures may not have been exposed long enough to accumulate impact glass in steady-state amounts (Adams and McCord, 1973). Such exposures occur in two main settings. The first is on steep slopes, where the new glass is shed and nonglassy material continuously exposed. The fresh material is brighter than the less disturbed material (fig. 6.57). As a result, lunar slopes are generally brighter than adjacent, more nearly level terrain composed of the same geologic unit (Shoemaker and Hackman, 1962). Second, relatively recent impacts exhume fresh material of mare lavas and redeposit it as bright crater rays. Rays darken more quickly in regoliths containing much Fe and Ti than they do in regoliths poor in these elements, explaining why the rays of the same crater are brighter on the terra than on Fe-Ti-rich mare units (fig. 6.57).

Color differences are subtle on the Moon. The visual and near-visual spectra of all areas are similar, and increase in reflectance toward longer wavelengths; that is, all lunar colors are reddish. However, differences do exist, and can be detected with instruments on Earth-based telescopes and enhanced by various photographic, instrumental, and computer image-processing techniques (McCord et al., 1976; Pieters, 1978). Color differences have proved to be valuable discriminators of lunar mare units, and can indicate the presence of some mineral compositions. Spectra of areas 10 to 20 km across are measured photometrically. The entire near side has also been photographed at two wavelengths in such a way as to indicate composition (fig. 6.58; bright = reddish surfaces; dark = bluish surfaces; Whitaker, *in* Hess et al., 1966, 1972). To a first approximation, the bluer the surface, the richer a mature mare regolith is in Fe and Ti (Whitaker, 1972; Pieters, 1978). Therefore, the dark areas in figure 6.58 are richer in these elements than the bright areas. Bright, reddish surfaces are low in Ti and Fe, but the amounts and proportions of the two elements may not be determinable from the color or albedo (Pieters, 1978). Table 6.7 (Pieters, 1978) summarizes the properties which can be inferred from the four wavelength bands which are most commonly used to interpret compositions by remote sensing. The properties are valuable for extrapolating the findings of sampling missions to unsampled areas.

Interiors of young craters on both mare and terra differ from the surrounding regions overlain by mature regoliths in having less agglutinitic and more crystalline material. These characteristics affect the general nature of the spectral continuum and also allow specific near-infrared absorption features around 1 and 2 μm to be detected (McCord et al., 1976).

Two instruments flown in lunar orbit on the Apollo 15 and 16 missions have also permitted extrapolations of sample compositions to unsampled parts of the Moon. The gamma-ray spectrometer and X-ray fluorescence spectrometer are currently the only means of estimating compositions on the far side. The compositions determined are those of surficial layers, but are thought to represent underlying materials, because the sharp boundaries between mare and terra and among mare units, as seen on the color-difference images (fig. 6.58), have persisted since the maria formed (Kuiper, *in* Heacock et al., 1965).

The gamma-ray spectrometer measures natural radioactivity of K, Th, and U, and also gamma rays emitted from other elements during nuclear reactions induced by high-energy cosmic ray bombardment (BVSP, 1981, ch. 2). The most useful results are obtained for Th, K, Fe, Mg, and Ti. The instrument integrated readings over areas of $2° \times 2°$ (3600 km^2) to $10° \times 10°$ (90 000 km^2) and analyzed about 22 percent of the total lunar surface. It showed that the western maria are more radioactive than the eastern (Soderblom et al., 1977). The X-ray spectrometer detects the elements Al, Mg, and Si from the intensity of the secondary X-ray fluorescence induced by solar X-rays. The results are reported as intensity ratios: Al/Si, Mg/Si, or Mg/Al. The eastern maria appear somewhat richer in Al than the western (Adler et al., 1972; Hubbard, 1979). The X-ray data are limited to illuminated terrane, and cover about 10 percent of the lunar surface. Data treatment has resolved areas

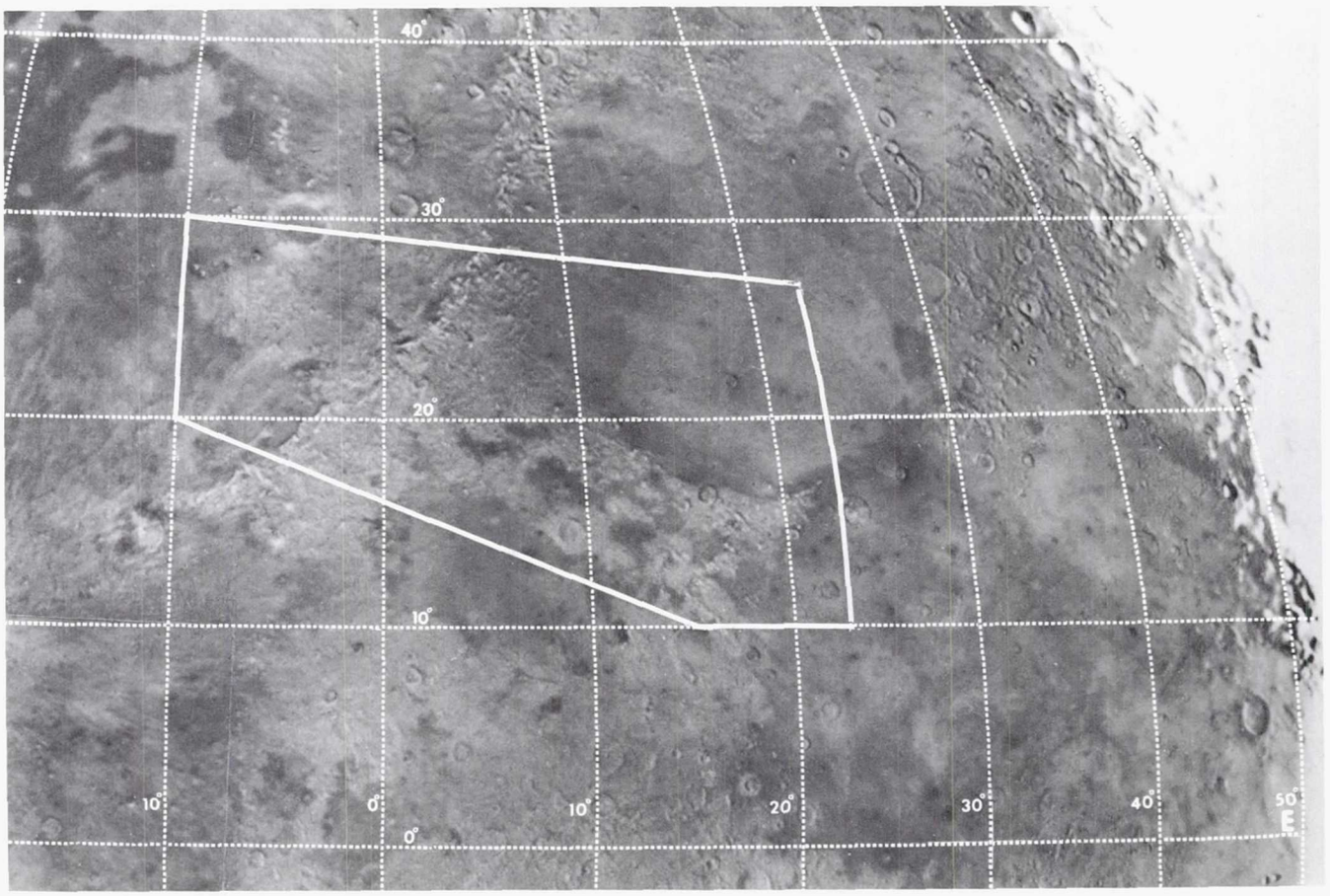

Figure 6.58. Color-difference photograph of north-central part of near side. Strong contrast between dark ("blue") and brighter ("red") maria evident in Mare Imbrium to left of white box and in Maria Serenitatis and Tranquillitatis inside and right of white box (white box encloses part of Apollo 15 and 17 ground tracks). Copernicus and its rays conspicuous (centered 10°N, 20°W). Courtesy E. A. Whitaker (1972).

Table 6.7. Properties of Mare Units

Unit[1]	D_L[2]	Crater density[3] (≥1-km craters/km²)	Location[4]	Spectral class[5]	Interpretation[6]
Em	100–240	$1–2.5 \times 10^{-3}$	E. Frigoris	LBSP	Very low Ti, high Fe or pyroxene
			W. Frigoris	LISP	Very low Ti
			Imbrium	hDSA	Med.-high Ti, prob. high Fe, radioactive
			N. Imbrium	LBSP	—
			Procellarum	hDSA	—
				HDSA	High Ti, prob. high Fe, radioactive
			Procellarum at long 35°W	hDSP	Similar to hDSA, maybe rich in pyroxene
			Serenitatis, Vaporum	hDWA	Medium Ti, maybe high Al
Im_3	240–280	$2.5–4.0 \times 10^{-3}$	Frigoris	LBSP	—
			E. Imbrium	LBSP	—
				LBG-	Very low Ti, high Al

Table 6.7 (continued). Properties of Mare Units

Unit[1]	D_L[2]	Crater density[3] (≥1-km craters/km²)	Location[4]	Spectral class[5]	Interpretation[6]
				LIG-(A15)	Low Ti, high radioactivity
			W. Imbrium	LBG-	—
				LBSP	—
			W. Procellarum	mISP	Low-medium Ti, maybe low Fe
			Procellarum E. of long	mISP	—
			35°W, Insularum,	mIG-	Diverse; low-medium Ti
			Nubium		(A12 type)
			W. Humorum	mISP	—
			Cent. Humorum	hDSP	—
			E. Humorum	mIG-	—
			Serenitatis	mISP	Maybe higher Fe than in Procellarum
			Tranquillitatis	HDWA	Very high Ti
			N. Fecunditatis	hDWA (L16)	—
			Crisium	LBG-	—
				LISP (L24)	—
				mIG-	—
				hDWA	—
Im_2	280–390	4×10^{-3}–2.6×10^{-2}	Roris, Iridum	LBG-	—
			NE Imbrium	LBG-	—
				LBSP	—
			Somniorum	LBG-	—
			NW, SW Tranquillitatis	HDWA (A11)	—
			SE, NE Tranquillitatis	mIG-	—
			Nectaris, S. Fecunditatis	mBG-	High Al
			Cent. Fecunditatis	mIG-	—
Im_1	>390	Not determined	Margin of NW Procell.	hDW-	—
			Somniorum	LBG-	—

NOTES:

1. Em = Eratosthenian mare material; Im = Imbrian mare material; subscripts denote age groups, 3 youngest, 1 oldest (not distinguished on plates).
2. Boyce and Dial (1973, 1975); Boyce et al. (1974, 1975); Boyce (1976); Moore et al. (1980).
3. Neukum et al. (1975a, b); Neukum and König (1976).
4. Refers to tracts of mare as mapped on plate D.
5. Pieters (1978) and BVSP (1981, ch. 2). First letter refers to UV/visual ratio (H = high; h = medium-high; m = medium; L = low); second letter refers to albedo (D = dark; I = intermediate; B = bright); third letter refers to 1-μm band (S = strong; W = weak; G = gentle); fourth letter refers to 2-μm band (P = prominent; A = attenuated; - = undetermined). A = Apollo; L = Luna.
6. Incorporates interpretations of color, gamma-ray, and X-ray data (BVSP, 1981, table 2.2.4). Interpretation given here only at first entry for each unit unless occurrences differ.

as small as about 1° wide (900 km²). With these resolutions, ejecta of individual craters, and therefore the subsurface materials exhumed and redeposited in the ejecta, can be analyzed (Andre et al., 1978).

Three other parts of the electromagnetic spectrum, accessible from Earth or with the aid of a spacecraft, have potential value in interpreting the maria. The first, in the thermal infrared part of the spectrum, measures temperatures during a total eclipse of the Moon (Saari et al., 1964; Winter, 1970) or from orbit (Low and Mendel, *in* NASA, 1973, sec. 24). These data are useful for detecting youthful craters because high eclipse temperatures result from fresh surfaces which may be undetectable in low-resolution photographs. For extended surfaces such as the maria, they may also indicate blockiness, resulting from thin

regolith, or may have a compositional significance (Moore et al., 1980).

Lunar applications of radar have been intensively studied. Earth-based signals in 3.8 cm and 70 cm bands have yielded the most detail, including radar maps of the whole nearside disc (Thompson, 1974, 1979; Zisk et al., 1974; Moore et al., 1980). So many factors affect echoes (Moore et al., 1980) that the interpretation of the data is still partly uncertain. Other factors being equal, the echoes measure depths of penetration and roughness at scales proportional to wavelength—larger than 70 cm for 70-cm radar and larger than 3.8 cm for 3.8-cm radar. Hence, the data may help determine blockiness of a regolith and therefore the age and target material of a crater (Thompson et al., 1979). Supplementary data are usually needed when interpreting radar data for maria (Zisk et al., 1977; Moore et al., 1980).

Figure 6.59. Thickness of mare basalts.
A. Western maria (De Hon, 1979).

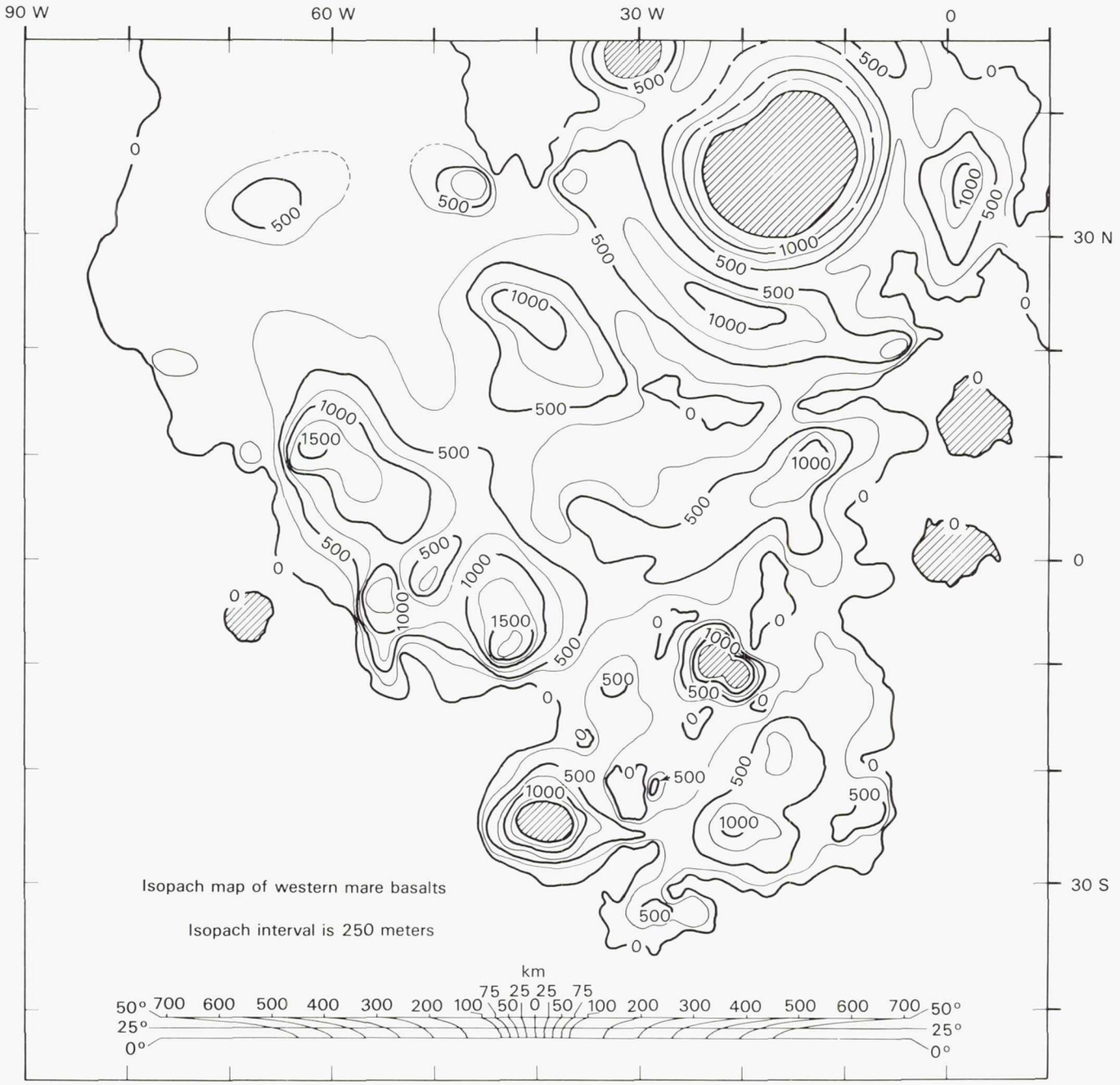

The remote sensing data are most valuable when examined together (Thompson et al., 1973, 1974; Zisk et al., 1977). Correlations among data sets are readily visualized when converted to a common format and displayed as false-color images showing any desired weighted combination of data sets (Eliason and Soderblom, 1977; La Jolla Consortium, 1977; Soderblom et al., 1977).

Elevation and thickness

Thicknesses of mare materials can be approximately measured by the degree of flooding of craters (fig. 6.59; Marshall, 1961; DeHon, 1974, 1979; DeHon and Waskom, 1976; Hörz, 1978; Head, 1979b). The crater depths are estimated from their diameters by assuming either that depth/diameter ratios and rim heights are the same as those of fresh craters (DeHon, 1974, 1979) or the same as those of a random population of craters (Hörz, 1978; Head, 1979b). Also, it is assumed that craters have not rebounded significantly and are superposed on the basin floor, not an earlier mare unit. Accordingly, thickness estimates vary. An average thickness of 0.4 km for all maria (DeHon, 1979) is equivalent to 2.4×10^6 km^3 of mare basalt on the whole Moon (0.4 km $\times$ 0.16 of the total lunar area of 38×10^6 km^2).

Mare-surface elevations decrease within a basin from the outer shelves to the center and therefore mimic the topography of the host basin (figs. 6.60, 6.61; Howard et al., 1974; Wilhelms, *in* NASA, 1973, sec. 29D). As shown by the diminished number of craters in the centers, the central mare deposits are also thicker than those on the shelves. The thickening is further demonstrated by positive gravity anomalies known as mascons (mass concentrations), detected by their perturbations on the orbits of spacecraft (Muller and Sjogren, 1968; 20 December 1968 issue of *Science*). Thicknesses in the mascon maria are estimated from modeling of the gravity data as 2 to 4 km (Sjogren et al., 1974). The largest mascons were modeled over Maria Imbrium, Serenitatis, Crisium, Humorum, Nectaris, Smythii, Orientale, and the mare in the center of the small Grimaldi basin (Solomon and Head, 1980).

B. Eastern maria (De Hon and Waskom, 1976). Scale applies to equator.

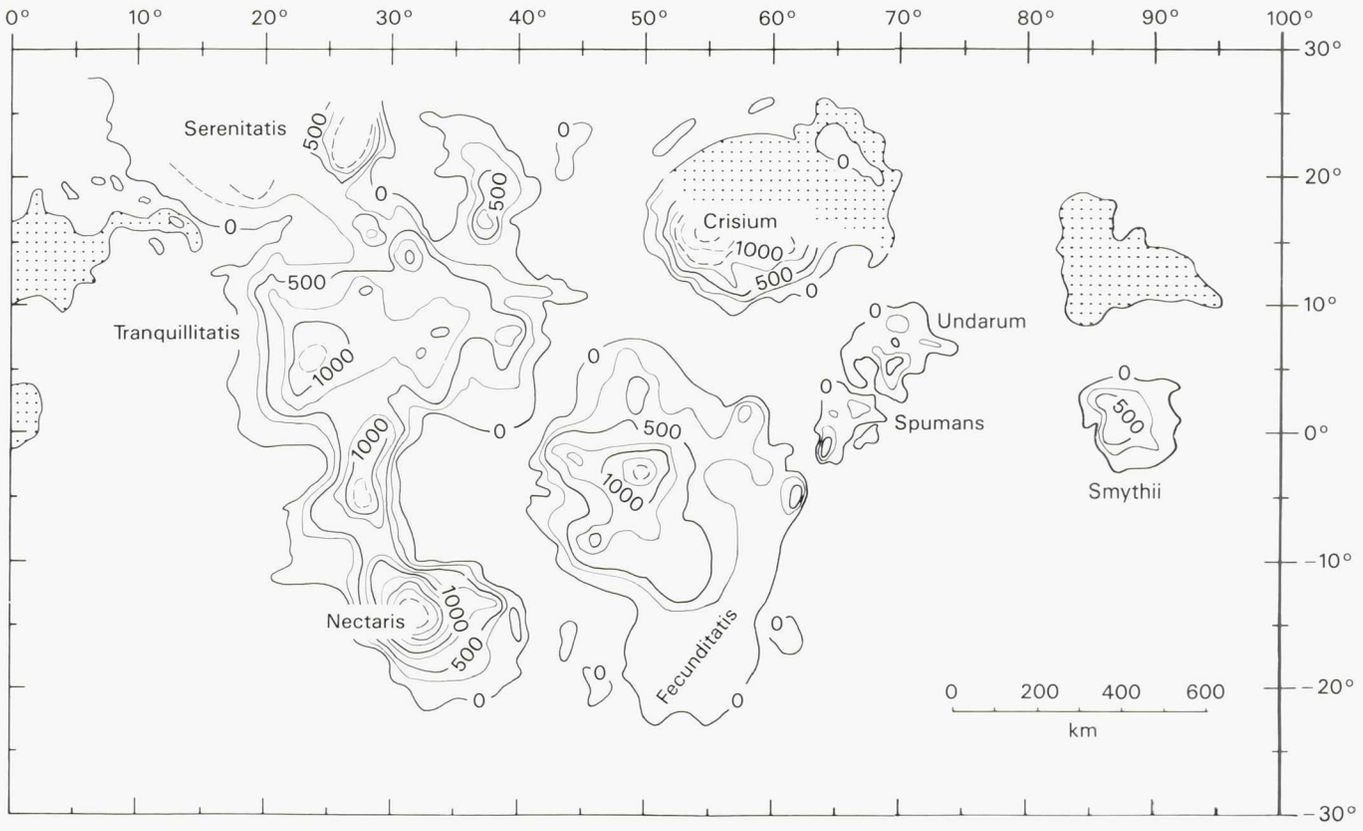

Isopach map of the eastern mare basalts

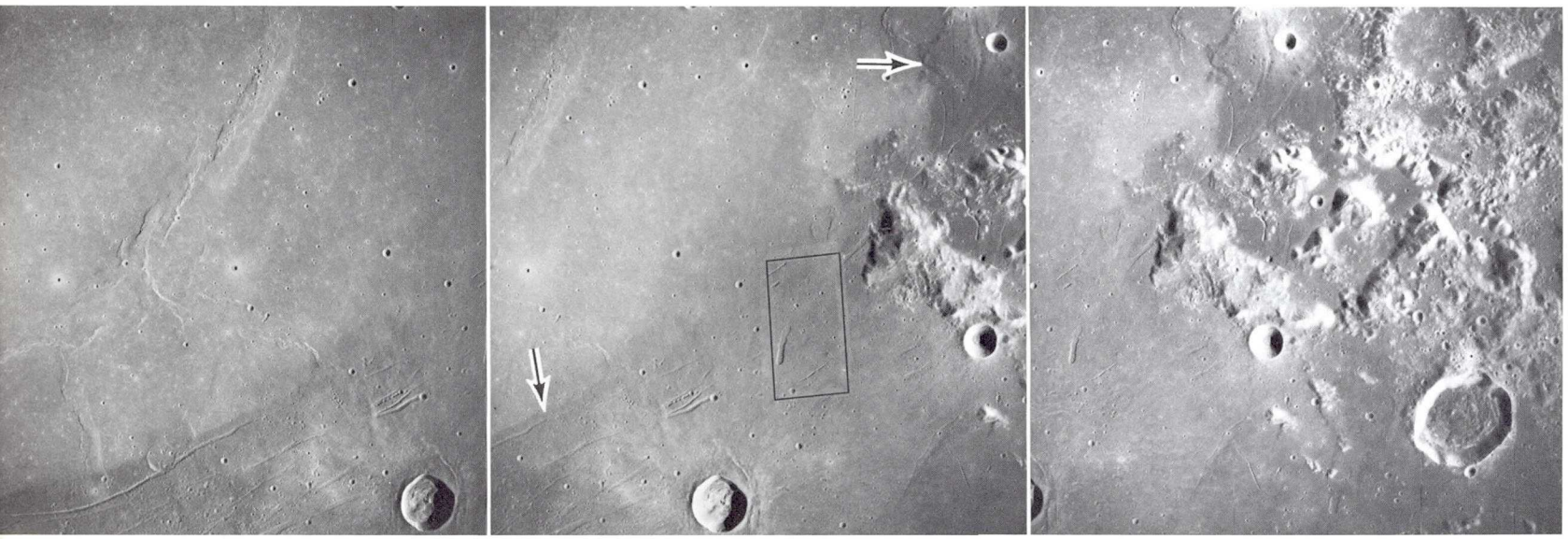

Figure 6.60. Southeastern border zone of Mare Serenitatis. Light-colored interior mare sharply abuts darker border (arrows). In left-hand frame, darker unit is "blue" mare lava; in right-hand frame, it is dark-mantling material. Apollo 17 site in right-hand frame (compare figure 6.47). Area of figure 6.55 outlined in center frame. Large crater in center and left frames is Dawes of Copernican age, (18 km, 17°N, 26°E). Stereoscopic pairs, Apollo 17 M-5000, M-5002, M-5004, right to left.

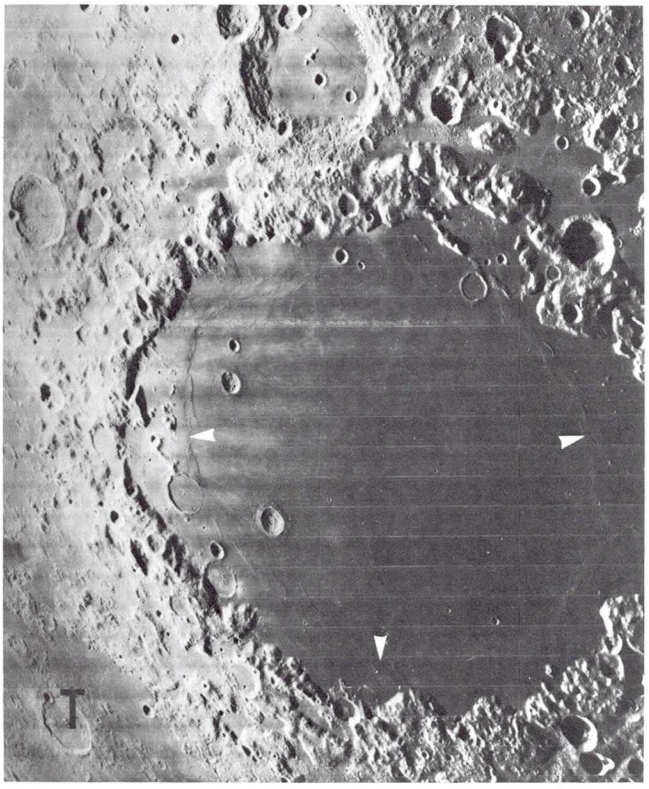

Figure 6.61. Mare Crisium. Arrowheads indicate mare ridges and scarps that formed between outer, shallow shelf and inner, thicker central mare. T = Taruntius (56 km, 6°N, 47°E), a Copernican crater having an uplifted, fractured floor. Orbiter 4 H-191.

A radar sounder flown on the Apollo 17 mission more directly measured depths to discontinuities in Maria Serenitatis and Crisium (Peeples et al., 1978). The depth figures are based on certain assumptions about the dielectric constant of the overflown materials and may not represent maximum depths. In Mare Serenitatis, one horizon lies about 1 km beneath the surface, and another lies 1.6 km deep in the west to 2.0 km deep in the east (Peeples et al., 1978). A horizon which appears to lie within the basalt section of Mare Crisium lies 0.8–1.0 km below the surface of the shelf which separates the conspicuous ridge system and the basin rim (fig. 6.61), then deepens to 1.4 km inward from the shelf (Maxwell and Phillips, 1978; Peeples et al., 1978).

Mare thicknesses are also inferred from the geochemical experiments. The craters Picard and Peirce (fig. 6.61) have penetrated the 1.4-km layer in Crisium and have excavated additional basalt whose Mg-rich chemistry is evident in the X-ray fluorescence data (Andre et al., 1978). These craters may also have excavated terra materials from beneath the mare (Head et al., 1978b). Based on the assumed excavation depth of Peirce, Maxwell and Phillips (1978) estimate the total mare thickness as 2.4 to 3.4 km.

Better thickness data are not available, but even an approximate estimate of mare volumes is useful in con-

sidering lunar geochemistry and petrology. The average thickness is probably less than 1 km, corresponding to less than 0.25 percent of a crust 75 km thick. Even if subsurface intrusions are added, the mare basalts are clearly volumetrically minor.

Terra mantling

Deposits called dark mantling materials or terra mantling materials are related to the mare materials but differ in several properties. They are as dark or darker than the maria, but their relief is partly rugged (fig. 6.62). The largest and most numerous tracts having this seemingly anomalous combination of properties lie around the southern periphery of the Imbrium basin (color plates C, D). Others are peripheral to almost all carefully scrutinized maria (Head, 1974d, 1976; Wilhelms, 1980a). The flat parts of maria may also contain dark mantling materials, but these are difficult to distinguish from mare lavas except by spectral techniques (Adams et al., 1974).

On both telescopic and spacecraft photographs, dark mantling deposits appear fine textured, relatively uncratered, and smoother than the underlying topography (fig. 6.62). No blocks are visible in the 2-m resolution of the best Apollo photographs. Radar and thermal-infrared observations also show an absence of blocks (Zisk et al., 1977). Mantles drape differentially over mountains, low hills, and flat surfaces, being thickest in depressions and thin or absent on sharp hills. Some hilltops surrounded by the deposits are bright, indicating shedding of the dark material. The action of mass wasting is further indicated by talus streaks which descend from the bright outcrops. The dark deposits are located near likely eruptive fissures in the form of rilles, endogenic craters, gashes, and dark cones (fig. 6.62). Such craters are much rarer in the mare lavas, which probably cover their sources as do flood-basalt lavas on Earth (Greeley, 1976). All these properties are consistent with pyroclastic origin for the dark mantling materials.

Stratigraphy and Distribution

The maria are (1) young relative to most other lunar stratigraphic units and (2) spatially related to basins. The visible maria are Late Imbrian, Eratosthenian, and Copernican in age; that is, they postdate the Orientale basin.

The general geographic relation between basins and maria is obvious. Few maria are located far from basins. Some basins were initially identified partly by the presence of small mare patches in seemingly isolated localities, and so undiscovered basins may also explain the remaining outliers. Continental sheets of basalt not occupying basins have been proposed, in particular for Oceanus Procellarum. But this large mare is probably contained within the Procellarum (Gargantuan) basin (fig. 6.63; Cadogan, 1974, 1981; Whitaker, 1981). The Procellarum basin additionally embraces all the large near-side or limb maria except Orientale, Nectaris, Crisium, Fecunditatis, and Smythii. The materials of all these maria except Crisium are thin.

Table 6.7 and the geologic and paleogeologic maps (color plates C and D) give some indication of the relations between age and spectral type of mare units (Boyce et al., 1974; Head, 1976; Head et al., 1978a, b; Whitford-Stark and Head, 1980; Pieters et al., 1980; BVSP, 1981, ch. 2). Most Eratosthenian and all known Copernican mare units (fig. 6.52; plate D) lie within the Procellarum basin and are bluish in color (some are marginal to the younger Imbrium and Serenitatis basins but central to Procellarum). Imbrian units (plates C and D) are more diverse spectrally

Figure 6.62. Dark-mantling material southwest of Mare Serenitatis. Arcuate rilles are Rimae Sulpicius Gallus. Many endogenic craters in scene (arrows). Steep slopes including sharp summits and the long, linear (Imbrium-radial) terra structure are bright because dark mantle has been shed. Apollo 17 H-23572.

(A)

(Pieters, 1978). Three subdivisions of Imbrian mare material can be distinguished on most of the Moon (table 6.7), and more than three in some well photographed maria (Boyce, 1976; Wilhelms, 1980a). Old Late Imbrian blue units are exposed in a few marginal embayments of Oceanus Procellarum (fig. 6.64). Intermediate-age Imbrian, blue, dark units characterize Mare Tranquillitatis and the adjoining border of Mare Serenitatis (figs. 6.57, 6.58, 6.60). Small patches of youngest Imbrian blue materials are scattered in most maria. Red units of all three Imbrian age subdivisions are in Oceanus Procellarum and in

Figure 6.63. The Procellarum basin according to Whitaker (1981).
A. Full-Moon photograph showing best-developed parts of three rings. Western shore of Oceanus Procellarum and northern shore of Mare Frigoris are especially well defined by Procellarum rings, which are centered about point P (23°N, 15°W). I = center of Imbrium basin.
B. Whitaker's (1981) interpretation of complete rings and relation to mare ridges.

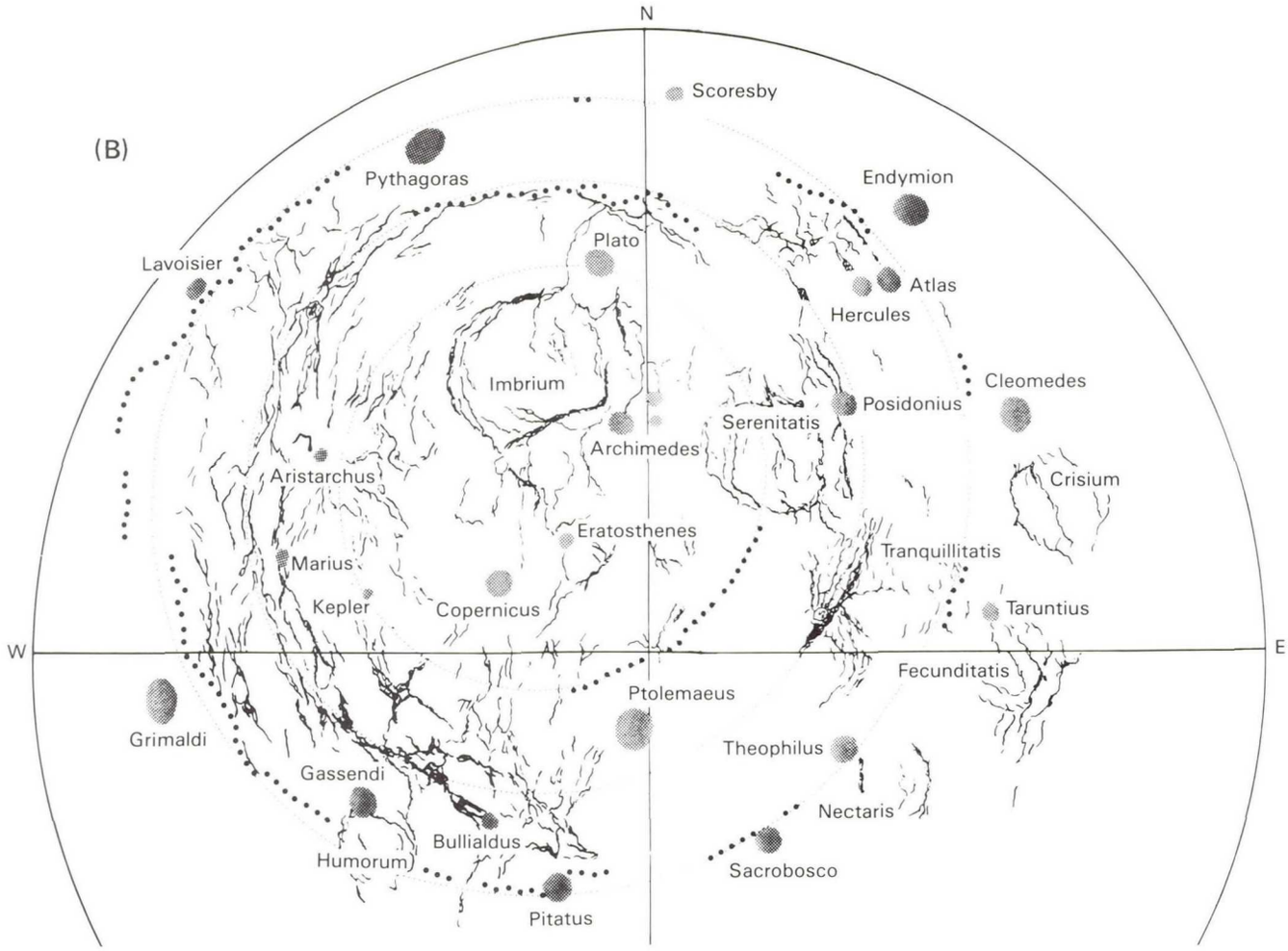

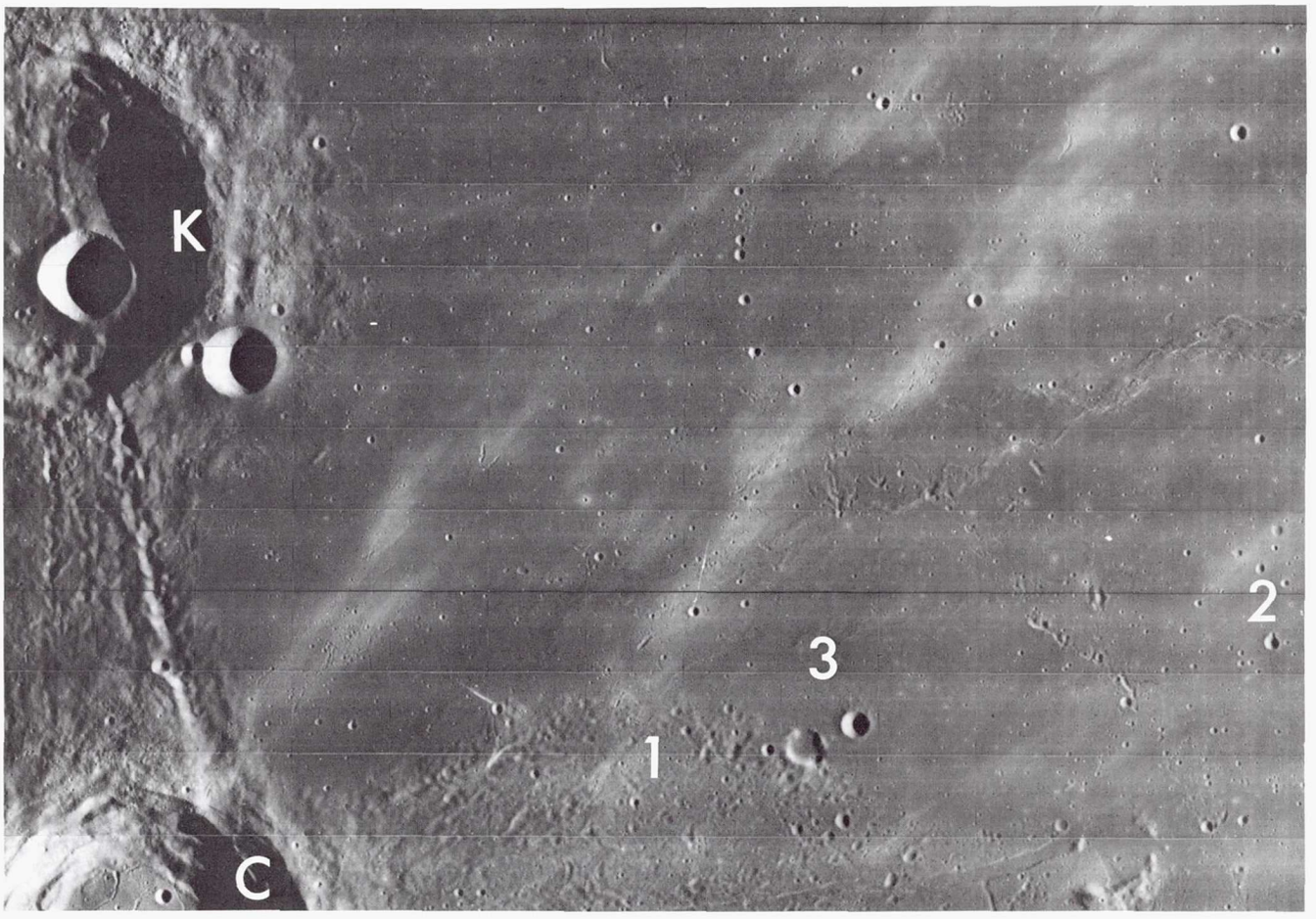

Figure 6.64. Mare stratigraphy in western Oceanus Procellarum. Oldest mare unit (1) is overlain by ejecta of crater Cardanus (C, 50 km, 13°N, 72°W; other large crater is Krafft, K, 51 km). Unit having fairly numerous superposed craters is probably next youngest (2). Sparsely cratered unit (3) sharply truncates unit 1 and probably is younger than unit 2, although contact is not distinct. Orbiter 4 H-169.

the maria occupying superposed basins. Some young Imbrian red patches are in Mare Crisium. An extensive reddish or orange mare-type of young Imbrian age fills central Mare Serenitatis and covers extensive tracts of Oceanus Procellarum (spectral class mISP; Pieters, 1978).

Therefore the most extensive maria and the most extensive red and blue units occur in the Procellarum basin or in basins superposed on that larger and older basin. In keeping with the distribution of KREEP, high radioactivity characterizes the western maria in Procellarum (Soderblom et al., 1977). High-Al, spectrally nondescript, weakly radioactive materials lie outside Procellarum in Maria Smythii, Fecunditatis, and Crisium (Hubbard, 1979). Little is known about farside mare compositions, except that the maria in the South Pole-Aitken basin are about as radioactive as eastern mare materials (Metzger et al., 1977).

MARE BASALTS

Introduction

Samples of mare basalt were returned by all landing missions. The largest amounts came from Apollos 11, 12, 15, and 17, which landed on maria (fig. 6.1). Small regolith cores were returned by Lunas 16 and 24, which also landed on maria. Apollos 14 and 16 and Luna 20 returned small amounts although they landed on terrae; fragments were thrown in by distant impacts. The basalts present considerably fewer problems than do the breccias from the terrae. Although the basalts also came from the regolith, with one exception (outcrops along Hadley Rille at the Apollo 15 site), they are much less severely reworked by impacts than the terra materials. Unlike most terra breccias, (1) the textures and compositions originated

in the same event, and (2) the radiometric age of a mare-basalt sample usually represents a crystallization age that is the same as the emplacement age of the source unit.

Composition, Mineralogy, Texture

Lavas

Lunar mare rocks are designated basalts by the same general criteria used to define terrestrial basalts: dark, mafic, extrusive rocks consisting primarily of (clino)pyroxene and plagioclase. In detailed elemental abundances, however, they differ from terrestrial basalts (table 6.8; Taylor, 1975, 1982; Papike et al., 1976; Papike and Vaniman, 1978; BVSP, 1981, ch. 1). The most important differences are that lunar basalts (1) contain no detectable H_2O; (2) are low in alkalis, especially Na_2O; (3) are high in TiO_2, TiO_2-poor lunar basalts having about the same amount of this oxide as average terrestrial basalts; (4) are low in Al_2O_3 and SiO_2, maximum contents of these oxides being about the same as average contents in terrestrial basalts; (5) are high in FeO, higher than terrestrial basalts; and (6) are generally richer in MgO than terrestrial basalts, the lowest contents being about the same as the terrestrial average. One additional important difference is in the extreme degree of reduction. Lunar basalts contain essentially no Fe^{3+}; most Fe occurs as Fe^{2+}, and native Fe metal, formed by reduction at or near the surface, is present.

Mare basalts are higher in FeO and MgO and lower in Al_2O_3, CaO, and Al_2O_3/CaO ratio than terra melt rocks of impact or volcanic origin (Taylor, 1975, 1982; BVSP, 1981, sec. 1.2.9). Most mare basalts have a negative europium anomaly, in contrast to the positive anomaly of the terrae. Both the mare and the terra materials, therefore the whole Moon, are very poor in volatiles (Taylor, 1982).

Textures of the returned mare basalts leave no doubt about their origin from magmas. They are similar to textures of terrestrial basalts, except that they lack alterations caused by chemical weathering and hydrothermal activity (fig. 6.65). They are typical of extrusive volcanic rocks produced by fairly rapid, near-surface crystallization of silicate melts. Most textural variations within each suite arose during second-order fractionation, crystallization, and cooling after extrusion (Lofgren et al., 1975).

Each sampling mission clarified details about mare origin, but also weakened generalizations which had been made earlier about compositional and age groups. Many authors have grouped mare basalts into two major, genetically significant compositional classes: (1) high-Ti (9–14 percent TiO_2), and (2) low-Ti (1.5–5 percent TiO_2; Papike et al., 1976). Basalt very low in titanium (VLT) was found in the Luna 24 sample in 1976 and may represent a third major group (Papike and Vaniman, 1978). The intermediate Ti contents are not well represented in the samples but apparently constitute extensive spectral units (table 6.7). Another major class are the high-alumina basalts (table 6.8; Ridley, 1975; Taylor, 1975, 1982). Small regolith fragments add more types to those identified among the rock-size (≥ 1 cm) samples. As many as two-thirds of the 15 spectral classes recognized telescopically may remain unsampled (Pieters, 1978). A complete range of compositions among lunar basalts now appears likely (Papike and Vaniman, 1978). Extrusion times were sometimes grouped into an early Apollo 11 and Apollo 17 high-Ti phase and a later Apollo 12 and Apollo 15 low-Ti phase; but basalts undoubtedly were extruded throughout the Late Imbrian Epoch, perhaps more sporadically in the Eratosthenian and Copernican Periods.

The heterogeneity already encountered among the mare-basalt samples and the number of unsampled compositional classes suggest that no two collection sites on the maria would furnish identical samples. For this reason and to avoid ambiguity in nomenclature, classification schemes generally include the sampling mission as one designator (table 6.8). The classification given here (BVSP, 1981, sec. 1.2.9; Taylor, 1982, table 6.1) incorporates the chief distinguishing chemical characteristic and, commonly, the name of a characteristic modal mineral (Apollo 12 and 15 low-Ti olivine or pigeonite basalts). Some literature refers to a characteristic texture (Apollo 11 "ophitic" or "intersertal" basalt). Trace-element chemistry is also used to classify some basalts, for example, those from the Apollo 17 site (Rhodes et al., 1976).

Pyroclastics

Sampling data substantiate the pyroclastic origin of the dark mantling materials. Pyroclastic materials in the form of glass droplets were found at all sampling sites; the most abundant from the Apollo 17 site. They are orange and black glasses that have been identified by distinctive spectral properties as similar to a telescopically observed dark mantling unit (Pieters et al., 1974; Adams et al., 1974). Orange and black droplets, derived from a sheet of pyroclastic material

Figure 6.65. Photomicrographs of thin sections of mare basalts from Apollo 12 and 15 sites showing diverse textures. Minerals are completely unaltered by chemical weathering despite their great age. Each view about 2-mm wide. Courtesy O. B. James.

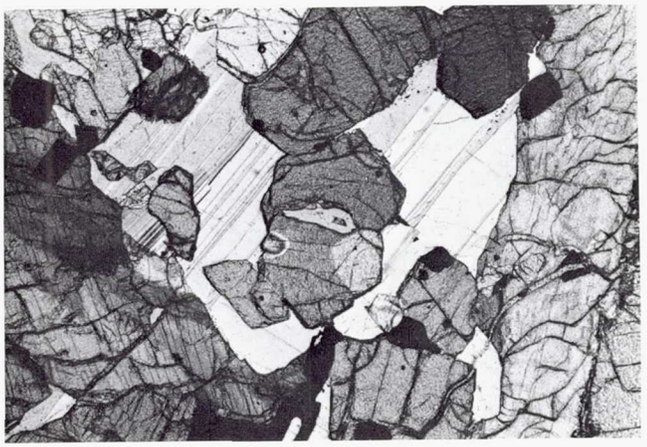

A. Sample 12035. Large anhedral crystals of plagioclase (light color; parallel twinning structure), large subhedral crystals of olivine (irregular structure), and large subhedral crystals of pyroxene (dark; parallel structure). Crossed polarizers.

C. Sample 12052. Large equant crystals at left and top are olivine, other large crystals are pyroxene. Groundmass of narrow, elongate grains consists of intergrowth of plagioclase, pyroxene, Fe-Ti oxides, and other trace phases. Same age as 12051 despite origin in separate, Si-rich flow. Plane polarized light.

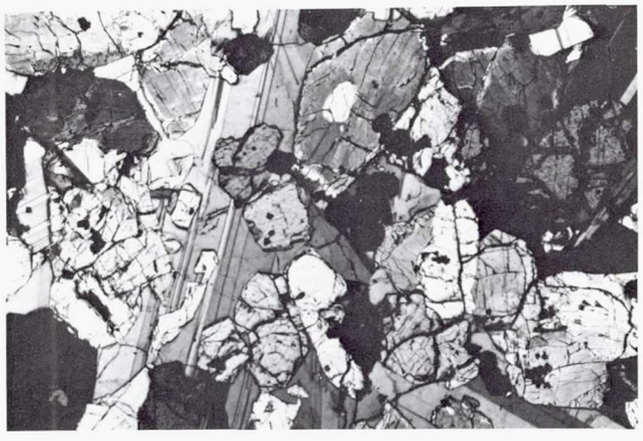

E. Sample 15538. Aggregates of large pyroxene grains "poikilitically" enclosed by large plagioclase crystals. Crossed polarizers.

B. Sample 12051. "Subophitic" texture in which laths of plagioclase (light color) are partly enclosed by pyroxene of approximately same size (dark). Black grains are ilmenite; chemically, rock is intermediate in TiO_2. Dated as 3.16 aeons old, the average age of the Apollo 12 basalts (table 6.6). Plane polarized light.

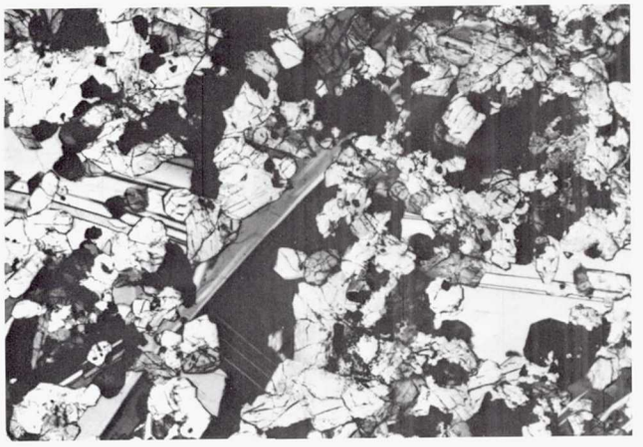

D. Sample 15535. "Granular" texture of pyroxene (irregular) and plagioclase (parallel twinning structure). Crossed polarizers.

F. Sample 15548. "Intergranular" texture consisting of aggregates of small, equant pyroxene grains enveloping plagioclase laths. Plane polarized light.

Table 6.8. Classification of Sampled Mare Basalts Widely Used by Lunar Investigators and in this Volume (after Basaltic Volcanism Study Project, 1981, sec. 1.2.9; Taylor, 1982, table 6.1). Includes major chemical and/or mineralogical characteristics that distinguish groups

Group name	Chemistry (oxides in weight percent)			
	Al_2O_3	TiO_2	K_2O	MgO
Apollo 11 high-K high-Ti	8–10	9–14	>0.3	7–10
Apollo 11 low-K high-Ti Apollo 17 low-K high-Ti			~0.1	
Apollo 12 ilmenite		5–9		
Apollo 12 low-Ti pigeonite Apollo 15 low-Ti pigeonite		1.5–5		
Apollo 12 low-Ti olivine Apollo 15 low-Ti olivine				10–18
Apollo 17, Luna 24 (very low Ti (VLT))	10–15	<1.5	<0.04	10–11
Apollo 12 feldspathic Luna 16 feldspathic Apollo 14 feldspathic		3–5	0.1–0.2	7–9

originally ≥1.5 m thick, are admixed with lava and terra fragments in the Apollo 17 regolith. The difference in color is due to more complete crystallization of the black droplets than the orange (Heiken et al., 1974). The devitrified black beads have a "blue" spectrum and the glassy orange beads have a "red" spectrum. Presumably this difference in devitrification accounts for similar spectra elsewhere, such as the "red" spectra on the Aristarchus Plateau (Zisk et al., 1977). The Apollo 17 droplets apparently were emplaced during an early "lava-fountain" or "fire-fountain" stage of mare eruption and were deposited on the mare basalt before most of the regolith formed (Heiken et al., 1974; Head, 1974d). Similar relations at other mare margins suggest that this volatile-driven stage was common in the early history of the filling of basins.

Green glasses collected by Apollo 15 are low in Ti and highly mafic. Pyroclastic rather than impact origin is indicated by the absence of fragments in the droplets (Delano, 1979). Delano (1979) proposes derivation from heterogeneous, volatile-rich sources at 400 ± 50 km depths.

Emplacement Ages and Petrologic Relations

Apollo 11

Only one of the sample suites contains basalts that clearly differ in age. These are the first samples returned from the Moon, the Mare Tranquillitatis materials brought back by Apollo 11 (figs. 6.66–6.68). Two types of basalt are distinguished by megascopic differences, microscopic texture, chemical composition, initial Sr ratio, and crystallization age (Schmitt et al., 1970; Papanastassiou et al., 1977). The older compositional class yielded the oldest lava ages of any site. It is commonly referred to as *low-K, high-Ti* basalt. Nine rock-size (≥1 cm) samples have been dated by Rb-Sr, ^{40}Ar-^{39}Ar, and Sm-Nd methods (Turner, 1977; Papanastassiou et al., 1977; Guggisberg et al., 1979; BVSP, 1981, table 7.3.1). They yield a range of ages from 3.55 to 3.92 aeons; table 6.6 gives the ages that the BVSP (1981) believes most reliable. The low-K group may consist of four separate flows (fig. 6.68; Guggisberg et al., 1979; Beaty and Albee, 1980). The oldest flow yields the same dates as the Imbrium basin (3.84 aeons), but must be younger unless exhumed from beneath a thin layer of Imbrium ejecta. Extrusion of the low-K, high-Ti basalts may have begun very soon after the Imbrium impact.

The younger, *high-K, high-Ti* group averages 3.57 aeons according to the preferred determinations (BVSP, 1981, pp. 950–955). The age determinations, rock textures, and bulk compositions are consistent with derivation of all the high-K rocks from a single flow (Papike et al., 1976; Beaty and Albee, 1978). Origin of the two groups from different magma reservoirs is indicated by the different initial Sr ratios (Papanastassiou et al., 1977).

Figure 6.66. Setting of Apollo 11 site in Mare Tranquillitatis. Landing site (arrow; 0.67°N, 23.5°E) lies 50 km north of nearest terra; arrow is 10 km long. Linear, broad-floored, en-echelon troughs (Rimae Hypatia) are part of graben system of the Tranquillitatis border; crater truncated by right edge is Moltke (compare figure 6.5). Irregular craters and crater clusters throughout view are secondary craters of Theophilus, centered 370 km south of landing site.

Apollo 12

Within each of the other three Apollo mare suites, there are some compositional differences but no clearly distinguished age differences. Apollo 12 collected the youngest suite of mare basalts. The landing site was in Mare Insularum, which at the time (November 1969) was considered part of Oceanus Procellarum (figs. 6.1, 6.69; Marvin et al., 1971). The geologic context of the sampled material is poorly known because the vicinity of the site, including almost all the sampled terrain, is occupied by the interiors or ejecta of several large craters (figs. 6.70–6.72; Sutton and Schaber, 1971; Rhodes et al., 1977). Materials of several types of basalt are mixed in the overlapping ejecta blankets of these craters, hindering determination of source beds of the samples and correlation of their compositions with telescopic spectra.

The most recent evaluations of the site (Rhodes et al., 1977) suggest that the samples fall into three major and one minor compositional types. Two of the types,

Figure 6.67. Traverses of Apollo 11 astronauts (shaded paths) relative to landed spacecraft "Eagle" (LM) and Little West crater. Traverses much shorter than for later missions. ALSCC = Apollo Lunar Surface Closeup Camera, used to take stereoscopic photographs of fine regolith structure; LRRR = Laser Ranging Retroreflector, used to accurately measure Earth-Moon distance; PSE = Passive Seismic Experiment; SWC = Solar Wind Composition experiment. Scale 1:250 refers to original map, drawn by U.S. Geological Survey and published by the Defense Mapping Agency for NASA.

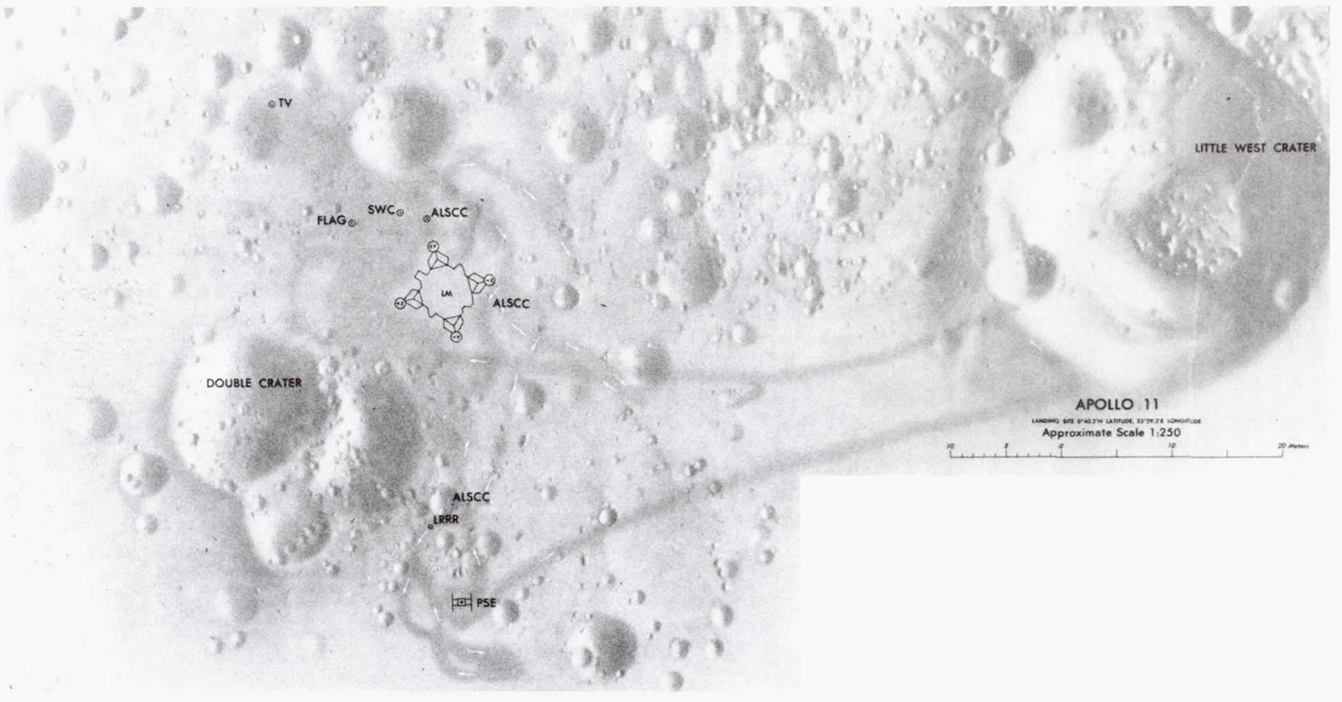

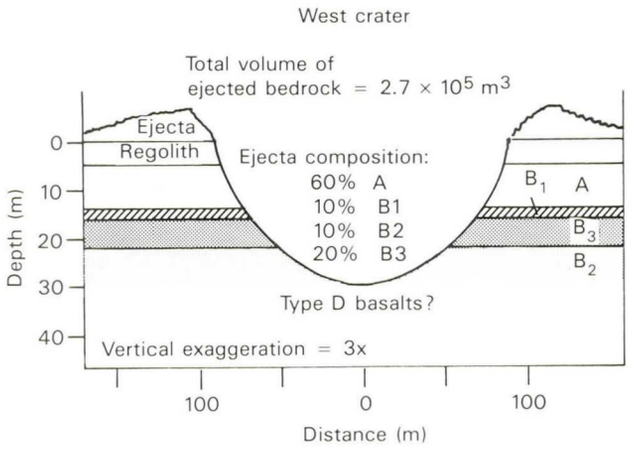

Figure 6.68. Mare stratigraphy in West crater (about 400 m east of Eagle) from which all or almost all large Apollo 11 basalt samples may have been derived (Beaty and Albee, 1978, 1980). After Beaty and Albee (1980).

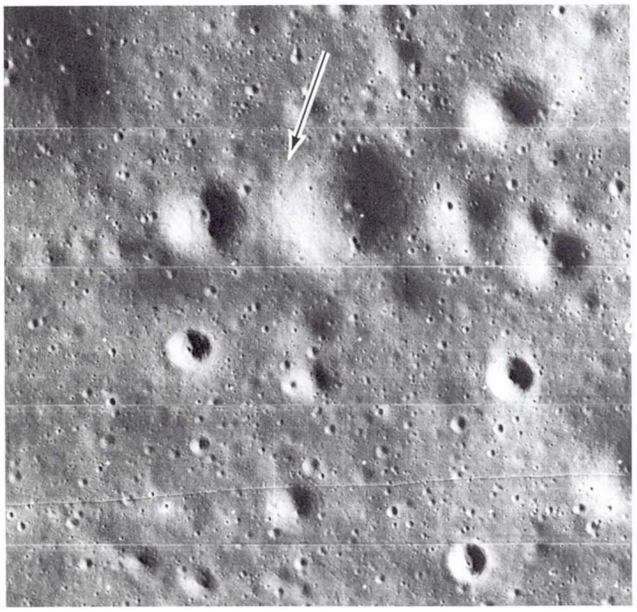

Figure 6.69. Vicinity of Apollo 12 landing site (arrow). Compare figure 6.71. Orbiter 3 H-154.

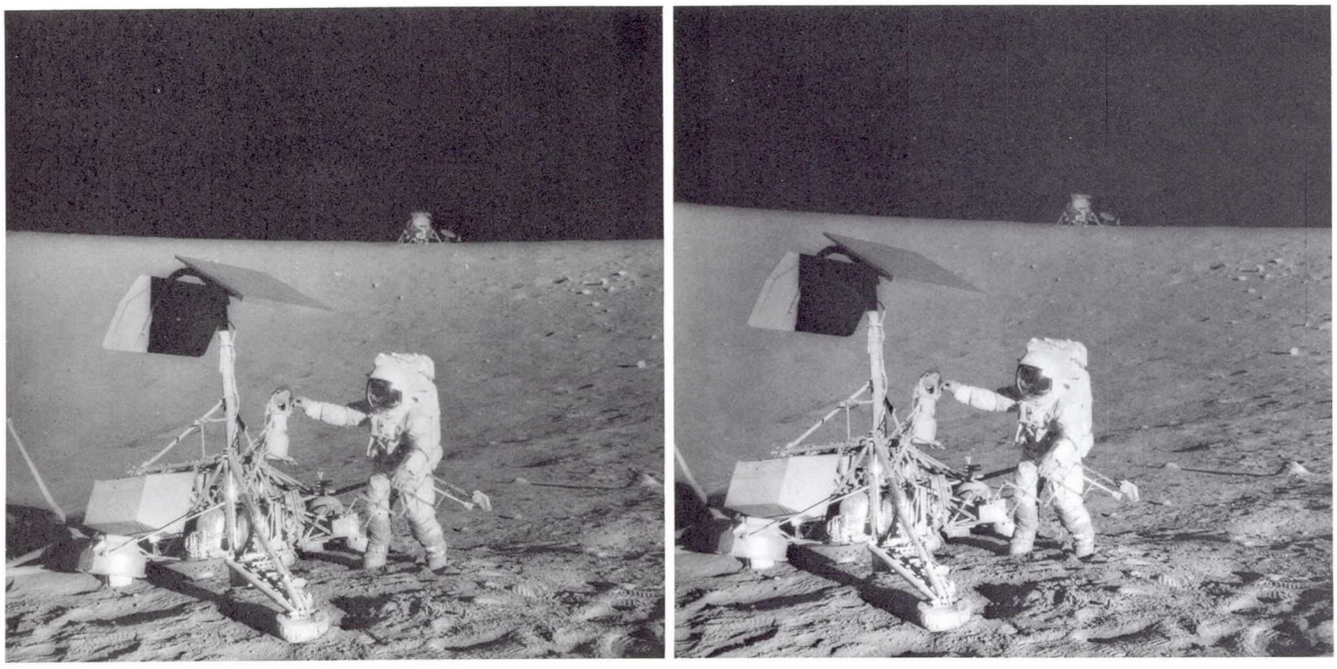

Figure 6.70. Apollo 12 astronaut examining Surveyor 3 spacecraft. LM in background on other side of Surveyor crater. Stereoscopic pair, Apollo 12 H-7134 (right) and H-7133 (left).

low-Ti olivine (Fe-Mg-rich) and *low-Ti pigeonite* (Si-rich) basalt, are probably parts of the same flow. Although some age determinations spread rather widely (Turner, 1977; BVSP, 1981, table 7.3.1), the combined chemical, textural, and petrologic evidence indicates common origin. Fractionation on the surface or in a shallow magma chamber is indicated (James and Wright, 1972; Rhodes et al., 1977).

Inferences about source depths of the craters' ejecta suggest that a *low- or intermediate Ti ilmenite* basalt (TiO_2 2.7–5.5 percent) was derived from a flow overlying the fractionated flow (fig 6.72; Rhodes et al., 1977).

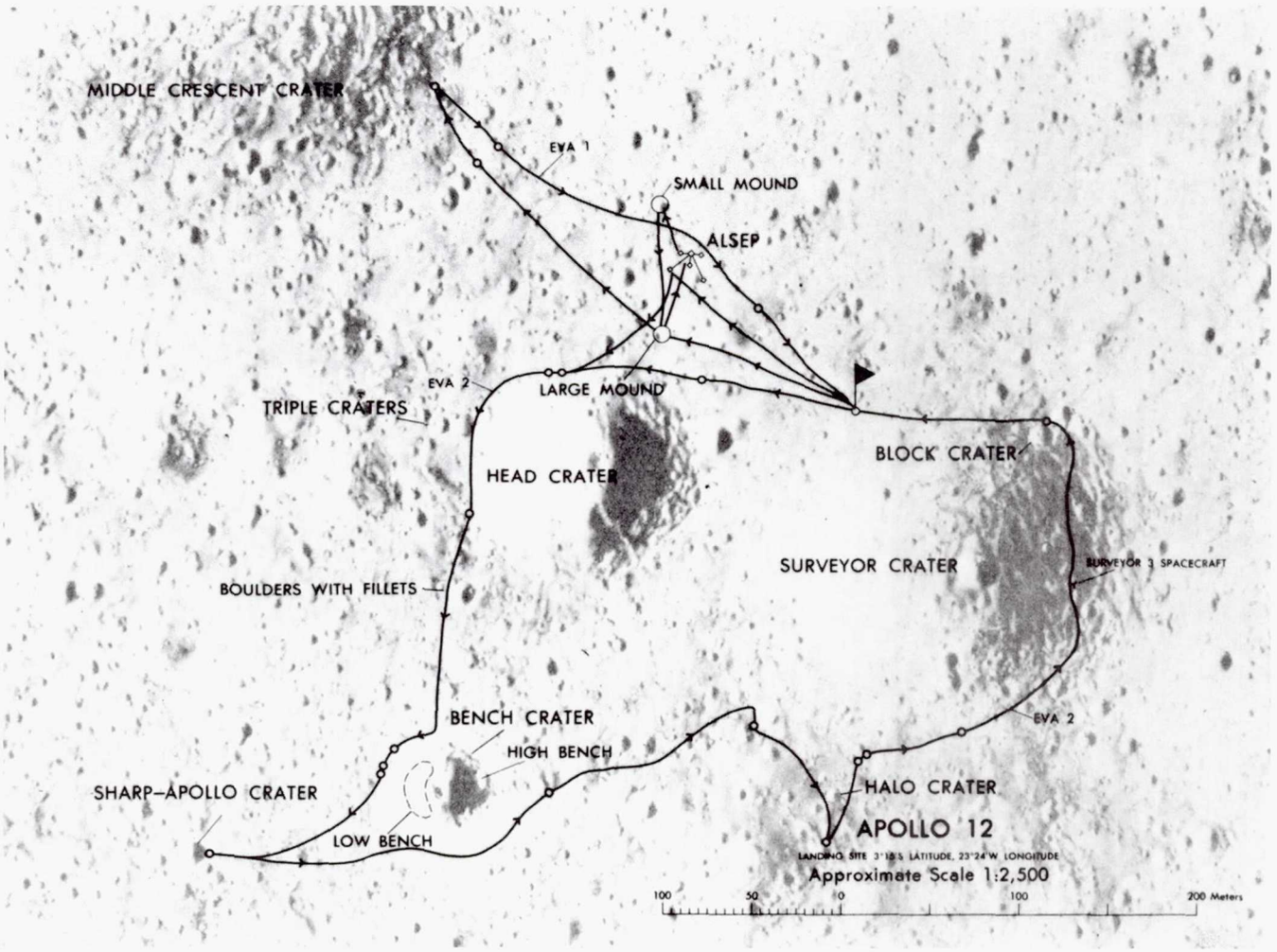

Figure 6.71. Apollo 12 astronaut traverses (EVA = extravehicular activity) relative to landing point (flag), the Surveyor 3 spacecraft, the ALSEP, and various named craters. Credits as for figure 6.67.

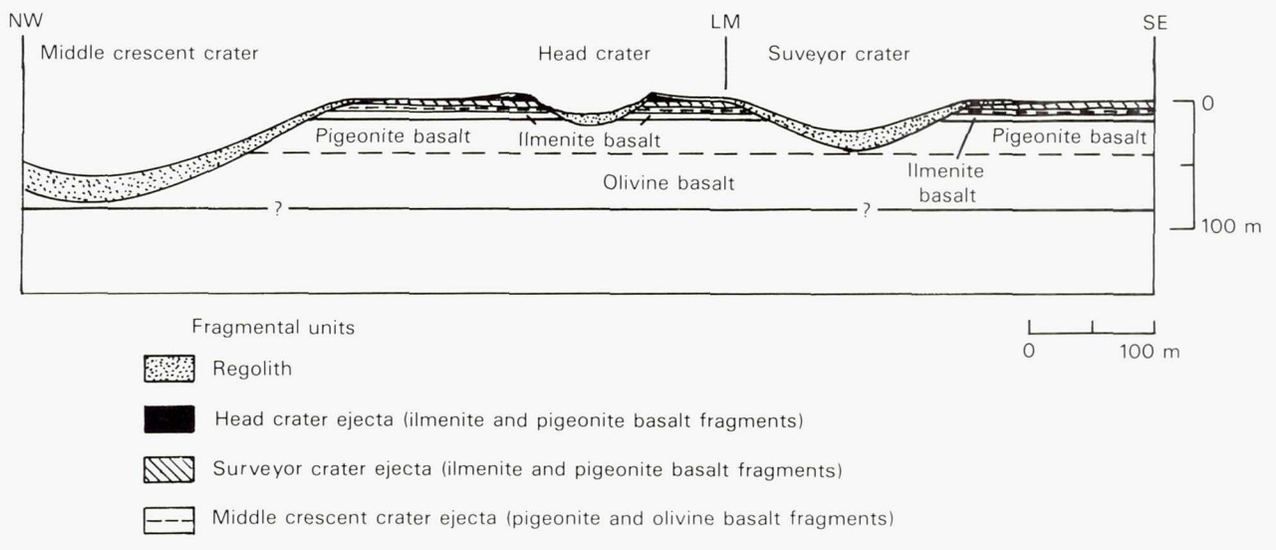

Figure 6.72. Geologic section showing hypothetical excavation of various basalt flows by three craters shown in figure 6.71 (based on Rhodes et al., 1977). Unit beneath olivine basalt may be Fra Mauro Formation or another basalt.

Compositional data indicate derivation from a different magma originating in a different mantle source than the olivine-pigeonite flow (James and Wright, 1972; Rhodes et al., 1977). However, the ages for the ilmenite basalt indicate eruption at the same time as the other flow. The 24 age determinations for the olivine-pigeonite and ilmenite flows, whose stated error ranges are <0.1 aeon, vary between 3.08 and 3.26 aeons. Their average, 3.17 aeons, is close to the most reliable determinations (BVSP, 1981) and is adopted here.

Finally, a fourth class, *feldspathic* (Al-rich) basalt, yielded at least one rock-size sample (12038). Again, Rb-Sr ages overlap with those of the other groups. A younger Ar-Ar age of 3.08 aeons for sample 12038 (Turner, 1977) is unlikely to indicate a true age difference, in view of the overlapping age determinations among the more abundant types. Petrologic relation to the other groups is uncertain (Rhodes et al., 1977). The few feldspathic fragments may be derived from beneath the other units (Nyquist et al., 1981) or from a unit not present within the traversed area.

Apollo 15

Two major classes of spectrally reddish low-Ti basalt were sampled by Apollo 15 in a small mare, Palus Putredinis, cut off from Mare Imbrium by the crater Archimedes (figs 6.1D, 6.41, 6.73, 6.74). An older, dominant type is characterized by abundant modal *pigeonite* and is Si-rich or quartz-normative (tables 6.6, 6.8). Although textures are diverse, they and the petrologic and chemical relations among the samples indicate moderate crystal fractionation of a single magma on or near the surface (Rhodes and Hubbard, 1973; Lofgren et al., 1975). Low-Ti pigeonite basalt constitutes all or part of the 60-m thick section of layered lavas exposed in the walls of Rima Hadley (fig. 6.73), and is exposed in boulders that are nearly in place at the rille's rim and in ejecta of two major craters (Howard et al., 1972; Swann et al., 1972; Lofgren et al., 1975). The other type is a *low-Ti olivine* (Fe-Mg-rich or olivine-normative) basalt which overlies the pigeonite flow except at the rille lip. The two flows apparently differ in parentage (Rhodes and Hubbard, 1973).

Despite the compositional and stratigraphic distinction, little difference emerges in the radiometric ages of the two flows (BVSP, 1981, table 7.3.1). The 0.03-aeon difference that does appear is consistent with the stratigraphic superposition, but may not be significant in view of the spread in age determinations for each flow and other lunar basalt flows. The green glass also appears to be about 3.3 aeons old (Huneke et al., 1974). All the sampled Apollo 15 basaltic materials thus seem to have been extruded at about the same time, 3.3 aeons ago.

Figure 6.73. Apollo 15 site. Southward view from station 10 across rim of Rima Hadley toward Apennine front. Exposed basalts (probably pigeonitic) are the largest in-place outcrops of lunar rock strata observed during Apollo surface exploration. Crosses are fiducial marks. Compare figures 6.1D and 6.41. Apollo 15 H-12115.

Apollo 17

Apollo 17 collected large amounts of mare basalt from a marginal embayment of Mare Serenitatis (figs. 6.1E, 6.46, 6 .47, 6.60). The samples were excavated by craters from as much as 100 m below the surface (fig. 6.48; Wolfe et al., 1981). The basalts are as rich or richer in TiO_2 (10–14 weight percent) than the Apollo 11 basalts and generally resemble them in chemistry, petrology, and age. Current information suggests that the major-element compositions span a continuous range, but some differences in trace elements can be recognized (Rhodes et al., 1976). No correlation of absolute age with any compositional or textural class is obvious. The isotopic ages as reported by the analysts range rather widely, but the best determinations (BVSP, 1981, pp. 957–959) cluster tightly between 3.68 and 3.72 aeons. An age of 3.7 aeons, in the middle of the Apollo 11 range, is adopted for

discussion purposes here. All the Apollo 17 basalts may have formed within a short time by partial melting of a heterogeneous source located in a small zone of the mantle (Rhodes et al., 1976).

Although the Apollo 17 sampling confirmed the pyroclastic origin of the dark mantling deposits, it refuted estimates of youth made before the mission (Scott et al., 1972). A number of ^{40}Ar-^{39}Ar ages from various laboratories average around 3.64 aeons (table 6.6). The low crater density which led to estimates of youth is due to initially subdued shapes and rapid degradation of impact craters in the noncohesive pyroclastic deposits (Lucchitta and Sanchez, 1975).

Premare basalts

Basalts were also extruded onto the lunar surface before the visible maria and KREEP basalts were formed (fig. 6.74; Hartmann and Wood, 1971; Shoemaker, 1972; Ryder and Taylor, 1976). The presence of premare basalt units is inferred from low albedos and distinctive remotely sensed chemistry in the ejecta of small craters that penetrate later deposits (Schultz and Spudis, 1979; Hawke and Spudis, 1980). The same phenomenon appears where impact craters penetrate ejecta or rays which are superposed on maria (fig. 6.75). Therefore, many lunar terra plains may consist of volcanic basalts overlain by impact ejecta (e.g., Wargentin, figs. 6.20E; fig. 6.22). More concrete evidence for premare volcanism has been found in the form of a few clasts in terra breccias (Ryder and Taylor, 1976; Ryder and Spudis, 1980). The source units of these fragments have been destroyed and redistributed by the basin impacts. The definitely volcanic early basalt samples are of a relatively aluminous type (Al_2O_3 11–14 percent), but nevertheless are mare-type basalts (Ridley, 1975; Taylor, 1982).

The early volcanism may even have been more extensive than the mare volcanism, which was volumetrically minor. The reason for the preservation of maria on 16 percent of the Moon is the stratigraphic accident that they postdate the Orientale basin and other large basins, which obscured earlier maria. This hypothesis is more likely than a sudden surge in internal heating and volcanism at 3.8 aeons.

Petrogenesis

The mantle source

Some early studies suggested that the mare basalts were derived from the primitive interior of the Moon, because the Moon, the mantle, and the mare basalts all have about the same density, 3.34 g/cm^3 (Taylor, 1982; see also BVSP, 1981). However, detection of the negative europium anomaly in the basalts and the positive anomaly in the terra materials showed that

Figure 6.74. Representative geologic section of Apollo 15 landing region probably applicable to traverse from foreground to background of figure 6.73. Rille profile based on Howard et al. (1972). Units beneath pigeonite basalt inferred on basis of regional stratigraphy.

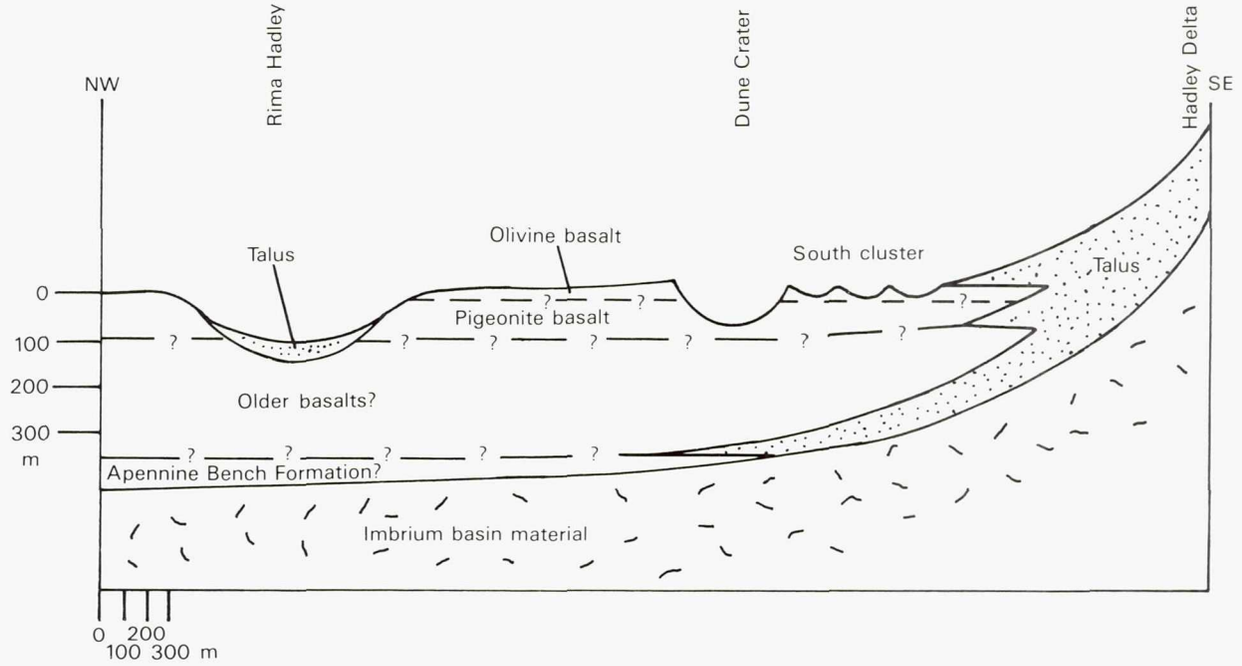

Figure 6.75. Exhumation of buried stratigraphic units.

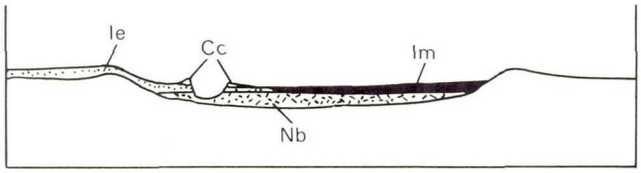

A. Diagrammatic geologic cross section. Nectarian basalt (Nb) covers crater floor, and Imbrian ejecta (Ie) covers parts of the crater and the basalt. Imbrian mare basalt (Im) fills deepest part of crater remaining after ejecta deposition. Copernican impact then strikes the ejecta and penetrates to unit Nb; as a result, the Copernican crater ejecta (Cc) contains material of the Nectarian basalt as well as Ie, hence appears dark.

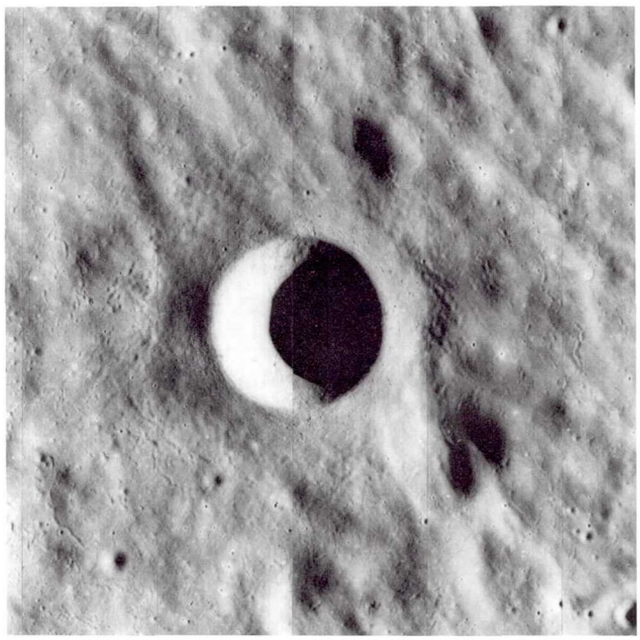

B. Copernicus H (4.3 km, 7°N, 18°W), a dark-halo crater thought volcanic before this picture was taken. Secondary craters and floor below level of adjacent terrain show that crater formed by impact. Dark halo results from exhumation of mare basalt from beneath the surface material (Copernicus ejecta). Orbiter 5 M-147.

the mare source had differentiated from the terra crustal material long before the mare basalts were extruded. This conclusion is confirmed by other isotopic and trace-element characteristics of mare and terra rocks. Most petrologists and geochemists believe that the mantle consists dominantly of olivine and pyroxene. The mare sources are generally thought to have lain at depths of less than 400 km (BVSP, 1981, sec. 3.4.2). Primitive, undifferentiated material may lie below those depths. A chemically distinct core is suggested by chemical (Taylor, 1982) and magnetic (Runcorn, 1980) evidence, but has not been established geophysically (Wiskerchen and Sonett, 1977; Goins et al., 1979; Taylor, 1982).

Partial melting

The mare-basalt magmas were formed by partial melting of small amounts of mantle material. The heat source was decay of radioactive K, Th, and U (Taylor, 1982) added to whatever primordial heat remained. High-Ti basalts and therefore their sources contain the greatest amounts of these radioactive elements (Taylor, 1975, 1982), probably explaining why they were the last types to be erupted in abundance. Derivation of the different compositional classes from different levels has been proposed, e.g., high-Al basalts from the highest level, high-Ti next highest, low-Ti deeper, and green glass deepest (Taylor, 1975, 1982). Several authors believe that certain geochemical characteristics require greater mixing and heterogeneity of the sources, and complex series of partial melting, fractional crystallization, contamination, and magma hybridization (reviews by BVSP, 1981; Taylor, 1982). Fine-scale original diversity of the mantle itself probably explains the Apollo 12, 15 and 17 observations that compositionally diverse magmas originated at the same time and were extruded on the same small part of the surface; small zones in the mantle apparently contained the compositionally diverse source materials. Compositions also changed after the flows were in place on the surface (e.g., Apollo 12), but these effects were less pronounced than in terrestrial magmas (Taylor, 1982).

Emplacement History

In summary, emplacement of a mare deposit depends on the following series of events.

1. The part of the mantle that would eventually produce the mare basalts differentiated from the bulk Moon some time before 4.4 aeons ago. The mare sources may have continued to evolve after this time (Nunes et al., 1975).
2. Basin impacts provided the settings for basalt extrusion by depressing the surface and thinning the lithosphere. Each basin stripped several kilometers or tens of kilometers from the terra crust, and the denser mantle rose to compensate isostatically for the lost mass. Later basins and craters thinned the crust additionally inside each older basin. The greatest crustal thinning, therefore, the greatest subsequent mare volcanism,

occurred where large basins are superposed on the Procellarum basin on the near side.

3. Small, compositionally diverse zones of the upper mantle partially melted. This stage lasted much longer than the first and also longer than the second. It probably began during the time of basin excavation. Its visible effects, the maria, began to be preserved after the last basin impact about 3.8 aeons ago. The extrusion stage lasted until at least 1.0 aeons ago within the Procellarum basin.

The dependence of basalt extrusion on crustal thinning by basins suggests that the Procellarum basin may explain much of the 15:1 nearside–farside difference in mare abundance. South Pole–Aitken on the far side was, by chance, struck by smaller impacts, and consequently contains less mare material than does Procellarum. However, a first-order hemispherical asymmetry in crustal thickness (Kaula et al., 1974; Bills and Ferrari, 1977) is not excluded as a cause of the dichotomy.

TECTONISM

Style and Extent

Endogenic forces have modified the depositional patterns of the Moon's stratigraphic units less than those of Mars and far less than those of Earth. The dominance of lunar geology by basins and maria extends to the endogenic structures which do exist. Most faults and folds are inside basins and transect mare materials. Some also transect the basin materials. The major folds are *mare ridges* (wrinkle ridges or dorsa). The major faults form arcuate or straight (not sinuous) *rilles* (rimae). The fractures that transect many crater floors are also concentrated in mare and basin settings. Some faults also described here do cut surfaces outside basins.

Speculations that the Moon might reveal something approaching earthlike internal activity were rampant before the Apollo instruments were emplaced (they were contained in the complex of instruments called ALSEP—Apollo Lunar Science Experiment Package). The seismometers showed hardly any internal seismicity; it is estimated as 10^{-7} to 10^{-12} that of Earth (French, 1977; Lammlein, 1977). The few repeating, weak, internal moonquakes seem to originate between about 50–200 and 700–1100 km depths, that is, mostly or entirely in the mantle (Goins et al., 1979; Nakamura et al., 1979). Their frequency shows that they are triggered by tidal stresses (Lammlein, 1977). The most energetic lunar seismic events result from impacts. Thus the Moon is essentially dead tectonically.[4]

Mare Ridges and Arcuate Rilles

The morphology of mare ridges attests to compressional origin. Most consist of a broad arch and a narrower, contorted spine; or one of these morphologies may occur alone (fig. 6.76; Strom, 1971; Lucchitta, 1976; Masursky et al., 1978). Ridges merge, overlap, or are arranged en-echelon. They consist of linear segments grouped in systems that are subconcentric and subradial to circular maria, or apparently straight and parallel, as in Oceanus Procellarum (fig. 6.76; Colton et al., *in* NASA, 1972c, sec. 29S). Whitaker (1981), however, notes that the Procellarum system is probably concentric with the Procellarum basin (fig. 6.63). Some ridges extend from mare margins into the terra, for instance, the "Lee-Lincoln" scarp at the Apollo 17 site (fig. 6.46; Wolfe et al., 1981). None are known to predate the visible mare materials.

Some circular ridges are formed by compaction over crater rims (fig. 6.76). Other, larger circular patterns of mare ridges are ascribed to settling of mare sections over buried basin rings (fig. 6.61). The ridges are, in fact, the only basis for locating the inner rings of thickly filled basins such as Imbrium, Serenitatis, and Crisium. Some ridges look like volcanic extrusions or intrusions and have been so interpreted (Fielder, 1965; Hartmann and Wood, 1971; Strom, 1971; several authors *in* NASA, 1972c, sec. 29).

Purely tectonic models have also been proposed and supported by considerable evidence. The basic cause may be settling of sections of mare basalt (Baldwin, 1963, 1968; Bryan, 1973; Maxwell et al., 1975). Thick sections of mare settle most, and the deformational stresses are concentrated where the basalts thin. Lucchitta (1976) suggested that ridges lie along steep faults, which apparently are normal in some places and reverse in others. This configuration indicates a basic origin by vertical tectonism, which may be manifested by compression of material near the surface (fig. 6.77).

Arcuate rilles are flat-floored, steep-walled grabens produced, in contrast to the ridges, by crustal extension. Like the ridges, most arcuate grabens occur in

[4]The largest recorded impact was recorded in July 1972 and probably excavated a 100-m crater on the Moon's far side. The opportunity to record further large moonquakes and thereby to better specify the impact rate and the state of the Moon's interior was lost when the ALSEPs were shut down in September 1977.

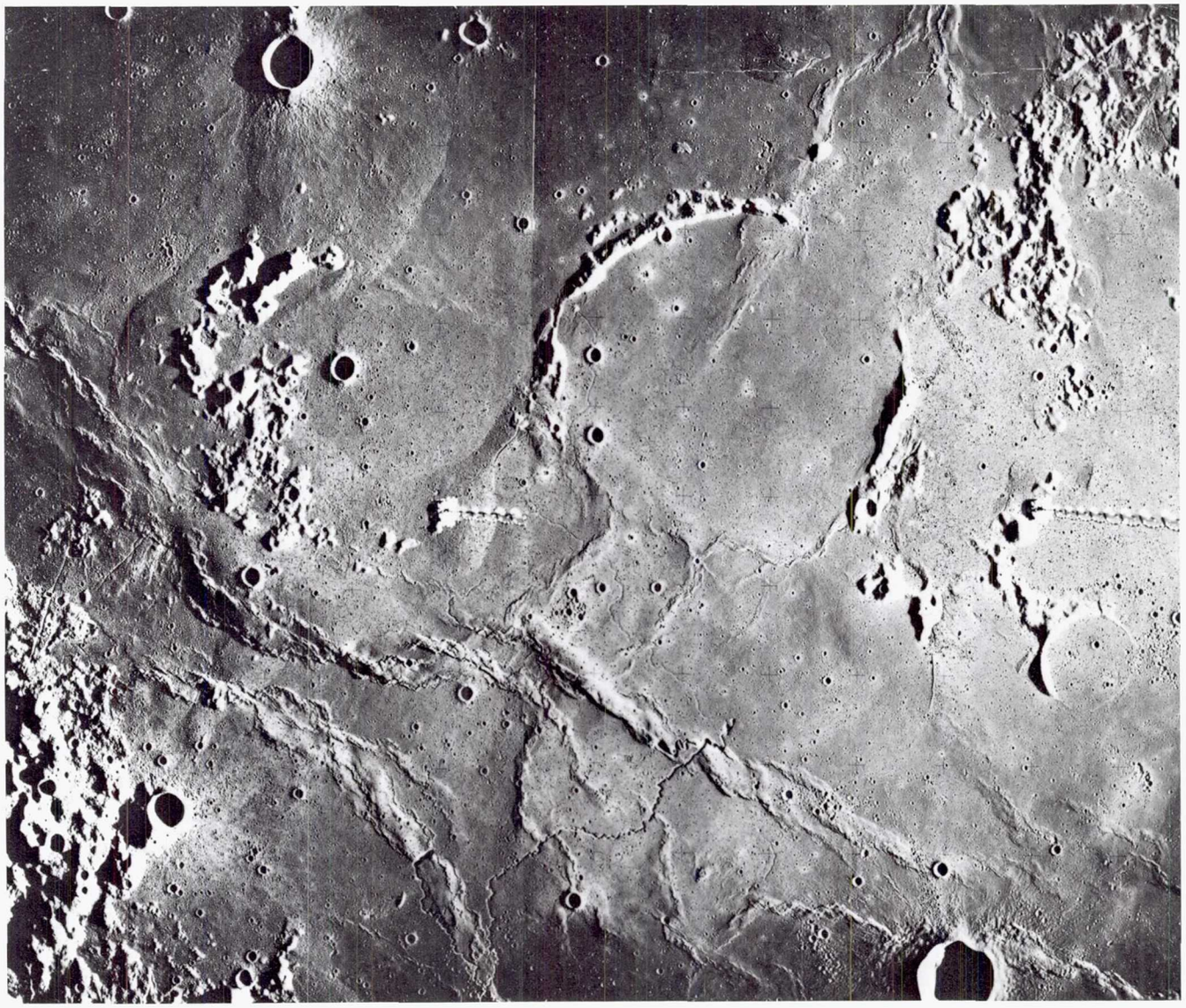

Figure 6.76. Mare ridges in southwestern Oceanus Procellarum (Colton et al., in *NASA, 1972c, sec. 29S). Large straight ridges in lower half of photograph approximately parallel to edge of Procellarum basin. Others formed over buried crater rims. Fresh crater truncated by lower edge of photograph is Herigonius (15 km, 13°S, 34°W). Rugged terra in lower left corner is part of rim of crater Letronne. Mosaic of Apollo 16 M-2836 (right) and M-2839 (left); gamma-ray spectrometer boom protrudes into view from right edges of both frames.*

Figure 6.77. Interpretation of mare ridges by Lucchitta (1976) based on models by A. R. Sanford. Thrust relations on surface originate by vertical displacements along steep faults in subsurface.

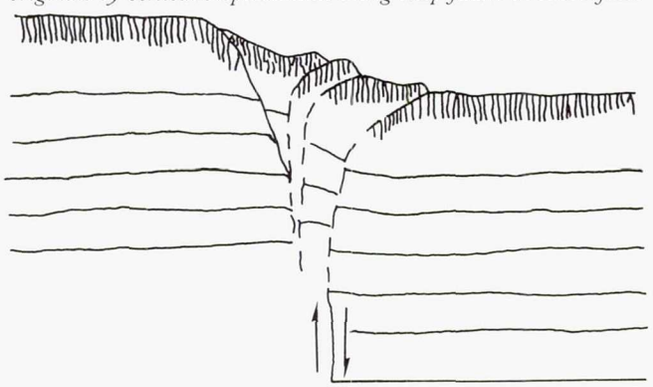

systems that consist of parallel, cross-cutting, or en-echelon sets, but some occur singularly. Most are concentric with basins (figs. 6.26, 6.60, 6.62, 6.66). They lie within the topographic basin rim as that rim is interpreted here, and cut both the mare and the basin material.

A recurring association of mare ridges and arcuate grabens suggests a genetic connection (Baldwin, 1963, 1968). In a given mare-filled basin, most ridges lie inward from most grabens. Sinking of the mare basalts apparently stretched the outer zones and compressed the inner (fig. 6.78; Baldwin, 1968; Bryan, 1973; Maxwell et al., 1975; Solomon and Head, 1979, 1980). The rilles cut old mare units and basin mate-

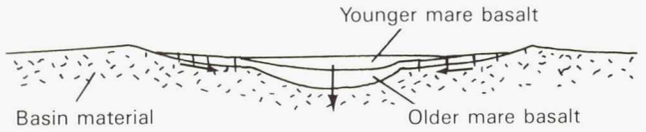

Figure 6.78. Diagrammatic cross section showing stresses responsible for graben opening and ridge formation during subsidence of mare basalts in a two-ring basin. Short vertical lines cutting older mare unit and the underlying basin material diagrammatically indicate grabens.

rials, whereas the ridges deform both old and young mare units (Lucchitta and Watkins, 1978). Therefore, compression continued longer than extension.

Crater Floor Fractures

Fractures in the floor materials of craters are among the commonest types of lunar structures. They are concentrated in and near maria and in basins without maria (figs. 6.56, 6.61, 6.79). Fractured-floor craters larger than about 150 km also occur in nonbasin settings, for example, Petavius (177 km; fig. 6.80) and Humboldt (205 km; fig. 6.32). Impact morphologies such as central peaks and even rays (fig. 6.61) show that most of the fractured craters are exogenic, despite their relatively shallow floors (Pike, 1980a). Anomalous uplift of impact-crater floors is the evident explanation.

The uplift interpretation also indicates the probable explanation for a wide range of more ambiguous lunar landforms (Brennan, 1975; Schultz, 1976b) such as the shallow, tilted floors and arcuate structures of 15 craters $\geq$20 km across in the Smythii basin (fig. 6.32; Wilhelms and El-Baz, 1977), and even the chaotic appearing, knobby, elevated interior of the crater Gaudibert along the border of Mare Nectaris. These peculiar craters are probably not calderas but impact craters modified by endogenic forces.

Straight Rilles and Scarps

Most of the radial Imbrium sculpture grooves undoubtedly formed by secondary impact (Baldwin, 1949, 1963), not faulting initiated by the Imbrium impact as widely believed during the 1960s. Nevertheless, some true faults are radial or subradial to Imbrium. Vallis Alpes (Alpine Valley; fig. 6.18A) has jagged walls consisting of linear segments, not the smoothly scalloped, matching walls and raised lips characteristic of low-angle secondary chains (figs. 6.18B, 6.20E, 6.81A). The valley is probably a graben somehow formed during the Imbrium impact as originally proposed for other sculpture.

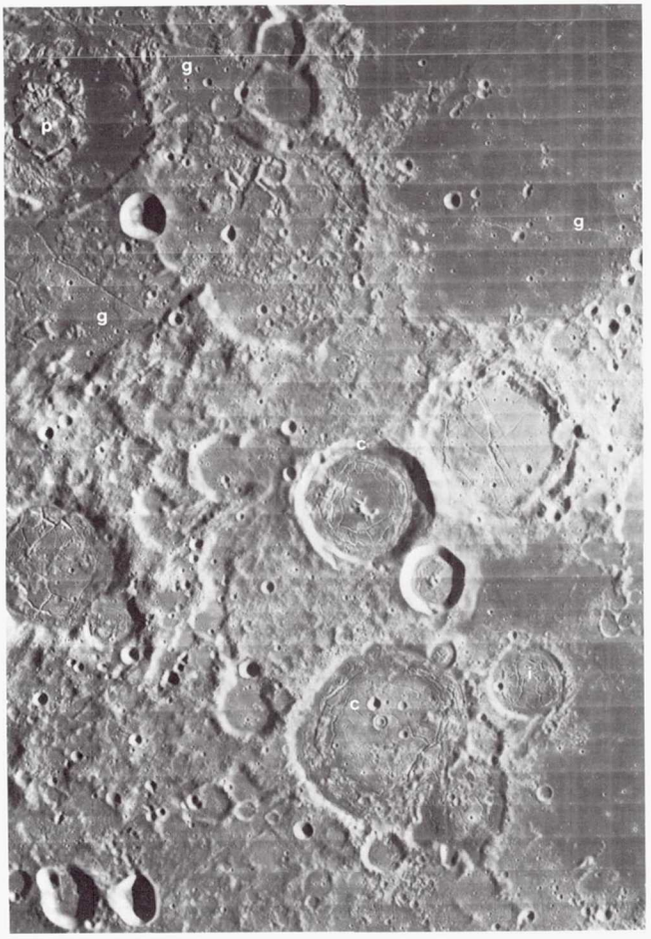

Figure 6.79. Subconcentric (c) and irregular (i) fractures, elevated central plateaus (p), and other crater-floor features evincing uplift. Linear grabens (g) between craters indicate further tectonic deformation in this border zone of northern Oceanus Procellarum. Crater labeled c in center of scene is Lavoisier E (49 km, 41°N, 80°W).

Radial or subradial faults, such as the Cauchy system in Mare Tranquillitatis, the Straight Wall (Rupes Recta, fig. 6.18B), and one leg of Rima Hyginus (fig. 6.81A), are more puzzling because they cut mare materials. They cannot be the direct product of the Imbrium impact. If they are related to Imbrium, they may form by some sort of rejuvenation of radial fractures (Mason et al., 1976).

An intricate system of long grabens occupies the terra adjacent to western and northwestern Oceanus Procellarum, amidst or near the numerous floor-uplift craters (fig. 6.79). The system includes grabens radial to Orientale and Imbrium, and others concentric with Procellarum. Most likely, the crater uplifts and the grabens are both related to anomalous properties of the lithosphere caused by Procellarum, though they lie outside the basin proper.

Figure 6.80. Petavius (177 km, 25°S, 60°E), a large, isolated crater having fractured floor resulting from floor uplift outside a basin environment. Orbiter 4 H-185.

Another system possibly related to Procellarum is in the center of the Moon's near side in Sinus Medii near the crater Triesnecker (fig. 6.81A). The system lies just inside the inner ring of the Procellarum basin (fig. 6.63). The Triesnecker system as a whole is oriented north-south, but the system includes many other trends, which mutual transection relations show to be contemporaneous. Regional extension is the apparent cause. The region may have been uplifted inside the Procellarum basin in the manner of a crater-floor uplift, or may have extended by deformation over the buried inner basin ring.

Other rilles or sets of rilles are long and straight and are not obviously related to any basin. A set of grabens, 1600 km long, extends from the terra east of Sinus Aestuum east southeast to Mare Fecunditatis (fig. 6.81). Like the rilles west of Oceanus Procellarum, they are younger than the terrae and the older Imbrian mare units they traverse, but older than the younger Imbrian mare units. Some are radial to basins but this orientation may be coincidental. For example, grabens east of Mare Fecunditatis are radial to the Nectaris basin but may be an extension of the long set (fig. 6.32). The trend is paralleled in other areas by several conspicuous chains in the south-central highlands (Abulfeda, Müller, Rima Bode II; fig. 6.81B) and by the Cauchy set. Rilles trending north of east are also known (fig. 6.81A). Whether the known rilles are grouped into genetically significant sets is unclear; tricks of lighting influence plotting of structures, even on good photographs. Concentration of the straight structures on the near side implies stresses either of hemispherical extent or related to the elevated mantle beneath the Procellarum basin.

Deformational History

Many lunar phenomena are ascribable to deformation ultimately initiated by basin impacts. When a basin forms, mass is lost by the excavation. The mantle rises in isostatic compensation (fig. 6.33B; Wise and Yates, 1970; Scott, 1974; Bowin et al., 1975). The compensation may not be complete; Orientale, the only young basin for which gravity data exist, has an annular negative gravity anomaly outside the mascon (Scott, 1974; Sjogren and Smith, 1976). Probably, no basin would have a mascon if it were not filled by mare basalt (Solomon and Head, 1980). This excess (superisostatic) mass subsides (fig. 6.78). In basins which lack large mascons but contain mare basalts, the basalts apparently sank far enough to achieve isostatic balance (Tranquillitatis, Procellarum). This occurred within the Procellarum basin where the crust (and presumably the elastic lithosphere) was thin. Only the very thickest maria in the youngest basins (Imbrium, Serenitatis) have persisted as mascons inside Procellarum, and the mascons are smaller than one would expect from the mare thickness (Solomon and Head, 1980). The subsidence created many arcuate grabens along the mare margins and in the adjacent basin terrain. Where the crust (lithosphere) was thick, the subsidence did not achieve balance, grabens did not form, and the mascon persists (Smythii, Orientale, Nectaris). Contraction caused by subsidence or some other factor was sufficient in all maria to wrinkle the basalts into ridges. An elevated crust-mantle discontinuity (lunar Moho) presumably was also a major factor in crater-floor uplifts and in accessibility of mare magmas to the surface.

Expansion or contraction of the hot, early Moon may have exerted strong global or regional stresses on whatever solid crust then existed. Since the oldest preserved features formed before 4.0 aeons ago (fig. 6.49), however, global stresses have been weak. For example, even the oldest lunar basins are not cut by long compressional scarps like those of Mercury. Graben formation ended in the middle part of the Late

Imbrian epoch about 3.6 aeons ago. Solomon and Head (1980) attribute the cessation of arcuate-graben opening to a thickening of the elastic lithosphere at this time. As the earlier lithosphere seems to have been equivalent to the terra crust, part of the mantle must have become rigid after 3.6 aeons.

The mascons show that the superisostatic loads are still there, but continued subsidence is unlikely because shallow endogenic moonquakes do not all correlate with mascon maria (Nakamura, et al., 1979; Solomon

Figure 6.81. Straight rilles (grabens) not obviously associated with a basin.

A. Center of lunar near side showing concentration of lunar straight rilles, including Rima Hyginus (H), Triesnecker system (T), an ENE set at the south margin of Sinus Medii (SM), and Rima Bode II (B). Conspicuous system trending NNW is radial to Imbrium ("Imbrium sculpture") and is of secondary-impact, not tectonic, origin. Rugged terra bordering Sinus Medii lies along ring of Procellarum basin. Telescopic photograph by Pic du Midi Observatory.

B. Detailed view of Rima Bode II. Cuts terra but is truncated by mare (of Sinus Aestuum). Irregular crater (7-km long, 13°N, 4°W) probably volcanic and possibly the source of the dark-mantling material on the adjacent terra. Pattern in lower left is artifact of photo processing in the spacecraft. Orbiter 5 M-120.

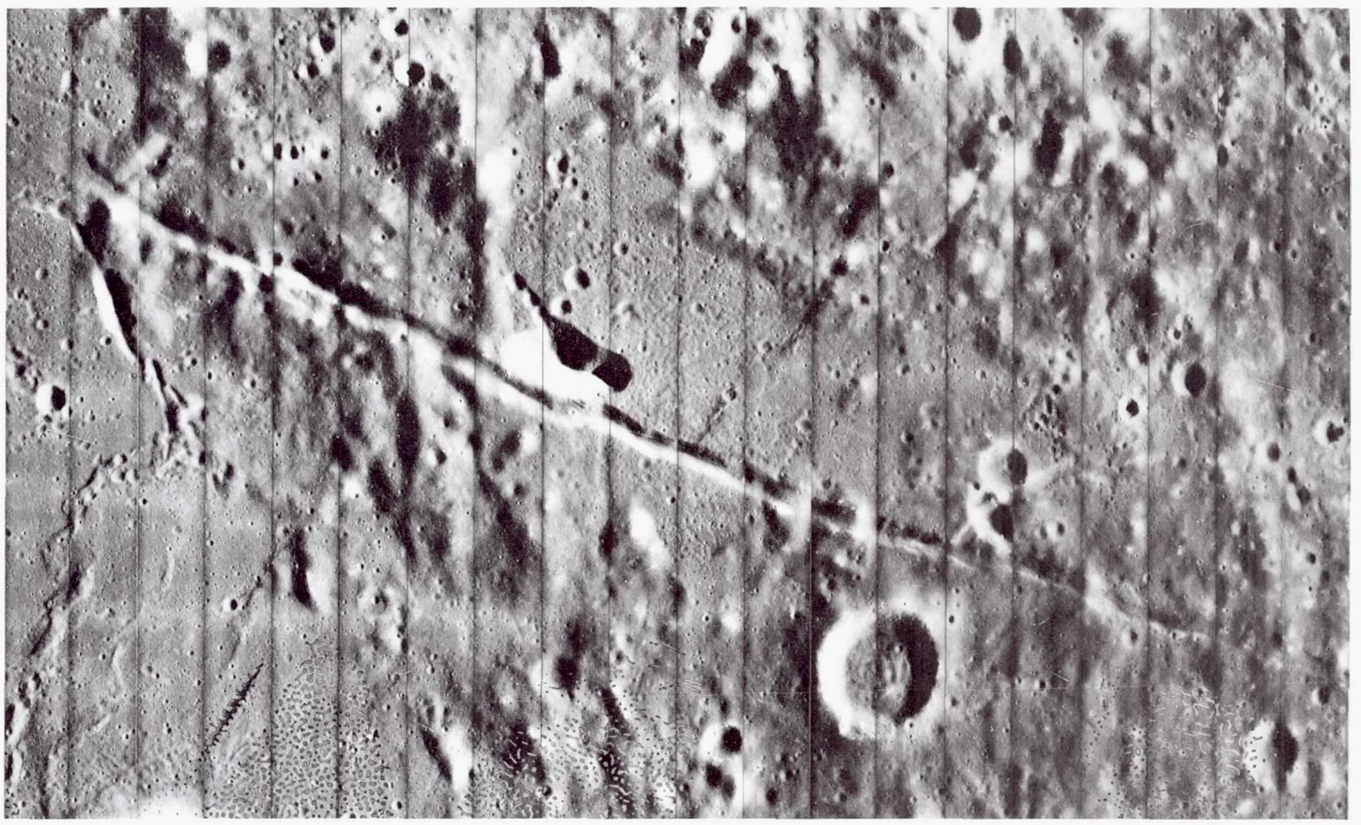

and Head, 1979). The lithosphere as defined by ability to transmit shear waves is at least 1000 ± 100 km thick. The only possible melted zones are below that depth and their existence is speculative (Goins et al., 1979).

GEOLOGIC HISTORY

Geologic Style of the Moon

Two decades of intensive study have drawn a consistent picture of the Moon's crustal style and the general outline of its evolution. It is now known that the upper part of a low-density, light-colored crust averaging about 75 km thick is composed of overlapping, interfingering beds of highly brecciated basin and crater ejecta. Each major impact has generated an extensive and complex deposit of breccia and impact melt. The deposit is thickest and continuous near the excavation rim, and thins progressively outward to an average distance of one basin or crater radius, where subdeposits around satellitic craters become more distinct. The satellitic craters were dug by secondary impact of ejecta from the parent, primary excavation. Near the primary's rim, and commonly beyond one radius of the primary, the secondary craters are buried by primary ejecta. The bedding and texture of the deposits probably become increasingly chaotic outward as more and more substrate material is intermixed. Each primary and secondary impact has excavated breccias that had been formed similarly and which therefore were already complex when excavated and redistributed. Basin deposits dominate this stratigraphic framework because basins are the largest impact cavities.

Each small crater is also the center of a more or less well-bedded deposit. Because many more small craters than large craters and basins form in any time interval, the deposits of the smaller craters accumulate as fine-grained regolith between the major deposits. Large and small impacts throw fragments of their ejecta in long rays far and wide over the Moon.

The second major lunar process, volcanism, has altered this impact-dominated stratigraphy. Most exposed volcanic rocks are mare basalts. Both mare and nonmare (KREEP) basalts were also produced before the visible maria formed. In the first half of lunar history, basalts were extruded into favorable depressions in the terrae when sufficient heat and access to the surface were available. Their presence on the surface implies that they are also interbedded with and intruded into the hidden parts of the crust.

The lunar crust has probably been constructed along this general pattern since its solidification. Relative stratigraphic relations determined by geologic techniques and absolute ages on returned samples (fig. 6.82) enable us to trace the evolution of this style through six periods of lunar history (table 6.1; fig. 6.83).

Pre-Nectarian Time

The first pre-Nectarian event was formation of the Moon. Isotopic ages of meteorites studied before the Apollo program yielded a solar system age of 4.55 aeons (Patterson, 1956) and this has not been altered by analyses of the lunar samples. Beyond its age of 4.55 aeons and the likelihood that it formed in the same part of the solar system as Earth (Clayton and Mayeda, 1975), little about the origin of the Moon is well established (Kaula, 1977; Hartmann, 1972, 1983; Wood, 1979; BVSP, 1981; Cadogan, 1981; Glass, 1982; Smith, 1982; Taylor, 1982).

The next pre-Nectarian event of geologic interest is the formation of the terra crust. Petrologists and geochemists favor differentiation of primitive material into an aluminous crust and a mafic mantle in the first 0.15–0.35 aeons. The oldest well-dated "pristine" rocks have crystallization ages of about 4.5 aeons. Impacts must have disrupted the forming crust and influenced the igneous petrogenesis (Wood, 1975b; Hartmann, 1980). Calibration of crater frequencies with estimates of the absolute age of the Nectaris basin suggests an age of 4.0–4.1 aeons for the oldest lunar surface on which craters have been counted (fig. 6.49). From this one might estimate appearance of the solid crust at roughly 4.2 aeons, in accord with one estimate for the end of the differentiation.

The first geologic features known to have been preserved are the giant South Pole-Aitken and Procellarum basins. Numerous earlier basins may have formed by impacts of large objects that must have been abundant in the early solar system (Wetherill, 1975, 1981). The South Pole-Aitken and Procellarum impacts raised high, arcuate mountain chains and must have covered most of the Moon with primary and secondary ejecta. The differences in crustal thickness inside and outside the basins are due partly to the excavation and partly to this accumulation of ejecta between the basins. The Procellarum basin, a little offset from the later Imbrium basin, may have unroofed KREEP-rich crustal layers or may have been the site of early extrusions of KREEP basalt that are

Figure 6.82. Fence diagram schematically showing stratigraphic relations of major dated lunar geologic units. Horizontal scale approximate; vertical scale approximate, greatly exaggerated.

Geologic Units

Em Eratosthenian mare basalt
Im Imbrian mare basalt
Iab Apennine Bench Formation
Ib Imbrium basin deposits (Fra Mauro Formation, material of Montes Apenninus, and interior material)
Nb Nectarian basin deposits (Serenitatis, Crisium, and Nectaris)

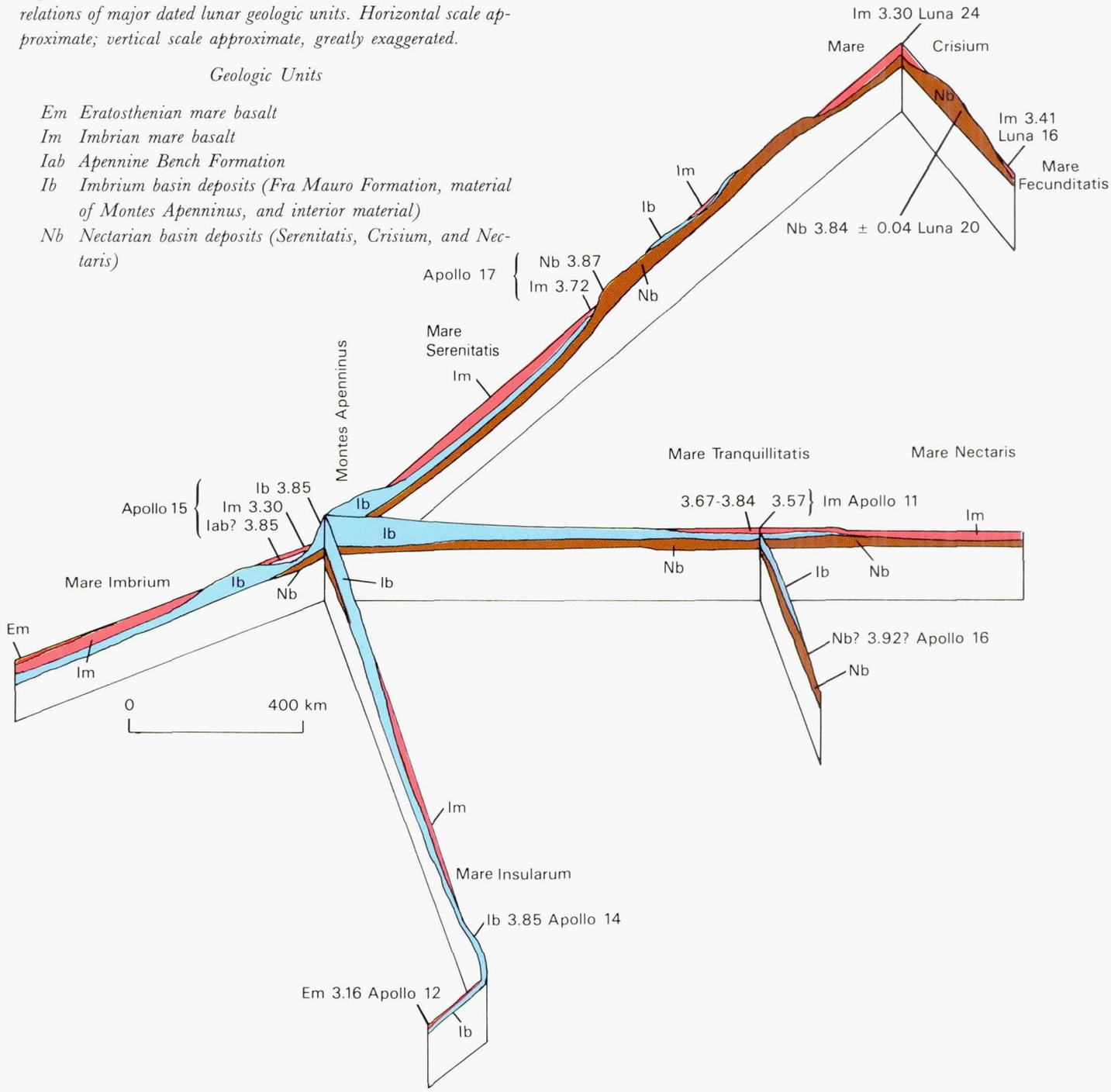

now concentrated in later deposits in the Imbrium-Procellarum region (Wood, 1972; Cadogan, 1974, 1981).

Thirty basins, including South Pole-Aitken and Procellarum, are here identified definitely or tentatively as pre-Nectarian. Nine age groups can be recognized among these basins by superposition relations, crater densities, and degree of preservation (table 6.4). The oldest are saturated by craters in the hundred-kilometer range and are recognizable as basins partly because later mare fill or light-plains deposits emphasize their outlines (e.g., Fecunditatis and Lomonosov-Fleming). The youngest have low superposed crater densities and well-defined ejecta and secondary craters (Freundlich-Sharonov). Basins of intermediate pre-Nectarian ages have been recognized

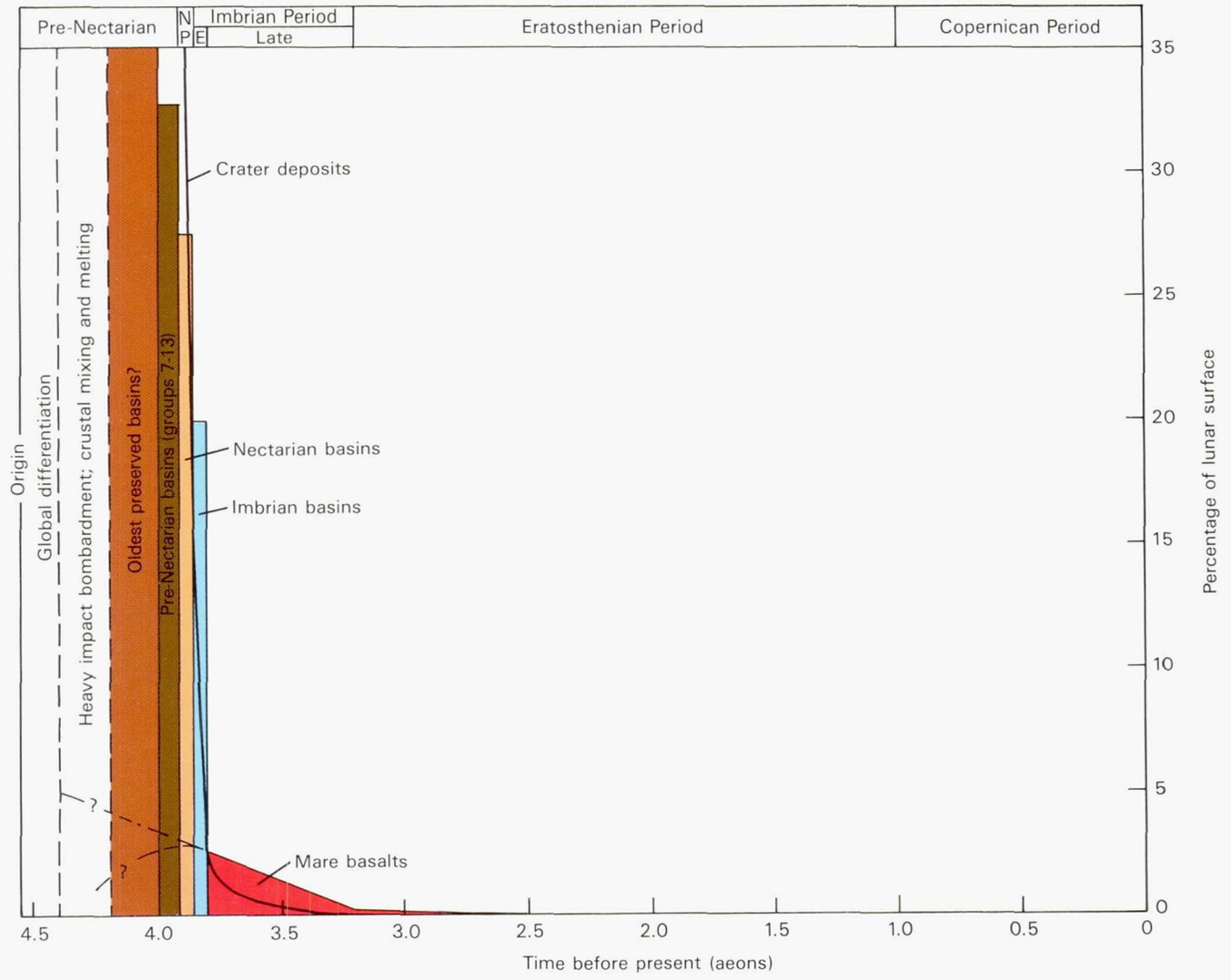

Figure 6.83. Geologic evolution of Moon. Age in aeons (horizontal axis) plotted against percentage of surface covered by each deposit or group of deposits (vertical axis; Wilhelms, in press b). Sequence of formation of individual basins given in table 6.4. Crater and basin materials are the interior deposits and the continuous inner facies of ejecta, assumed to extend one radius from rim crest. Extrusion of mare basalts arbitrarily shown to decline steadily throughout Late Imbrian Epoch and to level off abruptly at beginning of Eratosthenian Period. Eratosthenian and Copernican crater and mare deposits, if distributed evenly throughout time as assumed, cover barely enough area to be shown here. Extrapolations of basalt areas into periods of intense cratering show, alternatively, (1) steady decline throughout early history at same rate as in Late Imbrian (upper queried line), or (2) peak after 3.9 aeons caused by buildup of radiogenic heat (lower queried line).

by mapping that reveals ring patterns among disconnected elevated blocks or progressive diminishment in numbers of nearby craters toward the basin rim.

Nectarian Period

The Nectarian Period continued the general geologic style of the pre-Nectarian but with diminished activity. The period began with the formation of the Nectaris basin at a time that unfortunately is not well known. One estimate derived from isotopic dating of the fragmental breccias excavated by North Ray crater from the Descartes Mountains at the Apollo 16 site places the event at about 4.1 aeons and another at 3.92 ± 0.03 aeons. Possibly, however, Nectaris material was not, and may never be, dated by analyses of the Apollo samples. If Nectaris could be dated, the early impact history of the Moon would be much better understood than it is now, because the Nectaris deposits serve as a marker horizon in the older parts of the stratigraphic column. Numerous craters, 11 or 12 basins, and planar deposits superposed on Nectaris deposits but overlain by Imbrium deposits

are Nectarian (table 6.4). Mare-filled Nectarian basins are visually conspicuous features of the near side (Humorum, Serenitatis, Crisium, Nectaris), and unfilled or less deeply filled Nectarian basins are among the freshest large features of the far side (Mendeleev, Moscoviense, Korolev, Hertzsprung). Densities of Nectarian craters superposed on Nectaris-basin materials suggest that 1700 craters 20 km and larger formed on the whole Moon during the Nectarian Period (Wilhelms, 1976).

The extensive early plutonic and post-Nectarian volcanic activity, which is documented, implies that volcanism also occurred in Nectarian and pre-Nectarian time. Premare volcanic rock fragments have been recovered from later impact breccias and radiometrically dated as probably Nectarian. However, the extent of the early volcanic activity is unknown.

Early Imbrian Epoch

The catastrophic impact that excavated the Imbrium basin forever altered the near side of the Moon and provided another marker horizon for dividing lunar geologic history. Most of the northern and part of the southern near side were covered by the Fra Mauro Formation and related units, probably consisting mostly of primary basin ejecta, that contains earlier breccias, volcanic rock, regolith, and impact melt. Enough ejecta was melted by the impact to reset isotopic ages, thereby allowing dating of the Imbrium impact from the Apollo 14 and 15 samples. Most ages are in the 3.79–3.86 range. Such an age for Imbrium is confirmed by a date of 3.85 aeons for the last time that KREEP fragments at the Apollo 15 site were liquid. An age of 3.85 aeons is adopted here for the Imbrium basin (fig. 6.83).

The Early Imbrian epoch also was the time of the Schrödinger and Orientale impacts. The age of the double-ring Schrödinger is somewhat doubtful, but no doubt exists that Orientale is younger than Imbrium and is the youngest large lunar basin. The multi-ring Orientale affected the terra of the west limb of the Moon as strongly as Imbrium affected the northern near side; Orientale was subsequently filled by less mare material because its position outside the Procellarum basin placed it on a thicker crust. Continuous deposits (Hevelius Formation) and secondary craters of Orientale extensively cover deposits of the Imbrium and older basins. Post-Imbrium, pre-Orientale craters are also known and thus are also Lower Imbrian.

With the Orientale impact, the era of impact domination of the Moon ended and a temporary era of mare domination began. The transition is not coincidental and does not indicate a sudden surge in internal heating, but instead reflects the stratigraphic superposition of Orientale and pre-Orientale basin ejecta on any earlier mare basalts which formed. Certain maria such as the highly cratered patches in Mare Australe (Wilhelms and El-Baz, 1977) may have been spared an Orientale brightening and include pre-Orientale mare materials. But, in general, mare basaltic volcanism could become evident only after basin formation ceased.

Late Imbrian Epoch

Most of the present lunar maria formed in the Late Imbrian Epoch, which began around 3.8 aeons ago. The oldest exposed basalts, those from the Apollo 17 site, are about 3.7 aeons old. Some Apollo 11 basalts from a buried source bed have radiometric ages older than 3.8 aeons and may predate Orientale or even Imbrium. During the Imbrian Period, the rate of formation of impact craters declined greatly, such that the cumulative number of impacts in the first three-quarters aeon greatly exceeds the number that accumulated over the rest of the Moon's history (fig. 6.83).

In the Late Imbrian, available basins were filled by a variety of lava types generated by partial melting of heterogeneous zones in the mantle. The mare lavas are thinnest where the crust was thickest (Smythii, Fecunditatis) and thickest where the crust was thinnest (in Imbrium, Serenitatis, and other basins superposed on the Procellarum basin). In addition, lava fountains covered the margins of many basins with droplets of basaltic glass, and may have covered the basin centers as well. Some of the pyroclastic materials erupted from rilles and small craters that are still visible, including in the terrae. Subsidence of the basalts inside the Procellarum basin opened grabens in the mare margins and in the underlying basin floors. Sometime in the middle of the epoch, the arcuate grabens and straight grabens ceased forming, probably because the elastic lithosphere cooled and thickened. Impact craters also continued to form but in much smaller numbers than previously. Geometric relations observable on the surface show that deposits of craters such as Archimedes, Plato, and Lansberg must interfinger at depth with mare basalts.

Eratosthenian Period

For a time, the Eratosthenian Period continued the geologic style of the Late Imbrian Epoch. Crater and

mare deposits interfinger in Mare Imbrium and Oceanus Procellarum. Thin units of Eratosthenian basalt were sampled by Apollo 12 in Mare Insularum, within the Procellarum basin. Eratosthenian volcanism was most abundant and most persistent inside that giant basin, because the crust was thin and the mantle sources of the basalts elevated. Volcanism continued intermittently throughout the period. Graben formation had probably ceased by the Eratosthenian, but mare ridges continued to form because the central parts of the maria continued to subside slightly. Some crater floors continued to rise isostatically.

Copernican Period

The young age of many lunar craters is known from the fact that their rays cross all other terrain. These are also usually the freshest-appearing craters. Neither the absolute nor the relative ages of most prominent bright ray systems are well known. Copernicus may have formed about 0.85 aeons ago, based on dating of light-colored KREEP-rich material in the regolith at the Apollo 12 site, which is situated on a Copernicus ray (Eberhardt et al., 1973). The Copernicus origin of the light material is questioned, however (Quaide et al., 1971; Alexander et al., 1977). Autolycus or, less likely, Aristillus may have been dated by an Apollo 15 sample at 1.29 aeon (Bernatowicz et al., 1978). Some rayed craters (Timocharis, Theophilus, Langrenus) appear older than some nonrayed craters (Diophantus, Delisle) (Neukum and König, 1976; Wilhelms, 1980a). Eratosthenes itself has at least one faint ray. Hence, ray formation is a function of substrate composition as well as age; rays being preserved longer on units low in Fe and Ti than in mare units rich in these elements. Exposure times dated by the Kr-Kr method and nuclear fission tracks show that the landslide from South Massif at the Apollo 17 site formed 0.1 aeons ago (Arvidson et al., 1976). As the landslide was probably triggered by impact of ejecta from Tycho 2250 km away (figs. 6.46, 6.47; Wolfe et al., 1975; Lucchitta, 1977), Tycho may have formed "only" 100 million years ago. The smaller Copernican craters, Cone (Apollo 14; fig. 6.39), North Ray, and South Ray (Apollo 16; figs. 6.43, 6.44), which were sampled directly, are 25, 50, and 2 million years old, respectively (Arvidson et al., 1975).

Except in northwestern Oceanus Procellarum (Moore, 1967), no Copernican volcanic materials are known. Radiogenic and other internal heat has declined below levels capable of melting the mare sources or is too deep to affect the surface. Lithospheric thickening and cooling have shut off whatever subsurface cracks formerly served as access paths for ascending magmas. Mare volcanism has ceased.

Despite the paucity of absolute ages and the uncertainty about age relations of many units not in mutual contact, the general trend in lunar evolution is clear. Large and small impacts create fresh, blocky surfaces free of dust and then are slowly covered by dust and glass generated by later impacts until their forms, albedos, and spectra become blurred. In this way, units that formerly resembled Copernican units have become like those of the Imbrian and older systems. Catastrophic impacts—which still could occur at any time—more drastically change the Moon's face and redistribute its material.

Terrestrial Perspective

The slowness of lunar processes in almost the last four aeons gives us perspective on the differences between Moon and Earth. Impacts formed the Orientale and Imbrium basins before any rocks so far dated were preserved on Earth—probably because Earth was being similarly bombarded. The oldest mare rocks, from relatively young (Late Imbrian) lunar stratigraphic units, are as old as the oldest dated terrestrial rocks. Halfway through Earth-Moon history, in the Eratosthenian Period, the Moon's history had become almost quiescent while Earth had just left the Archean Era and began to leave a rich record of life and atmospheric changes (Cloud, 1968). The young-looking Copernicus formed sometime during Earth's Proterozoic, before life had emerged from the oceans. When the Cambrian Period began, all but a few of the present lunar landforms already existed. A Mesozoic impact formed the spectacularly fresh-appearing Tycho, whose rays extend over the whole near side of the Moon and whose secondary craters have not been degraded even on steep slopes. Continents were growing and moving and oceans were disappearing and reappearing while the only changes on the Moon were a few additional impacts. Some of the collected rocks had lain exactly in the same position where found for longer than *Homo sapiens* existed on Earth (French, 1977). Man has yet to see the Moon's surface change except by his own hand.

ACKNOWLEDGMENTS

Odette B. James (mare-basalt petrology), Henry J. Moore (cratering processes), Richard J. Pike (crater morphology and complex craters), and Paul D. Spudis (terra petrology) contributed writeups for other purposes which are adapted for use here. Discussions with Odette B. James, Gunther W. Lugmair, Paul D. Spudis, and S. Ross Taylor helped clarify the subjects of petrology and isotope geochronology, with which the author has not been directly involved. The stratigraphic aspects of lunar geology, closer to my research interests, have been worked out over two decades through collaboration among many colleagues in the U.S. Geological Survey, particularly John F. McCauley and the founder of the subject, Eugene M. Shoemaker. The chapter was reviewed by Charles H. Simonds and editor Michael H. Carr.

EXPLANATION FOR PLATES A-D

Cc	Copernican crater materials
Cm	Copernican mare materials
Ec	Eratosthenian crater materials
Em	Eratosthenian mare materials
Ic_2	Upper Imbrian crater materials
Im	Upper Imbrian mare materials
Id	Upper Imbrian dark-mantling materials
Iv	Upper Imbrian volcanic-dome complexes
Ip	Imbrian light-plains materials (mostly impact-melt rock inside basin and ejecta outside basin)
Ioi	Orientale-basin inner deposits (mostly primary ejecta)
Ioo	Orientale-basin outer deposits (mostly secondary craters and their ejecta)
Ic_1	Lower Imbrian crater materials
Iii	Imbrium-basin inner deposits (mostly primary ejecta and ring materials)
Iio	Imbrium-basin outer deposits (mostly secondary craters and their ejecta)
Nt	Nectarian terra-mantling and plains materials (probably thin basin ejecta, possibly overlying volcanic plains)
Nc	Nectarian crater materials
Nb	Nectarian basin materials younger than Nectaris (identified individually on plate A)
Nni	Nectaris-basin inner deposits (mostly primary ejecta and ring materials)
Nno	Nectaris-basin outer deposits (mostly secondary craters and their ejecta)
pNu	Pre-Nectarian materials, undivided
ob	Old basalts of Nectarian or Early Imbrian age, now buried (inferred)

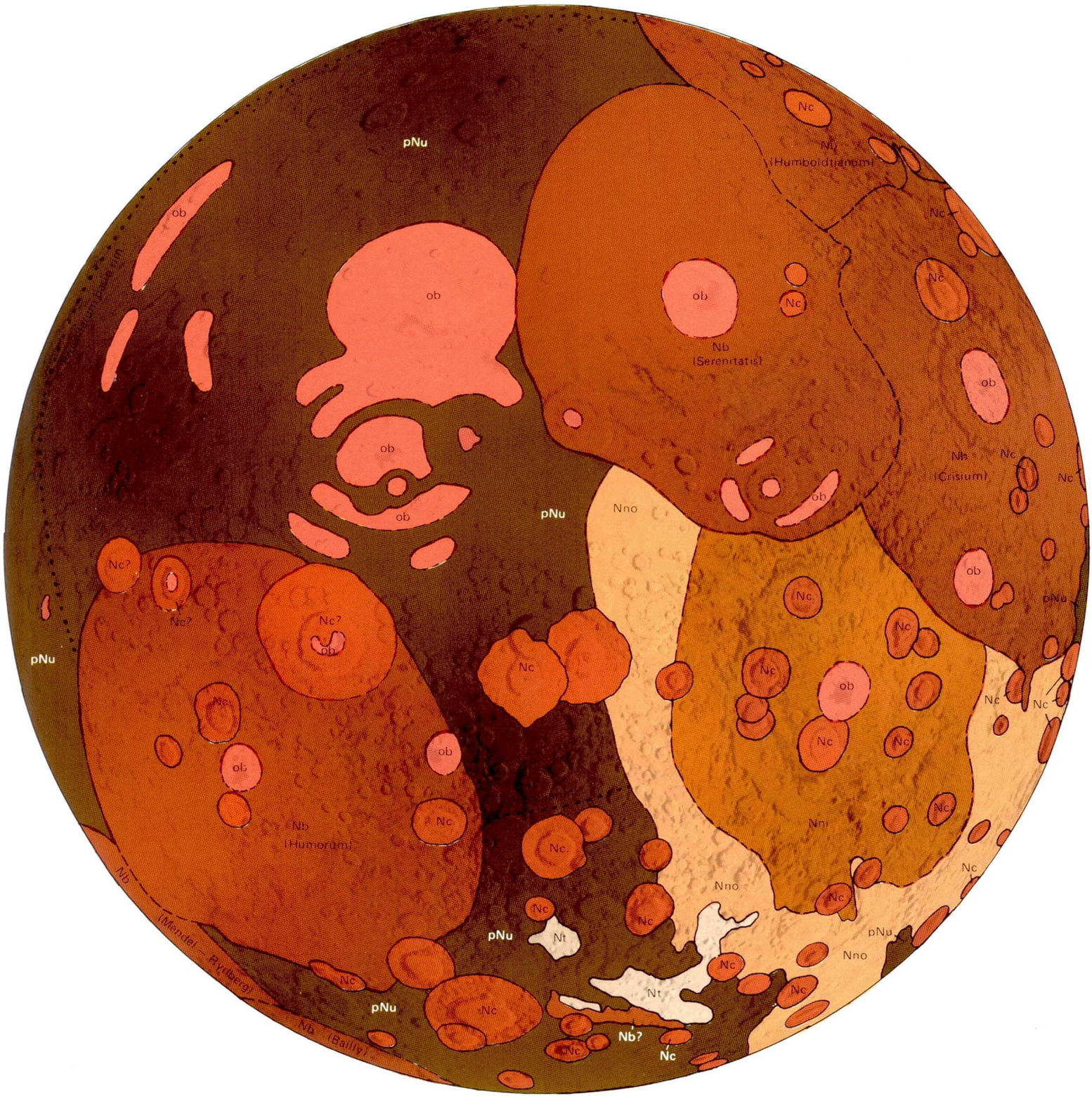
pNu
Nc
Nb
(Humboldtianum)
ob
Nb
(Serenitatis)
Nb
(Crisium)
Nno
Nc?
Nb
(Humorum)
Nb
(Mendel – Rydberg)
Nb (Bailly)
Nt
Nb?
Nni

PLATE A. Paleogeologic map representing lunar near side at end of Nectarian Period about 3.92 aeons ago. Deposits of Nectaris and six younger Nectarian basins superposed on pre-Nectarian terrane (undivided; only pre-Nectarian feature portrayed geologically is rim of Procellarum basin, dotted). Extent of old (now-buried) basalt (unit ob) inferred from likely extrusion rate (figure 6.83), age of underlying surface, and size of containing basin. Largest old maria are in center of Procellarum basin and in Insularum basin (multiring structure shown on base south of Procellarum center); these patches of old basalt probably both pre-Nectarian and Nectarian. Nectarian craters superposed on Nectarian basins in accord with the basins' ages; most on Nectaris, fewest on Serenitatis. Many additional Nectarian craters (and perhaps one or two basins) presumably present in northwest quadrant, where deeply buried by later deposits (plates B-D). Deposits of craters ≥ 50 km in rimcrest diameter shown here and in plates B-D. Contacts dashed where highly inferential. Base map by Donald E. Davis.

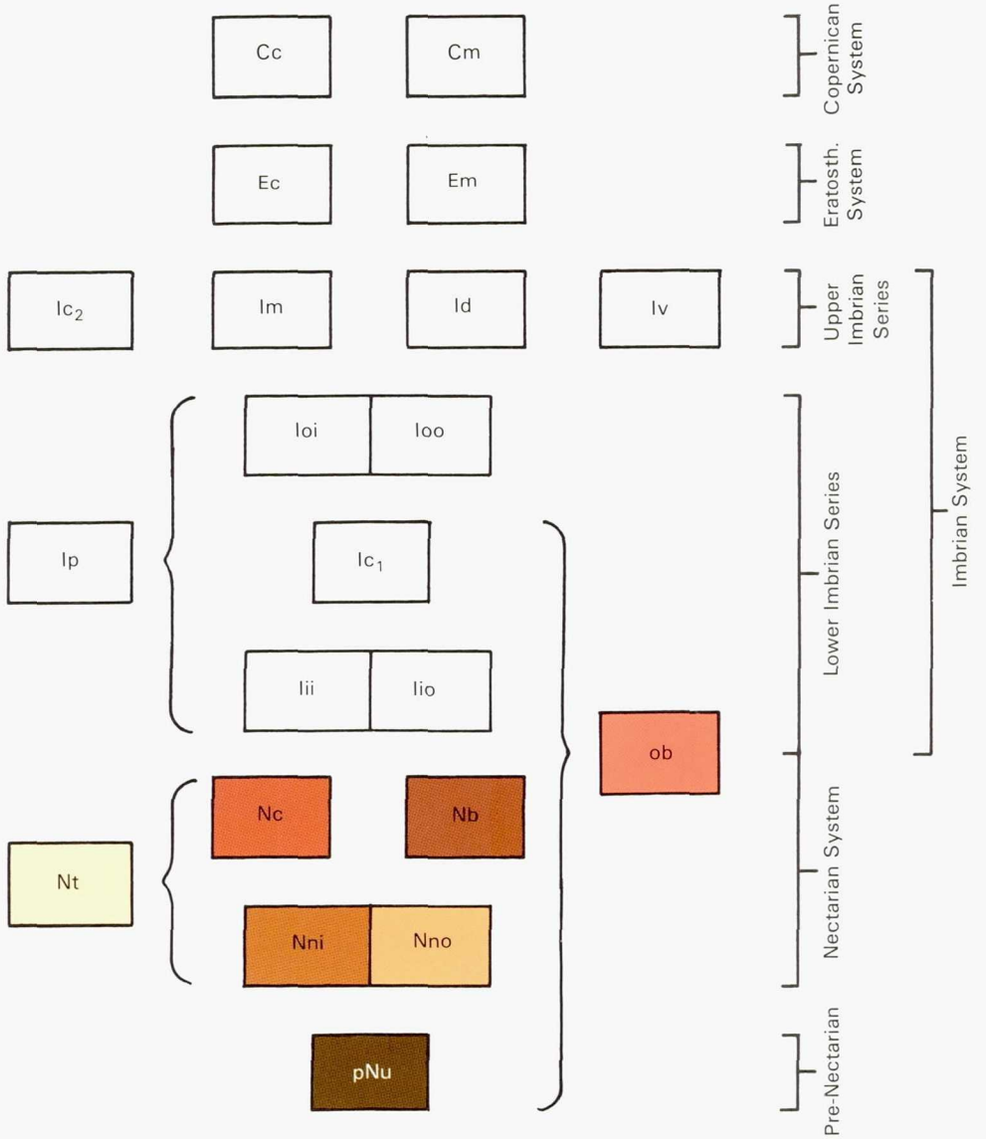

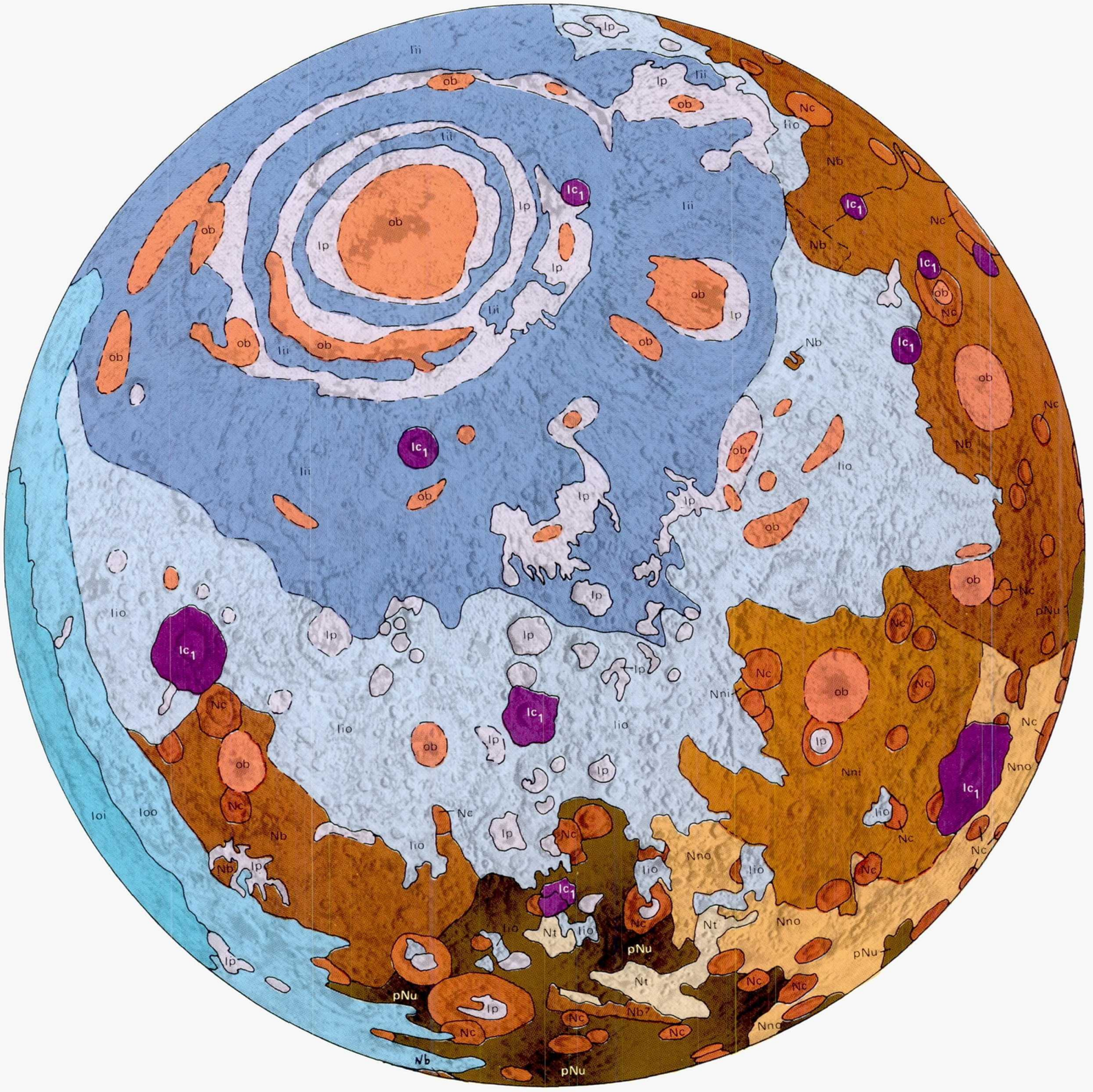
lp
lii
ob
lio
Nc
Nb
Ic_1
Nni
Nno
Nt
pNu
loi
loo
Nb?

PLATE B. Paleogeologic map representing lunar near side at end of Early Imbrian Epoch, after formation of Imbrium basin and just after formation of Orientale basin about 3.80 aeons ago. Imbrium basin excavated and redistributed target materials including pre-Nectarian material, old basalts, and Serenitatis deposits; Orientale target consisted mostly of thick pre-Nectarian material (plate A). Extrusions of old basalt on Nectarian surfaces have grown since Nectarian Period, and extrusions in area covered by Imbrian basin deposits have resumed at slightly different spots. Base from Wilhelms and Davis (1971); base shows Iridum crater (large expanse of unit Ic_2 in upper left of plates C and D) because thought older than Orientale when base was prepared.

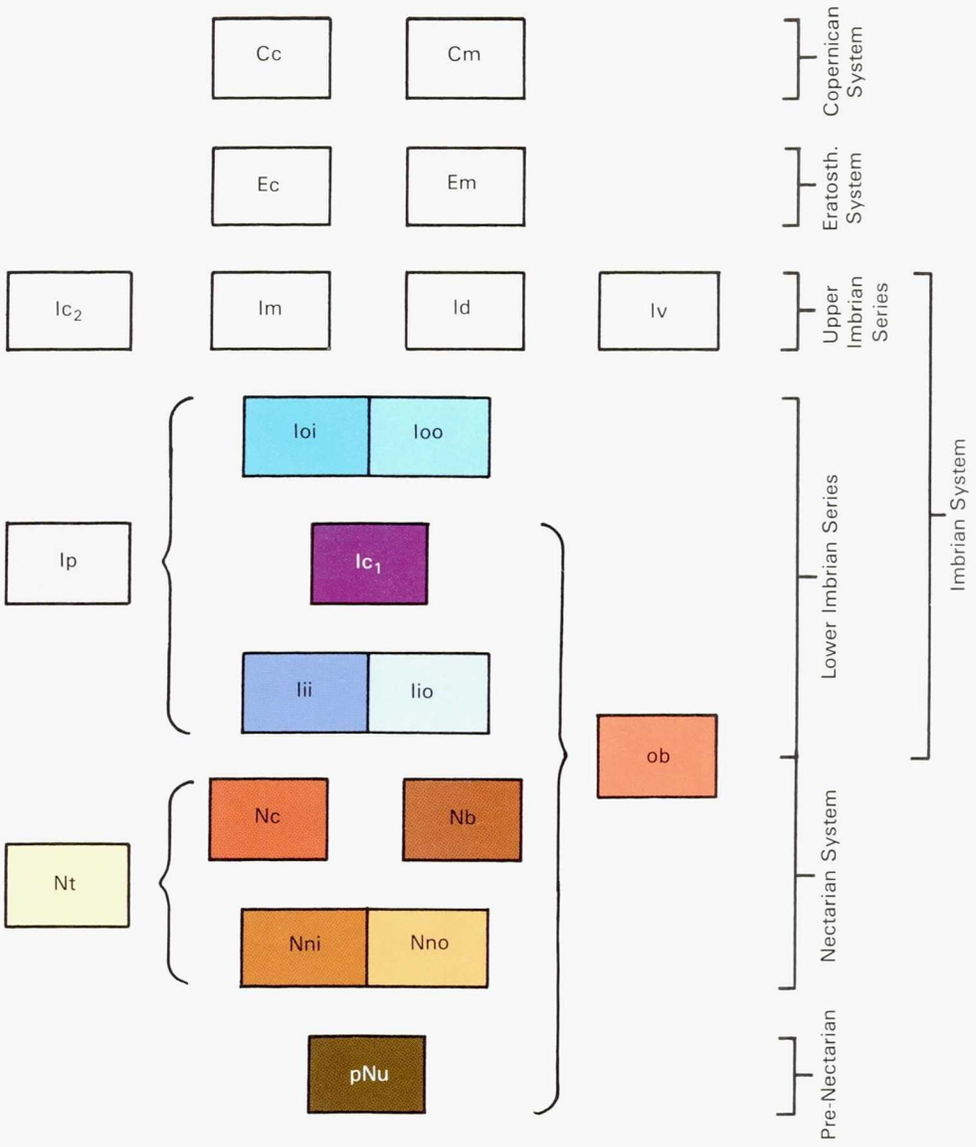

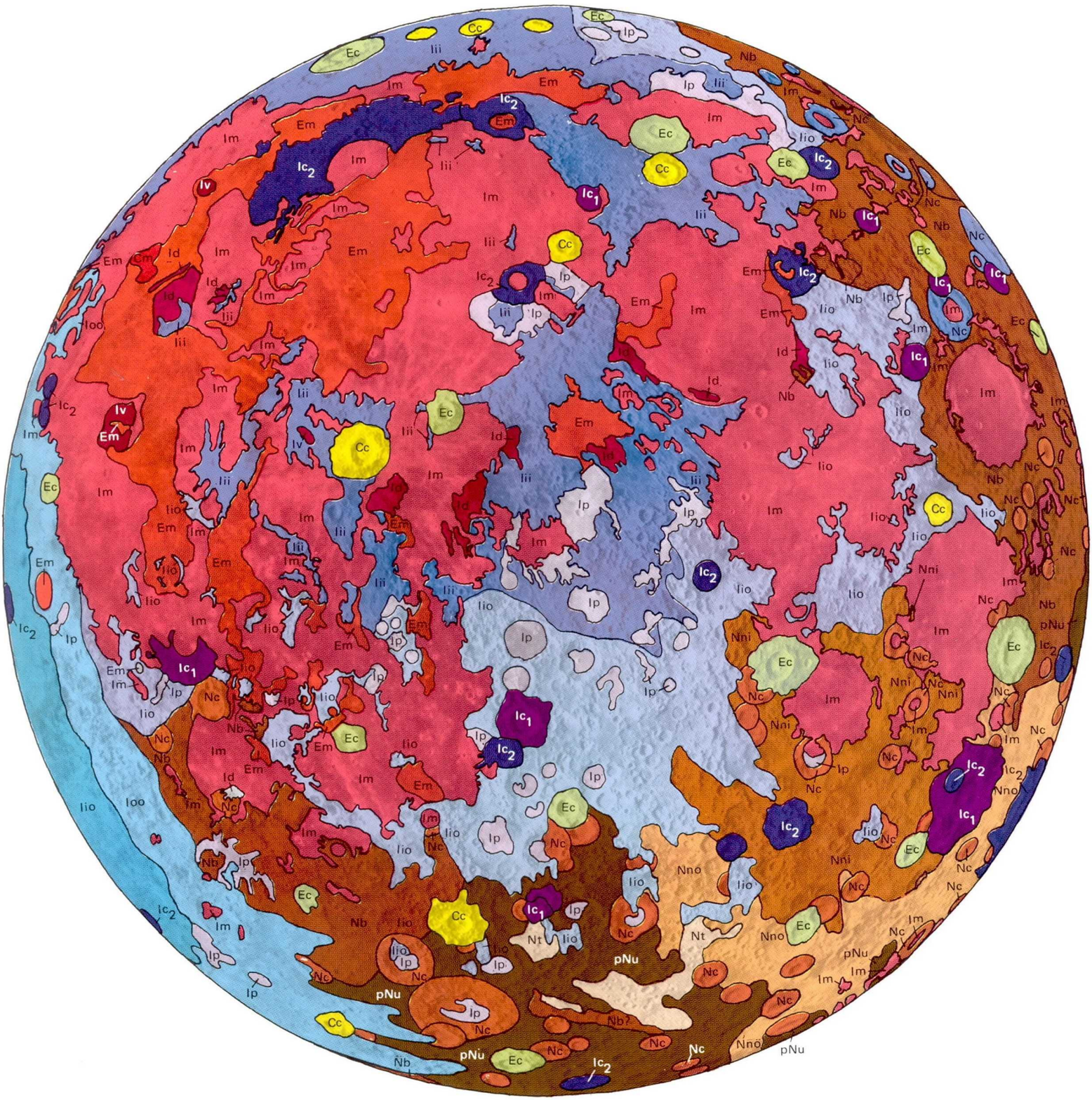
Ec
Cc
Ip
Nb
Iii
Im
Em
Ic2
Ic1
Nc
Iio
Id
Cm
Ioo
Iv
Nni
Nno
pNu
Nt
Nb?

PLATE C. Paleogeologic map representing lunar near side at end of Imbrian Period about 3.2 aeons ago. Extensive though thin mare basalts altered Moon's appearance during Late Imbrian Epoch. Base from Wilhelms and Davis (1971).

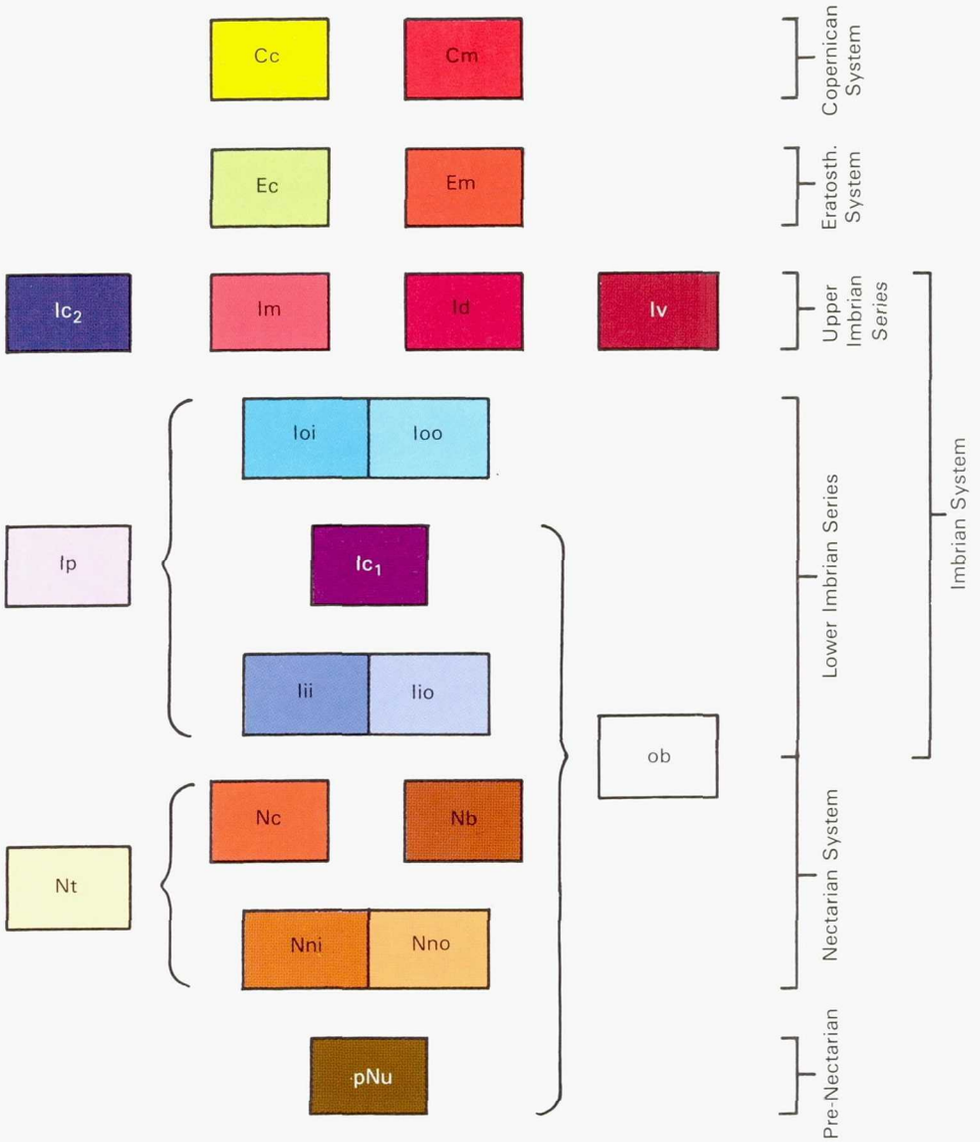

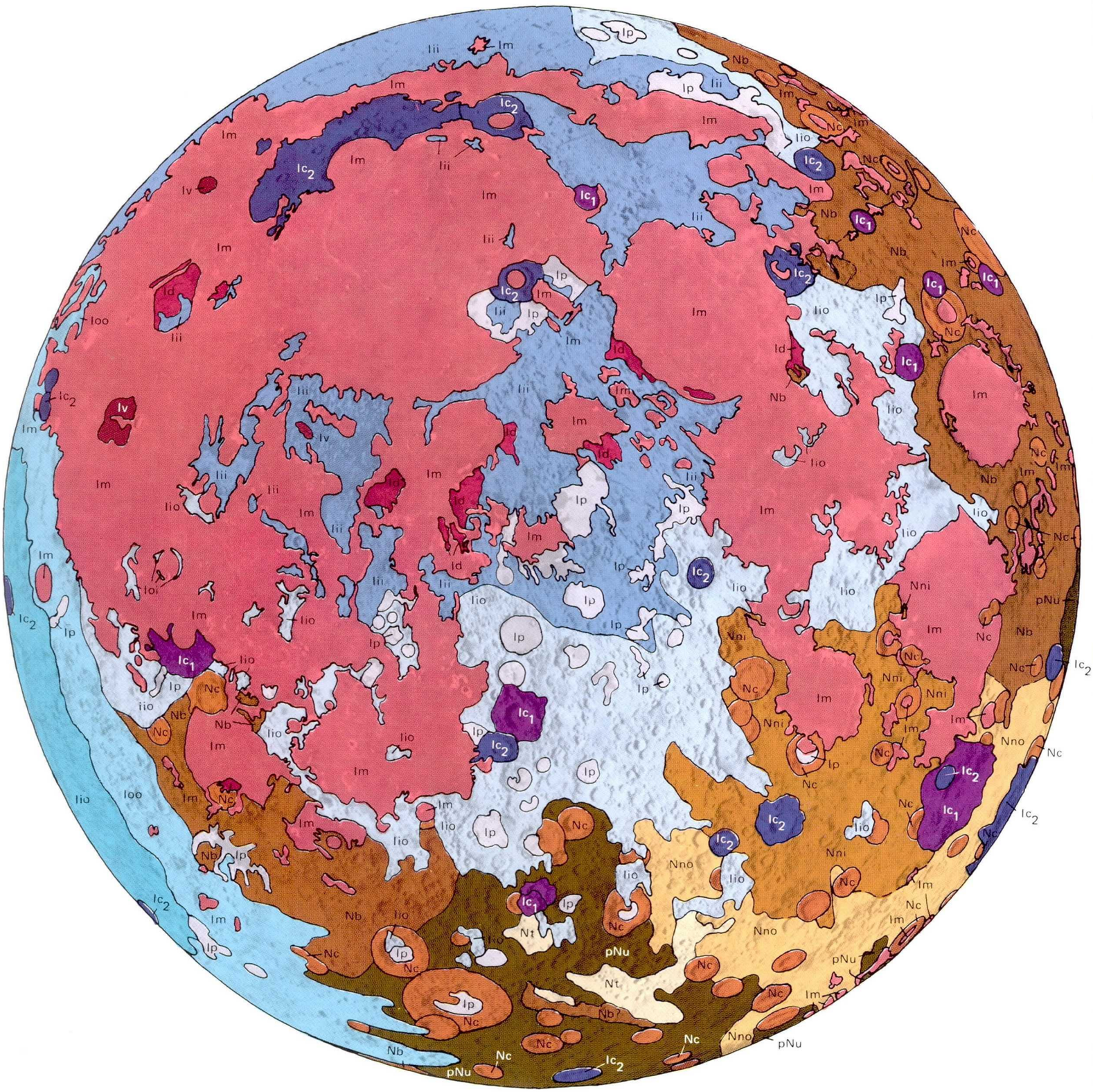
Iii
Im
Ip
Nb
Ic2
Ic1
Iv
Id
Ioo
Io
Ioi
Nc
Nt
Nb?
pNu
Nni
Nno

PLATE D. Geologic map of present lunar near side. Surface changed relatively little since ancient time portrayed in plate C. Base by U.S. Air Force Chart and Information Center.

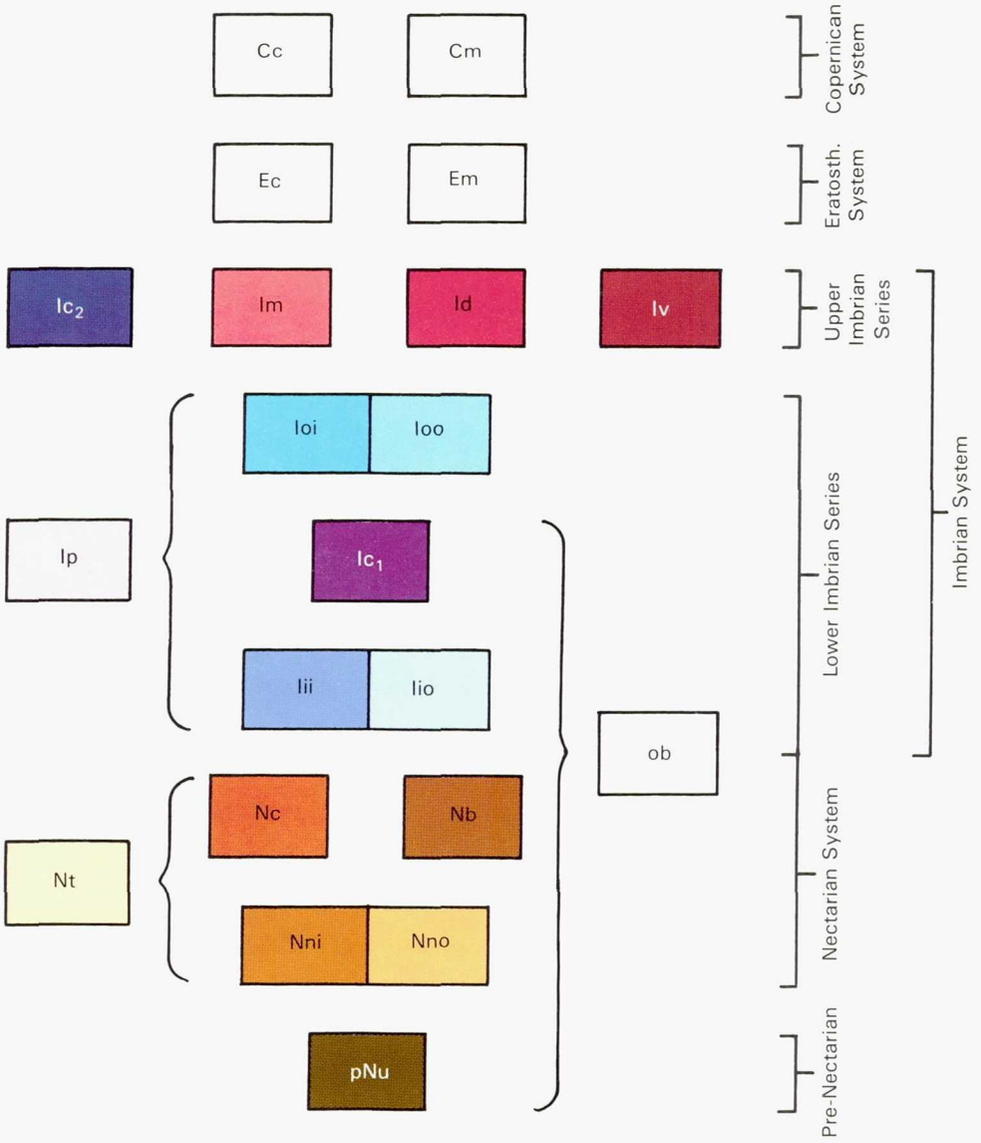

7
MARS

Michael H. Carr

INTRODUCTION

The last several years have seen an enormous increase in our knowledge of the geology of Mars. Although the planet has been observed through the telescope for centuries, during which time various surface markings were identified and atmospheric changes monitored, telescopic resolutions fall far short of those needed to detect topography. It was not until 1965, when pictures of the surface were first acquired by spacecraft, that interpretation of the planet's geology could realistically begin. Since that time we have acquired an enormous amount of information from a succession of missions. We now know that the planet has had a complex and varied geologic history. A wide variety of volcanic features, both ancient and geologically recent, attest to sustained volcanic activity. Dendritic channels and huge dry valleys suggest the widespread action of running water. Enormous canyons and extensive fracture systems are evidence of crustal deformation on a global scale. At the poles, layered sediments preserve evidence of sustained sedimentation. Elsewhere, collapsed ground, moraine-like features, scour, and vast sand seas indicate that the surface has been affected by the action of ice and wind. The planet thus resembles Earth in that it has been volcanically and tectonically active and has had its surface modified by wind, water, and ice. Differences between the two planets, however, remain profound.

The following discussion will attempt to identify the geologic processes that have affected the Martian surface and to trace how the surface has evolved. Because of the profusion of imaging data, the arguments are mainly geomorphic, although chemical and geophysical data are discussed where available. Emphasis is on the geology, but some other topics such as the chemical evolution of the atmosphere and the orbital and rotational motions are also examined where appropriate because of their influence on geologic processes. The discussion begins with some introductory remarks on telescope and spacecraft exploration, then goes on to discuss individually different geologic features of the planet. In most cases the origin of the features is only partly understood, and a variety of hypotheses are presented. Where possible, statistics on the number of asteroidal and cometary impacts are given as an indication of when the features formed. The chapter ends with a summary in which the evolution of the Martian surface is outlined and compared with that of Earth. The entire discussion draws heavily from other summaries, particularly those by Mutch et al. (1976), Arvidson et al. (1980), Snyder (1979), and Carr (1980, 1981).

Mars Within the Solar System

Mars is the fourth planet from the Sun after Mercury, Venus, and Earth. Its mean equatorial radius of 3390 km (Bills and Ferrari, 1978) is 0.51 times that of Earth and 1.88 times that of the Moon. In size, therefore, Mars is almost midway between Earth and the Moon. Its mass of 6.418×10^{26} g (Arvidson et al., 1980) gives the planet a mean density of 3.933 g/cm^3 as compared with 5.517 g/cm^3 for Earth (Bullen, 1975). The difference is due in part to the larger central pressure of Earth, but the Mars zero-pressure density of 3.72–3.78 g/cm^3 (Okal and Anderson, 1978) is also lower than Earth's value of 4.04 g/cm^3 (Ringwood, 1966). Probable causes are a lower iron content in the Mars core and a higher proportion of volatiles such as oxygen and sulfur (Arvidson et al., 1980).

Mars has a distinctly elliptical orbit with a period of 687 Earth-days or 1.861 Earth-years. The semi-major axis is 1.524 AU and the Mars–Sun distances at perihelion and aphelion are 1.381 and 1.666 AU, respectively. The time between successive close approaches to Earth (oppositions) is about 780 days (2.14 years). The exact time varies slightly because of the eccentricity. If opposition occurs at Mars perihelion, then the Earth–Mars distance may be as small as 55 million kilometers; if near aphelion, then the distance may be as large as 100 million kilometers. Particularly close oppositions in this century occurred in 1909, 1924, 1939, 1956, and 1971.

Variations in the orbital and rotational parameters have a significant effect on geologic processes. The rotation axis is currently inclined 25° to the plane of the orbit. The southern hemisphere is tilted toward the Sun at perihelion, causing southern summers to be hotter and shorter than those in the north. Precession of the rotation axis and the orbit plane, however, causes an alternation of climatic conditions between the two hemispheres on a 51 000 year cycle (Ward, 1973; Murray et al., 1973). Approximately 25 000 years from now the northern hemisphere will face the sun at perihelion and it will have the short hot summers. The alternation of the climatic characteristics of the two hemispheres causes the wind patterns to slowly shift in latitude, changes the preferred location of dust storm activity, modulates deposition of debris at the poles, and possibly affects the composition of the residual caps. An additional complication is that the magnitude of the eccentricity changes slowly, with a period of approximately 2 million years (Ward, 1973; Murray et al., 1973). The present value of 0.097 is close to the middle of the full range from 0.004 to 0.141. When the eccentricity is at the low end of the range, climatic differences between the two hemispheres are small; when the eccentricity is at the upper end of the range, differences are large and the effects of precession are amplified. Variations in the planet's obliquity, which is the angle between the equatorial plane and the orbital plane, may cause the largest climate changes. The present obliquity is 25°, but it ranges between 14.9° and 35.5° with a period of 1.2 million years (Ward, 1974). At high obliquities, a greater proportion of the Sun's radiation falls on the poles, and this may cause major changes in atmospheric pressure as the polar regions yield frozen and adsorbed CO_2 and H_2O to the atmosphere (Fanale and Cannon, 1974, 1979; Gierasch and Toon, 1973).

Telescopic Observations

The smallest feature that can be seen on Mars at the telescope under optimum conditions is around 150 km across; for most of the time the resolution is considerably poorer. At this scale numerous irregular surface markings are visible. Their pattern shows little obvious correlation with topography and is believed to be caused by variations in the distribution of surficial debris (Sagan et al., 1972); the bright areas being covered with a relatively thick cover of fine-grained debris, the dark areas being largely swept free. The overall pattern has remained fairly stable for over a century, although small changes are seen from year to year (e.g., see the maps of Inge et al., 1971a, 1971b; Inge, 1974, 1976, 1978). The general pattern must, however, change slowly as the circulation pattern of the atmosphere changes in response to long-term climate changes. Most of the dark markings are at present in the low southern latitudes, although two of the darkest regions, Syrtis Major and Mare Acidalium, are in the north. The albedo features of both hemispheres appear to have a greater contrast in summer than in winter (Focas, 1961; Thompson, 1973). The change in contrast was formerly attributed to a "wave of darkening," a progressive darkening of the markings that swept from pole to equator in spring, but the change is now believed to be due to an increase in brightness of the light areas, probably as a result of increased dust storm activity as summer conditions approach (Capen, 1976; Thompson, 1972, 1973; Boyce and Thompson, 1972).

Most of the seasonal changes in the telescopic image are due to either frost or atmospheric effects. The most obvious changes occur at the poles. At the beginning of northern fall, the northern cap is at its minimum, about 20° across. Clouds start to accumulate in the high northern latitudes to form a hood which covers much of the surface down to 45°N latitude. When the hood clears in spring the cap is at its maximum, extending down to 65°N latitude. At mid-spring the cap starts to retreat at a rate close to 20 km/day. In the south the events are somewhat different. The hood appears more discontinuous, and retreat of the seasonal cap is more ragged and asymmetric about the poles (Fischbacker et al., 1969). By the start of southern summer the cap has contracted to its minimum size and is about 10° across, considerably smaller than the northern cap, and displaced about 5° from the south pole.

Commonly observed transient brightenings appear to be caused by atmospheric effects. They are of two main types. White or blue clouds occur throughout most of the year preferentially in what we now know as areas of relatively high elevation, such as Tharsis, Elysium, and Alba. They appear to be formed mostly of water or carbon dioxide. Yellow clouds, on the other hand, tend to be only poorly visible in the blue and are generally restricted to late spring or summer in the south. They were correctly interpreted as dust clouds long before any spacecraft observations. The dust storm intensity seems to vary from year to year. In some years, such as 1957 and 1971, the dust storms become truly global and engulf the whole planet, obscuring all surface markings outside the polar regions. As we shall see later, the dust storms may be important in causing differences between the two residual polar caps and play an important role in the accumulation of layered sediments at the poles.

Spacecraft Exploration

Mars is by far the most intensively studied planet other than Earth. Spacecraft exploration started July 15, 1965, when Mariner 4 flew by the planet and returned 22 close-up pictures of a hazy, low contrast, cratered surface that superficially resembled the lunar highlands. The mission also confirmed that Mars had only a thin atmosphere with surface pressures in the 5–10 mb range, and demonstrated that its intrinsic magnetic field was less than 10^{-4} that of Earth. Two additional spacecraft, Mariners 6 and 7, were launched to the planet in 1969. Their pictures again revealed a cratered surface although "etch-pits," "chaotic terrain," and featureless areas (Leighton et al., 1969a; Collins, 1971) suggested processes distinctively different from those that have sculpted the Moon's surface. It was not until 1971, however, when the Mariner 9 spacecraft started taking pictures of the planet, that the full diversity of the Martian surface was revealed.

Mariner 9 was injected into Mars orbit on November 14, 1971. It carried several scientific instruments including a wide-angle camera (50 mm focal length), a narrow-angle camera (500 mm focal length), an ultraviolet spectrometer directed primarily at characterizing the scattering properties of the atmosphere, an infrared radiometer to measure temperatures, and an infrared spectrometer from which information could be obtained on the composition of the atmosphere and its entrained dust. In addition, temperature and pressure profiles in the atmosphere and surface elevations could be estimated from the attenuation of the radio signal from the spacecraft as it disappeared behind the planet and reappeared on each orbit.

As the spacecraft approached Mars the experimenters saw to their dismay that the entire planet was enveloped in an enormous dust storm that hid much of the surface from view. All that was visible was the south polar cap and four dark spots in the Tharsis region. All the carefully prepared plans to systematically explore the planet had to be set aside until the atmosphere cleared. Close examination of the four spots showed that each was a mountain top, visible because it stood above most of the obscuring dust in the atmosphere, and each contained what appeared to be a volcanic caldera. This was the first indication that the planet was not all lunar-like as it had appeared from the previous missions. Slowly the dust in the atmosphere settled, and by January 1972 the atmosphere was judged clear enough that adequate imagery of the surface could be acquired. Systematic mapping was accordingly begun and during the next several months the now-familiar canyons, volcanoes, channels, chaos, layered sediments, and volcanic plains were revealed. The mission ended on October 27, 1972, after more than 7300 pictures had been taken, including 1- to 3-km-resolution coverage of almost all the planet.

Meanwhile the Soviets had also sent two spacecraft to the planet. Mars 2 and Mars 3, launched in May 1971, entered orbit around the planet shortly after Mariner 9. Prior to orbit insertion each released a capsule which landed on the surface, but neither capsule returned any useful scientific data. The preplanned orbiter sequences also failed partly because of the global dust storms. The Soviets followed in 1973 with four separate launches of two orbiters and two landers. One of the orbiters returned 70 pictures of roughly Mariner 9 quality, and one of the landers reached the surface but again failed to return useful scientific data.

The most recent step in Mars exploration was taken by the Viking mission, which placed two landers on the surface and two additional vehicles in orbit around the planet. The main intent of the mission was to determine if life was present, and the array of experiments on the different vehicles reflects that goal. On each lander were two cameras to view the immediate surroundings of the spacecraft, a gas chromatograph-mass spectrometer (GCMS) to analyze organic compounds in the soil, an X-ray fluorescence experiment

to analyze the inorganics, a threefold biology experiment to detect different life processes, a seismometer, and an array of meteorological instruments. The lander capsule also included several entry experiments to measure the various properties of the atmosphere as the landers descended to the surface. The orbiters had two cameras, an array of infrared sensors, and a spectrometer to measure the water content of the atmosphere. The radios on both landers and orbiters could also be used for a variety of scientific purposes.

Each approaching spacecraft consisted of a combined orbiter and lander. The first went into orbit around Mars on June 19, 1976. After a three-week search for a safe landing site, the first lander was released, and it touched down in Chryse Planitia on July 20, 1976. Shortly thereafter the second spacecraft arrived, and its lander was released and set down in Utopia Planitia on September 3, 1976. Several months of intense activity followed during which the different biological and analytical experiments were successfully performed. Although no life was detected, the landers returned abundant data on the local geology around the landers, the chemistry of the soil and the atmosphere, local weather conditions, the planet's seismicity, and so forth. Contact with the last surviving lander was finally lost late in 1982 after six years of continuous operation on the planet.

Meanwhile the orbiters had been systematically observing the planet with their instruments. The cameras mapped the entire surface at a resolution of 200 meters and large areas at much higher resolutions, ranging down to 10 meters. The infrared instruments had mapped the areal and temporal variations, the temperature of the surface and atmosphere, and variations in the water content of the atmosphere over two full Martian years. The second orbiter ran out of attitude-control gas in July 1979, and the first in early August 1980, thereby terminating the orbiter mission. By that time the two orbiters had returned over 50 000 pictures of the planet, most of excellent quality.

GENERAL PROPERTIES OF THE SURFACE

Physiography and Topography

Mars is markedly asymmetric in the distribution of its physiographic features (fig. 7.1). Two-thirds of the planet is covered by an ancient, densely cratered terrain that superficially resembles the lunar highlands. A major difference from the Moon, however, is the presence of numerous valley networks that appear to have been cut by running water. The cratered terrain covers most of the southern hemisphere and a broad tongue extends into the north around 330°W longitude. The density of large craters (>30-km diameter) in the terrain is high but short of saturation, and most of the large craters are shallow, with flat floors and low rims. The number of smaller craters is proportionately less, and these are mostly bowl-shaped. Much of the remainder of the planet is covered by more sparsely cratered plains that in places resemble the lunar maria. They cover much of the high northern latitudes and large areas within the volcanic provinces of Tharsis and Elysium. Remnants of cratered terrain protrude through many parts of the plains, indicating that the cratered terrain is at a relatively shallow depth below the plains, although considerably disrupted. The plains differ in character according to latitude. Those in the equatorial regions have a relatively simple physiography, with numerous lava flows and ridges that resemble those on the lunar maria. The high-latitude plains, in contrast, are quite complex; they generally lack primary volcanic features and instead have numerous characteristics that suggest repetitive deposition and erosion.

Among the most impressive features of the Martian surface are the large shield volcanoes. Most occur in two broad provinces: around Tharsis, between latitudes 20°S and 50°N and longitudes 90°W and 140°W, and in Elysium between 10°N and 40°N and between 200°W and 220°W. Isolated volcanoes occur elsewhere, especially around the large impact basin Hellas, but these tend to be older and have less relief than those in Tharsis and Elysium. Several of the volcanoes are enormous by terrestrial standards; the main edifice of Olympus Mons, for example, is 550 km across and its summit is 25 km above the surrounding plains. Alba Patera, north of Tharsis, is over 1500 km across. For comparison the largest volcano on Earth, Mauna Loa, is 120 km across at its base and its summit is 9 km above the ocean floor.

The Tharsis volcanic province is on the northwest flank of a broad bulge in the planet's surface. Arranged around the bulge are numerous fractures roughly radial to the bulge and mostly concentrated in zones of closely spaced, parallel grabens or fossae. In addition, a series of interconnected canyons extends for over 3000 km from the summit of the bulge near Noctis Labyrinthus down its eastern flank. At its broadest and deepest, the system is over 600 km across and over 7 km deep. The canyons appear to be related

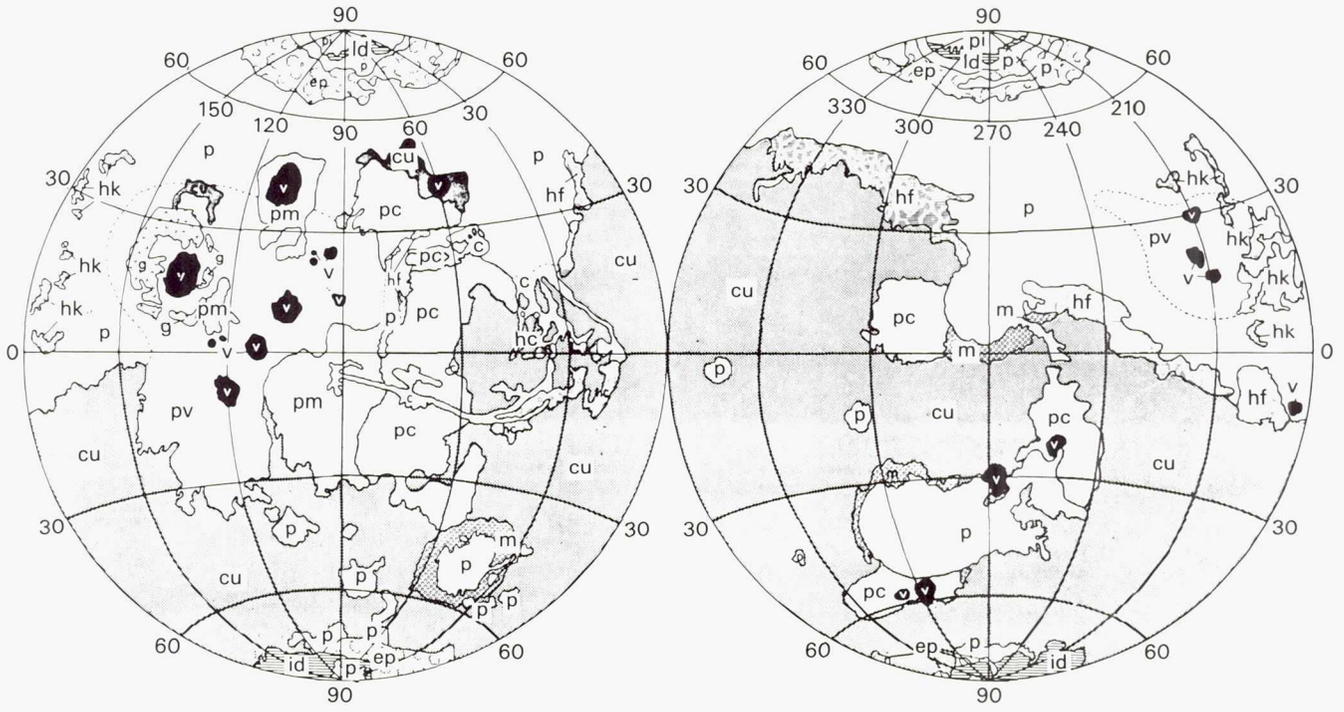

Figure 7.1. Physiographic map of Mars. Polar units include pi (permanent ice), ld (layered deposits), and ep (etched plains). Volcanic units include v (volcanic constructs), pv (volcanic plains), pm (moderately cratered plains), and pc (cratered plains). Modified areas include hc (chaotic terrain), hf (fretted terrain), hk (knobby terrain), c (channel deposits), p (plains undivided), and g (grooved terrain). Ancient units include cu (cratered terrain, undivided) and m (mountainous terrain) (from Mutch et al. 1976).

to the radial fractures since many of the walls are fault scarps and radial grabens are numerous close to and parallel with the canyon rim.

To the east the canyons merge with what has been termed chaotic terrain, areas where the ground has seemingly collapsed to form jostled blocks 1–2 km below the surrounding terrain. Most chaos occurs between 15°S and 5°N and between 15°W and 40°W. Several large channels emerge from the chaos, extend northward to Chryse Planitia, then across Chryse Planitia to die out around 45°N latitude. Other channels start in the box canyons north of the main canyon and also converge on Chryse Planitia, but from the west. Still other large channels occur in Memnonia, Amazonis, Hellas, and Elysium. The channels are enormous in size: where incised into the cratered upland south of Chryse Planitia, individual channels may be up to 25 km across; the scoured swath in the southern part of Chryse Planitia is in places over 600 km across.

At both poles and extending outward for a little over 10° are some layered deposits that appear unique to the polar region. In the south they overlie old cratered terrain; in the north they lie on plains. The layering is visible on escarpments and the walls of valleys that are arranged in a roughly spiral pattern around the poles. The deposits are almost devoid of impact craters, which suggests that they are younger than almost any other surface feature.

Around the layered terrain in the north is a nearly continuous collar of dunes, and in the high southern latitudes dune fields are common within large craters. Elsewhere, eolian landforms at a scale of few tens of meters or more are relatively rare, although occasional dune fields are found in sheltered areas, and fluted ground in some regions suggests the action of wind. One region where eolian features are common is southern Amazonis, where a thick sequence of seemingly friable deposits overlies the plains-upland boundary.

Mars' topography, like the physiography, is markedly asymmetric. The southern hemisphere is mostly higher than the northern, and a broad 10-km-high bulge is centered on the equator in the volcanic province of Tharsis. In addition the planet has considerable local relief. The summit of Olympus Mons stands 27 km above the datum and the floor of Hellas is over 10 km below it.

Since Mars has no sea level against which elevations can be referenced, an artificial datum has been

established. That chosen is a fourth-order, fourth-degree representation of the gravity field (Jordan and Lorell, 1975) fit to a 6.1-mb surface (Kliore et al., 1973; Christensen, 1975), which was picked because it is the partial pressure of water at its triple point. The datum is a triaxial ellipsoid with equatorial semi-major axes of 3394.6 km and 3393.3 km and a polar semi-minor axis of 3376.3 km.

A planet-wide topographic map has been constructed from data from several sources (Christensen, 1975; Wu, 1978). Radio occultations give the only absolute measures of elevations. They are derived from the timing and nature of the decay of the radio signal from a spacecraft as it passes behind the planet as viewed from Earth. The occultations from Mariner 9 provided a scattering of points across the surface where radii are known to within 1 km. The most precise measures (75–200 meters) of relative elevation are from Earth-based radar but these are restricted to east-west tracks within 25° of the equator (Downs et al., 1975). The Mariner 9 ultraviolet and infrared spectrometers have provided the most abundant elevation data (Hord et al., 1974; Hanel et al., 1972). The elevations are determined from the increase in atmospheric scattering or CO_2 absorption caused by the thicker atmosphere over regions of lower elevation. The precision of the measurements is around 1 km, but considerably larger inaccuracies may result from dust and condensates in the atmosphere. The global topographic map was constructed by using the occultation measurements to fix the east-west radar traces in absolute elevation, then hooking the roughly north-south UVS and IRIS traces to the radar profiles and occultation points, then contouring the result. Some discretion had to be exercised in the contouring because of the wide spacing of the data, and this largely accounts for differences between the maps of Christensen (1975) and Wu (1978). Errors in the global map are estimated at 1–2 km, but errors could be larger in areas of poor radar and occultation control, or where UVS and IRIS data are sparse. In a few areas more precise elevations are available because of good stereo coverage (Blasius, 1979; Wu, 1978) or because of dense Earth-based radar coverage (Roth et al., 1980).

Surface Temperatures and Thermal Inertia

Surface temperatures vary according to location, time of day, season, and surface properties as shown in figure 7.2 for typical cases. The temperatures are at a minimum just before dawn, rise rapidly to a peak just after noon, fall rapidly in the afternoon, and then more slowly to the pre-dawn low. Because of the orbital eccentricity, peak temperatures in southern summer are about 30° C higher than those in northern summer, and rise over 273° C for a wide range of latitudes. Temperatures are at their maximum of around 295 K at noon in midsummer at 25° S. The lowest temperatures recorded are on the southern cap at midwinter where they can fall as low as 140 K (Kieffer et al., 1977).

Thermal inertia is a measure of the responsiveness of a material to changes in thermal regime and is defined as $(kpc)^{1/2}$ where k is the thermal conductivity, p is the density, and c is the heat capacity. Differences in thermal inertia are most evident from the response of the surface to diurnal variations in insolation. Temperatures of surfaces with high thermal inertias respond only sluggishly to the insolation variations, so show only modest differences between day and night, whereas those with low thermal inertias have extreme day and night temperatures. The main cause of differences in thermal inertia is probably grain size. Course-grained materials tend to have relatively high thermal inertias; fine-grained materials tend to have low thermal inertias.

Kieffer et al. (1977) mapped variations in thermal inertia across the Martian surface from pre-dawn temperatures. For any given latitude, season and albedo, pre-dawn temperatures are highest (or lowest) when the thermal inertia is highest (or lowest). Thermal inertias were derived from differences between observed pre-dawn temperatures and those predicted by an idealized model of the surface after an appropriate correction for albedo, which was also measured by Kieffer et al. (1977). Subtracting out the model temperatures in effect corrects for latitude and season. The resulting thermal inertias show only partial correlation with physiographic features. Much of Tharsis, Elysium, and Amazonis, and a broad region termed Arabia, centered on 330°W longitude, have fine-grained materials at the surface. The canyons and canyon-chaos regions are relatively coarse grained. Thermal inertia and albedo show a negative correlation: bright areas tend to have low inertias, dark areas have high inertias. Interpretation of bright areas as regions with abundant fine-grained surficial debris at the surface is thus consistent with the thermal inertia measurements.

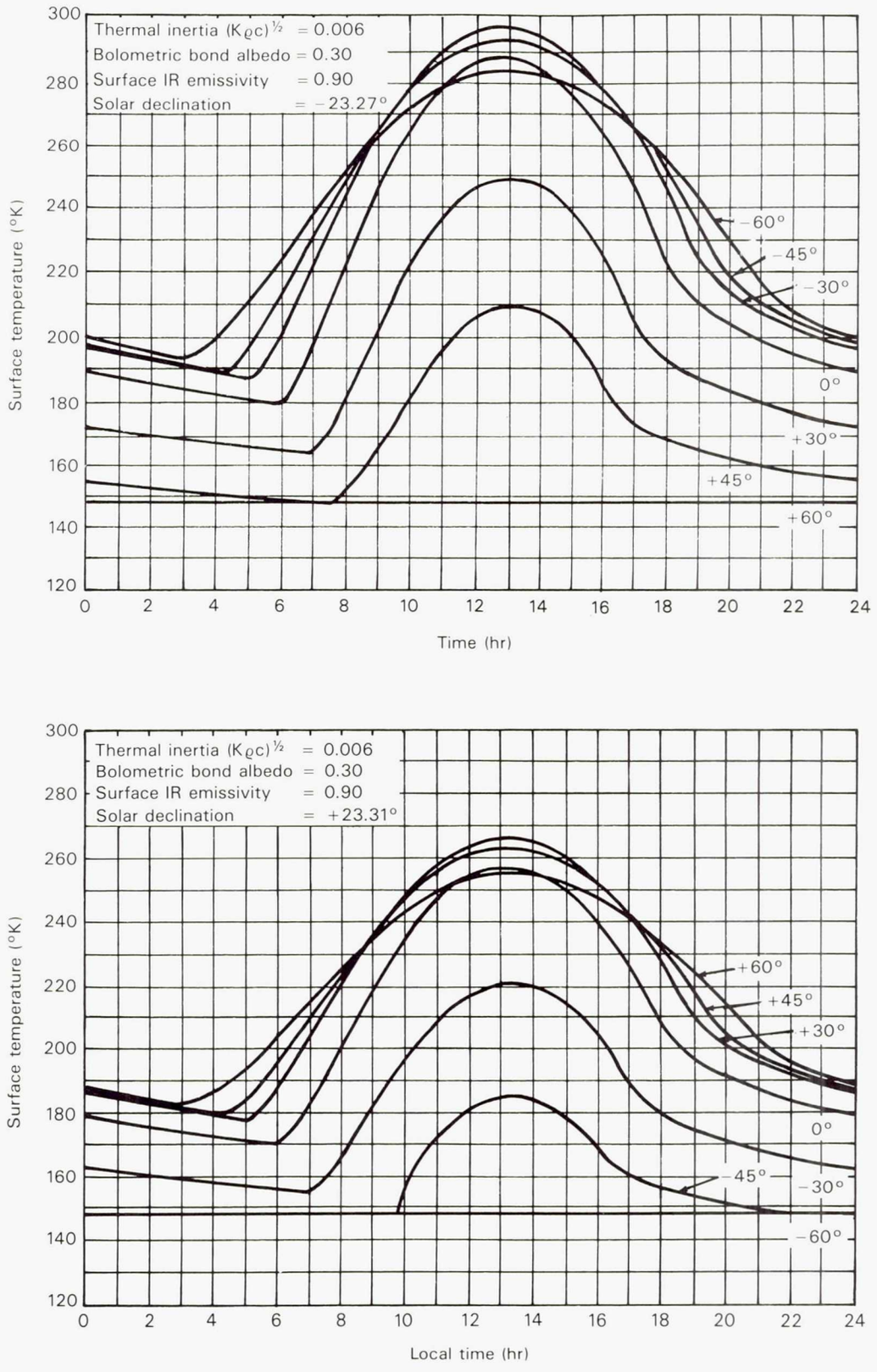

Figure 7.2. Models of the variation in surface temperature as a function of latitude. The upper diagram is for southern summer, the lower for northern summer. Peak summer temperatures in the south are higher than those in the north because of the coincidence of southern summer with perihelion.

Albedo and Color

The albedo of the Martian surface is markedly bimodal with peaks at 0.13 and 0.26 (Kieffer et al., 1977). Most dark areas are in the densely cratered terrain in the 0–40°S latitude belt. The darkest region of the planet is Syrtis Major with an albedo of 0.089, and the brightest region, just north of Ascraeus Mons, has an albedo of 0.429 (Kieffer et al., 1977). Estimates of the ratio of bright to dark areas range from 1.8 to 3.0 (McCord and Westphal, 1971; Binder and Jones, 1972).

The albedo is sensitive to wavelength, being considerably higher in the red than in the blue to give the planet its characteristic red color. At wavelengths below 0.5 μm the reflectivity ranges from 4 percent at 0.35 μm to around 10 percent at 0.5 μm (Adams and McCord, 1969; McCord and Westphal, 1971). At these wavelengths the dark and light areas have similar reflectivities, which accounts for the poor definition of surface markings in the blue, a phenomenon that early telescopic observers attributed to the presence of a blue haze. Above 0.5 μm the spectra from different areas diverge in such a way that bright areas have reflectivities around 30 percent at 0.85 μm as compared with 15 percent for the dark areas.

The difference in albedo between dark and light areas appears to be due largely to different amounts of fine-grained debris at the surface (Sagan et al., 1973). This conclusion, based on the disappearance and reappearance of dark markings during and after dust storms (see also Thomas and Veverka, 1979) and on the reflection properties of fine-grained and coarse-grained rock debris, is also consistent with the reflectivity of fine-grained debris at the Viking landing sites (Huck et al., 1977) and dust in the atmosphere (Pollack et al., 1979). Singer et al. (1979) attempted to derive spectra of the dark component uncontaminated by fine-grained debris by stripping from the dark area spectra various fractions of the spectra from light areas. They concluded that dark areas may be typically covered with 20–30 percent bright material. Soderblom et al. (1978) showed that significant spectral variability occurs in the areas of low albedo. Some variations are correlated with topography; crater rims in the densely cratered terrain, for example, tend to be more red than the intervening volcanic plains. Soderblom et al. suggested that these variations are caused by differences in the mineralogy of the exposed rocks and not simply by differences in the amounts of surficial debris.

The reflection spectrum is dominated by iron absorption bands in the visible, but at longer wavelengths bound water is important. The Fe^{3+} absorption between the UV and 0.75 μm causes the large contrast in reflectivity between the blue and the red. Bright areas generally show an additional Fe^{3+} absorption feature at 0.87 μm (Singer et al., 1979). These features have generally been attributed to ferric oxides (Binder and Jones, 1972). In dark areas the 0.87 μm band is weak, if present at all, and a Fe^{2+} band around 0.95 to 1.0 μm may be detectable. The strength of this band varies according to location, and the variation may indicate differences in mafic mineralogy, mainly the composition and proportions of pyroxenes and olivine (Adams and McCord, 1969; Huguenin et al., 1978; McCord et al., 1977; Singer et al., 1979). A broad absorption band centered at 2.85 μm was attributed by Houck et al. (1973) to bound water, a conclusion that is consistent with the evolution of water from heated soils at the Viking landing sites (Biemann et al., 1977). Soderblom and Wenner (1978) pointed out the strong resemblance of the spectra from bright areas with spectra from palagonite, a largely amorphous byproduct of the interaction of basaltic lava with water or ice.

THE VIEW FROM THE VIKING LANDERS

The Viking Lander 1 set down in the western part of Chryse Planitia at 22.5°W, 47.8°N in an area that from orbit looks like a lunar mare—a smooth, sparsely cratered volcanic plain with occasional wrinkle ridges. Farther to the west the Chryse plains are extensively scoured, seemingly by huge floods that cut deep gorges through the densely cratered terrain that separates Chryse Planitia from Lunae Planum. The scour, however, does not reach as far as the Viking site, which was placed by design in a relatively featureless area.

From the lander (fig. 7.3) the surface strongly resembles many rocky deserts of Earth, particularly those where volcanic rocks are exposed at the surface. The gently rolling landscape is yellowish-brown in color and strewn with rocks in the centimeter to meter size range. Between the rocks are drifts of fine-grained debris, which is also piled up on top of some of the larger boulders. Prominent in the scene are dune-like accumulations of debris, but these appear not to be dunes, which form by saltation of sand-size particles, but rather accumulations or drifts of much finer material in the lee of obstacles such as large boulders.

Figure 7.3. Drifts of fine-grained debris near the Viking 1 lander in Chryse Planitia. Layering visible in many of the drifts suggests that they are currently being eroded (Viking lander event 11A097).

Accumulations a few centimeters long are also common in the lee of many of the rocks. Layering exposed on the drifts indicate that they are not accumulating now but are being eroded. A small slump that occurred in one of the drifts after the landing showed that the drifts are stabilized by a thin coherent crust.

The loose rocks vary in color, shape, and texture. Most are angular with surfaces that are coarsely pitted, probably because of etching by the wind (Binder et al., 1977). The pits, which range in size from a few millimeters to 1 centimeter, may reflect the grain size of the rocks. Such a coarse grain could result from the low viscosity and high volatile content of the mafic lavas from which the rocks formed (Binder et al., 1977). Some rocks show features suggestive of layering and vesiculation. There is, 15–20 meters from the lander, an array of angular rocks that have a more bluish color and resemble terrestrial basalts. The origin of the strewn field is not known, but most of the rocks have probably been ejected from impact craters, the different rock types being derived from different locations or from different depths below the surface.

Craters are almost absent within the field of view, as was predicted before the landing by Gault and Baldwin (1970). They argued that primary craters smaller than 50 m across would be rare on the Martian surface because of the protective effects of the atmosphere. The atmosphere also protects the surface from much of the comminution and micro-erosion that occurs continuously on the Moon.

The fine-grained debris close to the surface is cemented to form a duricrust (Binder et al., 1977). This was well exposed beneath the spacecraft where the rocket exhaust removed the loose debris. Many of the pebble-size particles within reach of the lander also appear to be composed of duricrust (Toulmin et al., 1977). Its composition is almost identical to that of the loose debris except for a higher sulfur content and possibly slightly more chlorine. It is probably a caliche-like formation partly cemented by soluble salts, mainly $MgSO_4$, and possibly NaCl.

The view from the second lander in Utopia Planitia at 48°N, 225.6°W is superficially like the first in that it is of a rock-strewn landscape (fig. 7.4). However, the Utopia scene is flat and uniform, with no drifts or outcrops of bedrock. Slopes in the near field are less than 1° and on the horizon are all less than 2°. The scene has a remarkably uniform aspect, as similar size blocks with similar spacing continue across a level plain out to the horizon. The blocks are mostly subangular and more pitted than those at the Lander 1 site. They are also present in greater numbers than at the Lander 1 site. The most likely explanation for

Figure 7.4. View from the Viking 2 lander in Utopia Planitia. The spacecraft landed on a nearly level plain littered with angular blocky debris with a relatively narrow size range. Many of the blocks are deeply pitted (Viking lander 2 event 22A252).

the strewn field is that it is the surface of a debris flow from the 100-km-diameter crater Mie whose rim is 180 km to the east of the site. Orbiter pictures show that Mie, like other large Martian craters, has ejecta disposed around it in discrete lobes, one of which appears to cover the landing site.

Several trough-like depressions about a meter wide and 10 cm deep are visible from Lander 2. Although they cannot be traced for any great distance from the lander, they appear to form a roughly polygonal pattern. Much larger troughs, visible from orbit, also form a polygonal pattern over much of the Utopia region, with individual polygons ranging in size up to 5–10 km. The scale and form of the troughs visible from the lander are similar to those that form patterned ground in arctic regions of Earth, although the polygons visible from orbit are almost 100 times larger than any known on Earth. Terrestrial patterned ground forms by contraction of the frozen ground in winter, filling the resulting cracks by meltwater in the spring and summer, then refreezing, contraction, and cracking in the next winter. Present temperatures in the Utopia region, however, do not allow the melting of ice, even a salt-rich ice, so such a process cannot be operating there at present. If the troughs formed in an analogous manner to arctic patterned ground, then conditions must have been different in the past. Alternative ways to form the troughs are contraction by cooling of lava, although the lack of observable flows at the site argues against this, or contraction as a result of desiccation (Mutch et al., 1977). An additional possibility is that the troughs are tectonic and related in some way to regional warping (Pechmann, 1980).

The most obvious change observed at the Viking 2 landing site, after observations for over two full Martian years, was the appearance of frost, most likely water-ice. At the time the frost appeared, night-time temperatures at the surface were close to 150 K. At such temperatures the atmosphere could not contain sufficient water to form the water-ice observed. Jones et al. (1979) proposed, therefore, that the water-ice nucleated on dust particles in the warmer southern hemisphere where the water content was higher, and that the particles were swept into the northern hemisphere by the dust storm and ultimately deposited at the Lander 2 site, possibly after CO_2-ice evaporated during the day to leave a thin coating of water-ice around the site.

Surface Chemistry

The loose debris within reach of the Viking landers was analyzed by the landers' X-ray fluorescence spec-

trometers (Toulmin et al., 1977). The materials at both sites had remarkably similar compositions, and what was analyzed was probably a thin veneer of particulate debris that has been homogenized over the whole planet by repeated participation in global dust storms. The analyses (table 7.1) show a total-sum deficit of several percent, which is real. Only elements with atomic number greater than 11 could be analyzed, so such common elements as H, C, N, O, and Na were undetermined. The deficit probably results largely from H_2O and CO_2, which are suspected from the GCMS results (Biemann et al., 1977), although small amounts of Na and nitrate may also be present. The only significant variation between samples results from the presence of slightly more sulfur (and possibly chlorine) in duricrust samples.

The Viking landers carried no means of determining mineralogy so the mineralogy of the analyzed samples has to be inferred indirectly. The interpretation favored by the Viking experimenters is that the fine materials consist largely of Fe-rich smectite clays with minor amounts of sulfates, carbonates, and oxides. The presence of clays was initially suspected from reflectance spectra (Hunt et al., 1973; Logan et al., 1975). Houck et al. (1973) specifically pointed to the presence of an absorption feature at 2.85 μm that could be interpreted as caused by the presence of bound water. Detection of water in the soil at the two lander sites by the GCMS (Biemann et al., 1977) is also consistent with the clay model. Furthermore, Banin et al. (1981) demonstrated that Fe-rich clays can catalyze breakdown and synthesis of organic compounds, and successfully simulated the Viking results with sterile clay soils. One possible objection to interpreting the fines as dominantly clay is the absence of certain well-defined Fe^{3+} absorption bands in Mars spectra as demonstrated by Singer (1981), who alternatively suggested that the fines are predominantly palagonitic. Toulmin et al. (1977) and Soderblom and Wenner (1978) also suggested the presence of palagonite and proposed that devitrification of palagonite might be a major source of the clays. Whatever the precise mineralogy (or lack of it), it seems clear that the fines are largely Fe-rich weathering products and not primary minerals.

THE ATMOSPHERE AND SURFACE VOLATILES

The Atmosphere

The atmosphere at the surface contains 95.3 percent CO_2, 2.7 percent N_2, 1.6 percent Ar, and only small amounts of other constituents (table 7.2). The water vapor content is generally close to saturation for night time temperatures, ranging from 1 to 100 pr μm (the depth of water, measured in micrometers, that would be on the surface if all the water in the atmosphere above precipitated out) and averaging around 12 pr μm (Farmer and Doms, 1979). The surface pressure varies according to season because a significant fraction of the CO_2 in the atmosphere

Table 7.1. X-ray Fluorescence Analyses of Different Samples at the Two Viking Landing Sites (from Toulmin et al., 1977)

	Chryse Fines	Chryse Duricrust (1)	Chryse Duricrust (2)	Utopia Fines	Estimated Absolute Error
SiO_2, wt %	44.7	44.5	43.9	42.8	5.3
Al_2O_3, wt %	5.7	N/A	5.5	N/A	1.7
Fe_2O_3, wt %	18.2	18.0	18.7	20.3	2.9
MgO, wt %	8.3	N/A	8.6	N/A	4.1
CaO, wt %	5.6	5.3	5.6	5.0	1.1
K_2O, wt %	<0.3	<0.3	<0.3	<0.3	—
TiO_2, wt %	0.9	0.9	0.9	1.0	0.3
SO_3, wt %	7.7	9.5	9.5	6.5	1.2
Cl, wt %	0.7	0.8	0.9	0.6	0.3
Sum	91.8	N/A	93.6	N/A	—
Rb, ppm	<30			<30	
Sr, ppm	60 ± 30			100 ± 40	
Y, ppm	70 ± 30			50 ± 30	
Zr, ppm	<30			30 ± 20	

Table 7.2. Composition of the Atmosphere at the Surface (from Owen et al., 1977)

Gas	Proportion
Carbon dioxide (CO_2)	95.32%
Nitrogen (N_2)	2.7%
Argon (Ar)	1.6%
Oxygen (O_2)	0.13%
Carbon Monoxide (CO)	0.07%
Water vapor (H_2O)	0.03%
Neon (Ne)	2.5 ppm
Krypton (Kr)	0.3 ppm
Xenon (Xe)	0.08 ppm
Ozone (O_3)	0.03 ppm

Isotope Ratios

Ratio	Earth	Mars
$^{12}C/^{13}C$	89	90
$^{16}O/^{18}O$	499	500
$^{14}N/^{15}N$	277	165
$^{40}Ar/^{36}Ar$	292	3000
$^{129}Xc/^{132}Xc$	0.97	2.5

condenses on the winter polar caps. The changes are controlled largely by the southern cap because it is more extensive at its maximum and smaller at its minimum than that in the north. At the Lander 1 site, at an elevation 2 km below the datum, the pressure ranged from 6.9 mb at southern mid-winter to 9 mb at the end of southern spring when the southern cap had retreated to its minimum and before the northern cap had enlarged greatly. At the Lander 2 site, at an elevation of 3 km below the datum, the pressure ranged from 7.5 to 10 mb. The scale height of the atmosphere is close to 8 km (Seiff and Kirk, 1977). As a consequence, surface pressures vary by about a factor of 10 from the summit of Olympus Mons to the floor of Hellas.

Because the atmosphere is so thin it normally absorbs little radiation directly but is heated from below by contact with the ground, and since it has a low heat capacity it undergoes large diurnal oscillations in temperature close to the ground. The oscillations, however, damp out rapidly with elevation, and above the boundary layer the temperatures closely follow the adiabatic lapse rate. When large amounts of dust are in the atmosphere, during and after the large dust storms, the situation is quite different. The atmosphere is heated directly by absorption of sunlight by the dust, and the temperature oscillations near the ground are suppressed. The result is small temperature fluctuations at the surface, but larger fluctuations high in the atmosphere, and a more isothermal profile as compared with a clear atmosphere.

Winds vary considerably according to location and season, and result from a variety of causes. A general circulation of the atmosphere is driven largely by seasonal temperature gradients and movement of the atmosphere from pole to pole as 20–30 percent of it condenses on the winter cap. During winter, large temperature gradients around the poles create instabilities, resulting in the development of cyclonic and anticyclonic storm systems (Leovy and Mintz, 1969; Blumsack, 1971; Pollack et al., 1976). During the rest of the year winds that result directly from the general circulation are small. More important are tidal winds, slope winds, and those connected with the large dust storms.

Tidal winds result from differences in the day and night temperatures; they tend to blow from the cold night side of the terminator to the warm day side. The effect is considerably enhanced when the atmosphere is loaded with dust because the contrast in night and day temperatures extends throughout the atmosphere rather than being restricted to the thin boundary layer. Slope winds result from the heating of the clear atmosphere mainly by contact with the ground. Since ground temperatures are controlled largely by the reflectance properties of the surface, they are independent of elevation. Horizontal temperature gradients, therefore, develop in the atmosphere over sloping ground and give rise to slope winds, which blow upslope during the day and downslope at night.

At the Viking landing sites, winds were measured at a height of 1.3 m off the ground. As expected from the global circulation pattern, conditions were quiet at the start of the mission, in northern summer. Wind speeds ranged from 2 to 7 m/sec and tidal and slope winds appeared to dominate (Hess et al., 1977). During fall, the pattern changed as storm systems passed north of the landing sites every three to four days. During this period average wind speeds were around 5 m/sec with daily maxima around 10 m/sec (Ryan and Henry, 1979). The pattern changed dramatically with the onset of the first 1977 dust storm, when average speeds increased to 17 m/sec and gusts occurred up to almost 30 m/sec.

The existence of great dust storms has been known for many years from telescopic observations. They tend to occur each Martian year close to perihelion in the southern hemisphere and spread to cover much of the planet. During 1977, the Viking spacecraft

observed two major dust storms. The first started in Thaumasia early in southern spring and the second started near Argyre about three months later (Briggs et al., 1979). The atmosphere cleared to about its pre-storm opacity about four months after the start of the second storm. At the Viking landing sites, which were far north of the storm centers, the optical depth of the atmosphere increased greatly with the arrival of each storm, rising from a value of 0.5 before the storm to a value of 6 at the Lander 1 site after the second storm. Dust storm arrival was also evident from a sharp decrease in the diurnal temperature range. At the Lander 1 site diurnal temperatures ranged from 184 to 242 K just before the first storm arrived; after arrival of the second storm the range was 190 to 204 K.

The global dust storms probably occur as a result of a feedback mechanism between local dust storms and diurnal tides (Leovy and Zuruk, 1979). Dust storms appear to start where high winds are expected because of high slopes or because of high temperature gradients, such as along the edge of the polar cap. They are most common during southern summer when surface temperatures are at their highest. Dust raised into the atmosphere causes an increase in the tidal winds, which raises more dust, which further amplifies the winds, so that a storm can propagate itself and possibly engulf the whole planet. The storms probably end when they raise so much dust into the atmosphere that the atmosphere becomes almost isothermal. Then, convective coupling of the near-surface boundary layer with the tidal winds aloft diminishes, surface winds fall, and no more dust is raised. It then takes about four months for the dust to settle out and the atmosphere to return to its pre-storm clarity.

Volatiles in the Surface

Most of Mars' outgassed volatiles are trapped within the surface rather than in the atmosphere. Fanale and Cannon (1974, 1979) showed that clays and finely ground basalt have a considerable adsorptive capacity for CO_2. Estimates of the total volume of CO_2 in the surface are uncertain because of uncertainties in the structure and composition of the regolith. On the old cratered terrain is probably a megaregolith, several kilometers thick, in which finely pulverized and weathered debris near the surface gives way to breccia at greater depths and fine to fractured rock in place. Its total thickness may be as much as 10 km (Carr, 1979). On younger surfaces the megaregolith may be buried and a much thinner new regolith may develop on the fresh surface. This simple picture is complicated by redistribution of weathered debris by the wind, with surfaces at high latitudes being sites of preferential deposition. Fanale and Cannon (1979) attempted to model adsorption of CO_2 in the surface by assuming a relatively thick layer of strongly adsorptive materials (nontronite) at high latitudes, a relatively thin layer at low latitudes, and a mean regolith thickness of 150 m. According to their model, more than 100 mb of CO_2 is held within the hypothetical regolith, which implies that less than one-tenth of the CO_2 outgassed from the planet is in the atmosphere.

Exchange of CO_2 between the surface and atmosphere in response to diurnal and annual temperature changes is probably small because only the top meter of the surface is affected. Long-term climate changes may, however, cause significant exchange because their temperature effects penetrate to depths of several hundred meters. Obliquity variations are particularly important because of their effect on mean annual temperatures in the polar regions (Ward, 1974), where thick deposits of weathered debris, with a high adsorptive capacity for volatiles, are believed to reside. Fanale and Cannon estimated that as a result of such exchange the atmospheric pressure may range from 0.5 to 22 mb during the obliquity cycle.

The Martian surface may also contain significant amounts of water or water-ice. The evidence is mostly indirect, including geomorphic evidence such as the presence of channels, the nature of Martian ejecta patterns, various possible thermokarst features (Carr and Schaber, 1977), and geochemical evidence which suggests that on the order of 100 m of water, averaged over the whole planet, has been outgassed (Pollack and Black, 1979; McElroy et al., 1977). Liquid water is unstable everywhere on the Martian surface and ice is unstable in the equatorial regions. In addition, Farmer and Doms (1979) showed that at latitudes within 30° of the equator, ice is always unstable below the surface if in diffusive contact with the atmosphere. If ice is in the permafrost zone it must be isolated from the atmosphere. In contrast, within 40° of the poles, ice is stable at depths greater than 10 cm. At intermediate latitudes ice is stable near the surface for only parts of the year.

The capacity of the Martian surface to hold water depends therefore on the degree to which the deeper layers are isolated from the atmosphere. Smoluchowski (1968) estimated that ice could survive below a 100-

cm-thick fine-grained soil for a billion years, but his calculations did not take into account the flushing action of CO_2 as it moves in and out of the surface in response to long-term climate changes. Carr (1981) estimated that the equivalent of 30 m of water could be tied up in the poles, either in the permanent cap, the layered terrains, or as deeper ground ice. Another 15 m could be adsorbed or chemically bound within the regolith. The rest of the outgassed water probably exists as groundwater or ground ice in the megaregolith, which has a substantial, and probably largely unfilled, storage capacity.

CRATERS AND CRATER AGES

Martian craters superficially resemble craters on other terrestrial planets except for the frequent occurrence of central pits and for their patterns of ejecta. Most large Martian craters are, however, poorly preserved, so their primary characteristics are not well understood. As on other planets, craters on Mars pass from simple to complex to multi-ringed basins with increasing size. The simple-to-complex transition (fig. 7.5) takes place in the 5–10-km size range (Pike, 1979) as compared to about 20 km for the Moon. Martian complex craters are proportionately shallower than on the Moon and many, particularly those in the 30–45-km size range, contain central pits (Woods et al., 1978), a feature that has been attributed to the presence of large amounts of volatiles in the target materials. The transition to multi-ringed basins takes place at around 140 km (Wood and Head, 1976), but Mars has fewer impact basins (1.3 per 10^7 km^2) than the Moon (7.6 per 10^7 km^2) or Mercury (2.2 per 10^7 km^2).

The most distinctive characteristic of Martian craters is their ejecta patterns. On the Moon and Mercury, craters typically have coarse hummocky textures near the rim crest which become finer farther out and ultimately merge with strings of secondary craters. The patterns appear to be due in large part to ballistic sedimentation (Oberbeck, 1975). In contrast, most Martian ejecta patterns appear to result from flow across the surface (Carr et al., 1977b), and craters that have these patterns have been informally referred to as "fluidized ejecta craters" or "splosh craters." There are two main types (Carr, 1981). In the first, typified by Yuty (fig. 7.6), the ejecta is disposed around the crater in several sheets, each with a ridge or rampart at its outer margin. The sheets extend up to two crater diameters from the rim and during

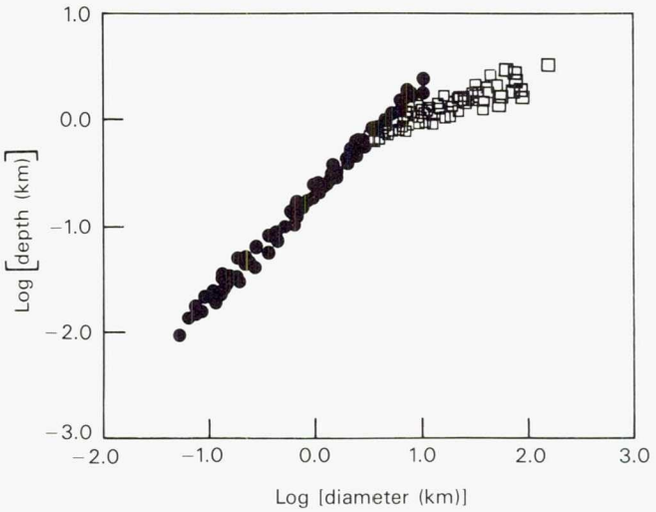

Figure 7.5. Depths of Martian craters as a function of diameter. Squares represent complex craters, dots represent simple craters (adapted from Pike, 1979).

emplacement appear to have been deflected by preexisting obstacles as they flowed across the surface (Carr et al., 1977b). In the second type, a continuous annulus of ejecta, commonly with a concentric fabric on the surface, surrounds the crater and overlies ejecta sheets with a strong radial fabric (fig. 7.7).

The conclusion that Mars ejecta is more fluid than that on the Moon or Mercury appears inescapable; there is abundant evidence of flow of the ejecta across the surface, and the continuous ejecta extends for considerably greater distances from the rim crest than on the Moon or Mercury (Carr et al., 1977b). Two factors could contribute to an enhanced fluidity: the presence of an atmosphere and the inclusion of ice or water in the ejected debris. Patterns similar to those on Mars have been simulated both with viscous targets (Gault and Greeley, 1978) and with impacts in the presence of an atmosphere (Schultz and Gault, 1981). The flow patterns occur only around craters larger than about 5 km in diameter, and Boyce (1979) suggested that the onset diameter may reflect the depth at which groundwater was encountered during crater formation.

As craters are exposed to conditions on the Martian surface they are slowly degraded. Yuty-type craters first lose the fine textures on the surfaces of the ejecta so that the crater becomes surrounded simply by ramparts that outline the position of the no-longer-visible ejecta sheets. Ultimately the ramparts also disappear and the crater is left with little evidence of ejecta around it. Craters that start with an annulus

Figure 7.6. Flow ejecta patterns around the 18-km-diameter crater Yuty, at 22°N, 34°W. The ejecta is mostly in thin sheets, each with a distal, lobate ridge. A pre-existing crater, adjacent to the Yuty rim, is only partly buried, indicating that the ejecta is thin. (3A07.)

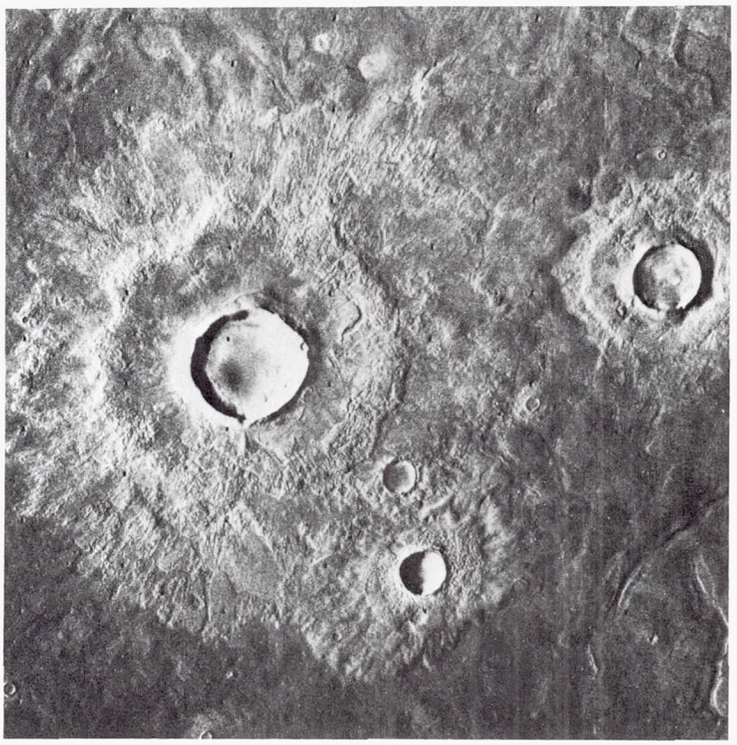

Figure 7.7. Impact craters in Utopia Planitia (41°N, 260°W). Most craters in this region have an inner annulus of ejecta with a distinct outward facing scarp beyond which the ejecta has a marked radial pattern. (10B81.)

of ejecta first lose all traces of ejecta other than the annulus itself, until they resemble the pedestal craters described below. Ultimately the annulus is also lost.

Pedestal craters are craters set into a circular platform several radii across and several tens of meters high. They appear to form by selective removal of easily erodible materials between craters. Erosion is thought to be inhibited around the crater because of armoring of the surface by ejecta (McCauley, 1973; Arvidson et al., 1976). They are most common at high latitudes but are also found at lower latitudes where friable, easily erodible materials are at the surface.

Surfaces on Mars can be divided into two types, according to crater densities: those with high densities of large (>50-km diameter) craters and those on which large craters are rare. The former surfaces are believed to have formed before the decline of an early, heavy bombardment, the latter after the decline, which by analogy with the Moon is thought to have occurred around 3.8 billion years ago. In principle, the more sparsely cratered surfaces can be dated relatively by the number of superposed craters. In practice, this turns out to be quite difficult because of complications arising from selective destruction of superposed craters after the surface being dated formed and by incomplete burial of pre-existing craters. Absolute dating is even more suspect because of great uncertainties in the crater production rate on Mars. This chapter includes several tables that give crater densities on different geologic features together with age estimates. The crater densities are given in terms of the number of craters larger than 1 km diameter per 10^6 km^2. This is a convenient reference diameter, for adequate statistics can generally be gathered for this size crater even on relatively sparsely cratered surfaces. Use of this "crater number" was pioneered by Wise et al. (1979a). They, however, derived their numbers by extrapolating from larger diameters down to the reference diameter, with the aid of a theoretical production function. Their extrapolated numbers are, in general, considerably higher than the actual numbers, and only actual numbers are given here. The crater number gives a valid relative age only if an insignificant number of 1-km craters has been destroyed since the surface formed and only if formation of the surface erased completely the pre-existing 1-km crater

population. Unfortunately, these two conditions cannot always be established so caution should be exercised in using estimated relative ages from these numbers.

Several attempts have been made to establish an absolute time scale for Mars based on crater counts (Neukum and Wise, 1976; Soderblom et al., 1974; Hartmann et al., 1980). The scheme adopted in this chapter is that of Carr (1981), in which a time scale based on the 1-km-diameter crater numbers is calibrated by ages from Hartmann et al. (1981). The Hartmann et al. ages are based on a model in which the rate of formation of craters on Mars is twice that on the Moon, at least for diameters larger than 4 km. Following Hartmann et al., errors are given, and these are large, faithfully reflecting the large uncertainties in the method.

DENSELY CRATERED TERRAIN

The surface of Mars can be divided into two units, densely cratered terrain and sparsely cratered plains. All other features such as volcanoes, channels, and canyons are either superposed upon or modifications of these two units. Distinction between the two components is not obvious everywhere. In several places the plains overlap the old cratered terrain such that plains form the low ground between rims of old craters, and in many parts of the cratered terrain are intercrater plains that are indistinguishable from the older plains of the sparsely cratered hemisphere. Nevertheless, the two units can generally be identified.

Cratered Plateau

The densely cratered terrain consists of two components: a more rugged, densely cratered plateau and intercrater plains. The cratered plateau almost certainly includes the planet's oldest surfaces. While it superficially resembles the lunar highlands, closer examination shows that the lunar and Martian highlands are distinctively different. Two obvious differences concern craters. First, the Martian craters generally are more subdued than those of the Moon, and, second, their size frequency distributions are different. Both distinctions have been attributed to more intense crater obliteration early in Mars' history as compared with the Moon. A third distinction is that the Martian highlands are dissected almost everywhere by branching valleys suggestive of fluvial erosion.

Craters larger than 20 km have a wide range in morphology. The most fresh-appearing, while not as well preserved as some large lunar craters, have coarse hummocky rims, terraced walls, central peaks, flat floors, and large secondary crater fields. The most degraded are barely visible, shallow, circular depressions. Most craters have an intermediate morphology with flat floors at a lower elevation than the surrounding terrain and a rim that has little, if any, relief or texture (fig. 7.8). The crater walls are commonly simple inward-facing escarpments. Superimposed on the larger craters is the array of smaller (<10 km) craters, which are mostly fresh-appearing. These gen-

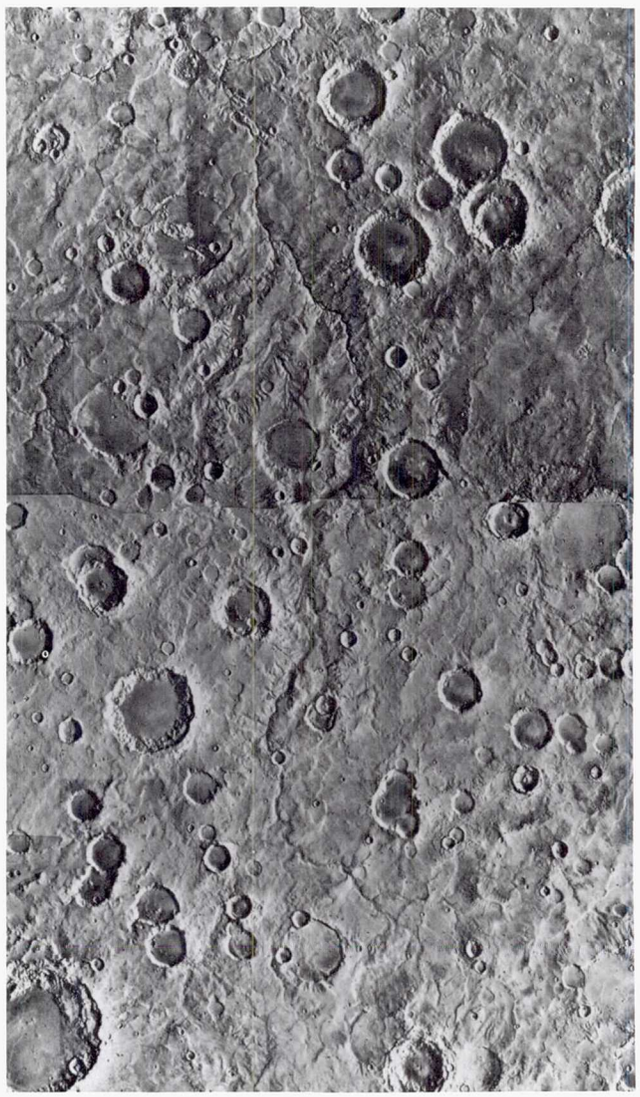

Figure 7.8. Cratered terrain around 30°S, 15°W, southeast of Margaritifer Sinus. The larger craters mostly have flat floors and low rims. Between the craters are commonly smooth plains with ridges like those on the lunar maria. Valleys drain northward toward the Margaritifer Chaos. The scene is 500 km across (from mosaic 211-5207).

erally have distinct rims and are surrounded by fluidized ejecta patterns. The patterns are less common around the large craters of the older population, but this may simply be a consequence of their usual poor state of preservation. The smaller craters also tend to have more internal relief, probably because most postdate an early era of intense crater obliteration and so retain their primary features.

Around the large impact basins of Argyre, Hellas, and Isidis are numerous closely spaced, rugged, irregular hills. They are most obvious around Argyre, where they form a 600-km-wide annulus around the basin. They probably comprise mainly uplifted, jostled blocks of the old pre-basin surface, although ejecta may also be present. However, there is no indication of extensive ejecta sheets such as those around the Orientale and Imbrium basins on the Moon, possibly because the atmosphere caused the ejecta to be widely dispersed.

The size-frequency distribution and morphology of craters in the old cratered terrain provide evidence of early, high rates of crater obliteration. Opik (1966) noted a break in slope on size-frequency curves for Mars at around 20 km and attributed it to an obliterative process, which he suspected had removed most of the small craters and modified the larger ones. The Mariner 6 and 7 investigators (Leighton et al., 1969; Murray et al., 1971) noted a bimodal distribution of craters, both in terms of morphology and number; the larger (>5 km) tended to be shallow with low rims, whereas the smaller craters were mostly bowl-shaped. In addition, on cumulative size-frequency plots the slopes for the large craters were shallower than those for the small craters. The global coverage of Mariner 9 permitted a more definitive description of the crater distribution. Hartmann (1973) showed that the size distribution curve for the cratered highlands can be divided into three segments. Below 5 km and above 30 km, the slope on cumulative size-frequency plots is generally steep with values of -2 or larger. Between 5 and 30 km, however, the slope of the curve is much shallower, around -1. This general picture is confirmed by more precise counts from Viking data (fig. 7.9).

Hartmann (1973), elaborating upon the previous proposals of Opik (1966), suggested that the part of the size-frequency curve above 30 km survives from an early era in the history of the planet when cratering and obliteration rates were high. The segment of the curve between 5 and 30 km, he suggested, represents an equilibrium curve between crater formation and crater destruction during this early era. Destruction could have been caused by several processes, such as eolian erosion and lava infilling, in addition to the crater-forming process itself. The curve has a low slope because small craters are destroyed more rapidly than larger ones. In contrast, most craters above 30 km are too large to have been destroyed by obliterative processes other than impact and so preserve a near-saturation distribution. Hartmann postulated further that some time early in Mars' history, probably around 4 billion years ago, both the cratering rate and the obliteration rate declined rapidly. The bowl-shaped craters smaller than 5 km represent the craters accumulated since that time. The decline in obliteration rates could not greatly postdate the decline in cratering rate, otherwise we would see large numbers of modified craters on the sparsely cratered plains, which we do not. Nor could the decline in obliteration rates greatly precede the decline in cratering rate, otherwise there would be large numbers of unmodified craters in the highlands. The decline in cratering and

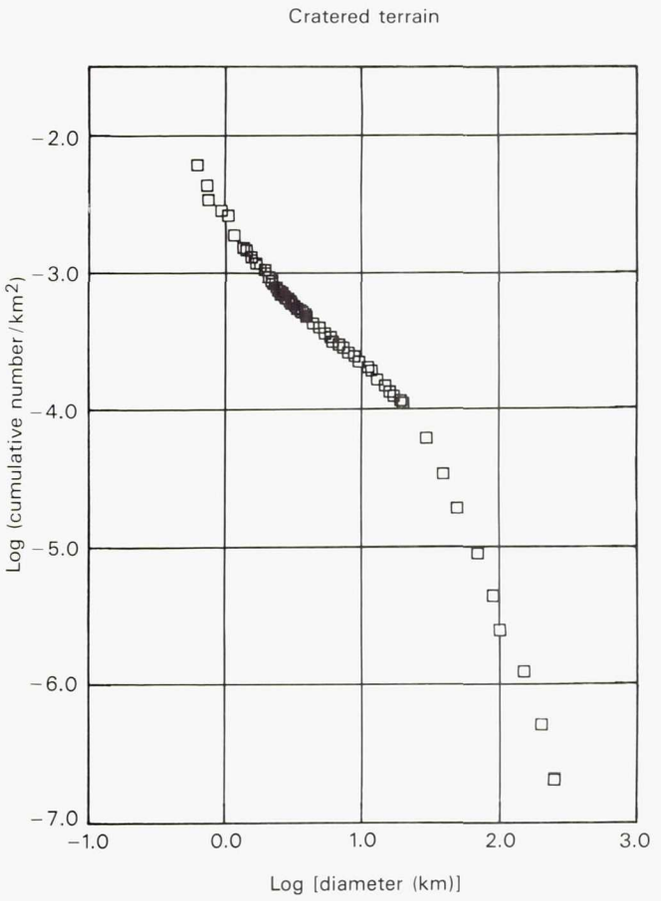

Figure 7.9. Cumulative size frequency distribution of craters in the old cratered terrain.

the decline in obliteration appear to have been roughly simultaneous.

Jones (1974) and Chapman and Jones (1977) presented a slightly different model for evolution of the densely cratered terrain. They suggested that, as in the Hartmann model, cratering rates were high early, then declined to leave a crater distribution that was close to saturation for all crater diameters. There followed then a discrete era of intense crater obliteration that destroyed all craters smaller than about 5 km and most in the 5–30-km size range, greatly modifying the rest. The population of fresh-appearing small craters formed after the obliteration event was over. Thus, in the Hartmann model, the high cratering and high obliteration rates occurred together; in the Jones/Chapman model an obliteration episode occurred some time after the cratering rates had declined.

Intercrater Plains

The intercrater plains in many places partly bury the cratered plateau so that the rims of old craters protrude through the plains to the surface. In many places the intercrater plains have wrinkle ridges like those on the Moon, which suggests a volcanic origin. Greeley and Spudis (1978) estimated that such ridged plains cover 36 percent of the old cratered terrain. The intercrater plains generally preserve only the population of craters that postdate the era of enhanced obliteration (fig. 7.10), and burial of the old craters by the plains may have been an important factor in the obliteration process. The proportion of intercrater plains to more primitive crust varies. Jones (1974) and Mutch et al. (1976) attempted to identify regions in the densely cratered terrain where the most primitive crust survives. They analyzed the distribution of relatively fresh-appearing craters larger than 15 km in diameter and degraded craters in the same size range and found higher proportions of only slightly modified craters in areas of high elevation and low albedo. They attributed the proportion of less modified craters in these areas to higher proportions of primitive crust not covered by the late intercrater plains.

The primitive cratered plateau and the intercrater plains are distinct in their level of dissection. The older unit is dissected almost everywhere by small branching valleys that range in preservation from those that are barely discernible to those that appear relatively fresh. The intercrater plains, on the other hand, appear somewhat less dissected, and most of the channels are well preserved. In this respect the intercrater plains differ from the plains of the opposite hemisphere, which are mostly undissected.

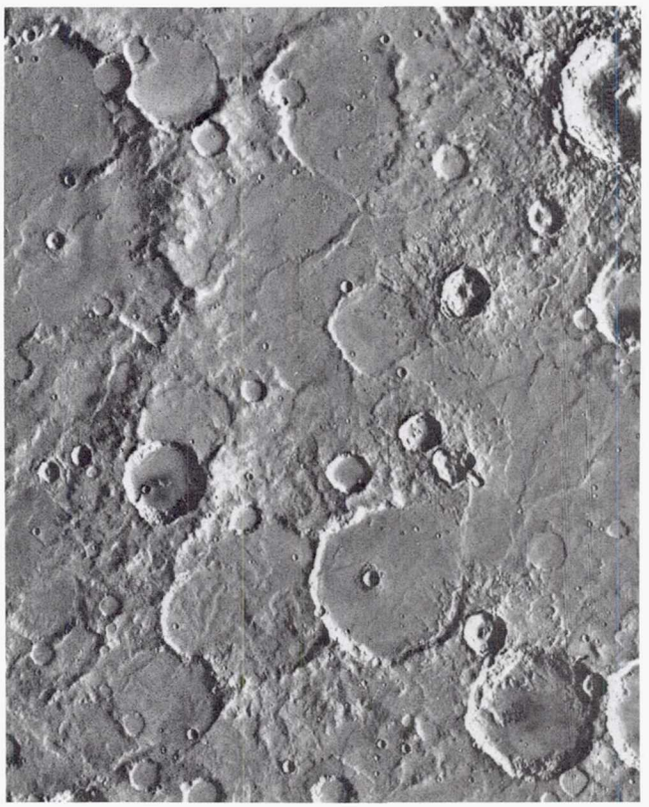

Figure 7.10. Intercrater plains within the old cratered terrain at 22°S, 175°W. Two different populations of craters are visible. Those older than the plains mostly have flat floors, low rims and little trace of ejecta. Those younger than the plains are mostly bowl-shaped with central peaks and flow ejecta patterns (635A66).

Malin (1976) pointed out that the intercrater plains are horizontally layered. The layering is evident mainly where the succession is seen in sections, such as in channel and canyon walls. Malin also suggested that some of the layers are unconsolidated, since features such as craters are occasionally exhumed along escarpments.

Many of the large craters, including the impact basins, have level floors. These differ greatly in character. Some are saturated with craters as small as a few tens of meters across. The number of craters suggests an ancient surface, and it is surprising that such small craters could survive on a surface as active as Mars. Other crater floors are filled with partly eroded layered deposits, and others by plains with wrinkle ridges. At the time of writing, little systematic work has been done on these deposits, and their range of characteristics and origin are not known.

Formation of the Densely Cratered Terrain

The sequence of events that resulted in densely cratered terrain cannot be reconstructed in detail, but the broad outlines can be inferred. Very early in the planet's history the surface was subject to high rates of bombardment, after which the impact rates declined rapidly to roughly their present level. The time of the decline is not known, but most authors argue that the decline occurred more or less simultaneously throughout the inner solar system as debris in roughly circular, heliocentric orbits was swept up by the planets. On the Moon the decline occurred around 3.9 billion years ago and the same date is widely assumed for Mars (Soderblom et al., 1974; Hartmann, 1977; Neukum and Wise, 1976). The decline must have been rapid, otherwise we would not see the sharp dichotomy between densely cratered uplands and sparsely cratered plains (Soderblom et al., 1974).

If the Hartmann (1973) model is correct, then prior to 3.9 billion years ago obliteration rates were also high, significantly higher than if obliteration were caused simply by craters destroying one another. Contributing to the high obliteration rates were almost certainly high rates of volcanism, although morphologic evidence of this early volcanism has been largely destroyed as on the Moon. The high rates of volcanism may have been induced in part by the brecciation and heating caused by the high rates of impact. In addition, heat flows must have been higher as a result of higher rates of heat production by radioactive decay (as recounted in the Earth chapter), and higher rates of dissipation of accretional energy. The atmosphere may also have been thicker during this period (Pollack, 1979), leading to enhanced eolian and fluvial activity. The channels are the most direct evidence of different atmospheric conditions, and their wide range of preservation suggests that they too were subject to the same obliterative processes that affected the craters. The relatively immature dissection pattern (see "Channels and Valleys") may represent an equilibrium between fluvial action and reworking of the landscape by impact. The high rates of impact probably caused the atmosphere to be permanently loaded with dust that was continually being sedimented onto the surface only to be reworked by more impacts. At around 3.8 billion years ago, the impact rate declined and the landscape stabilized, leaving a slightly dissected, densely cratered terrain brecciated to depths of several kilometers.

If the above reasoning is correct then the materials close to the surface of the cratered terrain are of diverse origin but have a narrow range in age. Only those features that formed relatively late in the high-cratering era, just before the decline, are likely to have survived. Those that formed earlier would have been destroyed by impact and their materials redistributed around the planet.

High rates of volcanism appear to have continued after the decline in cratering rates, but most of the activity was in the low areas of the northern hemisphere and in Tharsis and Elysium. Volcanism within the cratered plateau of the southern hemisphere appears to have tapered off fairly rapidly because most of the intercrater plains are as heavily cratered, if not more so, than any of the plains on the opposing hemisphere. Therefore, most date from soon after the decline in impact rates. Both craters and channels superposed on the intercrater plains are only slightly degraded, showing that the era of enhanced obliteration was over by the time most of the intercrater plains formed. Valley formation continued beyond the decline in cratering rate, but seemingly at lower rates since most of the sparsely cratered plains are undissected.

SPARSELY CRATERED PLAINS

Sparsely cratered plains is a general term referring to those regions of the planet without the dense population of large craters that characterizes the ancient upland just described. All the plains are cratered to some degree, but their relatively sparse cratering compared with the uplands indicates that they formed after the decline in early high cratering rates. The oldest plains have higher crater densities than most lunar maria and probably date from near the decline in the cratering rates, around four billion years ago. The youngest plains, such as those close to the large Tharsis shields, are barely cratered at all and appear to be a few hundred million years old at most. Thus, formation of the plains spans almost the entire history of the planet. Most plains are in the northern hemisphere, but a large area of plains extends into the southern hemisphere at the south end of the Tharsis bulge. Other plains form Hesperia Planum and the floors of Argyre and Hellas.

The character of the plains changes dramatically between latitudes 30° and 40° on both hemispheres. At lower latitudes the topography is crisp and surface forms are clearly delineated. Most of the landforms,

such as flow fronts, wrinkle ridges, craters, grabens, and channels, are relatively familiar from lunar and terrestrial experience even if their precise origin is not known. The albedo patterns also tend to be simple and comprehensible and mostly confined to crater-related streaks. The plains at high latitudes are quite different. Their topography is complex and many of their characteristics are difficult to relate to those elsewhere on Mars or on any other planetary surface. The albedo patterns are irregular at all scales from tens of meters to tens of kilometers. The net result is some of the most confusing terrains on the planet. In the equatorial latitudes, most of the plains appear to be volcanic, although some have undergone extensive fluvial and eolian modification. The origin of the plains at higher latitudes is unclear. They may also be volcanic, but if so, the primary volcanic features have been largely destroyed; they appear to have been extensively modified after their formation, and ice may have played a prominent role in the process.

Low-Latitude Plains

Most plains that occur within 30° to 40° of the equator are of two types: flow plains, which are composed of clearly delineated flows one on another, and ridged plains, which are generally featureless except for superposed craters and wrinkle ridges. Major exceptions are the plains of southern Amazonis, which do not fall into either category but more closely resemble those at higher latitudes, and the plains of Isidis Planitia, on which are numerous lines of lava cones with summit vents.

Flow plains

Most flow plains (fig. 7.11) occur on the flanks of the Tharsis and Elysium bulges, and those in Tharsis are the most extensive and best studied (Carr et al., 1977a; Schaber et al., 1978). On the east and southeast flanks of the Tharsis bulge, flows are visible as far east as 80°W longitude, both north and south of the canyon. On the west flanks, flows are mostly restricted to east of 150°W longitude. To the north, the Tharsis flows merge with a flow field around Alba Patera. The flows range in shape from narrow finger-shaped types with fairly smooth outlines to broad tabular types with irregular, multi-lobed peripheral scarps. Individual flows may be up to hundreds of kilometers long; flow thicknesses range from 10 to 80 meters but most are in the 30–60 meter range (Schaber et al., 1978). Slope appears to exercise strong control on morphology, the long thin flows being on steeper ground than the broad tabular flows (Carr et al., 1977a). The narrower flows are generally a few kilometers wide and commonly contain a central leveed channel; the broader flows range in width up to a few tens of kilometers and rarely contain channels. The pattern of flows is to some extent controlled by the large volcanoes. The three large volcanoes in central Tharsis have been the source of vast quantities of lava that form fan-shaped arrays of flows to the northeast and southwest of each of the shields. Elsewhere, however, and especially on the southeast flanks of the bulge in Syria and Sinai Planum, the flows show no obvious relation to discrete volcanoes.

Inferences can be made about the composition of the flows from their shape, spectral reflectance data, and the composition of weathered debris at the Viking landing sites. Most data suggest that the flows are iron-rich and basic to ultrabasic in composition. Several attempts have been made to estimate Si content from the morphology of lava flows (e.g., Hulme, 1974; Moore et al., 1978). Yield strengths of the flows are estimated by assuming that they behave as Bingham plastics, in which no flow occurs until a critical yield stress is reached within the flow. Initial estimates by Hulme (1974) suggested relatively high silica contents, 48–50 percent for some Olympus Mons flows. However, Moore et al. (1978) showed that the yield strength of a flow is dependent on local slopes and suggest that the Martian flows are more akin to terrestrial basalt than to the more silicic andesite, trachyte, or rhyolite. The presence of lava channels and levees, and the extreme length of many of the flows also suggest that they have rheological properties similar to basalt. Iron-rich basic lava is also consistent with the reflectance data and with the relatively low Al and K and high Fe and Mg in the weathered debris at the Viking landing sites (Toulmin et al., 1977).

The flow plains have a wide range in age and most are younger than the ridged plains. Schaber et al. (1978) divided the flow plains of Tharsis into 17 units and counted the number of superposed craters. On the oldest units, the number of craters larger than 1 km ranges from 2400 to 3200 per 10^6 km^2. The upper bound of 3200 is close to the maximum for any plains on the planet and probably represents an age close to the time when the impact rates declined. The youngest flows identified by Schaber et al., those immediately adjacent to Olympus Mons, have 90–135 craters larger than 1 km per 10^6 km^2. By the chronology outlined above, these are only a few hundred mil-

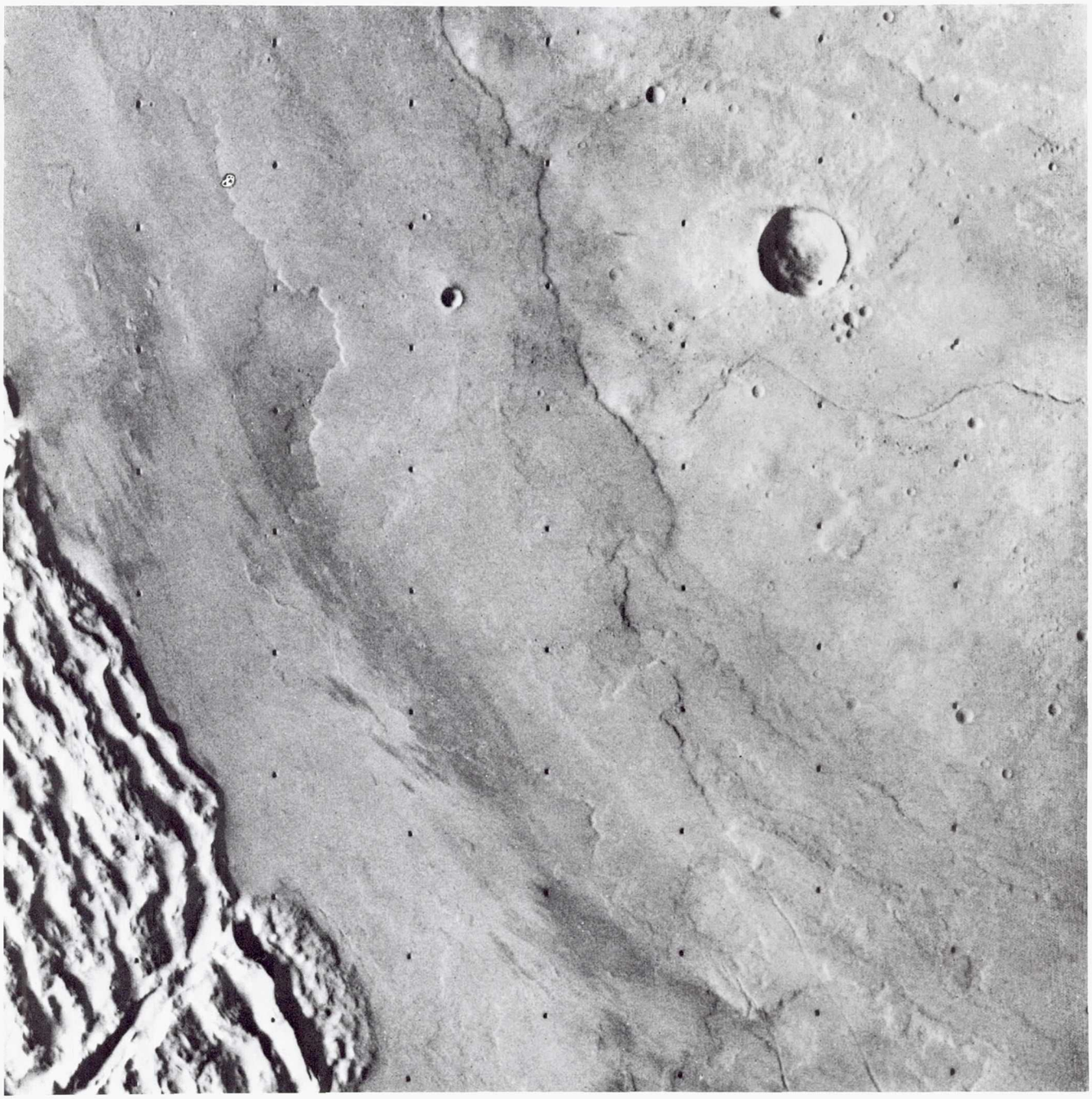

Figure 7.11. Flow plains northeast of Olympus Mons. Relatively young flows at the center transect older flows in the upper right. At the lower left is the edge of the Olympus Mons aureole. The frame is 86 km across (45B24).

lion years old, on average. Formation of the Tharsis plains may span almost the entire history of the planet; indeed, the plains are probably still being formed. It would be fortuitous for volcanism to have ceased shortly before we viewed the planet after such a long sustained history of eruption. Moreover, Martin (1981) claimed to have detected volcanic activity in the Tharsis region.

Ridged plains

In many plains areas flows cannot be seen, but wrinkle ridges like those on the lunar maria are common. Ridged plains (fig. 7.12) occur in a north-south belt around 1000 km wide on the eastern flank of the Tharsis bulge. The belt includes all of Lunae Planum and the eastern margin of Solis Planum and Sinai

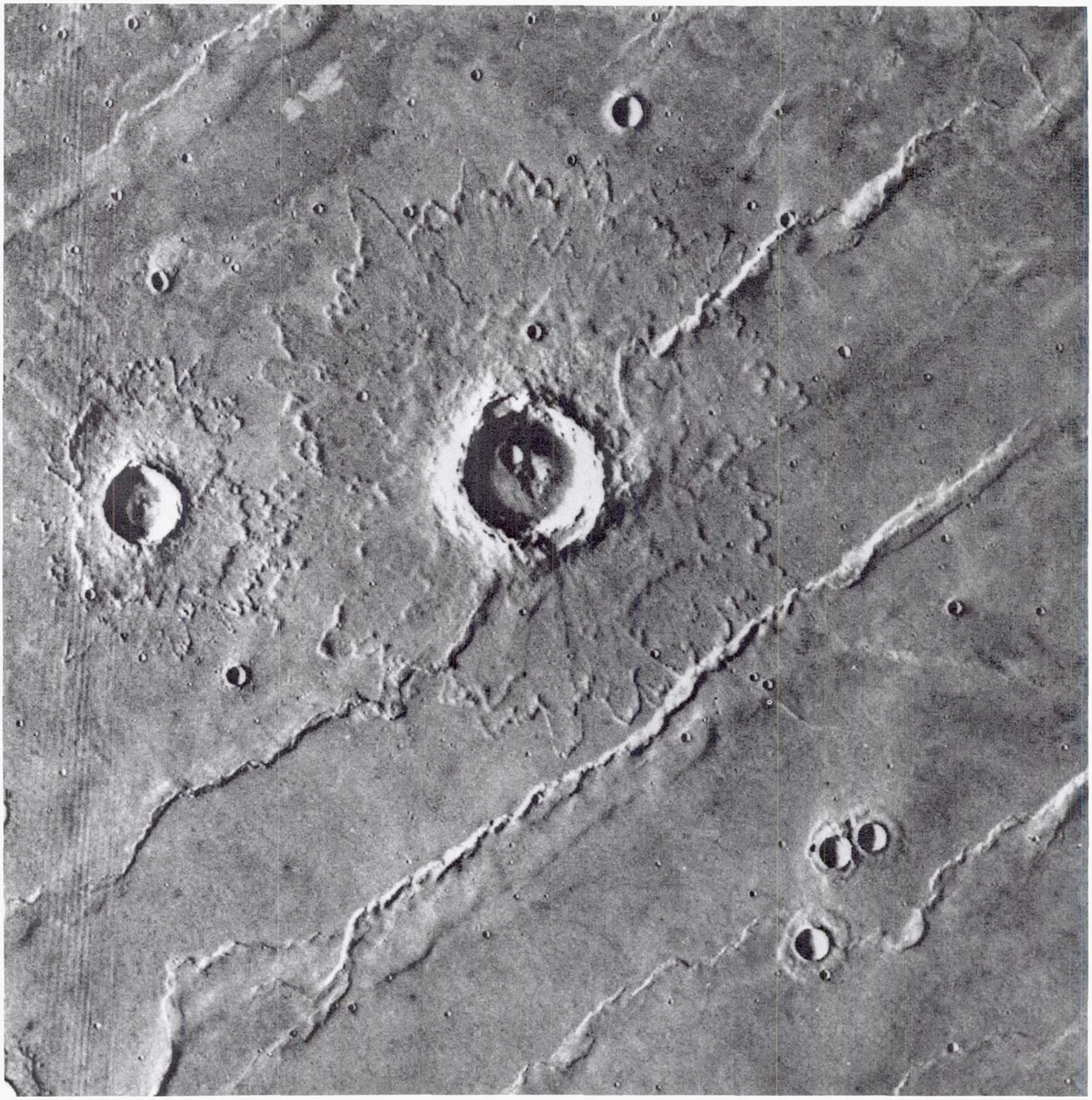

Figure 7.12. Ridged plains in Sinai Planum at 22°S, 79°W. The ridges are identical in form to those on the lunar maria; many consist of a sharply defined, crenulate ridge atop a broader low ridge. These ridges are concentric with the Tharsis bulge. The craters show the flow ejecta patterns typical of craters at low latitudes. The frame is 250 km across (608A45).

Planum. Other extensive areas of ridged plains occur in Syrtis Major Planitia, Elysium Planitia, and Hesperia Planum. As we saw previously, ridged plains also occur locally throughout the densely cratered terrain. Why evidence for flows on these plains is so sparse is uncertain. It might be argued that the flow fronts have been eroded away, but that is inconsistent with the preservation of small craters, which indicate low erosion rates on these plains (Arvidson et al., 1979). An alternative is that the lavas were more fluid and had lower yield strength than those on the flow plains, so formed thinner flows.

The precise way that lunar mare ridges form is not known. Most evidence suggests that they are tectonic

in nature, possibly resulting from stresses caused by deformation of the crust in response to eruption and deposition of the mare lavas (Lucchitta, 1977; Baldwin, 1963; Solomon and Head, 1979; Howard and Muehlberger, 1973). The Martian wrinkle ridges also appear to be tectonic. Formation of the ridges on the plains to the east of Tharsis is clearly related to the Tharsis bulge. Phillips and Lambeck (1980) modeled the stress distribution within the Martian lithosphere that results from the Tharsis load and found a strong orthogonal relationship between the direction of principal stress and the alinement of the wrinkle ridges. Similar but more qualitative results were obtained by Wise et al. (1979a) and Plescia and Saunders (1979). The implication is that the wrinkle ridges formed as a consequence of the presence of the Tharsis dome. The question is still open as to whether the deformation postdated the formation of the present surface or was penecontemporaneous. The ridges on the plains of Hesperia Planum, Syrtis Major Planitia, and the patches in the old cratered terrain are even less well understood, but they may be deformational features that formed in response to local stresses.

The ridged plains of Lunae Planum, Hesperia Planum, and Syrtis Major Planitia are among the oldest plains on the planet (table 7.3). Hartmann et al. (1981) gave an age of 3.2 billion years for Lunae Planum, 3.4 billion years for Hesperia Planum, and 3.6 billion years for Syrtis Major Planitia. The difference between the counts for each of these plains is small and they must be considered about the same age. Neukum and Hiller (1981) give an age of about 4 billion years for Lunae Planum and Soderblom et al. (1974) used Lunae Planum as a measure of the number of craters that have accumulated on the planet since the decline of the early high cratering rate. Chryse Planitia and the plains west of Elysium appear slightly younger than those just described. Chryse has 2100 craters larger than 1 km per 10^6 km^2 (Dial, 1978) and Elysium Planitia has 2000 (Neukum and Hiller, 1981) as compared with 2500 for Lunae Planum.

High-Latitude Plains

Between 30°N and 40°N, the appearance of the plains changes greatly, and the twofold classification of the equatorial plains into flow plains and ridged plains no longer applies. In the south the transition is not observed, but the plains of Argyre and Hellas have some of the characteristics of the high northern plains. The high-latitude plains are poorly understood and almost no literature exists about them. They have a greater areal variation than the equatorial plains, and generally a greater complexity. Primary volcanic features, which abound in the equatorial regions, are relatively rare; erosional rather than depositional characteristics usually dominate.

Several factors may contribute toward differences between the low and high latitudes. Soderblom et al. (1973) postulated that the high latitudes were covered with a blanket of debris several tens of meters to kilometers thick. They suggested that the equatorial regions, particularly the dark areas, are largely swept free of debris and that the "swept" areas move north and south with the 50 000-year precessional cycle, as

Table 7.3. Plains Ages. Crater counts are from Gregory (1979) and Dial (1978). Ages are based on the model of Hartmann et al. (1981) as modified by Carr (1981)

	No. of Craters <1 km/10^6 km^2	Crater Age (billions of years)		
		Minimum Likely	Best Estimate	Maximum Likely
Lunae Planum	2400	1.7	3.5	3.8
Chryse Planitia	2100	1.2	3.0	3.8
Sinai Planum	970	0.4	1.4	3.0
Hellas	2640	2.9	3.8	3.9
Mare Acidalium	830	0.2	1.2	1.7
Amazonis Planitia	1940	1.0	2.8	3.7
Noachis	1740	0.9	2.5	3.6
Hesperia Planum	2710	3.0	3.9	3.9
Utopia Planitia	1270	0.6	1.8	2.3
Syrtis Planitia	2053	1.2	2.9	3.7

the climatic regimes of the two hemispheres alternate. The boundary between the swept equatorial and unswept high-latitude regions should therefore have undergone repeated stripping and accumulation of debris. The evidence for the debris blankets is largely the smaller number of 4- to 10-km-diameter craters at the high latitudes. Soderblom et al. also cited a general loss of topographic detail as additional evidence for the blanketing, but this appears now to be an observational artifact. Differences between the high and low latitudes may also be affected by the stability of water. In the equatorial regions, water and water-ice are always unstable under present climatic conditions, so the near-surface materials are permanently dehydrated (Farmer and Doms, 1979). At high latitudes water-ice is stable for part of the year. The presence of CO_2 and H_2O ices on the surface during winter may also have affected how the surfaces at high latitudes evolved.

Extensive areas of the far northern plains, especially north of 50°N and most of Mare Acidalium, have a distinct mottled appearance. Most also have a polygonal fracture pattern, discussed separately below. The mottling is caused mainly by the sharp contrast in albedo between the ejecta around craters and the much darker surrounding plains, although bright remnants of the old cratered terrain also contribute. The mottling is best seen in Mare Acidalium between 30°N and 50°N. Most craters in this area have an inner, relatively thick, circular flap of ejecta which overlies a thinner, more extensive sheet with a strong radial pattern and jagged outline. The high albedo extends to the farthest extremity of the ejecta, commonly as far as six crater radii from the crater rim. The cause of the contrast in albedo between the ejecta blankets and the intervening plains is uncertain. It may result simply because the ejecta excavated from below the surface intrinsically has a high albedo, but another possibility is that the eject around craters acts as a trap for fine-grained wind-blown debris and so acquires a high albedo.

Within 500 km of the northern boundary of the old cratered terrain between 280°W and 0°W are some distinctively patterned plains that can be divided into two components, namely, a relatively smooth unit with gently rolling topography and—commonly at a slightly lower elevation—a stippled or dimpled unit. In places the surface has a striped appearance (fig. 7.13) or thumbprint texture (Guest et al., 1977); elsewhere are arrays of curvilinear, closely spaced ridges, several kilometers long and approximately a

Figure 7.13. Patterned plains at 33°N, 271°W. Low parallel ridges resemble glacial terminal moraines and may indicate successive stages in the removal of former ice-rich deposits. The frame is 170 km across (572A06).

kilometer across. Many of the features of these plains have been interpreted on the basis of the Soderblom et al. model of repeated episodes of deposition and removal of debris blankets or mantles (Arvidson et al., 1976; Guest et al., 1977). The smooth areas are interpreted as remnants of a former, more extensive cover of debris and the stippled regions as areas where the surficial debris layer has been removed. Carr and Schaber (1977) suggested that the striped patterns were analogous to recessional glacial moraines and marked successive positions of the edge of the blankets as they were removed. Some support for this interpretation is a rough parallelism, seen in some areas, between the stripes and the present boundary of the smooth and stippled ground.

To the west of the Viking 2 landing site, between latitude 40°N and 50°N and longitudes 240° to 290°W, the plains are extremely complex. At a scale of 1 km or larger, they have little obvious relief other than the craters, but at scales below 1 km the surface is highly textured. Irregular arrays of closely spaced, roughly equidimensional hills and hollows, a few hundred meters across, are separated by smooth areas,

and locally there are swarms of closely spaced, low linear ridges less than 1 km across. These plains are at the termination of some large channels which originate on the flanks of the Elysium dome over 1000 km to the southeast. Most of the channels, when traced into this area, become indistinct, dark, linear features and are recognizable as channels only because they merge southeastward into well-defined channels. Where the channels die out to the west, the character of the plains changes; thus, the peculiar characteristics of the area appear connected in some way with the channels. Whether the Elysium channels formed by water erosion or through the action of lava is unclear, but if by water then modification of ice-rich fluvial deposits could be the cause of the strange surface morphology in these areas.

Extensive areas of the northern plains, particularly in Mare Acidalium and Utopia Planitia, are cut by cracks which partly intersect to form a roughly polygonal pattern (fig. 7.14). Such fracturing is rare at low latitudes, although parts of Isidis Planitia are similarly fractured. The cracks divide the surface into a mosaic of blocks ranging in size from a few kilometers to about 10 km across. The blocks are generally angular but occasionally the cracks outline a circle, which probably is a reflection of a crater in the surface beneath the plains. In rare cases, features can be traced from the adjacent plains and across the troughs as though their floors had been downfaulted (Pechman, 1980). Toward the boundary of the plains with the old cratered terrain, the pattern of cracks becomes coarser and almost all the troughs have flat floors.

Figure 7.14. Fractured ground north of Isidis Planitia at 38°N, 253°W. The fractures form a network of flat-floored graben which suggests uniform horizontal extension in all directions. The largest crater is 10 km across (573A12).

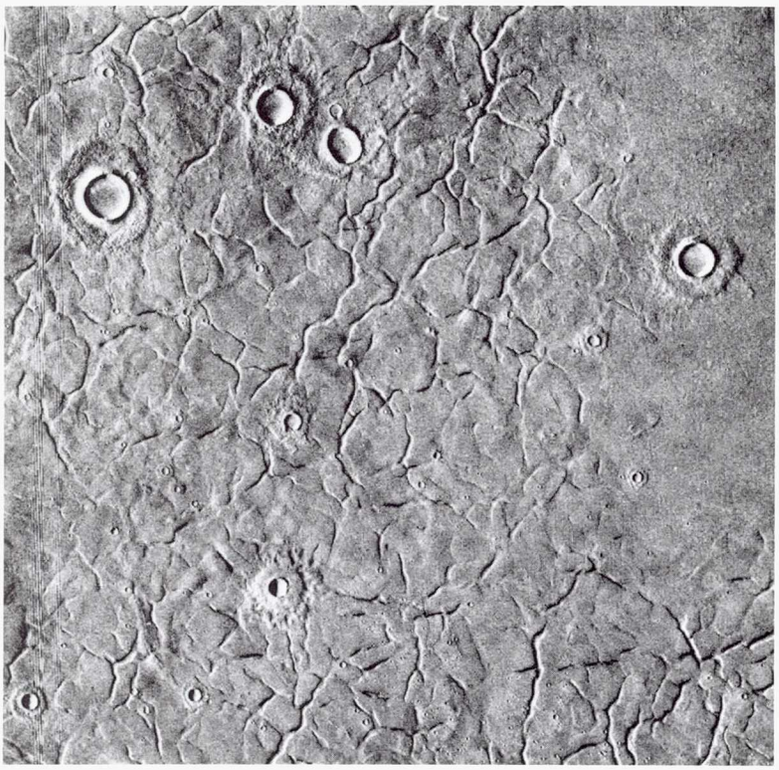

The origin of the fractured plains is not known. The observation that linear fractures can occasionally be traced from the surrounding plains, then across the flat floors of a trough, strongly suggests that the troughs are grabens and formed by faulting (Pechman, 1980). The pattern of cracks indicates uniform tension in all directions within the plane of the surface. Similar patterns commonly form on Earth, where horizontal tensional stresses develop because of cooling or desiccation. Examples are the cooling of horizontal sheets of lava or permanently frozen ground (Lachenbruch, 1962). In all terrestrial cases, however, the size of the individual polygons is at least two orders of magnitude smaller than the polygons observed on Mars. The scaling problem is so severe that formation of the Martian patterns simply by contraction is unlikely. A possible alternative is that the cracks result from some form of tensional tectonics caused by large-scale warping of the surface (Pechman, 1980).

The only plains of any significant extent in the high southern latitudes are in and to the south of Hellas, and within Argyre. The plains of Hellas are rarely seen without frost, clouds, or haze and so are poorly photographed; yet, in many places they have an etched appearance that suggests partly eroded layered deposits at the surface. Along the southern margin of the basin numerous ridges and valleys extend down into the basin from several volcanic centers. Parts of the floor of Argyre also have an etch-pitted appearance. Probably the most puzzling features of the Argyre plains are some long, interconnected ridges. These occur close and run almost parallel to the southern margin of the basin and maintain a uniform width of 1–2 km for hundreds of kilometers (fig. 7.15). Such ridges are rare elsewhere on Mars, although some are present at 3°S, 207°W. They may be simply volcanic intrusions or dikes that stand out as ridges after erosion of the intervening plains. A less likely alternative is that they are eskers—ridges of debris from subglacial rivers that are left standing after a former ice cover has been removed.

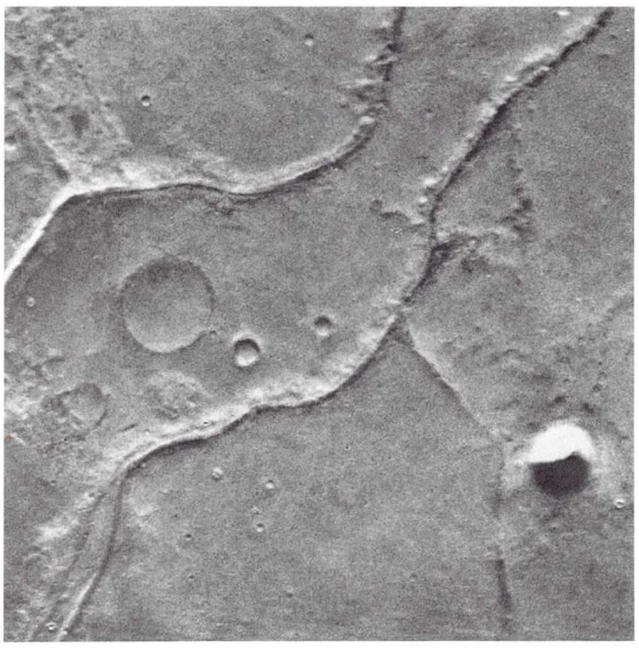

Figure 7.15. Ridges on the floor of Argyre. Many of the ridges extend for hundreds of kilometers and occasionally branch. Their origin is unknown but a possibility is that they are dikes left standing after removal of intervening material (56733).

Fretted Terrain

In most places along the boundary between the plains and the cratered terrain the plains simply lap onto the older terrain. If the slope of the pre-plains surface is steep, the boundary is abrupt; if shallow, then the boundary is transitional with numerous islands of old terrain protruding through the plains and patches of plains within the older cratered terrain. More intriguing is the section of the boundary that Sharp (1973a) termed fretted terrain. The most extensive occurrence is between latitudes 30° and 45°W. Typically fretted terrain consists of two components: high-standing remnants of the densely cratered terrain and—at a lower elevation—the more sparsely cratered plains (fig. 7.16). Separating the two is generally a steep escarpment 1–2 km high. The two components interfinger in complex patterns with broad, flat-floored, sinuous channels (fretted channels), reaching from the plains deep into the uplands and commonly merging with the floors of large upland craters. Along the boundary isolated remnants of old terrain form numerous flat-topped outliers surrounded by plains. There is, therefore, a transition from undisturbed cratered terrain, to cratered terrain that is dissected by broad flat-floored channels, to a region where the cratered terrain forms closely spaced, flat-topped mesas with intervening plains, and finally to an area of mostly plains with widely spaced outliers of cratered terrain.

Almost everywhere within the fretted terrain, debris aprons occur at the base of the escarpments that separate the cratered plateau from the plains (Carr and Schaber, 1977; Squyres, 1978). Where unconfined, such as around plateau outliers, the debris aprons extend 10 to 20 km across the surrounding plains. The surfaces of the aprons are almost devoid of craters and smooth except for fine striae oriented almost at right angles to the escarpment. Divergence and convergence of striae around obstacles suggest that the aprons are debris flows. Where the flows are confined, such as within the flat-floored valleys, the striae tend to run parallel to the length of the valleys, indicating flow away from the walls and down the valleys. The relations suggest that the old plateau has been eroded by a process of scarp retreat, in which lateral erosion at the face of an escarpment is rapid compared with erosion rates on the upper surface of the plateau. Erosion of the scarps provides materials which feed the debris flows.

Fretted terrain may form preferentially in areas where removal of debris by mass wasting is particularly efficient. Squyres (1979) showed that prominent debris flows, as seen in the fretted terrain, occur in two latitude bands 25° wide and centered on 40°N and 45°S. Squyres (1978) pointed out that in these regions ice is precipitated from the atmosphere onto the ground in mid-winter. He postulated that debris flows form because material eroded from the cliff faces becomes mixed with the annual ice deposits to form a rock-ice mixture that resembles a terrestrial rock glacier. Movement of the glacier is by creep, which is accomplished largely by flow of the interstitial ice. Although not explicitly stated by Squyres, such a mechanism may explain why the fretted terrain occurs only where the debris flows are found. The flows provide an efficient way of removing debris eroded from an escarpment, so that erosion can continue unhindered by a protective talus wedge.

In many plains areas are numerous outliers of cratered terrain surrounded by plains. Near the boundary with the cratered upland the outliers may be flat-topped mesas, but farther away the outliers are mostly small, rounded, equidimensional hills. Where the hills are spaced far apart their origin is unclear, but where close together the knobs outline large craters indicating that they are remnants of the old terrain (fig. 7.17). Such "knobby terrain" (McCauley et al., 1972; Carr et al., 1973), characterized by numerous

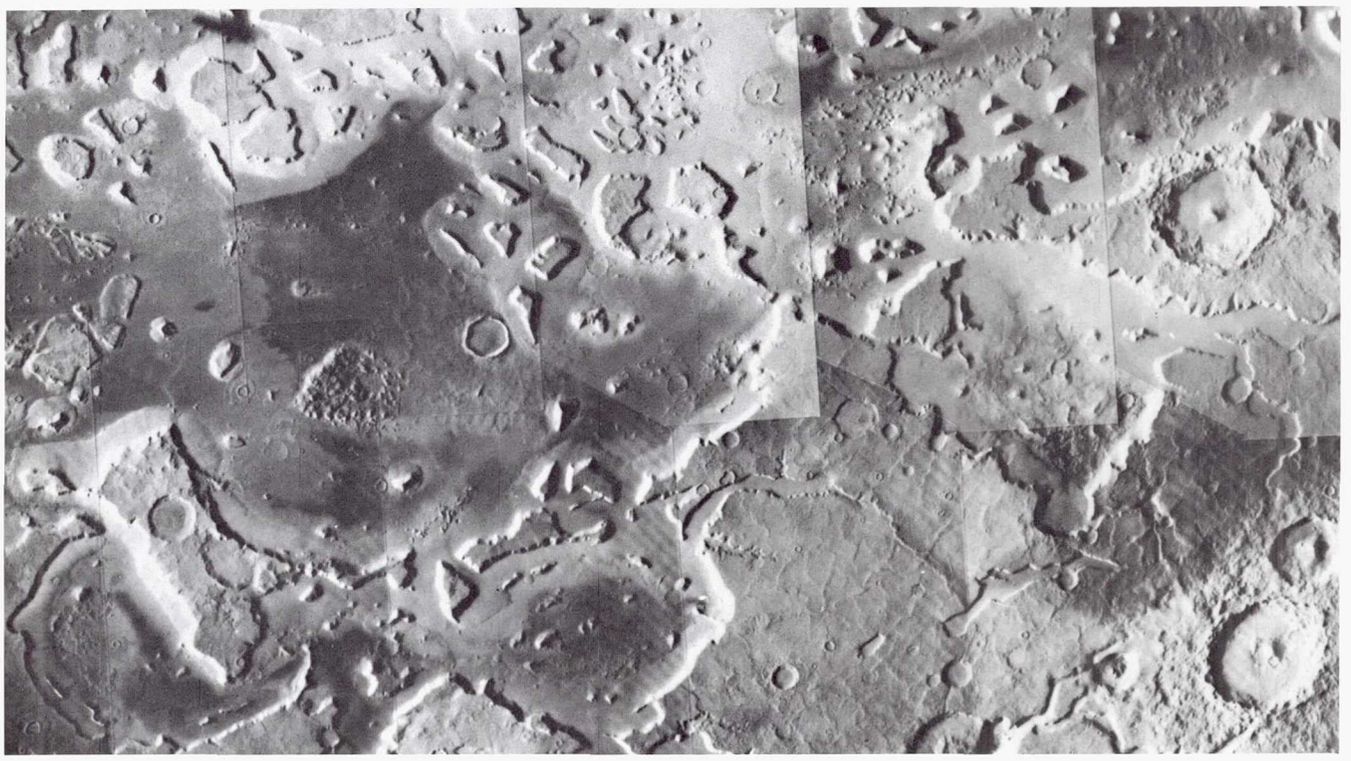

Figure 7.16. Fretted terrain at 38°N, 245°W. The terrain consists of two components: a high-standing, cratered plateau, which is essentially continuous to the south of this area, and low-lying plains, which are more extensive farther north. The two components complexly interfinger, with flat-floored valleys reaching deep into the plateau to the south, and isolated plateau remnants forming mesas at the top of the picture. Debris flows have formed at the bases of all the escarpments. (Rev. 529A).

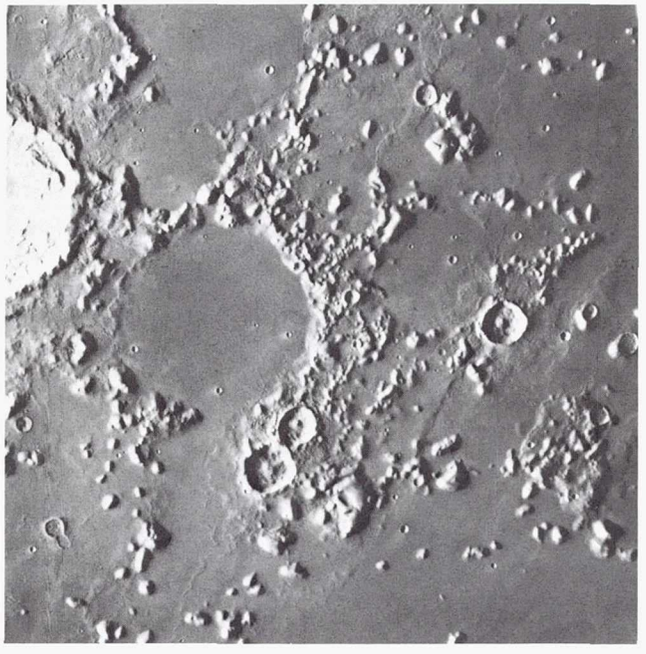

Figure 7.17. Knobby terrain at 24°N, 175°W. The knobs appear to be remnants of a former cratered surface now flooded by younger plains. The large crater remnant near the center is 50 km across (545A24).

closely spaced hills and intervening plains, is particularly extensive east of Elysium between latitudes 10°N and 40°N and longitudes 170°W and 200°W, and north of the Protonilus and Nilosyrtis Mensae between 280°W and 350°W.

Although the knobs are widely accepted as plateau remnants, the precise mechanism whereby the former ancient crust has been so extensively destroyed in the northern hemisphere is poorly understood. Evidence of erosion by mass wasting along the present plains–uplands boundary around plateau remnants is persuasive. Erosion alone, however, cannot explain the disappearance of the primitive crust in the north for there is no sink of sufficient size to accommodate the debris. Mutch et al. (1976) and Mutch and Saunders (1976) suggested that a phase change in the mantle could cause a volume increase and massive disruption of the crust on one hemisphere. Wise et al. (1979b) invoked sub-crustal erosion by mantle convection and foundering of the partially eroded crust in the north. A third alternative is that massive early melting, possibly connected with core formation (Arvidson et al., 1980), resulted in convection and

concentration of low-density crustal material in the southern hemisphere. The entire surface was subsequently saturated with craters, but only the low-lying northern hemisphere was deeply buried by flows that post-date the decline in cratering rate. Some support for this hypothesis is the lack of a gravity anomaly along the plains–upland boundary (Phillips and Lamback, 1980), which indicates that there is a difference in the density of the crust across the boundary.

VOLCANOES

Mars has a rich and diverse array of volcanic landforms that range in size from Alba Patera, over 1500 km across, down to features at the limit of resolution of the orbiter images. The largest volcanoes are in three broad provinces, Tharsis, Elysium, and the Hellas region, but several lesser provinces, in which small volcanoes may be concentrated, have also been identified. The youngest volcanoes, those in Tharsis, resemble terrestrial shield volcanoes, which form largely by eruption of relatively fluid basaltic lava. The typical terrestrial stratocone, which generally contains a much larger proportion of ash, is far less obvious. Differences between Mars and Earth in the volcano sizes, volcano types, and their distributions, appear to result largely from the absence of plate tectonics on Mars.

The Tharsis province includes far more volcanoes than the other provinces, also the largest and the youngest. The name Tharsis is used here in a broad sense to include Olympus Mons and Alba Patera, which are outside Tharsis proper. Most volcanoes in the Tharsis province occur toward the summit and around the northwest edge of the Tharsis bulge. No large volcanoes are on the southeast flank of the bulge, although there are extensive lava plains. The asymmetry may result in some way because the Tharsis bulge straddles the plains–upland boundary. On the southeast flank of the bulge, cratered terrain is at a relatively shallow depth and no volcanoes are found, whereas on the northwest flank and toward the summit of the bulge, the old cratered terrain appears to be at a considerably greater depth, and numerous volcanoes are present. The Elysium province is also centered on a bulge in the crust, but the Elysium bulge is considerably smaller than the Tharsis bulge, being only 2000 km across and 5 km high.

The Large Shield Volcanoes

The three main shields of central Tharsis—Arsia Mons, Pavonis Mons, and Ascraeus Mons—are spaced 700 km apart on what appears to be a northeast–southwest-trending fracture zone just to the northwest of the bulge summit. Each shield is 350–400 km in diameter and has a summit caldera 27 km above the datum. The summit calderas are large by terrestrial standards; that of Arsia Mons is 110 km across and that of Ascraeus Mons is 3.6 km deep. In comparison, the summit caldera of Mauna Loa at its widest and deepest is 2.7 km across and a little over 200 meters deep. The flanks of the shields have an average slope of 5° and a fine radial fabric, which is caused mainly by long, thin flows and lava channels. Wider spaced, concentric lineations result from low terraces, grabens, and lines of pits. On the northeast and southwest flanks of each shield are deep irregular embayments made up of numerous coalesced pits, fractures, and spatulate depressions (fig. 7.18). Each embayment appears to have been the source of vast quantities of lava, which flowed over the adjacent plains, burying the lower flanks of the shields and forming fan-shaped arrays of flows. The flows that originate in the embayment on the southwest flank of Arsia Mons form a spur several kilometers high (fig. 7.19) adjacent to the volcano and decreasing in

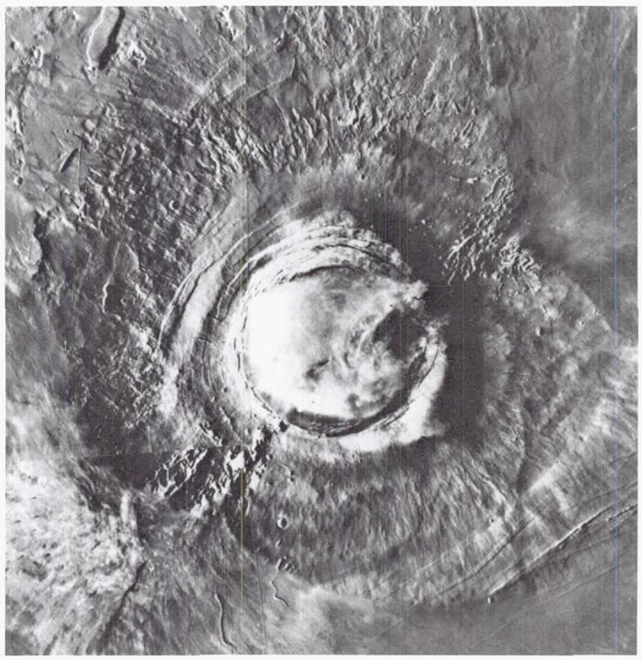

Figure 7.18. Arsia Mons. The main edifice is capped by a 120-km-diameter caldera. Embayments to the southeast and northwest have been the source of a vast array of flows that have partly buried the volcano. To the northwest the volcano flanks have a ragged appearance as though modified by mass wasting. (Rev. 90A).

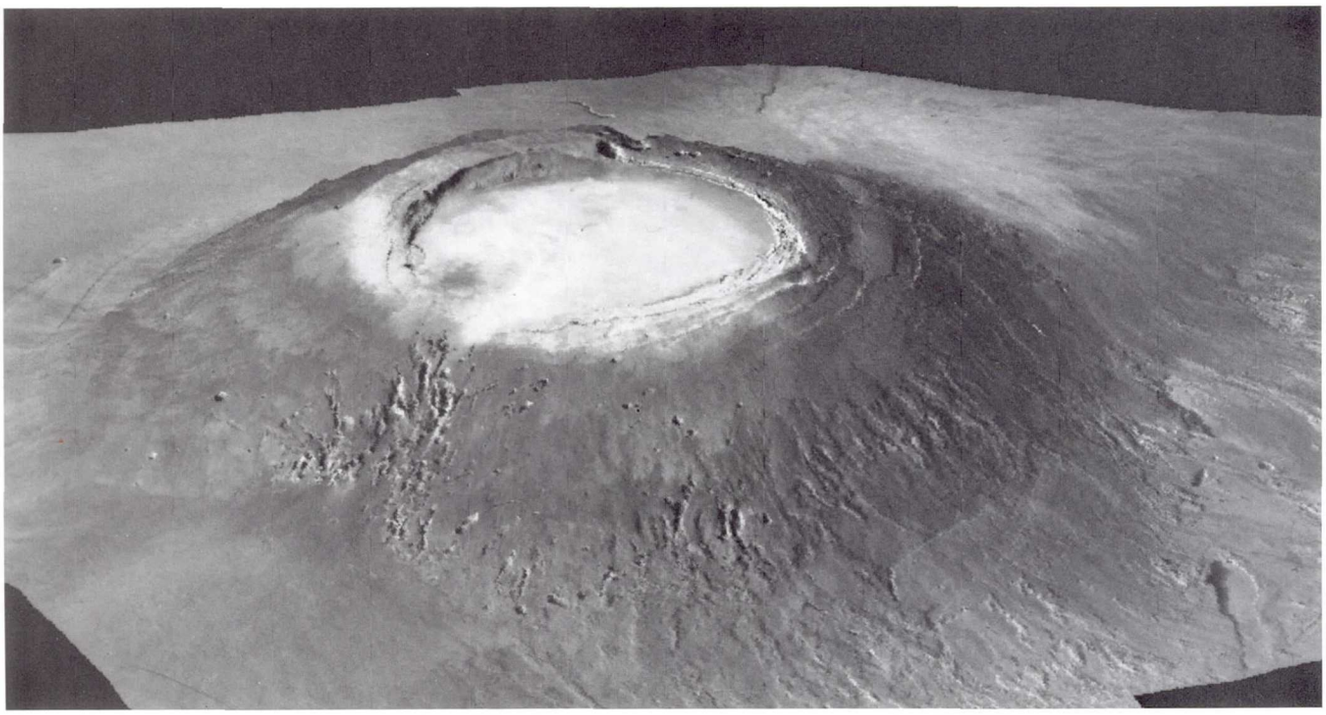

Figure 7.19. Oblique view of Arsia Mons from the northeast. The view was reconstructed from photogrametrically derived elevations. It shows the spur built to the southwest of the main edifice by eruptions from vents on the volcano flanks.

elevation away from it (Roth et al., 1980). The other volcanoes may have similar but smaller extensions to their central edifices.

One of the more puzzling features of Arsia Mons is to the west-northwest of the main edifice, where a lobe-shaped feature extends down the regional slope to approximately 350 km from the base of the volcano (fig. 7.20). The terrain within the lobe has a coarse, "sandpaper" texture except around the margins, where closely-spaced parallel ridges appear to be superposed on other features such as craters and lava flows. Adjacent to the lobe, the Arsia shield has a ragged appearance quite unlike the smooth, finely striated flank of the rest of the edifice. Carr et al. (1977a) suggested that the lobate feature is an enormous landslide or debris flow that swept over the plains following failure of the volcano flank. The landslide may have formed when the adjacent plains were covered with ice, which would have facilitated flow of the volcanic debris over large distances and, more importantly, superposed the flow pattern on the underlying topography when the ice dissipated. Similar, but smaller lobes occur on the northwest downslope sides of Pavonis Mons and Ascraeus Mons, thereby reinforcing the impression that gravity tectonics are involved.

The three Tharsis volcanoes appear to have gone through similar growth cycles. The first stage was building of the main edifice by the slow accumulation of fluid lava, which erupted both at the summit and along concentric fissures on the volcano flanks. During this stage, eruption must have been fairly symmetrical about the volcano center, with no marked radial rift zones as in Hawaii. After formation of the shields, eruption was concentrated along the line of the major northeast-southwest fracture zone on which the three volcanoes lie (Carr et al., 1977a; Crumpler and Aubele, 1978). Lava may have been transported laterally along the fracture zone from the main conduit under the center of each volcano. Eruptions on the northeast and southwest flanks caused repeated collapse of the surface of the shield, forming the large embayments or satellitic calderas. The satellite vents were the source of numerous flows which spread over the adjacent plains and built rounded ridges of lava to the northeast and southwest of each shield. Judging from the crater counts (table 7.4), building of the central edifice terminated earlier at Arsia Mons than at the other two shields, although eruptions from the embayments and within the central calderas of all the volcanoes continued into the recent geologic past and may still be continuing (Carr et al., 1977a).

Olympus Mons is 1600 km to the northwest of the line of Tharsis shields and barely on the Tharsis bulge. The surrounding plains are at elevations of 2–3 km above the datum, as compared with over 9 km around the Tharsis shields. The main shield is 550 km across as defined by a circular outward-facing escarpment up to several kilometers high (fig. 7.21). In some places the cliff transects surface flows; elsewhere flows are draped over the cliff and extend far beyond it. Like the Tharsis shields, Olympus Mons has a large complex summit caldera, gently sloping flanks, a fine radial texture caused by flows, and widely spaced, gentle, concentric terraces. Around the bounding escarpment are numerous lobate features suggestive of landslides (Blasius, 1976). The surface of Olympus Mons is one of the youngest on the planet. Plescia and Saunders (1979) estimated that there are 27 craters >1 km/10^6 km^2. Carr et al. (1977a) give numbers between 15 and 60 in the same units. According to the chronologies of Hartmann et al. (1981),

Figure 7.20. Detail of the lobe of debris that extends northwestward from the rugged northwest flank of Arsia Mons. Fine striations around the margin of the lobe appear to be superposed on pre-existing craters. The frame is 200 km across (42B35).

Table 7.4. Volcano Ages. Crater counts are from Plescia and Saunders (1979) and Crumpler and Aubele (1978). Ages are based on the model of Hartmann et al. (1981) as adapted by Carr (1981)

	No. of Craters >1 km/10^6 km^2	Crater Age (billions of years)		
		Minimum Likely	Best Estimate	Maximum Likely
Olympus Mons	27	<0.1	<0.1	0.3
Arsia Mons	78	<0.1	0.1	0.5
Arsia Mons summit	150	<0.1	0.2	0.9
Arsia Mons flanks	390	0.2	0.6	1.6
Pavonis Mons	350	0.1	0.5	1.4
Biblis Patera	1400	0.7	2.0	3.4
Alba Patera	1850	1.0	2.7	3.6
Jovis Tholus	2100	1.3	3.0	3.7
Uranius Patera	2480	1.7	3.6	3.9
Apollinaris Patera	990	0.4	1.4	3.0
Tharsis Tholus	1480	0.7	2.1	3.4
Albor Tholus	1500	0.7	2.2	3.4
Hecates Tholus	1800	1.0	2.6	3.6
Elysium Mons	2350	1.6	3.4	3.8
Uranius Tholus	2480	1.7	3.6	3.9
Ceraunius Tholus	2600	1.8	3.8	3.9
Ulysses Patera	3200	2.6	3.9	4.0
Hadriaca Patera	2100	1.2	3.0	3.7
Tyrrhena Patera	2400	1.7	3.5	3.9

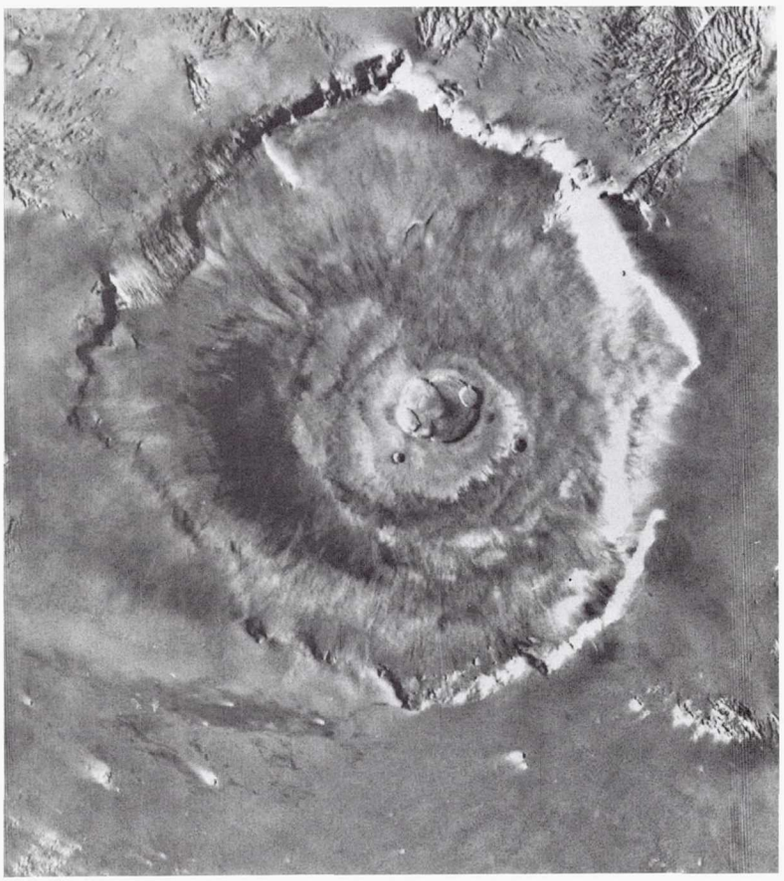

Figure 7.21. Olympus Mons. The central edifice has a summit caldera 24 km above the surrounding plains. Surrounding the volcano is an outward-facing scarp 550 km in diameter and several kilometers high. Beyond the scarp is a moat filled with lava, most derived from Olympus Mons. Farther out is an aureole of characteristically grooved terrain, just visible at the top of the frame (648A28).

Soderblom et al. (1974) and Neukum and Hiller (1981), these counts indicate ages of a few hundred million years. Such young ages imply that the volcano is still active.

Origin of Elysium Mons by eruptions of fluid lava is less convincing than in the case of the other large volcanoes. Its flanks have low hummocks but otherwise there is little surface detail apart from craters, even at high resolution. The summit of the volcano is estimated to be 9 km above the surrounding plain, which gives an average slope of 3.5° for the flanks (Blasius, 1979). Malin (1977) compared Elysium Mons to the terrestrial volcano Emi Koussi in the Tibetsi region of the Sahara and suggested that Elysium Mons, like Emi Koussi, is a composite volcano built of both ash and lava. He further suggested that andesitic and rhyolitic lavas may have been involved in its formation. This latter suggestion now appears less likely in view of the chemistry of the soils at the Viking landing sites (see "Surface Chemistry").

A fracture ring, approximately 400 km in diameter and centered on the summit caldera, almost completely surrounds Elysium Mons. The ring is probably caused by flexure of the crust under the volcano load, as suggested by Thurber and Toksöz (1978) for Olympus Mons. Outside the ring are numerous west-northwest to east-southeast trending, flat-floored troughs with straight walls much like grabens. The troughs are roughly parallel to some much larger fractures, the Cerberus Rupes, southwest of Elysium. A startling aspect of these troughs is that they change northwestward into fluvial-like channels which branch, rejoin, and meander for several hundred kilometers across the plains to the northwest. Similar but smaller channels also arise close to the northwest flank of Hecates Tholus. The channels are discussed separately below.

Although the surfaces of many of the large volcanoes are young, the volcanoes themselves may be quite ancient, having accumulated possibly for billions of years. The fan-shaped arrays adjacent to the central Tharsis volcanoes contain flows that have a range of ages. Those that form the spur to the southwest of Arsis have a range of crater densities from 100 to over 2000 larger than 1 km/10^6 km^2. By almost all chronologies, the larger number implies an age in excess of 3 billion years. Thus, Arsia Mons appears to have been active for billions of years. The accumulation rate must have been considerably lower than that for the Hawaiian shields. Assuming a 2 billion year age and a volume of 10^6 km^3 for Arsia Mons (Blasius and Cutts, 1976), give an accumulation rate of 5×10^{-4} km^3/yr. For comparison, the accumulation rate of Mauna Loa is estimated as 10^{-2} km^3/yr.

Olympus Mons and the Tharsis shields appear to have had eruptive styles similar to the Hawaiian volcanoes, but there are differences. The overall shape of the edifices with their low slopes and summit calderas suggests eruption primarily of fluid lava with little ash. The presence of complex summit calderas indicates that the summits have undergone cycles of inflation and deflation, like the Hawaiian volcanoes. Although the significance of the much larger size of the Martian calderas is not known, it surely must be due in part to a larger magma chamber. The outlines of individual flows on the Hawaiian and Martian volcanoes are similar, and the presence of leveed channels and channels atop ridges suggests similar processes whereby the magma is distributed from the source vents. However, lines of pits, indicative of lava

tubes, which are relatively common on the Hawaiian volcanoes, are rare on the Martian volcanoes. Another apparent difference is the relative scarcity of vents on the Martian shields. Rimless depressions, which could be vents, are common adjacent to the embayments on the northeast and southwest flanks of the Tharsis shields, and some pits form concentric lines elsewhere on the flanks, but in general vents are scarce. Certainly, radial lines of vents such as those on the Hawaiian rift zones are rare. Moreover, evidence of build-up of spatter around vents is almost completely lacking.

But the most obvious difference between the Hawaiian and Martian shields concerns size. Flows on the Martian shields commonly can be traced for tens of kilometers and central channels may be hundreds of meters across. Conversely, Hawaiian flows are rarely more than 30 kilometers long and their channels rarely are more than a few tens of meters wide. Walker (1973) suggested that effusion rate is the most important factor determining the length of a lava flow, with high effusion rates resulting in long flows. If true, then high effusion rates are implied for the Martian shields (Carr et al., 1977a), which is consistent with the large size of the lava channels. The high effusion rates also imply long intervals between eruptions if the accumulation rates given above are even approximately valid.

The great size of large shield volcanoes almost certainly results from the stability and thickness of the Martian lithosphere. Hawaiian volcanoes are relatively short-lived because motion of the Pacific plate carries them northwestward away from the magma source presently beneath Kilauea. The result is a long line of extinct volcanoes of modest size that stretch across the Pacific and become progressively older to the northwest. In contrast, on Mars, a volcano remains fixed over its magma source and will grow to a large size if magma remains available and under sufficient pressure to be pumped to the surface. The height to which a volcano can grow depends on the depth of origin of the magma and the density contrast between the lava and the rocks through which it passes on its way to the surface. Lava is pumped to the top of a shield volcano largely by the lithostatic pressure at the magma source (Eaton and Murata, 1960). A volcano can continue to grow in elevation so long as the pressure exerted by the column of magma between the volcano summit and the magma source is less than the lithostatic pressure at the source depths. When the pressure at the base of the column equals the lithostatic pressure, then the lava can be pumped no higher and any further growth of the volcano must be lateral. Eaton and Murata (1968) suggested that Mauna Loa is at its height limit because it is almost the same height as the nearby volcanoes Mauna Kea and Haleakala. Taking plausible values for the densities of the crust, mantle, and lava, they calculated that the Hawaiian lavas originate at depths of around 60 km.

Similar calculations are uncertain for Mars since estimates of the densities are largely guesswork. Taking terrestrial values of 2.8 g/cm^{-3} for the density of lava and 3.2 g/cm^{-3} for the average density of the rocks above the magma source, including both crust and mantle, then the 23-km height of Olympus Mons gives a 160-km depth to melting. Presence of a crust with densities close to that of the lava could significantly increase this figure. Blasius and Cutts (1976) showed, in addition, that irrespective of what densities are assumed, the greater elevation of Olympus Mons with respect to the surrounding plains as compared with the Tharsis shields implies a deeper source for its magma, which is geologically plausible. Steeper temperature gradients and shallower depths to melting are expected in Tharsis, which is closer to the center of the volcanic province. The Martian lithosphere, therefore, appears to be considerably thicker than Earth's, which ranges up to about 100 km at the thickest parts of the continents, and thicker under Olympus Mons than central Tharsis. Because of the great height of the youngest Martian volcanoes and the much lesser heights of the older ones, Carr (1976) suggested that the thickness of the Martian lithosphere has increased with time. Solomon and Head (1982), however, made several estimates of lithosphere thickness from the deformation of the lithosphere caused by volcanic loading and found no systematic change with time. They suggested that lithosphere thickness depends more on proximity to the main volcanic provinces.

Olympus Mons Aureole

The aureole of Olympus Mons consists of several huge lobes of distinctively ridged terrain that extend out from the base of the volcano for several hundred kilometers (fig. 7.22). The surface of each lobe appears to dip gently inward toward Olympus Mons, so that the inner sections are embayed by younger plains and the outer margins form outward-facing escarpments. Only the outer margins of the older lobes are visible, mainly because of burial by younger lobes

Figure 7.22. Synoptic view of Olympus Mons and its aureole. The aureole consists of several large lobes of grooved terrain, each bound by an outward-facing escarpment. The regional slope of the Tharsis bulge is from southeast to northwest, and the aureole is best developed to the northeast of Olympus Mons, down the regional slope.

closer in. The aureole deposits extend for 700 km to the northwest of Olympus Mons and for 300 to 400 km from the scarp around the rest of the volcano. A positive free-air gravity anomaly of several tens of milligals appears to coincide with the aureole, at least to the northwest (Sjogren, 1979).

Several suggestions have been made as to the origin of the aureole. King and Riehle (1974) proposed that Olympus Mons is a composite volcano that has erupted large volumes of ash and lava from its central vent and that the scarp of Olympus Mons is erosional, having formed at the zone of transition between dominantly lava and indurated ash deposits, close in, and dominantly ash deposits farther out. By implication, the aureole deposits are wind-eroded remnants of the distal parts of the tuff sheets. A major objection to this hypothesis is the lack of evidence of pyroclastic activity of any kind on the main Olympus shield. In a related hypothesis, Morris (1982) suggested also that the aureole deposits are vast, partly eroded, tuff sheets but that they were erupted from several volcanic vents around the Olympus shield. This hypothesis fails, however, to explain the cliff around the volcano, and the sources of the postulated pyroclastic flows are not convincingly identified. Harris (1977) proposed that the lobes are vast gravity-assisted thrust sheets caused by squeezing out of material from beneath Olympus Mons along planes of weakness and suggested that the aureole materials are concentrated to the northwest because this is down the regional slope caused by the Tharsis bulge. In a similar hypothesis, Lopes et al. (1980) proposed that the deposits are vast landslides that detached from the cliff around Olympus Mons. The main problem with the last two hypotheses is that they do not explain the positive gravity anomaly over the aureole. Hodges and Moore (1979) speculated that Olympus Mons is analogous to Icelandic tablemountains, volcanoes that form partly under ice. They propose that there was formerly a thick ice sheet around Olympus Mons, that the main shield formed subaerially, and the aureole under ice. The height of the cliff, 4–6 km, indicates the thickness of the ice. The difficulties with this hypothesis are numerous, including why no subaerial eruptions occurred over the vast area of the aureole, why the ice left no trace other than the aureole and the cliff, and why the thick ice should be preferentially located around Olympus Mons. Other suggestions are that the aureole is the erosional remnant of an ancient shield (Carr, 1973) or an unroofed pluton (Blasius, 1976), but both of these suggestions appear to require higher erosion rates than are found elsewhere on the planet and so appear implausible. Thus, we are left with no satisfactory explanation for the feature.

Small Shield-like Volcanoes

Several shield-like volcanoes considerably smaller than the large shields are present in Tharsis and Elysium. Most resemble the larger shields except that they usually have a proportionately larger summit caldera. Three of the volcanoes, however, the 60-km-diameter Uranius Tholus, the 120-km-diameter Ceraunius Tholus in Tharsis, and the 180-km-diameter Hecates Tholus in Elysium, are distinctively different. They have relatively steep slopes that average 9° (Blasius, 1979) and numerous fine radial channels on their flanks. Most of the channels lack the levees that characterize many of those on the larger shields and the plains, nor are there channels atop ridges as on Alba and Olympus Mons. The Ceraunius channels, for example, are simply inset into the volcanic surface (fig. 7.23). Most are a few hundred meters across or less, but a particularly large channel 2 km across starts at the summit caldera, extends

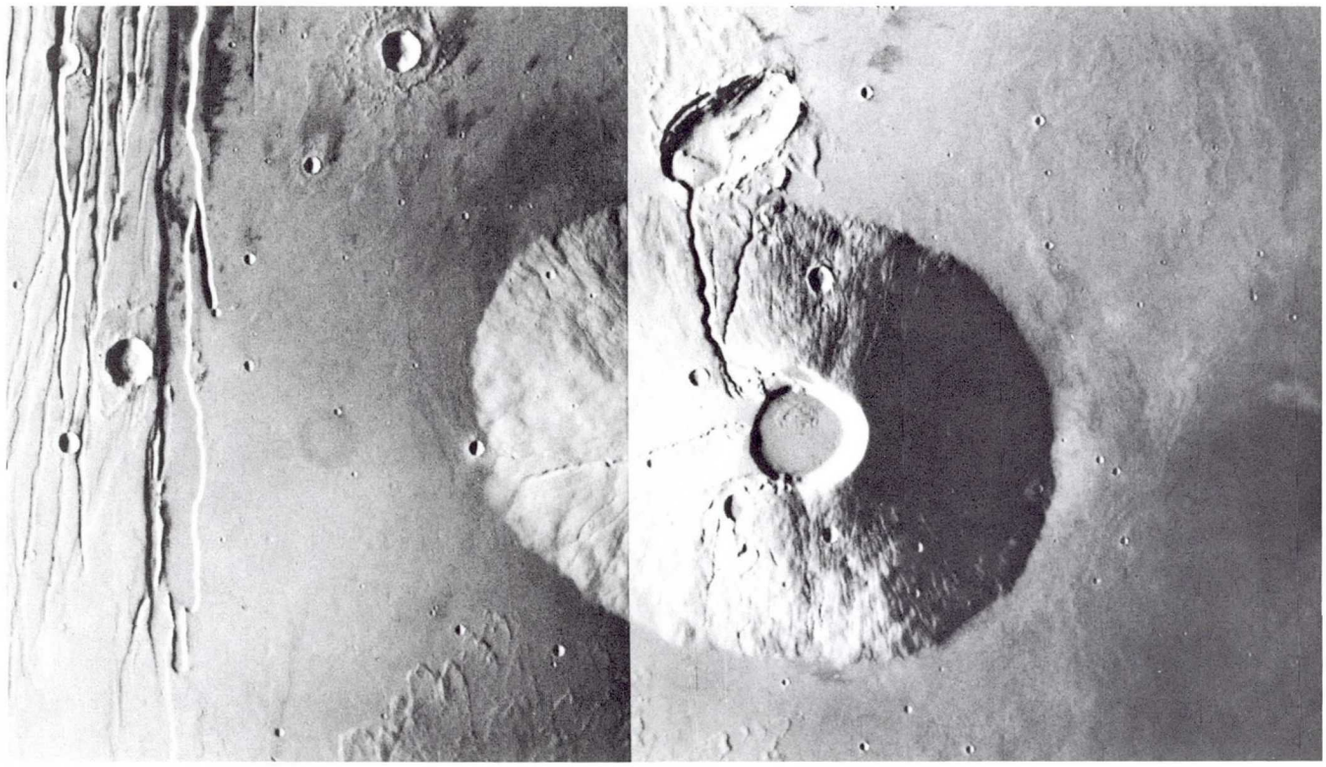

Figure 7.23. Ceraunius Tholus. The volcano has a 22-km-diameter summit caldera and on its flanks are numerous channels. A particularly large one on the northern flank terminates in what is seemingly an impact crater (516A22,24).

down the northern flank of the volcano, then into a large impact crater in the surrounding plain. As no large deposits occur within the crater at the end of the channel, the material eroded to form the channel must have been mostly removed. Several smaller channels on the volcano flanks have conical accumulation of debris at their lower ends.

Reimers and Komar (1979) suggested that the channels on Ceraunius Tholus were cut by volcanic density currents, mixtures of gas and particulate debris that move radially outward from a volcanic center either as a direct result of explosive activity at the vent or as a result of collapse of a gas and ash column over the volcano. They point out the similarity between the array of channels on the flanks of Ceraunius Tholus and those on the flanks of Barcena Volcano, Mexico, which were cut by density currents. They also point out that the large channel on Ceraunius cannot be formed by lava since there are no volcanic constructs within the crater in which it terminates. Nor is it likely to have been carved by water as suggested by Sharp and Malin (1975) because there is no catchment area and erosion by seepage at a volcano summit is unlikely. Reimers and Komar proposed that the density currents could form by explosive activity resulting either from rapid exsolution of juvenile water or interaction of magma with groundwater or ground ice. The Reimers and Komar hypothesis does not necessarily imply a distinctive composition for Uranius and Ceraunius Tholus for, although nuees ardentes on Earth are more common in non-basaltic lava such as andesite and rhyolite, they can form with basaltic magmas, particularly if there is strong interaction of the magma with groundwater.

Alba Patera

The 1600-km-diameter Alba Patera, at the northern edge of the Tharsis bulge, far exceeds any other volcano in areal extent, but its height is probably less than 6 km (Carr, 1976) and its slopes less than half a degree. At the center is a 100-km-diameter caldera, around which splay numerous north–south and northeast–southwest-trending fractures, which form a ring 600 km in diameter. One of the most striking characteristics of the volcano are the large, perfectly preserved lava flows on its flanks. Several types of flow features are present (Carr et al., 1977a). Most common are sharp-crested radial ridges up to 400 km long and averaging 8 km across. At the ridge crest is generally a channel usually less than 500 meters across,

or a line of pits, suggesting the presence of a lava tube (fig. 7.24). The ridges appear to have been built slowly by lava carried down the central channel. The ridge flanks are striated, probably as a result of overflow of lava from the main channel. Overflow may have occurred relatively often as a consequence of the shallow longitudinal profile of the central channel. Occasional channels leave the crest of the ridge and continue between the ridges. Presumably, lava overflowed the channel on the ridge crest and subsequent flow was between the ridges. In this manner, new ridges probably formed between the old ones as the volcano grew. Tabular sheet flows are present also, with well-defined, steep flow fronts. These may have formed when eruption rates were higher than those which resulted in the long ridges. Relatively short, narrow flows, less than 2 km across and with a central channel similar to those in Olympus Mons and the large Tharsis shield volcanoes, constitute a third type of flow. They occur mostly near the volcano summit and may indicate steeper slopes there. All the flow features just described have close terrestrial analogs, though Alba's are mostly an order of magnitude larger than any of their terrestrial counterparts.

Figure 7.24. Flows on the northwest flank of Alba Patera. In the lower left, lava channels are visible on the crest of radial ridges. During eruptions of modest discharge lava was transported northwestward, down the ridge-top channels, from vents off the picture to the southeast. During eruptions of higher discharge, the channels probably overflowed to form the large tabular flows seen in the central part of the picture.

Ancient Volcanoes in the Southern Hemisphere

Around Hellas are several old, sprawling volcanoes with little vertical relief (Peterson, 1978). Included are Hadriaca Patera at 264°W, 30°S, and Amphitrites Patera at 58°S, 298°W. Each has a vague circular depression at its center and, extending outward, numerous low radial ridges similar to, but more subdued than, those around Alba Patera. Ridges around the volcanic centers on the southern rim of Hellas extend over the rim and well into the Hellas basin. The volcanoes merge outward with the surrounding volcanic plains and appear to be sources for some of the flows that constitute the plains.

About 800 km to the northwest of Hadriaca Patera is a quite different volcano, Tyrrhena Patera, which has a central circular caldera 12 km in diameter surrounded by what appear to be layered deposits that extend as far as 300 km from the volcano center (fig. 7.25). The deposits are, in places, deeply eroded to form irregular escarpments, flat-floored radial valleys, and mesa-like outliers. The extreme dissection of the volcano as compared with the almost total lack of dissection of other volcanoes suggests that it is composed of friable, easily eroded materials. A strong possibility is that the volcano produced vast quantities of ash but little lava.

At 9°S, 186°W is yet another large volcano, Apollinaris Patera. It is 400 km across and surrounded by a low escarpment except to the south, where a broad spur extends from close to the summit caldera rim southward for about 350 km. It appears to have had a similar history to Arsia Mons in that after the main edifice was built, eruption continued on the volcano flank to build a broad ridge adjacent to and overlapping the original shield.

Small Volcanic Features

Most of the literature on Martian volcanoes has focused on the large shield volcanoes. These are large enough that secondary characteristics, such as calderas, lava flows, levees, flow fronts, and so forth, can be readily identified and a volcanic origin can hardly be doubted. In many areas, however, there are numerous small (<5 km) features that can also

Figure 7.25. Tyrrhena Patera at 20°S, 252°W. At the volcano center is a 45-km-diameter caldera. The caldera is surrounded by partly eroded horizontal sheets suggestive of ash-flow deposits (211-5730).

plausibly be interpreted as volcanic (West, 1974; Peterson, 1978; Hodges, 1979). In Isidis Planitia, for example, numerous cratered domes are arrayed in long strings, apparently along faults. They are generally several hundred meters across and resemble spatter cones and ramparts both in size and shape. East of Hellas many similar domes are elongated, darker than their surroundings, and have slot-like vents. Others are found in Mare Acidalium and Utopia Planitia (Hodges, 1979).

Some cratered cones in the knobby terrain at the southeastern edge of Elysium Planitia were called volcanoes by West (1974). These are somewhat ambiguous. As we saw in the previous chapter, formation of the knobby terrain by the breakup of an old cratered surface is well established. The presence of occasional knobs with summit craters should therefore not be surprising, as craters in the original surface may have partly controlled the breakup. Nevertheless, some of the cratered knobs do resemble stratocones and the possibility of a volcanic origin should be left open. Less ambiguous are low conical constructs with slot-like vents in the Tempe region (fig. 7.26). These are commonly astride grabens and merge outward with the surrounding volcanic plains. Many of the grabens in the Tempe region have, in addition, lines

Figure 7.26. Small volcano at 36°N, 86°W in the Tempe region. An old cratered plateau to the right is faulted by Tharsis radials and embayed by younger plains to the left. The frame is 60 km across (627A28).

of craters on their floors, and these may also be volcanic. Additional examples are some flat-topped pitted mountains in southwest Utopia and southwest of Olympus Mons, which show a remarkable resemblance to terrestrial tablemountains formed by intrusions under ice (Hodges and Moore, 1979; Allen, 1979b), and some low pancake-like structures in Chryse Planitia (Greeley et al., 1977).

Volcanic History

The type and location of terrestrial volcanoes is governed largely by plate motion. On Mars there is no evidence of plate motion. The arcuate chains of mountains that characterize terrestrial subduction zones are absent and compressional features of any type are rare. Evidence of strike-slip movement, such as occurs on Earth where plates move laterally with respect to one another, is also absent on Mars, despite the survival of large areas of ancient, cratered terrain in which such movements could easily be detected. The crust of Mars appears to be stable and not broken into moving plates like Earth's. The type of volcanism on Mars is correspondingly different. Volcanic cones, which typically occur along subduction zones on Earth, are relatively rare, and it is not unreasonable to assume that the andesitic and alkalic magmas that typify subduction-zone volcanism are also rare. Such an assumption is consistent with the limited compositional data we have for Mars, which suggests that most of the primary rocks are iron-rich and basic or ultrabasic. The most prominent features on Mars are shield volcanoes and flood basalts, both of which occur within plates on Earth and appear to be caused by processes deep within the mantle rather than shallow tectonics.

The history of volcanic activity on Mars can be reasonably well reconstructed from crater ages on different volcanic features. The oldest recognizable volcanic features are the ridged plains of the old cratered terrain. Flow fronts are rare on these plains but their vast extent, smooth surface, spectral signature, and wrinkle ridges all support a volcanic origin. Most are ancient; they have in excess of 2800 craters 1 km/10^6 km^2, which suggests that they date from shortly after the time that the impact rate declined about 3.8 billion years ago. Volcanism is, however, unlikely to have started at that time. More probably, volcanic activity was continuous throughout this era and we can only recognize as volcanic those surfaces that formed after the landscape stabilized. All evidence of the volcanism that occurred before 3.9 billion years ago has been lost or is unrecognized.

The next oldest identifiable volcanic features are the floors of Hellas, Hesperia Planum, and Tyrrhena Patera, all having crater numbers in excess of 2600. These are still within the cratered hemisphere. Slightly younger, with crater numbers between 2000 and 2600, are most of the ridged plains of the sparsely cratered hemisphere, including Lunae Planum, Solis Planum, Isidis Planitia, and Syrtis Major Planitia. Some of the more intensely cratered plains peripheral to Tharsis and most of the small Tharsis shields also formed at this time. In terms of absolute age, this is probably in the 2.5–3.5 billion years range. At a slightly younger age are the Elysium, Amazonis, and Noachis plains, Alba Patera, and the Elysium volcanoes, all having crater numbers close to 2000 and probably still date from before 2.5 billion years ago.

Volcanic activity after this time has been almost completely restricted to Tharsis. The only major exceptions are the plains of Mare Acidalium and Utopia, which have crater numbers between 800 and 1500, and possibly Apollinaris Patera with a crater number of 990. Within Tharsis, volcanic plains appear to range in age from in excess of 3 billion years to the present. The surfaces of the large Tharsis shields and Olympus Mons appear to be very young with average ages of a few hundred million years or younger. As we saw above, however, the edifices have probably been accumulating for billions of years. Volcanic activity on the southeast flanks of the Tharsis bulge terminated earlier than Tharsis proper. Counts in the Sinai-Solis Plains range from approximately 2300 down to 1000, indicating an approximate age range of 3 billion to 1.5 billion years.

Thus, the history of volcanic activity on Mars is one in which activity became progressively more restricted with time. Between 2.5 and 4 billion years ago, extensive volcanic activity resulted in formation of most of the sparsely cratered plains of the northern hemisphere and the ridged plains of the densely cratered terrain. After 2.5 billion years ago, activity was largely restricted to around the Tharsis bulge and to some of the northern plains; in the last billion years volcanism occurred only near the crest and northwest flank of the bulge.

THE THARSIS BULGE

The Tharsis bulge has clearly played a major role in the evolution of Mars. Radial fractures around the rise affect almost an entire hemisphere. The largest and youngest volcanoes are on its flanks, as is the vast

system of equatorial canyons. The bulge has even influenced surficial processes by perturbing wind regimes, and possibly controlling migration of groundwater and the location of fluvial features. But the bulge is of interest not only for its effects on surface geology but for the clues it provides concerning the nature of the planet's interior. A large gravity anomaly, coincident with the bulge, gives a means of assessing the structure of the crust and the density distribution down to depths of several hundred kilometers. The anomaly, in addition, gives some indication of whether the bulge is being actively supported from below, perhaps by convection, or whether it is supported passively by the strength of the crust.

The Tharsis bulge is a broad, gentle rise on which smaller features such as volcanoes, craters, and canyons are superposed. Its crest, around 0° latitude, 105°W (Christensen, 1975; Wu, 1978), is at an elevation of 10–11 km above the datum. To the north, regional slopes range from 0.2° to 0.4° and continue down below the −1 km level into the plains of Chryse and Amazonis Planitia. To the south, the slopes are half these values and continue down only to about the 4 km level, where they merge with the relatively high southern uplands. The bulge is therefore asymmetric, being steeper and more extensive to the north, probably as a result of straddling the plains–upland boundary. If the 4-km contour is taken as the base of the bulge, it is 5500 km across and 7 km high, but to the north it is far more extensive.

Numerous radial fractures occur around the bulge (fig. 7.27). Several attempts have been made to reconstruct the sequence and timing of faulting around the bulge from transection relations and crater densities on fractured and unfractured units (Wise et al., 1979a; McGill, 1978; Frey, 1979; Plescia and Saunders, 1982). Surfaces younger than the cratered plains of Scott and Carr (1976) are mostly only sparsely fractured. These plains average 2400 >1 km/10^6 km^2 (Gregory, 1979), which suggests ages in the 2.5 to 3.5 billion years range. On the other hand, where the oldest plains are in contact with densely cratered terrain as in the Tempe plateau, the plateau and the plains are usually fractured to an equal extent. The two relations imply that the fracturing peaked shortly after the decline in cratering rates.

Fracturing continued to a much later date, however, but with considerably less intensity. Occasional fractures are visible, for example, among the young lava flows of central Tharsis, where many flows that clearly transect fractures are themselves cut by fractures with similar orientations. Volcanic activity and faulting took place simultaneously and apparently continued into the geologically recent past.

Although the general region of Tharsis remained at the center of the fracture system, the precise location of the center may have, on occasion, shifted slightly as is evident from the different orientations of different aged fractures. Plescia and Saunders (1980) suggested that the center of the Tharsis bulge was originally at 8°S, 100°W, near the west end of Noctis Labyrinthus. Faults that formed at this time are mainly exposed in the Ceraunius, Claritas, and Thaumasia Fossae and just north of Noctis Labyrinthus. They suggest that the center of faulting then shifted to 4°S, 110°W, close to Pavonis Mons. Relatively early, intense faulting about this center results in the Memnonia, Sirenum, and Mareotis Fossae and the faults within the canyon. After this early, intense episode, faulting continued about the same center at a relatively low level up to the present time, resulting in the fractures among the young flows of central Tharsis. A similar sequence of faulting was deduced by Wise et al. (1979a), although they gave a somewhat different location, 14°S–101°W, for the center of the fracture system.

The fractures appear to be caused by stresses that result from the presence of the Tharsis bulge. Phillips and Ivins (1979) calculated the stresses in the Martian lithosphere that are caused by the present surface gravity and topography. The excellent agreement between the predicted orientations of the fractures and those actually observed demonstrates conclusively that the fractures and ridges around Tharsis are caused by the present topographic and gravity highs and not by some process of updoming.

Gravity

A long wavelength free-air gravity anomaly of approximately 500 mGal exists over the Tharsis province and gravity lows of around 200 mGal are over the adjacent lowlands of Chryse and Amazonis (Lorrel et al., 1972; Gapcynski et al., 1977; Sjogren et al., 1975). Other lows occur over Hellas and Isidis. High-resolution data derived by direct measurements of the accelerations of Viking Orbiter 2 (Sjogren, 1979) show that there are also large local positive anomalies over individual volcanoes. The largest is over Olympus Mons, which has a 344 mGal anomaly as measured at an altitude of 275 km. Alba Patera has a positive anomaly of close to 70 mGal, and somewhat smaller

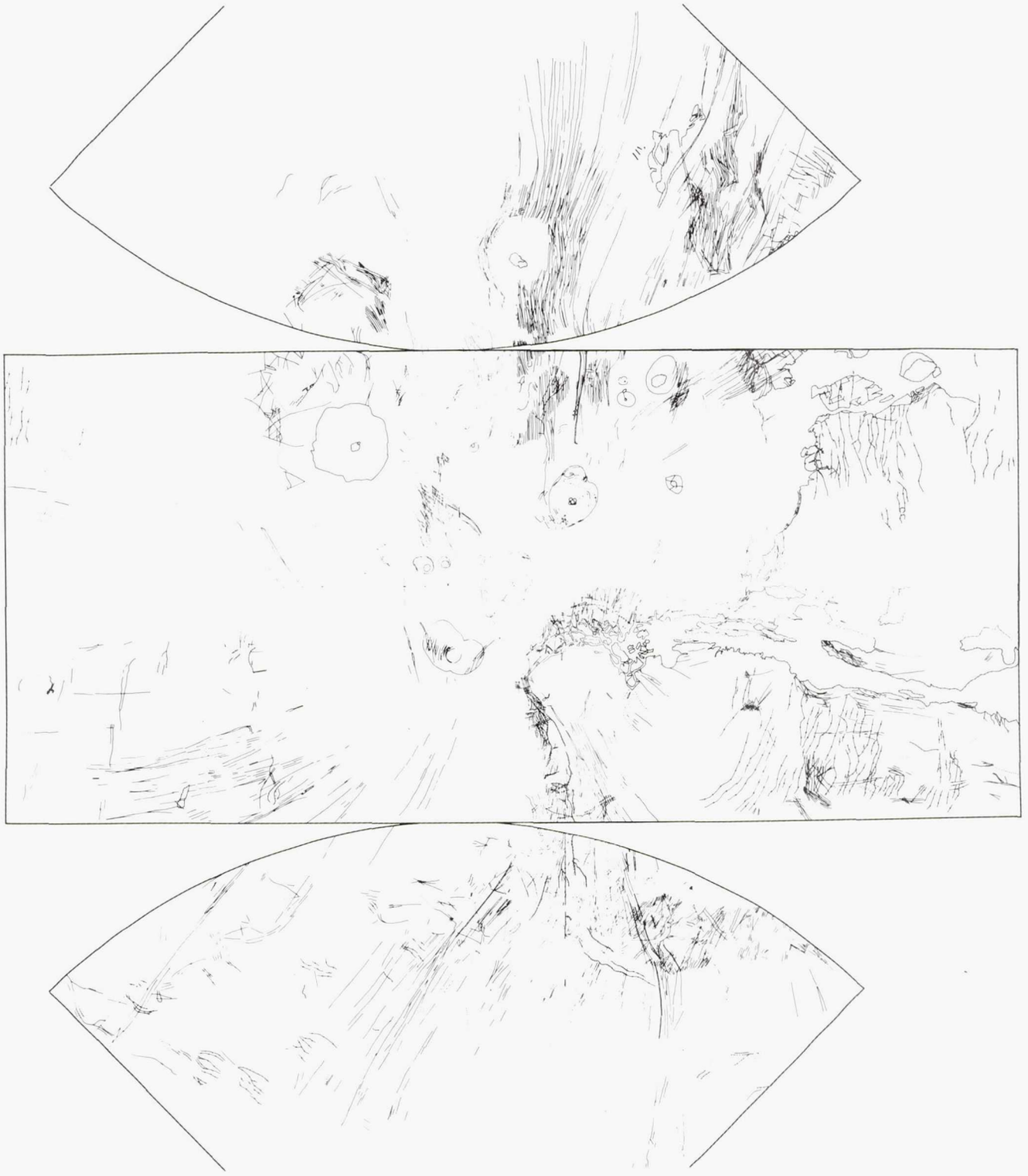

Figure 7.27. Structural features around the Tharsis bulge. The area shown extends from 60°N to 60°S and from 45°W to 180°W. The major volcanoes are outlines; faults are shown as plain lines, ridges as beaded lines (Courtesy J. Plescia, JPL).

anomalies are associated with the other large volcanoes. Local negative gravity lows occur over Isidis and the canyons.

The gravity data from Tharsis show a distinct correlation with topography (fig. 7.28), showing that the topography is only partly compensated, at least at a shallow depth (Phillips and Saunders, 1975). The data from the Amazonis and Chryse basins follow the same trend as the Tharsis data, indicating that formation of these basins was somehow coupled to the formation of the bulge. Outside Tharsis, topography and gravity are uncorrelated, so the topography must be compensated at a relatively shallow depth. Phillips et al. (1973) and Phillips and Saunders (1975) examined the Mars gravity data in terms of a simple Airy model. They calculated the gravitational effects of the observed topography and subtracted these from the measured gravity to get a Bouguer anomaly. The result is a large negative Bouguer anomaly over Tharsis and positive anomalies over some of the surrounding lowlands. Thus, although the topography is not completely compensated it is at least partly compensated. They suggested that the anomaly could be the result of a crust of variable thickness. Taking 50 km for the thickness of the crust where the Bouguer anomaly is zero and crust and mantle densities of 3.0

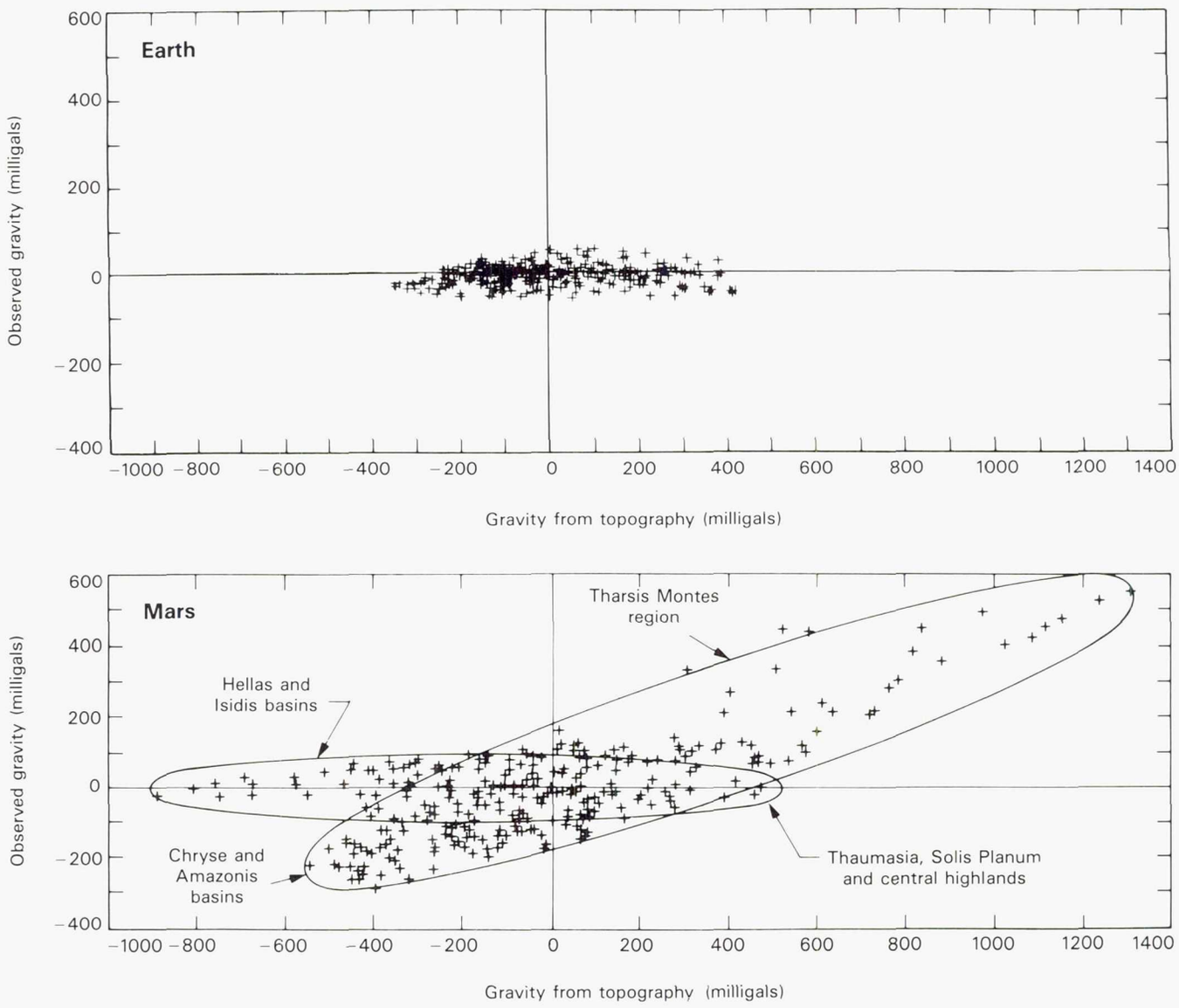

Figure 7.28. Relation between observed gravity and gravity computed from topography for Mars and Earth. On Earth the observed and computed gravities show no correlation because of isostatic compensation. On Mars a strong correlation exists for the Tharsis region indicating lack of isostatic compensation at shallow depths (from Phillips and Saunders, 1975).

and 3.3 g/cm^{-3}, respectively, they calculated crustal thicknesses as high as 130 km under Tharsis. They recognized that compensation is incomplete and calculated the "isostatic deviation," the fraction of the gravity anomaly that remains after correcting for isostatic compensation at some relatively shallow depth. The deviation has significant values only for the Tharsis region and its surroundings as anticipated from figure 7.28.

Compensation of both the high and low frequencies of the Martian topography cannot be achieved with either simple Pratt or Airy models (Phillips and Lambeck, 1980). As an alternative, Sleep and Phillips (1979) proposed a compensation mechanism which combines the Pratt and Airy concepts. They assumed that a crust of variable thickness (Airy model) overlies an upper mantle with lateral variations in density (Pratt model). In their model the crust is thinner under Tharsis than elsewhere and the upper mantle is less dense. They point out that low mantle densities under Tharsis are plausible because of the higher temperatures and different compositions expected under a volcanic region. The model is similar to that proposed by Thompson and Burke (1974) for the Basin and Range province of the United States. Sleep and Phillips were able to achieve compensation under Tharsis at depths as shallow as 300 km.

Several suggestions have been proposed (Phillips, 1978) for the formation of the Tharsis bulge. These include compression due to global shrinking, an antipodal reaction to the formation of Hellas, and lateral inhomogeneities in the Mars mantle. The two most plausible hypotheses are (1) that the lithosphere in Tharsis was uplifted as a result of mantle convection, or (2) that the Tharsis bulge is a thick accumulation of volcanics. Soon after the existence of the bulge was recognized, it was proposed that the Mars lithosphere had been actively uplifted and that the fractures formed as a result of the uplift (Hartmann, 1973; Carr, 1974a). We have seen, however, that the fractures are more plausibly explained as the result of stresses established in the lithosphere as a result of the presence of the bulge. Nevertheless, updoming of the lithosphere as a result of mantle convection is still a possible cause of the bulge. Several mechanisms could trigger the convection and localize upwelling under Tharsis. Convection could result simply from radiogenic heating of the mantle and establishment of a supercritical vertical temperature gradient. Alternatively, inhomogeneous accretion of the planet could lead to a lower mantle that is less dense than the upper, and as a result a "chemical plume" forms which carries radiogenically rich materials upward under Tharsis. Convection may also have been triggered by formation of the core. Elsasser (1963) proposed that as Earth heated up early in its history, an Fe-FeS-rich layer separated out at intermediate depths. Further heating allowed the Fe-FeS to melt, fall inward, and form the core. Such collapse would be accompanied by convective overturn of the mantle. In the case of Mars, the core-forming process could cause major upwelling and heat release under the Tharsis region.

In an alternative hypothesis, Solomon and Head (1982) proposed that the Tharsis dome is not caused by uplift but is instead a vast accumulation of volcanics. They suggest that the elastic lithosphere of Mars was laterally heterogeneous early in Mars history. Stresses of both global and local origin caused preferential fracturing where the lithosphere was thin, most notably in Tharsis. The fractures provided easy access for magma to the surface, so that the regions of thin lithosphere became regions of especially active volcanism. Volcanic heating maintained a thin lithosphere in the active regions, thereby sustaining the fracturing and volcanism. The process led to permanent topographic and gravity highs and a greatly thickened crust in the Tharsis region. A major advantage of this model is that anomalous dynamical or chemical properties need not be sustained for billions of years in the Martian mantle beneath Tharsis, as is required by most of the other models.

CANYONS

On the eastern flanks of the Tharsis bulge is the vast system of interconnected canyons termed Valles Marineris (Sharp, 1973b; Blasius et al., 1977). The canyons extend from Noctis Labyrinthus at 7°S, 96°W, eastward for a distance of 4500 km until the canyons merge with the main area of chaotic terrain south of Chryse Planitia (fig. 7.29). The entire length is almost one-quarter of the circumference of the planet. The canyon system is widest in the central section between 65°S and 80°W, where three parallel canyons, the Ophir, Candor, and Melas Chasmas, merge to form a continuous depression over 600 km across and in places over 7 km deep. Ophir and Candor Chasmas are closed to the east and west, but Melas Chasma connects with Noctis Labyrinthus to the west via Ius Chasma and with the chaotic areas to the east via the Coprates, Capri, and Eos Chasmas. In general, the depths become shallower away from the cen-

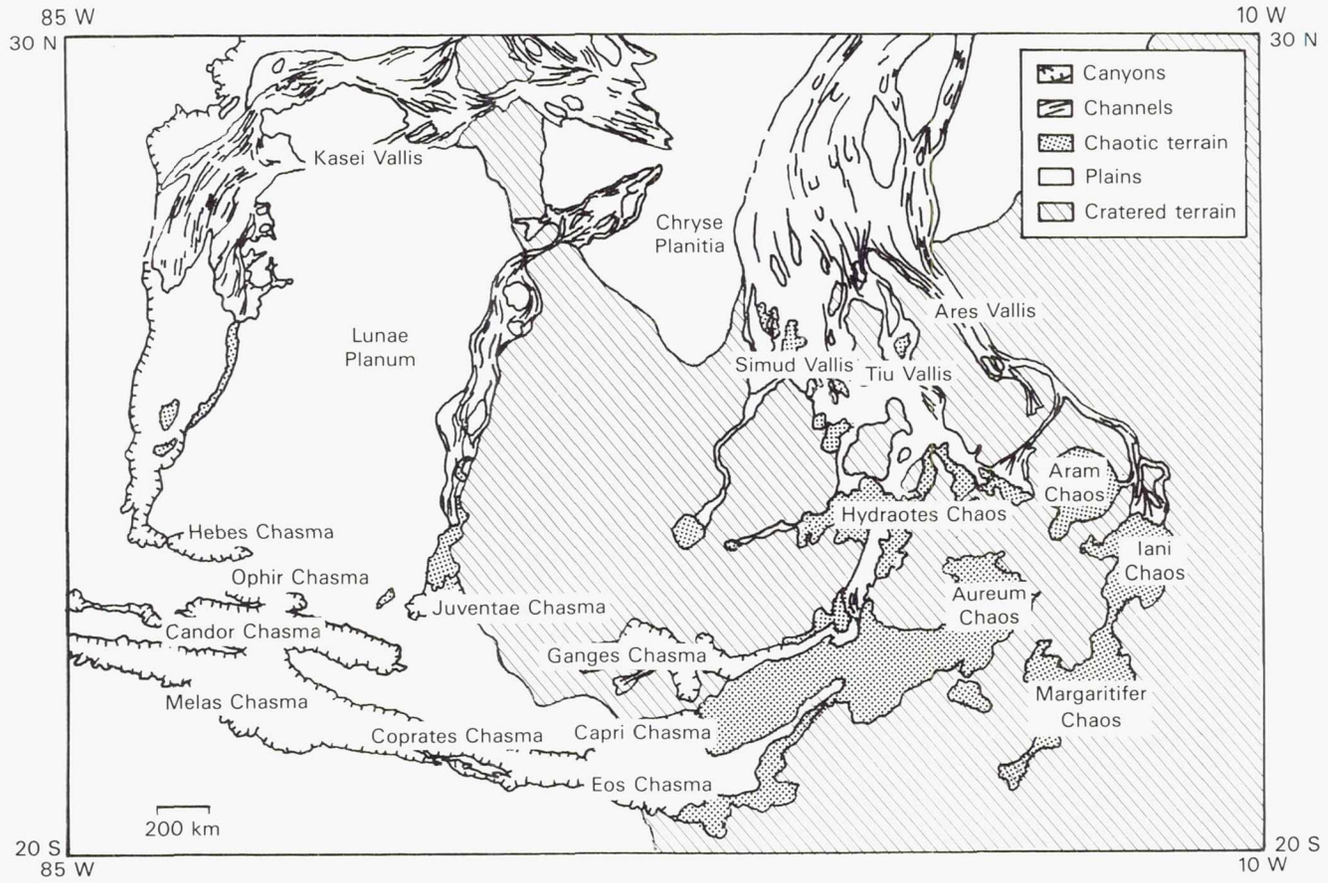

Figure 7.29. Sketch map of the canyons, chaos, and channels around the Chryse basin.

tral section such that the distal portions are only 2 to 3 km deep.

Most of the canyon walls are steeply gullied. The gully walls are generally smooth whereas the spurs between are steep and have sharp, fluted, branching spines. At the head of many gullies are cirque-like embayments in the surrounding plateau. The general morphology is similar to steep terrestrial scarps in desert or alpine environments where the dominant process of landscape evolution is dry mass wasting (Sharp, 1973b; Lucchitta, 1978b). In many places, but especially in Coprates Chasma, the bases of the spurs are truncated by a low scarp that produces a triangular facet at the end of each spur. The scarps are almost certainly formed by faulting and indicate that at least some faulting occurred after the gullies formed, although faulting and erosion probably continued simultaneously. In many places whole sections of the walls have collapsed to form gigantic landslides (fig. 7.30), leaving alcoves in the walls and fan-shaped tongues of debris on the floor (Carr et al., 1976; Lucchitta, 1978a). One slide at the west end of Ius Chasma is 100 km wide and extends completely across the canyon floor. Several of the slides are transected by low inward-facing escarpments, again demonstrating that downfaulting of the floor continued as the walls were eroded.

From the dimension of overridden obstacles, Lucchitta (1978a) estimated that emplacement velocities of the landslides were about 100 to 140 km/hr. She also showed that the effective coefficients of friction are low (<0.1) compared with most terrestrial landslides, which have coefficients in the 0.1–0.5 range. Riding on a cushion of air, or inclusion of various proportions of air, water, or ice within the moving debris have been suggested to explain the low coefficients of friction of terrestrial landslides (Shreve, 1966; Heim, 1932; Varnes, 1958; Kent, 1966; Plafker and Erikson, 1978). Water and ice may have played a similar role in Martian landslides, but atmospheric effects are less likely to have been important on Mars because of the much thinner atmosphere. Water or ice may have played an additional role in triggering the landslides. The depth of the canyons is greater than the depth of the base of the permafrost (Fanale, 1976). Thus, water-saturated materials with relatively low shear

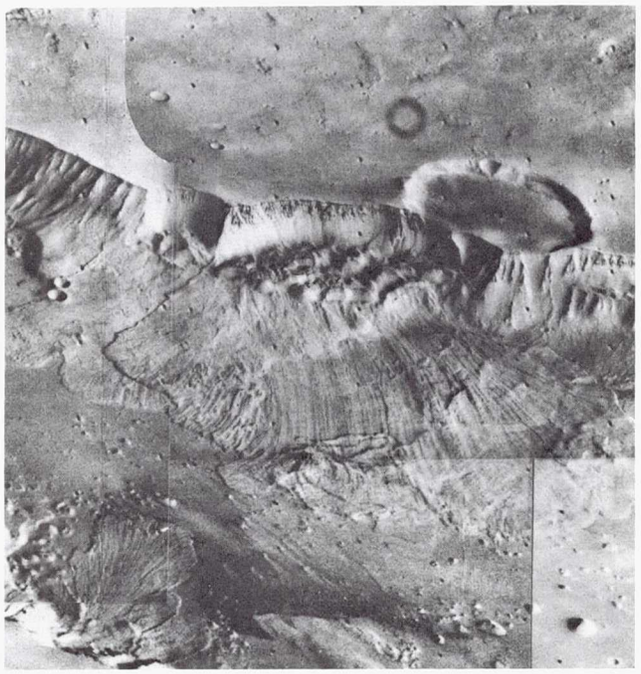

Figure 7.30. Oblique view across Capri Chasma showing landslides on the far wall. The canyon is about 130 km wide and 2 km deep. The landslides have two components: a fan-shaped lower lobe with radial striations, and a blocky, upper cap. The landslides leave alcove-like indentations in the canyon wall (14A29-14A32).

strengths may occur behind the canyon walls making them susceptible to collapse.

In some places, especially on the south side of Ius Chasma, the walls of the main canyon are deeply dissected by tributary canyons (fig. 7.31). The tributaries typically have blunt terminations, V-shaped cross sections, and steep walls that are generally smooth except for some fluting on the upper parts. Sharp (1973b) and Sharp and Malin (1975) suggested that the tributaries formed by sapping, a result of groundwater seepage or melting of ground ice. The recurrent intersection of the tributaries at right angles suggests strong structural control of the erosion. Some of the valleys meet the canyon floor discordantly and appear to be offset by faults. No sizable accumulations of eroded debris from these valleys have been identified on the floor of the main canyon.

The characteristics of the canyon floors change from west to east. In Noctis Labyrinthus, at the western end, the troughs are commonly discontinuous and many individual troughs consist of partly coalesced pits separated by septa. The western parts of Ius and Tithonium Chasmas have similarly segmented floors, and some landslides reach completely across the canyons, creating obstructions. The eastern part of Tithonium Chasma, however, has a relatively flat floor that is continuous with the similarly flat floors of the Melas and Coprates Chasmas to the east. Vague circular structures, resembling buried craters, suggest that parts of the smooth floors are downfaulted segments of the former plateau surface (Blasius et al., 1977).

Within Ius Chasma and Coprates Chasma are ridges several hundred kilometers long, parallel to the length of the canyons. The ridges are gullied in a style identical with that of the canyon walls and are almost certainly remnants of the upland surface. At the east end of the canyons numerous low rounded hills become common on the canyon floors. In the Capri and Eos Chasmas the hills are abundant and merge eastward with chaotic terrain. The low hills also appear to be remnants of the upland surface, but here they have been disturbed by whatever processes caused formation of the chaos. In the eastern parts of the Eos

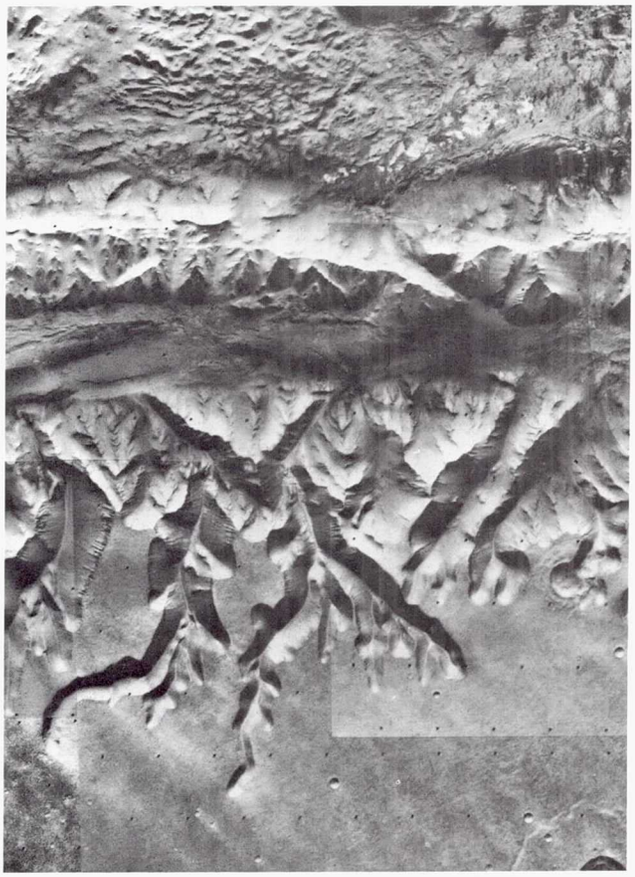

Figure 7.31. Tributary canyons on the south wall of Ius Chasma. Each tributary has an alcove-like termination and the plateau areas between tributaries are undissected, both of which suggest origin by sapping. Note the lack of deposits on the main canyon floor at the mouths of the tributaries. The frame is 110 km across (211-5158).

and Capri Chasmas are some smooth linear features within the rubble on the canyon floors. When traced northeastward, the smooth features merge with channels that contain teardrop-shaped islands. Therefore, there is a transition eastward, from poorly graded discontinuous depressions to channel-like features with graded floors and streamlined landforms.

Layered Canyon Deposits

Layered deposits occur at numerous places within the canyons; they are especially common within the Ophir, Candor, Melas, and Hebes Chasmas but also are present elsewhere (Blasius et al., 1977; Sharp, 1973b; Masursky, 1973). The thickest deposits form flat-topped mesas within the canyon. The flat upper surface resembles that of the surrounding plateau except that it appears to be less cratered and is unfaulted. The sides of the hills formed of the layered deposits have a fine vertical fluting that is distinctively different from the pattern of erosion on the canyon walls. A fine horizontal banding suggests layering on a scale down to the resolution limit of the available photography. In some places, as at the junction of Ophir and Candor Chasmas, the layered deposits appear to rest unconformably on typical dissected remnants of the plateau.

The layered deposits could be simply erosional remnants of the materials into which the canyon is cut. However, this interpretation appears unlikely in view of the relations at the Ophir-Candor divide, where the contrasting erosional styles and discordant layering between sediments and canyon wall are striking. Sharp (1973b) and McCauley (1978) both agree that the layered deposits formed after the canyons and have since been partly eroded themselves. Sharp (1973b) suggested that they may have been formed by materials derived by recession of the canyon walls after formation of the main canyon. McCauley (1978) proposed that the canyon sequences were deposited within lakes, asserting that no other process can explain the horizontality and continuity of the beds and the subtle differences in reflectance and competence of the various members in the sequence. While the idea of lakes within the canyons is highly speculative, lakes conceivably could form by release of groundwater, either catastrophically or by seepage, provided they were stabilized by formation of a thick ice cover. Wallace and Sagan (1979) pointed out that under present climatic conditions a lake on Mars will rapidly ice over and its lifetime would depend on the balance between seepage into the lake and sublimation of the overlying ice. McCauley further proposed that the lakewaters in the central section were catastrophically released, that they flooded down Coprates Chasma and ultimately formed some of the flood features observed in the chaotic terrain to the east.

Schultz and Lutz-Garihan (1981), noting the close resemblance between the layered deposits in the canyons and those at the poles, proposed that the canyons were formerly located at the poles and acquired their layered deposits at that time. This seems highly unlikely. The layered deposits in the canyons are relatively young and there is evidence from several other sources, such as crater morphology and differing erosional styles at high and low latitudes, that suggests that the poles have been stable for most of Mars' decipherable history. Moreover, as we have seen, the Tharsis bulge is an ancient feature, and for the planet to be dynamically stable, the pole must have been in such a position that Tharsis was centered on the equator for most of Mars' history. A final possible explanation of the canyon sediments is that they are layered ash deposits or ignimbrites.

Formation of the Canyons

The precise way in which the canyons formed is not known, but faulting and secondary enlargement by mass wasting have clearly been important. Evidence of faulting is strong, and includes alignment of the canyons parallel to the Tharsis radial faults, apparent fault-scarps at the bases of many of the walls, and the presence on the canyon floors of indistinct craters which suggests that the floors are, in places, downfaulted sections of the former plateau surface. A number of authors (Allegre et al., 1974; Sengor and Jones, 1975; Courtillot et al., 1975; Masson, 1977) have suggested that the Valles Marineris are analogous to terrestrial rift valleys and opened up as a consequence of lateral movement of the Syria-Solis Planum block to the south and west. As pointed out by Sharp (1973b) and Wise et al. (1979b), however, the general configuration of the canyons is inconsistent with large amounts of lateral extension. Particularly difficult to explain are the large central canyons, Ophir and Candor, which by the extension hypothesis should have transform faults at their east and west ends, and evidence of extension in the plateau beyond their terminations. Since neither of these conditions is fulfilled, formation of the canyons by simple extension appears unlikely.

Sharp (1973b) suggested that the canyons formed by a combination of faulting and scarp recession. He proposed that the first step was formation of parallel, roughly east–west-trending grabens. Then, differential subsidence caused lines of pits to form within the grabens. Continued subsidence and perhaps wall recession enlarged the pits until they merged longitudinally to form narrow troughs with scalloped walls. Lateral enlargement by sustained subsidence and further wall recession caused adjacent troughs to merge and form wider canyons, sometimes leaving longitudinal ridges along the former divides. Several such lateral mergers would be required to form the wide central troughs. Wall recession could have resulted from a combination of several processes, including dry mass wasting, groundwater sapping, and sublimation or melting of ground ice.

The main problem with any mechanism involving large-scale erosion is removal of the erosion products. The volume of the canyons is close to 10^6 km^3 (Sharp, 1973a). Some of the material may have been removed by the wind. Cutts (1973) noted that the volume of the polar layered terrains is almost identical to the volume of the canyons and suggested that wind was mainly responsible for removal of material to create the canyons, and that most of the debris was ultimately deposited at the poles. Sharp (1973b) pointed out, however, that deflation tends to turn itself off by forming a protective lag concentrate of the coarser debris, and he questions that deflation could have been a significant factor in the excavation. We have already discussed the possibility that water could have transported material through the eastern sections of the canyons, where smooth floors merge with distinctly fluvial features to the east. Nevertheless, water does not appear to have been important in creating the poorly graded western parts of the canyons or the completely closed Hebes Chasma to the north of the main canyon. The negative volume may have been caused mainly by tectonic subsidence, with the materials eroded from the walls mostly accumulating on the canyon floors, which continued to subside as erosion proceeded. The contribution of other processes, such as deflation and fluvial transport, toward removal of debris is unclear.

CHANNELS AND VALLEYS

The channels of Mars have posed some of the most controversial questions of Martian geology. The main issue is whether or not the channels were formed by running water. Liquid water is unstable under the conditions that currently prevail at the surface of the planet. With surface temperatures that range from 130 K to 300 K (Leighton and Murray, 1966; Kliore et al., 1965; Hess et al., 1977), liquid water will rapidly evaporate or freeze depending on location, time of day, and season. Several authors have therefore suggested alternative means of forming channels such as faulting, lava erosion, and wind action. The general consensus, however, still remains that many of the channels were formed by running water so different conditions in the past may be implied.

Sharp and Malin (1975) identified three main types of channels: fretted channels, runoff channels, and outflow channels. Fretted channels are broad, flat-floored valleys with steep walls and intersection relations with the surrounding terrain that suggest that they have grown in width by some process of scarp retreat. Most possess tributaries and become narrower upstream. They occur within the so-called fretted terrain, which is in two belts, 25° latitude wide and centered on 40°N and 45°S. In these belts, debris flows are common adjacent to steep slopes. The relations suggest that the fretted channels form by lateral enlargement of other channels by mass wasting, although precisely how the eroded wall materials are transported for great distances downstream is not clear.

Runoff channels start small, increase in size downstream, and have V-shaped cross sections (fig. 7.32).

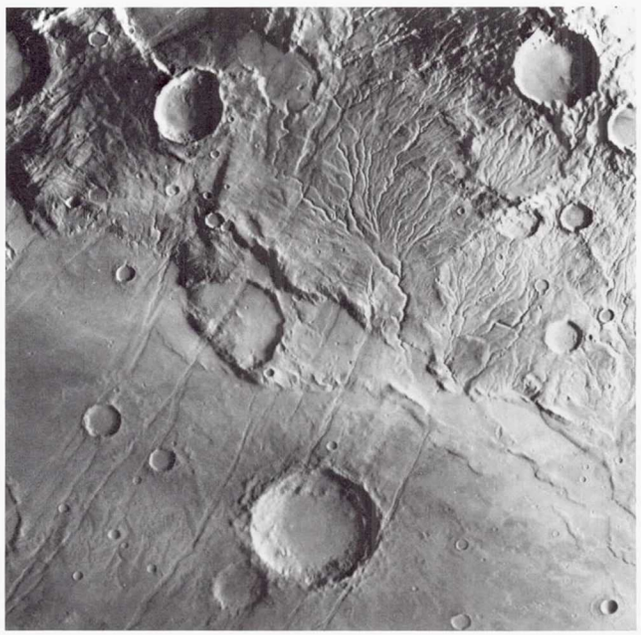

Figure 7.32. Dense tributary networks in the old cratered terrain at 48°S, 98°W. The frame width is 320 km (606A56).

The most common type is a simple gully, but complex, branching networks with a hierarchy of tributaries that feed one another are common. Runoff channels occur almost exclusively in the old cratered terrain, which has few areas that are left undissected. In contrast, more sparsely cratered regions of the planet are almost devoid of runoff channels, although some are present as on the south rim of Ius Chasma and on the flanks of Alba Patera. Runoff channels are almost certainly valleys and not true channels, and will be referred to as such in the subsequent discussion (Pieri, 1976).

The valley networks are probably largely restricted to the oldest terrain because they themselves are mostly old (Pieri, 1976; Carr and Clow, 1981). Other explanations such as a greater erodibility of the old terrain, or a preferred location of water there, while possible, are less likely. Certainly an old age for the valleys is the simplest explanation of the repeatedly observed truncation of valleys in the old cratered terrain by younger plains.

Martian valley systems superficially resemble terrestrial river valleys and are difficult to reconcile with any origin other than erosion by running water. Several alternatives have been explored to explain Martian channels in general. These include erosion by lava (Carr, 1974b; Schonfeld, 1977); erosion by liquid hydrocarbons (Yung and Pinto, 1978); erosion by wind (Cutts and Blasius, 1981); erosion by ice (Lucchitta, 1980); and origin by faulting (Schumm, 1974). While some of the alternatives may plausibly explain some of the features of the outflow channels, as discussed below, they fail to explain the integrated tributary networks. Volcanism would require lava sources at the heads of each tributary in areas where there is no indication of volcanic activity. Wind does not form complicated drainage networks, particularly with branches meeting at large angles, because of the strong coupling of flow near the surface with regional flow patterns higher in the atmosphere. Ice generally does not form well-integrated, finely branching networks. Faulting can occasionally simulate drainage patterns, but the repetitive mimicry from network to network is hardly plausible. Finally, there is no direct evidence of hydrocarbons on the Martian surface despite attempts to analyze for them, so invoking hydrocarbons raises more problems than it solves. Running water seems to be the most plausible erosive agent.

The pattern of dissection of the old cratered terrain suggests an immature drainage system. The drainage networks are generally open with wide, undissected interfluves between the branches. The networks are widely spaced and in most cases the distance from the most distal tributary to termination of the trunk valleys is short (<300 km) compared with valley systems on Earth, although exceptions occur. There appears to have been little competition between adjacent basins. Thus, single streams have not grown to dominate drainage over large areas. Drainage patterns are generally local with the channels converging on some local sink. The only areas with consistent drainage directions are those close to the plains–upland boundary, where drainage is toward the plains and in Margaritifer Sinus, where drainage is toward the chaotic terrain. Most valleys end abruptly with no indications of deposits at their mouths.

Several characteristics of the drainage networks, such as cirque-like terminations to tributaries, undissected interfluves, and drainage through crater walls into craters, suggest that groundwater sapping has been important in their development (Pieri, 1979). However, surface runoff was probably also involved. Sustained erosion is required to carve the valleys, and in order to sustain seepage from a groundwater system some recharge mechanism is needed; the water that passes over the surface must somehow be returned to the ground. Because the ground is currently frozen to substantial depths, replenishment of groundwater from surface runoff is difficult. Clifford (1981) noted that water on the surface will ultimately enter the atmosphere then freeze out at the poles, and suggested that the global groundwater system is recharged by basal melting of the polar ice. Another possibility is that, at the time the valleys formed, climatic conditions were such that the groundwater system could be recharged directly from precipitation and that the valleys formed by a combination of sapping and runoff. Recycling does not necessarily imply rain. Precipitation out of the atmosphere could be as ice, such as was observed on a small scale at the Lander 2 site (Jones et al., 1979).

Formation of the valley networks almost certainly requires climatic conditions different from today's. Lingenfelter et al. (1968) showed that with large discharges, flow of water could be sustained even across the lunar surface, where conditions are less permissive of flow than on Mars. Wallace and Sagan (1979) also demonstrated that flow of moderate discharge could be sustained under present Martian conditions provided the stream was covered with 10–30 m of ice. However, neither of these conditions is likely to apply to the formation of the valley net-

works. The distal parts of the tributary systems were probably composed of small streams as in terrestrial river systems, and such streams would freeze quickly under present climates. The valley networks appear to indicate more temperate conditions early in the planet's history.

The third class of channel identified by Sharp and Malin (1975), the outflow channels, include those that are widely interpreted as having been formed by catastrophic floods (McCauley et al., 1972; Masursky, 1973; Masursky et al., 1977; Milton, 1973; Baker and Milton, 1974; Hartmann, 1974; Sharp and Malin, 1975; Nummedal, 1976; Baker, 1977; Carr, 1979; Nummedal and Prior, 1981). Outflow channels typically emerge full born from chaotic terrain; they are widest and deepest close to their sources and have few, if any tributaries. Many are very large by terrestrial standards. An unnamed channel which emerges from Juventae Chasma and extends northward for several hundred kilometers across Lunae Planum has scoured a swath that is in places over 100 km wide. Sections of Kasei Vallis (fig. 7.33) are over 200 km wide, although the wider areas may result from the merging of several channels. Ares Vallis, which is a single discrete channel deeply incised into the uplands south of Chryse Planitia, is 20 to 30 km wide over much of its length. Most outflow channels occur around the Chryse basin (fig 7.29); however, several occur elsewhere, such as northwest of Elysium, along the plains-upland boundary in Memnonia, and in Amazonis Planitia.

Figure 7.33. Synoptic view of the upper reaches of Kasei Vallis. The channel originates in a vague depression in the left of the picture, where numerous streamlined islands are visible. The channel then continues to the east where it is deeply incised into Lunae Planum. The scene is 700 km across (211-5642).

The large channel that arises in Juventae Chasma, in southeastern Lunae Planum, illustrates many of the characteristics of outflow channels. It arises full scale from some chaotic terrain in the northern part of Juventae Chasma. North of the chaotic area the surface of Lunae Planum is modified by branching channels which diverge and converge around obstacles such as low hills and craters. Longitudinal grooves, teardrop-shaped islands, and arcuate escarpments can be traced about 1000 km northward, where the flow lines turn northeastward and converge in several channels cut in the old cratered terrain between Lunae Planum and Chryse Planitia (fig. 7.34). On Chryse Planitia the flow lines diverge across the plains to form a complex pattern of broad shallow channels, elongate islands, and longitudinal grooves (fig. 7.35). Scour is especially marked where flow lines converge around craters and in the gaps of ridges that have partly blocked the flow. Similar relations occur farther north where Kasei Vallis enters Chryse Planitia, and at the south end of Chryse Planitia where the plains have been modified by several large channels that emerge from the main areas of chaos at the east end of the equatorial canyons. The northward extent of the Chryse channels is unclear, but sculptured forms can be traced as far as 40°N.

Of somewhat different morphology are the channels that start to the northwest of Elysium (fig. 7.36). These arise in graben-like depressions, adjacent to Elysium Mons and Hecates Tholus, then wind their way northwestward, branching and rejoining in a complex pattern. Flow was restricted to discrete channels so that broad swaths of the surface were not eroded, as around Chryse Planitia.

Unlike the runoff channels, which appear to be mostly old, the outflow channels have a wide range of ages (Masursky et al., 1977). Some large discontinuous channels such as Ladon Vallis in the cratered uplands may predate the decline in impact rates around 3.9 billion years ago. Others, such as Mangala

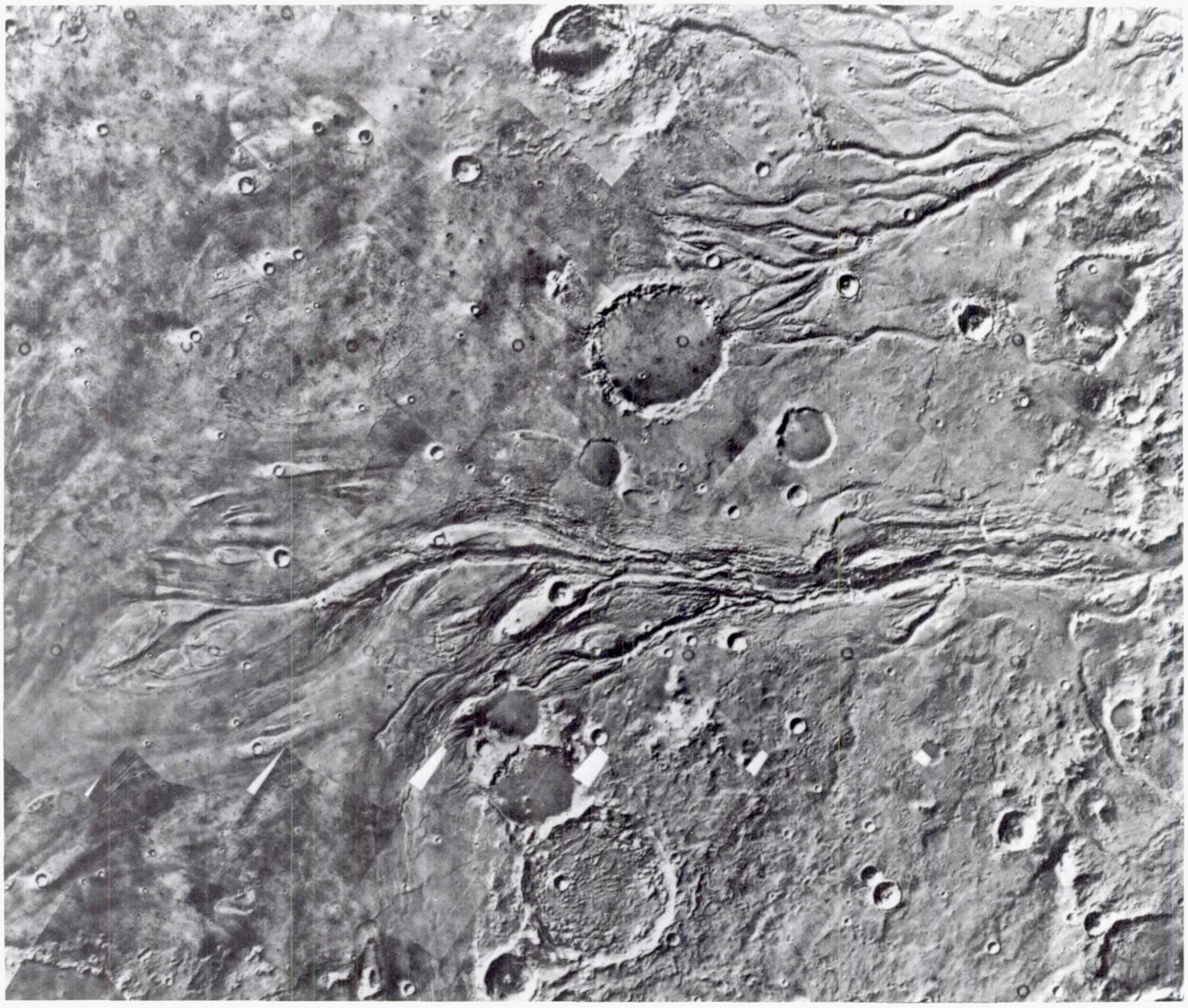

Figure 7.34. Valleys in the old cratered terrain between Lunae Planum on the left and Chryse Planitia, off the picture to the right. Maja Vallis is in the center of the scene; Vedra Vallis is toward the top. The picture is 300 km across (211-5190).

Vallis and the unnamed Amazonis channel, are only sparsely cratered. Mangala Vallis has 650 craters >1 km per 10^6 km^2; the Amazonis channel even fewer (Carr and Clow, 1981). Most of the large channels around the Chryse basin have crater numbers of 2000–3000 craters, which places their probable time of formation before 2.5 billion years ago.

The outflow channels have been compared (Baker and Milton, 1974; Baker and Kochel, 1978; Milton, 1973) with the channeled scablands of eastern Washington (Bretz, 1923, 1969; Baker, 1973), the largest known terrestrial flood feature. The scablands formed in the late Pleistocene following failure of an ice dam behind which had ponded Lake Missoula, an enormous lake that covered large parts of Idaho and western Montana. Baker (1973) estimated that peak discharges during the flood were close to 10^7 m^3/sec. The high discharges accomplished an enormous amount of erosion in a few days, creating streamlined islands, inner channel cataracts, longitudinal scour, and an anastomozing pattern of channels that cover close to 100 000 km^2. Baker and Milton (1974) made a detailed comparison of the channeled scablands and large Martian channels and concluded that the resemblance between the two was so close that a common origin—catastrophic flooding—was inescapable.

Several mechanisms have been proposed for the massive release of water onto the Martian surface.

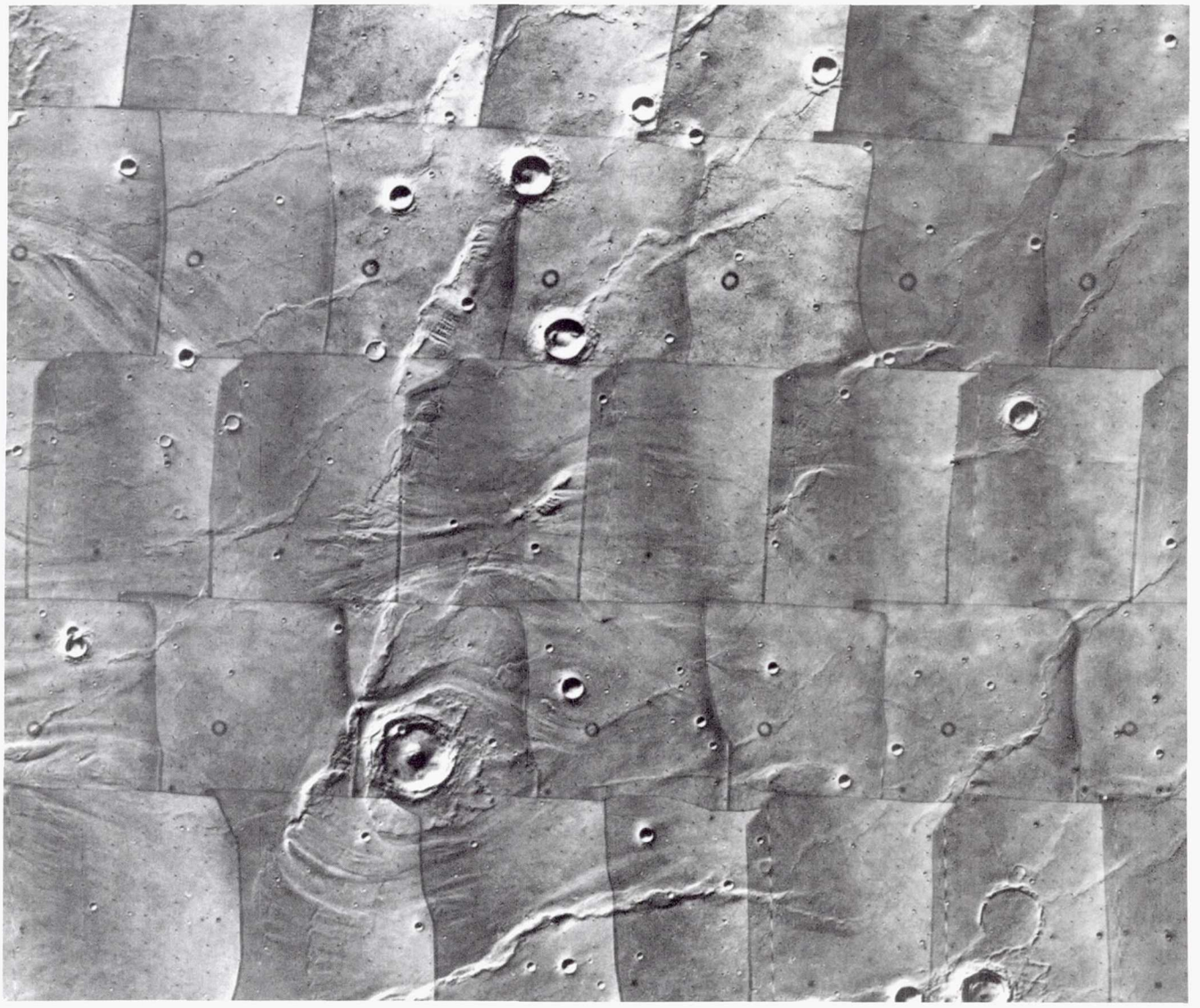

Figure 7.35. Chryse Planitia just to the east of Maja Vallis. Flow from Maja Vallis seemingly spread over the Chryse plains, was temporarily dammed by low ridges, then funneled through gaps where extensive scour took place. The large crater at bottom center is 13 km across (P-17002).

McCauley et al. (1972) and Masursky et al. (1977) proposed that the floods are analogous to Icelandic *jokulhlaups* or glacial bursts. These result from melting of an ice sheet at the base by volcanic heat. The water accumulates under the ice and then is released periodically as massive floods. As applied to Mars, high heat flows or volcanic eruptions in the chaos regions would melt near-surface ice and cause floods. However, the lack of evidence for either volcanic activity or ice in the source regions undermines the credibility of this hypothesis. Clark (1978) suggested that the water could be derived from subsurface heating of hydrated minerals. He suggested that water from a deep-baked zone could migrate upward and accumulate below the frozen near-surface layers and periodically break out to form the flood features. Clark acknowledged, however, that the existence of a deep, hydrated regolith is not certain and that the kinetics of the process are poorly understood. Carr (1979) suggested that the floods could form by breakout of water contained under high pressure within aquifers. Water, trapped below the thick permafrost that is everywhere present on Mars, would percolate slowly to low areas where a hydrostatic head would slowly build. Because of the large relief on the Martian surface, pressures could become so large as to disrupt the aquifer and

Figure 7.36. Channels northeast of Elysium Mons. The channels start in graben-like depressions close to the volcano but become more fluvial-like to the northwest, as in this scene. The picture is 150 km across.

enable the water to reach the surface under great pressure. Nummedal (1979) suggested that the channels and chaos are liquefaction scars caused by disintegration and flow of waterlogged near-surface materials. By this hypothesis, the scour and streamlining within the channels are caused by slurries of material that have broken away from cliff faces in source regions and moved down the channel. Lucchitta (1980), in contrast, proposed that the channels were cut by ice fed by artesian springs. She pointed out the many similarities between the Martian channels and scoured glacial terrain in northern Canada and ice-rises in Antarctica. Finally, Cutts and Blasius (1981) proposed that the large circum-Chryse channels were cut by the wind, and Schonfeld (1977) suggested they were cut by lava, but neither of these two proposals has gained wide acceptance (Carr, 1981).

The above hypotheses are not mutually exclusive, and different processes may have dominated in different cases. The circum-Chryse channels which scour broad swaths of terrain may, for example, originate in a different manner from the channels northwest of Elysium, in which flow appears to have been confined to discrete channels. Moreover, several different processes may have contributed to formation of any one channel. Catastrophic break-out of ground water may have resulted in liquefaction of the aquifer so that a slurry is brought to the surface. This could initially have formed a flood but as the discharge rate dropped, the slurry could have frozen and formed a dirty glacier. Finally, the channel may have been modified by the wind after its formation. The channel would thus retain the imprint of a variety of processes, all having contributed to the final channel form.

In summary, the valley networks provide evidence of an early period of temperate climatic conditions under which liquid water could flow across the surface at relatively modest discharges. The duration of these conditions must have been relatively short or erosion rates were very low, because a mature drainage system never developed. Outflow channels appear to have formed throughout Martian history, although most are also old. They probably could form under present climatic conditions. The most plausible mechanism for their formation is catastrophic flooding, although other processes may have been involved. Fretted channels form by enlargement of other channels by mass-wasting.

WIND

Wind erosion and transport are among the few geologic processes that have been observed in action on Mars. The waxing and waning of dust storms have been followed, streaks have been observed to dissipate and reform, and wind speeds have been measured at the Viking landing sites. Large-scale wind erosion features are, however, relatively rare, and despite billions of years of wind action much of the old cratered terrain remains intact. Moreover, subtle features on the ejecta of impact craters are retained despite ages that must be in the many hundreds of millions of years. It appears that while the wind is effective in moving loose debris, erosion rates on consolidated rocks are extremely slow.

Debris is moved by the wind either as a suspended load, by saltation (bouncing of particles across the surface), or by creep (the slow shifting of material across the surface as it is impinged upon by saltating particles). On Earth, the optimum size for movement by the wind is around 0.08 mm (Bagnold, 1941). Larger particles are constrained by their inertial resistance; smaller particles resist dislodgment because of intergranular cohesion, drag inefficiencies due to the small size, and immersion of the particle in the very-near-

surface laminar flow regime. Wind tunnel studies show that on Mars the optimum size is near 0.1 mm, close to that on Earth. Threshold wind velocities to move the particles are, however, considerably higher, ranging from 2.4 m/sec for a 10 mb atmosphere to 4 m/sec for a 5 mb atmosphere (Greeley et al., 1980). The equivalent values for Earth are close to 0.2 m/sec. The 2.4 m/sec threshold velocity is equivalent to free-stream (above the boundary layer) winds of 45–125 m/sec (Greeley et al., 1980). Wind speeds at the 1.3-m height of the meteorology boom on the Viking landers should be half these values. Gusts as high as 25 m/sec were recorded at the Viking sites, which is only just within the range for particle movement, so the lack of observed movement at the sites is not surprising.

Saltating or sand-size particles typically form dunes (fig. 7.37). The most extensive array of dunes on Mars are around the north pole, where the dunes form an almost continuous collar, in places hundreds of kilometers wide, around the layered deposits (Cutts et al., 1976). At high southern latitudes dunes are also common, but they are mostly restricted to within craters or adjacent to escarpments. In low to mid latitudes, dunes are less common but still present in sheltered areas, such as within the canyons or in valleys along the plains–upland boundary. The dunes appear to be mostly transverse types which break up into individual barchans around the dune-field edges; longitudinal dunes are rare or absent (Breed et al., 1979). The barchanoid types are identical in shape to terrestrial barchans, suggesting that they form by the same process, that is, by saltation of sand grains up the windward slope and repetitive collapse of the lee slope.

Figure 7.37. Dunes at 47°S, 340°W. A group of barchanoid dunes at right center merge with a field of transverse dunes in the upper parts of the frame, which is 60 km across (575B60).

The source of sand grains on Mars is puzzling. On Earth, most dunes are of quartz or, less commonly, calcite; other minerals tend to cleave or weather more easily so rarely accumulate as sand. On Mars, quartz-rich rocks are probably rare and although abundant particulate debris was observed at both Viking landing sites, the particles were in the micrometer rather than millimeter size range. Sand-size particles could form by electrostatic aggregation (Krinsley, 1979), or by cementation by frost; however, Sagan et al. (1977) argued that such aggregates could not long survive the continual reworking by the wind. Alternatively, the sand may, like most terrestrial sand, be of fluvial origin and derived from the large flood channels that drain northward toward the north polar region.

Movement of fine-grained debris across the surface results in changes in the albedo markings. In some areas such as Syria Planum, sharp albedo boundaries extend for long distances and show no obvious relation to topography. The most common markings are, however, splotches and streaks that are clearly related to local relief. Splotches are irregular dark markings within craters or adjacent to low cliffs or escarpments; streaks extend downwind from craters, and may be light or dark.

Attempts have been made to model crater-related streaks in wind tunnel experiments. As air flows over and around a crater, two vortices separate, wrap tightly around the upwind half of the crater rim, then trail off downstream. Erosion takes place preferentially along the line of the vortices and deposition takes place in the dead zone between. The dimensions and shape of the dead zone depend on wind velocity, with lower velocities resulting in more rapid convergence of trailing vortices. Three main types of wind streak have been recognized (Thomas and Veverka, 1979; Sagan et al., 1973; Greeley et al., 1978; Veverka and Thomas, 1981). Bright streaks are interpreted as the result of preferential deposition of dust in the lee of obstacles and removal in the intervening areas. Some indication of how bright streaks may look on the

ground is provided by the view from Viking Lander 1 (fig. 7.3). Many rocks have tails of debris associated with them and the larger drifts may be in dead zones between large boulders. Dark streaks may be of two kinds. Erosional dark streaks are believed to occur where a thin veneer of bright dust has been removed by turbulence downwind of obstacles. In contrast splotch-related dark streaks originate at a dark splotch, usually within a crater. Thomas and Veverka (1979) interpreted most of these as deposits of material deflated from dunes within the crater. Commonly the dunes can be seen. Other splotches and their associated dark streaks may, however, be erosional, as demonstrated by their color signature (Soderblom et al., 1978), so splotch-related streaks may result from different causes.

The planet-wide streak pattern was observed during and after the 1971 dust storm and before, during, and after the 1977 dust storms. In general, light streaks are more stable than dark streaks (Sagan et al., 1973). The dark streaks tend to disappear while the dust storm is in progress and reform as it wanes, preserving a record of winds during late southern summer. The pattern after the 1971 and 1977 storms was similar (Thomas and Veverka, 1979). Between the equator and 30°N, flow is from the northeast; south of the equator, winds become more northerly and swing around to come from the northwest between 20° and 30°S. At higher southern latitudes the winds are mostly east to west.

Although the loose debris on the Martian surface is continually being reworked by the wind, erosion of competent rocks is remarkably slow. Arvidson (1979) pointed out that preservation of craters and wrinkle ridges in Chryse Planitia limits the amount of erosion since the plains formed to a few meters at most. Assuming an age of around 3 billion years, he estimated erosion rates are only 10^{-3} μm/yr. Even if this estimate is off by a factor of 100, it is still low compared to some early estimates of 3×10^3 μm/yr for Martian erosion rates (Sagan, 1973). Chryse Planitia appears to be typical of equatorial plains in general, for they commonly have well-preserved, delicate lava flow textures and impact features preserved on seemingly ancient surfaces.

In some areas wind erosion may have been more efficient, probably because of friable, easily eroded rocks at the surface. As we saw earlier, many of the characteristics of the high-latitude plains, particularly pedestal craters, suggest repeated deposition and stripping by the wind. Etched terrain at the south pole (Sharp, 1973c), and on the floors of Argyre and Hellas, also suggests wind action. But where wind erosion features are best developed is in southern Amazonis between latitudes 5°S and 10°N and longitudes 135°W and 185°W (Ward, 1979). In this area a seemingly thick, sparsely cratered deposit cuts across the plains–upland boundary (fig. 7.38). On the surface of the unit are numerous wind erosion features such as irregular hollows, fluted escarpments, yardangs, and pedestal craters. The yardangs, double-tapered, flat-topped ridges up to 50 km long and 1 km across, are mostly slightly sinuous and occur in closely packed fields (fig. 7.39). Ward (1979) suggested that the preferential development of yardangs in this unit indicates that it is friable and easily eroded and suggested ignimbrites, porous lava or palagonite-rich mudflows as possible materials.

Late in the Viking mission, Orbiter 1 acquired high-resolution (10–40 m) coverage over a broad swath of terrain between 30° and 40°N and between longitudes 280° and 320°W. Much of this terrain has an etched

Figure 7.38. Synoptic view of friable, easily eroded deposits, that overlap the boundary between the old cratered terrain and younger plains at 6°S, 157°W. The scene is 710 km across (606A62).

Figure 7.39. Wind fluting and possible etch-pits in the plains just south of Olympus Mons. The frame is 24 km across (693A38).

appearance as though layered near-surface rocks had been partly eroded by the wind. Irregular flat-floored pits are surrounded by near-vertical walls, and irregularly shaped mesas appear to be remnants of a former continuous cover (fig. 7.40). How typical this is of the whole Martian surface is not known, but similar textures are occasionally seen in high-resolution pictures from other areas. It appears that in these areas the morphology of the surface at a scale of 100 m is controlled by processes such as impact and volcanism, but at scales of around 10 to 20 m the effects of wind start to dominate.

THE POLES

The most distinctive geologic features of the poles are thick layered deposits that extend from each pole outward to about 80° latitude. The deposits are believed to be mixtures of volatiles and dust that have been reworked late in the history of the planet; their layering and surface relief record variations in deposition and erosion, hence, climates, in the recent geologic past. Before examining the layered deposits in detail we will look briefly at the present conditions at the poles and then assess what impact climatic variations might have on the formation of the layered deposits.

A seasonal cap of carbon dioxide forms around the pole each fall and dissipates in spring. Formation in the fall generally cannot be seen because of clouds of condensed CO_2 over the growing cap. From variations in atmospheric pressure caused by condensation of the seasonal cap, Hess et al. (1979) calculated that the seasonal cap averages only a few tens of centimeters in thickness. The southern cap is more extensive than that in the north because of the relatively long southern winters. At its maximum it reaches 50°S; in contrast, the northern cap extends only to about 65° latitude at its maximum.

The retreat in spring is nonuniform in longitude, yet reproducible from year to year. Temporary outliers are left behind, particularly in the south where the terrain is more rugged, but these generally dissipate within days. At both poles a permanent or remnant cap is left behind in summer and the final stage of the retreat is the defrosting of valleys, walls, and escarpments within the remnant cap, which gives the

Figure 7.40. Cratered terrain at 29°N, 295°W. The surface has an etched appearance as though horizontal layers had been partly stripped away. Picture width is 50 km (184S21).

cap its characteristic swirl texture. The residual cap in the south is about 350 km across and its center is offset 4° from the pole along 30°W longitude. In the north, the residual cap is around 1000 km across and comparable in extent to the layered deposits. As a result, in mid-summer the southern layered terrains are partly frost-free, whereas those in the north are never seen without a frost cover.

The residual caps differ from one another in composition. The northern residual cap is almost certainly water-ice. Relatively large amounts of water vapor (80–100 pr μm) occur in the atmosphere over the cap in summer (Farmer et al., 1976) and temperatures on the frosted areas are around 205 K, close to the frost point of water in an atmosphere containing a few tens of precipitable microns of water (Kieffer et al., 1976). The temperature is well above the frost point of CO_2 (148 K) so little is likely to be present. In contrast, the measured temperatures over the southern residual cap are around 160 K, which probably result from CO_2-frost-point temperatures (148 K) on the frosted ground and higher temperatures on the defrosted ground (Kieffer and Palluconi, 1979). Little water was detected over the cap, but at these temperatures the vapor pressure of water is extremely small. Even if the atmosphere was saturated the amounts present would be below the detection limit of the instruments on the Viking orbiters (Farmer and Doms, 1979).

The differences between the two residual caps are probably caused by the global dust storms (Kieffer and Palluconi, 1979). The northern seasonal cap forms when large amounts of dust are in the atmosphere, so it may incorporate a significant amount of dust. Indeed, Pollack et al. (1979) suggested that condensation of the northern cap may play a significant role in scavenging dust from the atmosphere. In contrast the atmosphere is clear when the southern cap forms. In the north during spring and summer, therefore, dirty CO_2-ice is exposed to the Sun's radiation through a clear atmosphere and all the CO_2 dissipates, leaving only a remnant water cap. In contrast, during summer in the south clean ice is shielded from the Sun by a dirt-laden atmosphere and as a consequence CO_2 is still retained in the remnant cap. Whether the southern remnant cap also incorporates significant amounts of water is not known. The behavior of the caps must alternate with the precessional cycle so that 25 000 years from now the south pole should have the water-rich remnant cap.

The layered deposits lie mostly within the 80° latitude circle. They have a roughly horizontal layering best seen on defrosted escarpments or on slopes within valleys that are set into the layered sequence. The surfaces of the deposits are very sparsely cratered, and impact scars are not seen in the layers exposed in the valley walls. The lack of craters appears, therefore, to be truly an indication of a young age and not the result of some annealing process. The valleys spiral out from the pole, counterclockwise in the north and clockwise in the south, to give the remnant caps their characteristic swirl texture. Two especially large valleys, Chasma Boreale in the north and Chasma Australe in the south, cut across the general valley pattern. The thickness of the deposits has been estimated at 1–2 km in the south and 4–6 km in the north (Dzurisin and Blasius, 1975). The layering continues down to the limiting resolution of the available photographs. The outer boundary of the deposits is sharply demarcated by a generally convex-outward escarpment (fig. 7.41).

The layered deposits are believed to be accumulations of volatiles and dust, with the layering possibly caused by variations in accumulation rates of the two components (Murray et al., 1972; Cutts, 1973; Cutts et al., 1976; Sharp, 1974). The deposits may be accumulating at the north pole because the atmosphere is dusty when it forms and CO_2 may scavenge dust from the atmosphere as it condenses to form the seasonal cap. In 25 000 years dust storms will be occurring in northern summer, and dust accumulating at the south pole.

Climatic conditions are, however, subject to longer term changes because of the eccentricity and obliquity cycles (Murray et al., 1973; Ward, 1974). Variations in eccentricity affect the magnitude of the differences between the two poles; variations in obliquity affect the latitudinal distribution of the Sun's radiation. Clearly, such variations could have a major effect on the incidence and intensity of dust storms, on the stability of volatiles at the poles and the magnitude of the local winds, and so greatly affect depositional and erosional rates. Precisely how they are affected is not known.

The apparently young age of the layered deposits is also puzzling. It is unlikely that we happen to be viewing the poles just after deposition at the poles started. More likely deposition has occurred throughout geologic time but older deposits have been erased. Support for this conclusion is the evidence of scarp

Figure 7.41. Edge of the south polar layered deposits at 86°S, 357°W. The edge of the layered deposits is indicated by an outward-facing escarpment in the left of the picture. Layering is visible on defrosted areas in the right of the picture. Pits in the layered deposits may be secondary cratered or caused by the wind. The scene is 250 km across (421B77-80).

retreat around the edge of the southern layered deposits, the etch-pitted terrain in the south (Sharp, 1973c), which appears to be a remnant of former layered deposits, and outliers of layered terrain outside the main body, in the north.

The origin of the escarpments and valleys within the layered deposits has been the subject of some debate. Murray and Malin (1973) suggested that the swirl pattern is the result of deposition around the poles and that the pole position has slowly shifted with time. This now seems unlikely in view of the young age of the topography and inconsistency in pattern of movement indicated at each pole. Cutts (1973) and Sharp (1973c) suggested that the valleys are eroded by the wind, although they noted that in the north the valleys mostly curl in the anti-coriolis direction. Howard (1978) proposed that the present topography is in dynamic equilibrium with present climatic conditions. He suggested that ice sublimes on equator-facing slopes and recondenses on adjacent flats. As a result, escarpments are continually being eroded while moving slowly across the layered sequence. Their curvature is caused by slight differences in morning and afternoon temperatures, which results in slightly greater erosion on scarps with a westward component. Cutts et al. (1979) alternatively suggested that the valleys and escarpments are not caused by erosion, but rather, represent areas where deposition did not occur because of higher surface temperatures on the darker sloping ground.

In summary, deposition and erosion rates of the layered deposits may sensitively depend on climatic variations, which in turn depend on perturbations in the motions of the planet. The climatic variations did not necessarily result in large deviations from the present conditions; alternation of conditions between the two hemispheres, rather than major global changes, may have been the dominant factor. The young age

of the deposits suggests that they are erased and reform on relatively short (< 100 million years) time scales. Although their volatile content is not known, they may constitute a reservoir that, if dissipated, could affect atmospheric conditions over the entire planet.

CONCLUSIONS

Mars in many ways resembles Earth. It has an atmosphere, although a much thinner one than Earth, and a surface that has been modified by the wind. There is abundant evidence of near-surface water and ice. Moreover, water has eroded parts of the surface and reacted with the near-surface materials to produce weathered products. Deformation and volcanism have been extensive, and both have seemingly continued into the relatively recent geologic past. Despite these similarities, enormous differences between Mars and Earth remain.

A major cause of differences between the two planets is their contrasting tectonics. The geology of Earth's surface is dominated by plate tectonics. Interaction between lithospheric plates controls the distribution of continents, the formation of mountain chains, the location of volcanic and tectonic activity, and the general style of crustal deformation. Indeed, there are few geologic processes on Earth that are not affected in some way by plate tectonics. In contrast, the Mars crust is fixed, and all those features such as mountain chains, transcurrent fault zones, and linear ocean deeps, that on Earth characterize interaction between the plates, are absent. The stability also results in preservation of an ancient record in almost all areas of the planet.

A second reason for differences between the surfaces of Mars and Earth is the presence of abundant liquid water on Earth. Water plays an essential role in two major processes on Earth: weathering—the chemical breakdown of rock-forming minerals to form assemblages more in equilibrium with conditions at the surface; and gradation—the steady reduction of surface relief by erosion and sedimentation. Both processes are complemented by opposing processes such as metamorphism, in which low-temperature mineral assemblages are reconstituted into high-temperature assemblages, and tectonic activity, which tends to accentuate relief. Earth's surface is thus a complicated system; material is being recycled both through the mantle by subduction and sea-floor spreading, and within the lithosphere and hydrosphere by weathering, metamorphism, erosion, and deposition.

The dynamics of the Martian crust are totally different. Although the planet has been volcanically and tectonically active through much of its history, the lithosphere appears not to have been recycled through the underlying asthenosphere. Huge volcanoes have formed, as well as vast fracture systems, but the activity has not been concentrated in linear zones as on Earth. Instead, it has affected broad areas. Furthermore, although water has probably flowed across the Martian surface at times in the past, fluvial erosion has been trivial. Where channels are present, they mostly wind between the craters or down the crater rims. Rarely has erosion been sufficient to wear away the craters themselves. Erosion of young features, such as the large volcanoes, is imperceptible.

On Earth, uplift is followed by enhanced erosion and downwarping by rapid sedimentation, so that a rough equilibrium is maintained by the relief-forming processes and gradation by running water. On Mars, because of the limited fluvial erosion, no such equilibrium is achieved. If relief is created, such as by volcanic, tectonic, and impact processes, it largely remains. If any equilibrium is achieved, it is not with the surficial processes of erosion and deposition, but with the ability of the lithosphere to sustain the loads created by the relief. As a consequence, Mars, despite its small size, has considerable relief. Volcanoes have grown to almost three times the height of Mt. Everest, canyons several kilometers deep have survived for billions of years, and a broad 10-km high upwarp of continental dimensions has persisted in Tharsis for most of the planet's history.

The lack of significant sediment transport implies, in addition, that weathering products are not recycled. Chemical analyses of the surface materials indicate that weathered products, such as clays and evaporites, are present. Where subsurface rocks are in contact with groundwater, weathering may occur, but without erosion and removal of the weathered products, alteration must slow as a protective rind of weathered material accumulates around the unaltered rocks.

Thus, in addition to the lack of cycling of the Martian lithosphere through the underlying asthenosphere, cycling of surface materials within the lithosphere and hydrosphere is hindered by climatic conditions which inhibit flow of water across the surface. The result is an active planet, with considerable surface relief, on

which geologic features with a wide range of origin and age are preserved.

ACKNOWLEDGMENTS

This chapter benefited from excellent reviews by E. Shoemaker, L. Soderblom and D. Wilhelms of the U.S. Geological Survey. The work was supported by a grant from the Planetary Geology Programs Office, NASA Headquarters.

Page intentionally left blank

8
SUMMARY

Although our knowledge of the Moon and the terrestrial planets is incomplete and each has evolved differently, some general conclusions can be stated. The evolution of planetary surfaces depends on the interplay of four types of geologic processes: (1) impact cratering, (2) volcanism, (3) tectonism, and (4) interaction with the atmosphere and hydrosphere. The relative roles of the different processes vary with time, the size of the planetary body, and with atmospheric conditions at the surface.

IMPACT CRATERING

The Moon, Mercury, and Mars all have heavily cratered surfaces, which record a period of intense bombardment early in their histories. Since these bodies span the entire range of inner planet distances (0.38–1.5 AU), there can be little doubt that both Venus and Earth were also subjected to the same bombardment. Absolute ages of returned lunar samples demonstrate that, at least for the Moon, the period of heavy bombardment ended about 3.8 billion years ago. Presumably it ended at about the same time on all the terrestrial planets. On Earth, the record of early, heavy bombardment has been entirely erased because of high rates of volcanism, deformation, erosion, and burial. The oldest areas of Earth's surface, the Precambrian shields, are mostly 1 to 3 billion years old; the oldest rocks so far dated are 3.8 billion years old. The shields retain numerous old impact scars but even these post-date the heavy bombardment. Information on Venus is still inadequate to determine the extent to which its cratering record has been preserved, but radar images show large circular features which have been interpreted as impact craters and basins.

The shapes of the crater size/frequency distribution curves for the heavily cratered regions of the Moon, Mercury, and Mars are similar, suggesting that the population of objects responsible for the heavy bombardment was the same throughout the inner solar system. Conversely, the shapes of the size/frequency distributions of the younger craters that are superposed on the lunar maria and Martian plains are similar to each other but somewhat different from those of the highlands, which suggests a different population of objects may have caused the later craters. The origin of the two populations of impacting bodies is uncertain. Orbit dynamical studies suggest the period of heavy bombardment may be due to (1) the impact of a long-lived tail of accretional remnants left over from the formation of the terrestrial planets, or (2) the impact of fragments of large planetesimals perturbed into the inner solar system by the outer planets and tidally disrupted by close approaches to Earth or Venus. The present orbits of comets and Apollo and Amor asteroids have orbits that cross those of the terrestrial planets and these objects must have been dominant contributors to the cratering record in the inner solar system, at least during the last 3.8 billion years. If these families of objects were also responsible for the period of heavy bombardment, then their flux rates must have been orders of magnitude higher before 3.8 billion years ago than at present.

No matter what the origin of the impacting objects, cratering has clearly had major effects on the surfaces of all the terrestrial planets. Mercury, the Moon, and Mars reveal direct evidence that impacts excavated large volumes of material and fractured deeply into the lithosphere, redistributing material over broad areas and providing foci for later volcanic activity. Similar catastrophic events must also have occurred

widely on Earth and Venus during the first 600 million years of their histories, perhaps causing early separation of continental and oceanic areas on Earth, and profoundly influencing the style of deformation. Impacts probably continued to affect geologic and biologic evolution on Earth after 3.8 billion years ago, although to a far lesser extent than before, as suggested by recent debate over the nature of the Cretaceous-Tertiary boundary.

VOLCANISM

The style, mode of occurrence, and duration of volcanism vary considerably among the terrestrial planets. Volcanism on Earth occurs primarily at plate boundaries or in intraplate areas over mantle hot spots. At divergent boundaries, intrusion and eruptions occur along the mid-oceanic ridges as the plates separate. The eruptions are mostly basaltic and formed all the oceanic crust during the last 250 million years. Volcanism at convergent boundaries is more varied, including eruptions of volatile-rich andestic and rhyolitic materials in addition to basalts. Pyroclastic activity is far more common than at divergent junctions, and a greater variety of volcanic landforms are produced. The magmas at convergent junctions are generated, at least in part, by partial melting of the descending plate as it slides beneath the leading edge of the opposing plate. Hot spot volcanism in the interior of plates gives rise primarily to large basaltic shield volcanoes (particularly in oceanic areas) whose sizes are governed by the thickness of the lithosphere and the rate of plate motion relative to the fixed hot spot. Flood basalts are located primarily at the margins of continents where they form extensive plains derived from voluminous fissure eruptions. They appear to be associated with extensive deep-seated fracturing that accompanies breakup of continental plates.

Volcanism on the Moon is dominated by flood basalts primarily in impact basins on the nearside. These lavas originated at subcrustal depths and apparently worked their way through an essentially passive, but fractured crust without storage in shallow magma reservoirs. The concentration of maria on the nearside is probably related to a thinner crust there as indicated by the offset of the center of mass from the center of figure. The thinner crust may be the result of an enormous impact that occurred before most of the more prominent impact basins formed. A thicker farside lithosphere probably prohibited extensive volcanism there except in the deepest basins. Absolute ages of returned samples show that volcanism lasted from at least 3.0–4.0 billion years ago; crater densities suggest that it may have continued to 1 to 2 billion years ago in some areas. After that time, cooling and lithospheric thickening precluded further volcanic activity. The lack of large shield volcanoes suggests that localization of melting in discrete hot spots within the mantle was not important on the Moon.

If both the smooth and intercrater plains on Mercury are volcanic deposits, then volcanic activity was more extensive than on the Moon, and the rate of highland volcanism was higher. The morphology of these deposits and the apparent lack of large volcanic constructs suggests, however, that the style of volcanism was similar on the two bodies. The more extensive volcanic activity postulated for Mercury as compared with the Moon may be related to the formation of Mercury's enormous core, which would have greatly raised internal temperatures and thus caused extensive melting and global expansion. This, in turn, caused tensional fracturing in the thin lithosphere, thereby allowing easy access of magma to the surface. Albedo and color suggest that the Mercurian volcanic deposits are depleted in iron and titanium relative to lunar lavas possibly as a result of more thorough melting and differentiation. How long volcanism persisted on Mercury is unclear; it almost certainly was confined to very early in the planet's history and may have been of shorter duration than on the Moon.

Volcanism on Mars has been dominated by two main types of activity: the formation of lava plains and the building of shield volcanoes. Other types of activity, possibly of a more pyroclastic nature, may have also occurred. Large areas of the northern plains and some intercrater areas of the southern highlands appear to have been flooded by basalts. Unlike the Moon, these plains are not necessarily contained within impact basins and in this respect are more akin to the intercrater plains on Mercury. Large shield volcanoes occur principally in the Hellas, Elysium, and Tharsis regions. The largest and youngest are associated with the Tharsis uplift where they reach heights of about 24 km above their surroundings. The enormous size of the shields is probably the result of a thick lithosphere and the lack of plate tectonics. A thicker lithosphere on Mars, as compared to Earth, results in greater hydrostatic pressures in the magma source regions, which can force magma to higher levels on Mars; while in the absence of plate tectonics the shields remain fixed over the hot spots to allow more

lava to accumulate in the same area. Volcanism appears to have persisted throughout most of Martian history although at a progressively declining rate. It was widespread during the first half of the planet's history, forming intercrater plains in the cratered uplands and extensive lava plains elsewhere. During the second half of the planet's history, volcanism was restricted to the main volcanic provinces of Tharsis and Elysium. The most recent volcanism appears confined to the large shield volcanoes in and around Tharsis.

The history of volcanic activity on Venus is still uncertain. At least one mountain mass (Beta Regio) has two components (Rhea and Theia Mons) with shapes like shield volcanoes and one has a summit depression. Both mountains are rough at radar wavelengths, and chemical analyses by Venera spacecraft near the flanks of Beta Regio indicate a basaltic composition. Whether or not floor basalts or forms of more sialic volcanism are also present is not known.

TECTONICS

Each planet has had a distinctive tectonic history. Geologic activity on Earth is at present dominated by plate tectonics. The lithosphere is divided into plates that move relative to one another at rates mostly in the range of 1–15 cm/yr. At divergent junctions, along the crests of mid-oceanic ridges, new lithosphere forms as the plates move apart. Tensional tectonics dominate at these junctions, the most obvious manifestation being the enormous rift valleys along the ridge crests. At most convergent junctions are subduction zones where one plate slides beneath the other and is consumed in the hot mantle below. Mainly compressional tectonics occur at these junctions, creating the linear mountain chains that dominate the topography of the continents and many ocean margins. At other boundaries the plates may move by one another along transform faults, so that each plate is conserved. Plate tectonics has controlled the evolution of Earth's surface for at least the last 500 million years, and possibly for most of its history.

Neither interconnected ridges nor linear mountain chains have been observed on any other planet but Earth. On the Moon, most crustal deformation results from basin subsidence due to loading of the lithosphere by high density flood basalts. Tensile stresses have produced concentric graben at the margins of basins and compressive concentric wrinkle ridges in the interior of basins. Crustal deformation probably ceased shortly after emplacement of most of the mare basalts had been accomplished, around 3 billion years ago.

The tectonic framework of Mercury is unique among the terrestrial planets and is characterized by the widespread (probably global) distribution of thrust or reverse faults. These faults appear to be a manifestation of crustal shortening primarily caused by core/lithosphere cooling aided by planet despinning early in Mercury's history. Thermal history models suggest that extensive melting, global expansion, and tensional fracturing resulted from core formation, although the surface lacks evidence from this early period. Thus, Mercury's tectonic activity appears to be largely the result of formation of the large iron core, and activity probably terminated early in the planet's history.

The tectonics of Mars is dominated by the Tharsis bulge. Radial fractures (mostly graben) centered on Tharsis affect nearly an entire hemisphere, and compressional wrinkle ridges occur around the bulge periphery. Tharsis is also the site of the most recent volcanic activity and a large positive gravity anomaly. Deformation appears to have been most intense during the first half of Martian history but continued to the present at a lower level. Volcanism and faulting took place simultaneously. This extraordinary long period of deformation implies a stable stress system was sustained over much of Martian history. The stresses appear to be caused by the presence of the bulge, that is, by its topography and gravity anomaly rather than the mechanics of its formation. The bulge may have resulted from overturn in the mantle during core formation.

The tectonic framework of Venus is poorly understood. Extensive rifting has occurred, primarily in Aphrodite Terra and Beta Regio, but the rifts do not form a planet-wide network as on Earth. There are also continent-like masses, large mountains, and escarpments, but linear mountain chains or deep linear trenches have yet to be identified. Most of the Venus surface consists of rolling plains with a rather high density of possible impact craters which suggests an ancient surface. These limited data imply a more stable surface than on Earth and no present plate tectonics.

INTERACTION WITH THE ATMOSPHERE AND HYDROSPHERE

Among the terrestrial planets only Earth, Mars, and Venus have significant atmospheres. On Earth the at-

mosphere has a marked effect on the surface, mainly through the action of water which plays an essential role in two major processes: (1) weathering, the chemical breakdown of rock-forming minerals into mineral assemblages in equilibrium with surface conditions, and (2) gradation, the reduction of surface relief by erosion of the highs and deposition in the lows. The two processes are mutually dependent in that erosion exposes new surfaces to weathering, and weathering makes the surfaces more susceptible to erosion. The rates of erosion and weathering on Earth are so high, compared to most other geologic processes, that on the continents the small scale relief is almost everywhere dominated by the effects of dissection, mainly by water. Only at the larger scales does the imprint of primary processes of tectonism and volcanism dominate.

The Martian surface also retains abundant evidence of interaction with the atmosphere and hydrosphere. Vast sand seas surround the poles, debris blankets appear to have been repeatedly deposited and stripped away at high latitudes, the old terrain is everywhere dissected by valley networks, flood features are present in places, and numerous features suggest the action of ground-ice. Nevertheless, the rate of interaction appears to be orders of magnitude less than on Earth. An ancient cratered surface is well preserved over extensive areas. Where fluvial erosion has occurred its effects are small, having generally been insufficient to erode away the craters. On young surfaces (<2.5 billion years) erosion is almost imperceptible, except at high latitudes. Similarly, weathering has occurred as suggested by probable presence of clay minerals in the regolith, but without erosion to continually re-expose fresh material, weathering is likely to proceed far more slowly than on Earth. The relatively modest role of water in the evolution of the Martian surface results from its instability under the climatic conditions that prevailed for most of the planet's history.

Evidence of the nature of surface-atmosphere interaction on Venus is sparse, but since temperatures are too high for liquid water to exist, rates of interaction may be low. This viewpoint is supported by preservation of a seemingly ancient cratered surface on the planet. However, some interaction must occur. Winds are sufficient to move loose debris; the surface probably reacts with carbon dioxide in the atmosphere; and chemical activity of water at the surface may be comparable to Earth, despite the extremely low humidity. Moreover, early conditions may have been significantly different from those at present, and liquid water could have been stable at one time.

PLANETARY EVOLUTION

During accretion, around 4.6 billion years ago, the growing planets were heated by impacts and compression. Ultimately, internal temperatures reached the melting temperature of iron (or iron oxide or sulfide). The melted iron-rich materials then began gravitating toward the center, thereby releasing large amounts of energy and causing pervasive melting of the silicates of the interior. This in turn led to extensive outgassing and separation of aluminum and silicon rich materials to form the crust. These events probably all took place within the first few hundred million years, during which the planet continued to be heavily bombarded by interplanetary debris.

By the time the impact rates started to decline, around 3.8 billion years ago, each planet had a rigid crust able to retain a record of the impacts. Also by this time, Mercury and the Moon had lost any volatiles that had outgassed. The subsequent history of each planet depended to a large extent on the balance between heat dissipation and heat production by radioactive decay. Internal activity on the smaller, more efficient heat dissipators, Moon and Mercury, declined rapidly. Activity on the somewhat larger Mars declined more slowly, while activity on the much larger Earth was sustained at a high level. By this reasoning internal activity on Venus should have continued.

Two circumstances caused Earth to evolve along a path radically different from the other planets. First was development of plate tectonics and second was maintenance of conditions at the surface such that liquid water is stable. Why these two circumstances should have coincided only on Earth is unclear. Plate tectonics and the action of water have caused relatively rapid recycling of Earth's near-surface materials, partly through ingestion of the entire lithosphere at subduction zones and the re-emergence of the materials close to the surface as volcanic and plutonic rocks, and partly through mixing within the lithosphere by the processes of weathering, erosion, transport, burial, and metamorphism. No comparable recycling occurs on Mars, Moon, or Mercury; their surfaces are orders of magnitude more stable than Earth's. The extent to which the Venusian surface materials have been recycled is unclear. Water is now unstable at the sur-

face and most evidence suggests that there are no plate tectonics. But our perception of the style of current geologic activity on Venus is still very vague. Moreover conditions could have been very different in the past.

Thus, Earth is a dynamic planet on which is preserved a rich and diverse record from the recent geologic past, but only a poor record from the first half of its history. In contrast, the other terrestrial planets, with the possible exception of Venus, preserve a rich record from their early history, after which time their surfaces remained essentially unchanged.

Page intentionally left blank

APPENDIX

Maps of the Terrestrial Planets

Mercury

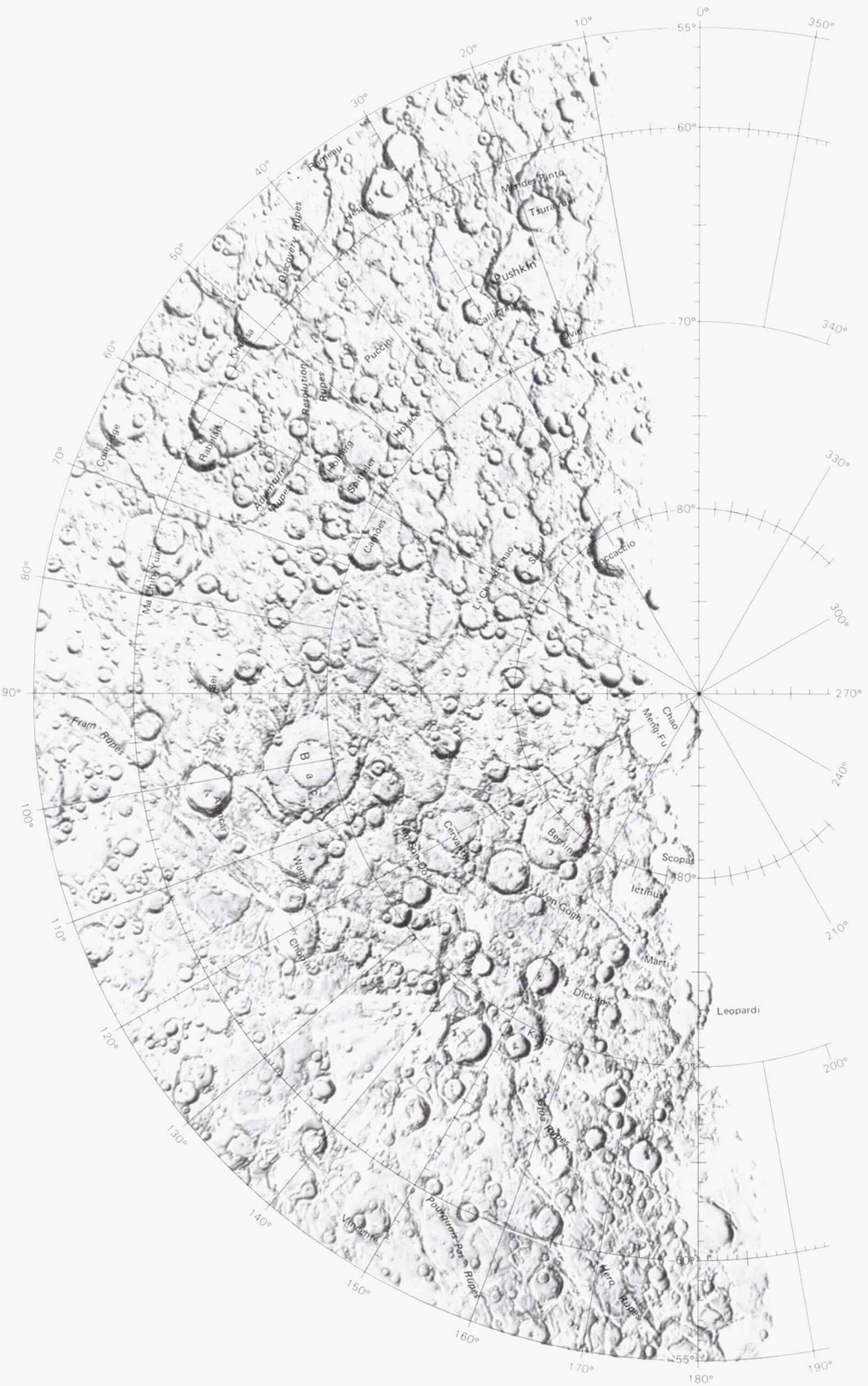

SOUTH POLAR REGION

SCALE 1 8388000 AT 56° LATITUDE
POLAR STEREOGRAPHIC PROJECTION

±90°
±80°
±70°
±60°
±55°

0 200 KILOMETERS 400 600 800 1000 2000

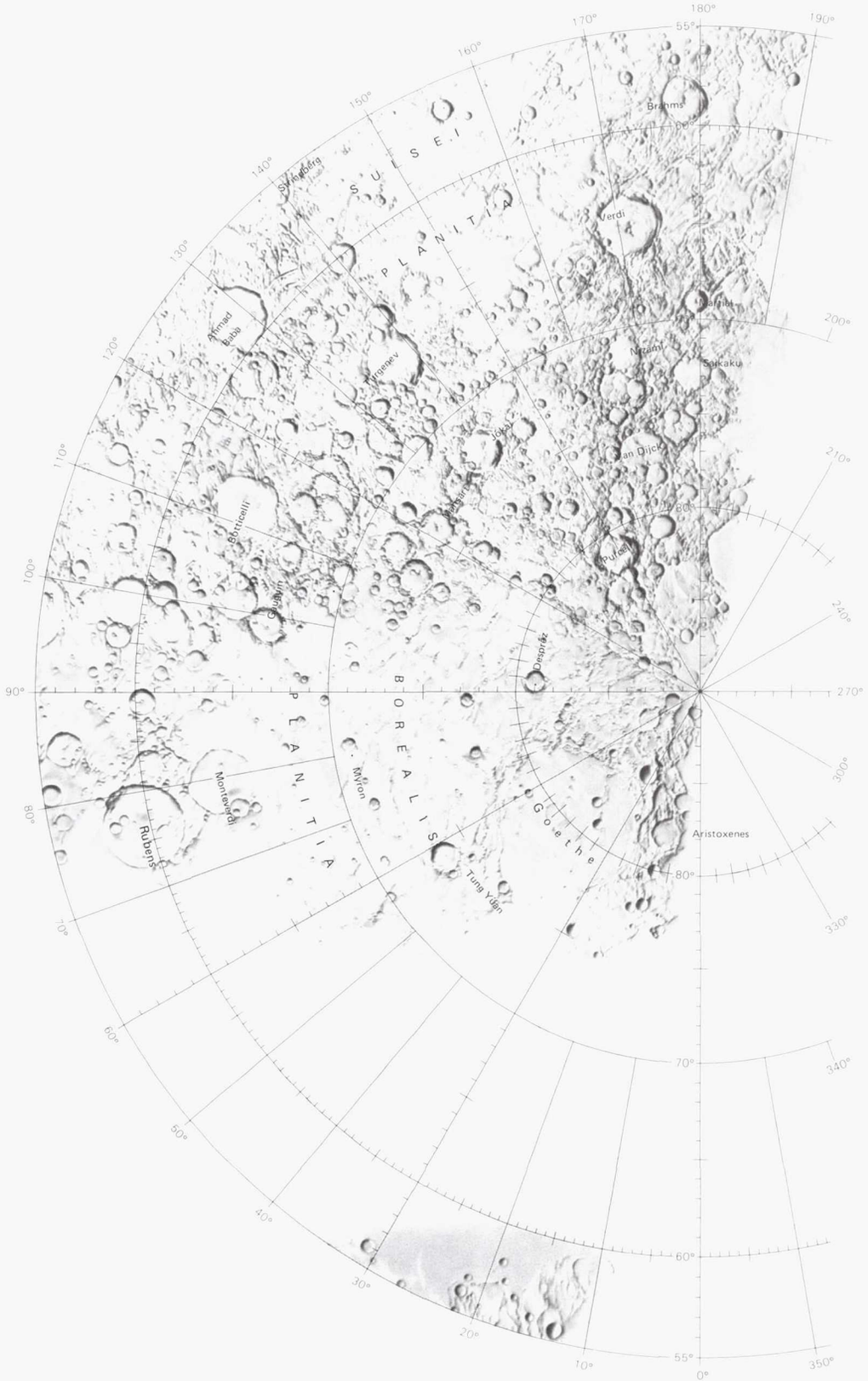

NORTH POLAR REGION

Mercury

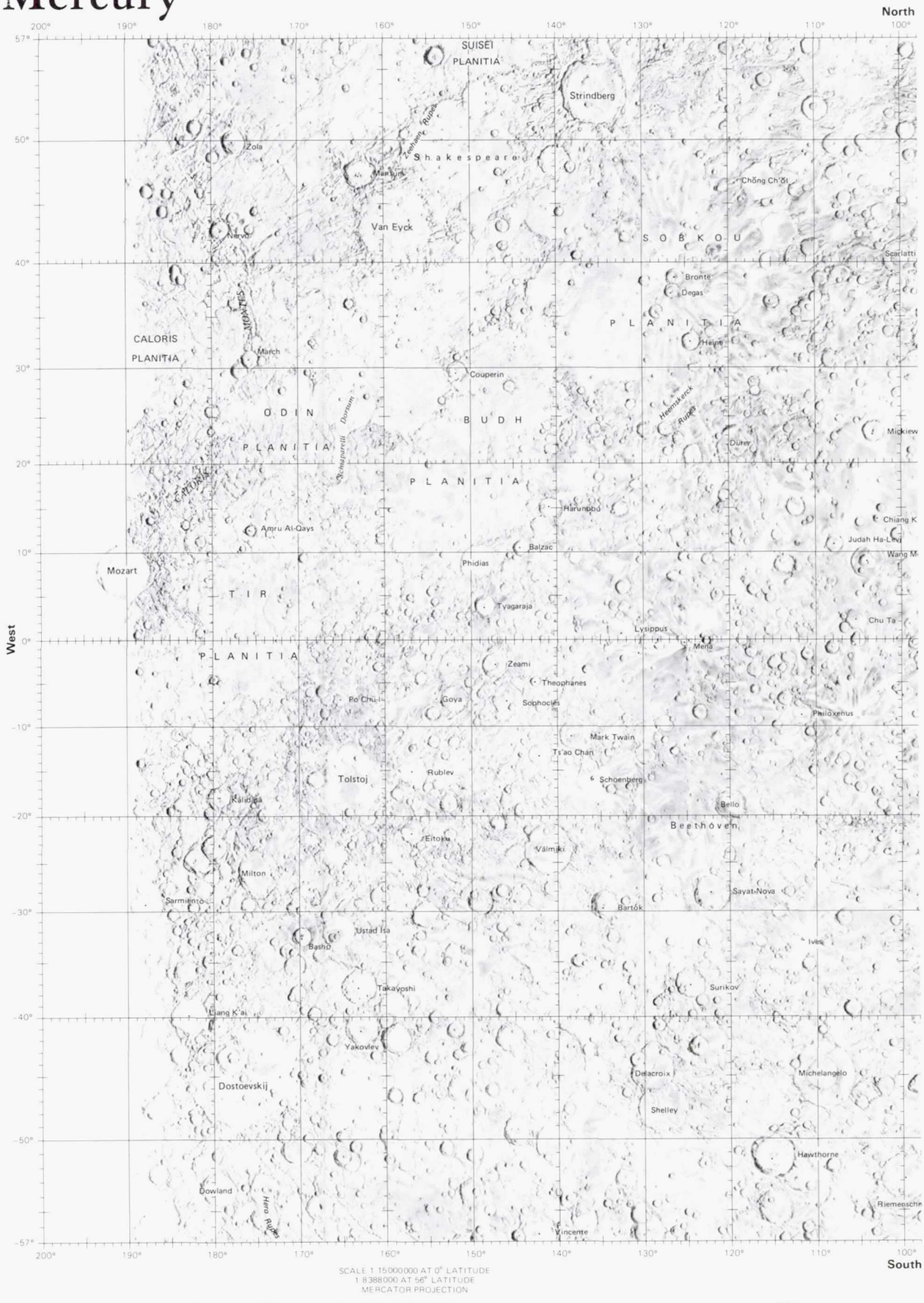

SCALE 1:15000000 AT 0° LATITUDE
1:8388000 AT 56° LATITUDE
MERCATOR PROJECTION

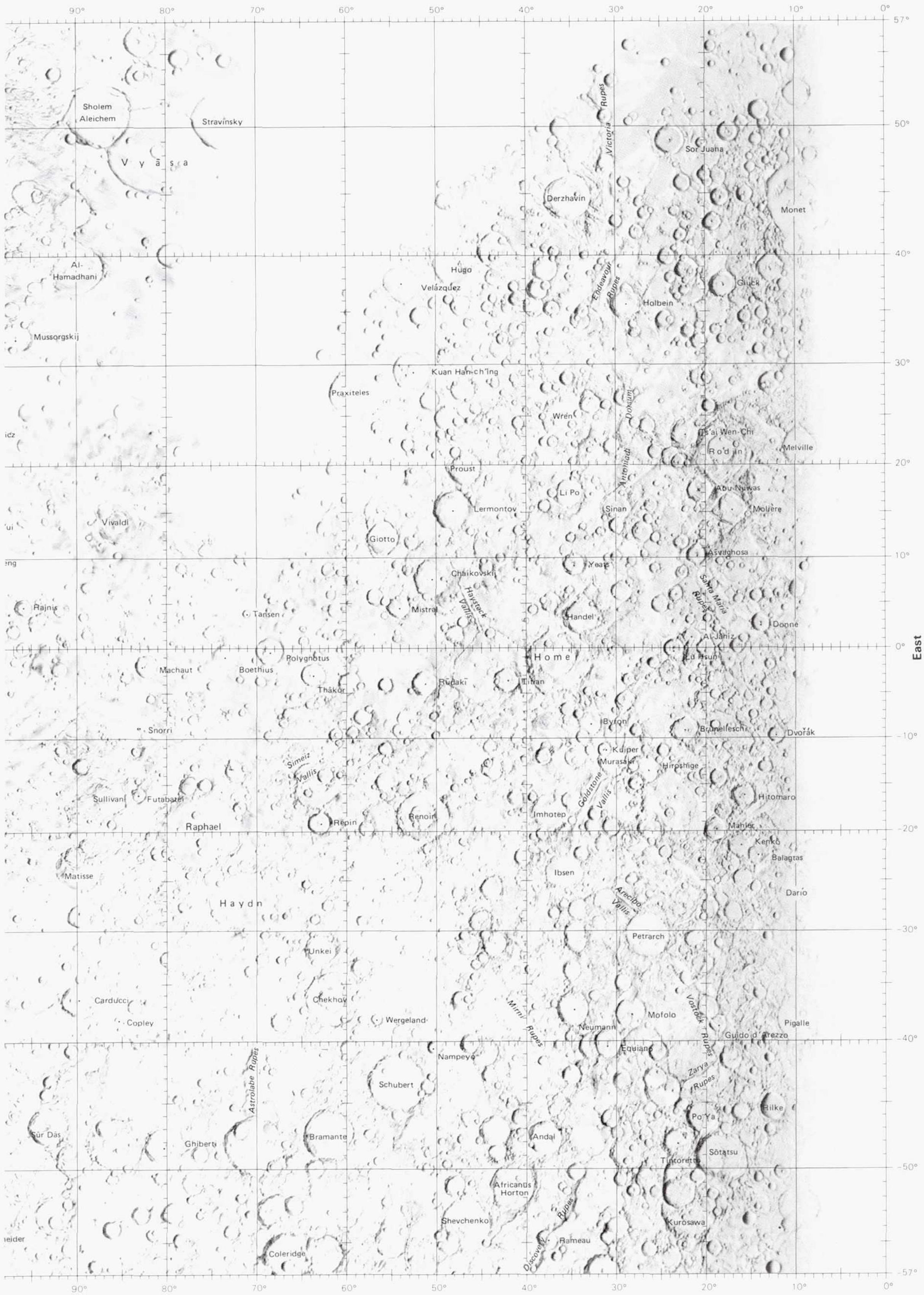
90°
80°
70°
60°
50°
40°
30°
20°
10°
0°
57°
50°
40°
30°
20°
10°
0°
-10°
-20°
-30°
-40°
-50°
-57°
East
Sholem Aleichem
Stravinsky
V y ā s a
Victoria Rupes
Sor Juana
Derzhavin
Monet
Al-Hamadhani
Hugo
Velázquez
Endeavour Rupes
Holbein
Gluck
Mussorgskij
Kuan Han-ch'ing
Praxiteles
Wren
Ts'ai Wen-Chi
Ro'd in
Melville
Antoniadi
Proust
Li Po
Abu-Nuwas
Lermontov
Sinan
Molière
Vivaldi
Giotto
Yeats
Asvaghosa
Chaikovskij
Haystack Vallis
Santa Maria Rupes
Rajnis
Tansen
Mistral
Handel
Donne
Al-Jahiz
Polygnotus
Machaut
Boethius
Lu Hsun
H o m e
Rudaki
Tir
Thākur
Byron
Brunelleschi
Dvořák
Snorri
Kuiper
Murasaki
Hiroshige
Simeiz Vallis
Goldstone Vallis
Hitomaro
Sullivan
Futabatei
Repin
Renoir
Imhotep
Raphael
Mahler
Kenkō
Balagtas
Matisse
Ibsen
Dario
Arecibo Vallis
H a y d n
Petrarch
Unkei
Carducci
Chekhov
Mirni Rupes
Mofolo
Vostok Rupes
Copley
Wergeland
Neumann
Guido d'Arezzo
Pigalle
Nampeyo
Equiano
Zarya Rupes
Schubert
Po Ya
Rilke
Astrolabe Rupes
Sūr Dās
Ghiberti
Bramante
Andal
Sōtatsu
Tintoretto
Africanus Horton
Shevchenko
Kurosawa
Rameau
Discovery Rupes
Coleridge

Venus

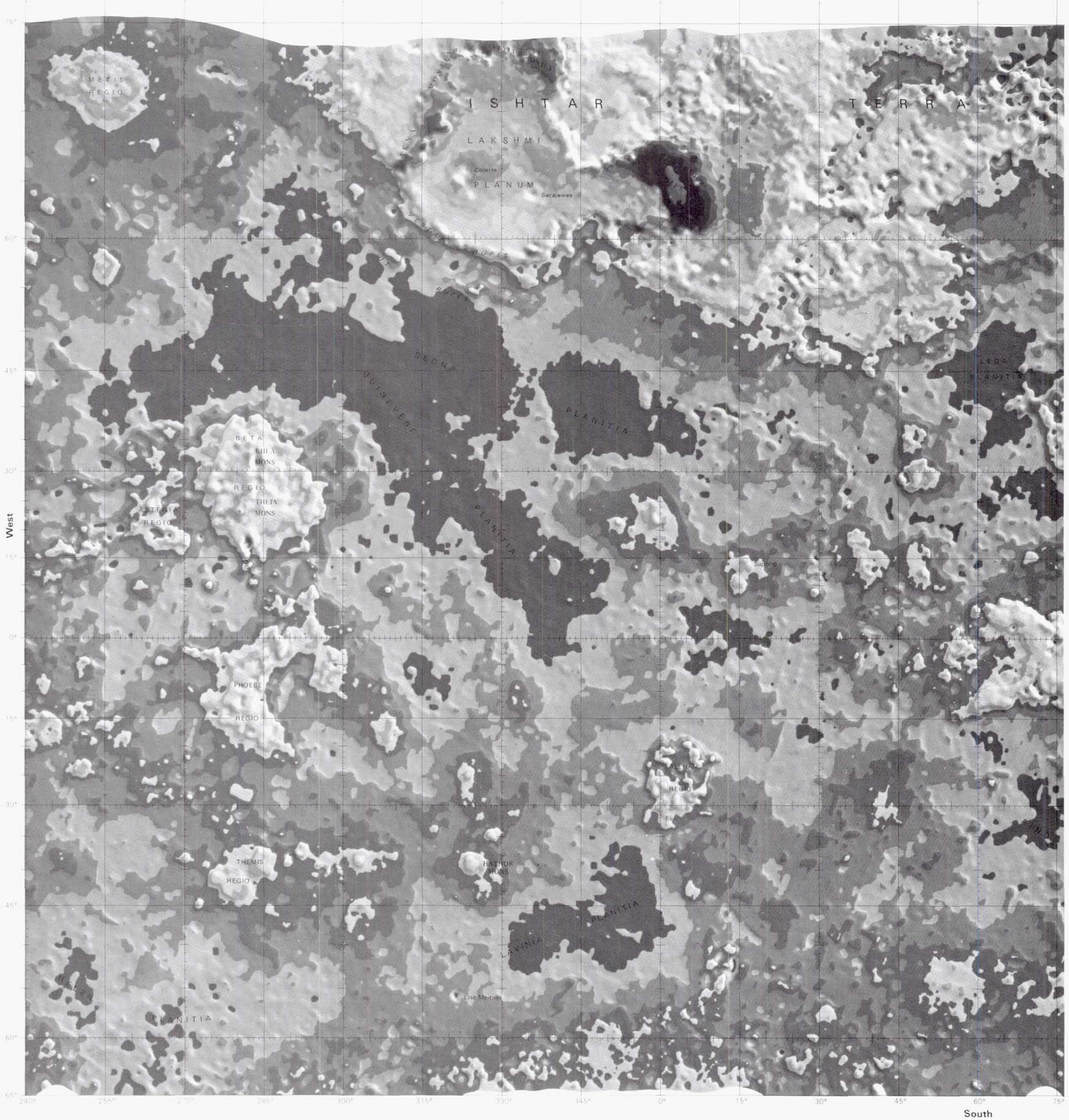
North
South
West
240°
255°
270°
285°
300°
315°
330°
345°
0°
15°
30°
45°
60°
75°
78°
65°
30°
0
METIS REGIO
ISHTAR TERRA
LAKSHMI PLANUM
Colette
Sacajawea
VESTA RUPES
RUPES
SEGMA
GUINEVERE
PLANITIA
LEDA PLANITIA
BETA REGIO
RHEA MONS
THIA MONS
ASTERIA REGIO
Sapphe
PHOEBE REGIO
THEMIS REGIO
HATHOR MONS
LAVINIA PLANITIA
Lise Meitner
PLANITIA
SCALE 1:50 000 000 (1mm = 50 km) AT 0° LATITUDE
MERCATOR PROJECTION
6000
5000
4000
3000
2000
1000
0
KILOMETERS

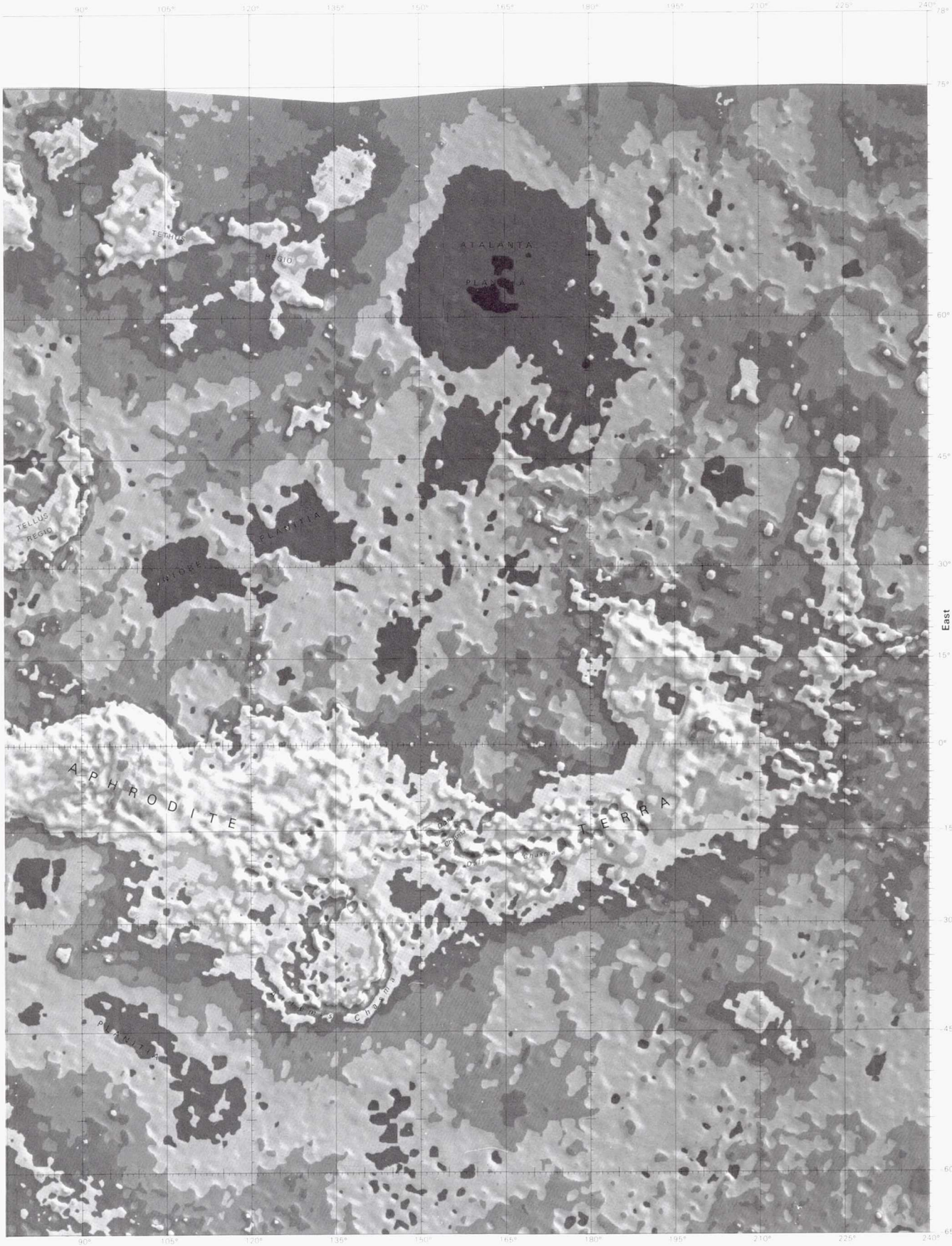

CONTOUR ELEVATION (Kilometers)	PLANET RADIUS (Kilometers)
12	6063
11	6062
10	6061
9	6060
8	6059
7	6058
6	6057
5	6056
4.5	6055.5
4	6055
3.5	6054.5
3	6054
2.5	6053.5
2	6053
1.5	6052.5
1	6052
0.5	6051.5
0	6051
−0.5	6050.5
−1	6050
−1.5	6049.5
−2.5	6048.5

Earth

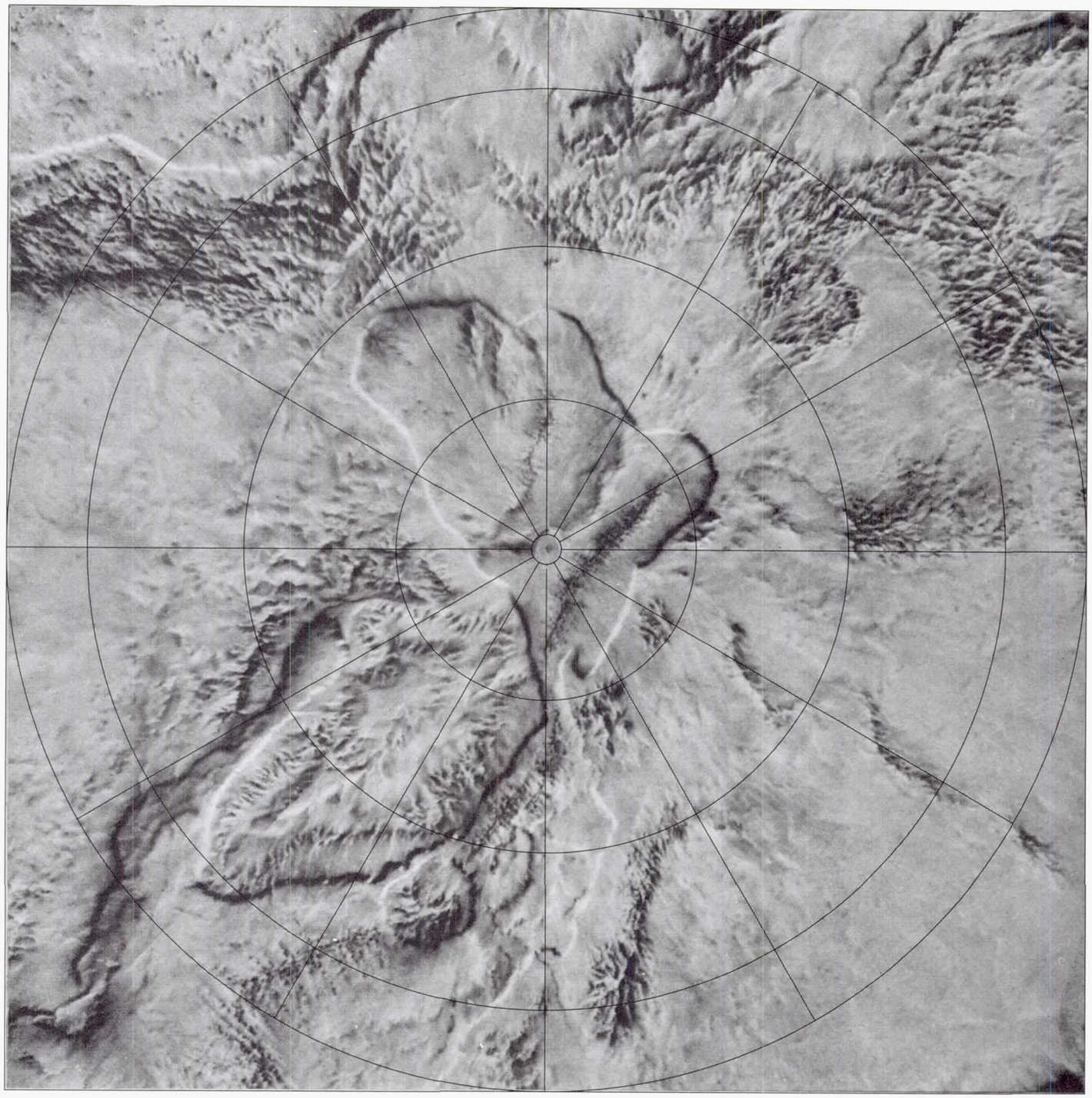

North Pole

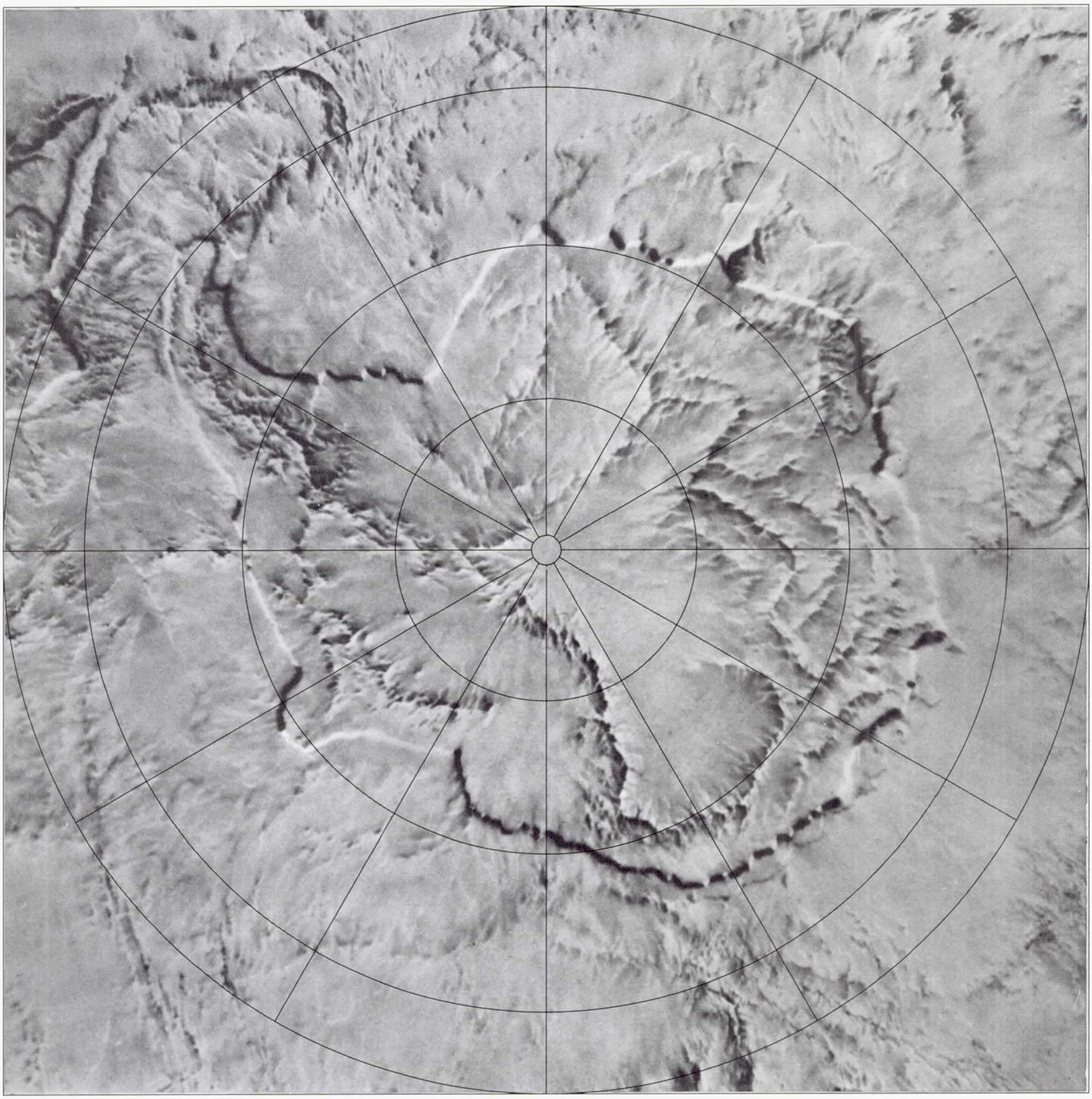

South Pole

Earth

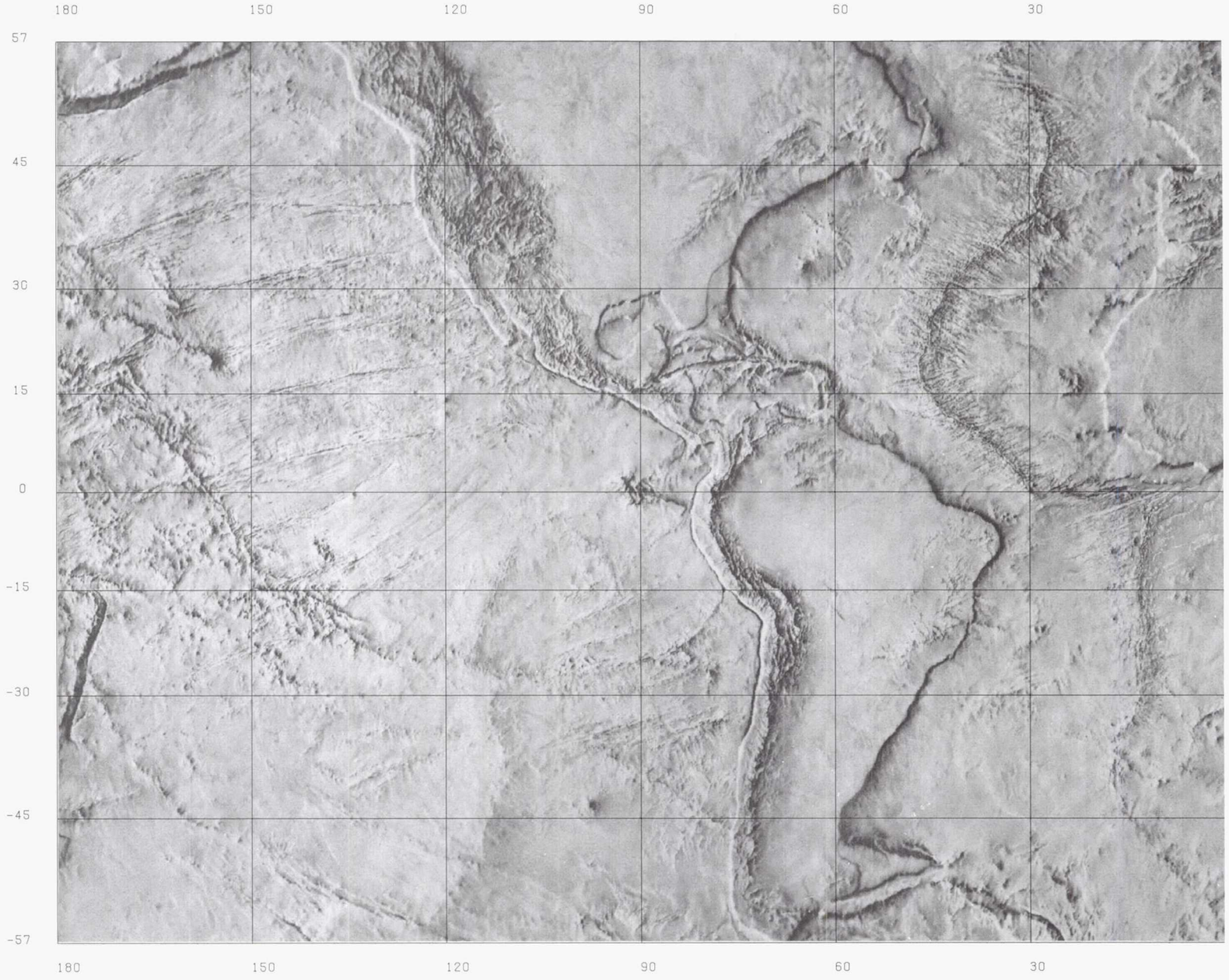


0
330
300
270
240
210
180
57
45
30
15
0
-15
-30
-45
-57
0
330
300
270
240
210
180

Moon

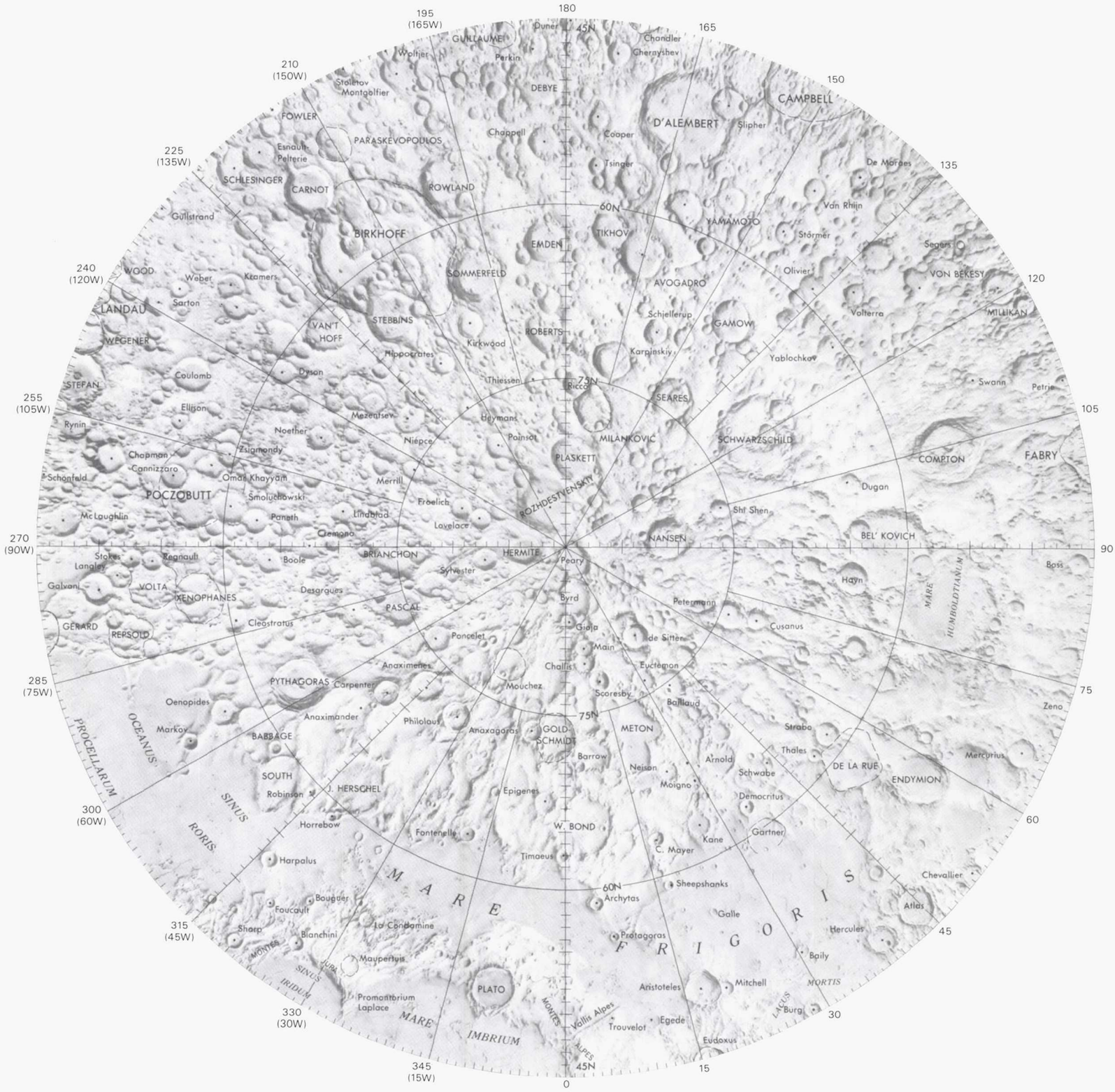

NORTH POLAR REGION

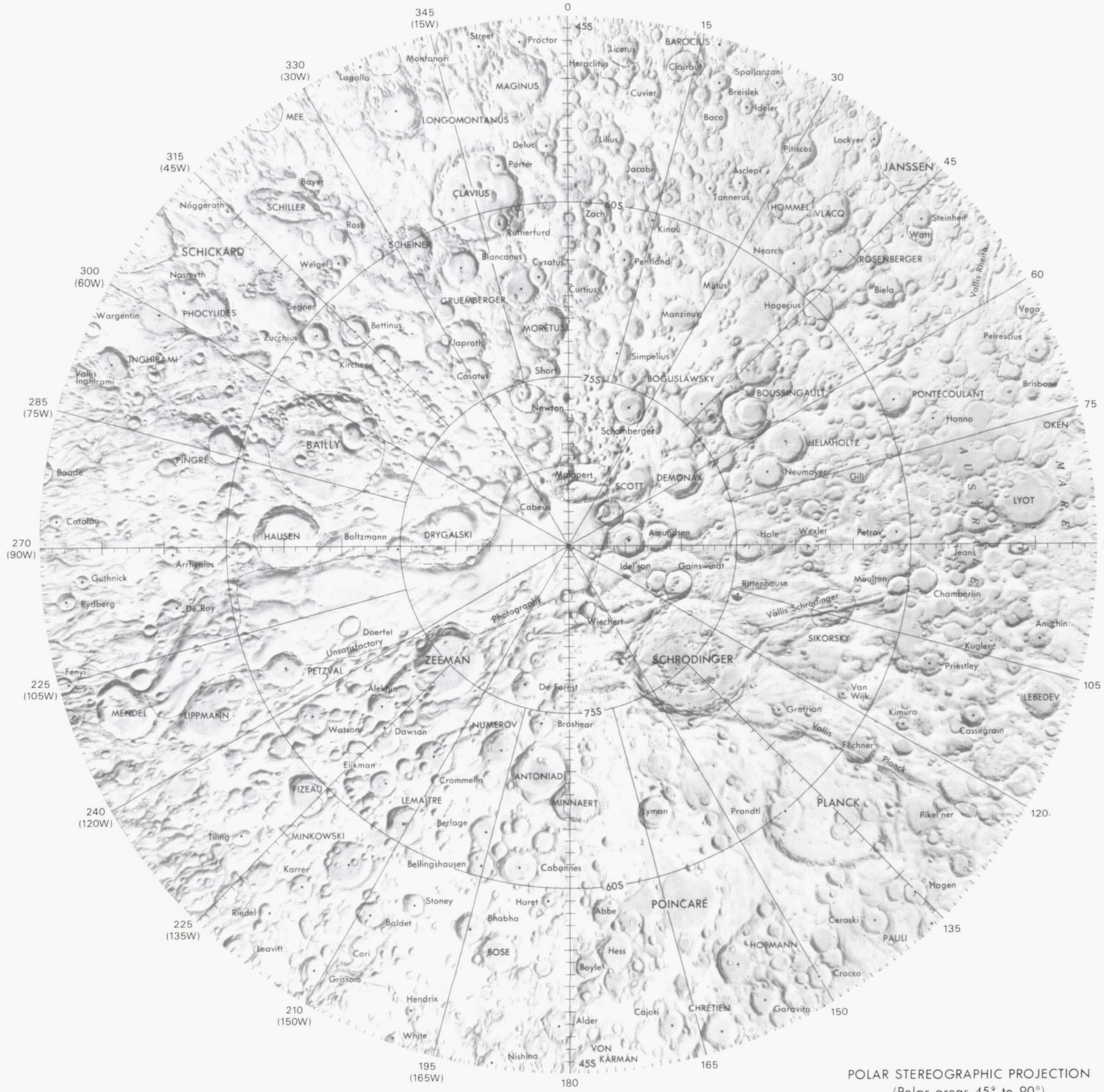

SOUTH POLAR REGION

POLAR STEREOGRAPHIC PROJECTION
(Polar areas 45° to 90°)
Scale 1:10,000,000 at the Poles.

Moon

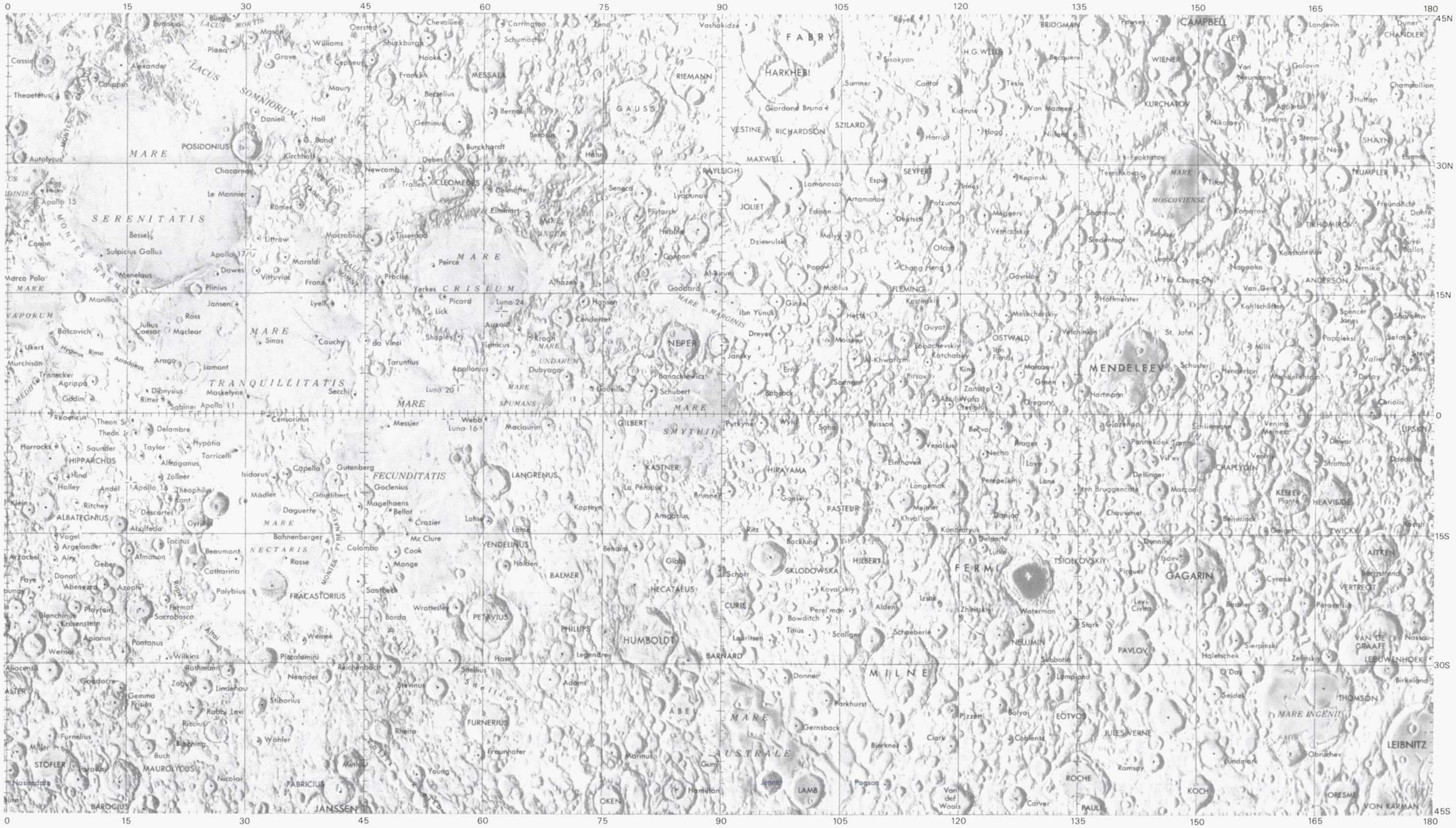

0
15
30
45
60
75
90
105
120
135
150
165
180
45N
30N
15N
0
15S
30S
45S
MARE SERENITATIS
MARE TRANQUILLITATIS
MARE CRISIUM
MARE FECUNDITATIS
MARE NECTARIS
MARE SMYTHII
MARE MARGINIS
MARE AUSTRALE
MARE MOSCOVIENSE
MARE INGENII
MARE UNDARUM
MARE SPUMANS
LACUS SOMNIORUM
FABRY
HARKHEBI
GAUSS
MESSALA
RIEMANN
CAMPBELL
POSIDONIUS
CLEOMEDES
NEPER
MENDELEEV
LANGRENUS
HUMBOLDT
PETAVIUS
FERMI
GAGARIN
MILNE
JANSSEN
LEIBNITZ
HIPPARCHUS
ALBATEGNIUS
FRACASTORIUS
VENDELINUS
TSIOLKOVSKIY
SKLODOWSKA
HIRAYAMA
PASTEUR
PAVLOV
KURCHATOV
MAURALYCUS
STOFLER
Apollo 11
Apollo 15
Apollo 16
Apollo 17
Luna 16
Luna 20
Luna 24

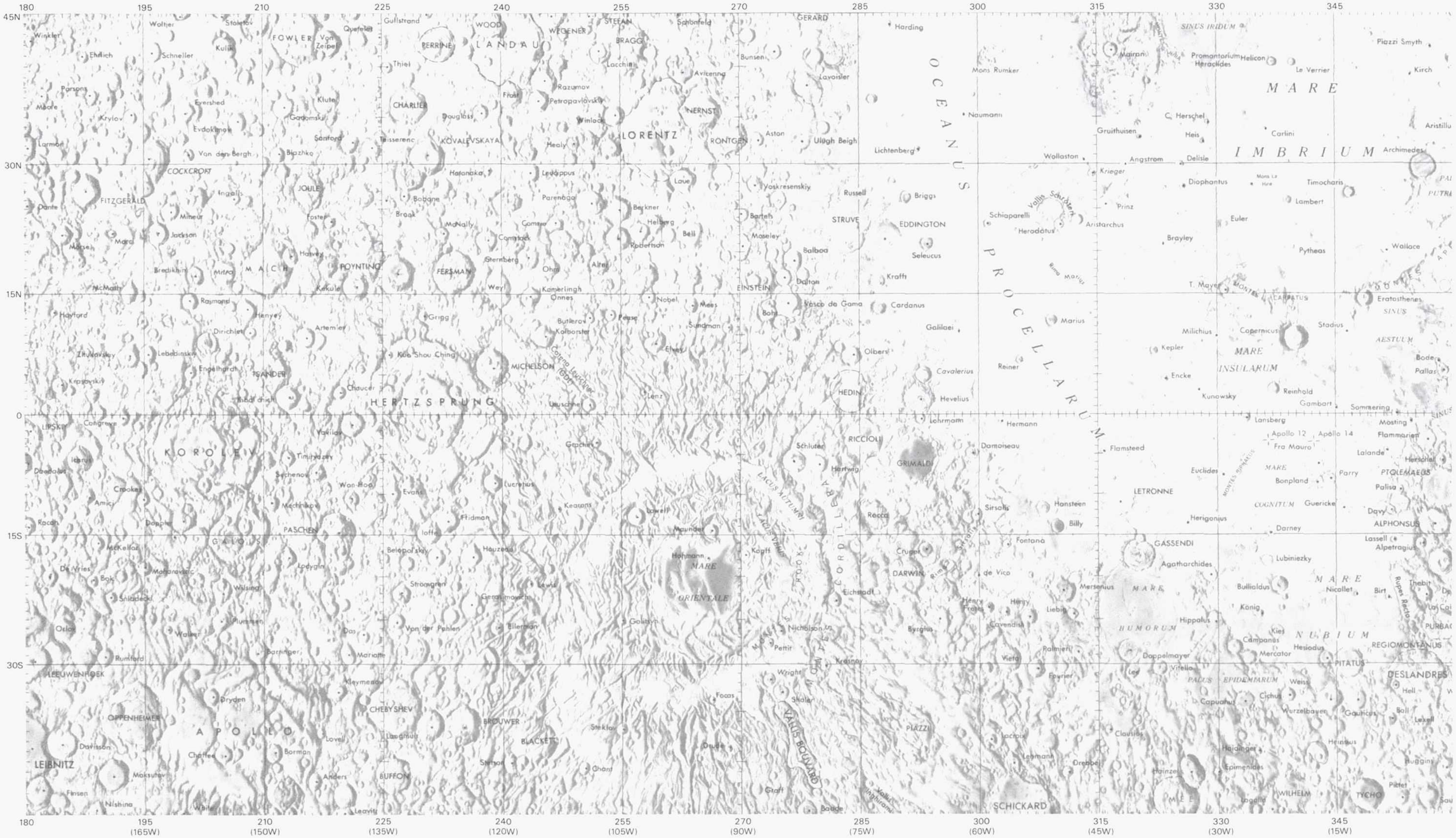

MERCATOR PROJECTION (45°N to 45°S)
Scale 1:10,000,000 at 34°N and S Latitudes.

Mars

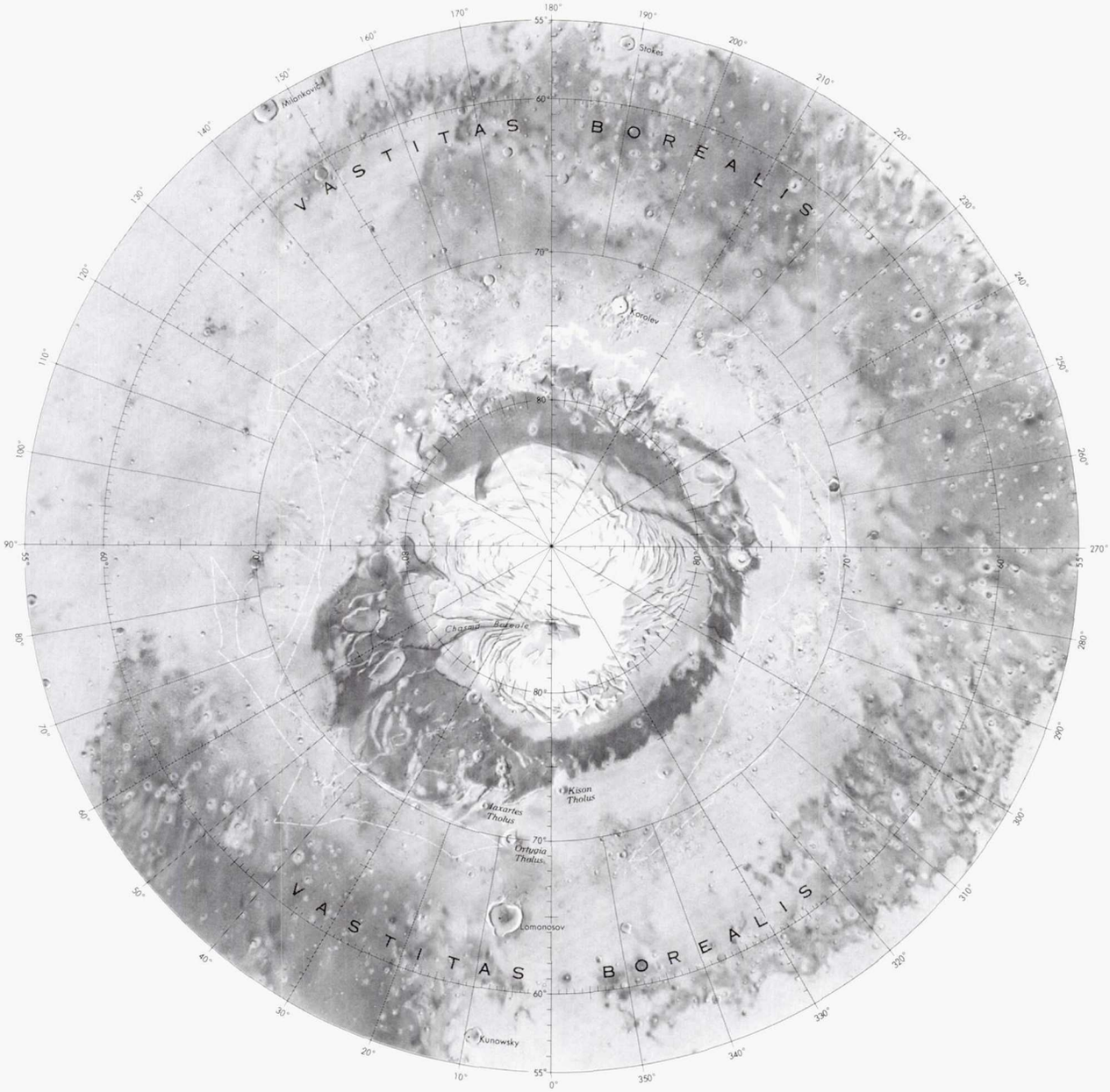

NORTH POLAR REGION
Polar cap as it appeared on August 4, 1972

SCALE 1:12,549,000 AT 60° LATITUDE
POLAR STEREOGRAPHIC PROJECTION

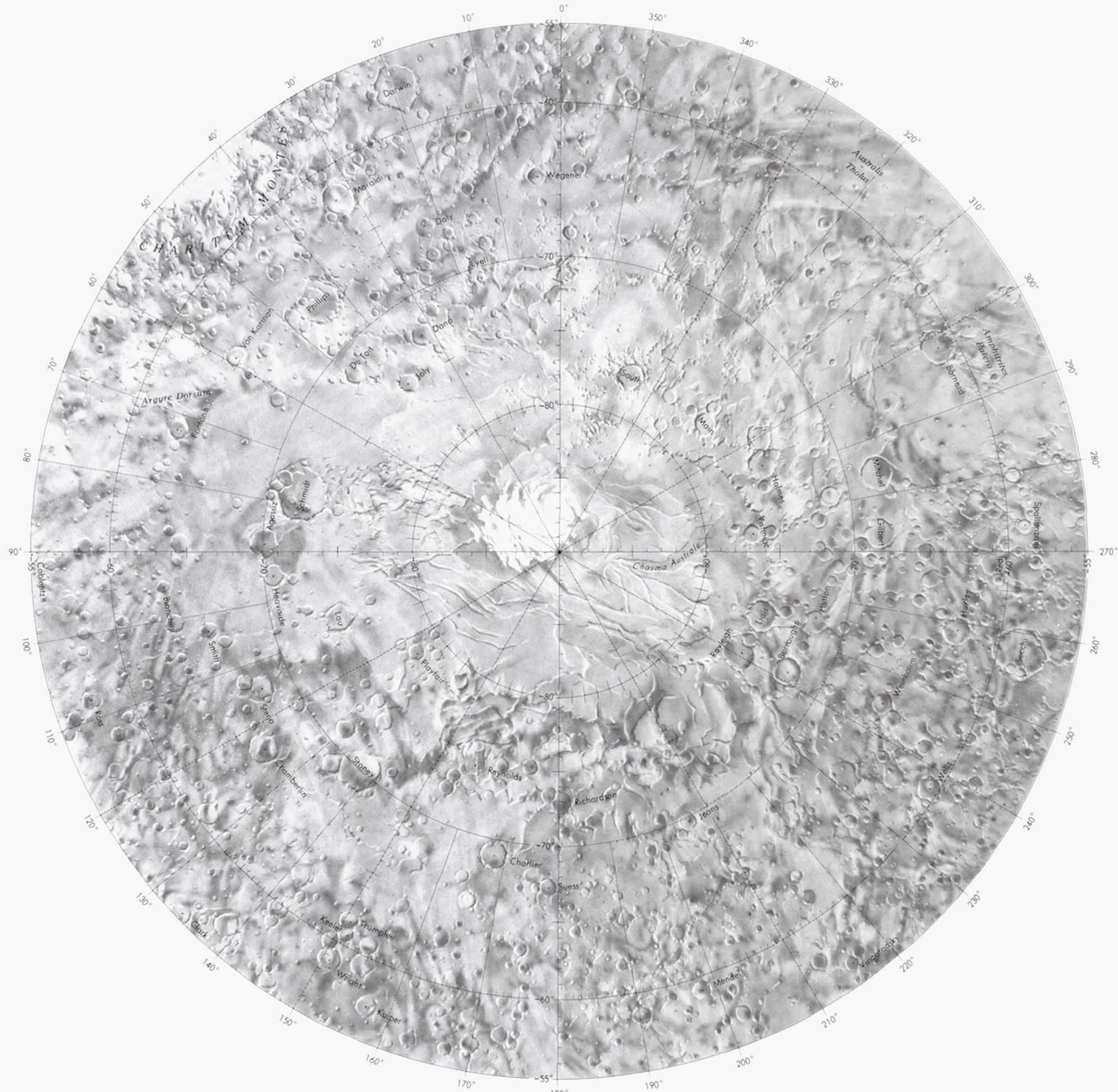

SOUTH POLAR REGION

Polar cap as it appeared on February 28, 1972

Mars

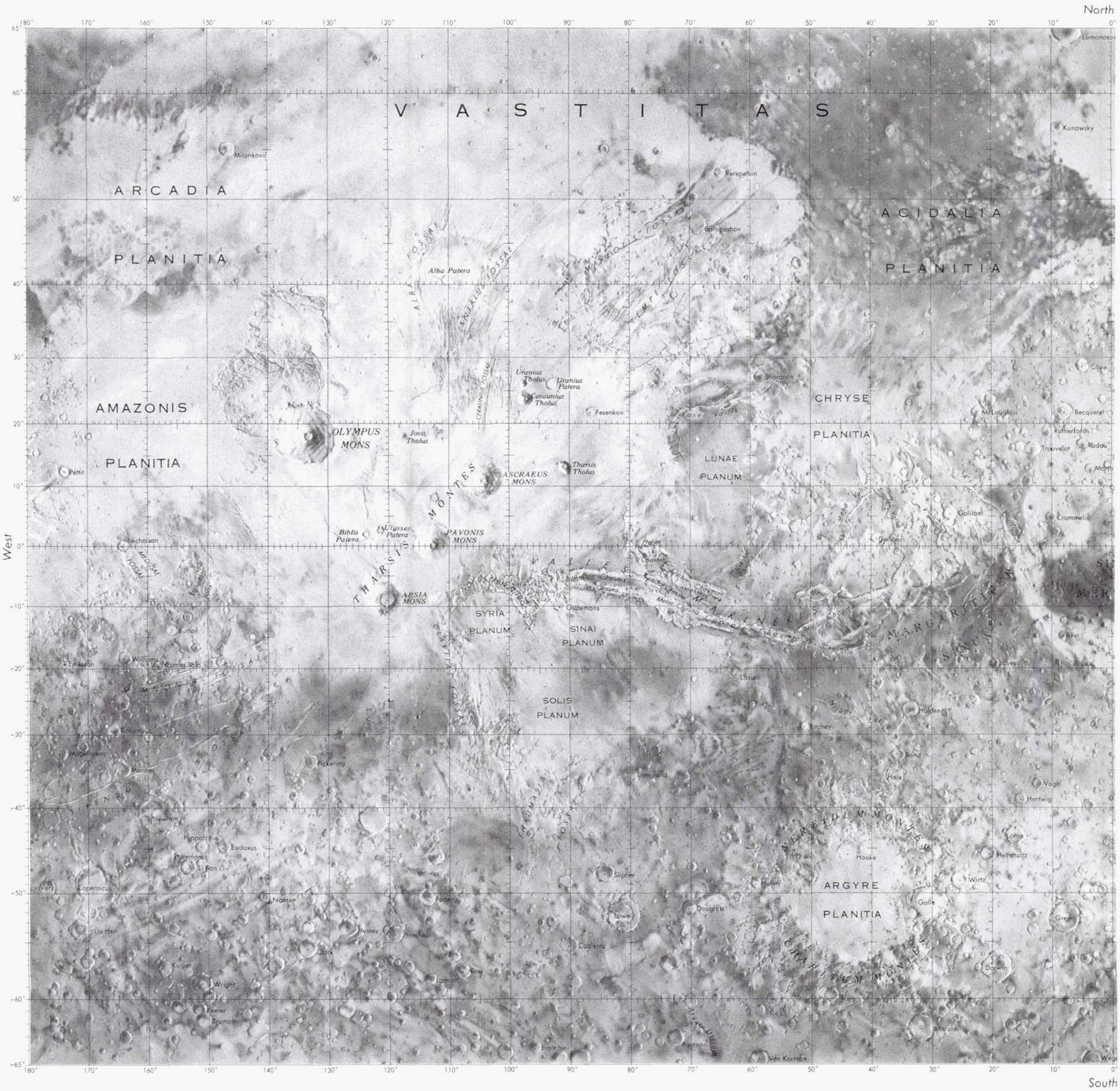
North
South
West
V A S T I T A S
ARCADIA
PLANITIA
ACIDALIA
PLANITIA
Alba Patera
AMAZONIS
PLANITIA
OLYMPUS MONS
Jovis Tholus
Uranius Tholus
Uranius Patera
Ceraunius Tholus
ASCRAEUS MONS
Tharsis Tholus
THARSIS MONTES
Biblis Patera
Ulysses Patera
PAVONIS MONS
ARSIA MONS
CHRYSE
PLANITIA
LUNAE
PLANUM
SYRIA
PLANUM
SINAI
PLANUM
SOLIS
PLANUM
ARGYRE
PLANITIA
Milankovic
Perepelkin
Lomonosov
Kunowsky
Fesenkov
Nicholson
Galilaei
Crommelin
Lowell
Von Kármán
Bianchini

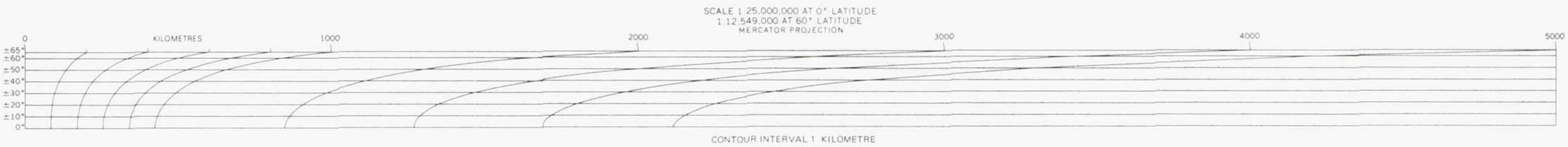
SCALE 1:25,000,000 AT 0° LATITUDE
1:12,549,000 AT 60° LATITUDE
MERCATOR PROJECTION
KILOMETRES
0
1000
2000
3000
4000
5000
CONTOUR INTERVAL 1 KILOMETRE

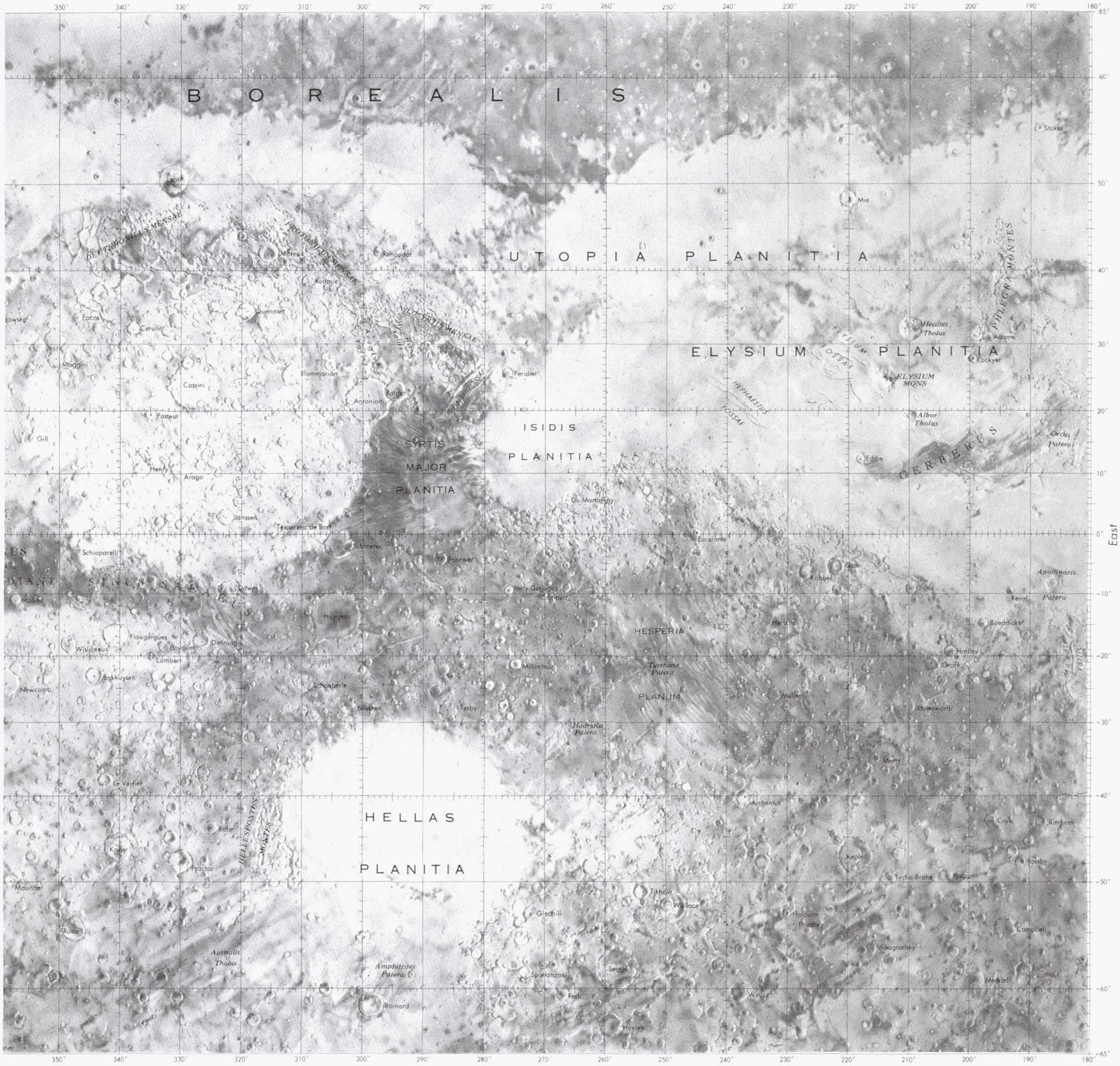
B O R E A L I S
U T O P I A P L A N I T I A
E L Y S I U M P L A N I T I A
ELYSIUM MONS
Hecates Tholus
Albor Tholus
PHLEGRA MONTES
CERBERUS
ISIDIS PLANITIA
SYRTIS MAJOR PLANITIA
HESPERIA PLANUM
Tyrrhena Patera
Hadriaca Patera
H E L L A S
P L A N I T I A
HELLESPONTUS MONTES
Amphitrites Patera
Australis Tholus
Apollinaris Patera
Orcus Patera
Mie
Stokes
Tyndall
Adams
Lockyer
Eddie
Escalante
Gale
Herschel
Huygens
Schiaparelli
Cassini
Flammarion
Peridier
Antoniadi
Pasteur
Gill
Arago
Janssen
Teisserenc de Bort
Schroeter
Fournier
Millochau
Schaeberle
Tesby
Kepler
Tycho Brahe
Gledhill
Barnard
Proctor
Maunder
Le Verrier
Newcomb
Bakhuysen
Lambert
Flaugergues
Wislicenus
Molesworth
Mendel
Campbell
Vinogradsky
Weber
Huxley
Secchi
Spallanzani
Arrhenius
Rossby
Bjerknes
Crivs
Boeddicker
Hadley
Graff
350° 340° 330° 320° 310° 300° 290° 280° 270° 260° 250° 240° 230° 220° 210° 200° 190° 180°
65° 60° 50° 40° 30° 20° 10° 0° −10° −20° −30° −40° −50° −60° −65°
East

Page intentionally left blank

REFERENCES

CHAPTER 1

Beatty, J. K., B. O'Leary, and A. Chaikin, 1981. *The New Solar System:* Sky Publishing Corp., Cambridge, Mass.

Shoemaker, E. M., 1962. Interpretation of lunar craters: *Physics and Astronomy of the Moon* (Kopal, Z., ed.), Academic Press, N.Y., pp. 283–359.

Shoemaker, E. M., and R. J. Hackman, 1962. Stratigraphic basis for a lunar time scale: *The Moon* (Z. Kopal and Z. K. Mikhailov, eds.), Academic Press, N.Y., pp. 289–300.

CHAPTER 2

Chapman, C. R., 1975. The nature of asteroids: *Sci. Amer.,* v. 232, no. 1, pp. 24–33.

Grossman, L., 1972. Condensation in the primitive solar nebula: *Geochim. et Cosmochim. Acta,* v. 36, pp. 597–619.

Grossman, L., and J. W. Larimer, 1974. Early chemical history of the Solar System: *Rev. Geophys. Space Phys.,* v. 12, pp. 71–101.

Lewis, J. S., 1974. The Chemistry of the Solar System: *Sci. Amer.,* v. 230, no. 3, pp. 51–65.

Wasson, J. T., 1974. *Meteorites:* Springer-Verlag, New York, 316 pp.

Whipple, F. L., 1974. The nature of Comets: *Sci. Amer.,* v. 230, no. 2, pp. 49–57.

Wood, J. A., 1979. *The Solar System,* Prentice-Hall, New Jersey, 196 pp.

CHAPTER 3

Adams, J., and T. McCord, 1977. Mercury: Evidence for an anorthositic crust from reflectance spectra: *Bull. Amer. Astron. Assoc.,* (abstract), v. 9, p. 457.

Allen, C. C., 1977. Rayed craters on the Moon and Mercury: *Phys. Earth Planet. Interiors,* v. 15, pp. 179–188.

Arthur, D. W. G., A. P. Agnieray, R. A. Horvath, C. A. Wood, and C. R. Chapman, 1963. The system of lunar craters, Quadrant 1: *Comm. Lunar Planet. Lab.,* v. 2 (30), pp. 71–78.

Broadfoot, A. L., 1976. Mercury's atmosphere from Mariner 10: Preliminary Results: *Rev. Geophys. Space Phys.,* v. 14, p. 625.

Broadfoot, A. L., S. Kumar, M. J. S. Belton, and M. B. McElroy, 1974. Mercury's atmosphere from Mariner 10: Preliminary Results: *Science,* v. 185, p. 166.

Broadfoot, A.L., D. E. Shemansky, and S. Kumar, 1976. Mariner 10: Mercury atmosphere: *Geophys. Res. Lett.,* v. 3 (10), pp. 577–580.

Burns, J. A., 1976. Consequences of tidal slowing of Mercury: *Icarus,* v. 28, pp. 453–458.

Carr, M. H., L. S. Crumpler, J. A. Cutts, R. Greeley, J. E. Guest, and H. Masursky, 1977. Martian impact craters and emplacement of ejecta by surface flow: *J. Geophys. Res.,* v. 82, p. 4055.

Chapman, C. R., 1976. Chronology of terrestrial planet evolution: The evidence from Mercury: *Icarus,* v. 28, pp. 523–536.

Chase, S. C., Jr., E. D. Miner, D. Morrison, and G. Munch, 1974. Preliminary Infrared Radiometry of the night side of Mercury from Mariner 10: *Science,* v. 185, p. 142.

Cintala, M. J., J. W. Head, and T. A. Mutch, 1976. Characteristics of fresh Martian craters as a function of diameter: comparison with the Moon and Mercury: *Geophys. Res. Lett.,* v. 3, p. 117.

Cintala, M. J., C. A. Wood, and J. W. Head, 1977. The effects of target characteristics on fresh crater morphology: Preliminary results for the Moon and Mercury: *Proc. Lunar Sci. Conf. 8th,* p. 3409.

Cordell, B., and R. G. Strom, 1977. Global tectonics of Mercury and the Moon: *Phys. Earth Planet. Interiors,* v. 15, p. 146.

Danjon, A., 1949. Photometrie et colorimetrie des planetes Mercure et Venus: *Bull. Astr.,* v. 14, p. 315.

Davies, M. E., S. E. Dwornik, D. E. Gault, and R. G. Strom, 1978. *Atlas of Mercury, NASA SP-423.*

DeHon, R. A., 1978. In search of ancient astroblemes: Mercury, (abstract), *Repts. Planet. Geol., NASA TM-79729,* p. 150.

Dollfus, A., and M. Auriere, 1974. Optical polarimetry of planet Mercury: *Icarus,* v. 23, p. 465.

Dzurisin, D., 1976. *Scarps, ridges, troughs and other lineaments on Mercury,* Ph.D. Dissertation, California Institute of Technology.

———, 1977. Mercurian bright patches: Evidence for physicochemical alteration of surface material? *Geophys. Res. Lett.,* v. 4, p. 383.

Fjeldbo, G., A. Kliore, D. Swetnam, P. Esposito, B. Seidel, and T. Howard, 1976. The occultation of Mariner 10 by Mercury: *Icarus,* v. 29, p. 439.

Fricker, P. E., R. T. Reynolds, A. L. Summers, and P. M. Cassen, 1976. Does Mercury have a molten core? *Nature,* v. 259, p. 2934.

Gault, D. E., G. E. Guest, J. B. Murray, D. Dzurisin, and M. C. Malin, 1975. Some comparisons of impact craters on Mercury and the Moon: *J. Geophys. Res.,* v. 80, p. 2444.

Gault, D. E., W. L. Quaide, and V. R. Oberbeck, 1968. Impact cratering mechanics and structures, *Shock Metamorphism.*

Goldreich, P., and S. L. Peale, 1968. The dynamics of planetary rotations: *Ann. Rev. Astron. Astrophys.* v. 6, p. 287.

Goldreich, P., and S. Soter, 1966. Q in the Solar System: *Icarus,* v. 5, p. 375.

Goldstein, R. M., 1971. Radar observations of Mercury: *Astron. J.,* v. 76, p. 1152.

Grossman, L., 1972. Condensation in the primitive solar nebula: *Geochim. et Cosmochim. Acta,* v. 36, p. 597.

Grossman, L., and J. W. Larimer, 1974. Early chemical history of the solar system: *Rev. Geophys. Space Phys.,* v. 12, p. 71.

Gubbins, D., 1977. Speculations on the origin of the magnetic field of Mercury: *Icarus,* v. 30, p. 186.

Haines, E. L., M. I. Etchegaray-Ramirez, and A. E. Metzger, 1978. Thorium concentrations in the lunar surface II: Deconvolution modeling and its application to the regions of Aristarchus and Mare Smythii: *Proc. Lunar Planet. Sci. Conf. 9th,* p. 2985.

Hale, W., and J. W. Head, 1980. Central peaks in Mercurian Craters: Comparisons to the Moon: *Proc. Lunar Planet. Sci. Conf. 11th,* pp. 2191-2205.

Hapke, B., 1977. Interpretation of optical observations of Mercury and the Moon: *Phys. Earth Planet. Interiors,* v. 15, p. 264.

Hapke, B., B. Chjristman, B. Rava, and J. Mosher, 1980. A color-ratio map of Mercury: *Proc. Lunar Planet. Sci. Conf. 11th* p. 87.

Hapke B., G. E. Danielson, K. Klassen, and L. Wilson, 1975. Photometric observations of Mercury from Mariner 10: *J. Geophys. Res.,* v. 80, p. 2431.

Hartmann, W. K., and G. P. Kuiper, 1962. Concentric structures surrounding lunar basins: *Comm. Lunar Planet. Lab.,* v. 1, p. 51.

Hawke, B. R., and J. J. Cintala, 1978. Impact melts on Mercury and the Moon: *Bull. Amer. Astron. Soc.,* v. 9, p. 531.

Hawke, B. R., and J. W. Head, 1978. Lunar KREEP Volcanism: Geologic evidence for history and mode of emplacement: *Proc. Lunar Planet. Sci. Conf. 9th,* pp. 3285-3309.

Head, J. W., 1976. Lunar Volcanism in Space and Time: *Rev. Geophys. Space Phys.,* v. 14, p. 265.

Herbert, F., 1980. Time dependent lunar density models: *Proc. Lunar Planet. Sci Conf. 11th,* pp. 2015-2030.

Hostetler, C. J., and M. J. Drake, 1980. On the early global melting of the terrestrial planets: *Proc. Lunar Planet. Sci. Conf. 11th,* pp. 1915-1929.

Howard, K. A., D. E. Wilhelms, and D. H. Scott, 1974. Lunar basin formation and highlands stratigraphy: *Rev. Geophys. Space Phys.,* v. 12, p. 309.

Hughes, H. G., F. M. App, and T. R. McGetchin, 1977. Global seismic effects of basin-forming impacts: *Phys. Earth Planet. Interiors,* v. 15, p. 251.

Kaula, W. M., 1976. Comments on the origin of Mercury: *Icarus,* v. 28, p. 429.

Klassen, K. P., 1975. Mercury rotation period determined from Mariner 10 photography: *J. Geophys. Res.,* v. 80, p. 2415.

———, 1976. Mercury's rotation axis and period: *Icarus,* v. 28, p. 469.

Leake, M. A., 1981. *The intercrater plains of Mercury and the Moon: Their nature, origin and role in terrestrial planet evolution,* Ph.D. Dissertation, University of Arizona.

Leake, M. A., C. R. Chapman, S. J. Weidenschilling, D. R. Davis, and R. Greenberg, 1981. Mercury's History Revisited: *Rpts. Planet. Geol. Prog., NASA TM-84211,* pp. 408-410.

Lewis, J. S., 1972. Metal/silicate fractionation in the Solar System: *Earth Planet. Sci. Lett.,* v. 15, p. 286.

———, 1973. Chemistry of the Planets: *Ann. Rev. Phys. Chem.,* v. 24, p. 339.

Malin, M. C., 1976a. Observation of intercrater plains on Mercury: *Geophys. Res. Letter,* v. 3, p. 581.

———, 1976b. Comparison of large crater and multi-ringed basin populations: *Proc. Lunar Sci. Conf. 7th,* p. 3589.

———, 1978. Surfaces of Mercury and the Moon: Effects of resolution and lighting conditions on the discrimination of volcanic features: *Lunar Planet. Sci. Conf. 9th* (Abstract), p. 686.

Malin, M. C., and D. Dzurisin, 1976c. Landform degradation on Mercury, the Moon and Mars: Evidence from crater depth/diameter relationships: *J. Geophys. Res.,* v. 82, p. 376.

———, 1978. Modification of fresh crater landforms: Evidence from the Moon and Mercury: *J. Geophys. Res.,* v. 83, p. 233.

Masson, P., and P. Thomas, 1977. Preliminary results of structural lineament pattern analysis of Mercury: *Rpts. Planet. Geol. Prog., NASA TMX-3511,* p. 54.

McCauley, J. F., 1967. U.S. Geol. Sur. Map I-491.

McCauley, J. F., J. E. Guest, G. G. Schaber, N. J. Trask, and R. Greeley, 1981. Stratigraphy of the Caloris basin, Mercury: *Icarus,* v. 47, pp. 184-202.

McCauley, J. R., 1977. Orientale and Caloris: *Phys. Earth Planet. Inter.,* v. 15, p. 220.

McCord, T., and J. Adams, 1972. Mercury: Surface composition from the reflectance spectrum: *Science,* v. 178, p. 745.

McCord, T. B., and R. N. Clark, 1979. The Mercury Soil: Presence of Fe^{2+}: *J. Geophys. Res.,* v. 84, p. 7664.

McKinnon, W. B., 1979. Caloris: Ring load on the elastic lithosphere, *EOS,* abstract, v. 60, p. 871.

———, 1981. Application of ring tectonic theory to Mercury and other solar system bodies. *Multi-ring Basins: Proc. Lunar Planet. Sci.,* v. 12A, pp. 259-273.

Melosh, H. J., 1977. Global tectonics of a despun planet: *Icarus,* v. 31, p. 221.

Melosh, H. J., and D. Dzurisin, 1978a. Tectonic implications for the gravity structure of the Caloris Basin, Mercury: *Icarus,* v. 33, pp.141-144.

———, 1978b. Mercurian global tectonics: A consequence of tidal despinning: *Icarus,* v. 35, p. 227.

Murray, B. C., M. J. S. Belton, G. E. Danielson, J. E. Davies, D. E. Gault, B. Hapke, B. O'Leary, R. G. Strom, V. Suomi, and N. Trask, 1974. Mercury's surface: Preliminary description and interpretation from Mariner 10 pictures: *Science,* v. 185, p. 169.

Murray, B. C., R. G. Strom, N. J. Trask, D. E. Gault, 1975. Surface history of Mercury: Implications for terrestrial planets: *J. Geophys. Res.,* v. 80, p. 2508.

Ness, N. F., 1978. Mercury: Magnetic field and interior: *Space Sci. Rev.,* v. 21, p. 527.

Ness, N. F., K. W. Behannon, R. P. Lepping, and T. C. Whang, 1975. The magnetic field of Mercury: *J. Geophys. Res.,* v. 80, p. 2708.

———, 1976. Observations of Mercury's magnetic field: *Icarus,* v. 28, p. 479.

Ness, N. F., K. W. Behannon, R. P. Lepping, T. C. Whang, and K. H. Schatten, 1974. Magnetic Field Observations near Mercury: Preliminary Results from Mariner 10: *Science,* v. 185, p. 151.

Oberbeck, V.R., W.L. Quaide, R. E. Arvidson, and H. R. Ag-

garwal, 1977. Comparative studies of lunar, martian and mercurian craters and plains: *J. Geophys. Res.,* v. 82, p. 1681.

Peale, S. J., 1974. Possible histories of the obliquity of Mercury: *Astron. J.,* v. 79, p. 722.

———, 1976. Inferences from the dynamical history of Mercury's rotation: *Icarus,* v. 28, p. 459.

Pechmann, J. B., and H. J. Melosh, 1979. Global fracture patterns of a despun planet: Application to Mercury: *Icarus,* v. 38, p. 243.

Pettingill, G. H., and R. B. Dyce, 1965. A radar determination of the rotation of the planet Mercury: *Nature,* v. 206, p. 1240.

Pike, R. J., 1980. Control of crater morphology by gravity and target type: Mars, Earth, Moon: *Proc. Lunar Planet. Sci. Conf. 11th,* pp. 2159–2189.

Pohn, H. A., and R. L. Wildey, 1970. A photoelectric-photographic study of the normal albedo of the Moon: *U.S. Geological Survey Professional Paper, 599-E,* pp. 1–20.

Schaber, G. G., J. M. Boyce, and N. J. Trask, 1977. Moon-Mercury: Large impact structures, isostasy and average crustal viscosity: *Phys. Earth Planet. Interiors,* v. 15, p. 189.

Schultz, P. H., 1977. Endogenic modification of impact craters on Mercury: *Phys. Earth Planet. Interiors,* v. 15, p. 202.

Schultz, P. H., and D. E. Gault, 1975. Seismic effects from major basin formations on the Moon and Mercury: *Moon,* v. 12, p. 159.

Scott, D. H., 1972. Geologic map of the Maurolycus Quadrangle, U.S. Geol. Surv. Geologic Atlas of the Moon: *U.S. Geol. Surv. Misc. Inv.* Map I-695.

———, 1977. Moon-Mercury: Relative preservation states of secondary craters: *Phys. Earth Planet. Interiors,* v. 15, p. 173.

Scott, D. H., J. F. McCauley, and M. N. West, 1977. Geologic Map of the west side of the Moon: *U.S. Geo. Surv. Misc. Inv. Map* I-1034.

Siegfried, R. W., and S. C. Solomon, 1974. Mercury: Internal structure and thermal evolution: *Icarus,* v. 23, p. 192.

Siscoe, G., and L. Christopher, 1975. Variations in the solar wind stand-off distance at Mercury: *Geophys. Res. Lett.,* v. 2, p. 158.

Siscoe, G. L., N. F. Ness, and C. M. Yeates, 1975. Substorms on Mercury? *J. Geophys. Res.,* v. 80, pp. 4359–4363.

Smith, E. I., and J. A. Hartnell, 1979. Crater size-shape profiles for the Moon and Mercury: Terrain effects and interplanetary comparisons: *Moon and Planets,* v. 19, p. 479.

Solomon, S. C., 1977. The relationship between crustal tectonics and evolution in the Moon and Mercury: *Phys. Earth Planet. Interiors,* v. 15, p. 135.

———, 1978. On volcanism and thermal tectonics on one plate planets: *Geophys. Res. Lett.,* v. 5, p. 461.

Spudis, P., 1978. Composition and origin of the Apennine Bench formation: *Proc. Lunar Planet. Sci. Conf. 9th,* pp. 3379–3394.

Stephenson, A., 1976. Crustal remanence and the magnetic moment of Mercury: *Earth Planet. Sci. Letter.,* v. 28, p. 454.

Stevenson, D. J., 1974. Planetary Magnetism: *Icarus,* v. 22, p. 403.

———, 1980. Core formation dynamics and primordial planetary dynamos: *Lunar Planet. Sci. Conf. 11th* (Abstract), pp. 1088–1090.

Strom, R. G., 1964. Analysis of lunar lineaments, I: Tectonic maps of the Moon: *Comm. Lunar Planet. Lab.,* v. 2, p. 205.

———, 1977. Origin and relative age of lunar and mercurian intercrater plains: *Phys. Earth Planet. Interiors,* v. 15, p. 156.

———, 1979. Mercury: A post Mariner 10 assessment: *Space Sci. Rev.,* v. 24, p. 3.

Strom, R. G., B. C. Murray, M. J. S. Belton, G. E. Danielson, M. E. Davies, D. Gault, G. Hapke, B. O'Leary, N. Trask, J. E. Guest, J. Anderson, and K. Klaasen, 1975a. Preliminary imaging results from the second Mercury encounter: *J. Geophys. Res.,* v. 80, p. 2345.

Strom, R. G., N. F. Trask, and J. E. Guest, 1975b. Tectonism and Volcanism on Mercury: *J. Geophys. Res.,* v. 80, p. 2478.

Strom, R. G., A. Woronow, and M. Gurnis, 1981. Crater populations on Ganymede and Callisto: *J. Geophys. Res.,* v. 86, pp. 8659–8674.

Toksöz, M. N., and D. H. Johnston, 1977. The evolution of the Moon and terrestrial planets, *The Soviet-American Conference on Cosmochemistry of the Moon and Planets, NASA SP-370,* Part 1, p. 295.

Toksöz, M. N., A. T. Hsui, and D. H. Johnston, 1978. Thermal evolution of the terrestrial planets: *The Moon and Planets,* v. 18, p. 281.

Trask, N. J., 1975. Cratering history of the heavily cratered terrain on Mercury: *Proc. Intern. Coll. Planet. Geol.: Geol. Rom.,* v. 15, p. 471.

Trask, N. J., and J. E. Guest, 1975. Preliminary geologic terrain map of Mercury: *J. Geophys. Res.,* v. 80, pp. 2461–2477.

Trask, N. J., and R. G. Strom, 1976. Additional evidence of mercurian volcanism: *Icarus,* v. 28, p. 559.

Vilas, F., and T. B. McCord, 1976. Mercury: Spectral Reflectance Measurements (0.33–1.06 μm) 1974/75: *Icarus,* v. 28, p. 593.

Ward, W. R., G. Colombo, and F. A. Franklin, 1976. Secular resonance solar spin down and the orbit of Mercury: *Icarus,* v. 28, p. 441.

Watkins, J. A., and R. G. Strom, 1984. Relative age of the smooth plains and Caloris Basin of Mercury: *Icarus,* (in press).

Wetherill, G. W., 1975. Late heavy bombardment of the Moon and terrestrial planets: *Proc. Lunar Sci. Conf. 6th,* p. 1539.

Whitaker, E. A., 1972. Lunar color boundaries and their relation to topographic features: A preliminary survey: *The Moon,* v. 4, pp. 348–355.

Wildey, R. L., 1977. A digital file of the lunar normal albedo: *The Moon,* v. 16, p. 231.

Wilhelms, D. E., 1974. Comparison of martian and lunar geologic provinces: *J. Geophys. Res.,* v. 79, p. 3933.

———, 1976. Mercurian volcanism questioned: *Icarus,* v. 28, p. 551.

Wilhelms, D. E., and J. F. McCauley, 1971. Geologic map of the near side of the Moon: *U.S. Geol. Surv. Misc. Inv. Series Map 1-703.*

Wood, C. A., 1980. Martian double ring basins: New Observations: *Proc. Lunar Planet. Sci. Conf. 11th,* pp. 2191–2205.

Wood, C. A., and J. W. Head, 1976. Comparisons of impact basins on Mercury, Mars, and the Moon: *Proc. Lunar Sci. Conf. 7th,* p. 3629.

Wood, C. A., J. W. Head, and M. J. Cintala, 1977. Crater degradation on Mercury and the Moon: Clues to surface evolution: *Proc. Lunar Sci. Conf. 8th,* p. 3503.

———, 1978. Interior morphology of fresh martian craters: the effects of target characteristics: *Proc. Lunar Planet. Sci. Conf. 9th,* pp. 3691–3709.

Woronow, A., 1978. A general cratering history model and its implications for the lunar highlands: *Icarus,* v. 34, p. 76.

Woronow, A., R. G. Strom, and M. Gurnis, 1982. Interpreting

the Cratering Record: Mercury to Ganymede and Callisto: *The Satellites of Jupiter,* Univ. of Arizona Press.

Wright, F. E., F. H. Wright, and H. Wright, 1963. The lunar surface: Introduction: *Moon, Meteorites and Comets,* Univ. Chicago Press, 1.

Wu, H. H., and A. L. Broadfoot, 1977. The extreme ultraviolet albedos of the planet Mercury and the Moon: *J. Geophys. Res.,* v. 82, p. 759.

Zohar, S., and R. M. Goldstein, 1974. Surface features on Mercury: *Astron. J.,* v. 79, p. 85.

CHAPTER 4

Ananda, M. P., W. L. Sjogren, R. J. Phillips, R. N. Wimberley, and B. G. Bills, 1980. A low-order global gravity fields of Venus and dynamic implications: *J. Geophys. Res.,* v. 85, pp. 8303-8318.

Anderson, D. L., 1981. Plate tectonics on Venus: *Geophys. Res. Lett.,* v. 8, pp. 309-311.

Anderson, J. D., L. Efron, and G. E. Pease, 1968. Mass dynamical oblateness, and position of Venus as determined by Mariner V tracking: *Astron. J., 73(II),* v. S162.

Anderson, J. D., G. W. Null, and C. T. Thornton, 1964. The evaluation of certain astronomical constants from the radio tracking of Mariner II: *Prog. in Astronaut. Aeron.,* v. 14, pp. 131-155.

Arvidson, R. E., and G. F. Davies, 1981. Effects of lateral resolution on the identification of volcano tectonic provinces on Earth and Venus: *Geophys. Res. Lett.,* v. 8, pp. 741-744.

Ash, M. E., D. B. Campbell, R. B. Dyce, R. P. Ingalls, R. Jurgens, G. H. Pettengill, I. I. Shapiro, M. A. Slade, and T. W. Thompson, 1968. The case for the radar radius of Venus: *Science,* v. 160, pp. 985-987.

Barsukov, V. L., 1982. New Venera results: Paper presented at the 13th Lunar and Planetary Science Conference, Houston, Tex., March 15-19, 1982.

Brass, G. W., and C. G. A. Harrison, 1982. On the possibility of plate tectonics on Venus: *Icarus,* v. 49, pp. 86-96.

Cameron, A. G. W., 1963. Formation of the solar nebula: *Icarus,* v. 1, pp. 339-342.

———, 1973. Accumulation processes in the primitive solar nebula: *Icarus,* v. 18, pp. 407-450.

Campbell, D. B., and B. A. Burns, 1980. Earth-based radar imagery of Venus: *J. Geophys. Res.,* v. 85, pp. 8271-8281.

Campbell, D. B., B. A. Burns, and V. Boriakoff, 1979. Venus: Further evidence of impact cratering and tectonic activity from radar observations: *Science,* v. 204, pp. 1424-1427.

Campbell, D. B., J. W. Head, J. K. Harmon, and A. A. Hine, 1984. Volcanism and rift formation in Beta Regio, Venus: (in press).

Campbell, D. B., R. F. Jurgens, R. B. Dyce, F. S. Harris, and G. H. Pettengill, 1970. Radar interferometric observations of Venus at 70-cm wavelength: *Science,* v. 170, pp. 1090-1099.

Carpenter, R. L., 1964. Studies of Venus by CW radar: *Astron. J.,* v. 69, pp. 2-11.

Colin, L., 1980. The Pioneer Venus Program: *J. Geophys. Res.,* v. 85, pp. 7575-7598.

Counselman, C. C., S. A. Gourevitch, R. W. King, G. B. Loriet, and E. S. Ginsberg, 1980. Zonal and meridional circulation of the lower atmosphere of Venus determined by radio interferometry: *J. Geophys. Res.,* v. 85, pp. 8026-8030.

Cutts, J. A., T. W. Thompson, and B. H. Lewis, 1981. Origin of bright ring shaped craters in radar images of Venus: *Icarus,* v. 48, pp. 428-452.

De Vaucouleurs, G., 1964. Geometric and photometric parameters of the terrestrial planets: *Icarus,* v. 3, pp. 187-235.

Downs, G. S., R. M. Goldstein, R. R. Green, G. A. Morris, and P. E. Reichley, 1973. Martian topography and surface properties as seen by radar: the 1971 opposition: *Icarus,* v. 18, pp. 8-21.

Downs, G. S., P. E. Reichley, and R. R. Green, 1975. Radar measurements of martian topography and surface properties: the 1971 and 1973 oppositions: *Icarus,* v. 26, pp. 273-312.

Drake, F. D., 1964. Microwave observations of Venus, 1962-1963: *Astron. J.,* v. 69, pp. 62-64.

Esposito, P. B., W. L. Sjogren, N. A. Mottinger, B. G. Bills, and E. Abbott, 1982. Venus gravity: Analysis of Beta Regio: *Icarus,* v. 51, pp. 448-459.

Florensky, C. P., L. B. Ronca, A. T. Basilevsky, G. A. Burba, O. V. Nikolaeva, A. A. Pronin, A. M. Trakhtman, V. P. Volkov, and V. V. Zazetsky, 1977. The surface of Venus as revealed by Soviet Venera 9 and 10: *Bull. Geol. Soc. America,* v. 88, pp. 1537-1545.

Geottel, K. A., J. A. Shields, and D. A. Decker, 1981. Density constraints on the composition of Venus: *Proc. Lunar Planet. Sci. Conf., 12B,* pp. 1507-1516.

Goldstein, R. M., 1964. Venus characteristics by Earth-based radar: *Astron. J.,* v. 69, pp. 12-18.

———, 1965. Preliminary Venus radar results: *Radio Sci., 69D,* pp. 1623-1625.

Goldstein, R. M., R. R. Green, and H. C. Rumsey, 1976. Venus radar images: *J. Geophys. Res.,* v. 81, pp. 4807-4817.

———, 1978. Venus radar brightness and altitude images: *Icarus,* v. 36, pp. 334-352.

Goldstein, R. M., and H. C. Rumsey, 1970. A radar snapshot of Venus: *Science,* v. 169, pp. 974-977.

———, 1972. A radar image of Venus: *Icarus,* v. 17, pp. 699-703.

Greeley, R., S. Williams, J. D. Iverson, R. Leach, B. R. White, and J. Pollack, 1982. Windblown sand on Venus: Preliminary laboratory simulations: *EOS,* v. 63, p. 1021.

Head, J. W., and D. B. Campbell, 1982. Identification of banded terrain in the mountains of Ishtar Terra: *Venus, NASA TM-85127,* pp. 80-82.

Head, J. W., S. E. Yuter, and S. C. Solomon, 1981. Topography of Venus and Earth: A test for the presence of plate tectonics: *Am. Sci.,* v. 69, pp. 614-623.

Jurgens, R. F., R. M. Goldstein, H. R. Rumsey, and R. R. Green, 1980. Images of Venus by three station radar interferometry—1977 results: *J. Geophys. Res.,* v. 85, pp. 8282-8294.

Kaula, W. H., 1981. Inferences from other bodies for the Earth's composition and evolution: *Evolution of the Earth, Geodynamics Series,* v. 5, pp. 141-146.

Kaula, W. H., and L. M. Muradian, 1982. Could plate tectonics on Venus be concealed by volcanic deposits? *Geophys. Res. Lett.* v. 9, pp. 1021-1024.

Keldysh, M. V., 1977. Venus exploration with Venera 9 and Venera 10 spacecraft: *Icarus,* v. 30, pp. 605-625.

Kuzmin, A. D., and Marov, M. Ya., 1974. *Physics of the planet*

Venus, Nauka, Moscow, (in Russian).

Lewis, J. S., 1972. Metal/Silicate fractionation in the solar system: *Earth Planet. Sci. Lett.,* v. 15, pp. 286–290.

———, 1974. The chemistry of the solar system: *Sci. Amer.,* v. 230, pp. 50–65.

Lewis, J. S., and F. A. Kreimendahl, 1980. Oxidation state of the atmosphere and crust of Venus from Pioneer-Venus results: *Icarus,* v. 42, pp. 330–337.

Malin, M. C., 1981. Speculations on the geology of Venus, *Trans. Am. Geophys. Union, EOS,* in press.

Malin, M. C., and R. S. Saunders, 1977. Surface of Venus: Evidence of diverse landforms from radar observations: *Science,* v. 196, pp. 987–990.

Masursky, H., E. Eliason, P. G. Ford, G. E. McGill, G. H. Pettengill, G. G. Schaber, and G. Schubert, 1980. Pioneer-Venus radar results: Geomorphology from imagery and altimetry: *J. Geophys. Res.,* v. 85, pp. 8232–8260.

McGill, G. E., 1979. Venus tectonics: Another Earth or another Mars? *Geophys. Res. Lett.,* v. 6, pp. 739–741.

McGill, G., S. Steenstrup, C. Barton, and P. Ford, 1981. Continental rifting and the origin of Beta Regio, Venus: *Geophys. Res. Lett.,* v. 8, pp. 737–740.

McGill, G. E., J. L. Warner, M. C. Malin, R. E. Arvidson, E. Eliason, S. Nozette, and R. D. Reasenberg, 1982. Topography, surface properties, and tectonic evolution: in *Venus,* D. M. Hunten, L. Colin, and T. M. Donahue, eds., University of Arizona Press, Tucson.

Moore, H. J., J. M. Boyce, G. G. Schaber, and D. H. Scott, 1980. Lunar remote sensing and measurements: *U.S. Geological Survey Prof. Paper* 1046B.

Moore, P., 1960. A defence of Schroter: *J. Brit. Astron. Assoc.,* v. 70, p. 363.

———, 1961. *The planet Venus,* 3rd ed., Macmillan, New York.

Mueller, R. F., 1969. Effect of temperature on the strength and composition of the upper lithosphere of Venus: *Nature,* v. 224, pp. 354–356.

Muhleman, D. O., 1964. Radar scattering from Venus and the Moon: *Astron. J.,* v. 69, pp. 34–41.

Nozette, S., and J. S. Lewis, 1982. Venus: Chemical weathering of igneous rocks and buffering of atmospheric composition: *Science,* v. 216, pp. 181–183.

Pettengill, G. H., E. Eliason, G. G. Ford, G. B. Loriot, H. Masursky, and G. E. McGill, 1980. Pioneer-Venus radar results: Altimetry and surface properties: *J. Geophys. Res.,* v. 85, pp. 8261–8270.

Pettengill, G. H., P. G. Ford, W. E. Brown, W. M. Kaula, C. H. Keller, H. Masursky, and G. E. McGill, 1979a. Pioneer-Venus radar mapping experiment: *Science,* v. 203, pp. 806–808.

Pettengill, G. H., P. G. Ford, W. E. Brown, W. M. Kaula, H. Masursky, E. Eliason, and G. E. McGill, 1979b. Venus: Preliminary topographic and surface imaging results from the Pioneer Orbiter: *Science,* v. 205, pp. 90–93.

Pettengill, G. H., P. G. Ford, and S. Nozette, 1982. Venus: Global surface radar reflectivity: *Science,* v. 217, pp. 640–642.

Phillips, R. J., and M. C. Malin, 1982. The interior of Venus and tectonic implications, in *Venus,* D. M. Hunten, L. Colin, and T. M. Donahue, eds., University of Arizona Press, Tucson.

Phillips, R. J., W. Kaula, G. McGill, and M. C. Malin, 1981. Tectonics and evolution of Venus: *Science,* v. 212, pp. 879–887.

Phillips, R. J., W. L. Sjogren, E. A. Abbot, J. C. Smith, and R. N. Wimberly, 1979. Gravity field of Venus: A preliminary analysis: *Science,* v. 205, pp. 93–96.

Pollack, J. B., and B. C. Black, 1979. Implications of the gas compositional measurements of Pioneer Venus for the origin of planetary atmospheres: *Science,* v. 205, pp. 56–59.

Reasenberg, R. D., Z. M. Goldberg, P. E. MacNeil, and I. I. Shapiro, 1981. Venus gravity: A high-resolution map: *J. Geophys. Res.,* v. 86, pp. 7173–7179.

Ringwood, A. E., and D. L. Anderson, 1977. Earth and Venus: A comparative study: *Icarus,* v. 30, pp. 243–253.

Rogers, A. E., and R. P. Ingalls, 1969. Venus: mapping the surface reflectivity by radar interferometry: *Science,* v. 165, pp. 797–799.

———, 1970. Radar mapping of Venus with interferometric resolution of the Range-Doppler ambiguity: *Radio Sci.,* v. 5, pp. 425–433.

Rumsey, H. C., G. A. Morris, R. R. Green, and R. M. Goldstein, 1974. A radar brightness and altitude image of a portion of Venus: *Icarus,* v. 23, pp. 1–7.

Saunders, R. S., and M. C. Malin, 1977. Geologic interpretation of new observations of the surface of Venus: *Geophys. Res. Lett.,* v. 4, pp. 547–550.

Schaber, G. G., 1982. Venus: Limited extension and volcanism along zones of lithospheric weakness: *Geophys. Res. Lett.,* v. 9, pp. 499–502.

Shapiro, I. I., S. H. Zisk, A. E. Rogers, M. A. Slade, and T. W. Thomspon, 1972. Lunar topography: global determination by radar: *Science,* v. 178, pp. 939–948.

Simpson, R. A., G. L. Tyler, and D. B. Campbell, 1978. Arecibo observations of Mars surface characteristics in the northern hemisphere: *Icarus,* v. 36, pp. 153–173.

Sjogren, W. L., R. J. Phillips, P. W. Birkeland, and R. N. Wimberley, 1980. Gravity anomalies on Venus: *J. Geophys. Res.,* v. 85, pp. 8295–8302.

Solomon, S. C., and J. W. Head, 1982. Mechanisms for lithospheric heat transport on Venus: Implications for tectonic style and volcanism: *J. Geophys. Res.,* v. 87, pp. 9236–9246.

Solomon, S. C., S. K. Stephens, and J. W. Head, 1982. On Venus impact basins: Viscous relaxation of topographic relief: *J. Geophys. Res.,* v. 87, pp. 7763–7771.

Surkov, Yu. A., F. F. Kirnozov, V. K. Khristianov, B. N. Glzov, F. Ivano, and B. N. Korchuganov, 1977. Investigations of the density of the venusian surface rocks by Venera 10: *COSPAR Space Res.,* v. 17, pp. 651–657.

Tauber, M. E., and D. B. Kirk, 1976. Impact craters on Venus: *Icarus,* v. 28, pp. 352–357.

Thompson, T. W., J. A. Cutts, R. W. Shorthill, and S. H. Zisk, 1980. Infrared and radar signatures of lunar craters: implications about crater evolution: *Proc. Conf. Lunar Highlands Crust,* pp. 483–499, Lunar Planet Inst., Houston, Tex.

Thompson, T. W., H. Masursky, R. W. Shorthill, G. L. Tyler, and S. H. Zisk, 1974. A comparison of infrared, radar and geologic mapping of lunar craters: *The Moon,* v. 10, pp. 87–117.

Thompson, T. W., S. H. Zisk, R. W. Shorthill, P. H. Schultz, and J. A. Cutts, 1981. Lunar craters with radar bright ejecta: *Icarus,* v. 46, pp. 201–225.

Tyler, G. L., 1979. Comparison of quasi-specular scatter from the Moon with surface parameters obtained from images: *Icarus,*

v. 37, pp. 29–45.

Urey, H. C., 1952. *The Planets,* Yale University Press, New Haven, Conn.

Vinogradov, A. P., Yu. A. Surkov, and F. F. Kirnozov, 1973. The content of Uranium, Thorium and Potassium in the rocks of Venus as measured by Venera 8: *Icarus,* v. 20, pp. 253–259.

Warner, J. L., 1980. Venus: Do sediments cover lowlands? *Bull. Amer. Astron. Soc.,* v. 12, p. 691.

———, 1983. Sedimentary processes and crustal cycling on Venus: *Proc. Lunar Planet. Sci. Conf. 13th,* A495–A500.

Weertman, J., 1979. Height of mountains on Venus and the creep properties of rock: *Phys. Earth Planet. Interiors.,* v. 19, pp. 197–207.

Wetherill, G. W., 1981. Solar wind origin of ^{36}Ar on Venus: *Icarus,* v. 46, pp. 70–80.

White, B. R., 1979. Soil transport by winds on Mars: *J. Geophys. Res.,* v. 84, pp. 4643–4651.

White, B. R., R. Greeley, J. D. Iverson, and J. B. Pollack, 1976. Estimated grain saltation in a martian atmosphere: *J. Geophys. Res.,* v. 81, pp. 5643–5650.

Williams, S., and R. Greeley, 1982. Saltation flux on Venus: Laboratory results: *EOS,* v. 63, p. 1021.

Young, L., and A. T. Young, 1971. Comments on "The composition of the Venus cloud tops in light of recent spectroscopic data": *Astrophys. J.,* v. 179, L39–43.

Zisk, S. H., 1972. Lunar topography: first radar interferometer measurements of Alphonsus-Ptolemaeus-Arzechal region: *Science,* v. 178, pp. 977–980.

Zisk, S. H., G. H. Pettengill, and G. W. Catura, 1974. 3.8-cm radar atlas of the Moon: *The Moon,* v. 10, pp. 17–50.

CHAPTER 5

Anhaeusser, C. R., 1971. Cyclic volcanicity and sedimentation in the evolutionary development of Archean greenstone belts of shield areas: *Geol. Soc. Australia Sp. Publ. no. 3,* pp. 57–70.

———, 1973. The evolution of the early precambrian crust of southern Africa: *Phil. Trans. Roy. Soc.,* London, v. A273, pp. 359–388.

———, 1975. Precambrian tectonic environments: *Ann. Rev. Earth Planet. Sci.,* v. 3, pp. 31–55.

Anhaeusser, C. R., R. Mason, M. J. Viljoen, and R. P. Viljoen, 1969. A reappraisal of some aspects of Precambrian shield geology: *Bull. Geol. Soc. America,* v. 80, pp. 2175–2200.

Armstrong, R. L., 1968. A model for the evolution of strontium and lead isotopes in a dynamic earth: *Rev. Geophys. Space Phys.,* v. 6, pp. 175–199.

Armstrong, R. L., and S. M. Hein, 1973. Computer simulation of Rb and Sr evolution of the Earth's crust and upper mantle: *Geochim. et Cosmochim. Acta,* v. 37, pp. 1–18.

Arvidson, R. E., E. A. Guiness, and S. W. Lee, 1979. Differential aeolian redistribution rates on Mars: *Nature,* v. 278, pp. 533–535.

Atwater, T., 1970. Implications of plate tectonics for the Cenozoic tectonic evolution of North America: *Bull. Geol. Soc. America,* v. 81, pp. 3513–3535.

Baranzangi, M., and J. Dorman, 1969. World seismicity maps compiled from ESSA, Coast and Geodetic Survey, Epicenter Data 1961–1967: *Bull. Seism. Soc. Amer.,* v. 59, pp. 369–380.

Berkner, L. V., and L. C. Marshall, 1967. The rise of oxygen in the Earth's atmosphere with notes on the martian atmosphere: *Adv. Geophys.,* v. 12, pp. 309–331.

Blackett, P. M. S., J. A. Clegg, and P. H. S. Stubbs, 1960. An analysis of rock magnetic data: *Proc. Roy. Soc.* (London), v. A-256, pp. 291–322.

Boyd, F. R., 1973. A pyroxene geotherm: *Geochim et Cosmochim. Acta,* v. 37, pp. 2533–2546.

Burke, K., J. F. Dewey, and W. S. F. Kidd, 1976. Dominance of horizontal movements, arc and midcontinent collisions during the later permobile regime: in *The Early History of the Earth,* B. F. Windley, ed., Wiley, New York, pp. 113–129.

Burke, K, and A. M. C. Sengor, 1979. Review of plate tectonics: *Rev. Geophys. Space Phys.,* v. 17, pp. 1081–1090.

Cameron, A. G. W., 1964. Interpretation of Xe measurements: in *The origin and evolution of atmospheres and oceans,* P. Branczio and A. G. W. Cameron, eds., Wiley, New York, pp. 235–248.

Card, K. D., W. R. Church, J. M. Franklin, M. J. Frarey, J. A. Robertson, G. F. West, and G. M. Young, 1972. The southern province: *in* Variations in tectonic styles in Canada: *Geol. Assoc. Canada Sp. Paper 2,* pp. 335–380.

Clark, S. P., K. K. Turekian, and L. Grossman, 1972. Model for the early history of the Earth: in *The nature of the solid Earth,* E. C. Robertson, ed., McGraw Hill, New York, pp. 3–18.

Clifford, T. N., 1970. The structural framework of Africa: in *African magmatism and tectonics,* T. N. Clifford and I. G. Glass, eds., Oliver and Boyd, London, pp. 1–26.

Cloud, P. E., 1968. Atmospheric and hydrospheric evolution on the primitive Earth: *Science,* v. 160, pp. 729–736.

———, 1972. A working model for the primitive Earth: *Am. J. Sci.,* v. 272, pp. 537–548.

Condie, K. C., 1976. *Plate tectonics and crustal evolution,* Pergamon Press, New York.

Coney, P. J., 1971. Cordilleran tectonic transitions and motion of the North American plate: *Nature,* v. 233, pp. 462–465.

Cox, A. V., and G. B. Dalrymple, 1967. Statistical analysis of geomagnetic reversal data and the precision of potassium argon dating: *J. Geophys. Res.,* v. 72, pp. 2603–2614.

Cox, A. V., R. R. Doell, and G. B. Dalrymple, 1963. Geomagnetic polarity reversals: *Science,* v. 142, p. 382.

Damon, P. E., and J. L. Kulp, 1958. Excess helium and argon in beryl and other minerals: *Am. Mineralogist,* v. 43, pp. 433–459.

Davidson, A., 1972. The Churchill Province: in *Variations in tectonic styles in Canada,* R. A. Price and R. J. W. Douglas, eds., *Geol. Assoc. Canada Sp. Paper 2,* pp. 381–434.

Dewey, J. F., 1972. Plate tectonics: *Sci. Amer.,* v. 226, pp. 56–68.

———, 1979. Plate tectonics—a global view of the dynamics of the Earth: in *Rediscovery of Earth,* L. Motz, ed., Van Norstrand, New York, pp. 166–180.

Dewey, J. F., and J. M. Bird, 1970. Mountain belts and the new global tectonics: *J. Geophys. Res.,* v. 75, pp. 2625–2647.

Dewey, J. F., and K. C. A. Burke, 1973. Tibetan, Variscan and Precambrian basement reactivation products of continental collision: *J. Geol.,* v. 81, pp. 683–692.

Dewey, J. F., and W. S. F. Kidd, 1977. Geometry of plate accretion: *Bull. Geol. Soc. America,* v. 88, pp. 960–968.

Dickinson, W. R., 1971. Plate tectonics in geologic history: *Science,* v. 174, pp. 107–113.

———, 1971. Plate tectonic models of geosynclines: *Earth Planet. Sci. Lett.,* v. 109, pp. 165–174.

Du Toit, A. L., 1937. *Our wandering continents:* Oliver and Boyd, London.

Eade, R. E., and W. G. Fahrig, 1971. Geochemical evolutionary trends of continental plates—a preliminary study of the Canadian shield: *Geol. Survey Canada Bull.,* v. 179, p. 51.

Engel, A. E. J., and D. L. Kelm, 1972. Pre-permian global tectonics: a tectonic test: *Bull. Geol. Soc. America,* v. 83, pp. 2325-2340.

Fanale, F. P., 1971. A case for catastrophic early degassing of the Earth: *Chemical Geol.,* v. 8, pp. 79-105.

Ganapathy, R., and E. Anders, 1974. Bulk composition of the Moon and Earth estimated from meteorites. *Proc. Lunar Sci. Conf. 6th,* pp. 1181-1206.

Ganapathy, R., J. W. Morgan, V. Krahenbuhl, and E. Anders, 1973. Early intense bombardment of the Moon: Clues from meteoritic elements in Apollo 15 and 16 samples: *Proc. Lunar Sci. Conf. 4th,* pp. 1239-1261.

Gast, P. W., 1960. Limitations on the composition of the upper mantle: *J. Geophys. Res.,* v. 65, pp. 1287-1297.

Glickson, A. Y., 1976. Stratigraphy and evolution of primary and secondary greenstone: Significance of data from shields of the southern hemisphere: in *The Early History of the Earth,* B. F. Windley, ed., Wiley, New York, pp. 257-277.

Glickson, A. Y., and I. B. Lamberg, 1973. Relations in space and time between major Precambrian shield units: and interpretations of western Australia data: *Earth Planet. Sci. Lett.,* v. 20, pp. 395-403.

Goldich, S. S., 1973. Ages of precambrian banded iron formation: *Econ. Geol.,* v. 68, pp. 1126-1134.

Goldich, S. S., and C. E. Hedge, 1974. 3800 Myr granitic gneisses in southwestern Minnesota: *Nature,* v. 252, pp. 467-468.

Goodwin, A. M., 1973. Plate tectonics and evolution of Precambrian crust: in *Implications of continental drift to the Earth science, v. 2,* D. H. Tarling and S. K. Runcorn, eds., Academic Press, London, pp. 1047-1069.

———, 1976. Giant impacting and the development of the continental crust: in *The Early History of the Earth,* B. F. Windley, ed., Wiley, New York, pp. 77-95.

Green, D. H., 1972a. Archean greenstone belts may include terrestrial equivalents of lunar maria: *Earth Planet. Sci. Lett.,* v. 15, pp. 263-270.

———, 1972b. Magmatic activity as the major process in the chemical evolution of the Earth's crust and mantle: *Tectonophysics,* v. 13, pp. 47-71.

———, 1975. Genesis of Archean peridotitic magmas and constraints on Archean geothermal gradients and tectonics: *Geology,* v. 3, pp. 15-18.

Green, D. H., and A. E. Ringwood, 1968. Genesis of calc-alkaline igneous rock suites: *Contr. Mineral. and Petrol.,* v. 8, pp. 277-288.

Grossman, L., 1972. Condensation in the primitive solar nebula: *Geochim. et Cosmochim. Acta,* v. 36, pp. 597-619.

Grossman, L., and J. W. Larimer, 1974. Early chemical history of the solar system: *Rev. Geophys. Space Phys.,* v. 12, pp. 71-101.

Hallam, A., 1973. *A revolution in the Earth Sciences:* Clarendon Press, Oxford.

Hamilton, W., 1969. Mesozoic California and the underflow of Pacific mantle: *Bull. Geol. Soc. America,* v. 80, p. 2409.

Hargraves, R. B., 1981. Precambrian tectonic style: a liberal uniformitarian interpretation: in *Precambrian Plate Tectonics,* A. Kroner, ed., Elsevier, Amsterdam, pp. 21-56.

Hartmann, W. K., 1978. Planet formation: mechanisms of early growth: *Icarus,* v. 33, pp. 50-61.

Hawkesworth, C. J., S. Moorbath, R. K. O'Nions, and J. F. Wilson, 1975. Age relationships between greenstone belts and granites in the Rhodesian Archean craton: *Earth Planet. Sci. Lett.,* v. 25, pp. 251-262.

Heirtzler, J. R., G. O. Dickson, E. M. Herron, W. C. Pitman, and X. LePichon, 1968. Marine magnetic anomalies, geomagnetic field reversals and motions of the ocean floor and continents: *J. Geophys. Res.,* v. 73, pp. 2119-2136.

Hess, H. H., 1962. History of ocean basins: in *Petrologic Studies: a volume in honor of A. F. Buddington,* A. E. J. Engle, et al., eds, Geol. Soc. America, Boulder, Colo., pp. 599-620.

Hoffman, P., J. F. Dewey, and K. Burke, 1974. Aulacogensand their genetic relation to geosynclines, with a Proterozoic example from Great Slave Lake, Canada: in *Modern and Ancient Geosynclines,* R. H. Dott and R. H. Shaver, eds., *Soc. Econ. Paleon. Min. Sp. Publ. 19,* pp. 38-55.

Holland, H. D., 1976. The evolution of sea water: in *The Early History of the Earth,* B. F. Windley, ed., Wiley, New York, pp. 559-567.

Holmes, A., 1944. *Principles of physical geology:* Nelson, London.

Hunter, D. R., 1974. Crustal development in the Kaapvaal Craton. 2. The Proterozoic: *Precambrian Res.,* v. 1, pp. 295-326.

Hurst, R. W., 1978. Sr evolution in the west Greenland-Labrador craton: a model for early Rb depletion in the mantle: *Geochim. et Cosmochim. Acta,* v. 42, pp. 39-44.

Irving, E., R. F. Emslie, and H. Ueno, 1974. Upper Proterozoic paleomagnetic poles from Laurentia and the history of the Grenville structural province: *J. Geophys. Res.,* v. 79, pp. 5491-5502.

Irving, E., and P. L. Lapointe, 1975. Paleomagnetism of precambrian rocks of Laurentia: *Geoscience Canada,* v. 2, pp. 90-98.

Isacks, B., and P. Molnar, 1971. Distribution of stress in the descending lithosphere from a global survey of mantle earthquakes: *Rev. Geophys. Space Phys.,* v. 9, pp. 103-174.

Isacks, B., J. Oliver, and L. R. Sykes, 1968. Seismology and the new global tectonics: *J. Geophys. Res.,* v. 73, pp. 5855-5899.

Karig, D. E., 1971. Origin and development of marginal basins in the western Pacific: *J. Geophys. Res.,* v. 75, pp. 239-254.

———, 1974. Evolution of arc systems in the western Pacific: *Ann. Rev. Earth Planet. Sci.,* v. 2, pp. 51-75.

Kay, R., N. J. Hubbard, and P. W. Gast, 1970. Chemical characteristics and origin of oceanic ridge volcanic rocks: *J. Geophys. Res.,* v. 75, pp. 1585-1613.

Langseth, H. G., X. LePichon, and M. Ewing, 1966. Crustal structure of the mid-ocean floor and convection currents: *J. Geophys. Res.,* v. 17, p. 5321.

Larimer, J. W., 1971. Composition of the Earth: chondritic or achondritic: *Geochim. et Cosmochim. Acta,* v. 35, pp. 769-786.

Lee, W. H. K., 1967. *Thermal history of the Earth:* Unpublished Ph.D. Thesis, Univ. Calif., Los Angeles.

Leeds, A. R., L. Knopoff, and E. G. Kausel, 1974. Variations in upper mantle structures under the Pacific Ocean: *Science,* v. 186, pp. 141-143.

LePichon, X., 1968. Sea Floor Spreading and Continental Drift: *J. Geophys. Res.,* v. 73, pp. 3661-3667.

Lewis, J. S., 1972. Low temperature condensation from the solar

nebula: *Icarus,* v. 16, pp. 241-262.

McElhinny, M. W., ed., 1977. Past distribution of continents: *Tectonophysics,* Spec. Issue, v. 40, pp. 1-181.

McKenzie, D. P., and R. L. Parker, 1967. The North Pacific: an example of tectonics on a sphere: *Nature,* v. 216, pp. 1276-1279.

McKenzie, D. P., and N. Weiss, 1975. Speculation on the thermal and tectonic history of the Earth: *Geophys. J. Roy. Astron. Soc.,* v. 42, pp. 131-174.

Menard, H. W., 1961. Some rates of regional erosion: *J. Geol.,* v. 69, pp. 154-161.

Miyashiro, A., 1972. Pressure and temperature conditions and tectonic significance of regional and ocean floor metamorphism: *Tectonophysics,* v. 13, pp. 141-159.

———, 1973. Paired and unpaired metamorphic belts: *Tectonophysics,* v. 17, pp. 241-254.

Molnar, P., and T. Atwater, 1978. Interarc spreading and Cordilleran tectonics as alternates related to the age of subducted oceanic lithosphere: *Earth Planet. Sci. Lett.,* v. 41, pp. 330-340.

Moorbath, S., 1976. Age and isotope constraints for the evolution of Archean crust: in *The Early History of the Earth,* B. F. Windley, ed., Wiley, New York, pp. 351-360.

Moorbath, S., J. H. Allaart, and D. Bridgewater, 1977. Rb-Sr ages of early Archean supracrustal rocks and Amitsoq gneisses at Isua: *Nature,* v. 270, pp. 43-45.

Moorbath, S., R. K. O'Nions, and R. J. Pankhurst, 1973. Early Archean age for the Isua iron formation, West Greenland: *Nature,* v. 245, pp. 138-139.

Morgan, J. W., J. C. Laul, V. Krahenbuhl, R. Ganapathy, and E. Anders, 1972. Major impacts on the Moon: Characterization from trace elements in Apollo 12 and 14 samples: *Proc. Lunar Sci. Conf. 3rd,* pp. 1377-1395.

Morgan, W. J., 1968. Rises, trenches, great faults and crustal blocks: *J. Geophys. Res.,* v. 73, pp. 1959-1982.

Murthy, V. R., 1976. Composition of the core and the early chemical history of the Earth: in *The Early History of the Earth,* B. F. Windley, ed., Wiley, New York, pp. 21-31.

Murthy, V. R., and H. T. Hall, 1972. The origin and chemical composition of the Earth's core: *Phys. Earth Planet. Interiors,* v. 6, pp. 125-130.

Oliver, J., B. Isacks, M. Baranzangi, and W. Tronovas, 1973. Dynamics of the downgoing lithosphere: *Tectonophysics,* v. 19, pp. 133-147.

O'Nions, R. K., N. M. Evenson, and P. J. Hamilton, 1979. Geochemical modeling of mantle differentiation and crustal growth: *J. Geophys. Res.,* v. 84, pp. 6091-6101.

Oversby, V. M., and A. E. Ringwood, 1971. Time of the formation of the Earth's core: *Nature,* v. 234, pp. 463-465.

Ozima, Minoru, and Kiyoshi Nakazawa, 1980. Origin of rare gases in the Earth: *Nature,* v. 284, pp. 313-316.

Patterson, C., 1956. Age of meteorites and the Earth: *Geochim. et Cosmochim. Acta.,* v. 10, pp. 230-235.

Peterman, Z. E., and C. E. Hedge, 1971. Related strontium isotopic and chemical variations in oceanic basalts: *Bull. Geol. Soc. America,* v. 82, pp. 493-500.

Pettijohn, F. J., P. E. Potter, and R. Siever, 1972. *Sand and sandstone:* Springer-Verlag, Heidleberg.

Phillips, R. J., W. H. Kaula, G. E. McGill, and M. C. Malin, 1981. Tectonics and evolution of Venus: *Science,* v. 212, pp. 879-887.

Press, F., and R. Siever, 1978. *Earth:* Freeman, San Francisco.

Ringwood, A. E., 1966. Chemical evolution of the terrestrial planets: *Geochim. et Cosmochim. Acta,* v. 30, pp. 41-104.

———, 1975. *Composition and petrology of the Earth's mantle:* McGraw-Hill, New York.

———, 1977. Composition of the core and implications for the origin of the Earth: *Geochem. J.,* v. 11, pp. 111-135.

Ringwood, A. E., and A. Major, 1970. The system Mg_2SiO_4-Fe_2SiO_4 at high pressures and temperatures: *Phys. Earth Planet. Interiors,* v. 3, pp. 89-108.

Ronov, A. B., and A. A. Yaroshevsky, 1969. Chemical composition of the Earth's crust: *Am. Geophys. Union Mon. No. 13,* pp. 37-57.

Rubey, W. W., 1951. Geologic history of sea water: *Bull. Geol. Soc. America,* v. 62, pp. 1111-1148.

———, 1955. Development of the hydrosphere and atmosphere with special reference to probable composition of the early atmosphere: *Geol. Soc. America Sp. Paper 62,* pp. 631-650.

Runcorn, S. K., 1962a. Convection currents in the Earth's mantle: *Nature,* v. 195, pp. 1248-1249.

———, 1962b. Paleomagnetic evidence for continental drift and its geophysical causes: in *Continental Drift,* S. K. Runcorn, ed., Academic Press, New York.

Rutland, R. W. R., 1973. Tectonic evolution of the continental crust of Australia: in *Implications of continental drift to the Earth Sciences,* v. 2, D. H. Tarling and S. K. Runcorn, eds., Academic Press, London, pp. 1011-1033.

Safronov, V. S., 1977. Time scale for the formation of the Earth and planets and its rocks in their geochemical evolution: *NASA SP-370,* pp. 797-803.

Schidlowski, M., 1971. Probleme der atmospharischen Evolution in Prakambrium: *Geol. Rund.,* v. 60, pp. 1351-1384.

———, 1976. Archean atmosphere and evolution of the terrestrial oxygen budget: in *The Early History of the Earth,* B. F. Windley, ed., Wiley, New York, pp. 525-535.

Schopf, J. W., 1974. The development and diversification of precambrian life: *Origins of Life,* v. 5, pp. 119-135.

Sclater, J. G., 1972. New perspectives in terrestrial heat flow: *Tectonophysics,* v. 13, pp. 257-291.

Sclater, J. G., R. N. Anderson, and M. L. Bell, 1971. Elevation of ridges and evolution of the central eastern Pacific: *J. Geophys. Res.,* v. 76, pp. 7888-7915.

Sclater, J. G., and J. Francheteau, 1970. The implications of terrestrial heat flow observations on current tectonic and geochemical models of the crust and upper mantle of the Earth: *Geophys. J. Roy. Astron. Soc.,* v. 20, pp. 509-542.

Sclater, J. G., C. Jaupart, and D. Galson, 1980. The heat flow through oceanic and continental crust and the heat loss of the Earth: *Rev. Geophys. and Space Phys.,* v. 18, pp. 269-311.

Shackleton, R. M., 1973. Problems of the evolution of the continental crust: *Phil. Trans. Roy. Soc.,* London, v. A273, pp. 317-320.

Siever, R., 1974. Comparison of Earth and Mars as differentiated planets: *Icarus,* v. 29, pp. 312-324.

Sinha, A. K., 1972. U-Th-Pb systematics and the age of the Onvernacht Series, South Africa: *Earth Planet. Sci. Lett.,* v. 16, pp. 219-227.

Smith, A. G., J. C. Briden, and G. E. Drewry, 1973. Phanerozoic world maps: *Palaeont. Assoc. Sp. Paper in Palaeont. No. 12,* pp. 1-42.

Smith, J. V., 1977. Possible controls on the bulk composition of the Earth: implications for the origin of the Earth and Moon: *Proc. Lunar Sci. Conf. 8th,* pp. 333–369.

———, 1979. Mineralogy of the planets: *Min. Mag.*, v. 43, pp. 1–89.

Smith, J. V., and B. Mason, 1970. Pyroxene garnet transformation in Coorara meteorite: *Science,* v. 168, pp. 832–833.

Snider-Pellegrini, A., 1858. *La creation et ses mysteres devoiles:* Fraanck et Dentu, Paris.

Steiner, J., and E. Grillmair, 1973. Possible galactic causes for periodic and episodic glaciations: *Bull. Geol. Soc. America,* v. 84, pp. 1003–1018.

Stowe, C. W., 1974. Alpine type structures in the Rhodesian basement complex at Salukwe: *J. Geol. Soc. London,* v. 130, pp. 411–426.

Sykes, L. R., 1967. Mechanisms of earthquakes and nature of faulting in mid-oceanic ridges: *J. Geophys. Res.*, v. 72, p. 2131.

Talbot, C. J., 1973. A plate tectonic model for the Archean crust: *Phil. Trans. Roy. Soc.*, London, v. A273, pp. 413–428.

Tarling, D. H., 1978. *Evolution of the Earth's crust:* Academic Press, New York.

Tarney, J., I. W. D. Dalziel, and M. J. DeWit, 1976. Marginal basin 'Rocas Verdes' complex from S. Chile: a model for Archean greenstone belt formation: in *The Early History of the Earth,* B. F. Windley, ed., Wiley, New York, pp. 131–146.

Taylor, F. B., 1910. Bearing of the Tertiary mountain belt on the origin of the Earth's plan: *Bull. Geol. Soc. America,* v. 21, pp. 179–226.

Taylor, S. R., 1975. *Lunar Science: A post-Apollo view.* Pergamon Press, New York.

Tera, F., D. A. Papanastassiou, and G. J. Wasserburg, 1974. Isotopic evidence for a terminal lunar cataclysm: *Earth Planet. Sci. Lett.*, v. 22, pp. 1–21.

Turekian, K. K., 1976. *Oceans:* Prentice-Hall, Englewood Cliffs, New Jersey.

Turekian, K. K., and S. P. Clark, 1969. Inhomogeneous accretion of the earth from the primitive solar nebula: *Earth Planet. Sci. Lett.*, v. 6, pp. 346–348.

Ulrych, T. J., 1967. Oceanic basalt leads: a new interpretation and an independent age for the Earth: *Science,* v. 158, pp. 252–256.

Urey, H. C., 1952. The terrestrial planets: in *The Planets,* Yale University Press, New Haven, Conn., pp. 58–113.

Viljoen, M. H., and R. P. Viljoen, 1969. A collection of 9 papers on many aspects of the Barberton granite-greenstone belt: *South Africa. Geol. Soc. S. Africa, Sp. Publ. 2.*

Vine, F. J., and D. H. Matthews, 1963. Magnetic anomalies over ocean ridges: *Nature,* v. 199, pp. 947–949.

Von Herzen, R. P., and W. H. K. Lee, 1969. Heat flow in oceanic regions: in *The Earth's crust and upper mantle,* P. J. Hart, ed., Geophysical Monograph 13. American Geophysical Union, Washington, D.C.

Wasserburg, G. J., G. J. F. MacDonald, F. Hoyle, and W. A. Fowler, 1964. Relative contributions of uranium, thorium and potassium production in the Earth: *Science,* v. 143, pp. 465–467.

Wegener, A., 1966. *The origin of continents and oceans:* Translated from the 4th (1929) German edition by J. Biram, Dover, New York.

Wilson, J. T., 1965. A new class of faults and their bearing on continental drift: *Nature,* v. 207, pp. 343–347.

———, 1968. A revolution in the earth sciences: *Geotimes,* v. 13, pp. 10–16.

Windley, B. F., 1976. *The Early History of the Earth:* Wiley, New York.

———, 1977. *The Evolving Continents:* Wiley, New York.

Wyllie, P. J., 1971. *The dynamic Earth:* Textbook in geosciences: Wiley, New York.

Zeigler, A. M., C. R. Scotese, W. S. McKerrow, M. E. Johnson, and R. K. Bambach, 1979. Paleozoic paleogeography. *Ann. Rev. Earth Planet. Sci.*, v. 7, pp. 473–502.

CHAPTER 6

Adams, J. B., and T. B. McCord, 1973. Vitrification darkening in the lunar highlands and identification of the Descartes material at the Apollo 16 site: *Proc. Lunar Sci. Conf. 4th,* pp. 163–177.

Adams, J. B., C. Pieters, and T. B. McCord, 1974. Orange glass: Evidence for regional deposits of pyroclastic origin on the moon: *Proc. Lunar Sci. Conf. 5th,* pp. 171–186.

Adler, I., and 12 coauthors, 1972. The Apollo 15 X-ray fluorescence experiment: *Proc. Lunar Sci. Conf. 3rd,* pp. 2157–2178.

Adler, I., and 14 coauthors, 1973. Results of the Apollo 15 and 16 X-ray experiment: *Proc. Lunar Sci. Conf. 4th,* pp. 2783–2791.

Alexander, E. C., Jr., M. R. Coscio, Jr., J. C. Dragon, and K. Saito, 1980. K/Ar dating of lunar soils IV: Orange glass from 74220 and agglutinates from 14259 and 14163: *Proc. Lunar Planet. Sci. Conf. 11th,* pp. 1663–1677.

Alexander, E. C., Jr., M. R. Coscio, Jr., J. C. Dragon, R. O. Pepin, and K. Saito, 1977. K/Ar dating of lunar soils III: Comparison of ^{39}Ar-^{40}Ar and conventional techniques; 12032 and the age of Copernicus: *Proc. Lunar Sci. Conf. 8th,* pp. 2725–2740.

Alexander, E. C., Jr., and S. B. Kahl, 1974. ^{40}Ar-^{39}Ar studies of lunar breccias: *Proc. Lunar Sci. Conf. 5th,* pp. 1353–1373.

Alvarez, L. W., W. Alvarez, F. Asaro, and H. V. Michel, 1980. Extraterrestrial cause for the Cretaccous-Tertiary extinction: *Science,* v. 208, pp. 1095–1108.

Andre, C. G., R. W. Wolfe, and I. Adler, 1978. Evidence for a high magnesium subsurface basalt in Mare Crisium from orbital X-ray fluorescence data, in *Mare Crisium: The view from Luna 24: Geochim. et Cosmochim. Acta, Suppl. 9,* pp. 1–12.

Arvidson, R., G. Crozaz, R. J. Drozd, C. M. Hohenberg, and C. J. Morgan, 1975. Cosmic ray exposure ages of features and events at the Apollo landing sites: *The Moon,* v. 13, pp. 259–276.

Arvidson, R., R. J. Drozd, E. Guinness, C. M. Hohenberg, C. J. Morgan, R. H. Morrison, and V. R. Oberbeck, 1976. Cosmic ray exposure ages of Apollo 17 samples and the age of Tycho: *Proc. Lunar Sci. Conf. 7th,* pp. 2817–2832.

Baldwin, R. B., 1949. *The Face of the Moon:* Univ. Chicago Press, 239 pp.

———, 1963. *The Measure of the Moon:* Univ. Chicago Press, 488 pp.

———, 1965. *A Fundamental Survey of the Moon:* McGraw-Hill, New York, 149 pp.

———, 1968. Lunar mascons: Another interpretation: *Science,* v. 162, pp. 1407–1408.

———, 1972. The tsunami model of the origin of ring structures concentric with large lunar craters: *Phys. Earth Planet. Interiors,* v. 5, pp. 327–339.

———, 1974. On the origin of the mare basins: *Proc. Lunar Sci. Conf. 5th,* pp. 1–10.

Basaltic Volcanism Study Project (BVSP), 1981. *Basaltic Volcanism on the Terrestrial Planets:* Lunar and Planetary Institute, Houston, Texas, 1286 pp.

Beatty, J. K., B. O'Leary, and A. Chaikin (editors), 1981. *The New Solar System:* Sky Publishing Co., Cambridge, Mass., 224 pp.

Beaty, D. W., and A. L. Albee, 1978. Comparative petrology and possible genetic relations among the Apollo 11 basalts: *Proc. Lunar Planet. Sci. Conf. 9th,* pp. 359–463.

———, 1980. The geology and petrology of the Apollo 11 landing site: *Proc. Lunar Planet. Sci. Conf. 11th,* pp. 23–35.

Bernatowicz, T. J., C. M. Hohenberg, B. Hudson, B. M. Kennedy, and F. A. Podosek, 1978. Argon ages for lunar breccias 14064 and 15405: *Proc. Lunar Planet. Sci. Conf. 9th,* pp. 905–919.

Bills, B. G., and A. J. Ferrari, 1977. A lunar density model consistent with topographical, gravitational, librational, and seismic studies: *J. Geophys. Res.,* v. 82, pp. 1306–1314.

Bowin, Carl, B. Simon, and W. R. Wollenhaupt, 1975. Mascons: A two-body solution: *J. Geophys. Res.,* v. 80, pp. 4947–4955.

Boyce, J. M., 1976. Ages of flow units in the lunar nearside maria based on Lunar Orbiter IV photographs: *Proc. Lunar Sci. Conf. 7th,* pp. 2717–2728.

Boyce, J. M., and A. L. Dial, 1973. Relative ages of some nearside mare units based on Apollo 17 metric photographs, *in* NASA, 1973b, sec. 29C.

———, 1975. Relative ages of flow units in Mare Imbrium and Sinus Iridum: *Proc. Lunar Sci. Conf. 6th,* pp. 2585–2595.

Boyce, J. M., and D. A. Johnson, 1977. Ages of flow units in Mare Crisium based on crater density: *Proc. Lunar Sci. Conf. 8th,* pp. 3495–3502.

———, 1978. Ages of flow units in the far eastern maria and implications for basin-filling history: *Proc. Lunar Planet. Sci. Conf. 9th,* pp. 3275–3283.

Boyce, J. M., A. L. Dial, and L. A. Soderblom, 1974. Ages of the lunar nearside light plains and maria: *Proc. Lunar Sci. Conf. 5th,* pp. 11–23.

———, 1975. A summary of relative ages of lunar nearside and farside plains: *Astrogeology 66,* USGS interagency report (open file).

Bryan, W. B., 1973. Wrinkle ridges as deformed surface crust on ponded mare lava: *Proc. Lunar Sci. Conf. 4th,* pp. 93–106.

Brennan, W. J., 1975. Modification of premare impact craters by volcanism and tectonism: *The Moon,* v. 12, pp. 449–461.

Burnett, D. S., and D. S. Woolum, 1977. Exposure ages and erosion rates for lunar rocks: *Phys. Chem. Earth,* v. 10, pp. 63–101.

Cadogan, P. H., 1974. Oldest and largest lunar basin? *Nature,* v. 250, pp. 315–316.

———, 1981. *The Moon—Our Sister Planet:* Cambridge Univ. Press, 391 pp.

Carlson, R. W., and G. W. Lugmair, 1979. Sm-Nd constraints on early lunar differentiation and the evolution of KREEP: *Earth Planet. Sci. Lett.,* v. 45, pp. 123–132.

———, 1981. Time and duration of lunar highlands crust formation: *Earth Planet. Sci. Lett.,* v. 52, pp. 227–238.

Carr, M. H., 1966. Geologic map of the Mare Serenitatis region of the Moon: USGS Map I-489 (LAC 42; scale 1:1,000,000).

Carr, M. H., K. A. Howard, and Farouk El-Baz, 1971. Geologic maps of the Apennine-Hadley region of the Moon (Apollo 15 pre-mission maps): USGS Map I-723 (scales 1:250,000 and 1:50,000).

Chao, E. C. T., 1973. Geologic implications of the Apollo 14 Fra Mauro breccias and comparison with ejecta from the Ries crater, Germany: *USGS J. Res.,* v. 1, pp. 1–18.

———, 1974. Impact cratering models and their application to lunar studies—a geologist's view: *Proc. Lunar Sci. Conf. 5th,* pp. 35–52.

———, 1977. The Ries Crater of Southern Germany, a model for large basins on planetary surfaces: *Geologisches Jahrbuch,* Series (Reihe) A, n. (Heft) 43.

Clayton, R. N., and T. K. Mayeda, 1975. Genetic relations between the moon and meteorites: *Proc. Lunar Sci. Conf. 6th,* pp. 1761–1769.

Cloud, P. E., 1968. Atmospheric and hydrospheric evolution on the primitive Earth: *Science,* v. 160, pp. 729–736.

Cooper, M. R., R. L. Kovach, and J. S. Watkins, 1974. Lunar near-surface structure: *Rev. Geophys. Space Phys.,* v. 12, pp. 291–308.

Crozaz, G., 1977. The irradiation history of the lunar soil: *Phys. Chem. Earth,* v. 10, pp. 197–214.

DeHon, R. A., 1974. Thickness of mare material in the Tranquillitatis and Nectaris basins: *Proc. Lunar Sci. Conf. 5th,* pp. 53–59.

———, 1979. Thickness of the western Mare basalts: *Proc. Lunar Planet. Sci. Conf. 10th,* pp. 2935–2955.

DeHon, R. A., and J. D. Waskom, 1976. Geologic structure of the eastern mare basins: *Proc. Lunar Sci. Conf. 7th,* pp. 2729–2746.

Delano, J. W., 1979. Apollo 15 green glass: Chemistry and possible origin: *Proc. Lunar Planet. Sci. Conf. 10th,* pp. 275–300.

Dence, M. R., 1971. Impact melts: *J. Geophys. Res.,* v. 76, pp. 5552–5565.

Dence, M. R., and A. G. Plant, 1972. Analysis of Fra Mauro samples and the origin of the Imbrium Basin: *Proc. Lunar Sci. Conf. 3rd,* pp. 379–399.

Dennis, J. G., 1971. Ries structure, Southern Germany, a review: *J. Geophys. Res.,* v. 76, pp. 5394–5406.

DePaolo, D. J., 1981. Nd isotopic studies: Some new perspectives on Earth structure and evolution: *EOS,* v. 62, pp. 137–140.

Dowty, Eric, Klaus Keil, Martin Prinz, J. Gros, and H. Takahashi, 1976. Meteorite-free Apollo 15 crystalline KREEP: *Proc. Lunar Sci. Conf. 7th,* pp. 1833–1844.

Duke, M. B., and J. S. Nagle, 1975. Stratification in the lunar regolith—A preliminary view: *The Moon,* v. 13, pp. 143–158.

Eberhardt, P., J. Geiss, N. Grögler, and A. Stettler, 1973. How old is the crater Copernicus? *The Moon,* v. 8, pp. 104–114.

Eggleton, R. E., 1965. Geologic map of the Riphaeus Mountains region of the Moon: USGS Map I-458 (LAC 76; scale 1:1,000,000).

Eggleton, R. E., and C. H. Marshall, 1962. Notes on the Apenninian Series and pre-Imbrian stratigraphy in the vicinity of Mare Humorum and Mare Nubium: Astrogeologic Studies Semiannual Progress Report, Feb. 1961–Aug. 1961, pp. 132–137, USGS open-file report.

Eggleton, R. E., and T. W. Offield, 1970. Geologic maps of the Fra Mauro region of the Moon (Apollo 14 premission maps): USGS Map I-708; (scales 1:250,000 and 1:25,000).

Eggleton, R. E., and G. G. Schaber, 1972. Cayley Formation interpreted as basin ejecta, in NASA *Apollo 15 Prelim. Sci. Rep.* (1972b) sec. 29B.

Eichhorn, G., J. J. McGee, O. B. James, and O. A. Schaeffer, 1979. Consortium breccia 73255: Laser ^{39}Ar-^{40}Ar dating of

aphanite samples: *Proc. Lunar Planet. Sci. Conf. 10th,* pp. 763–788.

Eliason, E. M., and L. A. Soderblom, 1977. An array processing system for lunar geochemical and geophysical data: *Proc. Lunar Sci. Conf. 8th,* pp. 1163–1170.

Engelhardt, Wolf v., 1967. Neue Beobachtungen im Nördlinger Ries: *Geologische Rundschau,* v. 57, pp. 165–188.

Fielder, G., 1961. *Structure of the Moon's Surface:* Pergamon Press, New York, 266 pp.

———, 1965. *Lunar Geology:* London, Lutterworth Press, 184 pp.

———, ed., 1971. *Geology and Physics of the Moon:* Amsterdam, Elsevier, 159 pp.

French, B. M., 1977. *The Moon Book:* Penguin Books, 287 pp.

French, B. M., and N. M. Short, eds., 1968. *Shock Metamorphism of Natural Materials,* Baltimore, Mono, 644 pp.

Frondel, J. W., 1975. *Lunar mineralogy:* New York, Wiley, 323 pp.

Gault, D. E., 1974. Impact craters, in *A Primer in Lunar Geology,* Greeley and Schultz (eds.), 1974, pp. 137–175.

Gault, D. E., J. B. Adams, R. J. Collins, G. P. Kuiper, H. Masursky, J. A. O'Keefe, R. A. Phinney, and E. M. Shoemaker, 1968a. Lunar theory and processes, *in* Surveyor VII mission report Part II. Science results: *Jet Propulsion Laboratory Technical Report* 32-1264, pp. 267–313.

Gault, D. E., W. L. Quaide, and V. R. Oberbeck, 1968b. Impact cratering mechanics and structure, in *Shock Metamorphism,* French and Short (eds.) 1968, pp. 87–99.

Gault, D. E., and J. A. Wedekind, 1978. Experimental studies of oblique impact: *Proc. Lunar Planet. Sci. Conf. 9th,* pp. 3843–3875.

Gilbert, G. K., 1893. The Moon's face, a study of the origin of its features: *Bull. Philosophical Soc. Washington,* v. 12, pp. 241–292.

Glass, B. P., 1982. *Introduction to Planetary Geology:* Cambridge Univ. Press, 469 pp.

Goins, N. R., M. N. Toksöz, and A. M. Dainty, 1979. The lunar interior: A summary report: *Proc. Lunar Planet. Sci. Conf. 10th,* pp. 2421–2439.

Greeley, R., 1976. Modes of emplacement of basalt terrains and an analysis of mare volcanism in the Orientale basin: *Proc. Lunar Sci. Conf. 7th,* pp. 2747–2759.

Greeley, R., and P. H. Schultz, eds., 1974. *A Primer in Lunar Geology* (comment edition), NASA Ames Research Center, 574 pp.

Green, J. (conference chairman), 1965. Geological problems in lunar research: *Annals,* New York Academy of Sciences, v. 123, art. 2, pp. 367–1257.

Grieve, R. A. F., 1980. Cratering in the lunar highlands: Some problems with the process, record and effects: Proceedings, Conference on the Lunar Highlands Crust, *Geochim. et Cosmochim. Acta, Suppl. 12,* pp. 173–196.

Grieve, R. A. F., and R. J. Floran, 1978. Manicouagan impact melt, Quebec, 2. Chemical interrelations with basement and formational processes: *J. Geophys. Res.,* v. 83, pp. 2761–2771.

Grieve, R. A. F., A. G. Plant, and M. R. Dence, 1974. Lunar impact melts and terrestrial analogs: Their characteristics, formation, and implications for lunar crustal evolution: *Proc. Lunar Sci. Conf. 5th,* pp. 261–273.

Grolier, M. J., 1970. Geologic map of the Sabine D region of the Moon: USGS Map I-618 (scale 1:100,000).

Guest, J. E., and R. Greeley, 1977. *Geology on the Moon:* London and Basingstoke, Wykeham Publications, 235 pp.

Guest, J. E., and J. B. Murray, 1976. Volcanic features of the nearside equatorial lunar maria: *J. Geologic. Soc. London,* v. 132, pp. 251–258.

Guggisberg, S., P. Eberhardt, J. Geiss, N. Grögler, A. Stettler, G. M. Brown, and A. Pecket, 1979. Classification of the Apollo 11 mare basalts according to Ar^{39}-Ar^{40} ages and petrologic properties: *Proc. Lunar Planet. Sci. Conf. 10th,* pp. 1–39.

Guinness, E. A., and R. E. Arvidson, 1977. On the constancy of the lunar cratering flux over the past 3.3×10^9 yr: *Proc. Lunar Sci. Conf. 8th,* pp. 3475–3494.

Hackman, R. J., 1966. Geologic map of the Montes Apenninus region of the Moon: USGS Map I-463 (LAC 41; scale 1:1,000,000).

Hackman, R. J., and A. C. Mason, 1961. Engineer special study of the surface of the Moon: USGS Map I-351 (scale 1:3,800,000).

Haines, E. L., and A. E. Metzger, 1980. Lunar highland crustal models based on iron concentrations: Isostasy and center-of-mass displacement: *Proc. Lunar Planet. Sci. Conf. 11th,* pp. 689–718.

Hall, R. C., 1977. *Lunar Impact: A History of Project Ranger: NASA SP-4210,* 450 pp.

Hartmann, W. K., 1964. Radial structures surrounding lunar basins, II: Orientale and other systems; conclusions: *Communications, Lunar and Planetary Laboratory,* v. 2, pp. 175–191.

———, 1972. *Moons and Planets:* Wadsworth, Belmont, CA, 404 pp second edition (1983), 509 pp.

———, 1973. Ancient lunar mega-regolith and subsurface structure: *Icarus,* v. 18, pp. 634–636.

———, 1975. Lunar "cataclysm": A misconception? *Icarus,* v. 24, pp. 181–187.

———, 1980. Dropping stones in magma oceans: Effects of early lunar cratering: Proceedings, Conference on the Lunar Highlands Crust, *Geochim. et Cosmochim. Acta, Suppl. 12,* pp. 155–171.

Hartmann, W. K., and G. P. Kuiper, 1962. Concentric structures surrounding lunar basins: *Communications, Lunar and Planetary Laboratory,* University of Arizona, v. 1, n. 12, pp. 51–66.

Hartmann, W. K., and C. A. Wood, 1971. Moon: Origin and evolution of multi-ring basins: *The Moon,* v. 3, pp. 4–78.

Hawke, B. R., and J. W. Head, 1977. Pre-Imbrian history of the Fra Mauro region and Apollo 14 sample provenance: *Proc. Lunar Sci. Conf. 8th,* pp. 2741–2761.

———, 1978. Lunar KREEP volcanism: geologic evidence for history and mode of emplacement: *Proc. Lunar Planet. Sci. Conf. 9th,* pp. 3285–3309.

Hawke, B. R., and P. D. Spudis, 1980. Geochemical anomalies on the eastern limb and farside of the moon: Proceedings of Conference on Lunar Highlands Crust: *Geochim. et Cosmochim. Acta, Suppl. 12,* pp. 467–481.

Heacock, R. L., G. P. Kuiper, E. M. Shoemaker, H. C. Urey, and E. A. Whitaker, 1965. Ranger VII, Part II. Experimenters' Analyses and Interpretations: NASA, *Jet Propulsion Laboratory Technical Report 32-700,* 154 p.

———, 1966. Rangers VIII and IX, Part II. Experimenters' Analyses and Interpretations: NASA, *Jet Propulsion Laboratory Technical Report 32-800,* 382 p.

Head, J. W, 1974a. Orientale multi-ringed basin interior and implications for the petrogenesis of lunar highland samples: *The Moon,* v. 11, pp. 327–356.

———, 1974b. Stratigraphy of the Descartes region (Apollo 16):

Implications for the origin of samples: *The Moon,* v. 11, pp. 77–99.

———, 1974c. Morphology and structure of the Taurus-Littrow highlands (Apollo 17): Evidence for their origin and evolution: *The Moon,* v. 9, pp. 355–395.

———, 1974d. Lunar dark-mantle deposits: Possible clues to the distribution of early mare deposits: *Proc. Lunar Sci. Conf. 5th,* pp. 207–222.

———, 1976. Lunar volcanism in space and time: *Rev. Geophys. Space Phys.,* v. 14, pp. 265–300.

———, 1979a. Serenitatis multi-ringed basin: Regional geology and basin ring interpretation: *The Moon and the Planets,* v. 21, pp. 439–462.

———, 1979b. Lava flooding of early planetary crusts: *Lunar Planet. Sci.* X, pp. 516–521 (2 abstracts).

Head, J. W., J. B. Adams, T. B. McCord, C. Pieters, and S. H. Zisk, 1978a. Regional stratigraphy and geologic history of Mare Crisium, *in* Mare Crisium: The View from Luna 24: *Geochim. et Cosmochim. Acta, Suppl. 9,* pp. 43–74.

Head, J. W., and A. Gifford, 1980. Lunar mare domes: Classification and modes of origin: *The Moon and the Planets,* v. 22, pp. 235–258.

Head, J. W., and B. R. Hawke, 1975. Geology of the Apollo 14 region (Fra Mauro): Stratigraphic history and sample provenance: *Proc. Lunar Sci. Conf. 6th,* pp. 2483–2501.

Head, J. W., and T. B. McCord, 1978. Imbrian-age highland volcanism on the Moon: The Gruithuisen and Mairan domes: *Science,* v. 199, pp. 1433–1436.

Head, J. W., C. Pieters, T. B. McCord, J. B. Adams, and S. H. Zisk, 1978b. Definition and detailed characterization of lunar surface units using remote observations: *Icarus,* v. 33, pp. 145–172.

Heiken, G. H., 1975. Petrology of lunar soils: *Rev. Geophys. Space Phys.,* v. 13, pp. 567–587.

Heiken, G. H., D. S. McKay, and R. W. Brown, 1974. Lunar deposits of possible pyroclastic origin: *Geochim. et Cosmochim. Acta,* v. 38, pp. 1703–1718.

Herbert, Floyd, M. J. Drake, C. P. Sonett, and M. J. Wiskerchen, 1977. Some constraints on the thermal history of the lunar magma ocean: *Proc. Lunar Sci. Conf. 8th,* pp. 573–582.

Herzberg, C. T., and M. B. Baker, 1980. The cordierite- to spinel-cataclasite transition: Structure of the lunar crust: Proceedings of Conference on the Lunar Highlands Crust, *Geochim. et Cosmochim. Acta, Suppl. 12,* pp. 113–132.

Hess, W. N., D. H. Menzel, J. A. O'Keefe, eds., 1966. The Nature of the Lunar Surface: *Proceedings 1965 IAU-NASA Symposium:* The Johns Hopkins Press, 320 pp.

Hodges, C. A., and D. E. Wilhelms, 1978. Formation of lunar basin rings: *Icarus,* v. 34, pp. 294–323.

Hodges, C. A., W. R. Muehlberger, and G. E. Ulrich, 1973. Geologic setting of Apollo 16: *Proc. Lunar Sci. Conf. 4th,* pp. 1–25.

Hood, L. L., P. J. Coleman, Jr., and D. E. Wilhelms, 1979. Lunar nearside magnetic anomalies: *Proc. Lunar Planet. Sci. Conf. 10th,* pp. 2235–2257.

Hörz, F., 1978. How thick are lunar mare basalts? *Proc. Lunar Planet. Sci. Conf. 9th,* pp. 3311–3331.

Hörz, F., and G. S. Banholzer, Jr., 1980. Deep seated target material in the continuous deposits of the Ries Crater, Germany: Proceedings, Conference on the Lunar Highlands Crust, *Geochim. et Cosmochim. Acta, Suppl. 12,* pp. 211–231.

Howard, K. A., 1975. Geologic map of the crater Copernicus: USGS Map I-840 (scale 1:250,000).

Howard, K. A., M. H. Carr, and W. R. Muehlberger, 1973. Basalt stratigraphy of southern Mare Serenitatis, in NASA *Apollo 17 Prelim. Sci. Rep.* (1973), sec. 29A.

Howard, K. A., J. W. Head, and G. A. Swann, 1972. Geology of Hadley rille: *Proc. Lunar Sci. Conf. 3rd,* pp. 1–14.

Howard, K. A., D. E. Wilhelms, and D. H. Scott, 1974. Lunar basin formation and highland stratigraphy: *Rev. Geophys. Space Phys.,* v. 12, pp. 309–327.

Howard, K. A., and H. G. Wilshire, 1975. Flows of impact melt at lunar craters: *USGS J. Res.,* v. 3, pp. 237–257.

Hubbard, N. J., 1979. Regional chemical variations in lunar basaltic lavas: *Proc. Lunar Planet. Sci. Conf. 10th,* pp. 1753–1774.

Hubbard, N. J., C. Meyer, Jr., P. W. Gast, and H. Wiesmann, 1971. The composition and derivation of Apollo 12 soils: *Earth Planet. Sci. Lett.,* v. 10, pp. 341–350.

Hubbard, N. J., F. Vilas, and J. E. Keith, 1978. From Serenity to Langemak: A regional chemical setting for mare crisium, *in* mare crisium: The view from Luna 24: *Geochim. et Cosmochim. Acta, Suppl. 9,* pp. 13–32.

Huneke, J. C., 1978. ^{40}Ar-^{39}Ar microanalysis of single glass balls and 72435 breccia clasts: *Proc. Lunar Planet. Sci. Conf. 9th,* pp. 2345–2362.

Huneke, J. C., E. K. Jessberger, and G. J. Wasserburg, 1974. The age of metamorphism of a highland breccia (65015) and a glimpse at the age of its protolith: *Lunar Sci.* V, pp. 375–377.

Irving, A. J., 1975. Chemical, mineralogical and textural systematics of nonmare melt rocks: Implications for lunar impact and volcanic processes: *Proc. Lunar Sci. Conf. 6th,* pp. 363–394.

———, 1977. Chemical variation and fractionation of KREEP basalt magma: *Proc. Lunar Sci. Conf. 8th,* pp. 2433–2448.

James, O. B., 1973. Crystallization history of lunar feldspathic basalt 14013: USGS Professional Paper 841, 29 pp.

———, 1977. Lunar highlands breccias generated by major impacts, in *Soviet-American Conference on Cosmochemistry of the Moon and Planets, NASA SP-370,* pp. 637–658.

———, 1980. Rocks of the early lunar crust: *Proc. Lunar Planet. Sci. Conf. 11th,* pp. 365–393.

———, 1981. Petrologic and age relations of the Apollo 16 rocks: Implications for subsurface geology and the age of the Nectaris basin: *Proc. Lunar Planet. Sci. Conf. 12th,* pp. 209–233.

James, O. B., J. W. Hedenquist, D. P. Blanchard, J. R. Budahn, and W. Compston, 1978. Consortium breccia 73255: Petrology, major- and trace-element chemistry, and Rb-Sr systematics of aphanitic lithologies: *Proc. Lunar Planet. Sci. Conf. 9th,* pp. 789–819.

James, O. B., and T. L. Wright, 1972. Apollo 11 and 12 mare basalts and gabbros: Classification, compositional variations, and possible petrogenetic relations: *Bull. Geol. Soc. America,* v. 83, pp. 2357–2382.

Jessberger, E. K., T. Kirsten, and T. Staudacher, 1977. One rock and many ages—Further K-Ar data on consortium breccia 73215: *Proc. Lunar Sci. Conf. 8th,* pp. 2567–2580.

Kaula, W. M., 1977. On the origin of the moon, with emphasis on bulk composition: *Proc. Lunar Sci. Conf. 8th,* pp. 321–331.

Kaula, W. M., G. Schubert, R. E. Lingenfelter, W. L. Sjogren, and W. R. Wollenhaupt, 1974. Apollo laser altimetry and inferences as to lunar structure: *Proc. Lunar Sci. Conf. 5th,* pp. 3049–3058.

Kieffer, S. W., and C. H. Simonds, 1980. The role of volatiles

in the cratering process: *Rev. Geophys. Space Phys.,* v. 18, pp. 143–182.

King, E. A., 1976. *Space Geology:* Wiley, New York, 349 pp.

Kirsten, T., and P. Horn, 1974. Chronology of the Taurus-Littrow region III: Ages of mare basalts and highland breccias and some remarks about the interpretation of lunar highland rock ages: *Proc. Lunar Sci. Conf. 5th,* pp. 1451–1475.

Kopal, Z., ed., 1962. *Physics and Astronomy of the Moon:* Academic Press, New York and London, 538 pp.

Kopal, Z., and Z. K. Mikhailov, 1962. *The Moon* (Symposium No. 14 of the International Astronomical Union, Pulkova Observatory, U.S.S.R., December 1960): Academic Press, London and New York, 571 pp.

Kuiper, G. P., 1959. The exploration of the Moon: *Vistas in Astronautics,* v. 2, pp. 273–312.

Kuiper, G. P., D. W. G. Arthur, E. Moore, J. W. Tapscott, and E. Whitaker, 1960. *Photographic Lunar Atlas:* Univ. Chicago Press.

Kuiper, G. P., and B. M. Middlehurst, 1961. Planets and Satellites: *The Solar System,* v. 3, University of Chicago Press, 601 pp.

La Jolla Consortium, 1977. Global maps of lunar geochemical, geophysical and geologic variables: *Proc. Lunar Sci. Conf. 8th,* v. 1, frontispiece.

Lammlein, D. R., 1977. Lunar seismicity and tectonics: *Phys. Earth Planet. Interiors,* v. 14, pp. 224–273.

Langseth, M. G., S. J. Keihm, and K. Peters, 1976. Revised lunar heat-flow values: *Proc. Lunar Sci. Conf. 7th,* pp. 3143–3171.

Latham, G. V., H. J. Dorman, P. Horvath, A. K. Ibrahim, J. Koyama, and Y. Nakamura, 1978. Passive seismic experiment: a summary of current status: *Proc. Lunar Planet. Sci. Conf. 9th,* pp. 3609–3613.

Lofgren, G. E., C. H. Donaldson, and T. M. Usselman, 1975. Geology, petrology, and crystallization of Apollo 15 quartz-normative basalts: *Proc. Lunar Sci. Conf. 6th,* pp. 79–99.

Lowman, P. D., Jr., 1969. *Lunar Panorama—A Photographic Guide to the Geology of the Moon:* Reinhold Müller, Zurich, 101 pp.

Lucchitta, B. K., 1976. Mare ridges and related highland scarps—Result of vertical tectonism? *Proc. Lunar Sci. Conf. 7th,* pp. 2761–2782.

———, 1977. Crater clusters and light mantle at the Apollo 17 site: A result of secondary impact from Tycho: *Icarus,* v. 30, pp. 80–96.

———, 1978. Geologic map of the north side of the Moon: USGS Map I-1062 (scale 1:5,000,000).

Lucchitta, B. K., and A. G. Sanchez, 1975. Crater studies in the Apollo 17 region: *Proc. Lunar Sci. Conf. 6th,* pp. 2427–2441.

Lucchitta, B. K., and J. A. Watkins, 1978. Age of graben systems on the moon: *Proc. Lunar Planet. Sci. Conf. 9th,* pp. 3459–3472.

Lugmair, G. W., 1974. Sm-Nd ages: A new dating method: Meteoritics, v. 9, p. 369 (abstract).

Markov, A. V., ed., 1962. *The Moon—A Russian View:* University of Chicago Press, 391 pp. (Originally published in Russian as *Luna,* State Publishing House of Physical-Mathematical Literature, Moscow, 1960.)

Marshall, C. H., 1961. Thickness of the Procellarian System, Letronne region of the Moon: USGS Professional Paper 424-D, pp. D208–D211.

Marvin, U. B., J. A. Wood, G. J. Taylor, J. B. Reid, B. N. Powell, J. S. Dickey, and J. F. Bower, 1971. Relative proportions and probable sources of rock fragments in the Apollo 12 soil samples: *Proc. Lunar Sci. Conf. 2nd,* pp. 679–699.

Mason, R., J. E. Guest, and G. N. Cooke, 1976. An Imbrium pattern of graben on the Moon: *Proceedings Geologists' Assoc.,* v. 87, pp. 161–168.

Masursky, H., G. W. Colton, and F. El-Baz, eds., 1978. *Apollo Over the Moon: A View from Orbit: NASA SP-362,* 255 pp.

Maurer, P., P. Eberhardt, J. Geiss, N. Grögler, A. Stettler, G. M. Brown, A. Peckett, and U. Krähenbühl, 1978. Pre-Imbrian craters and basins: ages, compositions and excavation depths of Apollo 16 breccias: *Geochim. et Cosmochim. Acta,* v. 42, pp. 1687–1720.

Maxwell, T. A., F. El-Baz, and S. H. Ward, 1975. Distribution, morphology, and origin of ridges and arches in Mare Serenitatis: *Bull., Geol. Soc. of America,* v. 86, pp. 1273–1278.

Maxwell, T. A., and R. J. Phillips, 1978. Stratigraphic correlation of the radar-detected subsurface interface in Mare Crisium: *Geophys. Res. Lett.,* v. 9, pp. 811–814.

McCauley, J. F., 1967a. The nature of the lunar surface as determined by systematic geologic mapping, in *Mantles of the Earth and Terrestrial Planets:* S. K. Runcorn, ed., New York and London, Wiley, pp. 431–460.

———, 1967b. Geologic map of the Hevelius region of the Moon: USGS Map I-491 (LAC 56; scale 1:1,000,000).

———, 1968. Geologic results from the lunar precursor probes: *AIAA* (American Institute of Aeronautics and Astronautics) *Journal,* v. 6, pp. 1991–1996.

———, 1977. Orientale and Caloris: *Phys. Earth Planet. Interiors,* v. 15, pp. 220–250.

McCauley, J. F., and D. H. Scott, 1972. The geologic setting of the Luna 16 landing site: *Earth Planet. Sci. Lett.,* v. 13, pp. 225–232.

McCord, T. B., C. Pieters, and M. A. Feierberg, 1976. Multispectral mapping of the lunar surface using ground-based telescopes: *Icarus,* v. 29, pp. 1–34.

McGill, G. E., 1977. Craters as "fossils": the remote dating of planetary surface materials: *Bull. Geo. Soc. America,* v. 88, pp. 1102–1110.

Melosh, H. J., 1980. Cratering mechanics—Observational, experimental, and theoretical: *Annual Review of Earth and Planetary Science,* v. 8, pp. 65–93.

Metzger, A. E., E. L. Haines, R. E. Parker, and R. G. Radocinski, 1977. Thorium concentrations in the lunar surface. I: Regional values and crustal content: *Proc. Lunar Sci Conf. 8th,* pp. 949–999.

Metzger, A. E., J. I. Trombka, L. E. Peterson, J. C. Reedy, and J. R. Arnold, 1973. Lunar surface radioactivity: Preliminary results of the Apollo 15 and Apollo 16 gamma-ray spectrometer experiment: *Science,* v. 179, pp. 800–803.

Meyer, C., Jr., 1977. Petrology, mineralogy, and chemistry of KREEP basalt: *Phys. Chem. Earth,* v. 10, pp. 239–260.

Meyer, C., Jr., R. Brett, N. J. Hubbard, D. A. Morrison, D. S. McKay, F. K. Aitken, H. Takeda, and E. Schonfeld, 1971. Mineralogy, chemistry and origin of the KREEP component in soil samples from the Ocean of Storms: *Proc. Lunar Sci. Conf. 2nd,* pp. 393–411.

Middlehurst, B. M., and G. P. Kuiper, 1963. The Moon, Meteorites, and Comets. *The Solar System,* v. 4: University of Chicago Press, 810 pp.

Milton, D. J., B. C. Barlow, R. Brett, A. R. Brown, A. Y. Glikson, F. A. Manwaring, F. J. Moss, E. C. E. Sedmik, J. Van Son, and G. A. Young, 1972. Gosses Bluff impact struc-

ture, Australia: *Science,* v. 175, pp. 1199–1207.

Milton, D. J., and C. A. Hodges, 1972. Geologic maps of the Descartes region of the Moon: USGS Map I-748 (Apollo 16 pre-mission maps) (scales 1:250,000 and 1:50,000).

Moore, H. J., 1967. Geologic map of the Seleucus quadrangle of the Moon: USGS Map I-527 (LAC 38; scale 1:1,000,000).

———, 1976. Missile impact craters (White Sands, New Mexico) and applications to lunar research: USGS Professional Paper 812B, 47 pp.

Moore, H. J., J. M. Boyce, G. G. Schaber, and D. H. Scott, 1980. Lunar remote sensing and measurements: USGS Professional Paper 1046-B, 78 p.

Moore, H. J., C. A. Hodges, and D. H. Scott, 1974. Multiringed basins—illustrated by Orientale and associated features: *Proc. Lunar Sci. Conf. 5th,* pp. 71–100.

Morgan, J. W., R. Ganapathy, H. Higuchi, and E. Anders, 1977. Meteoritic material on the Moon, in *Soviet-American Conference on Cosmochemistry of the Moon and Planets: NASA SP-370,* pp. 659–689.

Morris, E. C., and D. E. Wilhelms, 1967. Geologic map of the Julius Caesar quadrangle of the Moon: USGS Map I-510 (LAC 60; scale 1:1,000,000).

Morrison, R. H., and V. R. Oberbeck, 1975. Geomorphology of crater and basin deposits—Emplacement of the Fra Mauro Formation: *Proc. Lunar Sci. Conf. 6th,* pp. 2503–2530.

Muehlberger, W. R., F. Hörz, J. R. Sevier, and G. E. Ulrich, 1980. Mission objectives for geological exploration of the Apollo 16 landing site: Proceedings, Conference on the Lunar Highlands Crust, *Geochim. et Cosmochim. Acta, Suppl. 12,* pp. 1–49.

Müller, H. W., T. Plieninger, O. B. James, and O. A. Schaeffer, 1977. Laser probe ^{39}Ar-^{40}Ar dating of materials from consortium breccia 73215: *Proc. Lunar Sci. Conf. 8th,* pp. 2551–2565.

Müller, P. M., and W. L. Sjogren, 1968. Mascons: Lunar mass concentrations: *Science,* v. 161, pp. 680–684.

Murray, B., M. C. Malin, and R. Greeley, 1981. *Earthlike Planets:* Freeman, San Francisco, 387 pp.

Murray, J. B., 1971. Sinuous rilles, in *Geology and Physics of the Moon:* G. Fielder, ed., Elsevier, Amsterdam, pp. 27–39.

———, 1980. Oscillating peak model of basin and crater formation: *The Moon and the Planets,* v. 22, pp. 269–291.

Mutch, T. A., 1970. *Geology of the Moon—A stratigraphic view:* Princeton University Press, 324 pp.; second edition (1972) 391 pp.

Nabelek, P. I., L. A. Taylor, and G. E. Lofgren, 1978. Nucleation and growth of plagioclase and the development of textures in a high-alumina basaltic melt: *Proc. Lunar Planet. Sci. Conf. 9th,* pp. 725–741.

Nakamura, Y., G. V. Latham, H. J. Dorman, A-B. K. Ibrahim, J. Koyama, and P. Horvath, 1979. Shallow moonquakes: Depth, distribution and implications as to the present state of the lunar interior: *Proc. Lunar Planet. Sci. Conf. 10th,* pp. 2299–2309.

NASA (National Aeronautics and Space Administration), 1969a. *Surveyor Program Results: NASA SP-184,* 425 pp.

———, 1969b. *Analysis of Apollo 8 Photographs and Visual Observations: NASA SP-201,* 337 pp.

———, 1969c. *Apollo 11 Preliminary Science Report: NASA SP-214,* 204 pp.

———, 1970. *Apollo 12 Preliminary Science Report: NASA SP-235,* 227 pp.

———, 1971a. *Analysis of Apollo 10 Photographs and Visual Observations: NASA SP-232.*

———, 1971b. *Apollo 14 Preliminary Science Report: NASA SP-272.*

———, 1972a. *Analysis of Surveyor 3 Materials and Photographs Returned by Apollo 12: NASA SP-284.*

———, 1972b. *Apollo 15 Preliminary Science Report: NASA SP-289.*

———, 1972c. *Apollo 16 Preliminary Science Report: NASA SP-315.*

———, 1973. *Apollo 17 Preliminary Science Report: NASA SP-330.*

Neukum, G., 1977. Different ages of lunar light plains: *The Moon,* v. 17, pp. 383–393.

Neukum, G., and B. König, 1976. Dating of individual lunar craters: *Proc. Lunar Sci. Conf. 7th,* pp. 2867–2881.

Neukum, G., B. König, and J. Arkani-Hamad, 1975a. A study of lunar impact crater size-distributions: *The Moon,* v. 12, pp. 201–229.

Neukum, G, B. König, H. Fechtig, and D. Storzer, 1975b. Cratering in the earth-moon system: Consequences for age determination by crater counting: *Proc. Lunar Sci. Conf. 6th,* pp. 2597–2620.

Norman, M. D., and G. Ryder, 1979. A summary of the petrology and geochemistry of pristine highlands rocks: *Proc. Lunar Planet. Sci. Conf. 10th,* pp. 531–559.

Nunes, P. D., M. Tatsumoto, and D. M. Unruh, 1975. U-Th-Pb systematics of anorthositic gabbros 78155 and 77017—implications for early lunar evolution: *Proc. Lunar Sci. Conf. 6th,* pp. 1431–1444.

Nyquist, L. E., 1977. Lunar Rb-Sr chronology: *Phys. Chem. Earth.,* v. 10, pp. 103–142.

Nyquist, L. E., J. Wooden, C.-Y. Shih, H. Wiesmann, and B. M. Bansal, 1981. Isotopic and REE studies of lunar basalt 12038: Implications for petrogenesis of aluminous mare basalts: *Earth Planet. Sci. Lett.,* v. 55, pp. 335–355.

Oberbeck, V. R., 1975. The role of ballistic erosion and sedimentation in lunar stratigraphy: *Rev. Geophys. Space Phys.,* v. 13, pp. 337–362.

Oberbeck, V. R., and R. H. Morrison, 1973. On the formation of the lunar herringbone pattern: *Proc. Lunar Sci. Conf. 4th,* pp. 107–123.

Oberbeck, V. R., R. H. Morrison, F. Hörz, W. L. Quaide, and D. E. Gault, 1974. Smooth plains and continuous deposits of craters and basins: *Proc. Lunar Sci. Conf. 5th,* pp. 111–136.

Oberbeck, V. R., W. L. Quaide, R. E. Arvidson, and H. R. Aggarwal, 1977. Comparative studies of lunar, Martian, and Mercurian craters and plains: *J. Geophys. Res.,* v. 82, pp. 1681–1698.

Offield, T. W., 1971. Geologic map of the Schiller quadrangle of the Moon: USGS Map I-691 (LAC 125; scale 1:1,000,000).

Offield, T. W., and H. A. Pohn, 1970. Lunar crater morphology and relative age determinations of geologic units—Part 2. Applications, *in* USGS Professional Paper 700-C, pp. C163–C169.

———, 1979. Geology of the Decaturville Impact Structure, Missouri: USGS Professional Paper 1042, 48 pp.

O'Keefe, J. D., and T. H. Ahrens, 1975. Shock effects from a large impact on the moon: *Proc. Lunar Sci. Conf. 6th,* pp. 2831–2844.

Öpik, E. J., 1960. The lunar surface as an impact crater: *Notices, Royal Astronomical Society,* v. 120, pp. 404–411.

Papanastassiou, D. A., and G. J. Wasserburg, 1971a. Lunar chronology and evolution from Rb-Sr studies of Apollo 11 and 12 samples: *Earth Planet. Sci. Lett.,* v. 11, pp. 37–62.

———, 1971b. Rb-Sr ages of igneous rocks from the Apollo 14

mission and the age of the Fra Mauro Formation: *Earth Planet. Sci. Lett.*, v. 12, pp. 36-48.

Papanastassiou, D. A., D. J. DePaolo, and G. J. Wasserburg, 1977. Rb-Sr and Sm-Nd chronology and geology of mare basalts from the Sea of Tranquility: *Proc. Lunar Sci. Conf. 8th,* pp. 1639-1672.

Papike, J. J., F. N. Hodges, A. E. Bence, M. Cameron, and J. M. Rhodes, 1976. Mare basalts: Crystal chemistry, mineralogy, and petrology: *Rev. Geophys. Space Phys.*, v. 14, pp. 475-540.

Papike, J. J., and D. T. Vaniman, 1978. Luna 24 ferrobasalts and the mare basalt suite: Comparative chemistry, mineralogy, and petrology: Mare Crisium: The View from Luna 24: *Geochim. et Cosmochim. Acta, Suppl. 9,* pp. 371-401.

Patterson, C., 1956. Age of meteorites and the earth: *Geochim. et Cosmochim. Acta,* v. 10, pp. 230-237.

Peeples, W. J., W. R. Sill, T. W. May, S. H. Ward, R. J. Phillips, R. L. Jordan, E. A. Abbott, and T. J. Killpack, 1978. Orbital evidence for lunar subsurface layering in Maria Serenitatis and Crisium: *J. Geophys Res.*, v. 83, B7, pp. 3459-3468.

Pieters, C. M., 1978. Mare basalt types on the front side of the Moon: A summary of spectral reflectance data: *Proc. Lunar Planet. Sci. Conf. 9th,* pp. 2825-2849.

Pieters, C., J. W. Head, J. B. Adams, T. B. McCord, S. H. Zisk, and J. L. Whitford-Stark, 1980. Late high-titanium basalts of the western maria: Geology of the Flamsteed region of Oceanus Procellarum, *J. Geophys. Res.*, v. 85, pp. 3913-3938.

Pieters, C., T. B. McCord, M. P. Charette, and J. B. Adams, 1974. Lunar surface: Identification of the dark mantling material in the Apollo 17 samples: *Science,* v. 183, pp. 1191-1194.

Pike, R. J., 1980a. Geometric interpretation of lunar craters: USGS Professional Paper 1046-C, 77 pp.

———, 1980b. Formation of complex impact craters: Evidence from Mars and other planets: *Icarus,* v. 43, pp. 1-19.

Podosek, F. A., J. C. Huneke, A. J. Gancarz, and G. J. Wasserburg, 1973. The age and petrography of two Luna 20 fragments and inferences for widespread lunar metamorphism: *Geochim. et Cosmochim. Acta,* v. 37, pp. 887-904.

Pohn, H. A., and T. W. Offield, 1970. Lunar crater morphology and relative age determination of lunar geologic units—Part I. Classification, *in* USGS Professional Paper 700-C, pp. C153-C162.

Pohn, H. A., R. L. Wildey, and G. E. Sutton, 1970. A photoelectric-photographic study of the normal albedo of the Moon: USGS Professional Paper 599-E, 20 pp.

Prinz, M., E. Dowty, K. Keil, and T. E. Bunch, 1973. Mineralogy, petrology, and chemistry of lithic fragments from Luna 20 fines: origin of the cumulate ANT suite and its relationship to high-alumina mare basalts: *Geochim. et Cosmochim. Acta,* v. 37, pp. 979-1006.

Prinz, M., and K. Keil, 1977. Mineralogy, petrology and chemistry of ANT-suite rocks from the lunar highlands: *Phys. Chem. Earth,* v. 10, pp. 215-237.

Quaide, W. L., V. R. Oberbeck, T. Bunch, and G. Polkowski, 1971. Investigations of the natural history of the regolith at the Apollo 12 site: *Proc. Lunar Sci. Conf. 2nd,* pp. 701-718.

Quaide, W. L., and R. Wrigley, 1972. Mineralogy and origin of Fra Mauro fines and breccias: *Proc. Lunar Sci. Conf. 3rd,* pp. 771-784.

Reid, A. M., A. R. Duncan, and S. H. Richardson, 1977. In search of LKFM: *Proc. Lunar Sci. Conf. 8th,* pp. 2321-2338.

Rhodes, J. M., D. P. Blanchard, M. A. Dungan, J. C. Brannon, and K. V. Rogers, 1977. Chemistry of Apollo 12 mare basalts: Magma types and fractionation processes: *Proc. Lunar Sci. Conf. 8th,* pp. 1305-1338.

Rhodes, J. M., and N. J. Hubbard, 1973. Chemistry, classification, and petrogenesis of Apollo 15 mare basalts: *Proc. Lunar Sci. Conf. 4th,* pp. 1127-1148.

Rhodes, J. M., N. J. Hubbard, H. Wiesmann, K. V. Rodgers, J. C. Brannon, and B. M. Bansal, 1976. Chemistry, classification, and petrogenesis of Apollo 17 mare basalts: *Proc. Lunar Sci. Conf. 7th,* pp. 1467-1489.

Ridley, W. I., 1975. On high-alumina mare basalts: *Proc. Lunar Sci. Conf. 6th,* pp. 131-145.

Roddy, D. J., 1976. High-explosion cratering analogs for bowl-shaped, central-uplift, and multiring impact craters: *Proc. Lunar Sci. Conf. 7th,* pp. 3027-3056.

Roddy, D. J., R. O. Pepin, and R. B. Merrill, 1977. *Impact and Explosion Cratering:* Pergamon Press, New York, 1301 pp.

Runcorn, S. K., 1980. An iron core in the moon generating an early magnetic field? *Proc. Lunar Planet. Sci. Conf. 10th,* pp. 2325-2333.

Ryder, G., and J. F. Bower, 1976. Poikilitic KREEP impact melts in the Apollo 14 site rocks: *Proc. Lunar Sci. Conf. 7th,* pp. 1925-1948.

———, 1977. Petrology of Apollo 15 black-and-white rocks 15445 and 15455—Fragments of the Imbrium impact melt sheet? *Proc. Lunar Sci. Conf. 8th,* pp. 1895-1923.

Ryder, G., and P. D. Spudis, 1980. Volcanic rocks in the lunar highlands: Proceedings, Conference on the Lunar Highlands Crust, *Geochim. et Cosmochim. Acta, Suppl. 12,* pp. 353-375.

Ryder, G., and G. J. Taylor, 1976. Did mare-type volcanism commence early in lunar history? *Proc. Lunar Sci. Conf. 7th,* pp. 1741-1755.

Ryder, G., and J. A. Wood, 1977. Serenitatis and Imbrium impact melts: Implications for large-scale layering in the lunar crust: *Proc. Lunar Sci. Conf. 8th,* pp. 655-668.

Saari, J. M., R. W. Shorthill, and T. K. Deaton, 1964. Infrared and visible images of the eclipsed Moon of December 19, 1964: *Icarus,* v. 5, pp. 635-659.

Schaber, G. G., 1969. Geologic map of the Sinus Iridum quadrangle of the Moon: USGS Map I-602 (LAC 24; scale 1:1,100,000).

———, 1973. Lava flows in Mare Imbrium: Geologic evaluation from Apollo orbital photography: *Proc. Lunar Sci. Conf. 4th,* pp. 73-92.

Schaber, G. G., J. M. Boyce, and H. J. Moore, 1976. The scarcity of mappable flow lobes on the lunar maria: Unique morphology of the Imbrium flows: *Proc. Lunar Sci. Conf. 7th,* pp. 2783-2800.

Schmitt, H. H., G. Lofgren, G. A. Swann, and G. Simmons, 1970. The Apollo 11 samples: Introduction: *Proc. Lunar Sci. Conf. 1st,* pp. 1-54.

Schultz, P. H., 1976a. *Moon Morphology:* Univ. Texas Press, Austin, 626 pp.

———, 1976b. Floor-fractured lunar craters: *The Moon,* v. 15, pp. 241-273.

Schultz, P. H., and P. H. Spudis, 1979. Evidence for ancient mare volcanism: *Proc. Lunar Sci. Conf. 10th,* pp. 2899-2918.

Scott, D. H., 1972a. Geologic map of the Maurolycus quadrangle

of the Moon: USGS Map I-695 (LAC 113; scale 1:1,000,000).

———, 1972b. Geologic map of the Eudoxus quadrangle of the Moon: USGS Map I-705 (LAC 26; scale 1:1,000,000).

———, 1974. The geologic significance of some lunar gravity anomalies: *Proc. Lunar Sci. Conf. 5th,* pp. 3025–3036.

Scott, D. H., B. K. Lucchitta, and M. H. Carr, 1972. Geologic maps of the Tarus-Littrow region of the Moon (Apollo 17 premission maps): USGS Map I-800 (scales 1:250,000 and 1:50,000).

Scott, D. H., J. F. McCauley, and M. N. West, 1977. Geologic map of the west side of the Moon: USGS Map I-1034 (scale 1:5,000,000).

Shoemaker, E. M., 1962a. Interpretation of lunar craters, *in* Kopal (1962) *Physics and Astronomy of the Moon:* Academic Press, New York, pp. 283–359.

———, 1962b. Exploration of the Moon's surface: *Amer. Sci.,* v. 50, pp. 99–130.

———, 1964. The geology of the Moon: *Sci. Amer.,* v. 211, pp. 38–47.

———, 1965. Preliminary analysis of the fine structure of the lunar surface in Mare Cognitum, *in* Heacock and others, 1965, pp. 75–134; also *in* Hess and others, 1966, pp. 23–77.

———, 1972. Cratering history and early evolution of the Moon: *Lunar Sci. III,* pp. 696–698.

Shoemaker, E. M., R. M. Batson, H. E. Holt, E. C. Morris, J. J. Rennilson, and E. A. Whitaker, 1969. Observations of the lunar regolith and the earth from the television camera on Surveyor 7: *J. Geophys. Res.,* v. 74, pp. 6081–6119.

Shoemaker, E. M., and R. J. Hackman, 1962. Stratigraphic basis for a lunar time scale, *in* Kopal and Mikhailov (1962), pp. 289–300.

Shoemaker, E. M., R. J. Hackman, and R. E. Eggleton, 1963. Interplanetary correlation of geologic time: *Adv. Astronautic. Sci.,* v. 8, pp. 70–89.

Shoemaker, E. M., and E. C. Morris, 1970. Geology: Physics of fragmental debris, *in* Surveyor Final Reports: *Icarus,* v. 12, pp. 188–212.

Short, N. M., 1975. *Planetary Geology:* Prentice Hall, Englewood Cliffs, N.J., 361 pp.

Short, N. M., and M. L. Forman, 1972. Thickness of impact crater ejecta on the lunar surface: *Modern Geology,* v. 3, pp. 69–91.

Shorthill, R. W., 1973. Infrared atlas of the eclipsed Moon: *The Moon,* v. 7, pp. 22–45.

Simonds, C. H., 1975. Thermal regimes in impact melts and the petrology of the Apollo 17 Station 6 boulder: *Proc. Lunar Sci. Conf. 6th,* pp. 641–672.

Simonds, C. H., W. C. Phinney, J. L. Warner, P. E. McGee, J. Geeslin, R. W. Brown, and J. M. Rhodes, 1977. Apollo 14 revisited, or breccias aren't so bad after all: *Proc. Lunar Sci. Conf. 8th,* pp. 1869–1893.

Simonds, C. H., J. L. Warner, W. C. Phinney, and P. E. McGee, 1976. Thermal model for impact breccia lithification: Manicouagan and the Moon: *Proc. Lunar Sci. Conf. 7th,* pp. 2509–2528.

Sjogren, W. L., and J. C. Smith, 1976. Quantitative mass distribution models for Mare Orientale: *Proc. Lunar Sci. Conf. 7th,* pp. 2639–2648.

Sjogren, W. L., R. H. Wimberly, and W. R. Wollenhaupt, 1974. Lunar gravity via the Apollo 15 and 16 subsatellites: *The Moon,* v. 9, pp. 115–128.

Smith, J. V., 1974. Lunar mineralogy: A heavenly detective story: *American Mineralogist,* v. 59, pp. 231–243.

———, 1979. Mineralogy of the planets: a voyage in space and time: *Mineralogical Magazine,* v. 43, pp. 1–89.

———, 1982. Heterogeneous growth of meteorites and planets, especially the Earth and Moon: *J. Geology,* v. 90, pp. 1–48.

Smith, J. V., A. T. Anderson, R. C. Newton, E. J. Olsen, P. J. Wyllie, A. V. Crewe, M. S. Isaacson, and D. Johnson, 1970. Petrologic history of the moon inferred from petrography, mineralogy, and petrogenesis of Apollo 11 rocks: *Proc. Lunar Sci. Conf. 1st,* pp. 897–925.

Smith, J. V., and I. M. Steele, 1975. Lunar mineralogy: A heavenly detective story, Part II: *American Mineralogist,* v. 61, pp. 1059–1116.

Soderblom, L. A., J. A. Arnold, J. M. Boyce, and R. P. Lin, 1977. Regional variations in the lunar maria: Age, remanent magnetism, and chemistry: *Proc. Lunar Sci. Conf. 8th,* pp. 1191–1199.

Soderblom, L. A., and J. M. Boyce, 1972. Relative ages of some near-side and far-side terra plains based on Apollo 16 metric photography, *in* NASA, *Apollo 16 Prelim. Sci. Rep.,* 1972c, sec. 29A.

Soderblom, L. A., and L. A. Lebofsky, 1972. Technique for rapid determination of relative ages of lunar areas from orbital photography: *J. Geophys. Res.,* v. 77, pp. 279–296.

Solomon, S. C., 1975. Mare volcanism and lunar crustal structure: *Proc. Lunar Sci. Conf. 6th,* pp. 1021–1042.

Solomon, S. C., and J. W. Head, 1979. Vertical movement in mare basins: Relation to mare emplacement, basin tectonics, and lunar thermal history: *J. Geophys. Res.,* v. 84, pp. 1667–1682.

———, 1980. Lunar mascon basins: Lava filling, tectonics, and evolution of the lithosphere: *Rev. Geophys. Space Phys.,* v. 18, pp. 107–141.

Spudis, P. D., 1978. Composition and origin of the Apennine Bench Formation: *Proc. Lunar Planet. Sci. Conf. 9th,* pp. 3379–3394.

Spudis, P. D., and G. Ryder, 1981. Apollo 17 impact melts and their relation to the Serenitatis basin, *in* Multi-ring Basins, *Proc. Lunar Planet. Sci.,* v. 12A, pp. 133–148.

Staudacher, T., E. K. Jessberger, I. Flohs, and T. Kirsten, 1979. ^{40}Ar-^{39}Ar age systematics of consortium breccia 73255: *Proc. Lunar Planet. Sci. Conf. 10th,* pp. 745–762.

Steiger, R. H., and E. Jäger, 1977. Subcommission on geochronology: Convention on the use of decay constants in geo- and cosmochronology: *Earth Planet. Sci. Lett.,* v. 36, pp. 359–362.

Stöffler, D., 1981. Cratering mechanics: Data from terrestrial and experimental craters and implications for the Apollo 16 site, *in* Workshop on Apollo 16: *Lunar and Planetary Institute Tech. Report 81-01,* pp. 132–141.

Stöffler, D., H.-D. Knöll, and U. Maerz, 1979. Terrestrial and lunar impact breccias and the classification of lunar highland rocks: *Proc. Lunar Planet. Sci. Conf. 10th,* pp. 639–675.

Stöffler, D., H.-D. Knöll, U. B. Marvin, C. H. Simonds, and P. H. Warren, 1980. Recommended classification and nomenclature of lunar highland rocks—a committee report: Proceedings, Conference on Lunar Highlands Crust, *Geochim. et Cosmochim. Acta, Suppl. 12,* pp. 51–70.

Stöffler, D., H.-D. Knöll, W. U. Reimold, and S. Schulien, 1976. Grainsize statistics, composition and provenance of frag-

mental particles in some Apollo 14 breccias: *Proc. Lunar Sci. Conf. 7th,* pp. 1965–1985.

Stöffler, D., R. Ostertag, W. U. Reimold, R. Borchardt, J. Malley, and A. Rehfeldt, 1981. Distribution and provenance of lunar highland rock types at North Ray Crater, Apollo 16: *Proc. Lunar Planet. Sci. Conf. 12B,* pp. 185–207.

Strom, R. G., 1964. Analysis of lunar lineaments, I: Tectonic maps of the Moon, *Commun. Lunar and Planet. Lab.,* v. 2, n. 39, pp. 205–216.

———, 1971. Lunar mare ridges, rings and volcanic ring complexes: *Modern Geology,* v. 2, pp. 133–157.

Stuart-Alexander, D. E., 1971. Geologic map of the Rheita quadrangle of the Moon: USGS Map I-694 (LAC 114; scale 1:1,000,000).

———, 1978. Geologic map of the central far side of the Moon: USGS Map I-1047 (scale 1:5,000,000).

Stuart-Alexander, D. E., and K. A. Howard, 1970. Lunar maria and circular basins—A review: *Icarus,* v. 12, pp. 440–456.

Stuart-Alexander, D. E., and D. E. Wilhelms, 1975. The Nectarian System, a new lunar time-stratigraphic unit: USGS *J. Res.*, v. 3, pp. 53–58.

Sutton, R. L., and G. G. Schaber, 1971. Lunar locations and orientations of rock samples from Apollo missions 11 and 12: *Proc. Lunar Sci. Conf. 2nd,* pp. 17–26.

Swann, G. A., and 19 coauthors, 1972. Preliminary geologic investigation of the Apollo 15 landing site, *in* NASA, *Apollo 15 Prelim. Sci. Rep.,* 1972b, sec. 5.

———, and 12 coauthors, 1977. Geology of the Apollo 14 landing site in the Fra Mauro highlands: USGS Professional Paper 880, 103 pp.

Taylor, G. J., M. J. Drake, J. A. Wood, and U. B. Marvin, 1973. The Luna 20 lithic fragments, and the composition and origin of the lunar highlands: *Geochim. et Cosmochim. Acta,* v. 37, pp. 1087–1106.

Taylor, S. R., 1975. *Lunar Science: A Post-Apollo View:* New York, Pergamon Press, 372 pp.

———, 1982. *Planetary Science: A lunar perspective:* Lunar and Planetary Institute, Houston, Texas, 481 pp.

Tera, F., D. A. Papanastassiou, and G. J. Wasserburg, 1974. Isotopic evidence for a terminal lunar cataclysm: *Earth Planet. Sci. Lett.,* v. 22, pp. 1–21.

Thompson, T. W., 1974. Atlas of lunar radar maps at 70-cm wavelength: *The Moon,* v. 10, pp. 51–85.

———, 1979. A review of Earth-based radar mapping of the Moon: *The Moon and the Planets,* v. 20, pp. 179–198.

Thompson, T. W., K. A. Howard, R. W. Shorthill, G. L. Tyler, S. H. Zisk, E. A. Whitaker, G. G. Schaber, and H. J. Moore, 1973. Remote sensing of Mare Serenitatis, *in* NASA, *Apollo 17 Prelim. Sci. Report,* 1973, sec. 33A.

Thompson, T. W., H. Masursky, R. W. Shorthill, G. L. Tyler, and S. H. Zisk, 1974. A comparison of infrared, radar, and geologic mapping of lunar craters: *The Moon,* v. 10, pp. 87–117.

Todd, T., D. A. Richter, G. Simmons, and H. Wang, 1973. Unique characterization of lunar samples by physical properties: *Proc. Lunar Sci. Conf. 4th,* pp. 2639–2662.

Toksoz, M. N., A. M. Dainty, S. C. Solomon, and K. R. Anderson, 1974. Structure of the Moon: *Rev. Geophys. Space Phys.,* v. 12, pp. 539–567.

Trask, N. J., 1966. Size and spatial distribution of craters estimated from Ranger photographs, *in* Heacock and others, 1966, pp. 252–263.

———, 1969. Geologic maps of early Apollo landing sites, *explanatory pamphlet in* USGS Maps I-616 to I-627.

———, 1971. Geologic comparison of mare materials in the lunar equatorial belt, including Apollo 11 and Apollo 12 landing sites, in *Geological Survey Research 1971,* USGS Professional Paper 750-D, pp. D138–D144.

Turkevich, A. L., 1971. Comparison of the analytical results from the Surveyor, Apollo, and Luna missions, *Proc. Lunar Sci. Conf. 2nd,* pp. 1209–1215.

Turner, G., 1977. Potassium-argon chronology of the Moon: *Phys. Chem. Earth,* v. 10, pp. 145–195.

Ulrich, G. E., C. A. Hodges, and W. R. Muehlberger, eds. 1981. Geology of the Apollo 16 area, central lunar highlands: USGS Professional Paper 1048, 539 pp.

Urey, H. C., 1952. *The Planets:* Yale University Press, New Haven, 245 pp.

Van Dorn, W. G., 1968. Tsunamis on the Moon? *Nature,* v. 220, pp. 1102–1107.

Walker, D., J. Longhi, and J. R. Hays, 1972. Experimental petrology and origin of Fra Mauro rocks and soil. *Proc. Lunar Sci. Conf. 3rd,* pp. 797–817.

———, 1975. Differentiation of a very thick magma body and implications for the source regions of mare basalts: *Proc. Lunar Sci. Conf. 6th,* pp. 1103–1120.

Warner, J. L., 1972. Metamorphism of Apollo 14 breccias: *Proc. Lunar Sci. Conf. 3rd,* pp. 623–643.

Warren, P. H., and J. T. Wasson, 1977. Pristine nonmare rocks and the nature of the lunar crust: *Proc. Lunar Sci. Conf. 8th,* pp. 2215–2235.

———, 1979a. Effects of pressure on the crystallization of a "chondritic" magma ocean and implications for the bulk composition of the Moon: *Proc. Lunar Planet. Sci. Conf. 10th,* pp. 2051–2083.

———, 1979b. The compositional-petrographic search for pristine nonmare rocks: Third foray: *Proc. Lunar Planet. Sci. Conf. 10th,* pp. 583–610.

———, 1979c. The origin of KREEP: *Rev. Geophys. Space Phys.,* v. 17, pp. 73–88.

———, 1980. Early lunar petrogenesis, oceanic and extraoceanic: Proceedings, Conference on the Lunar Highlands Crust, *Geochim. et Cosmochim. Acta, Suppl. 12,* pp. 81–99.

Wetherill, G. W., 1971. Of time and the Moon: *Science,* v. 173, pp. 383–392.

———, 1975. Late heavy bombardment of the Moon and terrestrial planets: *Proc. Lunar Sci. Conf. 6th,* pp. 1539–1561.

———, 1977. Pre-mare cratering and early solar system history, in *Soviet#American Conference on Cosmochemistry of the Moon and Planets, NASA SP-370,* pp. 553–567.

———, 1981. Nature and origin of basin-forming projectiles, *in* Multi-ring Basins, *Proc. Lunar Planet. Sci.,* v. 12A, pp. 1–18.

Whitaker, E. A., 1972. Lunar color boundaries and their relationship to topographic features: A preliminary survey: *The Moon,* v. 4, pp. 348–355.

———, 1981. The lunar Procellarum basin, *in* Multi-ring Basins, *Proc. Lunar Planet. Sci.,* v. 12A, pp. 79–90.

Whitford-Stark, J. L., and J. W. Head, 1980. Stratigraphy of Oceanus Procellarum basalts: Sources and style of emplacement: *J. Geophys. Res.,* v. 85, pp. 6579–6609.

Wilhelms, D. E., 1968. Geologic map of the Mare Vaporum quadrangle of the Moon: USGS Map I-548 (LAC 59; scale 1:1,000,000).

———, 1970. Summary of lunar stratigraphy—Telescopic observations: USGS Professional Paper 599-F, 47 pp.
———, 1972. Geologic mapping of the second planet: *Astrogeologic Studies 55,* USGS open-file report, 36 pp.
———, 1976. Secondary impact craters of lunar basins: *Proc. Lunar Sci. Conf. 7th,* pp. 2883–2901.
———, 1979. Relative ages of lunar basins, *in* Reports of Planetary Geology Program, 1978–1979: *NASA Tech. Memo. 80339,* pp. 135–137 (abstract).
———, 1980a. Stratigraphy of part of the lunar near side: USGS Professional Paper 1046-A, 71 pp.
———, 1980b. Geologic map of lunar ringed impact basins, *in* Papers Presented to Conference on Multi-Ring Basins (Houston, November 1980): Lunar and Planetary Institute Contribution 414, pp. 115–117 (abstract).
———, 1981. Relative ages of lunar basins (II); Serenitatis, *in* Reports of Planetary Geology Program—1981: *NASA Tech. Memo. 84211,* pp. 405–407 (abstract).
———, (in press a) Lunar geology in the space age: NASA SP, in press.
———, (in press b) Geologic history of the Moon; USGS Professional Paper, in press.
Wilhelms, D. E., and D. E. Davis, 1971. Two former faces of the Moon: *Icarus,* v. 15, pp. 368–372.
Wilhelms, D. E., and F. El-Baz, 1977. Geologic map of the east side of the Moon: USGS Map I-948 (scale 1:5,000,000).
Wilhelms, D. E., K. A. Howard, and H. G. Wilshire, 1979. Geologic map of the south side of the Moon: USGS Map I-1162.
Wilhelms, D. E., and J. F. McCauley, 1971. Geologic map of the near side of the Moon: USGS Map I-703 (scale 1:5,000,000).
Wilhelms, D. E., V. R. Oberbeck, and H. R. Aggarwal, 1978. Size-frequency distributions of primary and secondary lunar impact craters: *Proc. Lunar Planet. Sci. Conf. 9th,* pp. 3735–3762.
Wilshire, H. G., and E. D. Jackson, 1972. Petrology and stratigraphy of the Fra Mauro Formation at the Apollo 14 site: USGS Professional Paper 785, 26 pp.
Wilshire, H. G., and H. J. Moore, 1974. Glass-coated lunar rock fragments: *J. Geology,* v. 82, pp. 403–417.
Wilshire, H. G., T. W. Offield, K. A. Howard, and D. Cummings, 1972. Geology of the Sierra Madera cryptoexplosion structure, Pecos County, Texas: USGS Professional Paper 599-H, 42 pp.
Winter, D. F., 1970. The infrared moon: Data, interpretations, and implications: *Radio Science,* v. 5, pp. 229–240.
Wise, D. U., and M. T. Yates, 1970. Mascons as structural relief on a lunar "Moho": *J. Geophys. Res.,* v. 75, pp. 261–268.
Wiskerchen, M. J., and C. P. Sonett, 1977. A lunar metal core? *Proc. Lunar Sci. Conf. 8th,* pp. 515–535.
Wolfe, E. W., N. G. Bailey, B. K. Lucchitta, W. R. Muehlberger, D. H. Scott, R. L. Sutton, and H. G. Wilshire, 1981. The geologic investigation of the Taurus-Littrow valley: Apollo 17 landing site: USGS Professional Paper 1080, 280 pp.
Wolfe, E. W., B. K. Lucchitta, V. S. Reed, G. E. Ulrich, and A. G. Sanchez, 1975. Geology of the Taurus-Littrow valley floor: *Proc. Lunar Sci. Conf. 6th,* pp. 2463–2482.
Wood, C. A., and J. W. Head, 1976. Comparison of impact basins on Mercury, Mars and the Moon: *Proc. Lunar Sci. Conf. 7th,* pp. 3629–3651.
Wood, J. A., 1972. Fragments of terra rock in the Apollo 12 soil samples and a structural model of the Moon: *Icarus,* v. 16, pp. 462–501.
———, 1975a. The Moon: *Sci. Amer.,* v. 233, pp. 92–102.
———, 1975b. Lunar petrogenesis in a well-stirred magma ocean: *Proc. Lunar Sci. Conf. 6th,* pp. 1087–1102.
———, 1975c. The nature and origin of boulder 1, station 2, Apollo 17: *The Moon,* v. 14, pp. 505–517.
———, 1977. A survey of lunar rock types and comparison of the crusts of Earth and Moon, in *Soviet-American Conference on Cosmochemistry of the Moon and Planets: NASA SP-370,* pp. 35–53.
———, 1979. *The Solar System:* Englewood Cliffs, N.J., Prentice Hall, 196 pp.
Wood, J. A., J. S. Dickey, Jr., U. B. Marvin, and B. N. Powell, 1970. Lunar anorthosites and a geophysical model of the moon: *Proc. Lunar Sci. Conf. 1st,* pp. 965–988.
Young, R. A., 1975. Mare crater size-frequency distributions: Implications for relative surface ages and regolith development: *Proc. Lunar Sci. Conf. 6th,* pp. 2645–2662.
———, 1977. The lunar impact flux, radiometric age correlation, and dating of specific lunar features: *Proc. Lunar Sci. Conf. 8th,* pp. 3457–3473.
Zisk, S. H., C. A. Hodges, H. J. Moore, R. W. Shorthill, T. W. Thompson, and D. E. Wilhelms, 1977. The Aristarchus-Harbinger region of the Moon: Surface geology and history from recent remote-sensing observations: *The Moon,* v. 17, pp. 59-99.
Zisk, S. H., G. H. Pettengill, and G. W. Catuna, 1974. High-resolution radar maps of the lunar surface at 3.8 cm wavelength: *The Moon,* v. 10, pp. 17–50.

CHAPTER 7

Adams, J. B., and T. B. McCord, 1969. Mars: interpretation of spectral reflectivity of light and dark regions: *J. Geophys. Res.,* v. 74, pp. 4851–4856.
Allegre, C. J., V. E. Courtillot, and M. Matteur, 1974. Evidence for lateral movements of the martian crust [abs.]: *EOS,* Transactions American Geophysical Union, v. 55, p. 341.
Allen, C. C., 1979a. Areal distribution of martian rampart craters: *Icarus,* v. 39, pp. 111–123.
———, 1979b. Volcano-ice interactions on Mars: *J. Geophys. Res.,* v. 84, pp. 8048–8059.
Arvidson, R. E., 1979. A post-Viking view of martian geologic evolution: *NASA Tech. Memo. 80339,* pp. 80–81.
Arvidson, R. E., A. Carusi, A. Coradini, M. Coradini, M. Fulchignoni, C. Federico, R. Funicello, and M. Salomone, 1976. Latitudinal variation of wind erosion of crater ejecta deposits on Mars: *Icarus,* v. 27, pp. 503–516.
Arvidson, R. E., K. A. Goettel, and C. M. Hohenberg, 1980. A post-Viking view of the geologic evolution of Mars: *Res. Geophys. Space Phys.,* v. 18, pp. 565–603.
Arvidson, R. E., E. A. Guiness, and S. W. Lee, 1979. Differential aeolian distribution rates on Mars: *Nature,* v. 278, pp. 533–535.
Bagnold, R. A., 1941. *The physics of blown sand and desert dunes:* Methuen and Co., London, 265 pp.
Baker, V. R., 1973. Paleohydrology and sedimentology of Lake Missoula flooding of eastern Washington: *Geol. Soc. America Sp. Paper 144,* 79 pp.

———, 1977. Viking-slashing at the Martian Scabland problem: *NASA Tech. Memo. TM-X-3511,* pp. 169–172.

Baker, V. R., and R. C. Kochel, 1978. Morphometry of streamlined forms in terrestrial and martian channels: *Proc. Lunar Sci. Conf. 9th,* pp. 3193–3203.

Baker, V. R., and D. J. Milton, 1974. Erosion by catastrophic floods on Mars and Earth: *Icarus,* v. 23, pp. 27–41.

Baldwin, R. B., 1963. *The measure of the Moon:* Univ. of Chicago Press, Chicago, IL 488 pp.

Banin, A., J. Rishpon, and L. Margulies, 1981. Composition and properties of the Martian soil as inferred from Viking biology data and simulation experiments with smectite clays: *Proc. 3rd Internat. Colloq. on Mars,* Pasadena, CA, Lunar and Planet. Inst., Houston, TX, pp. 16–18.

Biemann, K., J. Oro, P. Toulmin, L. E. Orgel, A. O. Nier, D. M. Anderson, P. G. Simmonds, D. Flory, A. V. Diaz, D. R. Rushnak, J. E. Biller, and A. L. Lafleur, 1977. The search for organic substances and inorganic volatile compounds in the surface of Mars: *J. Geophys. Res.,* v. 82, pp. 4641–4662.

Bills, B. G., and A. J. Ferrari, 1978. Mars topography and geophysical implications: *J. Geophys. Res.,* v. 83, pp. 3497–3508.

Binder, A. B., R. E. Arvidson, E. A. Guiness, K. L. Jones, E. C. Morris, T. A. Mutch, D. C. Pieri, and C. Sagan, 1977. The geology of the Viking Lander 1 site: *J. Geophys. Res.,* v. 82, pp. 4439–4451.

Binder, A. B., and J. C. Jones, 1972. Spectrophotometric studies of the photometric function, composition and distribution of the surface materials of Mars: *J. Geophys. Res.,* v. 77, pp. 3005–3019.

Blasius, K. R., 1976. *Topical studies of the geology of the Tharsis region of Mars:* Calif. Inst. Tech., Ph.D. Thesis, 85 pp.

———, 1979. Topography of six martian volcanoes from high altitude systematic stereo imaging of Viking Orbier 1 [abs.]: *Bull. Amer. Astron. Soc.,* v. 11, p. 573.

Blasius, K. R., and J. A. Cutts, 1976. Shield volcanism and lithospheric structure beneath the Tharsis plateau, Mars: *Proc. Lunar Sci. Conf. 7th,* pp. 3561–3573.

Blasius, K. R., J. A. Cutts, J. E. Guest, and H. Masursky, 1977. Geology of Valles Marineris: First analysis of imaging from the Viking Orbiter primary mission: *J. Geophys. Res.,* v. 82, pp. 4067–4091.

Boyce, J. M., 1979. A method for measuring heat flow in the martian crust using impact crater morphology: *NASA Tech. Memo. 80339,* pp. 114–118.

Boyce, P. B., and D. T. Thompson, 1972. A new look at the martian "violet haze" problem. I. Syrtis Major-Arabia 1969: *Icarus,* v. 16, pp. 291–303.

Breed, C. S., M. J. Grolier, and J. F. McCauley, 1979. Morphology and distribution of common "sand" dunes on Mars: Comparison with the Earth: *J. Geophys. Res.,* v. 84, pp. 8183–8204.

Bretz, J. H., 1923. The channeled scablands of the Columbia plateau: *J. Geology,* v. 31, pp. 617–649.

———, 1969. The Lake Missoula floods and the channeled scablands: *J. Geology,* v. 17, pp. 505–543.

Briggs, G. A., W. A. Baum, and J. Barnes, 1979. Viking orbiter observations of dust in the martian atmosphere: *J. Geophys. Res.,* v. 84, pp. 2795–2820.

Bullen, K. E., 1975. *The Earth's density:* Wiley, New York, 420 pp.

Capen, C. F., 1976. Martian albedo feature variations with season: Data of 1971 and 1973: *Icarus,* v. 28, pp. 213–230.

Carr, M. H., 1973. Volcanism on Mars: *J. Geophys. Res.,* v. 78, pp. 4049–4062.

———, 1974a. Tectonism and volcanism of the Tharsis region of Mars: *J. Geophys. Res.,* v. 79, pp. 3943–3949.

———, 1974b. The role of lava erosion in the formation of lunar rilles and martian channels: *Icarus,* v. 22, pp. 1–23.

———, 1976. Changes in height of martian volcanoes with time: *Geologica Romana,* v. 15, pp. 421–422.

———, 1979. Formation of martian flood features by release of water from confined aquifers: *J. Geophys. Res.,* v. 84, pp. 2995–3007.

———, 1980. The morphology of the martian surface: *Space Sci. Rev.,* v. 25, pp. 231–284.

———, 1981. *The Surface of Mars:* Yale University Press, New Haven, Conn., 232 pp.

Carr, M. H., K. R. Blasius, R. Greeley, J. E. Guest, and J. E. Murray, 1977a. Observations on some martian volcanic features as viewed from the Viking Orbiters: *J. Geophys. Res.,* v. 82, pp. 3985–4015.

Carr, M. H., and G. D. Clow, 1981. Martian channels and valleys: their characteristics, distribution and age: *Icarus,* v. 48, pp. 91–117.

Carr, M. H., L. S. Crumpler, J. A. Cutts, R. Greeley, J. E. Guest, and H. Masursky, 1977b. Martian impact craters and emplacement of ejecta by surface flow: *J. Geophys. Res.,* v. 82, pp. 4055–4065.

Carr, M. H., H. Masursky, W. A. Baum, K. R. Blasius, G. A. Briggs, J. A. Cutts, T. Duxbury, R. Greeley, J. E. Guest, B. A. Smith, L. A. Soderblom, J. Veverka, and J. B. Wellman, 1976. Preliminary results from the Viking Orbiter imaging experiment: *Science,* v. 193, pp. 766–776.

Carr, M. H., H. Masursky, and R. S. Saunders, 1973. A generalized geologic map of Mars: *J. Geophys. Res.,* v. 78, pp. 4031–4036.

Carr, M. H., and G. G. Schaber, 1977. Martian permafrost features: *J. Geophys. Res.,* v. 82, pp. 4039–4065.

Chapman, C. R., and K. L. Jones, 1977. Cratering and obliteration history of Mars: *Ann. Rev. Earth Planet. Sci.,* v. 5, pp. 515–540.

Christensen, E. J., 1975. Martian topography derived from occultation radar, spectral and optical measurements: *J. Geophys. Res.,* v. 80, pp. 2909–2913.

Clark, B. C., 1978. Implications of abundant hygroscopic minerals in the Martian regolith: *Icarus,* v. 34, pp. 645–665.

Clifford, S. M., 1981. A model for the climatic behavior of water on Mars: *Proc. 3rd Int. Colloq. on Mars,* Pasadena. Lunar Planet. Inst. Contrib. 441, Houston, Tex.

Collins, S. A., 1971. *The Mariner 6 and 7 pictures of Mars: NASA SP-263,* 159 pp.

Courtillot, V. C., C. J. Allegre, and M. Matteur, 1975. On the existence of lateral relative motions on Mars: *Earth and Planet. Sci. Lett.,* v. 25, pp. 279–285.

Crumpler, L. S., and J. C. Aubele, 1978. Structural evolution of Arsia Mons, Pavonis Mons and Ascraeus Mons, Tharsis region of Mars: *Icarus,* v. 34, pp. 496–511.

Cutts, J. A., 1973. Nature and origin of layered deposits of the martian polar regions: *J. Geophys. Res.,* v. 78, pp. 4231–4249.

Cutts, J. A., and K. R. Blasius, 1981. Origin of martian outflow channels: the eolian hypothesis: *J. Geophys. Res.,* v. 86, pp.

5075-5102.

Cutts, J. A., K. R. Blasius, G. A. Briggs, M. H. Carr, R. Greeley, and H. Masursky, 1976. North polar regions of Mars: Imaging results from Viking 2: *Science,* v. 194, pp. 1329-1337.

Cutts, J. A., K. R. Blasius, and W. J. Roberts, 1979. Evolution of martian polar landscape: interplay of long term variation in perennial ice caps and dust storm activity: *J. Geophys. Res.,* v. 84, pp. 2975-2994.

Dial, A. L., 1978. The Viking 1 landing site crater diameter-frequency distribution: *NASA Tech. Memo. 79729,* pp. 179-181.

Downs, G. S., P. E. Reichley, and R. R. Green, 1975. Radar measurements of Martian topography and surface properties: The 1971 and 1973 oppositions: *Icarus,* v. 26, pp. 273-312.

Dzurisin, D., and K. R. Blasius, 1975. Topography of the polar layered deposits of Mars: *J. Geophys. Res.,* v. 82, pp. 4225-4248.

Eaton, J. R., and K. J. Murata, 1960. How volcanoes grow: *Science,* v. 132, pp. 925-938.

Elsasser, W. M., 1963. Early history of the Earth: in *Earth Science and Meteoritics,* North Holland Publ., Amsterdam, pp. 1-30.

Fanale, F. P., 1976. Martian volatiles: their degassing history and geochemical fate: *Icarus,* v. 28, pp. 179-202.

Fanale, F. P., and W. A. Cannon, 1974. Exchange of adsorbed H_2O and CO_2 between regolith and atmosphere of Mars caused by changes in surface insolation: *J. Geophys. Res.,* v. 79, pp. 3397-3402.

———, 1979. Mars: CO_2 adsorption and capillary condensation on clays—significance for volatile storage at atmosphere history: *J. Geophys. Res.,* v. 84, pp. 8404-8414.

Farmer, C. B., D. W. Davies, and D. D. LaPorte, 1976. Mars: Northern summer ice cap—water vapor observations from Viking 2: *Science,* v. 194, pp. 1339-1341.

Farmer, C. B., and P. E. Doms, 1979. Global seasonal variation of water vapor on Mars and the implications for permafrost: *J. Geophys. Res.,* v. 84, pp. 2881-2888.

Fischbacher, G. E., L. J. Martin, and W. A. Baum, 1969. Martian polar cap boundaries: Final rept., JPL Contract 951547, Lowell Observatory, Flagstaff, AZ.

Focas, J. H., 1961. Etude photometrique et polarimetrique des phenomenes saisonniers de la planete Mars: *Ann. d'Astrophys.,* v. 24, pp. 309-324.

Frey, H. 1979. Thaumasia: a fossilized early-forming Tharsis uplift: *J. Geophys. Res.,* v. 84, pp. 1009-1023.

Gapcynski, J. P., R. H. Tolson, and W. H. Michael, 1977. Mars gravity field: combined Viking and Mariner 9 results: *J. Geophys. Res.,* v. 82, pp. 4325-4327.

Gault, D. E., and B. S. Baldwin, 1970. Impact cratering on Mars—some effects of the atmosphere: *EOS,* Transactions American Geophysical Union, v. 51, p. 342.

Gault, D. E., and R. Greeley, 1978. Exploratory experiments of impact craters formed in viscous-liquid targets: Analogs for martian rampart craters? *Icarus,* v. 34, pp. 486-495.

Gierasch, P. J., and O. B. Toon, 1973. Atmospheric pressure variation and the climate of Mars: *J. Atmos. Res.,* v. 30, pp. 1502-1508.

Greeley, R., R. Leach, R. White, J. Iverson, and J. Pollack, 1980. Threshold wind speeds for sands on Mars: wind tunnel simulations: *Geophys. Res. Lett.,* v. 7, pp. 121-124.

Greeley, R., R. Papson, and J. Veverka, 1978. Crater streaks in the Chryse Planitia region of Mars: Early Viking results: *Icarus,* v. 34, pp. 556-567.

Greeley, R., and P. Spudis, 1978. Volcanism in the cratered terrain hemisphere of Mars: *Geophys. Res. Lett.,* v. 5, pp. 453-455.

Greeley, R., E. Theilig, J. E. Guest, M. H. Carr, H. Masursky, and J. A. Cutts, 1977. Geology of Chryse Planitia: *J. Geophys. Res.,* v. 82, pp. 4093-4109.

Gregory, T., 1979. A Martian global plains system represented by Lunae Planum surface units: *NASA Tech. Memo. 80339,* pp. 75-77.

Guest, J. E., P. S. Butterworth, and R. Greeley, 1977. Geological observations in the Cydonia region of Mars from Viking: *J. Geophys. Res.,* v. 82, pp. 4111-4120.

Hanel, R. A., B. J. Conrath, W. A. Hovis, P. D. Lowman, J. C. Pearl, C. Prabhakara, and B. Schlachman, 1972. Infrared spectroscopy experiment of the Mariner 9 missions: Preliminary results: *Science,* v. 175, pp. 305-308.

Harris, S. A., 1977. The aureole of Olympus Mons, Mars: *J. Geophys. Res.,* v. 82, pp. 3099-3107.

Hartmann, W. K., 1973. Martian cratering. 4. Mariner 9 initial analysis of cratering chronology: *J. Geophys. Res.,* v. 78, pp. 4096-4116.

———, 1974. Geological observations of martian arroyos: *J. Geophys. Res.,* v. 79, pp. 3951-3957.

———, 1977. Cratering in the solar system. *Sci. American,* v. 236, pp. 84-99.

Hartmann, W. K., et al. (12 authors), 1981. Chronology of planetary volcanism by comparative studies of planetary cratering: in *Basaltic Volcanism on the Terrestrial Planets,* Pergamon Press, New York.

Heim, A., 1932. *Bergsturz und Menschenleben:* Fretz and Wasmuth, Zurich, 218 pp.

Hess, S. L., R. M. Henry, C. B. Leovy, J. A. Ryan, and J. E. Tillman, 1977. Meteorological results from the surface of Mars: Viking 1 and 2: *J. Geophys. Res.,* v. 82, pp. 4559-4574.

Hess, S. L., R. M. Henry, and J. E. Tillman, 1979. The seasonal variation of atmospheric pressure on Mars as affected by the south polar cap: *J. Geophys. Res.,* v. 84, pp. 2923-2927.

Hodges, C. A., 1979. Some lesser volcanic provinces on Mars: *NASA Tech. Memo. 80339,* pp. 248-249.

Hodges, C. A., and H. J. Moore, 1979. The subglacial birth of Olympus Mons and its aureoles: *J. Geophys. Res.,* v. 84, pp. 8061-8074.

Hord, C. W., K. E. Simmons, and L. K. McLaughlin, 1974. Mariner 9 ultraviolet spectrometer experiment: Pressure altitude measurements on Mars: *Icarus,* v. 21, pp. 292-302.

Houck, J. R., J. B. Pollack, C. Sagan, D. Schaak, and J. A. Decker, 1973. High altitude infrared spectroscopic evidence for bound water on Mars: *Icarus,* v. 18, pp. 470-480.

Howard, A. D., 1978. Origin of the stepped topography of the martian poles: *Icarus,* v. 34, pp. 581-599.

Howard, K. A., and W. R. Muehlberger, 1973. Lunar thrust faults in the Taurus-Littrow region: *Apollo 17 Prelim. Sci. Rept., NASA SP-330,* pp. 31-22 to 31-25.

Huck, F. O., D. J. Jobson, S. K. Park, S. D. Wall, R. E. Arvidson, W. R. Patterson, and W. D. Benton, 1977. Spectrophotometric and color estimates of the Viking Lander sites: *J. Geophys. Res.,* v. 82, pp. 4401-4411.

Huguenin, R. L., J. B. Adams, and T. B. McCord, 1978. Mars: surface mineralogy from reflectance spectra [abs.]: *Lunar Science VIII,* pp. 478-480, Lunar Planetary Sci. Inst., Houston, TX.

Hulme, G., 1974. The interpretation of lava flow morphology: *Geophys. J. Roy. Astron. Soc.,* v. 39, pp. 361-383.

Hunt, G. R., L. M. Logan, and J. W. Salisbury, 1973. Mars:

components of infrared spectra and the composition of the dust cloud: *Icarus,* v. 18, pp. 459-469.

Inge, J. L., 1974. *Mars—1973* (albedo map, 1:25,000,000): Lowell Observatory, Flagstaff, AZ.

———, 1976. *Mars—1975-1976* (albedo map, 1:25,000,000): Lowell Observatory, Flagstaff, AZ.

———, 1978. *Mars—1978* (albedo map, 1:35,000,000): Lowell Observatory, Flagstaff, AZ.

Inge, J. L., C. F. Capen, L. J. Martin, and B. Q. Faure, 1971a. Mars—1969, A new map of Mars from planetary patrol photographs: *Sky and Telescope,* v. 41, pp. 336-339.

Inge, J. L., C. F. Capen, L. J. Martin, and D. T. Thompson, 1971b. Mars—1971 (albedo map, 1:25,000,000): Lowell Observatory, Flagstaff, AZ.

Jones, K. L., 1974. Evidence for an episode of martian crater obliteration intermediate in martian history: *J. Geophys. Res.,* v. 79, pp. 3917-3932.

Jones, K. L., S. L. Bragg, S. D. Wall, C. E. Carlson, and D. G. Pidek, 1979. One Mars year: Viking Lander imaging observations: *Science,* v. 204, pp. 799-806.

Jordan, J. F., and J. Lorell, 1975. Mariner 9: An instrument of dynamical science: *Icarus,* v. 25, pp. 146-165.

Kent, P. E., 1966. The transport mechanism in catastrophic rockfalls: *J. Geology,* v. 74, pp. 79-83.

Kieffer, H. H., S. C. Chase, T. Z. Martin, E. D. Miner, and F. D. Palluconi, 1976. Martian north pole summer temperature. Dirty water ice. *Science,* v. 194, pp. 1341-1344.

Kieffer, H. H., T. Z. Martin, A. R. Peterfreund, and B. M. Jakosky, 1977. Thermal and albedo mapping of Mars during the Viking primary mission: *J. Geophys. Res.,* v. 82, pp. 4249-4291.

Kieffer, H. H., and F. D. Palluconi, 1979. The climate of the martian polar caps: *NASA Conf. Publ. 2072,* pp. 45-46.

King, J. S., and J. R. Riehle, 1974. A proposed origin of the Olympus Mons escarpment: *Icarus,* v. 23, pp. 300-317.

Kliore, A., D. L. Cain, G. S. Levy, V. R. Eshleman, G. Fjeldbo, and F. D. Drake, 1965. Occultation Experiment: results of the first direct measurements of Mars' atmosphere and ionosphere: *Science,* v. 149, pp. 1243-1248.

Kliore, A. J., G. Fjeldbo, B. L. Seidel, M. J. Sykes, and P. M. Woiceshyn, 1973. S-band radio occultation measurements of the atmosphere and topography of Mars with Mariner 9: Extended mission coverage of polar and intermediate latitudes: *J. Geophys. Res.,* v. 78, pp. 4331-4351.

Krinsley, D. H., 1979. Simulated martian aeolian abrasion and the creation of aggregates: *NASA Tech. Memo. 80339,* pp. 313-315.

Lachenbruch, A. H., 1962. Mechanics of thermal contraction cracks and ice wedge polygons in permafrost. *Geo. Soc. America Spec. Paper 70,* 69 pp.

Leighton, R. B., N. H. Horowitz, B. C. Murray, R. P. Sharp, A. G. Herriman, A. T. Young, B. A. Smith, M. E. Davies, and C. G. Leovy, 1969. Mariner 6 and 7 television pictures: Preliminary analysis: *Science,* v. 166, pp. 49-67.

Leighton, R. B., and B. C. Murray, 1966. Behavior of carbon dioxide and other volatiles on Mars: *Science,* v. 153, p. 136.

Leovy, C. B., and Y. Mintz, 1969. Numerical simulation of the weather and climate of Mars: *J. Atmos. Sci.,* v. 26, pp. 1167-1190.

Leovy, C. B., and R. W. Zuruk, 1979. Thermal tides and martian dust storms direct evidence for coupling: *J. Geophys. Res.,* v. 84, pp. 2956-2968.

Lingenfelter, R. E., S. J. Peale, and G. Schubert, 1968. Lunar rivers: *Science,* v. 161, pp. 366-369.

Logan, L. M., G. R. Hunt, and J. J. Salisbury, 1975. The use of mid infrared spectroscopy in remote sensing of space targets: in *Infrared and Raman Spectra of Lunar and Terrestrial Minerals* (C. Karr, ed.), Academic Press, New York.

Lopes, R. M., J. E. Guest, and C. J. Wilson, 1980. Origin of the Olympus Mons aureole and perimeter scarp: *The Moon and the Planets,* v. 22, pp. 221-234.

Lorrell, J., G. H. Born, E. J. Christensen, J. F. Jordan, P. A. Laing, W. L. Martin, W. L. Sjogren, I. I. Shapiro, R. D. Reasonberg, and G. L. Slater, 1972. Mariner 9 celestial mechanics experiment: Gravity field and pole direction of Mars: *Science,* v. 175, pp. 317-320.

Lucchitta, B. K., 1977. Topography, structure and mare ridges in southern Mare Imbrium and northern Oceanus Procellarum: *Proc. Lunar Sci. Conf. 8th,* pp. 2691-2703.

———, 1978a. A large landslide on Mars: *Bull. Geol. Soc. America,* v. 89, pp. 1601-1609.

———, 1978b. Morphology of Chasma walls, Mars: *J. Research,* U.S. Geological Survey, v. 6, pp. 651-662.

———, 1980. Martian outflow channels sculpted by glaciers: *Lunar and Planetary Science XI,* Lunar and Planet. Sci. Inst., Houston, TX, pp. 634-636.

Malin, M. C., 1976. *Nature and origin of intercrater plains on Mars: in* Unpublished Ph.D. Thesis, Calif. Inst. Tech., Pasadena, CA, 176 pp.

———, 1977. Comparison of volcanic features: Elysium (Mars) and Tibetsi (Earth): *Bull. Geol. Soc. America,* v. 84, pp. 908-919.

Martin, L. J., 1981. Possible volcanic activity on Mars during the Viking mission: *Proc. 3rd Internat. Colloq. on Mars,* Pasadena, CA, Lunar and Planet. Inst., Houston, TX, pp. 145-147.

Masson, P., 1977. Structural pattern analysis of the Noctis Labyrinthus-Valles Marineris regions of Mars: *Icarus,* v. 30, pp. 49-62.

Masursky, H., 1973. An overview of geologic results from Mariner 9: *J. Geophys. Res.,* v. 78, pp. 4037-4047.

Masursky, H., J. M. Boyce, A. L. Dial, G. G. Schaber, and M. E. Strobell, 1977. Formation of martian channels: *J. Geophys. Res.,* v. 82, pp. 4016-4038.

McCauley, J. F., 1973. Mariner 9 evidence for wind erosion in the equatorial and mid-latitude regions of Mars: *J. Geophys. Res.,* v. 78, pp. 4123-4137.

———, 1978. Geologic map of the Coprates quadrangle of Mars: U.S. Geological Survey, Misc. Inv. Map I-897.

McCauley, J. F., M. H. Carr, J. A. Cutts, W. K. Hartmann, H. Masursky, D. J. Milton, R. P. Sharp, and D. E. Wilhelms, 1972. Preliminary Mariner 9 report on the geology of Mars: *Icarus,* v. 17, pp. 289-327.

McCord, T. B., R. L. Huguenin, and G. L. Johnson, 1977. Photometric imaging of Mars during the 1973 opposition: *Icarus,* v. 31, pp. 293-314.

McCord, T. B., and J. A. Westphal, 1971. Mars: narrow band photometry from 0.3 to 2.5 microns of surface regions during the 1969 apparition: *Astrophys. J.,* v. 168, pp. 141-153.

McElroy, M. B., T. Y. Kong, and Y. L. Yung, 1977. Photochemistry and evolution of Mars' atmosphere: A Viking perspective: *J. Geophys. Res.,* v. 82, pp. 4379-4388.

McGill, G. E., 1978. Geologic map of the Thaumasia Quadrangle of Mars: U.S. Geological Survey Sp. Inv. Map I-1077.

Milton, D. J., 1973. Water and processes of degradation in the Martian landscape: *J. Geophys. Res.*, v. 78, pp. 4037–4047.

Moore, H. J., D. W. G. Arthur, and G. G. Schaber, 1978. Yield strengths of flows on the Earth, Mars and Moon: *Proc. Lunar Planet. Sci. Conf. 9th,* pp. 3351–3378.

Morris, E. C., 1982. Aureole deposits of the martian volcano Olympus Mons: *J. Geophys. Res.*, v. 87, pp. 1164–1178.

Murray, B. C., and M. C. Malin, 1973. Polar wandering on Mars: *Science,* v. 179, pp. 997–1000.

Murray, B. C., L. A. Soderblom, J. A. Cutts, R. P. Sharp, D. J. Milton, and R. B. Leighton, 1972. Geologic framework of the south polar region of Mars: *Icarus,* v. 17, pp. 328–345.

Murray, B. C., L. A. Soderblom, R. P. Sharp, and J. A. Cutts, 1971. The surface of Mars: I. Cratered terrains: *J. Geophys. Res.*, v. 76, pp. 313–330.

Murray, B. C., W. R. Ward, and S. C. Young, 1973. Periodic insolation variations on Mars: *Science,* v. 180, pp. 638–640.

Mutch, T. A., R. E. Arvidson, A. B. Binder, E. A. Guiness, and E. C. Morris, 1977. The geology of the Viking Lander 2 site: *J. Geophys. Res.*, v. 82, pp. 4452–4467.

Mutch, T. A., R. E. Arvidson, J. W. Head, K. L. Jones, and R. S. Saunders, 1976. *The geology of Mars:* Princeton Univ. Press, Princeton, N.J.

Mutch, T. A., and R. S. Saunders, 1976. The geologic development of Mars: a review: *Space Sci. Rev.*, v. 19, pp. 3–57.

Neukum, G., and K. Hiller, 1981. Martian ages: *J. Geophys. Res.*, v. 86, pp. 3097–3132.

Neukum, G., and D. U. Wise, 1976. Mars: A standard crater curve and possible new time scale: *Science,* v. 194, pp. 1381–1387.

Nummedal, D., 1976. Fluvial erosion on Mars: *Proc. Colloquium on Water in Planetary Regoliths,* Hanover, N.H., pp. 47–54.

Nummedal, D., and D. B. Prior, 1981. Generation of martian chaos and channels by debris flows: *Icarus,* v. 45, pp. 77–86.

Oberbeck, V. R., 1975. The role of ballistic erosion and sedimentation in lunar stratigraphy: *Rev. Geophys. and Space Phys.*, v. 13, pp. 337–362.

Okal, F. A., and D. L. Anderson, 1978. Theoretical models for Mars and their seismic properties: *Icarus,* v. 33, pp. 514–528.

Opik, E. J., 1966. The martian surface: *Science,* v. 153, pp. 255–265.

Owen, T., K. Biemann, D. R. Rushneck, J. E. Biller, D. W. Howarth, and A. L. Lafleur, 1977. The composition of the atmosphere at the surface of Mars: *J. Geophys. Res.*, v. 81, pp. 4635–4639.

Pechmann, J. C., 1980. The origin of polygonal troughs on the northern plains of Mars: *Icarus,* v. 42, pp. 185–210.

Peterson, J. E., 1978. Volcanism in the Noachis-Hellas region of Mars, 2: *Proc. Lunar Planet. Sci. Conf. 9th,* pp. 3411–3432.

Phillips, R. J., 1978. Report on the Tharsis Workshop: *NASA Tech. Memo. 79719,* pp. 334–336.

Phillips, R. J., and E. R. Ivins, 1979. Geophysical observations pertaining to solid state convection in the terrestrial planets. *Phys. Earth Planet. Interiors,* v. 19, pp. 107–148.

Phillips, R. J., and K. Lambeck, 1980. Gravity fields of the terrestrial planets: Long wavelength anomalies and tectonics: *Rev. Geophys. and Space Phys.*, v. 18, pp. 27–76.

Phillips, R. J., and R. S. Saunders, 1975. The isostatic state of martian topography: *J. Geophys. Res.*, v. 80, pp. 2893–2897.

Phillips, R. J., R. S. Saunders, and J. E. Conel, 1973. Mars: Crustal structure inferred from Bouguer gravity anomalies: *J. Geophys. Res.*, v. 78, pp. 4815–4820.

Pieri, D. C., 1976. Martian channels: Distribution of small channels on the Martian surface: *Icarus,* v. 27, pp. 25–50.

———, 1979, *Geomorphology of martian valleys:* Ph.D. Thesis, Cornell University, Ithaca, N.Y., 288 pp.

Pike, F. J., 1979. Simple to complex craters: the transition on Mars: *NASA Tech. Memo. 80339,* pp. 132–134.

Plafker, G., and G. E. Erickson, 1978. Mechanism of catastrophic avalanches from Nevados Huascaran, Peru: in *Rock Slides and Avalanches,* Elsevier, Amsterdam.

Plescia, J. B., and R. S. Saunders, 1979. The chronology of martian volcanoes: *Proc. Lunar Planet. Sci. Conf. 10th,* pp. 2841–2859.

———, 1982. Tectonic history of the Tharsis region, Mars: *J. Geophys. Res.*, v. 87, pp. 9775–9791.

Pollack, J. B., 1979. Climate change on the terrestrial planets: *Icarus*, v. 37, pp. 479–553.

Pollack, J. B., and D. C. Black, 1979. Implications of the gas compositional measurements of Pioneer Venus for the origin of planetary atmospheres: *Science,* v. 205, pp. 56–59.

Pollack, J. B., D. S. Colburn, M. Flaser, R. Kahn, C. E. Carlston, and D. Pidek, 1979. Properties and effects of dust particles suspended in the Martian atmosphere: *J. Geophys. Res.*, v. 84, pp. 2929–2945.

Pollack, J. B., C. B. Leovy, Y. H. Mintz, and W. Van Camp, 1976. Winds on Mars during the Viking season: Predictions based on a general circulation model with topography: *Geophys. Res. Lett.*, v. 3, pp. 479–482.

Reimers, C. E., and P. D. Komar, 1979. Evidence for explosive volcanic density currents on certain martian volcanoes: *Icarus,* v. 39, pp. 88–110.

Ringwood, A. E., 1966. Chemical evolution of the terrestrial planets: *Geochim. et Cosmochim. Acta,* v. 30, pp. 41–104.

Roth, L. E., G. S. Downs, and R. S. Saunders, 1980. Radar altimetry of south Tharsis, Mars: *Icarus,* v. 42, pp. 287–316.

Ryan, J. A., and R. M. Henry, 1979. Mars atmospheric phenomena during major dust storms as measured at the surface: *J. Geophys. Res.*, v. 84, pp. 2821–2829.

Sagan, C., 1973. Sandstorms and eolian erosion on Mars: *J. Geophys. Res.*, v. 78, pp. 4155–4161.

Sagan, C., D. Pieri, P. Fox, R. E. Arvidson, E. A. Guiness, 1977. Particle motion on Mars inferred from Viking Lander cameras: *J. Geophys. Res.*, v. 78, pp. 4155–4161.

Sagan, C., J. Veverka, P. Fox, R. Dubisch, R. French, P. Gierasch, L. Quam, J. Lederberg, E. Levinthal, R. Tucker, B. Eross, and J. B. Pollack, 1973. Variable features on Mars 2. Mariner 9 global results: *J. Geophys. Res.*, v. 78, pp. 4163–4196.

Sagan, C., J. Veverka, P. Fox, R. Dubisch, J. Lederberg, E. Levinthal, L. Quam, R. Tucker, J. B. Pollack, and B. A. Smith, 1972. Variable features on Mars: Preliminary Mariner 9 results: *Icarus,* v. 17, pp. 346–372.

Schaber, G. G., K. C. Horstmann, and A. L. Dial, 1978. Lava flow materials in the Tharsis region of Mars: *Proc. Lunar Planet. Sci. Conf. 9th,* pp. 3433–3458.

Schonfeld, E., 1977. Martian volcanism: *Lunar Sci. Conf. XVIII,* Pt. II, pp. 843–845, Lunar and Planet. Sci. Inst., Houston, TX.

Schultz, P. H., and D. E. Gault, 1981. Ejecta emplacement and atmospheric pressure: Laboratory experiments: *Proc. 3rd Internat. Colloq. on Mars,* Pasadena, CA, Lunar and Planet. Inst., Houston, TX, pp. 226–228.

Schultz, P. H., and A. B. Lutz-Garihan, 1981. Ancient polar locations on Mars: Evidence and implications: *Proc. 3rd Internat. Colloq. on Mars,* Pasadena, CA, Lunar and Planet. Inst., Houston, TX, pp. 229–231.

Schumm, S. A., 1974. Structural origin of large martian channels: *Icarus,* v. 22, pp. 371–384.

Scott, D. H., and M. H. Carr, 1978. Geologic map of Mars: U.S. Geological Survey, Misc. Inv. Map I-1083.

Seiff, A., and D. B. Kirk, 1977. Structure of the atmosphere of Mars in summer at mid-latitudes: *J. Geophys. Res.,* v. 82, pp. 4364–4378.

Sengor, A. M. C., and E. C. Jones, 1975. A new interpretation of martian tectonics with special reference to the Tharsis region [abs.]: *Geol. Soc. America,* Abstracts with Program, v. 7, p. 1264.

Sharp, R. P., 1973a. Mars: Fretted and chaotic terrain: *J. Geophys. Res.,* v. 78, pp. 4073–4083.

———, 1973b. Mars: Troughed terrain: *J. Geophys. Res.,* v. 78, pp. 4063–4072.

———, 1973c. Mars: South polar pits and etched terrain: *J. Geophys. Res.,* v. 78, pp. 4222–4230.

———, 1974. Ice on Mars: *J. Glaciology,* v. 13, pp. 173–185.

Sharp, R. P., and M. C. Malin, 1975. Channels on Mars: *Bull. Geol. Soc. America,* v. 86, pp. 593–609.

Shreve, R. L., 1966. Sherman Landslide, Alaska: *Science,* v. 154, pp. 1639–1643.

Singer, R. B., 1981. Some observational constraints on iron mineralogy in Martian bright soils. *Proc. 3rd Int. Colloq. on Mars,* Pasadena, CA: Lunar Planet. Inst. Contrib. 441, Houston, TX.

Singer, R. B., T. B. McCord, R. N. Clark, J. B. Adams, and R. L. Huguenin, 1979. Mars surface composition from reflectance spectroscopy: A summary: *J. Geophys. Res.,* v. 84, pp. 8415–8426.

Sjogren, W. L., 1979. Mars gravity: high resolution results from Viking Orbiter 2: *Science,* v. 303, pp. 1006–1009.

Sjogren, W. L., J. Lorell, L. Wong, and W. Downs, 1975. Mars gravity field based on a short arc technique: *J. Geophys. Res.,* v. 80, pp. 2899–2908.

Sleep, N. H., and R. J. Phillips, 1979. An isostatic model for the Tharsis province, Mars: *Geophys. Res. Lett.,* v. 6, pp. 803–806.

Smoluchowski, R., 1968. Mars. Retention of Ice: *Science,* v. 159, pp. 1348–1350.

Snyder, C. W., 1979. The extended mission of Viking: *J. Geophys. Res.,* v. 84, pp. 7917–7933.

Soderblom, L. A., C. D. Condit, R. A. West, B. M. Herman, and T. J. Kriedler, 1974. Martian planet-wide crater distributions: Implications for geologic history and surface processes: *Icarus,* v. 22, pp. 239–263.

Soderblom, L. A., K. Edwards, E. M. Eliason, E. M. Sanchez, and M. P. Charette, 1978. Global color variations on the martian surface: *Icarus,* v. 34, pp. 446–464.

Soderblom, L. A., T. J. Kriedler, and H. Masursky, 1973. Latitudinal distribution of a debris mantle on the Martian surface: *J. Geophys. Res.,* v. 78, pp. 4117–4122.

Soderblom, L. A., and D. B. Wenner, 1978. Possible fossil H_2O liquid-ice interfaces in the martian crust: *Icarus,* v. 34, pp. 622–637.

Solomon, S. C., and J. W. Head, 1979. Vertical movement in mare basins: relation to mare emplacement, basin tectonics, and lunar thermal history: *J. Geophys. Res.,* v. 84, pp. 1667–1682.

———, 1982. Evolution of the Tharsis Province of Mars: The importance of heterogeneous lithospheric thickness and volcanic construction: *J. Geophys. Res.,* v. 87, pp. 9755–9774.

Squyres, S. W., 1978. Martian fretted terrain: flow of erosional debris: *Icarus,* v. 34, pp. 600–613.

———, 1979. The evolution of dust deposits in the martian north polar regions: *Icarus,* v. 40, pp. 244–261.

Thomas, P., and J. Veverka, 1979. Seasonal and secular variations of wind streaks on Mars: An analysis of Mariner 9 and Viking data: *J. Geophys. Res.,* v. 84, pp. 8131–8146.

Thompson, D. T., 1972. Brief history of the martian "violet haze" problem: *Rev. Geophys. Space Sci.,* v. 10, pp. 919–933.

———, 1973. Time variations of martian regional contrasts: *Icarus,* v. 20, pp. 42–47.

Thompson, G. A., and D. B. Burke, 1973. Regional geophysics of the Basin and Range Province: *Ann. Rev. Earth and Planet. Sci.,* v. 2, pp. 213–238.

Thurber, C. H., and M. N. Toksöz, 1978. Martian lithosphere thickness from elastic flexure theory: *Geophys. Res. Lett.,* v. 5, pp. 977–980.

Toulmin, P., A. K. Baird, B. C. Clark, K. Keil, H. J. Rose, R. P. Christian, P. H. Evans, and W. C. Kelliher, 1977. Geochemical and mineralogical interpretation of the Viking inorganic chemical results: *J. Geophys. Res.,* v. 82, pp. 4625–4634.

Varnes, D. J., 1958. Landslide types and process: in *Landslides and Engineering Practice* (Eckel, E. H., ed.). National Res. Council, Highway Research Board, Special Rept. 29, pp. 20–47.

Veverka, J., P. Gierasch, and P. Thomas, 1981. Wind streaks on Mars: Meteorological control of occurrences and mode of formation: *Icarus,* v. 45, pp. 154–166.

Walker, G. P. L., 1973. Lengths of lava flows: *Phil. Trans. Roy. Soc.,* London, Ser. A., v. 274, pp. 107–118.

Wallace, D., and C. Sagan, 1979. Evaporation of ice in planetary atmospheres: Ice-covered rivers on Mars: *Icarus,* v. 39, pp. 385–400.

Ward, A. W., 1979. Yardangs on Mars: evidence of recent wind erosion: *J. Geophys. Res.,* v. 84, pp. 8147–8166.

Ward, W. R., 1973. Large scale variations in the obliquity of Mars: *Science,* v. 181, pp. 260–262.

———, 1974. Climatic variations on Mars. 1. Astronomical theory of insolation: *J. Geophys. Res.,* v. 79, pp. 3375–3386.

West, M., 1974. Martian volcanism: additional observations and evidence of pyroclastic activity: *Icarus,* v. 21, pp. 1–11.

Wise, D. U., M. P. Golombek, and G. E. McGill, 1979a. Tharsis province of Mars: Geologic sequence, geometry and a deformation mechanism: *Icarus,* v. 38, pp. 456–472.

———, M. P. Golombek, and G. E. McGill, 1979b. Tectonic evolution of Mars: *J. Geophys. Res.,* v. 84, pp. 7934–7939.

Wood, C. A., and J. W. Head, 1976. Comparison of impact basins on Mercury, Mars and Moon: *Proc. Lunar Sci. Conf. 7th,* pp. 3629–3651.

Wood, C. A., J. W. Head, and M. J. Cintala, 1978. Interior morphology of fresh martian craters: The effects of target characteristics: *Proc. Lunar Planet. Sci. Conf. 9th,* pp. 3691–3709.

Wu, S. S. C., 1978. Mars synthetic topographic mapping: *Icarus,* v. 33, pp. 417–440.

Yung, Y. L., and J. P. Pinto, 1978. Primitive atmosphere and implications for the formation of channels on Mars: *Nature,* v. 273, pp. 730–732.

Page intentionally left blank

INDEX